Vol. 45 No. 4 (2024)

ARCHIVES OF THERMODYNAMICS

ISSN: 1231-0956
ISSN: 2083-6023 (Online)

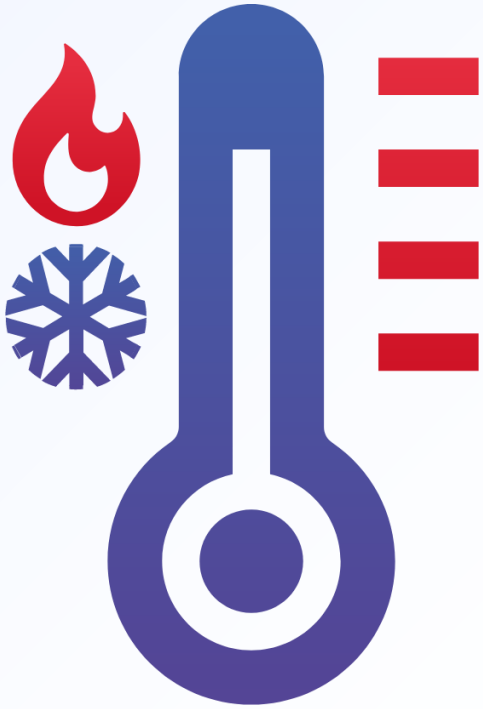

Co-published by

Institute of Fluid Flow Machinery
Polish Academy of Sciences

Committee on Thermodynamics and Combustion
Polish Academy of Sciences

WYDAWNICTWO IMP PAN

Aims and Scope

The aim of the quarterly journal Archives of Thermodynamics (AoT) is to disseminate knowledge between scientists and engineers worldwide and to provide a forum for original research conducted in the field of thermodynamics, heat transfer, fluid flow, combustion and energy conversion in various aspects of thermal sciences, mechanical and power engineering. Besides original research papers, review articles are also welcome.

The journal scope of interest encompasses in particular, but is not limited to:

- Classical and extended non-equilibrium thermodynamics
- Thermodynamic analysis including exergy
- Thermodynamics of heating and cooling
- Thermodynamics of nuclear power generation
- Thermodynamics in defence engineering
- Advances in thermodynamics
- Experimental, theoretical and numerical heat transfer
- Thermal and energy system analysis
- Renewable energy sources including solar energy
- Secondary fuels and fuel conversion
- Heat and momentum transfer in multiphase flows
- Nanofluids
- Energy transition
- Advanced energy carriers
- Energy storage and efficiency
- Energy in buildings
- Hydrogen energy
- Combustion and emissions
- Turbomachinery
- Thermal and energy system analysis
- Integrated energy systems
- Distributed energy generation
- Thermal incineration of wastes
- Waste heat recovery.

Vol. 45 No. 4 (2024)

ARCHIVES OF THERMODYNAMICS

ISSN: 1231-0956
ISSN: 2083-6023 (Online)

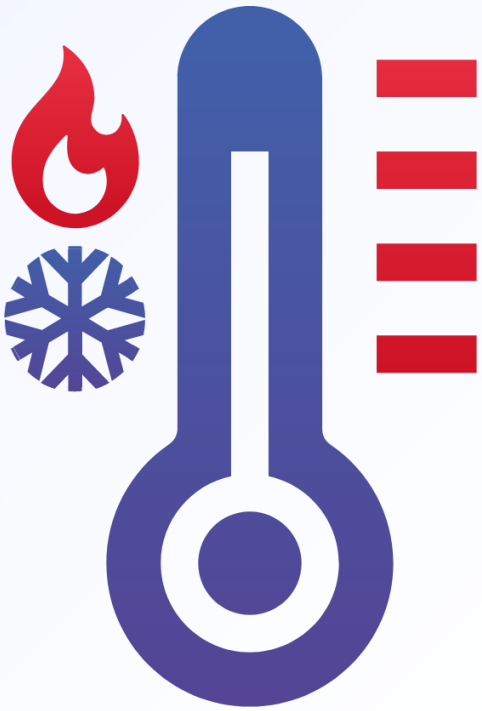

Co-published by

Institute of Fluid Flow Machinery
Polish Academy of Sciences

Committee on Thermodynamics and Combustion
Polish Academy of Sciences

WYDAWNICTWO IMP PAN

Editorial Office
IMP PAN Publishers
Institute of Fluid Flow Machinery, Fiszera 14, 80-231 Gdańsk, Poland,
Phone: (+48) 58-341-12-71 int. 230, e-mail: redakcja(at)imp.gda(.)pl
https://www.imp.gda.pl/archives-of-thermodynamics/
Journals PAS – Electronic Library Polish Academy of Sciences
https://journals.pan.pl/ather

Subscription outside Poland
From 2024, Archives of Thermodynamics appear only in electronic version as an open access journal. However, printed archive volumes or issues are still available. The price of a full volume outside Poland is **120 EUR**. The price of a single issue is **30 EUR**. Archived volumes or issues are available on request. Orders should be sent directly to IMP PAN Publishers:
Institute of Fluid-Flow Machinery,
Fiszera 14, 80-231 Gdansk, Poland,
e-mail: redakcja(at)imp.gda.pl or jfrk(at)imp.gda(.)pl or jrybka(at)imp.gda(.)pl.
Payments should be transferred to the bank account of IMP PAN:
IBAN 28 1130 1121 0006 5498 9520 0011 at Bank Gospodarstwa Krajowego; Code SWIFT: GOSKPLPW.

Prenumerata w Polsce
Od 2024, czasopismo ukazuje się tylko w formie elektronicznej otwartej. Osiągalne są jednak wydania papierowe archiwalne. Cena pojedynczego numeru wynosi **50 PLN**. Cena rocznika **200 PLN**. Zamówienia z określeniem numeru (rocznika), nazwiskiem i adresem odbiorcy należy kierować bezpośrednio do Wydawcy:
Instytut Maszyn Przepływowych PAN
ul. Fiszera 14, 80-231 Gdańsk,
e-mail: redakcja(at)imp.gda(.)pl lub jfrk(at)imp.gda(.)pl lub jrybka(at)imp.gda(.)pl.
Wpłaty prosimy kierować na konto Instytutu Maszyn Przepływowych PAN:
nr 28 1130 1121 0006 5498 9520 0011 w Banku Gospodarstwa Krajowego.

Articles in Archives of Thermodynamics are abstracted and indexed within:
Applied Mechanics Reviews • Arianta • Baidu Scholar • BazTech • Cabell's Directory • Celdes • Chemical Abstracts Service (CAS) – CAplus • CNKI Scholar (China National Knowledge Infrastucture) • CNPIEC • EBSCO (relevant databases) • EBSCO Discovery Service • Elsevier – SCOPUS • ESCI (Emerging Sources Citation Index) • Genamics JournalSeek • Google Scholar • Inspec • Index Copernicus • J-Gate • Journal TOCs • Naviga (Softweco) • Paperbase • Pirabase • POL-index • Polymer Library •Primo Central (ExLibris) • ProQuest (relevant databases) • ReadCube • Referativnyi Zhurnal (VINITI) • SCImago (SJR) • Summon (Serials Solutions/ProQuest) • TDOne (TDNet) • TEMA Technik und Management • Ulrich's Periodicals Directory/ulrichsweb • Web of Science • WorldCat (OCLC)

ISSN 1231-0956
ISSN 2083-6023 (Online)

Publication funding of this journal is provided by resources of the Polish Academy of Sciences and the Institute of Fluid Flow Machinery

Contents

Co-published by
Institute of Fluid-Flow Machinery
Polish Academy of Sciences
Committee on Thermodynamics and Combustion
Polish Academy of Sciences

http://www.imp.gda.pl/archives-of-thermodynamics/

Application of machine learning for reconstruction of multiphase fluid structure measured by a capacitance multi-electrode sensor

Remigiusz Ornowski[a,b], Marcin Lackowski[a], Roman Kwidzinski[a*]

[a]Institute of Fluid Flow Machinery, Polish Academy of Sciences, Heat Transfer Department, Fiszera 14, 80-231 Gdańsk, Poland
[b]TERCJA Measuring and Computer Systems, Dywizjonu 303 5B/24, 80-462 Gdańsk, Poland
*Corresponding author email: roman.kwidzinski@imp.gda.pl

Received: 10.06.2024; revised: 19.08.2024; accepted: 08.10.2024

Abstract

Non-invasive real-time measurements of phase content in the reservoir fluid are highly advantageous in the oil and gas industry and remain a current research topic. The paper presents an innovative, self-designed multi-electrode capacitance meter intended for detecting multiphase flow patterns in a low-permittivity medium, such as the reservoir fluid. The capacitance sensor is built with delta-sigma charge modulators capacitance-to-digital converters. Machine learning is applied to convert the capacitance measurements into a tomographic image of the flow pattern. At present, the meter is built with eight electrodes. It is shown that the measurements are repeatable and have a good signal-to-noise ratio. The implemented neural network is capable of correctly reconstructing the tomographic images for a test tube filled with reservoir fluid and placed in various locations inside the test section.

Keywords: Electrical capacitance tomography; Multiphase reservoir flow; Neural networks; Machine learning; Deep learning

Vol. 45(2024), No. 4, 5–12; doi: 10.24425/ather.2024.151993

Cite this manuscript as: Ornowski, R., Lackowski, M., & Kwidzinski, R. (2024). Application of machine learning for reconstruction of multiphase fluid structure measured by capacitance multi-electrode sensor. *Archives of Thermodynamics*, 45(4), 5–12.

1. Introduction

The extraction of hydrocarbons by well drilling is accompanied by tests of the physical properties of the reservoir fluid, which are performed both during the testing of a new well and during the field production phase. One of the important parameters determined during well testing and productivity monitoring is the phase composition of the reservoir fluid. The phase composition significantly influences the technique that can be used for measuring the fluid flow rate. In the oil (petroleum) and gas industry, processed reservoir fluids are mixtures that in addition to hydrocarbons include water (frequently with dissolved salts) and non-condensable gases (like hydrogen sulfide) [1]. The hydrocarbons form a mixture that may be a liquid, gas or two-phase medium. Hydrocarbon liquid is typically crude oil, while dominating hydrocarbon gases are methane and butane (commonly known as natural gas). Natural gas can be dissolved (partially or completely) in the liquid phase and the amount of dissolved and free gases in the reservoir fluid strongly depends on the fluid pressure and temperature. Under certain thermodynamic conditions, heavy hydrocarbons (paraffin) and asphalts present in the reservoir fluid may solidify.

The traditional and most common method in oil and gas exploration for measuring the phase composition of the reservoir fluid involves the use of a separator enabling the measurement of each phase separately. This method is expensive and requires ongoing maintenance by qualified personnel. Due to the dimensions of the separator, it also requires considerable space, which

Nomenclature

Greek symbols

ε_r – relative permittivity

Abbreviations and Acronyms

ECT – electrical capacitance tomography
fF – femtofarad (10^{-15} F)
FPGA – field-programmable gate array
GVF – gas volume fraction
MFMS – multiphase flow metering systems
WLR – water-in-liquid ratio

may be a problem on offshore drilling platforms. Measurements acquired with this method have low time resolution due to the high inertia of the separator operation but they offer high measurement accuracy for quasi-steady flows. This is because only single-phase flows are measured, for which high accuracy commercial flowmeters are readily available.

The development of electronics and computers in the 1980s resulted in intensified research on the direct measurement of multiphase flow rate, without prior phase separation. In the 1990s, the first multiphase flow metering systems (MFMS) appeared commercially that attracted the interest of the oil & gas industry [2, 3]. The usefulness of such systems has been appreciated in the event of depletion of rich fields and the need to exploit less efficient and less accessible fields that were previously considered unprofitable. The use of MFMS instead of an expensive measurement separator offers a reduction in production costs on such marginal fields. MFMS also enable monitoring of a well production continuously and in real time.

Measuring the volumetric flow rate of a multiphase medium requires determining the volumetric (void) fraction and velocity for each phase. These local quantities determine the flow pattern (structure) in the test cross-section or volume of the flow channel for the pressure and temperature conditions prevailing there. The flow velocities of individual phases may be the same but they are often different (so-called slip). Therefore, a volumetric MFMS most often consists of a sensor measuring the void fraction and a module measuring velocity. To determine the mass flow rate, it is also necessary to measure or evaluate the density of each phase [4, 5].

Available information shows that MFMS are or were offered for the oil & gas industry by several companies. Their design details are often protected by the manufacturers and sometimes even their basic principles of operation are concealed [6]. One of the commercially popular and elaborated multiphase flow meters is marketed under the trademark Roxar 2600 [7]. The basic Roxar model uses impedance measurement to determine phase content and velocity. The velocity is determined based on the cross-correlation of measurements in two planes (flow cross-sections). In the more advanced models, a Venturi tube is added to measure differential pressure and a gamma radiation source (Cesium 137) to measure density. As additional modules, a salinity sensor (for water-dominated flows) and an acoustic sensor for sand monitoring are also available. Roxar 2600 MPFM can be used in three-phase oil, water and gas flows, in the full range of values (from 0% to 100%) of water-in-liquid ratio (WLR) and gas volume fraction (GVF). Under certain conditions, the lowest flowrate measurement uncertainty is 5% for gas, 3% for liquid phase and 2% for WLR [7].

The multiphase flow sensor of the Roxar meter consists of two sets of plate electrodes flush-mounted on the inner wall of the vertical test section. The lower (downstream) set contains six electrodes with a height comparable to the diameter of the test section. Their width is similar to the spaces between them. The upper set consists of two electrodes placed opposite to each other, with the same height as in the lower set and a width covering a segment of a circle (approx. 70–90°). Depending on the electrical properties of the fluid, the same electrodes are used to measure capacitance (when the fluid is dielectric) or conductivity [6]. The measurement in the lower set is rotational and at a time only one electrode is active and the other five are passive. The rotation in the measurement means that the source voltage is switched at equal time intervals from the active electrode to the next (neighbouring) one. According to the manufacturer, processing of the sensor signals allows the determination of the volume occupied by large gas bubbles or slugs and the volume of the dispersed phase in a homogeneous liquid-gas mixture with small bubbles. For large bubbles/slugs, their deviation from the central flow axis is detected. The measurements are also sensitive to the near-wall flow composition. The time of a single measurement is short enough to determine the velocity of large bubbles and the dispersed phase separately. The continuous phase can be either oil or water, and the instrument automatically detects which liquid is present at a given moment.

Non-invasive, fast-response and continuous methods for measuring phase content continuously and in real time remain a current research topic. Particular attention is paid to improving measurement accuracy, extending the measurement range and reliably recognizing multiphase flow structures. This work focuses on the tomographic method using measurements of the electrical capacitance of a multiphase medium. Basic information on multi-electrode capacitive phase content meters can be found, for example, in [8, 9].

Capacitance measurements acquired by tomographic meters can be used to reconstruct the multiphase flow patterns from permittivity distribution, which is equivalent to the spatial distribution of phases in the tested flow domain. An algorithm suitable for this task can be derived considering a set of equations describing the relation between the capacitance (c) and the permittivity (ε). Assuming linear approximation, the change in capacitance (Δc) vector can be related to the changes of permittivity ($\Delta\varepsilon$) according to the equation $\Delta c = S\Delta\varepsilon$, where S is the sensitivity matrix of the transducer [10]. Determining the permittivity from capacitance measurements, known as an inverse problem, can be formally treated as calculating the inverse of the sensitivity matrix (S). However, the problem is ill-posed and ill-conditioned, that is there is no unique solution of the equation

$\Delta c = S\Delta\varepsilon$, and small changes in c (e.g. due to measurement noise) can result in great discrepancies in ε [11]. Therefore, computing the inverse S is a challenging task for which many solution methods have been proposed, among which two classes can be distinguished: direct and iterative. Direct methods include for example linear back-projection, singular value decomposition, and Tikhonov regularization. Examples of the iterative algorithms are Newton–Raphson and iterative Tikhonov methods, Landweber iteration or other steepest descent methods [10].

Apart from the above direct and iterative algorithms, unconventional reconstruction methods based on machine learning have been developed. Nooralahiyan et al. [12] were among the pioneers of using an artificial neural network for solving the inverse image reconstruction problem. Their paper describes the basic principles of an artificial neuron, the multilayer perceptron network and the back-propagation training algorithm, applied in real-time to electrical capacitance tomography (ECT) measurement of multicomponent flows with small (gas/oil) and large (water/oil) difference in permittivity. Later, Marashdeh et al. [13], used a multilayer feed-forward neural network combined with an analog Hopfield field network for solving the nonliner inverse problem. At the same time, Flores et al. [14] investigated the application of neural networks in ECT used in the oil industry. Imaging using the least squares support vector machine (LSSVM) with a self-adaptive particle swarm optimization algorithm was proposed by Chen et al. [15]. On the other hand, Wang et al. [16] studied multiphase flow monitoring by combining the LSSVM with a bacterial colony chemotaxis algorithm. A three-layer feed-forward neural network with radial basis function activation was used by Chen et al. [17] to reconstruct the permittivity distribution from the measured capacitance. Xu et al. [18] proposed a convolutional neural network to predict the oil flow rate, gas flow rate and gas void fraction from measurements with dual ECT sensors and a Venturi tube. A brief overview of other machine learning-based methods can be found in [11].

Based on an own-design unique multi-electrode capacitance meter and machine learning, this article describes the application of tomographic image reconstruction of a low-permittivity material. Reservoir fluid was used as an example of such material. The capacitance sensor is a novel construction built with eight ΔΣ charge modulators capacitance-to-digital converters (CDC).

2. Multi-electrode capacitance sensor

Electrical capacitance tomography is based on measurements of electrical capacitance between electrodes placed around the measured object. In the case of measurements on pipes [9], a set of electrodes is most often used in the form of identical thin plates, distributed evenly around the outer circumference of a non-conductive pipe. Mutual capacitances between individual electrodes are measured, so a single measurement result is a square data matrix of dimension $n \times n$, where n is the number of electrodes. However, the diagonal of the matrix is not taken into account because it represents measurements with one electrode, which have no physical meaning. Therefore, a single measurement produces $N = n^2 - n$ values of electrical capacitance. An exemplary electrical capacitance tomography system is shown in Fig. 1. In this example, the excitation signal from module (3) is sent via the switches (2) to one of the electrodes mounted on the outer wall of pipe (1). This produces a signal proportional to the mutual capacitances on the other electrodes. These signals are amplified (4) and converted to digital (5). The switches (2) then reconnect the excitation (3) and amplifiers (4) to the next electrodes, one by one. Reconnections and measurements are repeated by signal control and measuring system (6) until the capacitance matrix is completed.

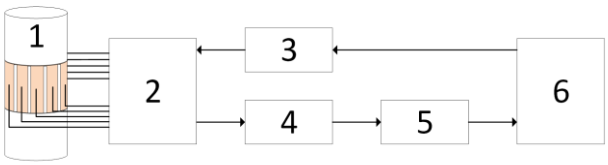

Fig. 1. Electrical capacitance tomograph: 1 – pipe with electrodes, 2 – switches, 3 – excitation, 4 – amplifiers, 5 – analog-to-digital converters, 6 – signal control and processing system.

The own-designed and built capacitance measurement system is based on the NEXYS-A7 digital circuit development platform, the main component of which is the XC7A100T-1CSG324C field-programmable gate array (FPGA) manufactured by Xilinx [19]. The block diagram of the capacitance sensor is shown in Fig. 2.

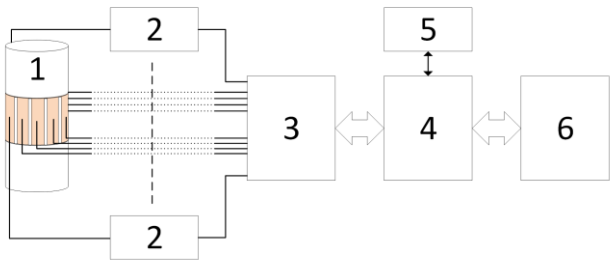

Fig. 2. Block diagram of the multi-electrode capacitance sensor: 1 – pipe with electrodes, 2 – ΔΣ modulators with excitation, 3 – LVDS interface, 4 – NEXYS-A7, 5 – local display, 6 – computer.

The NEXYS-A7 board (4 in Fig. 2) has a number of additional circuits that allow it to be used directly in a wide range of applications. For the multi-electrode capacitance sensor, two eight-bit input-output ports, a USB interface and a numeric display were used together with the graphic Pmod MTDS (Multi-Touch Display System) [20] add-on board (5). Moreover, the sensor set is supplemented with an original interface system of own design that is connected to two input-output ports and allows the connection of up to 16 measurement modules via LVDS (low-voltage differential signalling) interfaces (3). Eight identical measurement modules (2) were built as ΔΣ charge modulators capacitance-to-digital converters (CDC) and used in the research. The modulators were connected to eight electrodes mounted evenly around measuring pipe segment (1). Local display (5) can show current information, e.g. on actual capacitance values. The measured capacitance values are transmitted in real time to the computer (6) where they are stored and processed. Details of the used electronic components are summa-

Table 1. Electronic modules used to build the multi-electrode capacitance sensor.

No. in Figs. 2 & 4	Name	Manufacturer	Type	Specification
2	ΔΣ charge modulator capacitance to digital converter	own design and construction	–	sampling frequency 100–1200 kHz, output resolution 1bit, second order ΔΣ modulator
3	low-voltage differential signalling interface	own design and construction	–	16 channels, two transmission lines and one receiving line in each channel, maximum transmission frequency 400 MHz
4	digital circuit development platform	Digilent	NEXYS-A7	Artux-7 FPGA (clock >450 MHz), 129 MB DDR2 memory, USB, Ethernet, temperature sensor [19]
5	local display	Digilent	Pmod MTDS	2.8“ touchscreen display with QVGA resolution (320×240), PIC32MZ Microcontroller [20]

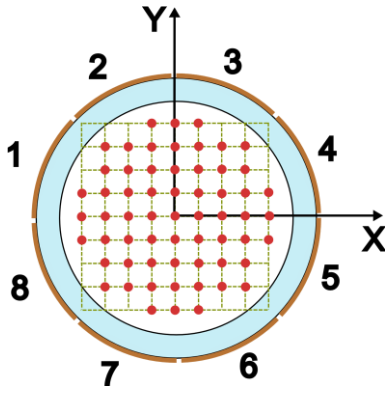

Fig. 3. Arrangement of electrodes in the test section: 1 to 8 – electrodes, XY – coordinate system. Red dots indicate 61 positions of the rod during reference measurements.

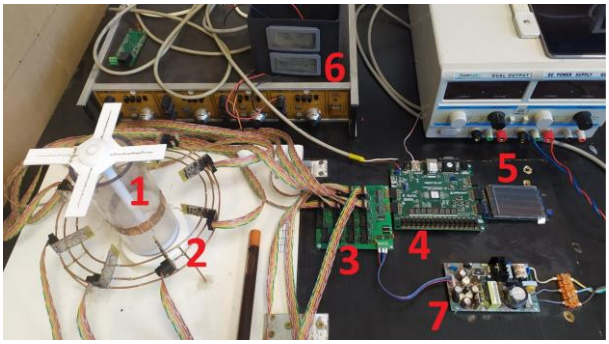

Fig. 4. Photograph setup: 1 – pipe with electrodes, 2 – ΔΣ modulators with excitation, 3 – LVDS interface, 4 – NEXYS-A7 FPGA, 5 – local display, 6 – 5 V power supply, 7 – +15 V and −15 V power supply of the capacitance sensor.

rized in Table 1. The arrangement of the measuring electrodes on the pipe wall in the test section is shown in Fig. 3 together with an XY coordinate system used in the subsequent discussion of tomograms.

A single measurement in the proposed device involves generating an excitation signal on one of the electrodes and simultaneously collecting responses on the remaining seven electrodes. This is followed by a program-controlled change of the excitation electrode. The complete measurement cycle requires eight partial measurements and returns 56 individual results for inter-electrode capacitances. The capacitance sampling frequency is 8 kHz, therefore a single measurement is done in 1 ms. At present, not all measurements are processed further and single measurements are transmitted once per second to the computer where they are written to a file. This is sufficient to analyze the stationary capacitance field in the test section.

A complete measuring system is shown in Fig. 4. Operation of the sensor set (No. 1 in Fig. 4) requires proper programming of the FPGA circuit (4). This includes the generation of signals necessary for the proper operation of ΔΣ modulators with excitation (2), i.e. reference clock signals with a frequency of 1.024 MHz, signals switching the modulator systems between the generation of the excitation signal and the capacitance measurement, and the collection and processing of digital outputs from the modulators. These signals are connected to ΔΣ modulators through an LVDS interface (3). Local display (5) is used for a quick overview of the sensor condition, e.g. actual capacitance values. For correct operation, the measuring system requires three supply voltages, which are provided by power supplies (6) and (7). The numbers 1 to 5 in Fig. 4 and in Fig. 2 showing the block diagram correspond to each other. In addition, the MicroBlaze soft-core microprocessor was programmed in the FPGA (4). The microprocessor is responsible for collecting the measurements and sending them to the cooperating computer. The FPGA software was created using the VIVADO Design Suite, while the program for the Microblaze microprocessor was written in the Xilinx Software Development Kit (SDK) environment.

3. Measurements

The constructed measuring system was installed on the wall of a polycarbonate pipe segment with an internal diameter of 60 mm and a wall thickness of 5 mm, Figs. 3 and 4. The pipe dimensions were selected to withstand the target operating conditions, i.e. temperature up to 70°C and pressure up to 4 bar. Eight electrodes mounted around the outer wall of the pipe were made of thin copper sheets measuring 20 mm × 25 mm. Two series of measurements were carried out. The first series was intended to generate reference data for reconstruction of the ca-

pacitance field, while the second one was intended to generate control data.

The reference data included 62 measurements of electrical capacity in the inter-electrode space: one measurement for an empty pipe and 61 measurements with a polyamide rod placed vertically in various locations relative to the longitudinal axis of the pipe, see Fig. 3. To define the position of the rod in the pipe cross-section, a rectangular grid was used with the origin in the pipe axis, grid size of 5 mm × 5 mm and a range from −20 mm to 20 mm. Some of the rod positions at the grid nodes were omitted because they were outside the pipe. The diameter of the rod was 12 mm and its relative permittivity was $\varepsilon_r = 3.6$.

The control data included a certain number of measurements, one for an empty pipe and the rest with a glass test tube filled with reservoir fluid and placed in different positions inside the pipe. The outer and inner diameter of the test tube was 15.5 mm and 13.3 mm, respectively. The relative permittivity of glass is $\varepsilon_r = 5.2$, while the relative permittivity of the reservoir fluid determined from the measurement of the change in the capacity of the air capacitor is $\varepsilon_r = 4.3$. Table 2 shows capacitances measured with the empty pipe. As expected, measured values are in the range from a tenth femtofarad to sub-picofarad.

4. Flow pattern reconstruction by artificial neural network

A neural network was used to analyze the collected data and generate tomographic images. A neural network consists of interconnected neurons, which are functions, most often non-linear, that convert the input signal. In the most commonly used networks, a neuron has *n* inputs and one output. Then, the weighted sum of *n* inputs is fed to the input of the function, and the output of the neuron is the result of the function. Neurons are stacked into layers, and the processed signals pass through subsequent layers of the neural network. The connections between the outputs and inputs of neurons, along with the weights assigned to them, are called synapses. Synapses also connect the outputs of the previous layer with the inputs of the next layer, with the first layer, the input layer, receiving the external input signals, and the last one, the output layer, generating the final result of the example neural network, Fig. 5.

The most important operation when creating a neural network is its training or learning procedure. To put it simply, it involves feeding a known signal to the input of a neural network and comparing the result of the network's operation with the expected one. Then, the synapse weights and sometimes the parameters of neuron functions are changed so that the result obtained is as close to the expected result as possible. This procedure is repeated many times for different sets of input and expected signals. A properly trained neural network produces correct results for all, or at least the vast majority, of the data sets used for training and, more importantly, can correctly process other similar input data.

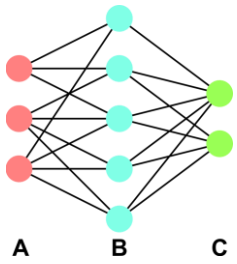

Fig. 5. Example neural network: A – input layer, B – hidden (internal) layer, C – output layer.

The collected measurement data was processed using libraries written in Python. The sequential model in TensorFlow library with the Keras interface was used to generate and train the neural network [21]. The input data is a square matrix of dimension 8 with a zeroed diagonal, representing the measured capacitances between the sensor electrodes. The output is the coordinates of the polyamide test rod position. In order to simplify the neural network, the output data was written as a vector whose elements corresponded to specific positions of the rod, and detection of one specific position of the rod was assumed. The finally applied single neural network has the following structure:

- input layer of 64 neurons,
- hidden (internal) layer of 256 neurons,
- output layer of 2 neurons.

The designed neural network was subjected to a training process using model data normalized to the range from 0 to 1, after which it generated the correct result. The created single neural network was multiplied to detect all 61 standard positions of the rod, then all 62 partial neural networks were sequentially subjected to the training process and combined into one network

Table 2. Sample matrix of measured capacitances in pF.

		Measuring electrode							
		1	2	3	4	5	6	7	8
Excitation electrode	1		0.7428	0.0515	0.0736	0.1211	0.0750	0.1078	0.7246
	2	0.7260		0.6860	0.0305	0.1061	0.0781	0.1409	0.0461
	3	0.0408	0.6536		0.7132	0.0592	0.0718	0.1522	0.0936
	4	0.0774	0.0418	0.7009		0.6967	0.0278	0.1443	0.1007
	5	0.0869	0.0775	0.0481	0.8124		0.7047	0.0982	0.0925
	6	0.0781	0.0831	0.0829	0.0327	0.6167		0.6889	0.0440
	7	0.0338	0.0762	0.0883	0.0727	0.0509	0.6616		0.5091
	8	0.6815	0.0316	0.0796	0.0803	0.0920	0.0277	0.5540	

with the 8 × 8 input matrix and the output vector of 62 elements. An untypical structure of the neural network was forced by the low quantity of reference data, which caused problems with correct training of a single neural network.

The output of the neural network was used to generate a tomographic image of the flow patterns. For this purpose, pattern images corresponding to the pattern sensor outputs were prepared. Sample patterns assigned to position Y = −10 mm and X = −10 mm, −5 mm or 0 mm are shown, respectively, as A, B, C images in Fig. 6.

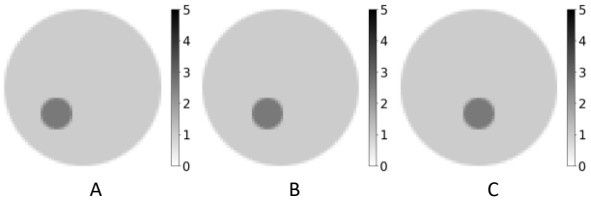

Fig. 6. Pattern tomographic images for three rod positions: A) X = −10 mm, Y = −10 mm; B) X = −5 mm, Y = −10 mm; C) X = 0 mm, Y = −10 mm.

The output of the network was a tomographic image, which was a weighted composite of the pattern images. In the first stage of checking the operation of the trained network, the pattern input data were reused and a practically accurate reproduction of the training data was received at the output, see Fig. 7, in which the rod positions correspond well with those in Fig. 6.

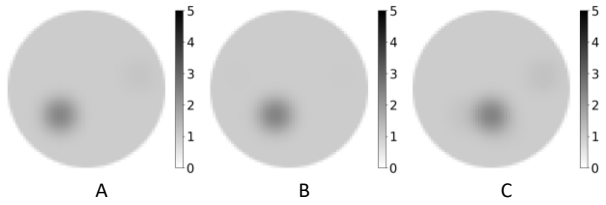

Fig. 7. Output tomographic images for three rod positions (shown in Fig. 6): A) X = −10 mm, Y = −10 mm; B) X = −5 mm, Y =−10 mm; C) X = 0 mm, Y = −10 mm.

5. Results

Measured data were statistically interpreted. Tables 3 and 4 show, respectively, the standard deviation and mean square deviation averaged from all measuring series for the full measuring matrix. It can be seen in Table 3 that the maximum value of the standard deviation equals 2.40 fF, the minimum value is 0.12 fF, and the average is 0.73 fF. Corresponding values for the mean square deviation in Table 4 are 2.18 fF, 0.10 fF and 0.75 fF. Table 5 shows absolute values of differences between capacitances measured with an empty pipe and one (typical) of the control measurements. For other control measurements, these values are similar. For the capacitance differences in Table 5, the corresponding maximum, minimum and average values are 22.82 fF, 0.68 fF and 8.48 fF.

More detailed analysis of the data presented in the tables leads to the conclusion that the average measured signal from

Table 3. Standard deviation of capacitance measurements in fF.

		Measuring electrode							
		1	2	3	4	5	6	7	8
Excitation electrode	1		0.9465	0.6765	0.1540	0.8125	1.1692	1.3954	0.8430
	2	1.2858		0.2860	0.2849	1.8582	0.2939	0.5941	1.3948
	3	1.0592	0.6496		0.2422	2.3983	0.2765	0.7954	0.5175
	4	1.1722	0.6917	0.8948		0.5086	0.3282	0.9162	0.4026
	5	0.7041	0.3241	0.3874	0.3495		0.3030	0.4687	0.7894
	6	0.6404	0.5667	0.8571	0.1727	0.9604		0.3967	0.6847
	7	2.0634	1.0953	0.1753	0.1232	0.4049	0.2758		0.3988
	8	1.0237	1.3063	0.8782	0.2486	0.4358	0.5352	1.2783	

Table 4. Mean square deviation of capacitance measures in fF.

		Measuring electrode							
		1	2	3	4	5	6	7	8
Excitation electrode	1		1.2879	0.5747	0.1293	0.6867	1.0652	1.2212	1.3083
	2	1.2172		0.3106	0.2402	1.8729	0.2571	0.5805	1.3344
	3	0.9432	1.0397		0.2072	2.1757	0.2502	0.8396	0.5796
	4	1.0591	0.9880	1.5000		0.5102	0.2795	0.8297	0.3988
	5	0.7558	0.3809	0.3352	0.6598		0.2650	0.4137	0.7610
	6	0.7116	0.5934	0.7754	0.1466	1.5413		0.3963	0.5763
	7	1.7749	0.9771	0.1639	0.1040	0.3774	0.2766		0.3470
	8	0.8583	1.2919	0.7816	0.2335	0.5941	0.4506	1.7812	

Table 5. Absolute value of differences between capacitance measures in fF.

		Measuring electrode							
		1	2	3	4	5	6	7	8
Excitation electrode	1		11.8022	0.6839	7.2696	21.7938	9.6818	4.6344	4.6308
	2	9.3650		1.4642	9.9730	20.4479	10.3518	8.5031	0.9020
	3	8.1539	10.8116		10.1570	22.5006	10.2041	8.4872	2.9265
	4	10.7341	9.6308	5.3480		2.1794	6.1330	9.7855	5.4407
	5	5.8758	6.1259	5.2418	14.4025		13.7443	9.9298	9.1028
	6	4.5810	2.9266	3.5715	4.2926	4.2589		10.2454	8.3952
	7	6.6521	4.9662	5.8284	1.6801	22.7186	17.8655		7.2578
	8	9.4027	9.2358	2.1333	3.0383	22.8179	7.7296	6.6307	

those presented in Table 5 is about 11 times greater than the noise represented in Tables 3 and 5, and varies from about 0.65 to 65. It might seem that these values are not very good but it should be noted that the average ε_r changes only by 25% when the filled glass test tube is inserted into the empty pipe. Moreover, the thickness of the pipe wall additionally decreases the system sensitivity to changes inside the pipe. The comparison of standard deviation or mean square deviation and the measurement range of 1 pF gives the average noise level at −63dB.

The prepared neural network was used for processing of control measurements. In this case, the test filled with reservoir fluid was used. Photographs in Fig. 8 show a few pipe and test tube configurations used to create control data for the reconstruction software. The images are aligned with the XY coordinate directions shown in Fig. 3. Figure 9 shows corresponding tomographic reconstructions. It can be seen in the tomographic images that the system reproduces correctly the real test tube location in the pipe cross-section.

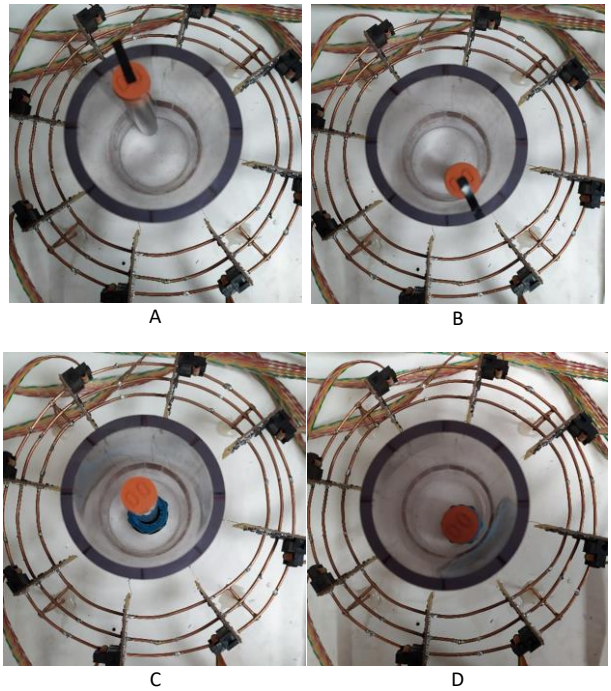

Fig. 8. Pictures of control pipe configurations with the test tube: A) close to electrode no. 2, B) close to electrode no. 6, C) close to the pipe centre, D) close to electrodes no. 5 and 6.

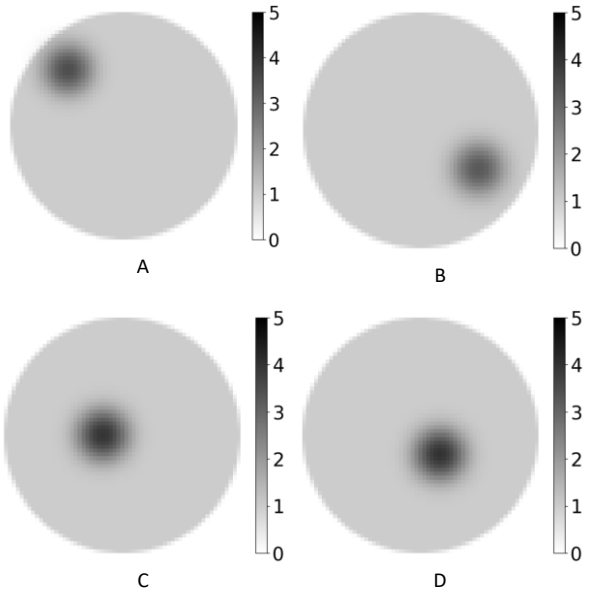

Fig.9. Output tomographic images of control pipe configurations shown in Fig. 8 with the test tube: A) close to electrode no. 2, B) close to electrode no. 6, C) close to the pipe centre, D) close to data electrodes no. 5 and 6.

6. Conclusions

The paper presents a novel eight-electrode capacitance meter designed to detect multiphase flow patterns in a medium with low permittivity, such as the reservoir fluid. Its operation was tested in laboratory conditions for static capacitance fields generated by introducing a polyamide rod or a glass test tube filled with reservoir fluid sample into the inter-electrode space.

The measurement system performed very well. The results were repeatable and had a good signal-to-noise ratio. The reconstruction of tomographic images in the case of data used to train the neural network was error-free, which confirms the selection of the appropriate structure of the neural network and the correctness of the training procedure. Reconstruction of target images with reservoir fluid also worked well. The position of the test tube was properly detected and the electrical permittivity was read at a noticeably higher level than in the case of data training the neural network. Both of these observations correspond to the actual measurement arrangement.

However, attention should be paid to the limitations of the proposed measurement system and the tomographic image reconstruction method. The use of only eight electrodes to measure capacitance significantly limits the accuracy and resolution of the reconstructed flow image. Moreover, the applied tomographic image reconstruction algorithm forces the detection of phase structures with a circular cross-section. For disturbances with a different shape, an approximation using a circle will be done. However, it should be expected that increasing the number of electrodes combined with more extensive training of the neural network should lead to better results.

Nevertheless, the designed capacitance meter has several significant advantages. The most important of them are a good signal-to-noise ratio and high sampling rate. The presented system can achieve signal-to-noise ratio of 63 dB at a sampling frequency of 1 kHz. For comparison, according to previous works, a generator-based two-electrode capacitance meters give signal-to-noise ratio of about 30 dB at a sampling frequency about 10 Hz. It should be noted that the capacitances measured here are very small, in the femtofarad range, which is difficult to measure accurately. Considering the above mentioned advantages, it should also be mentioned that the designed multichannel capacitance meter requires a specialized measuring system based on an expensive field-programmable gate array platform. The other meters can usually use commercially available integrated measurement circuits.

Acknowledgements

The research was supported by the third edition of the Programme of the Polish Ministry of Education and Science entitled "*Doktorat wdrożeniowy"* ("Industrial Doctoral Programme") − DWD/3/26/2019.

References

[1] Hu, X., Hu, S., Jin, F., & Huang, S. (Eds.) (2017). *Physics of Petroleum Reservoirs*. Petroleum Industry Press and Springer-Verlag. doi: 10.1007/978-3-662-53284-3

[2] Falcone, G., Hewitt, G.F., Alimonti, C., & Harrison B. (2002). Multiphase flow metering: current trends and future developments. *Journal of Petroleum Technology*, 54(4), 77–84. doi: 10.2118/74689-JPT

[3] Falcone, G., Hewitt, G.F., & Alimonti, C. (2009). *Multiphase Flow Metering*. Elsevier B.V.

[4] Thorn, R., Johansen, G.A., & Hjertaker, B.T. (2013). Three-phase flow measurement in the petroleum industry. *Measurement Science and Technology*, 24(1), 012003. doi: 10.1088/0957-0233/24/1/012003

[5] Hansen, L.S., Pedersen, S., & Durdevic, P. (2019). Multi-phase flow metering in offshore oil and gas transportation pipelines: trends and perspectives. *Sensors*, 19(9), 2184, doi: 10.3390/s19092184

[6] Meribout, M., Azzi, A., Ghendour, N., Kharoua, N., Khezzar, L., & AlHosani, E. (2020). Multiphase flow meters targeting oil & gas industries. *Measurement*, 165, 108111. doi: 10.1016/j.measurement.2020.108111

[7] *Roxar 2600 Multiphase Flow Meters*. Product Data Sheet RXPS-002516, Rev B (October 2022). Emerson Electric Co. https://www.emerson.com/ documents/automation/product-data-sheet-mpfm-2600-mvg-datasheet-roxar-en-us-170812.pdf [accessed 24 Nov 2023].

[8] Reinecke, N., & Mewes, D. (1996). Recent developments and industrial/research applications of capacitance tomography. *Measurement Science and Technology*, 7(3), 233−246. doi: 10.1088/0957-0233/7/3/004

[9] Rahman, N.A.Abd., Rahim, R.A, Nawi, A.M., Pei Ling, L., Pusppanathan, J., Mohamad, E.J., Seong, C.K., Din S.M., Ayob, N.M.N., & Yunus, F.R.M. (2015). A review on electrical capacitance tomography sensor development. *Jurnal Teknologi (Sciences & Engineering)*, 73(3), 35–41. doi: 10.11113/jt.v73.4244

[10] Yang, W.Q., & Peng, L. (2003). Image reconstruction algorithms for electrical capacitance tomography. *Measurement Science and Technology*, 14(1), R1–R13, doi: 10.1088/0957-0233/14/1/201

[11] Rasel, R.K., Shah, M., Chowdhury, S.M., Marashdeh, Q.M., & Teixeira, F.L. (2022). Review of selected advances in electrical capacitance volume tomography for multiphase flow monitoring. *Energies*, 15(14), 5285. doi: 10.3390/en15145285

[12] Nooralahiyan, A.Y., Hoyle, B.S., & Bailey N.J. (1994). Neural network for pattern association in electrical capacitance tomography. *IEE Proceedings – Circuits, Devices and Systems*, 141(6), 517–521. doi: 10.1049/ip-cds:19941190

[13] Marashdeh, Q., Warsito, W., Fan, L.S., & Teixeira F.L. (2006). A nonlinear image reconstruction technique for ECT using a combined neural network approach. *Measurement Science and Technology*, 17(8), 2097−2103. doi: 10.1088/0957-0233/17/8/007

[14] Flores, N., Kuri-Morales, A., & Gamio, C. (2006). An application of neural networks for image reconstruction in electrical capacitance tomography applied to oil industry. In *Progress in Pattern Recognition, Image Analysis and Applications*" (pp. 371–380). *Proceedings of the 11th Iberoamerican Congress on Pattern Recognition*, CIARP 2006, 14–17 November, Cancún, Mexico. Springer-Verlag, doi: 10.1007/11892755

[15] Chen, X., Hu, H., Liu, F.& Gao, X.X. (2011). Image reconstruction for an electrical capacitance tomography system based on a least-squares support vector machine and a self-adaptive particle swarm optimization algorithm. *Measurement Science and Technology*, 22(10), 104008. doi: 10.1088/0957-0233/22/10/104008

[16] Wang, H., Hu, H., Wang, L., & Wang, H. (2012). Image reconstruction for an Electrical Capacitance Tomography (ECT) system based on a least squares support vector machine and bacterial colony chemotaxis algorithm. *Flow Measurement and Instrumentation*, 27, 59–66. doi: 10.1016/j.flowmeasinst.2012.05.006

[17] Chen, X., Hu, H., Zhang, J. & Zhou, Q., (2012). An ECT system based on improved RBF network and adaptive wavelet image enhancement for solid/gas two-phase flow. *Chinese Journal of Chemical Engineering* 20(2), 359–367. doi: 10.1016/S1004-9541(12)60399-1

[18] Xu, Z., Wu, F., Yang, X., & Li Y. (2020). Measurement of gas-oil two-phase flow patterns by using CNN algorithm based on dual ECT sensors with Venturi tube. *Sensors*, 20(4), 1200. doi: 10.3390/s20041200

[19] *Nexys A7 FPGA Board Reference Manual*, Revised July 10, 2019. Digilent Inc. https://digilent.com/reference/programmable-logic/nexys-a7/reference-manual [accessed 24 Nov. 2023].

[20] *Pmod MTDS Reference Manual*. Digilent Inc. https://digilent.com/reference/pmod/pmodmtds/reference-manual [accessed 24 Nov. 2023].

[21] *TensorFlow Core Guide – The Sequential model*. TensorFlow. https://www.tensorflow.org/guide/keras/sequential_model [accessed 24 Nov. 2023].

Co-published by
Institute of Fluid-Flow Machinery
Polish Academy of Sciences
Committee on Thermodynamics and Combustion
Polish Academy of Sciences

http://www.imp.gda.pl/archives-of-thermodynamics/

Simplified mathematical model of oxy-fuel combustion of municipal solid waste in the grate furnace: effect of different flue gas recirculation rates and comparison with conventional mode

Paulina Copik[a*], Andrzej Szlęk[a], Mario Ditaranto[b]

[a]Department of Thermal Technology, Silesian University of Technology, Konarskiego 22, Gliwice 44-100, Poland
[b]SINTEF Energy Research, Sem Sælands vei 11, 7034 Trondheim, Norway
*Corresponding author email: paulina.wienchol@polsl.pl

Received: 13.02.2024; revised: 07.07.2024; accepted: 16.07.2024

Abstract

Bioenergy carbon capture technology (BioCCS or BECCS) plays a key role in the European Green Deal, which aims to decarbonize industry and energy sectors, resulting in the production of energy with negative CO_2 emissions. Due to the biogenic origin of carbon contained in municipal solid waste (MSW), the application of carbon capture in waste incineration plants can be classified as BioCCS. Thus, this technology has attracted scientists' attention recently since it reduces excessive waste and emissions of carbon dioxide. Currently, there are four incineration plants in the Netherlands, Norway and Japan, in which CO_2 capture is implemented; however, they are based on the post-combustion technique since it is the most mature method and not requires many changes in the system. Nevertheless, the separation of CO_2 from the flue gas flow, which contains mostly nitrogen, is complex and causes a large drop in the total performance of the system. Oxy-fuel combustion technology involves the replacement of air as an oxidizer into high purity oxygen and recirculated exhaust gas. As a result, CO_2-rich gas is produced that is practically ready for capture. The main goal of the study is to develop a mathematical model of oxy-waste combustion to answer the research questions, such as how the composition of oxidant that is supplied to the process affects the combustion performance. The model includes all important processes taking place within the chamber, such as pyrolysis, char burnout and gas combustion over the grate. The results of the work will contribute to the development of oxy-waste incineration plants and will be useful for design purposes.

Keywords: Oxy-fuel combustion; Mathematical modelling; Municipal solid waste; Carbon capture

Vol. 45(2024), No. 4, 13–25; doi: 10.24425/ather.2024.151233

Cite this manuscript as: Copik, P., Szlęk, A., & Ditaranto, M. (2024). Simplified mathematical model of oxy-fuel combustion of municipal solid waste on the grate furnace: effect of different flue gas recirculation rates and comparison with conventional mode. *Archives of Thermodynamics*, 45(4), 13–25.

1. Introduction

Municipal solid waste (MSW) is recognised as an inevitable result of human activity, rapid urbanisation, and economic growth. By 2050, global waste production is expected to increase from 2.01 billion tonnes in 2016 to 3.40 billion tonnes [1]. The waste-to-energy (WtE) industry is of unquestionable significance for non-recyclable waste disposal and plays a key role in the waste management hierarchy established in the European Union (EU) Waste Framework Directive [2].

A grate furnace is a mature and reliable technique for waste

Nomenclature

$\bar{a}$ – Planck-mean absorption coefficient
A_i – pre-exponential factor or frequency factor, 1/s
c – specific heat capacity, J/(kg K)
E_i – energy activation, kJ/mol
H – enthalpy, kJ/kg
k – kinetic rate constant, 1/s
k_{diff} – coefficient of mass transfer
$\dot{m}$ – mass flow, kg/s
$\dot{Q}_{rad}$ – heat of radiation, kW
$\dot{Q}_{reac}$ – heat of reaction, kW
$\dot{Q}_{comb}$ – heat of combustion, kW
r – rate of reaction, kg/s
r_c – ratio of CO/CO_2 formation rate
R – universal gas constant, J/(mol K)
t – time, s
T – temperature, K
x – coordinate

Subscripts and Superscripts

bed – bed
dev – devolatilization
evp – evaporation
gas – surrounding gases
ox – oxidiser

Abbreviations and Acronyms

ASU – air separation unit
BECCS – bioenergy carbon capture and storage
CCS – carbon capture and storage
CHP – combined heat and power
GDP – gross domestic product
LCA – life cycle assessment
LHV – lower heating value
MEA – monoethanolamine
MSW – municipal solid waste
OFC – oxy-fuel combustion
TGA – thermogravimetric analysis
WtE – waste-to-energy

incineration that is also able to destroy and remove toxic organic substances [3]. As stated in [4], in the EU, the proportion of MSW incineration plants making use of moving grate technology is 88%.

A step forward in the development of WtE plants is the integration of incinerators with carbon capture and storage (CCS) technology to become carbon dioxide (CO_2) negative [5]. The described system is called bio-energy carbon capture technology (BioCCS or BECCS) and consists of CO_2 removal from the atmosphere through feedstock with biological origin, which is then thermally converted to obtain energy. The resulting biogenic carbon dioxide is captured and permanently stored, for instance, in a geologic formation, and the biomass is regrown [6].

The opportunities and challenges that need to be addressed to fully exploit the great potential of BECCS technologies based on MSW are summarised in our previous work [7], in which we concluded that among all CCS techniques, oxy-fuel combustion (OFC) is a promising technology in terms of energy efficiency and environmental impact. OFC involves increasing the partial pressure of carbon dioxide in the exhaust gases in order to facilitate and reduce the costs of its sequestration [8]. The schematic diagram of the oxy-MSW incineration plant is presented in Fig. 1. The process involves the employment of oxygen (O_2) instead of air as an oxidizer, resulting in a temperature increase. In the case of waste usually having a moderated or low calorific value, oxy-incineration is favourable since it reduces the consumption of auxiliary fossil fuels (it is often used to keep the required temperature in the MSW combustor, causing inevitable CO_2 emissions). Moreover, due to the absence of nitrogen (N_2), the volume of the flue gas stream is about 5 times lower, which facilitates the cleaning of flue gas and allows for reducing the size of equipment [9]. It can also be foreseen that an increase in the partial pressure of oxygen will intensify the oxidation of complex hydrocarbons. However, the issue with ash melting may occur due to the elevated temperature of the process. To control the temperature in the furnace, oxygen can be diluted with flue gas, which mainly consists of carbon dioxide and water vapour.

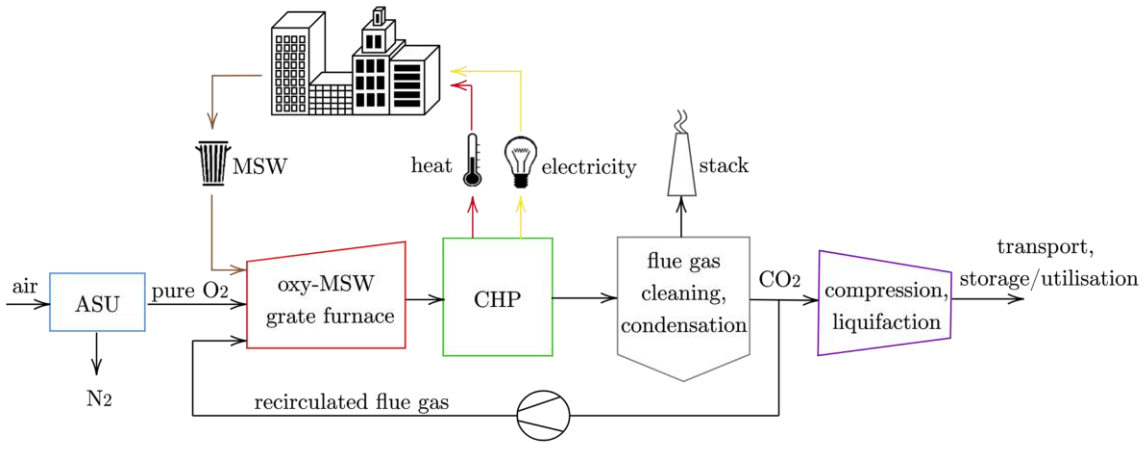

Fig. 1. Schematic diagram of the oxy-fuel incineration plant.

Till now, studies on oxy-waste combustion were focused on the assessment of the operation of the entire system, e.g. authors in [10–12] simulated the MSW incineration plant working under oxy-fuel combustion conditions and using exergy and life cycle assessment (LCA) analyses evaluated its exergy and energy efficiency as well as its effect on the environment. Results indicated that the total weighted resource consumption and total weighted environment potential of MSW oxy-fuel incineration were lower than MSW incineration with CO_2 capture via monoethanolamine (MEA) absorption. The authors also emphasized that the electric power consumption of the air separation unit (ASU) was the major influencing parameter, followed by the electric power consumption of the CO_2 compressor, while transport distance had a small influence on the results.

Experience from previous research on the oxy-combustion of fossil fuels, like coal, has shown that combustion chemistry and radiative heat transfer are altered due to the significantly higher partial pressures of carbon dioxide and water vapour in the flue gas [9,13–15]. Therefore, in the studies on oxy-waste combustion, the thermogravimetric technique was widely employed by many researchers to assess the thermal behaviour of waste, determine chemical kinetics and study gaseous emission in O_2/N_2 and O_2/CO_2 atmospheres [16–20]. Authors indicated that at the same oxygen concentration, the DTG (differential thermogravimetry) peak values in the oxy-fuel atmosphere were lower than those in the air atmosphere indicating that CO_2 has a higher inhibitory effect, as well as NO_x and SO_2 emissions were reduced at some temperatures under the O_2/CO_2 atmosphere. Thermogravimetric analysis (TGA) plays a vital role in research on the oxy-waste combustion process since it allows for relatively cost-effective and straightforward experimental data collection compared to tests using full-scale furnaces. As stated in [7], kinetic data obtained from TGA can be further used in mathematical and numerical modelling of the oxy-MSW combustion process.

In the literature, few works on the experimental investigation of oxy-waste combustion using lab-scale reactors can be also found, for example in [21,22]. Based on the results, authors concluded that such challenges as combustion chamber design, local O_2 concentrations, flue gas recirculation strategy as well as primary and secondary measures for NO_x should be further investigated. By now, only one study concerns an experimental campaign on OFC of wood chips using a pilot-scale facility [23]. The results of the tests indicated that the OFC of the biomass fuel is feasible but differs significantly from that of air combustion. The CO_2 concentration in the dry flue gas could be increased to around 73% with 5.7% excess O_2. Compared to air combustion, the emission of CO was higher during oxy-fired conditions, and the maximum temperature along the combustion chamber was lower.

Mathematical modelling is a powerful tool for furnace design and performance optimisation for various combustion systems without having to resort to scaling up results from lab-scale experiments, which is generally complicated by the strong interaction between turbulence, reaction kinetics, heat release and radiation. Research focused on the mathematical modelling of waste and biomass combustion on the grate furnace (Fig. 2) can be found in several papers, for example in [24–29]. Authors developed models of non-fossil solid fuel combustion with various levels of complexity that can be used for different purposes. All established models include processes such as drying, devolatilization, and gas and char oxidation, based on chemical kinetic to study different combustion indicators, e.g. temperature profiles, ignition and emission of pollutants. Since biomass and municipal solid waste contain high proportions of volatile matter, Yang et al. [30] built a one-dimensional model of solid fuel bed combustion to examine the effect of the devolatilization rate of the waste fuels on the process. In [31], authors developed a two-dimensional unsteady state model to investigate the effects of moisture content on combustion characteristics. Studies showed that due to the high moisture content of the feedstock, the evaporation process consumes a large amount of heat and can take about 2/3 of the whole combustion process. Research presented in [32] compared 2D and 3D models of waste combustion and investigated the effects of particle size, waste throughput, and residence time on the bed incineration performance. Yu et al. [33] developed a three-dimensional mathematical model as a tool for furnace structure design and operation conditions optimization when the straw combustion is in oxygen-enriched or air atmospheres. Such parameters as temperature and concentrations of carbon monoxide (CO) and nitrogen monoxide (NO) were calculated. The results of simulations showed that combustion in an oxygen-enriched atmosphere is superior to combustion in conventional air. A comprehensive review of modelling approaches of biomass and waste combustion is presented in [34] and [35], respectively.

Up to now, one paper on computational fluid dynamics (CFD) simulation of biomass thermal conversion under air/oxy-fuel conditions in a reciprocating grate boiler was found in the

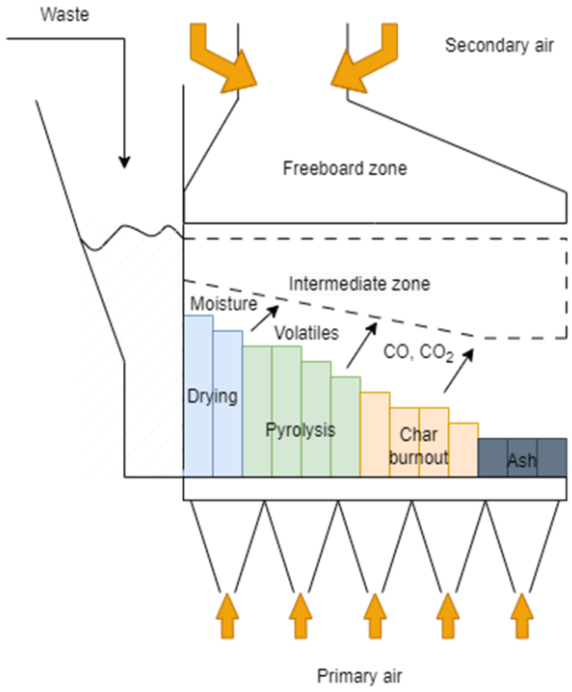

Fig. 2. Schematic diagram of the combustion chamber of a stoker boiler.

literature [36]. The effect of O_2/recycled flue gas (CO_2) ratios on flame temperature distribution, species concentration, char burnout, and fuel consumption have been studied and substantial differences were noticed compared with combustion in an air atmosphere. The numerical prediction showed that the gas temperature profile in oxy-fuel conditions with 25% oxygen concentration by volume in the oxidizer is closer to the referenced air-fired combustion.

To the best of the authors' knowledge, mathematical models of oxy-waste combustion in a moving grate furnace have not yet been described in the literature. Therefore, in this paper, a mathematical model of waste combustion for a full-scale moving grate MSWI plant under air- and oxy-fired conditions is demonstrated and compared. The model is developed using MATLAB Software. First, the air combustion model is validated by comparison with full-scale plant data. The validated model is then modified for an oxygen-fired system and used to study the effects of the atmosphere and oxidant distribution on important process outcomes.

2. Mathematical model development

2.1. Overview and assumptions

The scheme of considered MSW grate furnace is shown in Fig. 3. The combustion chamber is divided into three calculation sections: (a) grate, (b) intermediate zone, and (c) freeboard. In the model, the grate zone contains solid fuel particles. The oxidizer at the initial temperature and fresh fuel flow into the grate zone, where in the first stage the fuel is heated by surrounding gases by radiation, which provides energy for the evaporation and devolatilization. Then, the remained char reacts with oxidiser, which is supplied to the furnace, generating CO and CO_2. Therefore, fuel conversion processes take place in the grate zone, releasing or absorbing heat. This approach is consistent with most models of solid fuel combustion on the grate found in the literature [34,37]. The air in the grate zone is heated and partially consumed in the waste oxidation processes. The rest of the heated air and gases such as volatiles, water vapour, carbon dioxide and carbon monoxide escape from the grate zone. In the case of air combustion, the primary and secondary air is considered to be humid air. Temperature and relative humidity determine the absolute water content of air. For oxy-combustion, the oxidant is oxygen from the ASU and recycled exhaust gases. The composition of the oxidant that was adopted during the simulations is given in Table 2.

As Hoang et al. [35] stated, the coupling between the waste bed and the freeboard is a concern during mathematical modelling. Therefore, in this study, the intermediate zone is proposed, in which the released combustible gases like carbon monoxide and volatile matter are partially combusted with the surplus oxidizer from the grate zone; thus, heat is released above the grate. The reactions follow a chemical equilibrium. Such a solution has not yet been found in the literature.

In the freeboard, the oxidiser is supplied again to ensure the complete combustion of remaining combustible gases. The produced flue gas contains mainly CO_2, H_2O, and excess O_2. Thus, after water condensation, CO_2 can be easily compressed and transported.

The main assumptions are as follows:

- Waste is described by proximate and ultimate analysis.
- Model is steady state.

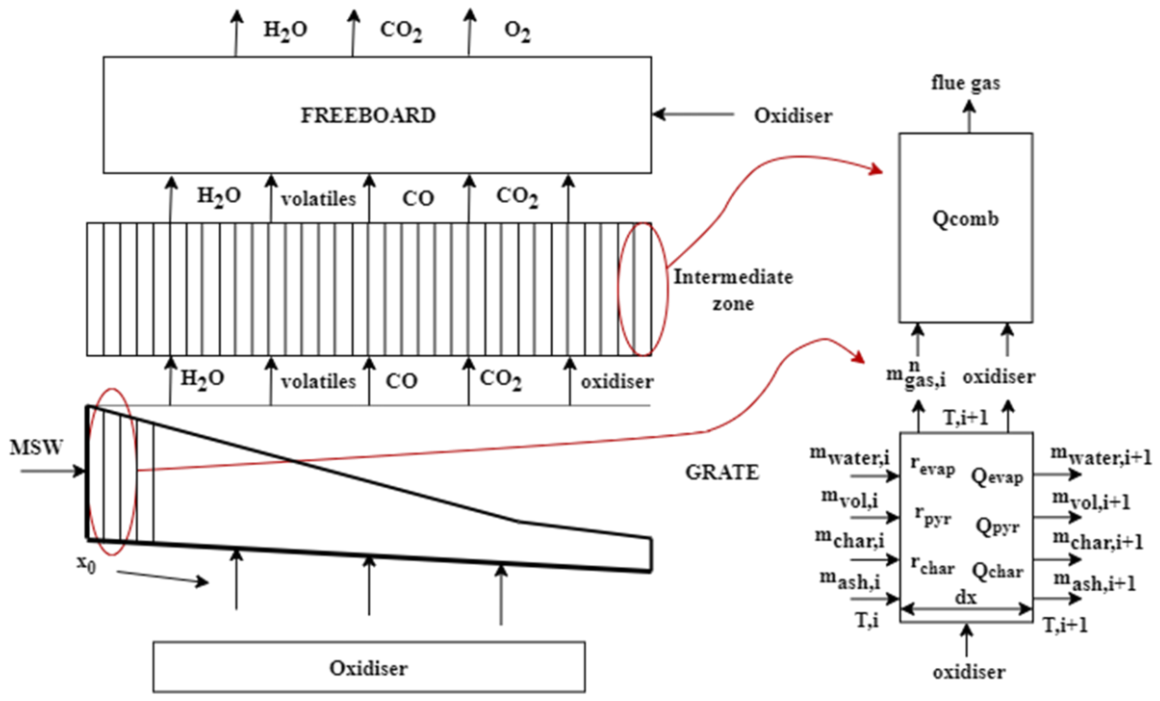

Fig. 3. Model of MSW combustion chamber.

- The modelled grate and intermediate zones are one-dimensional; the freeboard is modelled as 0D.
- Grate and intermediate zones are discretized in the direction of the moving grate as a series of control volumes. State variables within each control volume are homogeneous.
- Pyrolysis and char burnout that take place on the grate are taken into account based on one-step chemical kinetics.
- Combustion of volatiles and gases produced during char burnout that takes place over the grate is complete.

2.2. Materials

Municipal solid waste is a mixture of paper, plastic, food, textiles, tyres/rubber, glass and others. Determining the physicochemical properties of municipal solid waste is often problematic due to the high variability and heterogeneity of the feedstock [38]. The composition of waste varies depending on the level of gross domestic product (GDP) and the lifestyle of society, but may also vary depending on the season [7]. However, it can be assumed that the general properties of Europe's MSW are as follows: a) relatively high moisture content of 10–20%, b) high volatiles (VM) content at about 60–80% (dry basis), c) the ash fraction exceeding 10%, and d) fixed carbon (FC) level of about 10–20%. The average ultimate MSW composition can also be proposed (daf basis): 40–50% C; 25–35% O; 5–7% H; 0.5–2% N; 0.1–0.2% S; 0.1–0.2% Cl with a moisture content of 20–40% and an ash content of 15–30% [39].

In this study, we took the properties of waste, such as spent coffee grounds, described in detail in our previous study on kinetic analysis [20], but because the tested materials were dry, the amount of moisture was adjusted to match waste that is typically combusted in waste incineration plants. The proximate and ultimate analyses are presented in Table 1.

Table 1. Fuel composition.

Proximate analysis					
Moisture (ar, wt%)	Volatile matter (db, wt%)		Fixed carbon (db, wt%)		Ash (db, wt%)
20	57.77		7.62		34.61
Ultimate analysis (dry basis, wt%)					
LHV, kJ/kg	C	H	O	N	S
14 784	43.50	5.50	15.28	0.13	0.01

2.3. Mass and energy balances

The mass flow loss in each control volume is calculated as follows:

$$\frac{d\dot{m}_{tot,i}}{dx} = -k_j dt \dot{m}_{tot,i}, \quad (1)$$

where $d\dot{m}_{tot,i}$ is the mass flow loss of the fuel (kg/s), dx is the length of the control volume (m); k_j is the rate of the jth process (drying, pyrolysis, char burnout) (1/s); dt is the fuel residence time (s); described as

$$dt = \frac{dx}{v}, \quad (2)$$

where v is grate velocity (m/s).

The energy balance for the municipal solid waste bed is modelled as

$$\frac{\dot{m}_{tot,i} C_{tot,i} dT_i}{dx} = \dot{H}_{bed,i} - \dot{H}_{bed,i+1} + \dot{Q}_{rad,i} + \dot{H}_{ox,i}^{in,grate} - \dot{H}_{ox,i+1}^{out,grate} + \dot{Q}_{reac,i} - \dot{H}_{gas,i+1}^{out,grate}, \quad (2)$$

where $\dot{Q}_{rad,i}$ is the heat of radiation (kW/m), $\dot{H}_{ox,i}^{in,grate}$ and $\dot{H}_{ox,i+1}^{out,grate}$ denote the enthalpy flux of the oxidant at the inlet and outlet of the ith control volume (kW/m), respectively, $\dot{Q}_{reac,i}$ is the heat of the reactions (evaporation, pyrolysis, char oxidation) in the ith control volume (kW/m), $\dot{H}_{bed,i}$ and $\dot{H}_{bed,i+1}$ are the physical enthalpy fluxes of the solid bed at the inlet and outlet of the ith control volume (kW/m), respectively, $\dot{H}_{gas,i+1}^{out,grate}$ is the physical enthalpy of the gaseous phase escaping from the ith control volume (kW/m), and $\dot{m}_{tot,i}$ is defined as

$$\dot{m}_{tot,i} = \dot{m}_{water,i} + \dot{m}_{waste,i} + \dot{m}_{char,i} + \dot{m}_{ash,i}, \quad (4)$$

where $\dot{m}_{water,i}$, $\dot{m}_{waste,i}$, $\dot{m}_{char,i}$ and $\dot{m}_{ash,i}$ are the mass flow of the water, dry waste, char and ash in the solid bed, respectively. Parameters $c_{tot,i}$ (J/(kg K)) and T_i (K) denote specific heat capacity and temperature in the ith control volume, respectively.

2.3.1. Moisture evaporation zone

The rate of moisture release from solids can be expressed as [27,28,40]

$$r_{evp} = A_s h_s (C_{w,s} - C_{w,g}) \quad \text{when} \quad T_s < 100\ ^\circ\text{C} \quad (5)$$

or

$$r_{evp} = \frac{\dot{Q}_{rad}}{H_{evp}} \quad \text{when} \quad T_s \geq 100\ ^\circ\text{C}, \quad (6)$$

where H_{evp} is the heat of vaporisation of moisture contained in the solid (kJ/kg), h_s is the convective mass transfer coefficient (m/s), calculated according to [34], $C_{w,s}$ and $C_{w,g}$ is the moisture concentration in the solid phase and gas phase, respectively (kg/m^3), A_s is particle surface area (m^2), and Q_{rad} is radiation heat transfer (kW), and T_s is the temperature of the solid (°C).

2.3.2. Devolatilization zone

Pyrolysis is a crucial stage of combustion, where volatile compounds are released and the char is formed. Due to the complexity of the pyrolysis process, in this study, the devolatilization of waste is described by a one-step global reaction:

$$\text{MSW} \xrightarrow{r_{dev}} \text{char} + \text{volatiles}. \quad (7)$$

The rate constant of volatile release is taken from an Arrhenius type of expression:

$$k_{dev} = A_1 \exp\left(\frac{-E_1}{RT_{grate}}\right), \quad (8)$$

where A_1 is the pre-exponential factor or the frequency factor (1/s), E_1 is the energy activation (kJ/mol), and R is the universal gas constant (J/(mol K)). The data used for the calculation are presented in Table 3.

2.3.3 Char burnout zone

Due to the reactivity of CO_2 diluent, char combustion is influenced by various mechanisms, such as reduced oxygen mass transfer in CO_2, the lower temperature due to the higher heat capacity of CO_2 and the char-CO_2 gasification reactions [41]. In this study, the oxidizing (exothermic) reaction of char with oxygen is considered, in which CO_2 and CO are produced:

$$\mathrm{C} + \frac{1}{\theta}\mathrm{O_2} \xrightarrow{r_2} 2\left(1-\frac{1}{\theta}\right)\mathrm{CO} + \left(\frac{2}{\theta}-1\right)\mathrm{CO_2}, \quad (9)$$

where θ is the stoichiometric ratio for char oxidation defined as

$$\theta = \frac{1+\frac{1}{r_c}}{\frac{1}{2}+\frac{1}{r_c}}, \quad (10)$$

where r_c is the ratio of CO/CO_2 formation rate, which can be estimated by

$$r_c = \frac{\mathrm{CO}}{\mathrm{CO_2}} = 12\exp\left(-\frac{3300}{T_{char}}\right), \quad (11)$$

where T_{char} represents the char temperature.

The char reaction rate that can be generally expressed as [42]

$$k_i = \frac{k_{kin,i}k_{diff,i}}{k_{kin,i}+k_{diff,i}}, \quad (12)$$

where $k_{diff,i}$ is the coefficient of mass transfer for oxidizing and reductive reaction (kg/(m^{2}sPa), and

$$k_{kin,i} = A_{\mathrm{i}}\exp\left[\frac{-E_{\mathrm{i}}}{RT_{char}}\right] \quad (13)$$

is the kinetic rate constant for oxidizing and reductive reaction (kg/(m^{2}sPa)).

2.3.4. Intermediate zone – gaseous phase partial combustion

The energy balance of the intermediate zone is calculated as follows:

$$\frac{\dot{m}_{gas,i}c_{gas,i}dT_i}{dx} = \dot{H}_{ox,i}^{out,grate} + \dot{H}_{gas,i}^{out,grate} + \dot{Q}_{comb,i} - \dot{H}_{gas,i}^{out,intermediate\ zone}, \quad (14)$$

where $c_{gas,i}$ stands for the specific heat capacity of the gas produced in the *i*th control volume (J/(kg K)), $\dot{Q}_{comb,i}$ is the heat of partial combustion of volatiles and combustible gases (kW/m), $\dot{H}_{gas,i}^{out,intermediate\ zone}$ is the enthalpy of the produced gas at the outlet of the *i*th control volume (kW/m).

2.4. Heat transfer between solid and gaseous phases

Since high temperature occurs in the combustion chamber, this model assumes that radiation is the dominant heat transfer mechanism:

$$\dot{Q}_{rad,i} = \frac{\varepsilon_{bed}+1}{2}A\sigma\left(\varepsilon_{gas}T_{gas}^4 - \sigma_{gas}T_{bed}^4\right). \quad (15)$$

The emissivity ε_{bed} depends on the material, temperature and surface condition. In our simulations, we used a constant emissivity of ε_{bed} = 0.8 for waste bed, but different emissivities can be used for different fractions if data are available. In the above, A denotes surface (m^2), T_{gas} is the temperature of the freeboard (K), T_{bed} is the temperature of the grate (K), and σ is the Stefan-Boltzmann constant, $\sigma = 5.67\times10^{-8}$ W/(m^{2}K^4).

To calculate the radiative properties of gases in the furnace (ε_{gas} and α_{gas}), the weighted sum of the grey gases model (WSGGM) is used, which was introduced by Hottel and Sarofim [43] and due to its simplicity and relatively high accuracy, it was further developed and used by many researchers [38,44].

In the WSGG model, the Planck-mean absorption coefficient of the gas mixture over a path length is determined by [41,45]

$$\bar{a} = -\ln(1-\varepsilon/s), \quad (16)$$

where s is the radiation beam length, and ε the gas emissivity. The latter is calculated from

$$\varepsilon = \sum_i a_{\varepsilon,i}(T)(1-\exp(-\kappa_i p_i s)), \quad (17)$$

where $a_{\varepsilon,i}$ is the emissivity weighting factor for the *i*th grey gas component, κ_i and p_i are the pressure absorption coefficient (1/m·atm) and partial pressure (atm) of the *i*th absorbing gas, respectively.

The emissivity weighting factors are polynomial correlations that can be given as a function of the gas temperature:

$$a_{\varepsilon,i} = \sum_j b_{\varepsilon,i,j}T^{j-1}. \quad (18)$$

It should be noted that most of the already established coefficients of WSGGM are suitable only for the air-fired combustion conditions, where the molar fractions ratio of carbon dioxide and water vapour differs from oxy-fuel combustion, and using them in the oxy-fired conditions may lead to uncertain levels of inaccuracy. Therefore, with the growing popularity of oxygen-fired systems, some scientists have expanded the set of coefficients with those dedicated to oxy-fuel combustion, for example, in [45,46].

3. Calculation data

Physical data and process data (Table 2) of the full-scale incineration plant were provided by the Returkraft WtE plant in Kris-

Table 2. Physical and process data.

Parameter	Unit	Value
Grate length	m	10.2
Grate width	m	6.3
Height to the top of 1st pass	m	19.15
Waste throughput capacity	t/h	18
Primary air distribution (5 zones) (air-fired mode)	%	8 – 29 – 37 – 23 – 3
Primary air temperature	°C	110
Primary air flow rate	m_n^3/h	53669
Secondary air temperature	°C	110
Secondary air flow rate	m_n^3/h	39945
Grate speed	m/s	0.002
Oxidiser composition (air-fired mode)	vol. %	21% O_2 – 79% N_2
Relative humidity	%	95
Oxidiser composition (oxy-fired mode)	vol. %	95% O_2 – 5% N_2
Wet recirculated flue gas composition (oxy-fired mode)	mol %	55.5% CO_2 – 27.7% H_2O – 12.2% O_2 - 4.4% N_2
Flue gas molar flow	kmol/s	0.9429

tiansand (Norway). A description of the waste incineration process at the studied plant is available in [38].

As mentioned earlier, in this study individual steps of the fuel thermal decomposition were taken into account based on chemical kinetics. To determine the kinetic parameters of waste materials, an experimental campaign on the thermogravimetric instrument and lab-scale reactor was performed. Firstly, we performed the TGA analysis of sample pyrolysis in N_2 and CO_2 atmospheres and retrieved the kinetic data, employing isoconversional methods, also known as model-free (Friedman and Vyazovkin). According to the isoconversional principle, the process rate at a constant extent of conversion α is a function of temperature [47]. Then, we used a lab-scale reactor to produce waste chars and we subjected them to thermogravimetric analysis in air and oxy-fired conditions. These studies were in detail described in our previous works [20,21]. Table 3 shows the kinetic data used in the mathematical model in the air- and oxy-fired modes.

Other calculation data, such as, the physical properties of used waste used in the model are summarized in Table 4.

For the simulation of the waste combustion system, MATLAB software was used. The equations were solved using Newton-Raphson method and a mesh array of 10200 was employed.

Table 3. Kinetic data used in the mathematical model in the air- and oxy-fired mode.

Parameter	Unit	Value
$A_{dev,air}$	1/s	$10^{17.7}$
$E_{dev,air}$	kJ/mol	232100
$A_{dev,oxy}$	1/s	$10^{21.3}$
$E_{dev,oxy}$	kJ/mol	274700
$A_{char,air}$	1/s	$10^{4.79}$
$E_{char,air}$	kJ/mol	104372
$A_{char,oxy}$	1/s	136.56
$E_{char,oxy}$	kJ/mol	72137

4. Results and discussion

In the study, firstly simulations of the incineration chamber in the air-fired mode were performed, using assumptions and equations presented in Section 2 and input data presented in Section 3. The results of these calculations, such as the temperature of the grate and intermediate zone, as well as the mass flow of waste as a function of grate length, together with the model verification, are provided as a 'reference' and presented in Section 4.1. Validated model was then modified to the oxy-fired mode using the input data from Section 3. The results of the analysis of oxy-fired system are presented in Section 4.2.

4.1. Reference simulation and comparison with process data

Figure 4a presents the temperature of the grate and intermediate zone, as well as the fuel mass flow as a function of grate length. As can be observed, fuel combustion on the grate occurs gradually. Firstly, the fuel heats up and dries (Zone I), then when the grate reaches a temperature of around 450°C, volatiles are released. The drying and pyrolysis processes end at a distance of 2 m of the grate. Directly above the grate, in the intermediate zone, the volatiles partially burn, releasing heat and causing temperature growth up to 2000 K (Zone II). After the pyrolysis process, the waste char begins to slowly oxidize, and over the grate length of 8 m the fuel is burned out (Zones III and IV). In the fifth zone, the air mass flow is reduced and only ash remains. Similar findings regarding weight loss on the grate, burnout and grate temperatures have been found in the literature [27,28,30,38]. The different zones shown in Fig. 4a correspond to the air distribution according to data obtained from an incinerator in Norway (Table 2).

Figure 4b presents the molar fractions of gas species in the intermediate zone. As can be seen, oxygen quickly drops from 21% to below 1%, meaning that it is consumed during most of the process on the grate, which indicates that locally the air-lean (or fuel-rich) conditions dominate the bed combustion processes [33]. After the complete combustion of the fuel, the intermediate

Table 4. Physical properties of waste used in the model [24,27,29].

Parameter	Unit	Value
Heat capacity of water, c_{water}	kJ/kgK	4.187
Heat capacity of dry waste, c_{waste}		1.5+0.001T
Heat capacity of char, c_{char}		0.44+0.001T^{-7}×10^{-8} T^2
Heat capacity of ash, c_{ash}		0.8
Bed emissivity, ε_{bed}	–	0.8
Gas emissivity (air-fired system), $\varepsilon_{gas,air}$	–	0.4143
Gas emissivity (oxy-fired system), $\varepsilon_{gas,oxy}$	–	0.4816

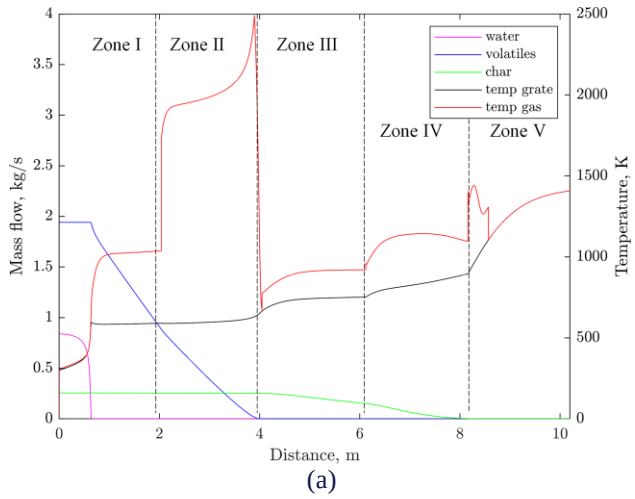

Fig. 4.(a) Temperature of the grate and intermediate zone and the mass flow of the fuel as a function of grate length; (b) Molar fractions of gas species in the intermediate zone.

zone is filled only with air. Results indicate that during the char oxidation CO_2 generation is more intensive. The produced carbon monoxide will be further combusted in the intermediate zone above the grate generating heat. Nevertheless, it is worth mentioning that in the char burnout zone, the temperature should not exceed 800°C due to the presence of organics in the waste, such as plant residues and food leftovers with a very low ash melting point temperature of around 825°C [48].

Figure 5 presents a comparison of the temperature of the

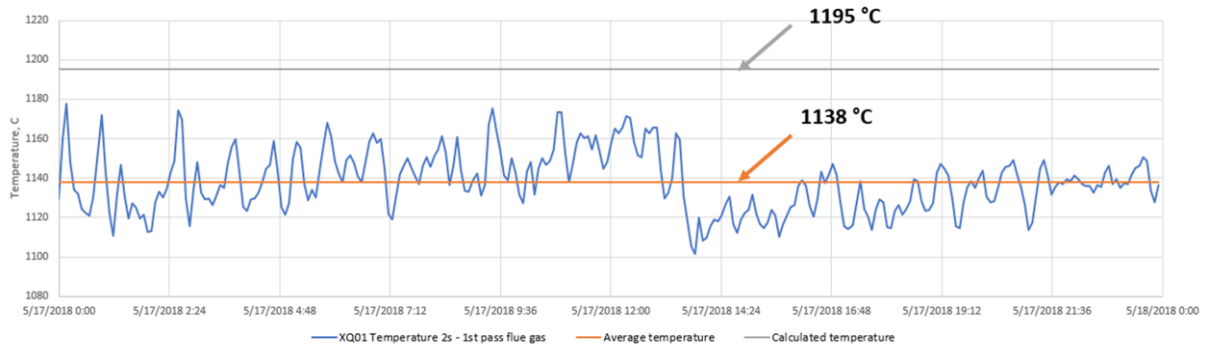

Fig. 5. Comparison between real temperature in the furnace (freeboard zone) and simulation results (WtE Returkraft plant data).

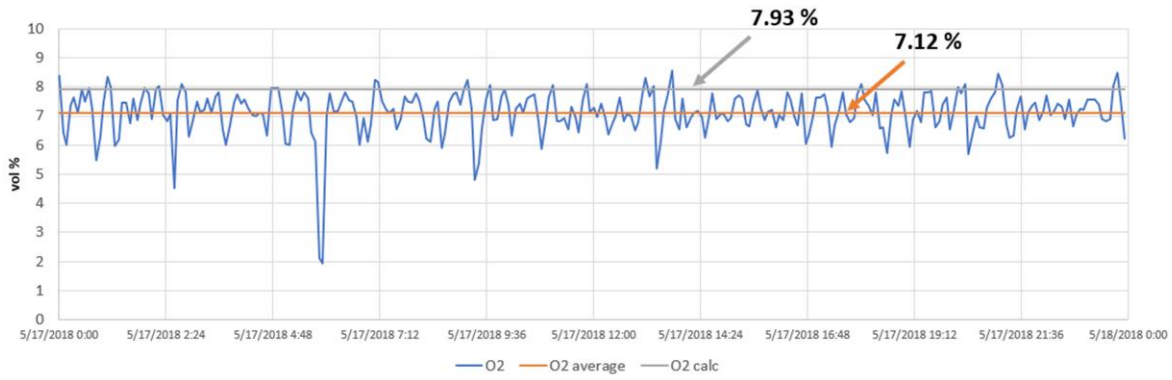

Fig. 6. Comparison between the measured and simulated oxygen content in the flue gas at the outlet (WtE Returkraft plant data).

freeboard between the air-fired model and the measurements (with the calculated average value) in the incineration plant. Figure 6 shows measurements and the calculated value of the oxygen content in the flue gas at the outlet. The relative difference between the calculated and measured values of temperatures and oxygen content is 4.8% and 10.2%, respectively. Thus, it was found that the air-fired model was sufficiently accurate and work on the model in the oxy-combustion mode began.

4.2. Oxy-combustion model

This section presents the results of simulations of the oxy-waste combustion chamber. To assess the influence of different factors, such as flue gas recirculation ratio, oxygen distribution, and oxidizer temperature, three different cases were studied:

1) The first one involved introducing oxygen into the combustion chamber in a sub-stoichiometric amount (λ equal to 0.52), along with recirculated exhaust gas in the ratio of 15, 20, and 25%.
2) The second one comprised checking the influence of oxidant distribution. This was achieved by first supplying recirculated flue gas to the combustion chamber, and only after the volatiles have been released, introducing oxygen (in the amount as in the first case).
3) In the third case, the most favourable oxygen distribution was taken (determined from the previous cases) and the influence of 3 different oxidant temperatures on the process was checked.

4.2.1. Effect of the flue gas recirculation

Oxy-fuel combustion changes many parameters inside the furnace due to the change in overall thermal environment in the furnace. A major effect is visible on temperature distribution which happens due to CO_2 rich combustion environment. Figure 7 presents the radiative heat transfer between gas and solid phase for air- and oxy-fired conditions. As can be observed, oxy-fired system is characterized by higher radiative heat flux than combustion in an air atmosphere, which can be also observed in other comparative studies on air- and oxy-fired systems [41,49].

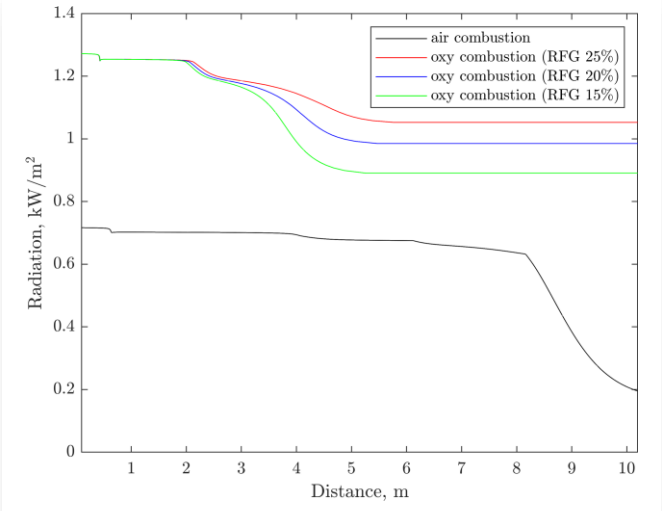

Fig. 7. Radiative heat transfer for air- and oxy-fired system.

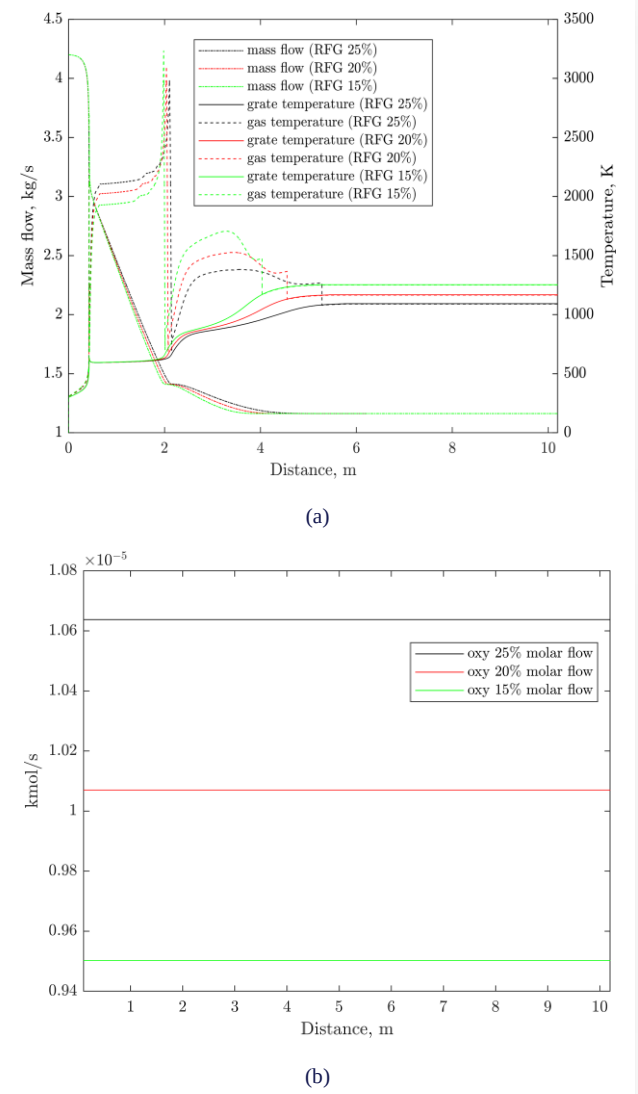

Fig. 8. a) Temperature of the grate and intermediate zone, and the mass flow of the fuel as a function of grate length; b) Oxidant distribution along the grate.

Figure 8 shows temperatures of the grate and intermediate zone, as well as the mass flow of waste as a function of grate length. As can be observed, the higher the degree of flue gas recirculation, the lower the temperature of the grate and the intermediate zone, which confirms that recirculation can effectively control the temperature in the combustion chamber. The reason for this is the change in the environment of the furnace, as the CO_2 and H_2O contained in flue gas have a different specific heat capacity than N_2. The increased amount of recycled flue gas decreases the temperature of the process [36,50].

The next finding obtained in this research is that using oxygen during waste combustion raises the temperature and speeds up the process. For instance, combustion ends at 4 m for a recirculation rate of 15%, at 4.5 m for a 20% rate, and at 5.5 m for

Table 5. Oxygen demand for different oxy-fired conditions.

Parameter	Unit	Value		
RFG ratio	%	15	20	25
Total oxygen demand	kmol/s	0.0969	0.1027	0.1085
Oxygen from ASU	kmol/s	0.0795		
Share of oxygen in the oxidant	%	33	37	43

25%. This means that, in addition to the lower exhaust gas volume and thus, smaller equipment used for flue gas cleaning (as discussed in Section 1), the size of the combustion chambers operating under oxy-fuel conditions may be lowered by 30–50% when compared to the conventional mode of combustion.

The oxygen needed to complete the oxy-waste combustion process (total and oxygen produced in ASU) is compiled in Table 5. A larger flue gas recirculation (RFG) ratio corresponds with a higher oxygen content in the oxidiser. This is because components that oxidize, like oxygen, carbon dioxide, and water vapour, are present in the recirculated gases. Additionally, the percentage of oxygen in the oxidant was determined for each case and ranged from 33% to 43%.

Nevertheless, we found that temperature in the intermediate zone can exceed as much as 3000 K, when the volatiles are partially combusted, and the temperature at the grate can exceed the temperature of the waste ash melting point. Thus we analysed the second case, in which we limited the oxygen supply only to char oxidation zone. The drying and devolatilization processes were carried out in the atmosphere of recycled flue gases (with ratios of 15, 20 and 25%).

4.2.2. Effect of oxygen distribution

Analogous to the previous results, Fig. 9 shows a comparison of radiative heat transfer between air- and oxy-fired conditions for different ratios of flue gas recirculation. The oxygen share in the oxidant for each case was equal to 25%. It can be observed that

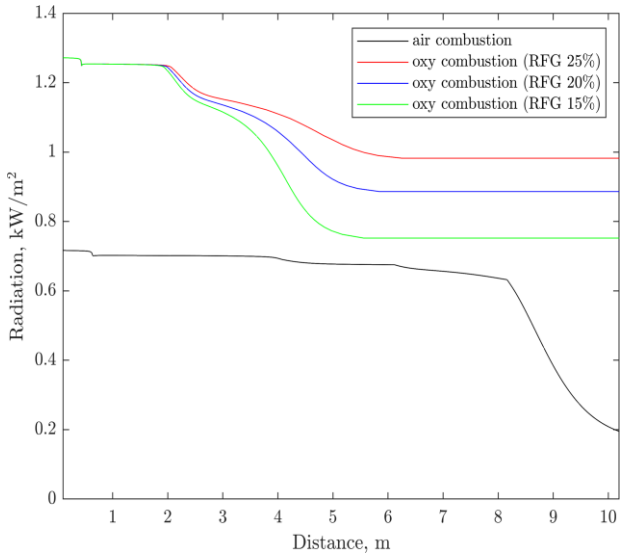

Fig. 9. Radiative heat transfer for air- and oxy-fired system.

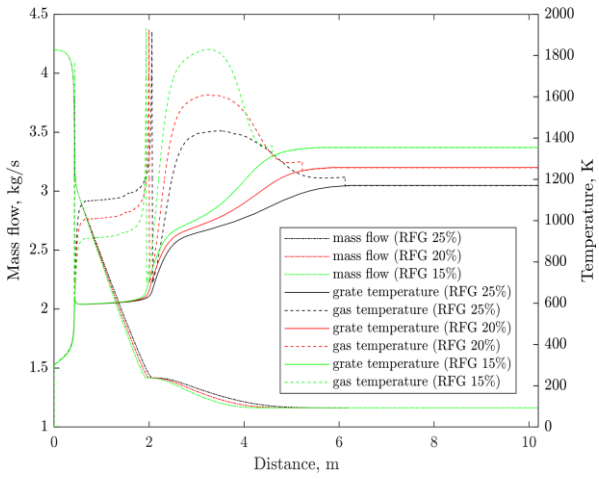

(a)

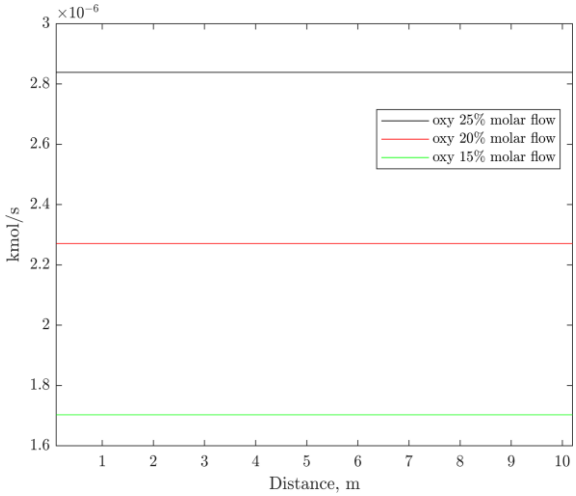

(b)

Fig. 10. a) Temperature of the grate and intermediate zone, and the mass flow of the fuel as a function of grate length; b) Oxidant distribution along the grate.

the radiative heat transfer profile for the oxy-fired system in this case is more similar to air combustion than that predicted in the first studied case (compare to Fig. 7). Similarly, Figure 10 displays the temperature of the grate and intermediate zone, and the mass flow of waste as a function of grate length for considered ratios of flue gas recirculation. The results imply that the use of recirculated flue gas for evaporation and pyrolysis processes is feasible. Limiting oxygen slightly extends the process and significantly decreases the temperature in the combustion chamber.

Regarding the oxygen demand in the second case studied, the required amount of oxygen in the process decreased significantly, as shown in Table 6. This results in a lower consumption of electricity to power the air separation unit, which is employed to produce pure oxygen. As various studies have shown [7,51], the ASU is the most energy-intensive device in the oxy-fuel combustion systems. Therefore, in studies on oxy-waste incineration, the key parameter that will allow the selection of the optimal oxidant distribution strategy should be the oxygen demand.

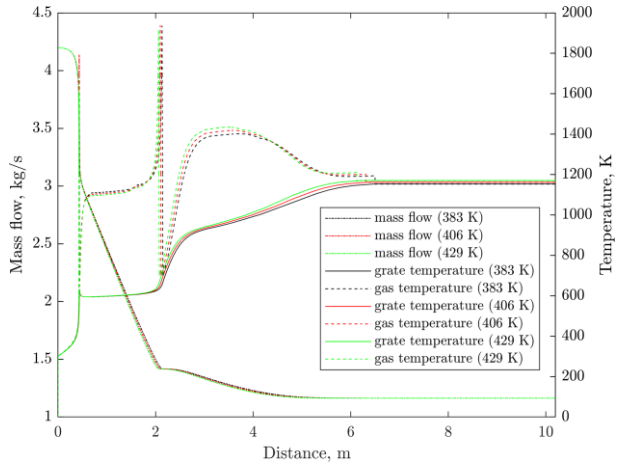

Fig. 11. Temperature of the grate and intermediate zone and the mass flow of the fuel as a function of grate length.

4.2.3. Effect of oxidizer temperature

In the last case, we analysed the influence of the oxidizer temperature on the process. We selected the conditions used in the second case (with the 25% of recirculated flue gas) and investigated three different temperatures of 383 K, 406 K and 429 K. The results presented in Fig. 11 indicate that the temperature of the oxidiser does not affect the process significantly.

5. Conclusions

This study presents the first attempt at mathematical modelling of real-scale oxy-waste incineration, which is a scientific novelty of this work. As a result, the 1D model of oxy-MSW combustion in a grate furnace is developed and analysed. The processes that were considered on the grate comprised waste drying, pyrolysis, the heterogeneous reactions of char and O_2/CO_2, based on the chemical kinetics, as well as homogeneous reactions between gases in the intermediate zone (above the grate). Besides, heat and mass transfer between the gas and solid phases are comprised.

The presented results showed that combustion parameters such as temperature and the duration of the process highly depend on oxidant composition:

- Increased content of oxygen in the supplied gas shortens the combustion process by around 30–50%.
- Increased content of oxygen elevates the temperature in the gaseous reactions area.
- Increased content of oxygen elevates the temperature in the grate.

Table 6. Oxygen demand for different oxy-fired conditions.

Parameter	Unit	Value		
RFG ratio	%	15	20	25
Total oxygen demand	kmol/s	0.0290	0.0232	0.0174
Share of oxygen in the oxidant	%	25		

- The study also confirmed that flue gas recirculation effectively control the temperature of the process.
- Moreover, the results indicate that the use of recirculated exhaust gases as an oxidant is sufficient for the drying and pyrolysis process.

Thus, oxy-fuel combustion of waste in a grate furnace can provide improved burnout and higher temperature with a sustainable 'CO_2-less' thermal conversion of fuel.

Results will be useful especially for the design purposes of the oxy-MSW combustion process since they show the duration of the various stages of waste incineration, the amount and composition of the obtained products, as well as the approximate temperature of the gaseous and solid phases depending on the used oxidant.

Acknowledgements

This research is supported by the National Science Centre (Project no. UMO-2021/41/N/ST8/02548) and Ministry of Education and Science (Poland) under statutory research funds of the Faculty of Energy and Environmental Engineering of SUT (08/060/RGZ200275-24). The work of MD is supported by the CLIMIT program of the Research Council of Norway (Grants number 281869 and 305062).
I would like to acknowledge the WtE Returkraft plant for providing the operational data.

References

[1] Kaza, S., Yao, L., Bhada-Tata, P., & Van Woerden, F. (2018). *What a Waste 2.0: A Global Snapshot of Solid Waste Management to 2050*. World Bank Publications.

[2] Cucchiella, F., D'Adamo, I., & Gastaldi, M. (2017). Sustainable waste management: Waste to energy plant as an alternative to landfill. *Energy Conversion and Management*, 131, 18–31. doi: 10.1016/j.enconman. 2016.11.012

[3] Kumar, A., & Samadder, S.R. (2017). A review on technological options of waste to energy for effective management of municipal solid waste. *Waste Management*, 69, 407–422. doi: 10.1016/ j.wasman.2017.08.046

[4] Makarichi, L., Jutidamrongphan, W., & Techato, K. (2018). The evolution of waste-to-energy incineration: A review. *Renewable and Sustainable Energy Reviews*, 91, 812–21. doi: 10.1016/j.rser. 2018.04.088

[5] Pour, N., Webley, P.A., & Cook, P.J. (2018). Potential for using municipal solid waste as a resource for bioenergy with carbon capture and storage (BECCS). *International Journal of Greenhouse Gas Control*, 68, 1–15. doi: 10.1016/j.ijggc.2017. 11.007

[6] Tanze, S.E., Blok, K., & Ramírez, A. (2021). Decarbonising industry via BECCS: Promising sectors, challenges, and techno-economic limits of negative emissions. *Current Sustainable Renewable Energy Reports*, 8, 253–262. doi: 10.1007/s40518-021-00195-3

[7] Wienchol, P., Szlęk, A., & Ditaranto, M. (2020). Waste-to-energy technology integrated with carbon capture – Challenges and opportunities. *Energy*, 198, 117352. doi: 10.1016/j.energy.2020. 117352

[8] Buhre, B.J.P., Elliott, L.K., Sheng, C.D., Gupta, R.P., & Wall, T.F. (2005). Oxy-fuel combustion technology for coal-fired power generation. *Progress in Energy and Combustion Science*, 31(4), 283–307. doi: 10.1016/ j.pecs.2005.07.001

[9] Toftegaard, M.B., Brix, J., Jensen, P.A., Glarborg, P., & Jensen, A.D. (2010). Oxy-fuel combustion of solid fuels. *Progress in*

Energy and Combustion Science, 36, 581–625. doi: 10.1016/ j.pecs.2010.02.001

[10] Ding, G., He, B., Cao, Y., Wang, C., Su, L., Duan, Z., Song, J., Tong, W., & Li, X. (2018). Process simulation and optimization of municipal solid waste fired power plant with oxygen/carbon dioxide combustion for near zero carbon dioxide emission. *Energy Conversion and Management*, 157, 157–168. doi: 10.1016/j.enconman. 2017.11.087

[11] Tang, Y.T., Ma, X.Q., Lai, Z.Y. & Chen, Y. (2013). Energy analysis and environmental impacts of a MSW oxy-fuel incineration power plant in China. *Energy Policy*, 60, 132–141. doi: 10.1016/j.enpol.2013.04.073

[12] Vilardi, G., & Verdone, N. (2022). Exergy analysis of municipal solid waste incineration processes: The use of O_2-enriched air and the oxy-combustion process. *Energy*, 239(B), 122147. doi: 10.1016/j.energy. 2021.122147

[13] Scheffknecht, G., Al-Makhadmeh, L., Schnell, U., & Maier, J. (2011). Oxy-fuel coal combustion — A review of the current state-of-the-art. *International Journal of Greenhouse Gas Control*, 5(1) 16–35. doi: 10.1016/ j.ijggc.2011.05.020

[14] Kosowska-Golachowska, M., Kijo-Kleczkowska, A., Luckos, A., Wolski, K., & Musiał, T. (2016). Oxy-combustion of biomass in a circulating fluidized bed. *Archives of Thermodynamics*, 37(1), 17–30. doi: 10.1515/aoter-2016-0002

[15] Kindra, V.O., Milukov, I.A.Shevchenko, I.V., Shabalova, S.I., & Kovalev, D.S. (2021). Thermo-dynamic analysis of cycle arrangements of the coal-fired thermal power plants with carbon capture. *Archives of Thermodynamics*, 42(4), 103–121. doi: 10.24425/ather. 2021.139653

[16] Lai, Z.Y., Ma, X.Q., Tang, Y.T., & Lin, H. (2011). A study on municipal solid waste (MSW) combustion in N_2/O_2 and CO_2/O_2 atmosphere from the perspective of TGA. *Energy*, 36(2), 819–824. doi: 10.1016/j.energy. 2010.12.033

[17] Tang, Y., Ma, X., Lai, Z., & Fan, Y. (2015). Thermogravimetric analyses of co-combustion of plastic, rubber, leather in N_2/O_2 and CO_2/O_2 atmospheres. *Energy*, 90(1), 1066–1074. doi: 10.1016/ j.energy.2015.08.015

[18] Lai, Z.Y., Ma, X.Q., Tang, Y.T., Lin, H., & Chen, Y. (2012). Thermogravimetric analyses of combustion of lignocellulosic materials in N_2/O_2 and CO_2/O_2 atmospheres. *Bioresource Technology*, 107, 444–450. doi: 10.1016/j.biortech.2011.12.039

[19] Tang, Y., Ma, X., Lai, Z., Zhou, D., & Chen, Y. (2013). Thermo-gravimetric characteristics and combustion emissions of rubbers and polyvinyl chloride in N_2/O_2 and CO_2/O_2 atmospheres. *Fuel*, 104, 508–514. doi: 10.1016/j.fuel.2012. 06.047

[20] Wienchol, P., Korus, A., Szlęk, A., & Ditaranto, M. (2022). Thermogravimetric and kinetic study of thermal degradation of various types of municipal solid waste (MSW) under N_2, CO_2 and oxy-fuel conditions. *Energy*, 248, 123573. doi: 10.1016/j.energy. 2022.123573

[21] Copik, P., Korus, Szlęk, A., & Ditaranto, M. (2023). A comparative study on thermochemical decomposition of lignocellulosic materials for energy recovery from waste : Monitoring of evolved gases, thermogravimetric, kinetic and surface analyses of produced chars. *Energy*, 285, 129328. doi: 10.1016/j.energy. 2023.129328

[22] Becidan, M., Ditaranto, M., Carlsson, P., Bakken, J., Olsen, M.N.P., & Stuen, J. (2021). Oxyfuel combustion of a model MSW – An experimental study. *Energies*, 14 (17), 5297. doi: 10.3390/en14175297

[23] Mack, A., Maier, J., & Scheffknecht, G. (2022). Modification of a 240 kW_{th} grate incineration system for oxyfuel combustion of wood chips. *Journal of the Energy Institute*, 104, 80–88. doi: doi: 10.1016/j.joei. 2022.07.011

[24] Shin, D., & Choi, S. (2000). The combustion of simulated waste particles in a fixed bed. *Combustion and Flame*, 121(1-2), 167–180. doi: 10.1016/S0010-2180(99)00124-8

[25] Yang, W., Ryu, C., & Choi, S. (2004). Unsteady one-dimensional model for a bed combustion of solid fuels. *Proceedings of the Institution of Mechanical Engineers, Part A: Journal of Power and Energy*, 218(8), 589–598. doi: 10.1243/0957650042584348.

[26] Zhou, H., Jensen, A.D., Glarborg, P., Jensen, P.A., & Kavaliauskas, A. (2005). Numerical modeling of straw combustion in a fixed bed. *Fuel*, 84(4), 389–403. doi: 10.1016/ j.fuel.2004.09.020

[27] Gu, T., Yin, C., Ma, W., & Chen, G. (2019). Municipal solid waste incineration in a packed bed: A comprehen-sive modeling study with experimental validation. *Applied Energy*, 247, 127–39. doi: 10.1016/j.apenergy. 2019.04.014

[28] Hoang, Q.N., Van Caneghem, J., Croymans, T., Pittoors, R., & Vanierschot, M. (2022). A novel comprehensive CFD-based model for municipal solid waste incinerators based on the porous medium approach. *Fue*l, 326, 124963. doi: doi: 10.1016/j.fuel. 2022.124963

[29] Wissing, F., Wirtz, S., & Scherer, V. (2017). Simulating municipal solid waste incineration with a DEM/CFD method – Influences of waste properties, grate and furnace design. *Fuel*, 206, 638–656. doi: 10.1016/j.fuel. 2017.06.037

[30] Yang, Y.B., Yamauchi, H., Nasserzadeh, V., & Swithenbank, J. (2003). Effects of fuel devolatilisation on the combustion of wood chips and incineration of simulated municipal solid wastes in a packed bed. *Fuel*, 82(18), 2205–2221. doi: 10.1016/S0016-2361(03) 00145-5

[31] Sun, R., Ismail, T.M., Ren, X., & Abd El-Salam, M. (2015). Numerical and experimental studies on effects of moisture content on combustion characteristics of simulated municipal solid wastes in a fixed bed. *Waste Management*, 39, 166–178. doi: 10.1016/j.wasman. 2015.02.018

[32] Xia, Z., Long, J., Yan, S., Bai, L., Du, H., & Chen, C. (2021). Two-fluid simulation of moving grate waste in-cinerator: Comparison of 2D and 3D bed models. *Energy*, 216, 119257. doi: 10.1016/j.energy.2020. 119257

[33] Yu, Z., Ma, X., & Liao, Y. (2010). Mathematical modeling of combustion in a grate-fired boiler burning straw and effect of operating conditions under air- and oxygen-enriched atmospheres. *Renewable Energy*, 35(5), 895–903. doi: 10.1016/ j.renene.2009.10.006

[34] Khodaei, H., Al-Abdeli, Y.M., Guzzomi, F., & Yeoh, G.H. (2015). An overview of processes and considerations in the modelling of fixed-bed biomass combustion. *Energy*, 88, 946–972. doi: 10.1016/j.energy.2015.05. 099

[35] Hoang, Q.N., Vanierschot, M., Blondeau, J., Croymans, T., Pittoors, R., & Van Caneghem, J. (2021). Review of numerical studies on thermal treatment of municipal solid waste in packed bed combustion. *Fuel Communications*, 7, 100013. doi: 10.1016/ j.jfueco. 2021.100013

[36] Karim, R., Ahmed, A., Alhamid, A., Sarhan, R., & Naser, J. (2020). CFD simulation of biomass thermal conversion under air/oxy-fuel conditions in a reciprocating grate boiler. *Renewable Energy*, 146, 1416–1428. doi: 10.1016/j.renene. 2019.07.068

[37] Yang, Y.B., Goh, Y.R., Zakaria, R., Nasserzadeh, V., & Swithenbank, J. (2002). Mathematical modelling of MSW incineration on a travelling bed. *Waste Management*, 22(4), 369–380. doi: 10.1016/S0956-053X(02)00019-3

[38] Magnanelli, E., Tranås, O.L., Carlsson, P., Mosby, J., & Becidan, M. (2020). Dynamic modeling of municipal solid waste incineration. *Energy*, 209, 118426. doi: 10.1016/j.energy.2020. 118426

[39] Becidan, M. (2007). *Experimental studies on municipal solid*

waste and biomass pyrolysis. PhD thesis, Norwegian University of Science and Technology, Trondheim.

[40] Ismail, T.M., Abd El-Salam, M., El-Kady, M.A., & El-Haggar, S.M. (2014). Three dimensional model of transport and chemical late phenomena on a MSW incinerator. *International Journal of Thermal Sciences*, 77, 139–157. doi: 10.1016/j.ijthermalsci. 2013.10.019

[41] Chen, L., Yong, S.Z., & Ghoniem, A.F. (2012). Oxy-fuel combustion of pulverized coal: Characterization, fundamentals, stabilization and CFD modeling. *Progress in Energy and Combustion Science*, 38(2), 156–214. doi: 10.1016/j.pecs.2011. 09.003

[42] Toporov, D.D. (2015). *Combustion of pulverised coal in a mixture of oxygen and recycled flue gas*. Elsevier. doi: 10.1016/C2013-0-19301-4

[43] Hottel H.C., & Sarofim, A.F. (1967). *Radiative transfer*. McGraw-Hill, New York.

[44] Sadeghi, H., Hostikka, S., Crivelli, G., & Bordbar, H. (2021). Weighted-sum-of-gray-gases models for non-gray thermal radiation of hydrocarbon fuel vapors, CH_4, CO and soot. *Fire Safety Journal*, 125, 103420. doi: 10.1016/j.firesaf.2021.103420

[45] Bordbar, M.H., Wecel, G., & Hyppänen, T. (2014). A line by line based weighted sum of gray gases model for inhomogeneous CO_2-H_2O mixture in oxy-fired combustion. *Combustion and Flame*, 161(9), 2435–2445. doi: 10.1016/j.combustflame.2014. 03.013

[46] Alberti, M., Weber, R., & Mancini, M. (2020). New formulae for gray gas absorptivities of H_2O, CO_2, and CO. *Journal of Quantitative Spectroscopy and Radiative Transfer*, 255, 107227. doi: 10.1016/j.jqsrt. 2020.107227

[47] Vyazovkin, S. (2015). *Isoconversional kinetics of thermally stimulated processes*. Springer.

[48] Butmankiewicz, T., Dziugan, P., Kantorek, M., Karcz, H., & Wierzbicki, K. (2012). Thermal disposal of municipal waste on a grid - is it a proper technology? *Archives of Waste Management and Environmental Protection*, 14(2), 13–28 (in Polish). https://bibliotekanauki.pl/articles/357104

[49] Smart, J.P., Patel, R., & Riley, G.S. (2010). Oxy-fuel combustion of coal and biomass, the effect on radiative and convective heat transfer and burnout. *Combustion and Flame*, 157(12), 2230–2240. doi: 10.1016/ j.combustflame. 2010.07.013

[50] Mureddu, M., Dessì, F., Orsini, A., Ferrara, F., & Pettinau, A. (2018). Air- and oxygen-blown characterization of coal and biomass by thermogravimetric analysis. *Fuel*, 212, 626–637. doi: 10.1016/j.fuel. 2017.10.005

[51] Skorek-Osikowska, A., Bartela, Ł., & Kotowicz, J. (2015). A comparative thermodynamic, economic and risk analysis concerning implementation of oxy-combustion power plants integrated with cryogenic and hybrid air separation units. *Energy Conversion and Management*, 92, 421–430. doi: 10.1016/ j.enconman.2014.12.079

Co-published by
Institute of Fluid-Flow Machinery
Polish Academy of Sciences
Committee on Thermodynamics and Combustion
Polish Academy of Sciences

http://www.imp.gda.pl/archives-of-thermodynamics/

Use of butanol, pentanol and diesel in a compression ignition engine: A review

Deepak Kumar[a*], Naveen Kumar[b], Rajiv Chaudhary[a]

[a]Department of Mechanical Engineering, Delhi Technological University, New Delhi, India, 110042
[b]Centre for Advanced Studies and Research in Automotive Engineering, Delhi Technological University, Delhi, India, 110042
*Corresponding author, kumar.deepak2501@gmail.com

Received: 12.07.2023; revised: 07.07.2024; accepted: 16.07.2024

Abstract

Using oxygenated alternative fuels in compression ignition (CI) engines is feasible for energy security problems and climate change. Alcohols are regarded as alternative fuels for compression ignition engines because of their excellent physicochemical features, emission, and combustion characteristics. Research on alcohols and their additions has progressed significantly in recent years. Several researchers have examined the combined effect of higher alcohol with diesel and their impact and challenged that concentrations of higher alcohol reduce harmful particulate emissions in CI engines. This paper mainly focused on the performance and emissions properties of higher alcohols like butanol and pentanol. Alcohol has a low energy content, typically affecting engine brake-specific fuel consumption (BSFC). Low-temperature combustion (LTC) in compression ignition engines can lower NO_x and smoke emissions, and improve the efficiency of the engine. LTC is done by combining higher alcohol with increased exhaust gas recirculation (EGR) rate and retarded fuel injection timing. The higher alcohol, along with the oxygen in the fuel reduces exhaust fumes, improves the air/fuel mixture by providing a longer ignition delay (ID), and can replace the fossil fuel like diesel (partially or whole) to allow efficient and clean combustion in CI engines. Finally, several significant findings and comments are provided regarding potential avenues for experimental research and future development. According to thorough analysis, bio-alcohols are considered to be a substitute fuel for CI engines.

Keywords: Diesel engines, Higher alcohol, Diesel, Butanol, Pentanol

Vol. 45(2024), No. 4, 27–35; doi: 10.24425/ather.2024.151994

Cite this manuscript as: Kumar, D., Naveen Kumar, N., & Chaudharya, R. (2024). Use of butanol, pentanol and diesel in a compression ignition engine: A review. *Archives of Thermodynamics*, 45(4), 27–35.

1. Introduction

The application of alternative fuels in the transportation and power-generating industries used in compression ignition (CI) engines is becoming increasingly significant [1]. This requirement becomes necessary because of two issues: decreased oil reserves, price instability, and emission regulations for human health and environmental preservation [2].

The petroleum industry is a crucial sector of the Indian economy, accounting for about 25% of the country's total energy consumption. However, India remains heavily reliant on imports to meet its domestic demand for crude oil, with nearly 80% of its crude oil requirements being imported [3]. India's oil demand is projected to rise from the current 4.7 million barrels per day (mb/d) to 6.7 mb/d in 2030 and 8.3 mb/d in 2050 [4]. Despite the high efficiency of CI engines, the primary pollutants emitted from diesel fuel are HC, NO_x, and CO [5].

Nomenclature

ABE – acetone-*n*-butanol-ethanol
ABED – ABE/diesel blends
BSFC – brake-specific fuel consumption
BTE – brake thermal efficiency
CI – compression-ignition
CN – cetane number
CO – carbon monoxide
CO_2 – carbon dioxide
CRDI – common rail direct injection
CV – calorific value
DI – direct injection
EGR – exhaust gas recirculation
HC – hydrocarbon
HCCI – homogeneous charge compression ignition
HRR – heat-release-rate
LHE – latent heat of evaporation
LHV – lower heating value
LTC – low-temperature combustion
NO_x – nitrogen oxides
PODEn – poly-oxy methylene dimethyl ethers
PPCI – partially-premixed-compression-ignition
RCCI – reactivity-controlled-compression-ignition
RSM – response surface methodology
SCR – selective catalytic reduction
HCOOH – formic acid
HCHO – formaldehyde

In recent years, various measures have been taken to reduce these exhaust gases from diesel engines by implementing regulations such as BS (brake-specific) standards, alternative fuels, etc. Among these measures, alternative biofuels have become essential because of the rising price of retrofitting CI (compression-ignition) engines, rising oil prices, and declining oil reserves [6]. Due to their abundant sources and self-contained oxygen properties, oxygenated fuels are gaining much attention as new alternative fuels. Alcohol [7], ester [8], ether [9], and other alcohol-based fuels are currently the primary oxygenated alternative fuels. Numerous experiments have shown that blending these fuels with diesel reduces smoke opacity and increases the ambiguous interactions between NO_x and soot [10,11].

Different alcohols, like methanol and ethanol, are currently used as alternative biofuels, and higher alcohols, like butanol, pentanol, etc. can also be used as alternative fuels in CI engines. By using these alcohols with diesel in CI engines, the particulate emissions can be decreased. Moreover, a few issues exist while using lower alcohol in diesel engines. Previous researchers have found that lower alcohols, such as methanol and ethanol, have less miscibility in diesel and might cause phase separation problems at low temperatures due to their poor chemical and physical characteristics [12]. Also, low-carbon alcohols have low CN (cetane number), low viscosity, and high latent heat of evaporation (LHE), impacting engine performance and emissions [13–15]. To address these issues, various approaches can be employed, including alcohol fumigation, dual injection, blending alcohol with diesel fuel, and creating alcohol-diesel fuel emulsions [16].

A double injection system or alcohol fumigation can productively solve the miscibility problems of alcohol/diesel fuel blends. Ghadikolaei et al. [17] examined that fumigation might solve the miscibility problem in the alcohol-diesel blend. In addition, Liu et al. [18] discovered the various consequences of ethanol/PODEn/diesel fuel blends on CI engines. They found that PODEn enhanced the emission and combustion features of CI engines. Phase separation problems can be reduced by adding co-solvents or emulsifiers in lower alcohol/diesel blends [19]. Higher alcohols have drawn more attention because of their high cetane number, energy density, mixing stability, and reduced moisture absorption compared to lower alcohols. Higher alcohols contain more carbon, are less hygroscopic, and are less polar. The suitability of neat butanol for CI engines is constrained by several factors. Its lower cetane number, diminished energy density, elevated heat of vaporization, potential corrosiveness to engine components, and compatibility issues with seals and gaskets all pose challenges. Moreover, the limited availability and underdeveloped infrastructure for butanol distribution exacerbate its practicality as a transportation fuel for CI engines. These properties contribute to ignition delays, incomplete combustion, reduced efficiency, heightened emissions, and reliability concerns. Nonetheless, despite these limitations, the environmental benefits of butanol, such as lower emissions, suggest potential avenues for improvement through fuel blending or the adoption of advanced engine technologies [20]. Therefore, the combination of higher alcohols such as butanol, pentanol, etc. along with diesel without the addition of emulsifiers or co-solvents does not cause phase separation problems. Higher alcohols can be utilized as solvents for alcohols like methanol and ethanol [21]. Secondly, they are less corrosive in nature because of their lower hygroscopicity and lower water content [22]. These alcohols have longer carbon chains than lower alcohols, which increases their CV (calorific values), CN, and density. Higher alcohol concentrations can also extend the ignition delay period, improving the premixed and diffusion combustion phases and thoroughly mixing the air and fuel.

Biobutanol and biopentanol are biofuels produced via fermentation processes, but they differ in microorganisms and pathways. Biobutanol, often derived from acetone-butanol-ethanol (ABE) fermentation by Clostridium bacteria, utilizes various feedstocks like sugar cane and cellulose-rich biomass. The process involves hydrolysis to break down feedstock into fermentable sugars, fermentation by bacteria yielding butanol, acetone, and ethanol, and distillation to separate butanol. Conversely, biopentanol production may involve the genetic engineering of microorganisms for pentanol synthesis, with similar feedstock options. Challenges include optimizing microbial strains for high yields and reducing production costs to compete with traditional fuels. Both biofuels represent promising alternatives necessitating ongoing research and development [23].

Integrating an economic analysis into the assessment of higher alcohol fuels entails evaluating their cost of production, including raw materials, processing, and infrastructure, alongside feedstock availability and price fluctuations. Assessing energy content and engine efficiency relative to conventional fuels is essential, as is considering the cost of infrastructure modifications. Market demand, price sensitivity, environmental and social costs, policy support, and long-term technological advancements all play pivotal roles in determining the economic viability and potential societal benefits of adopting higher alcohol

Table 1. Physicochemical properties of fuels [16,22,48].

Properties	Diesel	Methanol	Ethanol	*n*-Butanol	*n*-Pentanol
Mol. formula	$C_{12}H_{26}$-$C_{14}H_{30}$	CH_3-OH	C_2H_5-OH	C_4H_9-OH	C_5H_{11}-OH
Mol. weight (kg/kmol)	191–210	31.84	45.88	75.12	87.85
Density (kg/m^3) at 15℃	838	790.73	790.2	810.1	815.2
Flashpoint (℃)	72	11.5–12.5	14.5	27	48
Boiling point (℃)	181–358	65.2	79.3	116.2	138.1
Cetane number (CN)	51.5	5.5	8.2	16	17.82–20
LHE (kJ/kg)	252–288	1160.73	919.37	582.24	309.15
Water solubility at 20℃ (%weight)	Immiscible	Miscible	Miscible	8.1	1.9
C (%weight)	85.83	38.18	51.84	65.22	67.83
O (%weight)	0.0	50.10	35.23	22.15	19.05
H (%weight)	14.20	13.24	12.92	13.54	14.21
C/H ratio	5.98	3.08	3.92	5.02	5.06
Self-ignition temperature (°C)	248–302	385	363	343	298
LHV (MJ/kg)	44.15	20.04	27.08	34.17	34.92
Vapour pressure (mmHg)	0.42	126.5	54.6	6.8	6.8
Saturation pressure (kPa) at 38℃	2.08	32.02	14.06	2.94	4.18
Lubricity (µm corrected wear scar)	314.8	1109.2	1056.5	592.10	677.15
Kinematic viscosity at 40℃ (mm/s^2)	3.45	0.52	0.98	2.56	2.83

fuels. Higher alcohols have lower total production costs than lower alcohols in terms of price. To control fuelling in internal combustion engines using either fossil fuel or biodiesel, various strategies are employed to optimize engine performance and emissions. Two primary approaches are commonly focused on: maintaining a constant initial injection angle or optimizing the combustion phasing, typically measured by the CA50 angle (the crank angle at which 50% of the fuel mass has burned) [24]. Research trends indicate that while maintaining a constant initial injection angle provides a useful baseline, optimizing the CA50 angle generally yields better efficiency, performance, and emissions outcomes. This optimization is especially critical for biodiesel due to its distinct combustion properties compared to fossil fuels. Consequently, modern engine control strategies often include CA50 optimization to adapt to varying fuel characteristics and operating conditions, ensuring optimal engine performance and reduced environmental impact.

Yanai et al. [25] examined the consequences of neat butanol and found that the performance and emission features of the engine are affected by the spray characteristics and advanced injection angle strategy. Gautam et al. [26] have also found that the CO emission decreased and BTE (brake thermal efficiency) increased with the advancement in injection angle. By using RSM (response surface methodology), Kumar et al. [27] observed the impact of different factors on CI engines and concluded that fuel injection pressure seriously influences the performance and emissions behaviour of CI engines. Low-temperature combustion (LTC) is a promising strategy for simultaneously reducing NO_x and smoke emissions while enhancing combustion efficiency. LTC is characterized by a well-prepared premixed fuel/air mixture that combusts at lower temperatures after an extended ignition delay. The most effective methods to achieve LTC include using exhaust gas recirculation (EGR) and delaying the injection timing. Combustion tests were conducted in an optically accessible diesel engine using a 20% butanol/diesel blend under varying injection timings and EGR rates. A partially premixed low-temperature combustion (LTC) was achieved with late injection timing combined with a high EGR rate of 50%. This resulted in significant reductions in smoke and NO_x emissions, with a minor decrease in efficiency [28].

For instance, RCCI (reactivity-controlled-compression-ignition) [29], PCCI (partially-premixed-compression-ignition) [30], and HCCI (homogeneous charge compression ignition) [31] have demonstrated the ability to achieve the most stringent emissions standards in the transportation sectors. Higher alcohol PFI (port fuel injection) and diesel DI (direct injection) can produce RCCI. The combustion phase may be more readily controlled, a more comprehensive operating range is attained, the efficiency of diesel engines is substantially improved, and extremely low NO_x and particulate matter emissions are maintained. However, because of its physicochemical characteristics, increasing alcohol consumption in compression ignition engines typically impacts the performance of the engines. While using higher alcohols in compression ignition engines, including nanoparticles [32] and polymethyl dimethyl ether [33] can also enhance the performance of the engines.

The primary goal of this study is to present a thorough analysis of higher alcohol and its impacts on CI engines' performance, combustion, and emissions. Numerous researchers and scientists have examined butanol and pentanol in various ratios with diesel to see whether or not they are suitable as fuel for the current diesel engines. The recent research and prior results about replacing (fully or partially) fossil fuel with these alcohols in compression ignition engines were usually successful since they increased the fuel's renewable fraction while reducing regulated emissions and improving efficiency.

2. Butanol as fuel in CI engine

Butanol, saturated hydrocarbon, is a straight-chain alcohol having 4-carbon atoms mainly extracted from fossil fuels and bio-derived substances. Despite this, both butanol and pentanol have similar physicochemical properties and give identical results when used in CI engines. Butanol can be added in significant proportion to diesel fuel and used; however, it is not suitable for the complete replacement of diesel directly in diesel engines due to the different properties than diesel (see Table 1). Butanol/diesel blends are one of several possibilities for making diesel engines suitable with alcohol. Due to the hydrophilic nature of methanol and ethanol, it does not form a proper mixture with

diesel as they become separated into different liquid phases over several periods, and it gives undesirable effects while using them in diesel engines. Hence, it requires an additional co-solvent to attain a better blend with diesel. Butanol exhibits better miscibility characteristics with diesel blends because of its lower polarity [34]. No emulsifying agents are required for diesel/butanol blends as they do not undergo phase separation even after many days [35].

Moreover, it acts as a solvent for methanol/diesel fuel blends [36] and ethanol/diesel fuel blends [37–39] while used in CI engines. Although blending can be completed either splash-blended in the storage reservoir right before distribution or in-line at the terminal, a specific manufacturing facility is not required to handle the stable diesel/butanol fuel blend due to its ease of attainment [40]. Another significant benefit is that butanol may be blended into diesel at larger ratios, indicating that perhaps the fuel has a more substantial share of renewable energy. According to several studies, using butanol/diesel mixes, butanol can substitute up to 40% of diesel fuel without requiring significant changes to the current engine system [41].

The low heating value (LHV) of a fuel impacts the engine's power production. Because alcohol's heating value rises as carbon atoms increase, butanol has a higher heating value compared to lower alcohols like methanol and ethanol. However, butanol has a 23% lesser LHV than diesel; therefore, it requires a higher quantity of diesel-butanol blended fuels to obtain equal power output from the engine. As the number of carbon atoms grows, alcohol's volatility and auto-ignition temperature drop. Therefore, diesel/butanol mixtures do not impact the ignition issues at various low-load settings [42]. It lowers the CN of blends with diesel, reduces auto-ignition properties and lengthens ignition delay. Direct application of these higher alcohols in unmodified CI engines is prohibited for this very reason.

2.1. Combustion, performance and emission behaviour of butanol

An exhaustive research review on the effects of blending butanol with diesel in various kinds of CI engines is shown in Table 2.

2.2. Summary

According to the above literature review, adding butanol to diesel has various effects on the CI engine performance and emissions:

1. More butanol content in diesel/butanol blends lowers the fuel's CN, increases ignition delay (ID), and increases the maximum heat release rate (HRR).
2. The peak pressure inside the engine cylinder improves the premixed phase of combustion, increases BTE, reduces indicated torque, power and IMEP (indicated mean effective pressure), and increases CO and HC emissions.
3. Combustion temperatures of diesel/butanol blends are low at medium and low loads, and which also, due to the lower calorific value and higher LHE of butanol as compared to diesel, reduce NO_x emissions. Alternatively, increased NO_x emissions are caused by an extended premixed combustion phase due to the higher combustion temperatures at high loads.
4. Butanol increases combustion by increasing the distillation and viscosity of biodiesel/butanol blends, increasing the BTE and decreasing soot particles, CO, and unburnt hydrocarbon emissions but lowering BSFC. Its higher distillation temperature, in comparison to ethanol, aids in superior fuel vaporization, thereby enhancing the combustion process.
5. When PODEn is added to diesel blend (DB), it increases the CN, which decreases the delay period while increasing HC, NO_x, and exhaust emissions while reducing soot emissions. Reducing the time intervals between the pilot and direct injections can help lower hydrocarbons and carbon monoxide emissions.

Adding butanol to biodiesel improves the BTE and increases BSFC while reducing ID period, cylinder pressure, maximum HRR, and NO_x, HC, and CO emissions. Simultaneously, the current research also suggests that ABE has a high potential for reducing butanol recovery costs and lowering soot and NO_x emissions.

Oxygen in fuel affects combustion and emissions, promoting complete oxidation and reducing CO and hydrocarbon emissions while potentially increasing NO_x. It also influences soot and particulate matter formation, favouring smaller particles in oxygen-rich environments [43]. Understanding oxygen's role is crucial for emission control strategies, offering opportunities to mitigate emissions. Balancing oxygen content is essential for efficient combustion with minimal environmental impact, enhancing sustainability in combustion-related activities for cleaner air and improved environmental health.

The mixed results observed in studies on using higher alcohols as fuel in diesel engines – where some parameters increase in some studies and decrease in others – can be attributed to factors such as variations in fuel composition, engine types, measurement techniques, environmental conditions, and data analysis methods. Addressing these factors can help researchers reach more definitive conclusions about the use of higher alcohols in diesel engines, potentially leading to optimized formulations and enhanced performance and emissions profiles. Additionally, several studies indicated that combining higher alcohols with nanoparticles might enhance engine performance by boosting combustion and reducing emissions.

3. Pentanol as fuel in CI engine

Pentanol is also a saturated higher alcohol with 5-carbon atoms having a higher CN, a higher energy density, a more stable pentanol-diesel blend, and a less moisture-absorbing tendency than other lower alcohols. Pentanol is more similar to diesel fuel in comparison to other alcohols in terms of its latent heat of vaporisation, viscosity, and density. It can be manufactured using biological processes such as biosynthesis of glucose using bacteria (Escherichia coli) and natural fermentation using engineered microorganisms [44]. Pentanol is a fantastic sustainable fuel for CI engines.

Table 2. An overview of studies of blended butanol/diesel fuels in various types of compression ignition engines.

Ref.	Engine	Fuels used	Test conditions/ variables	Blend designation	Performance BSFC	Performance BTE	NOx	Soot	HC	CO
[49]	4-cylinders, 16-valve	Diesel + *n*-butanol	2000 rpm, 4000 rpm	20% NB	↑	↑	↑		↓	↑
				30% NB	↑	↑	↑		↓	↑
				40% NB	↑	↑	↑		↑	↑
[50]	4-stroke, 1-cylinder	Diesel + butanol isomers	3000 rpm	10% NB	↑	↑				
[51]	4-stroke, 1-cylinder	Diesel + butanol isomers	2000 rpm	8%, 16%, 24% NB			↓	↓		
[52]	4-stroke, 4-cylinder, 4-valve, VGT	Diesel + butanol isomers	1400 rpm	50% NB	↑		↑	↓	↑	↑
				50% IB	↑		↑	↓	↑↑	↑
				50% SB	↑		↑	↓	↑↑	↑↑
				50% TB	↑		↑	↓	↑↑	↑
[53]	4-stroke, 4-cylinder, DI	Diesel + methanol + *n*-butanol	2000 rpm	10%, 15% NB			↓	↓	↓	↓
[54]	4-cylinder, DI	Diesel + ethanol + *n*-butanol	1600 rpm	5 %, 10 %, 13 %, and 18 %NB	↑	↑	↓ LL ↑ HL	↓		↓
[55]	4-cylinders, 16 valves	Diesel + *n*-butanol + PODEn	Injection strategy 1600 rpm	20% NB 20% PODEn			↑	↓		↓
[56]	4-stroke, 2-cylinder, CRDI engine	Diesel + butanol + DEE	1600 rpm	85% diesel 15% NB doped with 0.3% DEE	↓	↑	↓			↓
[57]	4-stroke, 4-cylinder	Diesel + butanol	1800 rpm	80% diesel, 20% NB			↓		↑	↑
[58]	4-stroke, 1-cylinder, diesel engine	Diesel, mango seed, butanol	1500 rpm	75% diesel 20% MS 0%, 5%, 10%, and 15% butanol	↓	↑	↓		↓	↓
[59]	4-stroke, 1-cylinder	Diesel +ABE	1200 rpm	80 % diesel, 20 %ABE			↓	↑	↑	↑
[60]	4-stroke, 1-cylinder, DI, diesel engine	Diesel + alcohol + Al_2O_3 nanoparticles	1200 rpm	84% diesel, 16% *n*-butanol doped with Al_2O_3 nanoparticles			↑	↑ LL ↓ HL	↓	↓

Note: ↑↑ means increased substantially by, / – not changed significantly by, ↓ – decreased by, ↑ – increased by, NB – *n*-butanol, TB – *tert*-butanol, IB – isobutanol, DEE – diethyl ether, MS – mango seed, SB – *sec*-butanol, ABE – acetone–butanol–ethanol, VGT – variable geometry turbocharger, LL – low-load, HL – high-load.

Even after long days, pentanol diesel blend fuel exhibits improved blend stability without phase separation [45]. Pentanol and diesel have comparable viscosities; however, pentanol/diesel mixtures often have a lower density than pure diesel fuel. Pentanol/diesel blends could help to achieve better atomization and combustion of fuels in CI engines. Pentanol/diesel mixes have flashpoints exceeding 37.8°C, making them inflammable from a safety perspective. The CFPP (cold filter plugging point) behaviour of pentanol/diesel blends are below the limit as per EN 116 standards [46].

3.1 Combustion, performance and emission behaviour of pentanol

An exhaustive research review on the effects of blending pentanol along with diesel in various kinds of CI engines is shown in Table 3.

Table 3. An overview of studies on using blended pentanol/diesel fuels in various types of compression ignition engines (for legend see Table 2).

Ref.	Engine	Fuels used	Test conditions/ variables	Blend designation	Performance BSFC	Performance BTE	NO_x	Soot	HC	CO
[61]	1-cylinder	Diesel + *n*-pentanol	1500 rpm,		↑	↓	↓ LL ↑ HL		↑	↑
[62]	4-cylinder	Diesel + pentanol		Diesel/n-pentanol blends				↑		↑
[63]	4-stroke, 1-cylinder, DI	Diesel + pentanol	1500 rpm	Diesel/n-pentanol blends	↑	↓			↑	↑
[64]	4-stroke, 1-cylinder, DI	Diesel + pentanol	3000 rpm	10% NP	↑	↓				
[65]	1-cylinder diesel engine	1-pentanol/diesel blend	2000 rpm	10%, 20%, and 30%	↑	↓	↓	↓	↑	↑
[66]	4-stroke engine	Diesel-Jatropha-pentanol	1500 rpm	J20 D65 P15		↓	↑	↓	↓	↑
[67]	4-stroke, 4-cylinder, diesel engine	waste oil-derived biodiesel, diesel, and pentanol	1800 rpm indirect-injection	79.09% diesel, and 12.58% 1-pentanol 8.33% WOB	↑	↓	↓		↓	↓
[68]	4-stroke, 1-cylinder, diesel engine	Diesel–mahua methyl ester–pentanol	20 MPa to 50 MPa 2000 rpm	70% diesel 10% pentanol, and 20% MME biodiesel	↓	↑		↓	↓	↓
[69]	4 stroke, 1-cylinder	Diesel + biodiesel + pentanol		BD70 P30			↑		↓	↓
[66]	4-stroke 1-cylinder diesel engine	Diesel, Jatropha, biodiesel, and pentanol	1500 rpm	10%, 15% pentanol		↑	↑	↓	↓	↑

Note: WOB – waste oil-derived biodiesel, MME – mahua methyl ester, BD – diesel +biodiesel, P – pentanol.

3.2. Summary

According to the above literature review, adding pentanol to diesel has different effects on CI engine performance and emissions:

1. Pentanol-diesel blended up to 45% v/v can be used in CI engines without any modification or damage.
2. Pentanol-diesel blended up to 45% v/v can be used in CI engines without any modification or damage.
3. Several researchers conducted chemical modelling studies and kinetic tests to examine the principles of *n*-pentanol to employ pentanol as a next-generation biofuel. Data on oxidation, laminar flame velocity, reactivity flame instability, ignition delay time, species, and concentration are all included in the combustion modelling.
4. As the content of pentanol increases, the ID period increases due to the low CN of the pentanol/diesel blend fuel. Unlike diesel, higher peak cylinder pressures and higher premix HRRs are reported for pentanol-diesel blends.
5. Because of their lower viscosity and high oxygen concentration, pentanol/diesel blends enhance the performance of atomization and combustion compared to diesel. Generally, it offers much better thermal efficiency than other alcohols. However, the pentanol/diesel mixture slightly increases the engine's BSFC, so more fuel is required for the same performance.

The increased combustion temperature and oxygen content increase the NO_x emissions at very high loads while using pentanol/diesel blends as fuel. Pentanol/diesel blends have a lower cetane number due to the higher LHV of pentanol. Due to their increasing oxidizing properties, soot emissions decrease with increasing the pentanol content in diesel/pentanol blends. In CI engines, pentanol typically exhibits superior combustion, performance and emissions characteristics. Pentanol and its additives, like cetane number modifiers and nanoparticles, can simultaneously improve efficiency and reduce emissions in advanced combustion. Using pentanol in engines minimizes fossil fuel needs and reduces environmental pollution.

First-generation biofuels are derived from edible crops such as corn and sugarcane. Second-generation biofuels use non-edible sources, including plant materials like wood, agricultural residues, and municipal solid waste. Third-generation biofuels primarily come from algae and can also utilize carbon dioxide (CO_2) as a feedstock [47]. Oxygenated fuels and paraffinic fuels each have unique benefits and drawbacks. Oxygenated fuels are effective in lowering emissions and making use of renewable resources, although they struggle with lower energy density and compatibility issues. On the other hand, paraffinic fuels offer

high energy density and clean combustion, but they are more expensive to produce and less widely available. The decision to use one type of fuel over the other depends on the specific application, existing infrastructure, and environmental objectives.

4. Conclusions

Butanol and pentanol are second/third-generation biofuels made from lignocellulosic biomass in environmentally friendly ways that do not rely heavily on food crops. They are similar to traditional biofuels in that they can address environmental degradation and energy insecurity. The following findings have been derived from this thorough study of the applications of higher alcohols in CI engines:

- Compared to diesel, higher alcohol/diesel blends have higher premixed heat release rates and peak cylinder pressures. Brake thermal efficiency of engines is improved by applying higher alcohols such as butanol due to low cetane number. It also enhances the quality of fuel atomization as the mixture becomes less viscous and denser.
- The oxygenated nature of higher alcohols typically results in a reduction in particulate emissions. The use of pentanol in diesel engines reduces brake thermal efficiency.
- Increasing the amount of butanol in the butanol/diesel blend generally decreases NO_x emissions. However, at high loads, for pentanol-containing alcohol NO_x, emissions rise linearly with their content. Generally, higher alcohol levels lead to a rise in CO and HC emissions. For engines running on higher alcohol levels, EGR is the most common technique to reduce NO_x emissions, followed by delayed injection.
- Diesel/higher alcohols blended fuel that contains PODEn, or CN modifiers, increases the CN, shortens the ID, and reduces soot particles and CO emissions. Nanoparticles enhance the combustion chamber's superior mixing capability with fine atomization; due to this, their use improves engine brake thermal efficiency and reduces brake-specific fuel consumption. It has been discovered that the application of higher alcohols as well as nanoparticles can improve engine performance and lower its emissions.

The impact of butanol and pentanol blended with diesel is more significant on CI engine performance and emissions and requires further investigation at high altitudes and under time-dependent (transient) conditions such as changes in load, acceleration, and transient or rotary drive cycles. Furthermore, the study is necessary to apply higher alcohol levels in compression ignition engines, optimize combustion characteristics, and specify optimum blend fuel ratios for the stability and long-term durability of the engines.

References

[1] Singh, P., Varun, Chauhan, S.R., & Kumar, N. (2016). A review on methodology for complete elimination of diesel from CI engines using mixed feedstock. *Renewable and Sustainable Energy Reviews*, 57, 1110–1125. doi: 10.1016/j.rser.2015.12.090

[2] Panoutsou, C., Germer, S., Karka, P., Papadokostantakis, S., Kroyan, Y., Wojcieszyk, M., Maniatis, K., Marchand, P., & Landalv, I. (2021). Advanced biofuels to decarbonise European transport by 2030: Markets, challenges, and policies that impact their successful market uptake. *Energy Strategy Reviews*, 34, 100633. doi: 10.1016/j.esr.2021.100633

[3] IEA (2021), *India Energy Outlook 2021*. IEA, Paris. https://www.iea.org/reports/india-energy-outlook-2021

[4] IEA (2023), *Oil Market Report - April 2023*, IEA, Paris https://www.iea.org/reports/oil-market-report-april-2023.

[5] Nabi, Md.N. (2010). Theoretical investigation of engine thermal efficiency, adiabatic flame temperature, NO_x emission and combustion-related parameters for different oxygenated fuels. *Applied Thermal Engineering*, 30(8-9), 839–844. doi: 10.1016/ j.applthermaleng.2009.12.015

[6] Salvi, B.L., Subramanian, K.A., & Panwar, N.L. (2013). Alternative fuels for transportation vehicles: A technical review. *Renewable and Sustainable Energy Reviews*, 25, 404–419. doi: 10.1016/ j.rser.2013.04.017

[7] Yilmaz, N., Donaldson, A.B., & Johns, A. (2005). Some Perspectives on Alcohol Utilization in a Compression Ignition Engine. *SAE Technical Paper*, 2005-01-3135. doi: 10.4271/2005-01-3135

[8] Wu, G., Wang, X., Abubakar, S., Li, Y., & Liu, Z. (2021). A realistic skeletal mechanism for the oxidation of biodiesel surrogate composed of long carbon chain and polyunsaturated compounds. *Fuel*, 289, 119934. doi: 10.1016/j.fuel.2020.119934

[9] Jeevanantham, A.K., Nanthagopal, K., Ashok, B., Al-Muhtaseb, A.H., Thiyagarajan, S., Geo, V.E., Ong, H.C., & Samuel, K.J. (2019). Impact of addition of two ether additives with high speed diesel- *Calophyllum Inophyllum* biodiesel blends on NO_x reduction in CI engine. Energy, 185, 39–54. doi: 10.1016/j.energy.2019.07.013

[10] Atmanli, A., Ileri, E., & Yilmaz, N. (2016). Optimization of diesel–butanol–vegetable oil blend ratios based on engine operating parameters. *Energy*, 96, 569–580. doi: 10.1016/j.energy.2015.12.091

[11] Atmanli, A., & Yilmaz, N. (2018). A comparative analysis of n-butanol/diesel and 1-pentanol/diesel blends in a compression ignition engine. *Fuel*, 234, 161–169. doi: 10.1016/j.fuel.2018.07.015

[12] Fayyazbakhsh, A., & Pirouzfar, V. (2017). Comprehensive overview on diesel additives to reduce emissions, enhance fuel properties and improve engine performance. *Renewable and Sustainable Energy Reviews*, 74, 891–901. doi: 10.1016/j.rser.2017.03.046

[13] Li, L., Wang, J., Wang, Z., & Liu, H. (2015). Combustion and emissions of compression ignition in a direct injection diesel engine fueled with pentanol. *Energy*, 80, 575–581. doi: 10.1016/ j.energy.2014.12.013

[14] Ma, Y., Huang, R., Fu, J., Huang, S., & Liu, J. (2018). Development of a diesel/biodiesel/alcohol (up to n-pentanol) combined mechanism based on reaction pathways analysis methodology. *Applied Energy*, 225, 835–847. doi: 10.1016/j.apenergy.2018.05.065

[15] EL-Seesy, A.I., Waly, M.S., He, Z., El-Batsh, H.M., Nasser, A., & El-Zoheiry, R.M. (2021). Influence of quaternary combinations of biodiesel/methanol/n-octanol/diethyl ether from waste cooking oil on combustion, emission, and stability aspects of a diesel engine. *Energy Conversion and Management*, 240, 114268. doi: 10.1016/j.enconman.2021.114268

[16] Agarwal, A.K. (2007). Biofuels (alcohols and biodiesel) applications as fuels for internal combustion engines. *Progress in Energy and Combustion Science*, 33(3), 233–271. doi: 10.1016/j.pecs.2006.08.003

[17] Ghadikolaei, M.A., Yung, K.-F., Cheung, C.S., Ho, S.S.H., & Wong, P.K. (2020). Non-polar organic compounds, volatility and

oxidation reactivity of particulate matter emitted from diesel engine fueled with ternary fuels in blended and fumigation modes. *Chemosphere*, 249, 126086. doi: 10.1016/j.chemosphere.2020.126086

[18] Liu, H., Wang, X., Wu, Y., Zhang, X., Jin, C., & Zheng, Z. (2019). Effect of diesel/PODE/ethanol blends on combustion and emissions of a heavy duty diesel engine. *Fuel*, 257, 116064. doi: 10.1016/j.fuel.2019.116064

[19] Gao, Z., Wu, S., Luo, J., Zhang, B., Zhang, H., & Xiao, R. (2021). Optimize the co-solvent for methanol in diesel with group of oxygen-containing reagents: Molecular structure and intermolecular forces analysis. *Fuel Processing Technology*, 222, 106980. doi: 10.1016/j.fuproc.2021.106980

[20] Thakur, A.K., Kaviti, A.K., Singh, R., & Gehlot, A. (2020). An overview of butanol as compression ignition engine fuel. *International Journal of Energy for a Clean Environment*, 21(4), 333–354. doi: 10.1615/InterJEnerCleanEnv.2020033667

[21] Jin, C., Zhang, X., Han, W., Geng, Z., Tessa Margaret Thomas, M., Dankwa Jeffrey, A., Wang, G., Ji, J., & Liu, H. (2020). Macro and micro solubility between low-carbon alcohols and rapeseed oil using different co-solvents. *Fuel*, 270, 117511. doi: 10.1016/j.fuel.2020.117511

[22] Raman, R., & Kumar, N. (2019). The utilization of n-butanol/diesel blends in Acetylene Dual Fuel Engine. *Energy Reports*, 5, 1030–1040. doi: 10.1016/j.egyr.2019.08.005

[23] Visioli, L.J., Enzweiler, H., Kuhn, R.C., Schwaab, M., & Mazutti, M.A. (2014). Recent advances on biobutanol production. *Sustainable Chemical Processes*, 2, 15. doi: 10.1186/2043-7129-2-15

[24] Heywood, J.B. (2018). *Internal Combustion Engine Fundamentals* (2nd ed.). McGraw-Hill Education, New York.

[25] Yanai, T., Han, X., Reader, G.T., Zheng, M., & Tjong, J. (2015). Preliminary investigation of direct injection neat *n*-butanol in a diesel engine. *Journal of Energy Resources Technology*, 137(1), 012205. doi: 10.1115/1.4028519

[26] Gautam, R., Chauhan, B.S., & Chang Lim, H. (2022). Influence of variation of injection angle on the combustion, performance and emissions characteristics of Jatropha Ethyl Ester. *Energy*, 254C, 124436. doi: 10.1016/j.energy.2022.124436

[27] Kumar, M., Singh, V.K., Sharma, A., Ansari, N.A., Gautam, R., & Singh, Y. (2022). Effect of fuel injection pressure and EGR techniques on various engine performance and emission characteristics on a CRDI diesel engine when run with linseed oil methyl ester. *Energy & Environment*, 33(1), 41–63. doi: 10.1177/0958305X20983477

[28] Huang, H., Zhou, C., Liu, Q., Wang, Q., & Wang, X. (2016). An experimental study on the combustion and emission characteristics of a diesel engine under low temperature combustion of diesel/gasoline/n-butanol blends. *Applied Energy*, 170, 219–231. doi: 10.1016/j.apenergy.2016.02.126

[29] Žvar Baškovič, U., Vihar, R., Rodman Oprešnik, S., Seljak, T., & Katrašnik, T. (2022). RCCI combustion with renewable fuel mix – Tailoring operating parameters to minimize exhaust emissions. *Fuel*, 311, 122590. doi: 10.1016/j.fuel.2021.122590

[30] Nachippan, N.M., Parthasarathy, M., Elumalai, P.V., Backiyaraj, A., Balasubramanian, D., & Hoang, A.T. (2022). Experimental assessment on characteristics of premixed charge compression ignition engine fueled with multi-walled carbon nanotube-included Tamanu methyl ester. *Fuel*, 323, 124415. doi: 10.1016/j.fuel.2022.124415

[31] Gainey, B., Yan, Z., & Lawler, B. (2021). Autoignition characterization of methanol, ethanol, propanol, and butanol over a wide range of operating conditions in LTC/HCCI. *Fuel*, 287, 119495. doi: 10.1016/j.fuel.2020.119495

[32] Khan, H., Soudagar, M.E.M., Kumar, R.H., Safaei, M.R., Farooq, M., Khidmatgar, A., Banapurmath, N.R., Farade, R.A., Abbas, M.M., Afzal, A., Ahmed, W., Goodarzi, M., & Taqui, S.N. (2020). Effect of nano-graphene oxide and n-butanol fuel additives blended with diesel-Nigella sativa biodiesel fuel emulsion on diesel engine characteristics. *Symmetry*, 12(6), 961. doi: 10.3390/sym12060961

[33] Liu, X., Wang, H., Zheng, Z., & Yao, M. (2021). Development of a reduced primary reference fuel-PODE$_3$-methanol-ethanol-*n*-butanol mechanism for dual-fuel engine simulations. *Energy*, 235, 121439. doi: 10.1016/j.energy.2021.121439

[34] Lapuerta, M., García-Contreras, R., Campos-Fernández, J., & Dorado, M.P. (2010). Stability, Lubricity, viscosity, and cold-flow properties of alcohol−diesel blends. *Energy & Fuels*, 24(8), 4497–4502. doi: 10.1021/ef100498u

[35] Rakopoulos, D.C., Rakopoulos, C.D., Papagiannakis, R.G., & Kyritsis, D.C. (2011). Combustion heat release analysis of ethanol or n-butanol diesel fuel blends in heavy-duty DI diesel engine. *Fuel*, 90(5), 1855–1867. doi: 10.1016/j.fuel.2010.12.003

[36] Huang, Z., Lu, H., Jiang, D., Zeng, K., Liu, B., Zhang, J., & Wang, X. (2005). Performance and emissions of a compression ignition engine fueled with diesel/oxygenate blends for various fuel delivery advance angles. *Energy & Fuels*, 19(2), 403–410. doi: 10.1021/ef049855d

[37] Huang, J., Wang, Y., Li, S., Roskilly, A.P., Yu, H., & Li, H. (2009). Experimental investigation on the performance and emissions of a diesel engine fuelled with ethanol-diesel blends. *Applied Thermal Engineering*, 29(11-12), 2484–2490. doi: 10.1016/j.applthermaleng.2008.12.016

[38] Chandra, R., & Kumar, R. (2007). Fuel properties of some stable alcohol-diesel microemulsions for their use in compression ignition engines. *Energy & Fuels*, 21(6), 3410–3414. doi: 10.1021/ef0701788

[39] Asfar, K.R., & Hamed, H. (1998). Combustion of fuel blends. *Energy Conversion and Management*, 39(10), 1081–1093. doi: 10.1016/S0196-8904(97)00034-4

[40] Ahmed, I. (2001). Oxygenated diesel: Emissions and performance characteristics of ethanol-diesel blends in CI engines. *SAE Technical Paper*, 2001-01-2475. doi: 10.4271/2001-01-2475

[41] Al-Hasan, M.I., & Al-Momany, M. (2008). The effect of iso-butanol-diesel blends on engine performance. *Transport*, 23(4), 306–310. doi: 10.3846/1648-4142.2008.23.306-310

[42] Yao, M., Wang, H., Zheng, Z., & Yue, Y. (2010). Experimental study of n-butanol additive and multi-injection on HD diesel engine performance and emissions. *Fuel*, 89(9), 2191–2201. doi: 10.1016/j.fuel.2010.04.008

[43] Kozak, M., & Merkisz, J. (2022). oxygenated diesel fuels and their effect on PM emissions. *Applied Sciences*, 12(15), 7709. doi: 10.3390/app12157709

[44] Cann, A.F., & Liao, J.C. (2010). Pentanol isomer synthesis in engineered microorganisms. *Applied Microbiology and Biotechnology*, 85, 893–899. doi: 10.1007/s00253-009-2262-7

[45] Rajesh Kumar, B., & Saravanan, S. (2015). Effect of exhaust gas recirculation (EGR) on performance and emissions of a constant speed DI diesel engine fueled with pentanol/diesel blends. *Fuel*, 160, 217–226. doi: 10.1016/j.fuel.2015.07.089

[46] Campos-Fernandez, J., Arnal, J.M., Gomez, J., Lacalle, N., & Dorado, M.P. (2013). Performance tests of a diesel engine fueled with pentanol/diesel fuel blends. *Fuel*, 107, 866–872. doi: 10.1016/j.fuel.2013.01.066

[47] Dahman, Y., Dignan, C., Fiayaz, A., & Chaudhry, A. (2019). An introduction to biofuels, foods, livestock, and the environment. In *Biomass, Biopolymer-Based Materials, and Bioenergy* (pp. 241–

276). Woodhead Publishing. doi: 10.1016/B978-0-08-102426-3.00013-8

[48] Yilmaz, N., & Atmanli, A. (2017). Experimental evaluation of a diesel engine running on the blends of diesel and pentanol as a next generation higher alcohol. *Fuel*, 210, 75–82. doi: 10.1016/j.fuel.2017.08.051

[49] Chen, Z., Liu, J., Han, Z., Du, B., Liu, Y., & Lee, C. (2013). Study on performance and emissions of a passenger-car diesel engine fueled with butanol-diesel blends. *Energy*, 55, 638–646. doi: 10.1016/j.energy.2013.03.054

[50] Zhang, Z.-H., Chua, S.-M., & Balasubramanian, R. (2016). Comparative evaluation of the effect of butanol–diesel and pentanol-diesel blends on carbonaceous particulate composition and particle number emissions from a diesel engine. *Fuel*, 176, 40–47. doi: 10.1016/j.fuel.2016.02.061

[51] Rakopoulos, D.C., Rakopoulos, C.D., Giakoumis, E.G., Dimaratos, A.M., & Kyritsis, D.C. (2010). Effects of butanol–diesel fuel blends on the performance and emissions of a high-speed DI diesel engine. *Energy Conversion and Management*, 51(10), 1989–1997. doi: 10.1016/j.enconman.2010.02.032

[52] Pan, M., Tong, C., Qian, W., Lu, F., Yin, J., & Huang, H. (2020). The effect of butanol isomers on diesel engine performance, emission and combustion characteristics under different load conditions. *Fuel*, 277, 118188. doi: 10.1016/j.fuel.2020.118188

[53] Zhang, Z., Tian, J., Xie, G., Li, J., Xu, W., Jiang, F., Huang, Y., & Tan, D. (2022). Investigation on the combustion and emission characteristics of diesel engine fueled with diesel/methanol/n-butanol blends. *Fuel*, 314, 123088. doi: 10.1016/j.fuel.2021.123088

[54] Zhang, Z., Li, J., Tian, J., Dong, R., Zou, Z., Gao, S., & Tan, D. (2022). Performance, combustion and emission characteristics investigations on a diesel engine fueled with diesel/ ethanol /n-butanol blends. *Energy*, 249, 123733. doi: 10.1016/j.energy.2022.123733

[55] Huang, H., Li, Z., Teng, W., Zhou, C., Huang, R., Liu, H., & Pan, M. (2019). Influence of n-butanol-diesel-PODE$_{3\text{-}4}$ fuels coupled pilot injection strategy on combustion and emission characteristics of diesel engine. *Fuel*, 236, 313–324. doi: 10.1016/j.fuel.2018.09.051

[56] Sahu, T.K., & Shukla, P.C. (2022). Combustion and emission characteristics of butanol-diesel blend (B15) doped with diethyl ether, diglyme and ethyl diglyme in a CRDI diesel engine. *SAE Technical Paper*, 2022-01-1073. doi: 10.4271/2022-01-1073

[57] Yilmaz, N., Vigil, F., & Donaldson, B. (2022). Effect of n-butanol addition to diesel fuel on reduction of PAH formation and regulated pollutants. *Polycyclic Aromatic Compounds*, 43(10), 8785–8799. doi: 10.1080/10406638.2022.2153881

[58] Ahmad, K., & Saini, P. (2022). Effect of butanol additive with mango seed biodiesel and diesel ternary blends on performance and emission characteristics of diesel engine. *Energy Sources, Part A: Recovery, Utilization, and Environmental Effects*, 44(4), 9988–10005. doi: 10.1080/15567036.2022.2143954

[59] Duan, X., Xu, Z., Sun, X., Deng, B., & Liu, J. (2021). Effects of injection timing and EGR on combustion and emissions characteristics of the diesel engine fuelled with acetone-butanol-ethanol/diesel blend fuels. *Energy*, 231, 121069. doi: 10.1016/j.energy.2021.121069

[60] Chen, Q., Wang, C., Shao, K., Liu, Y., Chen, X., & Qian, Y. (2022). Analyzing the combustion and emissions of a DI diesel engine powered by primary alcohol (methanol, ethanol, *n*-butanol)/diesel blend with aluminum nano-additives. *Fuel*, 328, 125222. doi: 10.1016/j.fuel.2022.125222

[61] Rajesh Kumar, B., & Saravanan, S. (2015a). Effect of exhaust gas recirculation (EGR) on performance and emissions of a constant speed DI diesel engine fueled with pentanol/diesel blends. *Fuel*, 160, 217–226. doi: 10.1016/j.fuel.2015.07.089

[62] Huang, H., Lv, D., Zhu, J., Chen, Y., Zhu, Z., Pan, M., Huang, R., & Jia, C. (2018). Development and validation of a new reduced diesel/*n*-pentanol mechanism for diesel engine applications. *Energy & Fuels*, 32(9), 9934–9948. doi: 10.1021/ acs.energyfuels.8b02083

[63] Rajesh Kumar, B., & Saravanan, S. (2016). Effects of *iso*-butanol/diesel and *n*-pentanol/diesel blends on performance and emissions of a DI diesel engine under premixed LTC (low temperature combustion) mode. *Fuel*, 170, 49–59. doi: 10.1016/j.fuel.2015.12.029

[64] Zhang, Z.-H., Chua, S.-M., & Balasubramanian, R. (2016). Comparative evaluation of the effect of butanol-diesel and pentanol-diesel blends on carbonaceous particulate composition and particle number emissions from a diesel engine. *Fuel*, 176, 40–47. doi: 10.1016/j.fuel.2016.02.061

[65] Ashok, A., Gugulothu, S.K., Venkat Reddy, R., Burra, B., & Panda, J.K. (2022). A systematic study of the influence of 1-pentanol as the renewable fuel blended with diesel on the reactivity controlled compression ignition engine characteristics and Trade-off study with variable fuel injection pressure. *Fuel*, 322, 124166. doi: 10.1016/j.fuel.2022.124166

[66] Venkatesan, S.P., Sriharihara n, P., Rohith, B., Purusothaman, M., & Venkatesh, S. (2023). Study of the performance and emissions of diesel engines operating by blends of Jatropha biodiesel, diesel and pentanol. *Materials Today: Proceedings*, 72(4), 2513–2517. doi: 10.1016/j.matpr.2022.09.532

[67] Yilmaz, N., Atmanli, A., Hall, M.J., & Vigil, F.M. (2022). Determination of the optimum blend ratio of diesel, waste oil derived biodiesel and 1-pentanol using the response surface method. *Energies*, 15(14), 5144. doi: 10.3390/en15145144

[68] Ramachander, J., Gugulothu, S.K., Sastry, G.R., & Bhsker, B. (2022). An experimental assessment on the influence of high fuel injection pressure with ternary fuel (diesel-mahua methyl ester-pentanol) on performance, combustion, and emission characteristics of common rail direct injection diesel engine. *Environmental Science and Pollution Research*, 29, 119–132. doi: 10.1007/s11356-021-13909-3

[69] Ashok, A., Gugulothu, S.K., Reddy, R.V., & Burra, B. (2023). Influence of fuel injection timing and trade-off study on the RCCI engine characteristics of Jatropha oil-diesel blend under 1-pentanol dual-fuel strategies. *Environmental Science and Pollution Research*. 30, 98848–98857. doi: 10.1007/s11356-022-22039-3

Co-published by
Institute of Fluid-Flow Machinery
Polish Academy of Sciences
Committee on Thermodynamics and Combustion
Polish Academy of Sciences

http://www.imp.gda.pl/archives-of-thermodynamics/

Numerical Investigation of Increasing-Decreasing Stepped Micro Pin Fin Heat Sink Having Various Arrangements

Prabhakar Bhandari[1], Vineet Sharma[2], Lalit Ranakoti[3], Vijay Singh Bisht[4], Manish Kumar Lila[5], Shivasheesh Kaushik[6]*, Nikhil Kanojia[7], Ayushman Srivastava[7], Bhupendra Kumar[8], Shailesh Ranjan Kumar[9], Manish Kumar[10], Ashwarya Raj Paul[11]

[1]Department of Mechanical Engineering, School of Engineering and Technology, K. R. Mangalam University, Gurugram, Haryana-122103, India
[2]Department of Electrical Engineering, Poornima College of Engineering, Jaipur-302033, India
[3]Department of Mechanical Engineering, Graphic Era Deemed to University, Clement Town, Dehradun, Uttarakhand-248002, India
[4]Department of Thermal Engineering, Veer Madho Singh Bhandari Uttarakhand Technical University, Dehradun, Uttarakhand-248007, India
[5]Department of Mechanical Engineering, Graphic Era Hill University, Dehradun, Uttarakhand-248002, India
[6]Department of Mechanical Engineering, Shivalik College of Engineering, Dehradun, India
[7]Department of Mechanical Engineering, U.P.E.S, Dehradun, India
[8]Department of Mechanical Engineering, Dr. A.P.J.A.K.I.T. Tanakpur, India
[9]Department of Mechanical Engineering, Motihari College of Engineering, Motihari, India
[10]Department of Mechanical Engineering, Bakhtiyarpur College of Engineering, Bakhtiyarpur Dedaur, Bakhtiyarpur, Patna, India
[11]Department of Mechanical Engineering, V.I.T., Vellore, India
*Corresponding author email: skaushik@sce.org.in

Received: 01.02.2024; revised: 06.04.2024; accepted: 06.06.2024

Abstract

The ongoing trend of miniaturization of electronic devices, including computer processors, high-speed servers and micro-electro-mechanical system devices, should go hand in hand with their improved performance. However, managing heat remains a major challenge for these devices. In the present study, a numerical investigation was done on a micro-channel heat sink with an open-stepped micro-pin fin heat sink with various arrangements through ANSYS software. Pin fin was varied in a fashion of increasing and decreasing. The working fluid opted for was water in a single phase. The analysis takes into account varying thermo-physical properties of water. The operating parameters, i.e. the Reynolds number was taken as 100–350 and heat flux as 500 kW/m^2. Arrangements selected were staggered and inline. Observations revealed that the staggered 2 arrangement has shown better thermal performance than other arrangements within the entire investigated range of Reynolds numbers because of the effective mixing of fluids. Furthermore, the inline configuration of micro pin fin heat sink has the worst performance. It is interesting to note that a very small difference was observed in the heat transfer capability of both staggered configurations, while the pressure drop in the staggered 2 arrangement has shown an elevated value at a higher Reynold number value compared to the staggered 1 arrangement.

Keywords: Heat transfer augmentation; Thermo-hydraulic performance; Stepped micro-channel heat sink; Open micro-channel; Inline arrangement; Staggered arrangement

Vol. 45(2024), No. 4, 37–44; doi: 10.24425/ather.2024.151995

Cite this manuscript as: Bhandari, P., Sharma, V., Ranakoti, L., Bisht, V.S., Lila, M.K., Kaushik, S., Kanojia, N., Srivastava, A., Kumar, B., Kumar, S.R., Kumar, M., & Paul, A.R. (2024). Numerical Investigation of Increasing-Decreasing Stepped Micro Pin Fin Heat Sink Having Various Arrangements. *Archives of Thermodynamics*, 45(4), 37–44.

1. Introduction

Heat sinks, as per classical thermodynamics, are devices designed to dissipate heat without experiencing a temperature increase. Unfortunately, it's not feasible to construct such systems. In industrial and commercial settings, heat sinks function based on a common principle of thermal contact, they absorb excess heat generated during the operation of various systems. A significant decrease in the overall size of the component can be noticed in the industry of electronics because of the research and

Nomenclature

A_{bw} – surface area of the bottom wall, mm^2
A_{cw} – surface area of solid / liquid contact, mm^2
D_h – hydraulic diameter, mm
h – heat transfer coefficient, W/K
H_b – height of bottom substrate, mm
H_c – height of channel, mm
H_f – height of pin fin, mm
k_l – thermal conductivity of liquid, W/(m·K)
k_s – thermal conductivity of the substrate, W/(m·K)
L – length, mm
L_f – length of individual pin fin, mm
$\overline{\mathrm{Nu}}$ – average Nusselt number
ΔP – pressure drop, Pa
q – heat flux applied, W/m^2
q_{eff} – heat flux effective, W/m^2
Re – Reynolds number
u_{in} – fluid inlet velocity, m/s
$T_{avg,cw}$ – average temperature of the solid-liquid interface, K
$T_{bulk,l}$ – bulk temperature of the liquid, K
W – width, mm
W_f – width of individual pin fin, mm
W_{sw} – width of side wall, mm

Greek symbols

μ – dynamic viscosity, Pa·s
ρ – density, kg/m^3

Subscripts and Superscripts

bw – bottom wall
cw – constant wall
f – footprint
h.fx – flux
in – inlet
l – liquid

Abbreviations and Acronyms

CFD – computational fluid dynamics
FEM – finite element method
HTC – heat transfer coefficient
OSMPFHS – open stepped micro pin fin heat sink
M.C.H.S. – micro channel heat sink
P.V.T. – photovoltaic trough

development taking place in the field of transistors since 1948. The removal of heat from the electronic devices is an ongoing concern having connections with the current flow via any electrical component, leading to a notable surge in heat generation per unit volume in these devices. Shortly, it is highly likely to reach a power density of nearly 1000 W/cm² [1]. Excessive heat can reduce overall efficiency and possibly cause irreversible damage to equipment if heat dissipation is not carefully controlled. As stated by the author [2], inadequate thermal management accounts for over 50% of failures in electronic VLSI circuits. Therefore, it is imperative to develop an effective and long-lasting cooling system to address this issue. Traditional cooling methods that utilize natural or forced air with fans and fins are inadequate for dissipating heat in such devices, as they are incapable of handling the significant heat generated [3]. Therefore, there is a need for innovative solutions to efficiently disperse a substantial quantity of heat from the zones which are very much confined. Additionally, these traditional systems are often bulky, noisy and unstable.

Air has a limited thermal conductivity when compared to liquids, resulting in poor heat dissipation. According to the study, liquid cooling achieves around 4–10 times higher heat flux than air cooling.

Microchannels have garnered a lot of attention in the scientific community among the various innovative technologies for dispersing heat, e.g., cooling by jet impingement, heat pipe in size of microns, Carbon nanotubes, cooling by spraying, and microchannels [4–5]. This is because it has a high surface-to-volume ratio [6] and is simple to use. For example, in [7] the authors started using this microchannel for heat dispersion, emphasizing its use in electronic cooling. Since then, a lot of work has gone into improving the architecture of the device as well as its performance based on heat dissipation to improve its utility.

2. Literature review and objective

The literature outlines various strategies to enhance heat transfer through micro-channels, which can be categorized as active and passive methods. Active approaches involve integrating microchannels with additional techniques like vibration and electrostatic forces to boost heat transfer [8]. On the other hand, passive methods focus on altering the fundamental properties of microchannel heat sinks, applying techniques such as altering the microchannel structure [9,10], using different working fluids [11,12] such as nanofluids, and so on, and adjusting the coolant operating conditions [13]. Pin fin variations for microchannel heat sinks have been included in the design, like a higher area of convection, fluid mixing with an improved strategy, secondary flow, and disturbances of laminar flow, which are all benefits of micro pin-fin topologies [14,15].

To enhance the microchannel pin fin heat sink (MPFHS) performance, several studies with experimental details with varying fin height [16], tip clearance [17,18], pin fin forms, sizes, alignments and densities have been reported in the past few years [19,20]. It was found that the performance of thermal characteristics was improved whereas the pressure was minimized in the microchannel heat sink. Figure 1 illustrates the sequential utilization of pin fins to enhance the effectiveness of open microchannel configurations. Bhandari and Prajapati first studied the influence of stepped pin fin in open micro pin fin heat sinks [21]. They stated that out of all the variants they looked at, the pin fin with rising height performed better. Increased fluid mixing, which is also seen in the 1 mm channel height [22], is the cause of this behaviour. Variable tip clearance enhances the three-dimensionality of fluid flow, which aids in thermal augmentation. Variable tip clearance along channel length and width was added

to the work [23]. According to them, bidirectional steepness outperformed unidirectional steepness in terms of thermal performance factor value. The group has performed various numerical studies on open-stepped micro pin fin heat sinks. Some focused on the effect of pin fin arrangement [24], fluid flow and thermal transfer argumentation [25,26], and thermo-hydraulic performance of open-stepped micro pin fin heat sinks [27,28].

The design modifications in microchannel heat sinks are also motivated by other sectors like solar, space, automobile industries, etc. These sectors face challenges in heat transfer and heat absorption from diverse sources. Many researchers worked on specific designs and developed highly efficient and effective air heaters for their applications [29–33]. Modified designs utilized solar energy more during the day for diverse applications. The same literature presented the importance of rough shapes and perforation. It demonstrated the positive effects of roughness shapes and perforation utilized over absorber plates [29,30] and conical inserts installed inside circular heat pipes [31]. Some focused only on fins/inserts for heat transfer and absorption enhancement [32,33]. The working of solar air heaters is quite similar to heat sinks, so researchers can be inspired by it [34,36]. Some researchers have been encouraged by mini channels [37,38], microchannels [39,40], spiral tube concentric exchangers [41–43], exchangers using perforated and diverse shapes of inserts [44–46], and exchangers utilizing semi-hollow cylindrical-macro inserts [47]. In this study, we conduct simulations to assess how various arrangements impact the thermal and hydraulic performance of a heat sink with microchannels. We consider increasing and decreasing arrays of pin fins in a stepped configuration.

3. Novelty and objective

In previous works, researchers have performed analysis on pin fin heat sink having pin fin height variation throughout its length. The pattern is either in increasing style or decreasing style. However, in our works, we have considered increasing and decreasing arrays of pin fins in a stepped configuration. Further, the same configurations of pin fins were repeated throughout the length of the heat sink. Another novelty of the present geometry lies in a change in pin fin orientation (inline and staggered) along the channel width. The objective of these design alterations is to maximize the heat transfer rate in the heat sink at a minimum pressure drop penalty. In the later part, detailed dimensions of the heat sink model used in this study have been explained. The choice of the stepped configuration was made because it has demonstrated superior performance compared to uniform arrangements. This improvement is attributed to enhanced mixing of fluids, enhanced stability of 3-D fluid and distraction of thermal and hydraulic boundary layers. Based on these factors, a numerical study was conducted to compare three different arrangements containing the same fluid of single phase flowing in open microchannel pin fin heat sinks.

4. Geometry and numerical modeling

Figure 1 displays an isometric diagram of the micro pin fin heat sink (MPFHS). In Fig. 2(a), we can observe that the pin fins are shorter compared to the channel height. The study numerically analyzed the heat sink's three-dimensional geometry for various substrate materials. The overall dimensions of the computational domain are 22.50 × 12.50 × 2.00 mm (length × width × height).

Fig. 1. Isometric view of micro pin fin heat sink.

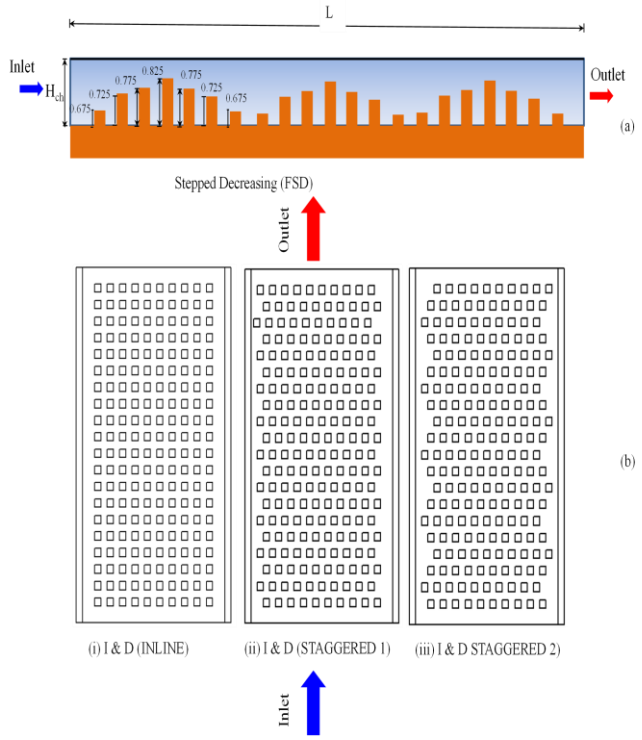

Fig. 2. (a) Side view of increasing and decreasing stepped micro pin fin heat sink.; (b) Top view of different cases considered (i) inline arrangement, (ii) staggered 1 arrangement, (iii) staggered 2 arrangement.

The heat sink consists of rows of pin fins with varying heights, with a total of 21 rows, each containing 10 fins. This results in a total of 210 pin fins of the same size, each with a footprint area of 0.5 × 0.5 mm², arranged at a pitch distance of 1.0 mm.

Two 0.5 mm thick and 1 mm high side walls are located on those sides of the heat sink which are opposite to each other to promote fluid passage between them. The intake and outflow plenums are 1 mm long to guarantee a smooth and controlled flow of the fluid, which in this case is water. Detailed dimensional information of the current study is given in Table 1.

For the current investigation, an open microchannel heat sink (MCHS) with a stepped design, specifically with increasing and

decreasing heights for the fins, as shown in Fig. 3(a), is used. The pin fin height variations in a unit array along the length in the heat sink are as follows: 0.675 mm, 0.725 mm, 0.775 mm, 0.825 mm, 0.775 mm, 0.725 mm, 0.675 mm. The various investigated configurations are illustrated in Fig. 2(b). Two different staggered configurations have been opted, one having alteration in consecutive fin rows in one direction while the other having fin alteration in both directions.

Table 1. The heat sink's dimensional parameters.

No.	Parameters	Range of value
1	Heat sink length (L)	22.50 mm
2	Heat sink width (W)	12.50 mm
3	Heat sink pin fin height (H_f)	0.6–0.9 mm
4	Width of side wall (W_{sw})	0.5 mm
5	Heat sink total height ($H = H_c+H_b$)	2 mm
6	Thickness of bottom wall (H_b)	1 mm
7	Dimension of fin footprint ($L_f \times W_f$)	0.5 × 0.5 mm
8	Gap between the fins (longitudinal and transverse)	0.50 mm
9	Total number of fins	210

5. Governing equations

To address the current problem with water as a single-phase working medium, the conjugate technique was employed. To streamline the analysis, certain simplifying assumptions were made, listed as follows:

a) fluid follows the law of Newtonian fluid and it is incompressible,
b) flow is assumed to be laminar at every region of analysis,
c) no slip condition was applied at the boundary,
d) the effect of thermal changes due to radiation was ignored,
e) surfaces are adiabatic except for the wall at the bottom.

The governing equations can be written as

$$\nabla \cdot (\rho_l \vec{V}) = 0, \tag{1}$$

$$\nabla \cdot (\rho_l \vec{V}\vec{V}) = -\nabla p + \nabla \cdot \mu_l[(\nabla \vec{V} + \nabla \vec{V}^t) - 2/3I\nabla \cdot \vec{V}] + \rho_l \vec{g}, \tag{2}$$

$$\nabla \cdot (\rho_l c_{p,l} \vec{V} T) = \nabla \cdot (k_l \nabla T). \tag{3}$$

Here, $\vec{V}$ is the velocity, t is used as a subscript representing the transpose of the matrix, while the numeric l resembles the liquid, I is the unit matrix. In the case of solid substrate, the energy equation becomes:

$$k_S \nabla^2 T = 0. \tag{4}$$

To simulate the current problem, ANSYS 18.0 was implemented with the scheme of SIMPLE being used with the criteria for convergence fixed to 10^{-4} in the case of the continuity equation, 10^{-6} for the momentum equation and 10^{-7} for the energy equation.

To predict the results, we utilized polynomial functions of temperature to represent the thermal and physical properties, as referenced by Bhandari and Prajapati [16]. These relationships are applicable within the temperature range of 5–95°C, which aligns with our assumed working conditions. Fluent considered these relationships while defining the characteristics of coolant. In this study, we calculated the Reynolds number:

$$Re = \frac{\rho_l u_{in} D_h}{\mu_l}, \tag{5}$$

where u_{in} is the uniform velocity at the inlet plenums. The hydraulic diameter (D_h) is 0.5 mm, and this value remains consistent for all three configurations. We determined the heat transfer coefficients using Eq. (6):

$$h = \frac{q_{eff}}{(T_{avg,\,cw} - T_{bulk,l})}. \tag{6}$$

The average Nusselt number is calculated as:

$$\overline{Nu} = \frac{hD_h}{k_l} = \frac{q_{eff} D_h}{(T_{avg,\,cw} - T_{bulk,l}) k_l}, \tag{7}$$

where $T_{bulk,l}$ represents the bulk fluid temperature and $T_{avg,cw}$ depicts the average temperature of the solid-liquid interface.

We calculate the area-weighted average temperature as "$T_{avg,cw}$" and estimate the volume-averaged temperature for the fluid domain "$T_{bulk,l}$". The heat flux (effective), denoted as "q_{eff}", is calculated with the help of Eq. (8) as follows:

$$q_{eff} = qA_{bw}/A_{cw}. \tag{8}$$

The heat sink's bottom wall surface area is denoted as A_{bw} and the surface area where the solid contacts the liquid is A_{cw}. It is important to note that the bottom wall surface area remains constant at 281.25 mm² for all configurations. Moreover, the convective surface area is also the same for all cases, i.e. 614.25 mm².

6. Validation

To validate the present work, the work of Mei et al. [48] was replicated. Mei et al. [48] considered the tip clearance of 0.5 mm and 1.00 mm in their studies. A comparison of the average Nusselt number obtained from the present work and that of Mei et al. work [48] is shown in Fig. 3. It is observed that the results remain in good agreement with the present model. The deviation between the studies may be due to several fins considered and shape variation.

7. Results and Discussion

To understand how pin fin arrangements affect the thermal and hydraulic characteristics, we selected three different configurations. Specifically, we simulated the increasing and decreasing stepped configurations for both inline and staggered arrangements, all at a heat flux of 500 kW/m². The variations in heat transfer coefficients for these different arrangements are illustrated in Fig. 4.

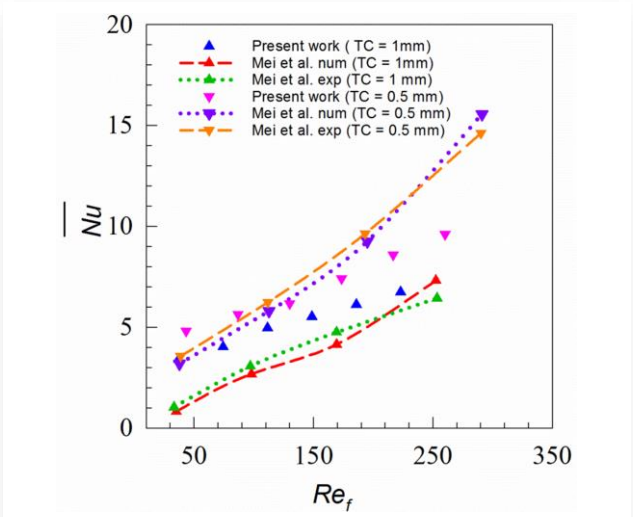

Fig. 3. Variation of average Nusselt number with fin Reynold number for different configurations.

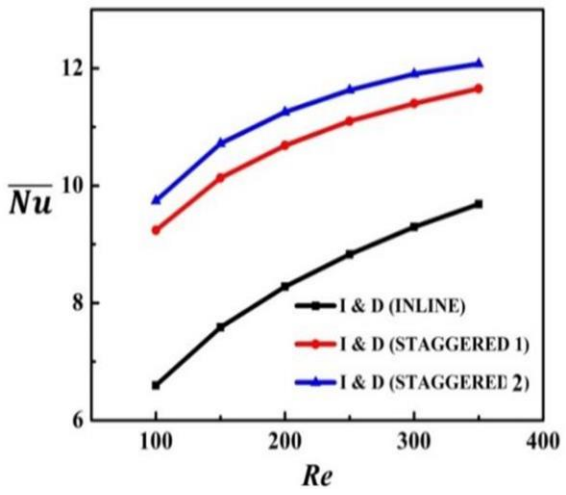

Fig. 5. Variation of $\overline{Nu}$ with Re for different configurations at heat flux of 500 kW/m^2.

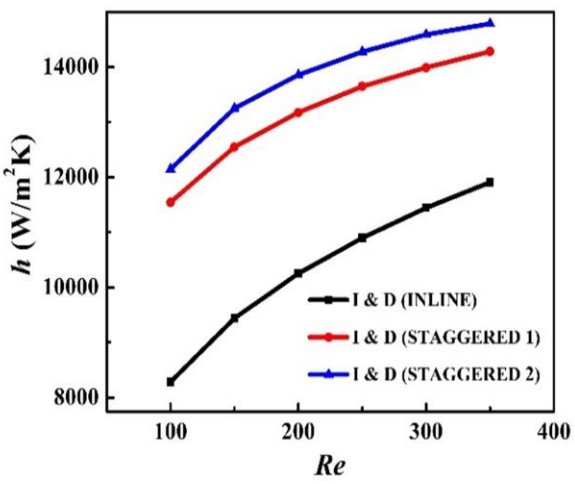

Fig. 4. Variation of heat transfer coefficients with Re for different configurations at heat flux of 500 kW/m^2.

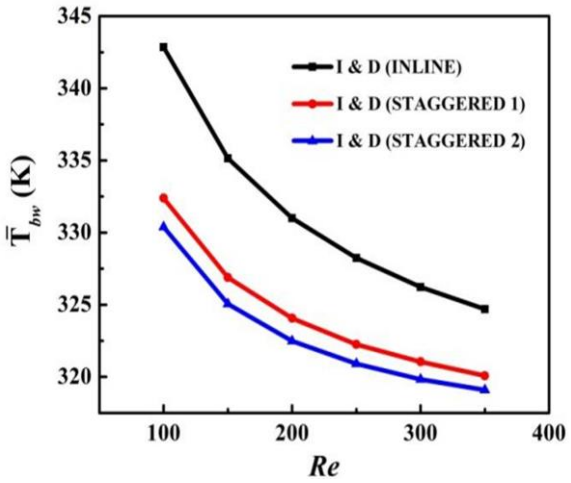

Fig. 6. Variation of $\overline{T_{bw}}$ with Re for different configurations at heat flux of 500 kW/m^2.

It is observed that increasing the Reynolds number results in higher heat transfer coefficients. It is obvious since at higher Re, fluid flow rate increases subsequently; more heat is carried out by the coolant. Furthermore, it is reported that the staggered layout has higher heat transfer coefficients than the inline layout. It is interesting to note that with an increase in Re value, the heat transfer coefficient slope decreases, and at a higher Re value, it is almost flat.

A similar trend was also observed for the average Nusselt number as revealed in Fig. 5. It is observed that orientation changes from inline to staggered one showed a substantial increase in average Nu. Moreover, with further modification in the staggered arrangement, the average Nusselt number increases due to augmented flow mixing.

The variation of $\overline{T_{bw}}$ for different configurations is depicted in Fig. 6. $\overline{T_{bw}}$ was calculated as the area-weighted average temperature at the bottom wall of the heat sink where heat flux has been applied. It is noticed that significant augmentation is achieved when the arrangement changes from inline to staggered. The minimum bottom wall temperature is observed for the staggered 2 configuration due to the higher value of the average Nusselt number. It is interesting to note that increasing Re resulted in high coolant velocity and mass flow rate causing more heat transfer from the heat sink. A smaller value of $\overline{T_{bw}}$ implies higher heat dissipation at any operating condition.

Pressure difference occurs at the outlet and the inlet was examined to acquire the actual pressure drop which has been illustrated in Fig. 7. Figure 7 depicts a variation of pressure drop with change in Re for all the arrangements that are made in the current study. Among all the configurations, the maximum pressure drop was obtained for the staggered 2nd case while the lowest pressure drop was obtained in the inline case. The obstruction that occurs in the flow of fluid at the staggered 2nd case could

be the reason behind this phenomenon. Furthermore, it is observed that with an increase in Re, pressure drop increases in all the configurations of the heat sink.

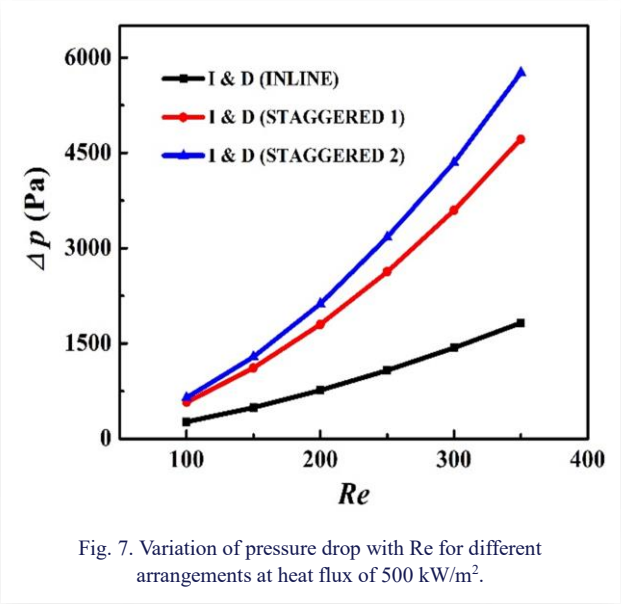

Fig. 7. Variation of pressure drop with Re for different arrangements at heat flux of 500 kW/m^2.

This is due to an increase in fluid velocity at higher Re which causes extensive flow resistance so higher pumping power is needed. From Fig. 7, it is observed that the pressure drop curve is not linear and is much steeper at higher values of Re explicitly in stepped staggered heat sinks.

It can be concluded that at low Re values, the pressure drop is low but the heat transfer capability is also low, while at high Re values, the heat transfer coefficient does not increase as much as the pressure drop. So, it is recommended to use an Increasing-Decreasing Stepped Micro Pin Fin Heat Sink for mid-range Re values.

8. Conclusions

In this study, we conducted simulations of a stepped microchannel heat sink having increasing and decreasing fin heights in various arrangements. We compared these arrangements using single-phase water as the working fluid, considering both inline and staggered configurations. The staggered arrangements included one with alterations in one direction only and another with changes in both directions. The working conditions involved a heat flux of 500 kW/m² and a Reynolds number range from 100 to 350.

Based on our findings, it can be concluded that the staggered arrangements, especially the staggered 2 arrangement, can significantly enhance the performance of the stepped microchannel configuration. This improvement is attributed to the three-dimensionality effect and improved fluid mixing.

At low Reynolds numbers, both the pressure drop and the heat transfer capability are minimal. At higher Reynolds numbers, the increase in the heat transfer coefficient involves a large rise in pressure drop. Therefore, it is advisable to use an Increasing-Decreasing Stepped Micro Pin Fin Heat Sink within a mid-range of Reynolds numbers.

Acknowledgements

This work was supported by the K. R. Mangalam University, Gurugram, Haryana (India) through a Seed research grant (KRMU/ADMIN/SEED/2022-23/3493(B). The author would like to express appreciation to the K. R. Mangalam University's Central Instrumentation Facility for facilitating the research work.

References

[1] Mudawar, I., & Lee, J. (2009). Low-Temperature Two-Phase Microchannel Cooling for High-Heat-Flux Thermal Management of Defense Electronics. *IEEE Transactions on Components Package. Technologies*, 32(2), 453–465. doi: 10.1109/TCAPT.2008.2005783

[2] Pedram, M., & Nazarian, S. (2006). Thermal modeling, analysis, and management in VLSI circuits: Principles and methods. *Proceedings of the IEEE. Institute of Electrical and Electronics Engineers*, 94(8), 1487–1501. doi: 10.1109/JPROC.2006.879797

[3] Ahmed, H.E., Salman, B.H., Kherbeet, A.S. & Ahmed, M. I. (2018). Optimization of thermal design of heat sinks: A review. *Intenational Journal of Heat and Mass Transfer*, 118, 129–153. doi: 10.1016/j.ijheatmasstransfer.2017.10.099

[4] Gururatana, S. (2012). Heat Transfer Augmentation for Electronic Cooling. *American Journal of Applied Sciences*, 9(3), 436–439. doi: 10.3844/ajassp.2012.436.439

[5] Bhandari, P., Rawat, K.S., Prajapati, Y.K., Padalia, D., Ranakoti, L., & Singh, T. (2023). A review on design alteration in microchannel heat sink for augmented thermohydraulic performance. *Ain Shams Engineering Journal*, 15(2), 102417. doi: 10.1016/j.asej.2023.102417

[6] Naqiuddin, N.H., Saw, L.H., Yew, M.C., Yusof, F., Ng, T.C. & Yew, M.K. (2018). Overview of micro-channel design for high heat flux application. *Renewable and Sustainable Energy Reviews*, 82, 901–914. doi: 10.1016/j.rser.2017.09.110

[7] Tuckerman D.B., & Pease, R.F.W. (1995). High-Performance Heat Sinking for VLSI, *IEEE Electron Device Letters*, 2(5), 126–129. doi: 10.1109/EDL.1981.25367

[8] Bhandari, P., Singh, J., Kumar, K., & Ranakoti, L. (2022). Active techniques in microchannel heat sink for miniaturization problem in electronic industry: A review. *Acta Innovations*, 45, 45–54. doi: 10.32933/actainnovations.45.4

[9] Japar, W.M.A.A., Sidik, N.A.C., Saidur, R., Asako, Y., & Yusof, S.N.A. (2020). A review of passive methods in microchannel heat sink application through advanced geometric structure and nanofluids : Current advancements and challenges. *Nanotechnology Reviews*, 9(1), 1192–1216. doi: 10.1515/ntrev-2020-0094

[10] Bhandari, P., Rawat, K.S., Prajapati, Y.K., Padalia, D., Ranakoti, L., & Singh, T. (2023). A review on design alteration in microchannel heat sink for augmented thermohydraulic performance. *Ain Shams Engineering Journal*, 15(2), 102417. doi: 10.1016/j.asej.2023.102417

[11] Kumar, N., Singh, P., Redhewal, A.K., & Bhandari, P. (2015). A review on nanofluids applications for heat transfer in microchannels. *Procedia Engineering*, 127, 1197–1202. doi: 10.1016/j.proeng.2015.11.461

[12] Chamkha, A. ., Molana, M., Rahnama, A., & Ghadami, F. (2018). On the nanofluids applications in microchannels: A comprehensive review. *Powder Technology*, 332, 287–322. doi: 10.1016/j.powtec.2018.03.044

[13] Prajapati, Y.K., & Bhandari, P. (2017). Flow boiling instabilities in microchannels and their promising solutions – A review. *Experimental Thermal and Fluid Science*, 88, 576–593. doi: 10.1016/j.expthermflusci.2017.07.014

[14] Bhandari, P., Rawat, K., Prajapati, Y.K., Padalia, D., Ranakoti, L., & Singh, T. (2023). Design modifications in micro pin fin configuration of microchannel heat sink for single phase liquid flow: A review. *Journal Energy Storage*, 66, 107548. doi: 10.1016/j.est.2023.107548

[15] Bhandari, P., Padalia, D., Ranakoti, L., Khargotra, R., András, K., & Singh, T. (2023). Thermo-hydraulic investigation of open micro prism pin fin heat sink having varying prism sides. *Alexandria Engineering Journal*, 69, 457–468. doi: 10.1016/j.aej.2023.02.016

[16] Bhandari, P., & Prajapati, Y.K. (2021). Thermal performance of open microchannel heat sink with variable pin fin height. *Intenational Journal of Thermal Sciences*, 159, 106609. doi: 10.1016/j.ijthermalsci.2020.106609

[17] Bhandari, P., & Prajapati, Y.K. (2022). Influences of tip clearance on flow and heat transfer characterstics of open type micro pin fin heat sink, *Intenational Journal of Thermal Sciences*, 179, 107714. doi: 10.1016/j.ijthermalsci.2022.107714

[18] Bhandari, P., & Prajapati, Y.K. (2021). Experimental Investigation of Variable Tip Clearance in Square Pin Fin Microchannel Heat Sink. *Proceedings of the 26th National and 4th International ISHMT-ASTFE Heat and Mass Transfer Conference* (pp. 1351−1356). IIT Madras, Chennai - 600036, Tamil Nadu, India. Begel House Inc. doi: 10.1615/IHMTC-2021.2040

[19] Chiu, H.C., Hsieh, R.H., Wang, K., Jang, J.H., & Yu, C.R. (2017). The heat transfer characteristics of liquid cooling heat sink with micro pin fins. *International Communications in Heat and Mass Transfer*, 86, 174–180. doi: 10.1016/j.icheatmasstransfer.2017.05.027

[20] Zhao, J., Huang, S., Gong, L., & Huang, Z. (2016). Numerical study and optimizing on micro square pin-fin heat sink for electronic cooling, *Applied Thermal Engineering*, 93, 1347–1359. doi: 10.1016/j.applthermaleng.2015.08.105

[21] Bhandari, P., & Prajapati, Y.K. (2021). Fluid flow and heat transfer behaviour in distinct array of stepped micro pin fin heat sink, *Journal of Enhanced Heat Transfer*, 28(4), 31–61. doi: 10.1615/JEnhHeatTransf.2021037008

[22] Bhandari, P., Prajapati, Y.K. & Uniyal, A. (2023). Influence of three dimensionality effects on thermal hydraulic performance for stepped micro pin fin heat sink. *Meccanica*, 58, 2113–2129. doi: 10.1007/s11012-022-01534-4

[23] Bhandari, P. (2022). Numerical investigations on the effect of multi-dimensional stepness in Open micro pin fin heat sink using single phase liquid fluid flow. *International Communications in Heat and Mass Transfer*, 138, 106392. doi: 10.1016/j.icheatmasstransfer.2022.106392

[24] Bhandari, P., & Prajapati, Y.K. (2020). Numerical Analysis of Different Arrangement of Square Pin-Fin Microchannel Heat Sink. In *Advances in Mechanical Engineering* (pp. 879–891). Singapore, Springer Publishing. doi: 10.1007/978-981-15-0124-1_79

[25] Bhandari, P., & Prajapati, Y.K. (2021). Numerical study of fluid flow and heat transfer in stepped micro-pin fin heat sink. In *Fluid Mechanics and Fluid Power*. *Lecture Notes in Mechanical Engineering* (pp. 373-381). Springer Publishing, Singapore. doi: 10.1007/978-981-16-0698-4_40

[26] Bhandari, P., Prajapati, Y.K., & Bisht, V.S. (2021). Heat transfer augmentation in micro pin fin heat sink using out of plane fluid mixing. *Proceedings of the 26th National and 4th International ISHMT-ASTFE Heat and Mass Transfer Conference* (pp. 1595−1600). IIT Madras, Chennai-600036, Tamil Nadu, India. Begel House Inc. doi: 10.1615/IHMTC-2021.2400

[27] Bhandari, P., Kumar, K., Ranakoti, L., Bisht, V.S., Lila, M.K., Joshi, K., Raju, N.V.G., Sobti, R., & Jayahari, L. (2023). Thermo-hydraulic investigation of two stepped micro pin fin heat sink having variable step size. *E3S Web of Conferences*, 430, 01177. doi: 10.1051/e3sconf/202343001177

[28] Bhandari, P., Vyas, B., Padalia, D., Ranakoti, L., Prajapati, Y.K., & Bangri, R.S. (2024). Comparative thermo-hydraulic analysis of periodic stepped open micro pin-fin heat sink. *Archives of Thermodynamics*, 45(3), 99−105. doi: 10.24425/ather.2024.151228

[29] Kaushik, S., & Singh, S. (2019). Analysis on Heat Transmission and Fluid Flow Attributes in Solar Air Accumulator Passage with Diverse Faux Jaggedness Silhouettes on Absorber Panel. I*nternational Journal of Engineering and Advanced Technology*, 8, 32−41. doi: 10.35940/ijeat.E1011.0785S319

[30] Kaushik, S., Panwar, K., & Vashisth, S. (2022). Investigating the Thermionic Effect of Broken Perforated Curved Ribs on Solar Preheater through CFD Simulation. *Res Militaris*, 12(5), 1508−1524.

[31] Uniyal, V., Joshi, S.K., Kaushik, S., & Kanojia, N. (2021). CFD Investigation of Transfer of the Heat and Turbulent Flow in Circular Copper Tube with Perforated Conical Rings of Aluminium Material. *Materials Today: Proceeding*, 46(15), 6719−6725. doi: 10.1016/ j.matpr.2021.04.217

[32] Thapa, R.K., Bisht, V.S., Bhandari P., & Rawat, K. (2022). Numerical study of car radiator using dimple roughness and nanofluid. *Archives of Thermodynamics*, 43(3), 125−140. doi: 10.24425/ather.2022.143175

[33] Kaushik, S., Singh, S., Kanojia, N., Naudiyal, R., Kshetri, R., Paul, A.R., Kumari, R., Kumar, A., & Kumar, S. (2021). Effect of introducing varying number of fins over LED light bulb on thermal behaviour. *Materials Today: Proceeding*, 46(19), 9794−9799. doi: 10.1016/j.matpr.2020.10.876

[34] Ghildyal, A., Bisht, V.S., Rawat K.S., & Bhandari, P. (2023). Effect of D-shaped, Reverse D-shaped and U-shaped turbulators in Solar Air Heater on thermo hydraulic performance. *Archives of Thermodynamics*, 44(2), 3−20. doi: 10.24425/ather.2023.146556

[35] Haldia, S., Bisht, V.S., Bhandari, P., Ranakoti, L., & Negi, A. (2024). Numerical assessment of solar air heater performance having broken arc and broken S-shaped ribs as roughness. *Archives of Thermodynamics*, 45(1), 23−31. doi: 10.24425/ather.2024.150435

[36] Kumar, S., Bisht, V.S., Bhandari, P., Ranakoti, L., Negi, A., Bist, A.S., & Padalia, D. (2024). Computational Analysis of Modified Solar Air Heater having Combination of Ribs and Protrusion in S-shaped Configuration. *International Journal Interactive Design and Manufacturing*, 1−12. doi: 10.1007/s12008-024-01972-2

[37] Kaushik, S., Uniyal, V., Ali, S., Kanojia, N., Verma A.K., Joshi S., Makhloga, M., Pargai, P.S., Sharma, S.K., Kumar, R., & Pal, S. (2023). Comparative analysis of fluid flow in mini channel with nano fluids and base fluid. *Materials Today: Proceedings.* doi: 10.1016/j.matpr.2023.05.363

[38] Kaushik, S., Uniyal, V., Verma, A.K., Jha, A.K., Joshi, S., Makhloga, M., Pargai, P.S., Sharma, S.K., Kumar, R., & Pal, S. (2023). Comparative Experimental and CFD Analysis of Fluid Flow Attributes in Mini Channel with Hybrid CuO+ZnO+H_2O Nano Fluid and (H_2O) Base Fluid. *EVERGREEN Joint Journal of Novel Carbon Resource Sciences & Green Asia Strategy*, 10(01), 182−195. doi: 10.5109/6781069

[39] Kaushik, S., Ali, S., Kanojia, N., Uniyal, V., Verma, A.K., Panwar, S., Uniyal, S., Goswami, S., Kindo, S., Som, D., & Yadav, N.K. (2023). Experimental and CFD analysis of fluid

flow in a rectangular strip-based microchannel with nanofluid. *Materials Today: Proceedings*. doi.: 10.1016/j.matpr.2023.05.647

[40] Kaushik, S., Verma, A., K., Singh, S., Kanojia, N., Panwar, S., Uniyal, S., Goswami, S., Kindo, S., Som, D., & Yadav, N.K. (2023). Comparative Analysis of Fluid Flow Attributes in Rectangular Shape Micro Channel having External Rectangular Inserts with Hybrid Al_2O_3+ZnO+H_2O Nano Fluid and (H_2O) Base Fluid. *EVERGREEN Joint Journal of Novel Carbon Resource Sciences & Green Asia Strategy*, 10(2), 851−862. doi: 10.5109/6792839

[41] Kaushik, S., Singh, S., & Panwar, K. (2021). Comparative analysis of thermal and fluid flow behaviour of diverse nano fluid using Al_2O_3, ZnO, CuO nano materials in concentric spiral tube heat exchanger. *Materials Today: Proceedings*, 46(15), 6625−6630. doi: 10.1016/j.matpr.2021.04.100

[42] Kaushik, S., Singh, S., & Panwar, K. (2022). Experimental Study of Fluid Flow Properties in Spiral Tube Heat Exchanger with varying Insert Shape over Spiral Tube Profile. *Materials Today: Proceedings*, 80(1), 78−84. doi: 10.1016/j.matpr. 2022.10.117

[43] Kaushik, S., Singh, S., Kanojia, N., Rawat, K., & Panwar, K. (2020). Comparative Study for Thermal and Fluid Flow Peculia rities in Cascading Spiral Inner Tube Heat Exchanger with or without Diverse Inserts over Spiral Tube. *IOP Conference Series: Materials Science and Engineering*, 802. doi: 10.1088/1757-899X/802/1/012009

[44] Singh, B.P., Bisht, V.S., & Bhandari, P. (2021). Numerical Study of Heat Exchanger Having Protrusion and Dimple Roughened Conical Ring Inserts. In *Advances in Fluid and Thermal Engineering, Lecture Notes in Mechanical Engineering* (pp. 151−162). Springer Publishing, Singapore. doi: 10.1007/978-981-16-0159-0_14

[45] Kharkwal, H., & Singh, S. (2022). Effect of serrated circular rings on heat transfer augmentation of circular tube heat exchanger. *Archives of Thermodynamics*, 43(2), 129−155. doi: 10.24425/ather.2022.141982

[46] Singh, B.P., Bisht, V.S., Bhandari, P., & Rawat, K.S. (2021). Thermo-fluidic modelling of a heat exchanger tube with conical shaped insert having protrusion and dimple roughness. *Aptisi Transactions on Technopreneurship*, 3(2), 127−143. doi: 10.34306/att.v3i2.200

[47] Kaushik, S., Mahar, V.S., Singh, S., Kshetri, R., Kumar, B., Mehta, J.S., Paul, A.R., Kumar, S., Vashisth, S., Pundir, R.S., & Kumar, A. (2024). Comparative experimental analysis of fluid flow in a concentric tube exchanger having semi hollow cylindrical macro inserts with nanofluid and base fluid. *Archives of Thermodynamics*, 45(2), 205–212. doi: 10.24425/ather.2024.150866

[48] Mei, D., Lou, X., Qian, M., Yao, Z., Liang, L., & Chen, Z. (2013). Effect of tip clearance on the heat transfer and pressure drop performance in the micro-reactor with micro-pin-fin arrays at low Reynolds number. *International Journal of Heat and Mass Transfer*, 70, 709–718. doi: 10.1016/j.ijheatmasstransfer.2013.11.060

Co-published by
Institute of Fluid-Flow Machinery
Polish Academy of Sciences
Committee on Thermodynamics and Combustion
Polish Academy of Sciences

http://www.imp.gda.pl/archives-of-thermodynamics/

Evaluating the mixed convection flow of Casson fluid from the semi-infinite vertical plate with radiation absorption effect

Sonam, Rajendra Singh Yadav*

University of Rajasthan, Department of Mathematics, Jaipur, Rajasthan-302004, India
*Corresponding author email: rajendrauor@gmail.com

Received: 25.04.2024; revised: 19.06.2024; accepted:16.07.2024

Abstract

This study examines a steady laminar Casson fluid flow induced by a semi-infinite vertical plate under the impact of the Darcy-Forchheimer relation and thermal radiation. The features of mixed convection, cross-diffusion, radiation absorption, heat generation, chemical reactions and viscous dissipation are also considered to explain the transport phenomenon. The resultant system of equations, concerned with the problem under consideration, is transformed into a group of non-linear ordinary differential equations (ODEs) by means of similarity variables. The bvp4c method, an instrument popular for its numerical accomplishments, is utilized to solve this problem. The effect of flow parameters on heat transfer, concentration and velocity is evaluated via diagrams. To validate our code, we have compared the present outcomes to the prevenient literature, and stable consent has been detected. Moreover, the friction coefficient C_{f_x}, Nusselt number Nu_x, and Sherwood number Sh_x are also computed to assess velocity gradient, efficiency of heat transfer and mass transfer process, respectively.

Keywords: MHD flow; Radiation; Cross-diffusion; Slippiness; Chemical reactions

Vol. 45(2024), No. 4, 45–59; doi: 10.24425/ather.2024.151996

Cite this manuscript as: Sonam, & Yadav, R.S. (2024). Evaluating the mixed convection flow of Casson fluid from the semi-infinite vertical plate with radiation absorption effect. *Archives of Thermodynamics*, 45(4), 45–59.

1. Introduction

The review of non-Newtonian fluids has attracted a lot of interest due to their wide applications in manufacturing and industrial areas, particularly in polymer processing, the food industry to optimize sensory aspects, the oil and gas industry, and the formulation of beauty products. The Casson fluid, a shear-thinning fluid with lower resistance under high strain rates, is one variant of non-Newtonian fluids. Casson [1] was the one who first discovered it. Later, it was developed by Heller [2] to anticipate the flow properties of a pigment-oil mixture. Since then, the Casson fluid flow has been discussed by several scientists and researchers under various conditions. Ramana et al. [3] investigated the influence of the melting processes on Casson liquid. They noted that the large values of melting parameter decrease fluid concentration. The flow of electrically conducting Casson hybrid nanofluid along a vertical moving surface was pioneered by Krishna et al. [4]. Kodi et al. [5] have expounded on the heat and mass transfer of Casson fluid over the vertical plate. The study specifically accounted for the influence of heat absorption. Recently, Jaffrullah et al. [6] investigated the impacts of Joule heating and MHD (magnetohydrodynamics) on Casson fluid flow.

Nomenclature

B_0 – constant magnetic field, T
B_c – concentration slip parameter
B_t – temperature slip parameter
B_u – velocity slip parameter
c_p – specific heat at constant pressure, J kg^{-1}K^{-1}
c_s – species susceptibility, J kg^{-1}K^{-1}
C – fluid concentration, kg m^{-3}
C_b – drag force coefficient
C_{f_x} – local skin friction coefficient, N m^{-2}
C_w – wall concentration, kg m^{-3}
C_∞ – ambient concentration, kg m^{-3}
D_m – mass diffusivity factor, m^{2}s^{-1}
Du – Dufour number
Ec – Eckert number
f – dimensionless stream function
f' – dimensionless velocity
Fr – Forchheimer number
g – gravitational acceleration, m s^{-2}
Gm – concentration Grashof number
Gr – temperature Grashof number
K_0 – porous medium permeability, m^2
K_1 – porosity parameter
K_c – chemical reaction constant, s^{-1}
K_c' – chemical reaction parameter
K_T – thermal diffusion ratio, m^{2}s^{-1}
k^* – mean absorption coefficient, m^{-1}
L_0 – velocity slip factor, m
M – magnetic parameter
M_0 – thermal slip factor, m
N_0 – concentration slip factor, m
Nu$_x$ – Nusselt number
Pr – Prandtl number
Q_0 – constant heat generation/absorption coefficient, W m^{-3}K^{-1}
Q^* – heat generation/absorption parameter
q_r – radiation heat flux, W m^{-2}
q_w – wall heat flux, W m^{-2}
R_0 – radiation absorption coefficient, W kg^{-1}
R^* – radiation absorption parameter
Re$_x$ – Reynolds number
S – suction/blowing parameter
Sc – Schmidt number
Sr – Soret number
Sh$_x$ – Sherwood number
T – temperature, K
T_m – mean temperature, K
T_w – wall temperature, K
T_∞ – ambient temperature, K
u, v – velocity components, m s^{-1}
v_0 – velocity suction/blowing, m s^{-1}
U_0 – velocity at wall, m s^{-1}
x, y – Cartesian coordinates, m

Greek Symbols

β_C – solute expansion coefficient, m^3 kg^{-1}
β_T – heat expansion coefficient, K^{-1}
γ – Casson parameter
θ – dimensionless temperature
η – similarity variable
k – thermal conductivity, W m^{-1}K^{-1}
μ – dynamic viscosity, Pa s
ρ – fluid density, kg m^{-3}
σ – electric conductivity, Ω^1 m^{-1}
σ^* – Stefan-Boltzmann coefficient, W m^{-2}K^{-4}
υ – viscosity, m^{2}s^{-1}
ψ – stream function. m^{2}s^{-1}
ϕ – dimensionless concentration

Subscripts and Superscripts

0 – condition at wall
w – condition at wall
∞ – ambient condition
' – differentiation with respect to η

Abbreviations and Acronyms

IVP – initial value problem
MHD – magnetohydrodynamics
ODE – ordinary differential equation
2D – two-dimensional

Fluids that exhibit boundary slippiness have numerous applications in tribology, influencing friction and reducing attrition in various mechanical systems such as engines and bearings. Furthermore, in the range of thermal exchangers, it significantly improves heat transfer efficiency across several industrial processes. Navier [7] initially came up with the concept of boundary slippiness. Later, Krishna and Chamkha [8] investigated the impact of slip on nanofluid flow from a vertical plate in the porous medium. Obalalu et al. [9] introduced the impact of velocity slip on the Casson nanofluid flow over a permeable surface. They noted a drop in velocity subject to large scales of slip parameters.

The theory of hydromagnetic flow has attracted a lot of sapidity in many industrial areas, particularly in the rate of cooling of ending materials [10]. The magnetic fields have also shown an appreciable interest in navigation systems, induction heating systems, MRI (magnetic resonance imaging) machines, and climate phenomenon management. Chamkha [11] deliberated on steady flow along a vertical plate under a magnetic field. Kumar et al. [12] have proposed the influence of magnetic fields on free convection fluid flow through porous sheets with chemical reactions. Lately, Raghunath et al. [13] have discussed MHD flow from an unbounded plate with radiation absorption. They reported a reversed effect on velocity subject to the magnetic parameter.

The phenomenon of fluid flow in porous media is utilized in many branches of engineering and applied sciences, particularly filtration, soil mechanics, petroleum engineering and water quality. The obtainable articles evidence that a lot of discussion has been stated about the problems of porous media that are developed by utilizing Darcy's theory. To forecast the effect of inertia, a quadratic term of velocity in the model of Darcian veloc-

ity is introduced by Forchheimer [14]. Aleem et al. [15] discussed the effects of chemical reactions and Newtonian heat on MHD nanofluids via Darcy medium. Nasir et al. [16] proposed a model by using Darcy-Forchheimer and entropy analysis effects on nanofluid.

The study of mixed convection flow plays a vital role in thermal engineering, especially in designing heating, cooling and ventilation systems for various applications. It is frequently found in extremely high-power output devices to dissipate all of the heat necessary. Bilal et al. [17] explored that the mixed convection of hybrid nanofluid increased the velocity profile. Sinha and Yadav [18] evaluated a numerical simulation of the convective slip flow over a porous plate. Roy et al. [19] focused on the transfer of heat via convection.

Engineering innovations like fluid gyroscopes and centrifuges involve suction and blowing, which is also in geophysics. In fact, chemical reactions use suction to eliminate reactor components [20]. On the contrary, blowing is applied to connect reactor components which chill planes and decrease drag [21]. Hussain et al. [22] have nicely explained the MHD flow of Williamson fluid with suction/blowing.

Chemical reactions have a major role in industrial processes due to their use in maximizing production and minimizing waste. Bejawada et al. [23] investigated the impact of radiation and chemical reactions on MHD Casson fluid flow over an inclined, non-linear surface. Raju et al. [24] analyzed the Soret impact on the water-based Jeffrey fluid flow from a semi-infinite vertical plate with chemical reactions and found an inverse behaviour of the reaction parameter on the concentration profile. Zhao et al. [25] had incurred chemical reactions in the flow of nanofluid to improve the concentration profile.

Thermal radiation is an essential concept in many engineering applications and significantly impacts the boundary layer flow due to its uses in technological and industrial fields such as polymer processing, re-entry vehicles, high-speed flights, furnace design and space technologies like aerodynamic rockets, propulsion systems, missiles, etc. Therefore, the effect of heat radiation cannot be disregarded. The word emission is widely used to signify the radiation of heat [26]. Asha and Sunitha [27] deliberated on the impact of radiation on peristaltic blood flow. In this literature, the approximation method (HAM – homotopy analysis method) is applied to explore the numerical solution. Later on, Abbas et al. [28] studied the Sakiadis flow with variable density and radiation impacts. Saravana et al. [29] analyzed the impact of radiation on fluid flow.

The phenomena of heat generation/absorption hold significant importance in various engineering and industrial processes, such as fertilization, filled-bed reactors, waste stowage materials and dissociating liquids. It is an essential characteristic of MHD Casson fluid flows. Gambo and Gambo [30] applied the influence of heat generation/absorption on fluid flow generated by a vertical annulus. This investigation took into account the existence of a magnetic field. Rao et al. [31] dealt with the effect of radiation absorption and heat sink/source on MHD free convective Casson fluid flow. They observed that the radiation absorption parameter adversely affects the Nusselt number. Thereafter, the idea of heat generation/absorption over ternary nanofluid flow was explored by Manjunatha et al. [32]. MHD heat transfer of Casson fluid over a moving wedge in the presence of internal heat generation/absorption impact is explored by Amar et al. [33].

The exploration of viscous dissipation and Joule heating has captured interest in their contribution to fluid flow and temperature distribution owing to their broad utility in many industrial and engineering applications [34]. These are the most significant thermal properties of fluid flow. Viscous dissipation is the modification of kinetic energy into heating energy under friction. Brinkman [35] initially came up with the concept of viscous dissipation. He also took into account the transportation of heat by convection. Later, Swain et al. [36] discussed the MHD flow of non-Newtonian fluid through a stretching sheet in the presence of viscous dissipation. They noted that the large values of the viscous parameter helped to raise the temperature. Das [37] observed the impacts of Joule heating and viscous dissipation on the Casson fluid's MHD convective slip flow over the inclined plate with thermal radiation. Sadia et al. [38] numerically analyzed the impact of Joule heating on the flow of Jeffrey fluid.

Thermo-diffusion, also known as thermophoresis or the Soret impact [39], is a phenomenon where particles migrate in a fluid through the interaction between the temperature and concentration gradients. It has applications in various fields such as heat transfer, particle separation and colloidal science. The diffusion-thermo or the Dufour effect [40] is the mutual phenomenon of thermo-diffusion. The presence of the Dufour effect is crucial in binary gas mixtures. A theoretical discussion of heat transfer on absorption kinetics with thermo-diffusion impact is explored by Krenn et al. [41]. The flow behaviour of hybrid nanofluid between two parallel plates was studied by Revathi et al. [42], with a specific focus on the impact of cross-diffusion. An increase in temperature is observed with an increasing Dufour number in this literature. Lately, Ullah et al. [43] conducted a study to explore the effect of cross-diffusion on Jeffery-Hamel flow in a stretching channel with Joule heating.

In sight of the extant literature, which primarily focuses on the discussions of steady flow of Casson fluid under different features [44–46], there is a notable gap in research regarding the examination of the combined impact of chemical reaction, radiation absorption, slip and heat source/sink on flow and heat transfer over a semi-infinite vertical plate in Darcy porous medium. This is the novelty of the present study. Inspired by this identified research gap, our goal is to yield a more elaborate understanding of the complex interplay between flow patterns and heat transfer conductors by incorporating these complex factors. The insights gained from this comprehensive analysis hold significance in various industrial processes like filtration, the food industry, climate phenomenon management, furnace design, and so forth. It can also aid our understanding of heat transfer in renewable energy systems.

2. Mathematical formulation

In order to construct our problem, we have made the following assumptions:

- The electrically conducting, non-compressible Casson fluid over a semi-infinite vertical plate in a Darcy porous medium is deemed.
- The plate is deemed to be along the vertical axis, i.e. the x-axis.
- The flow is regarded as steady, 2D, radiative, laminar, and mixed convective.
- T_w and C_w are the temperature and concentration at the plate, respectively.
- B_0 is the constant magnetic field employed at a right angle to the flow axis.
- In order to disregard the Hall impact and the propelled magnetic field, the magnetic Reynolds number is assumed to be low [47,48].
- T_∞ and C_∞ are the ambient temperature and mass, respectively.

The flow problem sketch is displayed in Fig. 1.

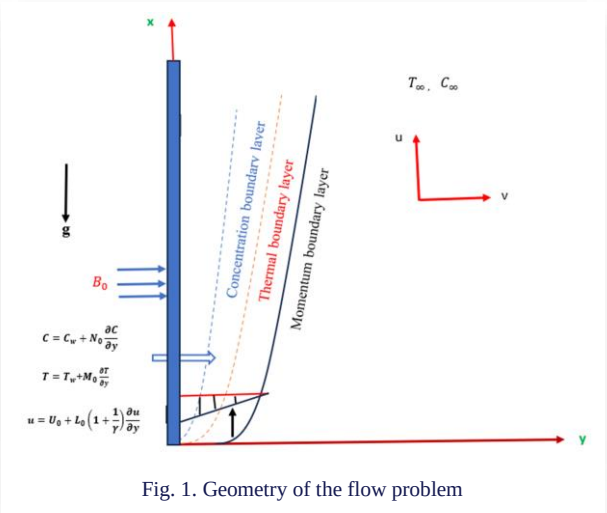

Fig. 1. Geometry of the flow problem

The rheological formula [3] for the Casson fluid model is:

$$\tau_{ij} = \begin{cases} 2\left(\mu_b + \frac{p_y}{\sqrt{2\pi}}\right)e_{ij}, & \pi > \pi_c, \\ 2\left(\mu_b + \frac{p_y}{\sqrt{2\pi_c}}\right)e_{ij}, & \pi < \pi_c, \end{cases} \quad (1)$$

where: τ_{ij} – $(i, j)^{th}$ component of the stress tensor, μ_b – plastic dynamic viscosity of the fluid, p_y – yield stress of the fluid, e_{ij} – $(i, j)^{th}$ component of the deformation rate, $\pi = e_{ij}e_{ij}$ – product of the component of deformation rate with itself, π_c – critical value of this product based on the non-Newtonian model.

To the impression as mentioned above, the modelling equations are described as follows [13,44,46]:

$$\frac{\partial u}{\partial x} + \frac{\partial v}{\partial y} = 0, \quad (2)$$

$$u\frac{\partial u}{\partial x} + v\frac{\partial u}{\partial y} = \frac{\mu}{\rho}\left(1+\frac{1}{\gamma}\right)\frac{\partial^2 u}{\partial y^2} - \frac{\sigma {B_0}^2}{\rho}u - \frac{\mu}{\rho K_0}u + \\ + g[\beta_T(T-T_\infty) + \beta_C(C-C_\infty)] - \frac{C_b}{\sqrt{K_0}}u^2, \quad (3)$$

$$\rho c_p\left(u\frac{\partial T}{\partial x} + v\frac{\partial T}{\partial y}\right) = k\frac{\partial^2 T}{\partial y^2} + \mu\left(1+\frac{1}{\gamma}\right)\left(\frac{\partial u}{\partial y}\right)^2 - \frac{\partial q_r}{\partial y} + \\ + \sigma {B_0}^2 u^2 + Q_0(T-T_\infty) + R_0(C-C_\infty) + \frac{\rho D_m K_T}{c_s}\frac{\partial^2 C}{\partial y^2}, \quad (4)$$

$$u\frac{\partial C}{\partial x} + v\frac{\partial C}{\partial y} = D_m\frac{\partial^2 C}{\partial y^2} + \frac{D_m K_T}{T_m}\frac{\partial^2 T}{\partial y^2} - K_c(C-C_\infty). \quad (5)$$

The associate boundary conditions:

$$\begin{cases} u = U_0 + L_0\left(1+\frac{1}{\gamma}\right)\frac{\partial u}{\partial y}, \ v = -v_0(x), \\ T = T_w + M_0\frac{\partial T}{\partial y}, \ C = C_w + N_0\frac{\partial C}{\partial y} \quad \text{at} \quad y = 0; \\ u \to 0, \ T \to T_\infty, \ C \to C_\infty \quad \text{as} \quad y \to \infty. \end{cases} \quad (6)$$

Here, u and v are the fluid speeds along x- and y-axes, respectively, c_s denotes the species susceptibility, K_T and K_c signifies the thermal-diffusion and constant of chemical reaction, respectively, heat expansion is expressed by β_T, μ, ρ are dynamic viscosity and liquid density, respectively, γ is the Casson parameter, K_0 is the porous medium permeability, q_r – heat fluctuation, C_b, β_C, D_m, T_m and σ stand for drag force factor, solute expression, mass diffusivity, mean temperature and fluid electric conductivity, respectively, R_0, Q_0, and c_p are the coefficients of radiation absorption, heat source/sink and specific heat, respectively, velocity suction/blowing is expressed by $v_0(x)$.

Incorporating the Rosseland approximation [49] for q_r as follows:

$$q_r = -\frac{4\sigma^*}{3k^*}\frac{\partial T^4}{\partial y}, \quad (7)$$

and extending the term T^4 in Taylor's expansion around T_∞ by ignoring high-order terms as

$$T^4 \cong 4T_\infty^3 T - 3T_\infty^4, \quad (8)$$

Eq. (4) can consequently be reformulated as

$$\rho c_p\left(u\frac{\partial T}{\partial x} + v\frac{\partial T}{\partial y}\right) = k\frac{\partial^2 T}{\partial y^2} + \sigma {B_0}^2 u^2 + \mu\left(1+\frac{1}{\gamma}\right)\left(\frac{\partial u}{\partial y}\right)^2 + \\ + \frac{16\sigma^* T_\infty^3}{3k^*}\frac{\partial^2 T}{\partial y^2} + Q_0(T-T_\infty) + R_0(C-C_\infty) + \frac{\rho D_m K_T}{c_s}\frac{\partial^2 C}{\partial y^2}. \quad (9)$$

Now, we introduce a dimensional variable η and functions $f(\eta), \theta(\eta)$, and $\phi(\eta)$ as follows:

$$\eta = \sqrt{\frac{U_0}{2\upsilon x}}\, y, \quad u = \frac{\partial \psi}{\partial y}, \quad v = -\frac{\partial \psi}{\partial x}, \quad \theta(\eta) = \frac{T-T_\infty}{T_w - T_\infty}, \\ \psi(x) = \sqrt{2\upsilon x U_0}\, f(\eta), \quad \phi(\eta) = \frac{C-C_\infty}{C_w - C_\infty}. \quad (10)$$

Enforcing Eq. (10) into Eqs. (3), (5), (6) and (9), we obtain the following set of ordinary differential equations (ODEs):

$$\left(1+\frac{1}{\gamma}\right)f''' + \mathrm{Gr}\,\theta - M\,f' - \mathrm{Fr}\,f'^2 + \mathrm{Gm}\,\phi + \\ - K_1\,f' + f\,f'' = 0, \quad (11)$$

$$\frac{1}{\mathrm{Pr}}\left(1+\frac{4}{3}N\right)\theta'' + f\,\theta' + \mathrm{Du}\,\phi'' + \mathrm{Ec}\left(1+\frac{1}{\gamma}\right)f''^2 + \\ + \mathrm{Ec}\,M\,f'^2 + Q^*\,\theta + R^*\,\phi = 0, \quad (12)$$

$$\frac{1}{\mathrm{Sc}}\,\phi'' + \mathrm{Sr}\,\theta'' + f\,\phi' - K_c'\,\phi = 0, \quad (13)$$

and the boundary conditions:

$$f(0) = S, \quad f'(0) = 1 + \left(1 + \frac{1}{\gamma}\right) B_u f''(0),$$

$$\theta(0) = 1 + B_t \theta'(0), \quad \phi(0) = 1 + B_c \phi'(0) \text{ at } \eta = 0, \quad (14)$$

$$f' \to 0, \quad \theta \to 0, \quad \phi \to 0 \qquad \text{as } \eta \to \infty. \quad (15)$$

The relevant parameters are further specified as:

$\mathrm{Gr} = \frac{2g\beta_T x(T_w - T_\infty)}{{U_0}^2}$ – heat Grashof number, $N = \frac{4\sigma^* T_\infty^3}{k\,k^*}$ – radiation parameter, $\mathrm{Fr} = \frac{2C_b x}{\sqrt{K_0}}$ – Forchheimer number, $K_1 = \frac{2\upsilon x}{K_0 U_0}$ – porosity parameter, $\mathrm{Gm} = \frac{2g\beta_C x(C_w - C_\infty)}{{U_0}^2}$ – mass Grashof number, $M = \frac{2\sigma {B_0}^2 x}{U_0 \rho}$ – magnetic parameter, $\mathrm{Ec} = \frac{{U_0}^2}{c_p(T_w - T_\infty)}$ – Eckert number, $Q^* = \frac{2Q_0 x}{U_0 \rho c_p}$ – heat generation/absorption factor, $\mathrm{Pr} = \frac{\upsilon \rho C_p}{k}$ – Prandtl number, $\mathrm{Du} = \frac{D_m K_T}{\upsilon c_s c_p} \frac{(C_w - C_\infty)}{(T_w - T_\infty)}$ – Dufour number, $Sc = \frac{\upsilon}{D_m}$ – Schmidt number, $Sr = \frac{D_m K_T}{\upsilon T_m} \frac{(T_w - T_\infty)}{(C_w - C_\infty)}$ – Soret number, $R^* = \frac{2R_0 x}{U_0 \rho c_p} \frac{(C_w - C_\infty)}{(T_w - T_\infty)}$ – radiation absorption parameter, $K_c' = \frac{2K_c x}{U_0}$ – reaction parameter, $S = v_0 \sqrt{\frac{2x}{\upsilon U_0}}$ – suction (> 0)/blowing (< 0) parameter, $B_u = L_0 \sqrt{\frac{U_0}{2\upsilon x}}$ – velocity slip factor, $B_t = M_0 \sqrt{\frac{U_0}{2\upsilon x}}$ – thermal slip factor, and $B_c = N_0 \sqrt{\frac{U_0}{2\upsilon x}}$ – concentration slip factor.

Our concentration is now directed towards the examination of vital physical quantities, specifically skin-friction factor (C_{f_x}), Nusselt number (Nu_x) and Sherwood number (Sh_x). These paramount parameters play a fundamental role in deciphering flow dynamics and heat attributes. Their explicit formulations are presented below:

$$C_{f_x} = \frac{2\mu\left(1 + \frac{1}{\gamma}\right)\left(\frac{\partial u}{\partial y}\right)_{y=0}}{\rho {U_0}^2}, \quad (16)$$

$$\mathrm{Nu}_x = -\frac{x\left(k + \frac{16\sigma^* T_\infty^3}{3k^*}\right)\left(\frac{\partial T}{\partial y}\right)_{y=0}}{k(T_w - T_\infty)}, \quad (17)$$

$$\mathrm{Sh}_x = -\frac{x\left(\frac{\partial C}{\partial y}\right)_{y=0}}{(C_w - C_\infty)}. \quad (18)$$

Enforcing the similarity transformations given in Eq. (10), we get:

$$C_{f_x} = \frac{1}{\sqrt{\mathrm{Re}_x}}\left(1 + \frac{1}{\gamma}\right) f''(0), \quad (19)$$

$$\mathrm{Nu}_x = -\sqrt{\mathrm{Re}_x}\left(1 + \frac{4}{3}N\right)\theta'(0), \quad (20)$$

$$\mathrm{Sh}_x = -\sqrt{\mathrm{Re}_x}\phi'(0), \quad (21)$$

where $\mathrm{Re}_x = \frac{U_0 x}{2\upsilon}$ is the Reynolds number.

3. Numerical methodology

To evaluate the flow problem, the numerical technique bvp4c is exploited in MATLAB software. The initial step is to transmute the group of higher-order ODEs provided in Eqs. (11)–(13) and the boundary conditions in Eqs. (14)–(15) into an initial value problem (IPV) via a first-order process:

$$f = y_1, \; f' = y_2, \; f'' = y_3, \; \theta = y_4, \; \theta' = y_5,$$

$$\phi = y_6, \; \phi' = y_7,$$

$$y_3' = \left(\frac{1}{1 + \frac{1}{\gamma}}\right)(M\, y_2 + Fr\, {y_2}^2 + K_1\, y_2 - y_1\, y_3 + -Gr\, y_4 - Gm\, y_6). \quad (22)$$

$$y_5' = -\mathrm{Pr}\left\{\frac{\mathrm{Ec}\left[\left(1 + \frac{1}{\gamma}\right) {y_3}^2 + M\, {y_2}^2\right] + y_1\, y_5 + Q^*\, y_4 + R^*\, y_6 + \mathrm{DuSc}\,(K_c'\, y_6 - y_1\, y_7)}{\left(1 + \frac{4}{3}N - \mathrm{Pr\,DuScSr}\right)}\right\}, \quad (23)$$

$$y_7' = -\mathrm{Sc}(y_1 y_7 + \mathrm{Sr} y_5' - K_c' y_6), \quad (24)$$

subject to:

$$\begin{cases} y_1(0) = S, \quad y_2(0) = 1 + \left(1 + \frac{1}{\gamma}\right) B_u\, y_3(0), \\ y_4(0) = 1 + B_t\, y_5(0), \quad y_6(0) = 1 + B_c\, y_7(0), \end{cases} \quad (25)$$

$$y_2 \to 0, \; y_4 \to 0, \; y_6 \to 0 \quad \text{as} \quad \eta \to \infty. \quad (26)$$

To provide a more precise estimate of the outcomes, the values of $y_3(0)$, $y_5(0)$ and $y_7(0)$ are improved with a maximum error of 10^{-5} and a step size of $h = 0.1$.

4. Validation of our code

In order to evaluate the precision of the proposed numerical technique, our results are compared with the outcomes achieved by

Table 1. Comparative analysis of C_{f_x}, Nu_x, and Sh_x with previous outcomes.

		Alam et al. [44]			Ram et al. [46]			Present result		
Sr	**Du**	C_{f_x}	Nu_x	Sh_x	C_{f_x}	Nu_x	Sh_x	C_{f_x}	Nu_x	Sh_x
2.0	0.030	6.2285	1.1565	0.1531	6.22686	1.15620	0.15352	6.2260	1.1561	0.1535
1.6	0.037	6.1491	1.1501	0.2283	6.14662	1.14971	0.22866	6.1466	1.1497	0.2287
1.2	0.050	6.0720	1.1428	0.3033	6.06948	1.14235	0.30358	6.0695	1.1423	0.3036
0.8	0.075	6.0006	1.1333	0.3781	5.99810	1.13285	0.37840	5.9981	1.1329	0.3784

Alam et al. [44] and Ram et al. [46]. The values of C_{f_x}, Nu_x and Sh_x are compared with the results of Alam et al. [44] and Ram et al. [46] for different levels of Sr and Du in Table 1 by taking $\mathrm{Sc} = 0.22$, $\mathrm{Pr} = 0.71$, $\mathrm{Gr} = 10$, $M = 0.3$, $\mathrm{Gm} = 4$, $S = 0.5$, $\mathrm{Fr} = K_c' = K_1 = Q^* = \mathrm{Ec} = N = R^* = B_u = B_t = B_c = 0$, $\gamma \to \infty$, $\mathrm{Re}_x = 1$. After making the comparisons, the bvp4c code was found to be precise and highly efficient.

5. Results and discussion

To figure out the physical understanding of the work, the numerical calculation is examined for various factors, and the possessed outcomes are manifested with the assistance of diagrams and tables. The context values in the existing study were chosen as $\gamma = 0.5$, $\mathrm{Gr} = 4$, $\mathrm{Gm} = M = \mathrm{Pr} = 2$, $N = 1.5$, $\mathrm{Sr} = \mathrm{Ec} = Q^* = 0.2$, $\mathrm{Du} = \mathrm{Sc} = 0.6$, $S = R^* = K_c' = 0.5$, $\mathrm{Fr} = K_1 = B_u = B_t = B_c = 1.0$, $\mathrm{Re}_x = 1$ and maintained fixed during the computations. Here,

- Schmidt number $\mathrm{Sc} = 0.6$, signifies water vapour;
- Prandtl number $\mathrm{Pr} = 2$, assents physically to water;
- Du and Sr are selected so that their multiplication is stable, and the mean temperature T_m remains stable as well;
- other values are selected at random.

The outcomes possessed from the numerical calculation are presented by figures displaying velocity $f'(\eta)$, temperature distribution $\theta(\eta)$ and concentration $\phi(\eta)$.

The change of the velocity amplitude $f'(\eta)$ for diverse Casson factor (γ) values is depicted in Fig. 2. Regarding that, an enhancement in γ decreases the flow rate magnitude. Because the augmentation in γ increases the yield stress, which bans the flow and molecules interplay, the substance develops a viscous bond. As a result, when γ increases, the flow rate decreases.

The effect of M on the velocity is verified in Fig. 3. It is explicit that velocity amplitude $f'(\eta)$ decreases with growth in M. The existence of magnetic induction in an electrically conducting liquid propels a protesting force named Lorentz force that

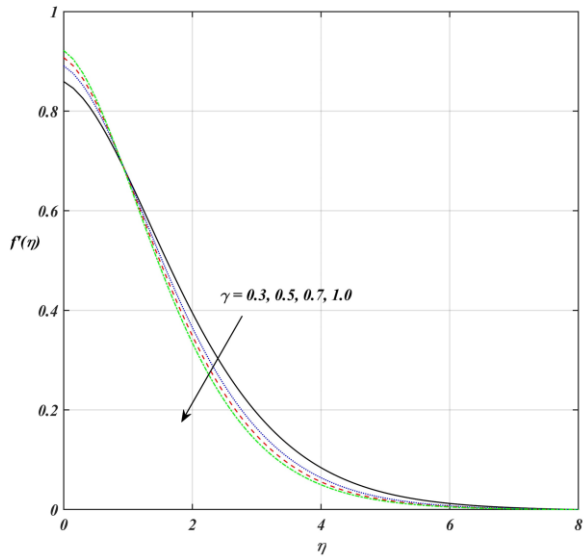

Fig. 2. The change of velocity with diverse values of γ.

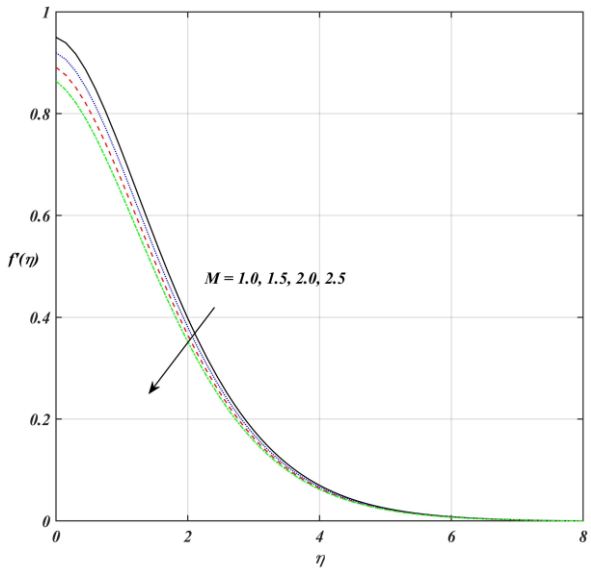

Fig. 3. The change of velocity with diverse values of M.

slows down the fluid motion. For the grater values of M, the Lorentz force becomes more apparent, leading to a damping in $f'(\eta)$. Conversely, the tiny values of M result in a significant augmentation in $f'(\eta)$. Hence, by adjusting the strength of the magnetic field, one can achieve the desired flow rate, which may be crucial for mechanical reasons when controlling fluid flow.

Figures 4 and 16 delineate the effect of S on dimensionless profiles $f'(\eta)$ and $\theta(\eta)$, respectively. It is noticed that suction $(S > 0)$ detracts flow rate and temperature phenomena, while blowing $(S < 0)$ augments them. This is because, suction $(S > 0)$ tends to thin the flake, while blowing $(S < 0)$ thickens it. This alteration in extent of the flake thickness influences fluid flow near the surface. Also, the thermal transmission rate (from the fluid to the surface) is slowed down. Thereby, suction or blowing can be used to control flow separation.

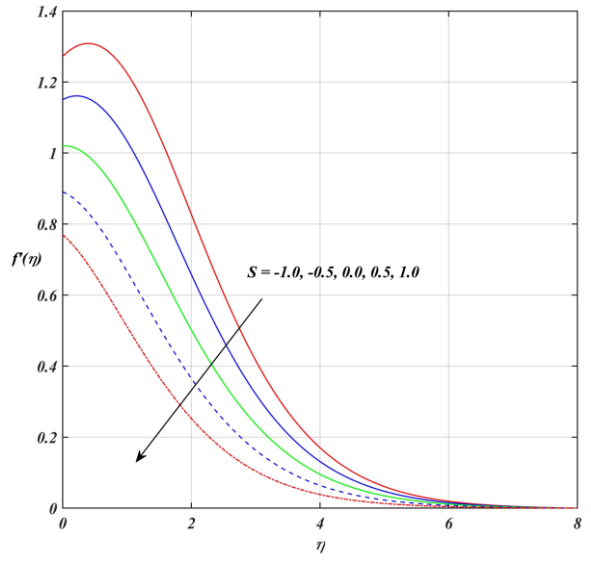

Fig. 4. The change of velocity with diverse values of S.

The change of the velocity amplitude $f'(\eta)$ for diverse values of heat (Gr) and mass (Gm) Grashof numbers is depicted in Figs. 5 and 6, respectively. It is manifested that a significant increase in surface refrigeration causes Gr and Gm to rise, resulting in an increase in velocity. Also, the growth in the value of Gr and Gm has the inclination to augment the thermal and mass buoyancy stress.

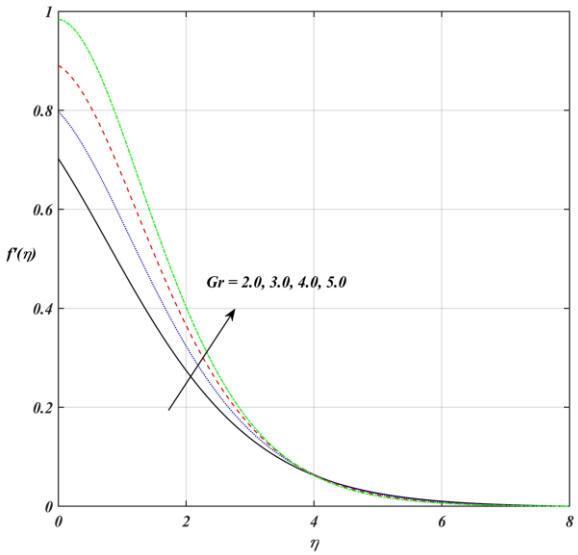

Fig. 5. The change of velocity with diverse values of Gr.

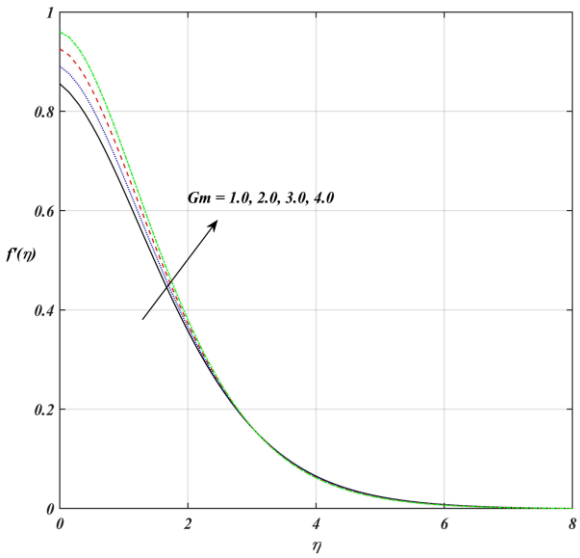

Fig. 6. The change of velocity with diverse values of Gm.

Figure 7 plots the behaviour of dimensionless profile $f'(\eta)$ with K_1. It should be noticed that the larger values of K_1 suggest a porous medium with low permeability and high dynamic viscosity as $K_1 = \frac{2\upsilon x}{K_0 U_0}$, which produces a higher fluid flow resistance. As seen in Fig. 7, rising values of K_1 result in a drop in $f'(\eta)$. Thus, the existence of porous media leads to a drop in flow velocity.

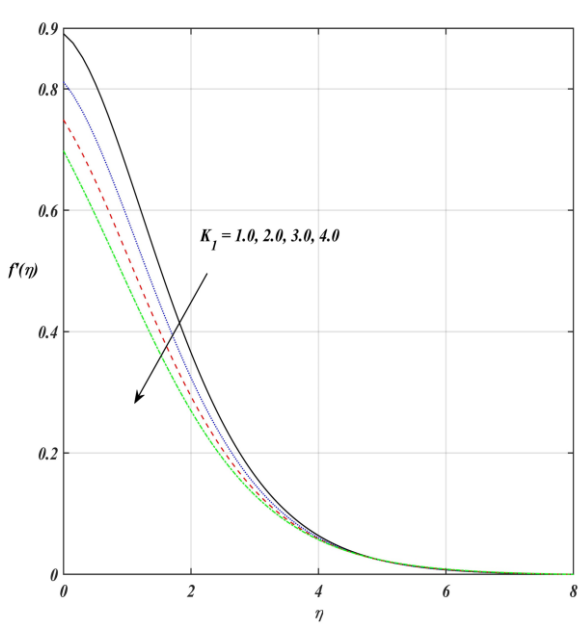

Fig. 7. The change of velocity with diverse values of K_1.

Figure 8 exhibits the effect of B_u on velocity profiles. Initially, the velocity decreases as B_u grows, but after $\eta = 1.5$, it slightly rises. This is because, as the slip stage happens, the velocity of the semi-infinite plate is not as analytic as the velocity of the flow near the plate.

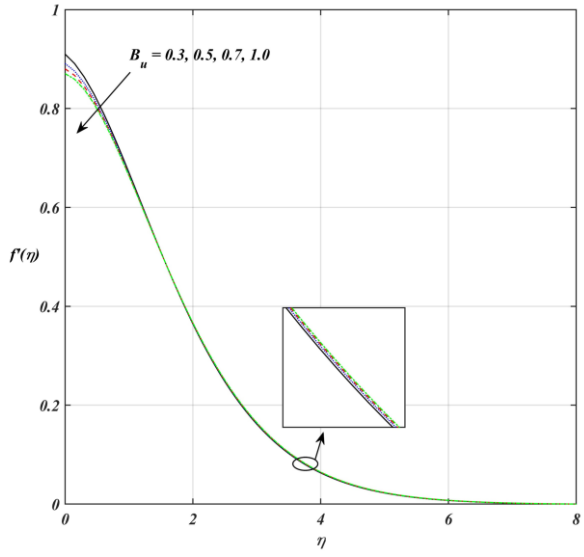

Fig. 8. The change of velocity with diverse values of B_u.

Figures 9 and 17 delineate the impressions of Dufour quantity Du on $f'(\eta)$ and $\theta(\eta)$, respectively. These profiles exhibit that $f'(\eta)$ and $\theta(\eta)$ both boost with rising values of Du. Physically, Du is the proportion of thermal diffusion and mass diffusion. For higher values of Du, thermal diffusion occurs much more effectively, and viscosity drops, leading to an augmentation in both $f'(\eta)$ and $\theta(\eta)$.

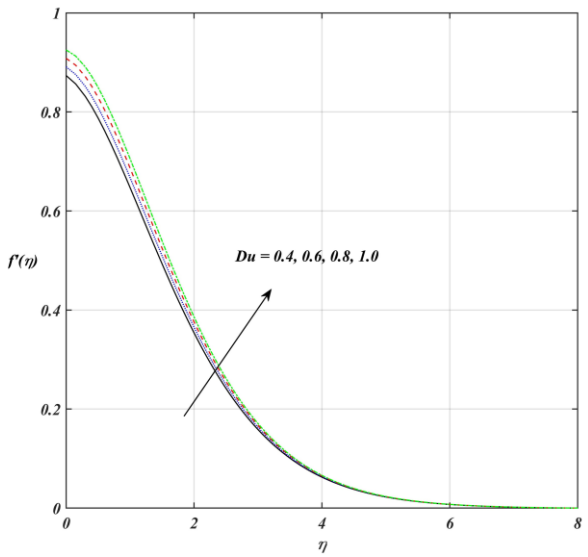

Fig. 9. The change of velocity with diverse values of Du.

Figure 10 declares the role of Fr on the momentum profile $f'(\eta)$. We detected that the momentum profile decreases as Fr rises, while it slightly increases away from the plate. Physically, grater values of Fr suggest a porous medium with low permeability and high dynamic viscosity as $\mathrm{Fr} = \frac{2C_b x}{\sqrt{K_0}}$, which produces a higher fluid flow resistance.

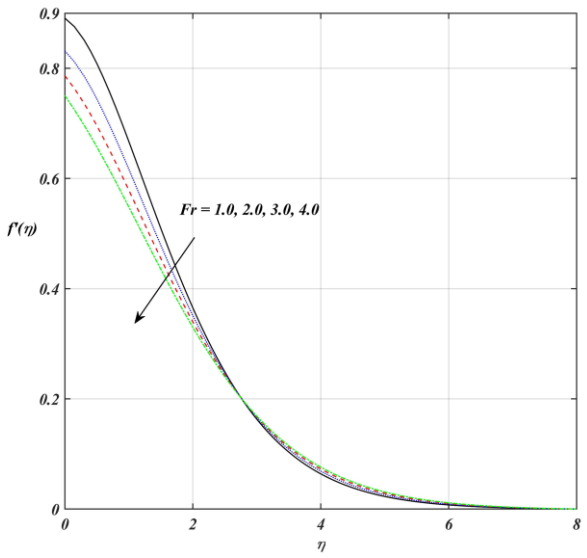

Fig. 10. The change of velocity with diverse values of Fr.

Figures 11 and 18 delineate the impressions of Ec on $f'(\eta)$ and $\theta(\eta)$, respectively. These profiles exhibit that velocity and temperature experience an increase with an increment in the dissipation parameter Ec. The existence of viscous dissipation causes the conversion of kinetic energy into internal energy as the fluid performs work against viscous forces. As a result, we may state that $f'(\eta)$ and $\theta(\eta)$ both are rising.

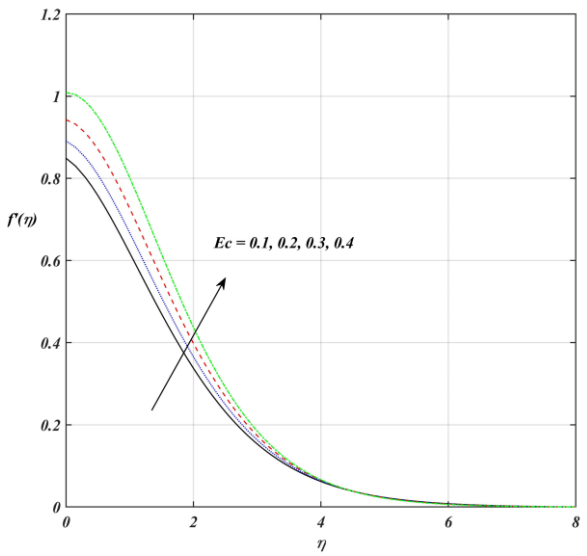

Fig. 11. The change of velocity with diverse values of Ec.

Figures 12 and 19 depict the responses of dimensionless profiles $f'(\eta)$ and $\theta(\eta)$ to diverse values of N within the boundary layer region, respectively. We detected that $f'(\eta)$ and $\theta(\eta)$ both rise as N increases. Physically, increasing values of N enhance the heat transfer performance from the plate to the fluid. Therefore, more heat is transmitted into the fluid for higher values of N. As a result, the surface temperature decreases, but the thermal boundary layer thickens.

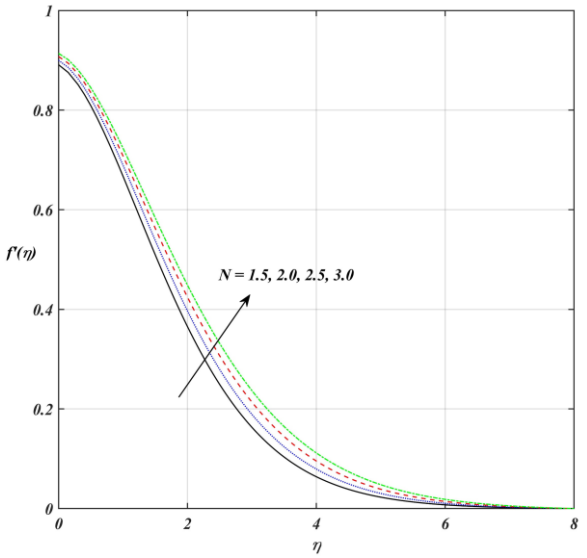

Fig. 12. The change of velocity with diverse values of N.

The change of the temperature $\theta(\eta)$ for diverse Casson factor (γ) values are depicted in Fig. 13. The yield stress or critical shear rate encourage molecular rigidity, which bans the liquid molecules from interplaying. In this context, when γ increases, the temperature distribution $\theta(\eta)$ decreases.

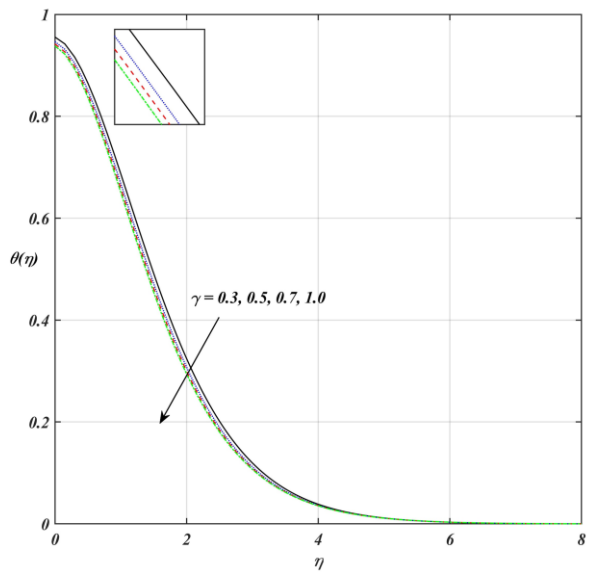

Fig. 13. The change of temperature with diverse values of γ.

Figure 14 is outlined to infer the effect of M on temperature. We found that the larger values of the magnetic parameter cause a rise in $\theta(\eta)$. This is because the higher values of the Lorentz force generate heat energy in flow, which promotes the increase of the thermal boundary layer.

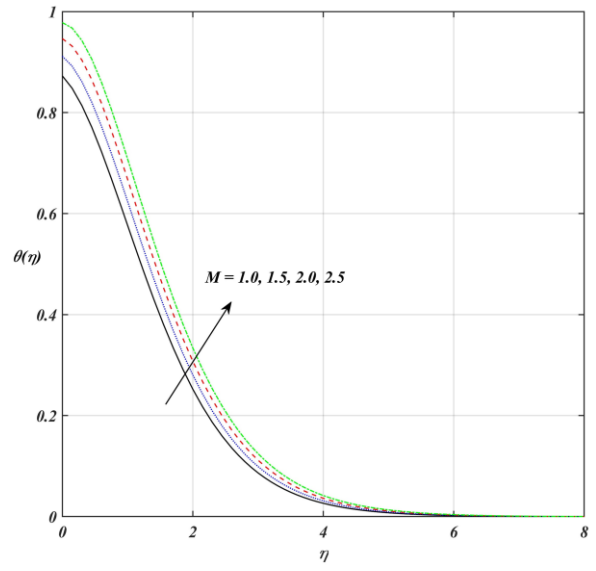

Fig. 14. The change of temperature with diverse values of M.

Figure 15 depicts the variation in dimensionless profile $\theta(\eta)$ for diverse values of Pr. It has been observed that fluid temperature reduces with enhanced Pr. This is due to the fact that the thermal conductivity of the substance is decreased with augmentation in Pr, resulting in a deficit in the thermal boundary layer. Additionally, Fig. 20 points out that the temperature $\theta(\eta)$ reduces as B_t rises because low heat is transported from the plate to the fluid.

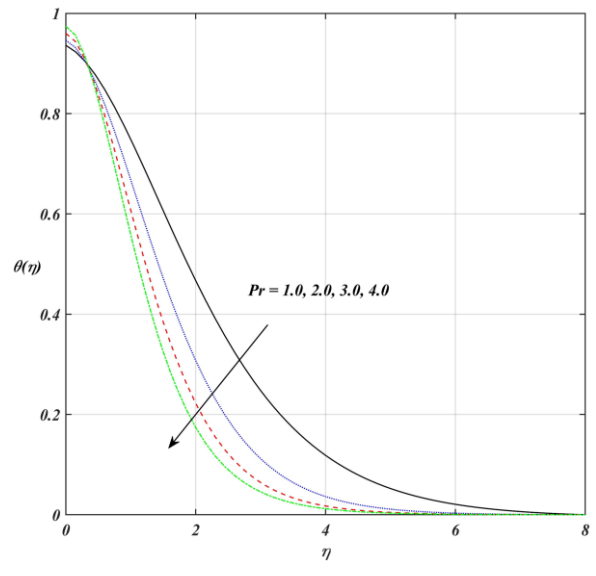

Fig. 15. The change of temperature with diverse values of Pr.

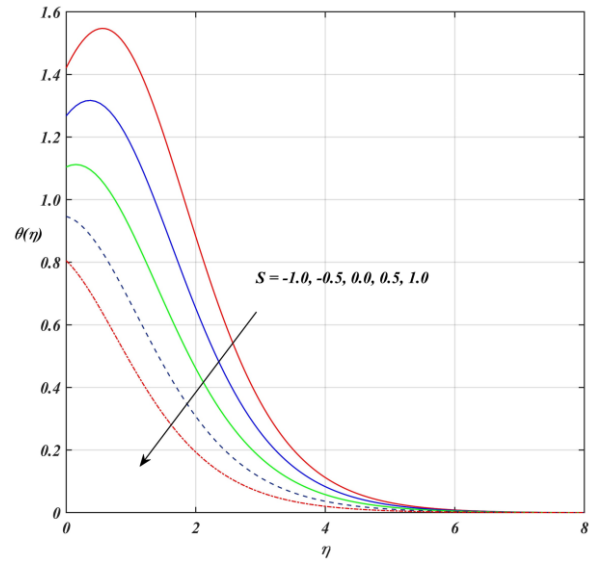

Fig. 16. The change of temperature with diverse values of S.

The effect of Q^* on $\theta(\eta)$ has been illustrated in Fig. 21. It indicates that heat transport is enhanced by internal heat generation ($Q^* > 0$). Consequently, the thermal boundary layer distends for greater values of Q^* (> 0). This phenomenon arises because an increase in the heat suction parameter amplifies the heat energy in the flow arrangement, thereby thickening the thermal boundary layer. It is also noted that increasing Q^* (> 0), causes a reduction in the heat transfer rate.

Figure 22 depicts the change of temperature $\theta(\eta)$ with varied values of R^*. It indicates that heat transport is enhanced by increasing values of R^* as heat is absorbed by the buoyancy accurate flow. Additionally, the thermal boundary layer thickness increases.

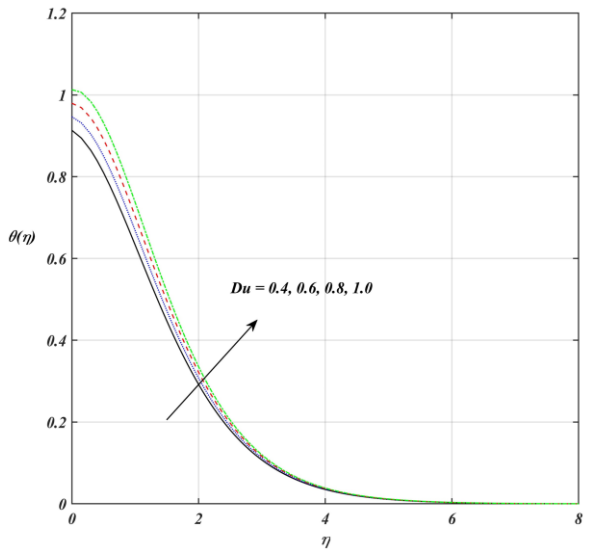

Fig. 17. The change of temperature with diverse values of Du.

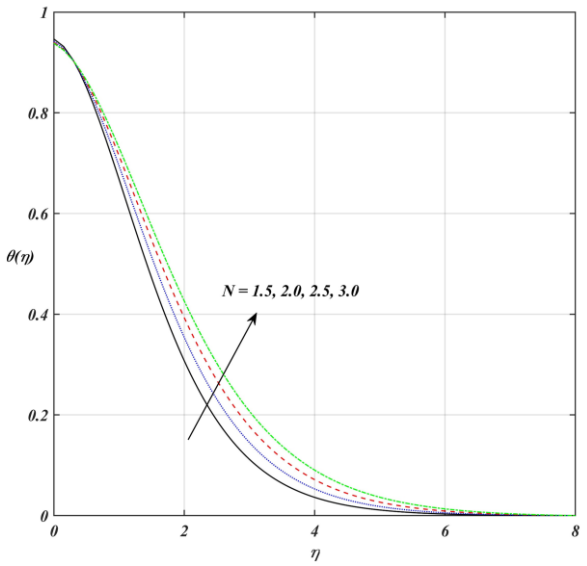

Fig. 19. The change of temperature with diverse values of N.

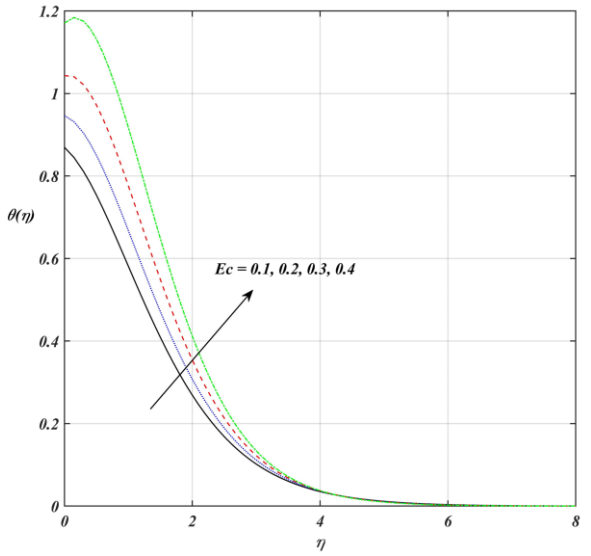

Fig. 18. The change of temperature with diverse values of Ec.

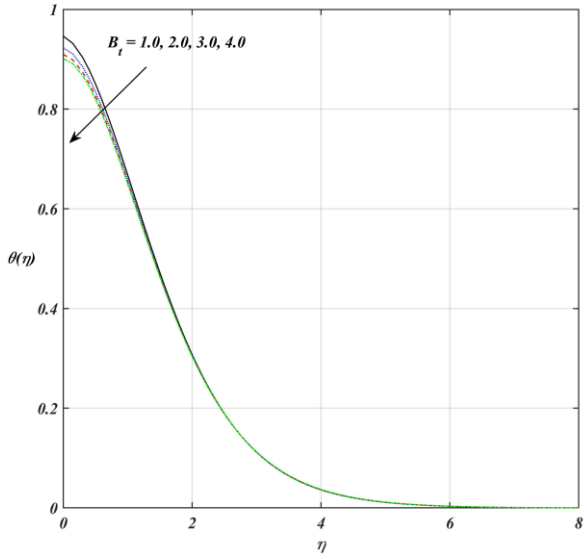

Fig. 20. The change of temperature with diverse values of B_t.

Figure 23 depicts the change of concentration $\phi(\eta)$ with different values of Sr. We detected that $\phi(\eta)$ is increased by augmentation of Sr. The impact of the Soret number is demonstrated by a dynamic molecule under the effect of temperature slope. This passes heavy molecules to a cold arrangement and slight molecules to a hot arrangement, which hereby leads to an enhanced concentration profile. Figure 24 portrays the change of concentration $\phi(\eta)$ with varied values of Sc. Physically, Sc is the proportion between kinematic viscosity and mass diffusivity, and the increment in mass diffusivity reduces Sc. So, the increasing trend in Sc reduces the species concentration. Additionally, Fig. 25 exhibits the effect of S on concentration $\phi(\eta)$. We detected that $\phi(\eta)$ is reduced by augmentation in S. This implies that the density of the concentration boundary layer decreases.

The effect of K_c' on concentration $\phi(\eta)$ is verified in Fig. 26. We explored that $\phi(\eta)$ diminishes as K_c' boosts. This is because as K_c' increases, the fluid becomes polarized, and the particles spread, decreasing the concentration of the fluid flow.

The change of C_{f_x} against K_1 for two values of M is shown in Fig. 27. It is observed that C_{f_x} reduces by raising both K_1 and M. Thus, the porous media with low permeability have a considerable role in enhancing the fluid flow resistance.

Figure 28 illustrates the tendency of Nu_x with the change of Pr for $\mathrm{Du} = 0.6, 1.0$. It is detected that Nu_x reduces by raising Pr and Du both. Moreover, Fig. 29 exhibits the behaviour of Sh_x against K_c' for two values of Sc. From this, it is noted that $\mathrm{Sh_x}$ grows with enhancing both K_c' and Sc.

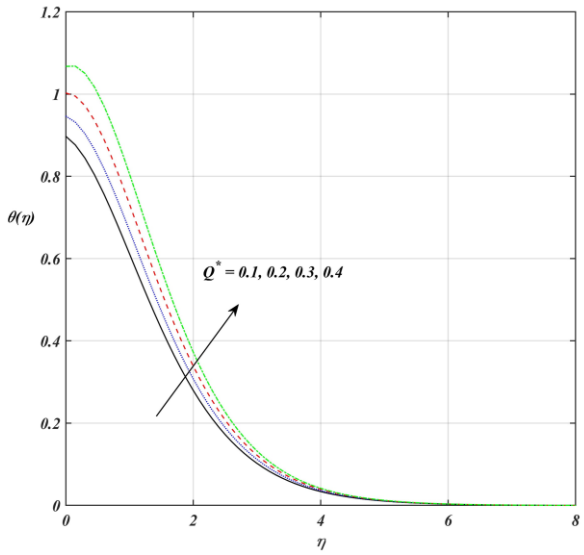

Fig. 21. The change of temperature with diverse values of Q^*.

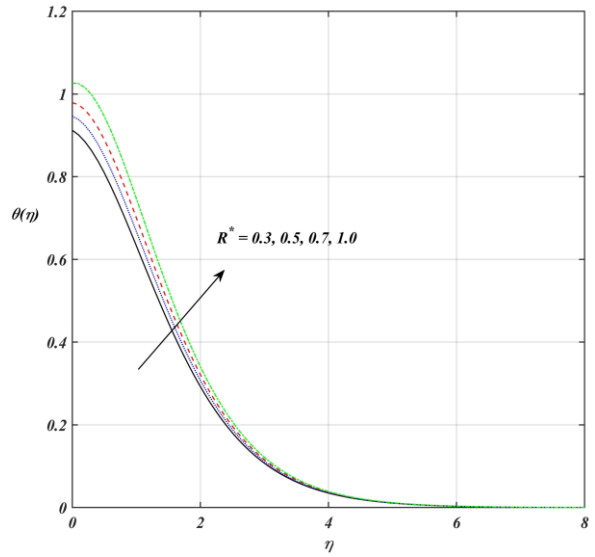

Fig. 22. The change of temperature with diverse values of R^*.

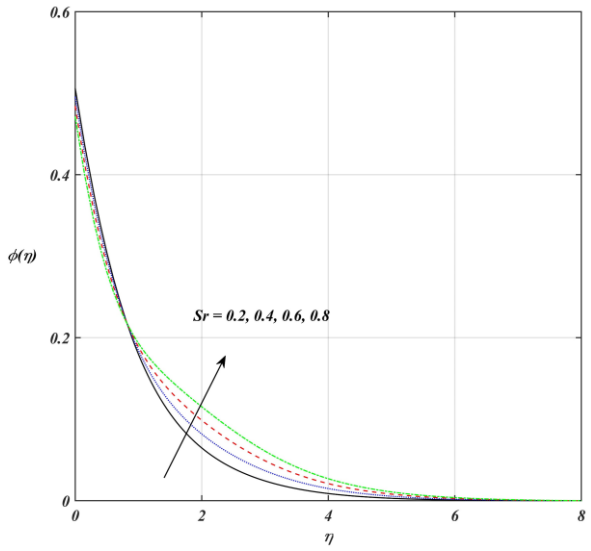

Fig. 23. The change of temperature with diverse values of Sr.

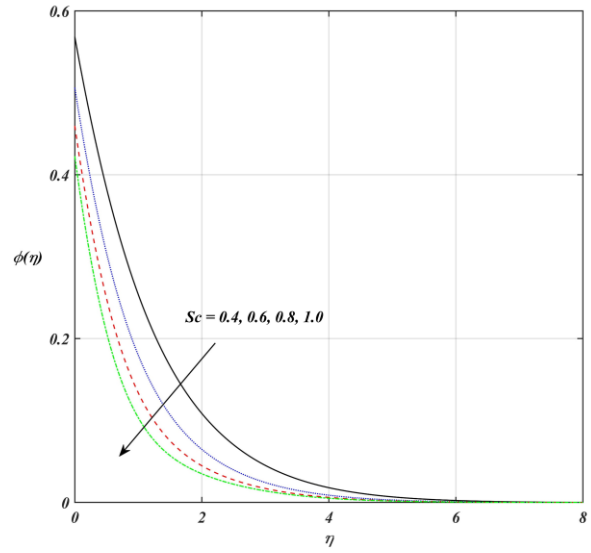

Fig. 24. The change of concentration with diverse values of Sc.

To comprehensively characterize the dynamics of flow and heat transfer, vital dimensionless physical quantities C_{f_x}, Nu_x and Sh_x are meticulously examined for varied governing parameters.

Tables 2 and 3 depict the reactions of C_{f_x} and Sh_x to varied values of governing parameters, respectively. A reduction in C_{f_x} is observed for enhancing values of M, Fr and K_1. Simultaneously, the Sherwood number Sh_x, another crucial quantity, exhibits a distinct pattern, i.e. it undergoes a notable escalation for increasing values of K_c', Sc and Sr.

In Table 4, we investigated how the parameters N, Q^*, R^*, and Du affect the Nusselt number Nu_x. It has been found that Nu_x decreases with an increase in the parameters Q^*, R^* and Du, while it grows under the influence of N.

Table 2. Data of C_{f_x} for varying levels of M, Fr, K_1 when $\mathrm{Re}_x = 1$.

M	Fr	K_1	C_{f_x}
1.0	1	1	-0.0998
1.5	1	1	-0.1606
2.0	1	1	-0.2178
2.0	1	1	-0.2178
2.0	2	1	-0.3367
2.0	3	1	-0.4268
2.0	1	1	-0.2178
2.0	1	2	-0.3764
2.0	1	3	-0.5016

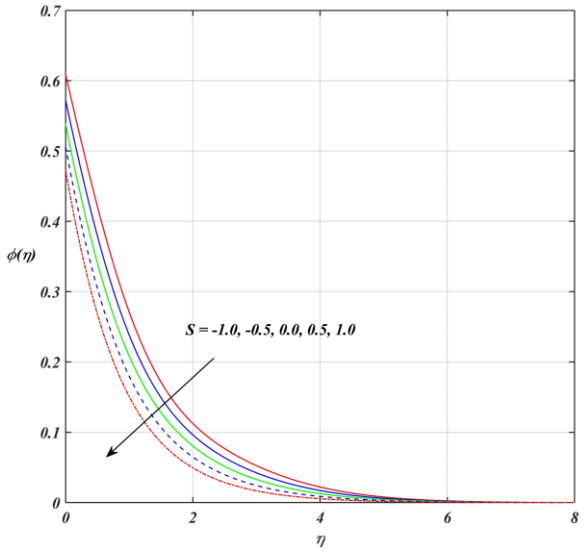

Fig. 25. The change of concentration with diverse values of S.

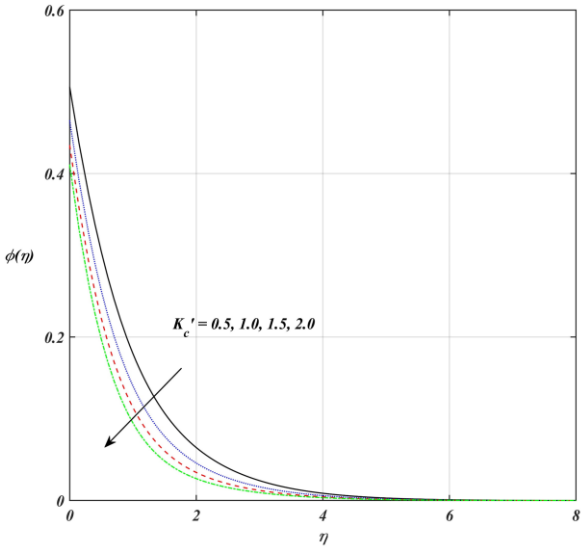

Fig. 26. The change of concentration with diverse values of K_c'.

Table 3. Data of Sh_x for several levels of $K_c', \mathrm{Sc}, \mathrm{Sr}$ when $\mathrm{Re}_x = 1$.

K_c'	Sc	Sr	Sh_x
0.5	0.6	0.2	0.4937
1.0	0.6	0.2	0.5348
1.5	0.6	0.2	0.5651
0.5	0.4	0.2	0.4314
2.0	0.6	0.2	0.4937
2.0	0.8	0.2	0.5402
2.0	0.6	0.2	0.4937
2.0	0.6	0.4	0.5042
2.0	0.6	0.6	0.5157

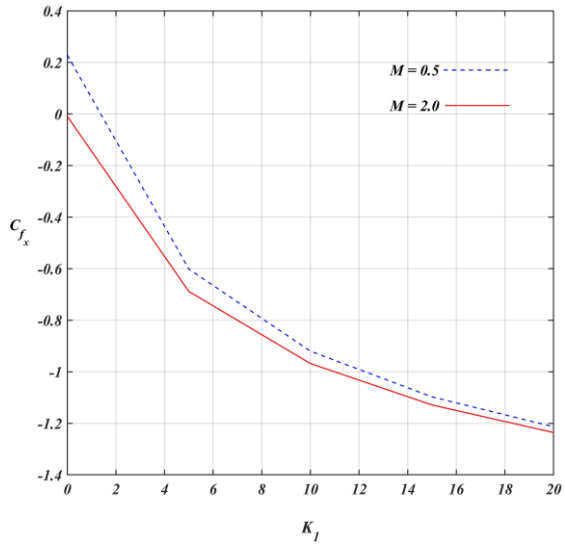

Fig. 27. Variance in C_{f_x} against K_1 and M.

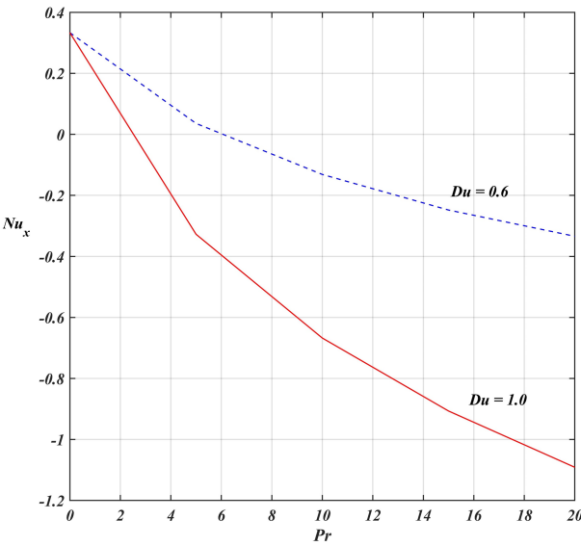

Fig. 28. Variance in Nu_x against Pr and Du.

Table 4. Data of Nu_x for different levels of N, Q^*, R^*, Du when $\mathrm{Re}_x = 1$.

N	Q^*	R^*	Du	Nu_x
1.5	0.2	0.5	0.6	0.1603
2.0	0.2	0.5	0.6	0.2116
2.5	0.2	0.5	0.6	0.2612
1.5	0.1	0.5	0.6	0.3073
1.5	0.2	0.5	0.6	0.1603
1.5	0.3	0.5	0.6	-0.0086
1.5	0.2	0.3	0.6	0.2627
1.5	0.2	0.5	0.6	0.1603
1.5	0.2	0.7	0.6	0.0617
1.5	0.2	0.5	0.4	0.2593
1.5	0.2	0.5	0.6	0.1603
1.5	0.2	0.5	0.8	0.0608

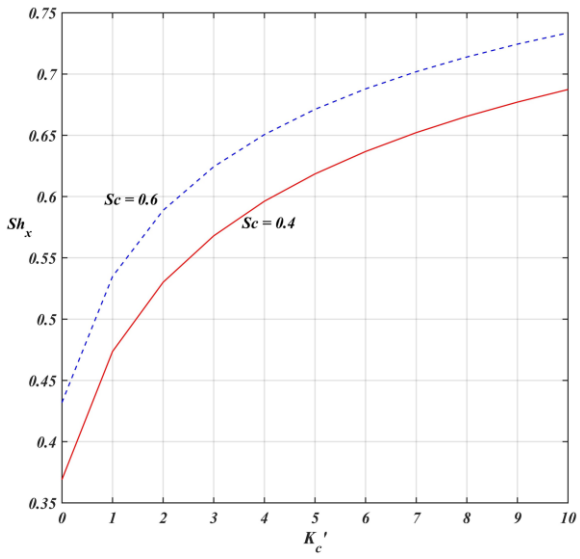

Fig. 29. Variance in Sh_x against K_c' and Sc.

6. Conclusions

In the current work, the influence of radiation absorption and viscous dissipation on the MHD mixed convection flow of Casson fluid from a semi-infinite vertical plate has been investigated mathematically. The governing equations were solved numerically employing an entirely inherent bvp4c method. The comparative interpretation was also noted pictorially. The effects of several physical parameters on $f'(\eta), \theta(\eta)$ and $\phi(\eta)$ are described as follows:

- Suction parameter $(S > 0)$ lowers the velocity, temperature and concentration profiles, while the effect of the blowing parameter $(S < 0)$ is reverse.
- An enhancement in the parameters N, Ec, and Du led to a rise in temperature and velocity, while the effect of the Casson parameter is opposite.
- A growth in the parameters K_1, B_u, M, and Fr led to a reduction in velocity, while the effect of Gr and Gm is reverse.
- A growth in the parameters $Q^*, R^*$and M led to an augmentation in temperature, while the effect of Pr and B_t is reverse.
- An increase in the reaction parameter and Schmidth number led to a reduction in the concentration profile, while the effect of the Soret number is opposite.
- The local skin friction decreased with improvements in magnetic parameter, Forchheimer number and porosity parameter.
- The local Nusselt number was reduced with an enhancement in Prandtl number, heat generation parameter, absorption parameter and Dufour number while increasing with the radiation parameter.
- The Sherwood number was enlarged with an enhancement in the Soret number, Schmidt number and reaction parameter.

Acknowledgements

This work was supported by Sonam by the CSIR- HRDG Ph.D. grant (09/149(0740)/2019-EMR-I), Ministry of Science & Technology, Government of India.

References

[1] Casson, N.A. (1959). A flow equation for the pigment-oil suspensions of the printing ink type. In: *Rheology of Disperse Systems* (C.C. Mill, ed.), (pp. 84–102). Pergamon Press.

[2] Heller, W. (1960b). Rheology of disperse systems, *Proceedings of a Conference Organized by the British Society of Rheology*, (C.C. MILL, ed.). Pergamon Press, New York, 1959, VII + 223. *Journal of Polymer Science*, 47(149), 537–538. doi: 10.1002/pol.1960.1204714975

[3] Ramana, R.M., Kumar, J.G., & Raju, K.V. (2020). Melting and radiation effects on MHD heat and mass transfer of Casson fluid flow past a permeable stretching sheet in the presence of chemical reaction. *AIP Conference Proceedings*, 2246(1), 020021. doi: 10.1063/5.0014732

[4] Krishna, M.V., Ahammad, N.A., & Chamkha, A.J. (2021). Radiative MHD flow of Casson hybrid nanofluid over an infinite exponentially accelerated vertical porous surface. *Case Studies in Thermal Engineering*, 27, 101229. doi: 10.1016/j.csite.2021.101229

[5] Kodi, R., Mopuri, O., Sree, S., & Konduru, V. (2021). Investigation of MHD Casson fluid flow past a vertical porous plate under the influence of thermal diffusion and chemical reaction. *Heat Transfer*, 51(1), 377–394. doi: 10.1002/htj.22311

[6] Jaffrullah, N.S., Sridhar, N.W., & Ganesh, N.G.R. (2023). MHD radiative Casson fluid flow through Forchheimer permeable medium with Joule heating influence. *CFD Letters*, 115(8), 79–199. doi: 10.37934/cfdl.15.8.179199

[7] Navier, H. (1827). Mémoire sur les lois du mouvement des fluides. *Mémoires de l'Académie des sciences de l'Institut de France*, 6.

[8] Krishna, M.V., & Chamkha, A.J. (2019). Hall and ion slip effects on MHD rotating boundary layer flow of nanofluid past an infinite vertical plate embedded in a porous medium. *Results in Physics*, 15, 102652. doi: 10.1016/j.rinp.2019.102652

[9] Obalalu, A.M., Ajala, O.A., Abdulraheem, A., & Akindele, A.O. (2021). The influence of variable electrical conductivity on non-Darcian Casson nanofluid flow with first and second-order slip conditions. *Partial Differential Equations in Applied Mathematics*, 4, 100084. doi: 10.1016/j.padiff.2021.100084

[10] Vajravelu, K., & Hadjinicolaou, A. (1997). Convective heat transfer in an electrically conducting fluid at a stretching surface with uniform free stream. *International Journal of Engineering Science*, 35(12–13), 1237–1244. doi: 10.1016/s0020-7225(97)00031-1

[11] Chamkha, A.J. (1999). Hydromagnetic three-dimensional free convection on a vertical stretching surface with heat generation or absorption. *International Journal of Heat and Fluid Flow*, 20(1), 84–92. doi: 10.1016/s0142-727x(98)10032-2

[12] Kumar, M.A., Reddy, Y.D., Goud, B.S., & Rao, V.S. (2022). An impact on non-Newtonian free convective MHD Casson fluid flow past a vertical porous plate in the existence of Soret, Dufour, and chemical reaction. *International Journal of Ambient Energy*, 43(1), 7410–7418. doi: 10.1080/01430750.2022. 2063381

[13] Raghunath, K., Obulesu, M., & Raju, K.V. (2023). Radiation absorption on MHD free conduction flow through porous medium over an unbounded vertical plate with heat source. *International*

Journal of Ambient Energy, 44(1), 1712–1720. doi: 10.1080/ 01430750.2023.2181869

[14] Forchheimer, P. (1901). *Wasserbewegung durch boden*. Zeitschrift des Vereins deutscher Ingenieure, 45, 1782–1788.

[15] Aleem, M., Asjad, M.I., Shaheen, A., & Khan, I. (2020). MHD influence on different water based nanofluids (TiO2, Al2O3, CuO) in porous medium with chemical reaction and Newtonian heating. *Chaos, Solitons & Fractals/Chaos, Solitons and Fractals*, 130, 109437. doi: 10.1016/j.chaos.2019.109437

[16] Nasir, S., Berrouk, A.S., Tassaddiq, A., Aamir, A., Akkurt, N., & Gul, T. (2023). Impact of entropy analysis and radiation on transportation of MHD advance nanofluid in porous surface using Darcy-Forchheimer model. *Chemical Physics Letters*, 811, 140221. doi: 10.1016/j.cplett.2022.140221

[17] Bilal, M., Khan, I., Gul, T., Tassaddiq, A., Alghamdi, W., Mukhtar, S., & Kumam, P. (2021). Darcy-Forchheimer hybrid nano fluid flow with mixed convection past an inclined cylinder. *Computers, Materials & Continua*, 66(2), 2025–2039. doi: 10.32604/cmc.2020.012677

[18] Sinha, S., & Yadav, R.S. (2022). MHD mixed convective slip flow along an inclined porous plate in presence of viscous dissipation and thermal radiation. *Trends in Sciences*, 19(4), 2685. doi: 10.48048/tis.2022.2685

[19] Roy, P.P., Chowdhury, S., Raj, M.H., Islam, M.Q., & Saha, S. (2023). Forced, natural and mixed convection of non-Newtonian fluid flows in a square chamber with moving lid and discrete bottom heating. *Results in Engineering*, 17, 100939. doi: 10.1016/ j.rineng.2023.100939

[20] Mukhopadhyay, S. (2009). Unsteady boundary layer flow and heat transfer past a porous stretching sheet in presence of variable viscosity and thermal diffusivity. *International Journal of Heat and Mass Transfer*, 52(21-22), 5213–5217. doi: 10.1016/ j.ijheatmasstransfer.2009.04.013

[21] Mukhopadhyay, S., & Vajravelu, K. (2012). Effects of transpiration and internal heat generation/absorption on the unsteady flow of a Maxwell fluid at a stretching surface. *Journal of Applied Mechanics*, 79(4), 044508. doi: 10.1115/1.4006260

[22] Hussain, M., Jahan, S., Ranjha, Q.A., Ahmad, J., Jamil, M.K., & Ali, A. (2022). Suction/blowing impact on magneto-hydrodynamic mixed convection flow of Williamson fluid through stretching porous wedge with viscous dissipation and internal heat generation/absorption. *Results in Engineering*, 16, 100709. doi: 10.1016/j.rineng.2022.100709

[23] Bejawada, S.G., Reddy, Y.D., Jamshed, W., Nisar, K.S., Alharbi, A.N., & Chouikh, R. (2022). Radiation effect on MHD Casson fluid flow over an inclined non-linear surface with chemical reaction in a Forchheimer porous medium. Alexandria Engineering Journal, 61(10), 8207–8220. doi: 10.1016/ j.aej.2022.01.043

[24] Raju, K.V., Mohanaramana, R., Reddy, S.S., & Raghunath, K. (2023). Chemical radiation and SoRET effects on unsteady MHD convective flow of Jeffrey nanofluid past an inclined semi-infinite vertical permeable moving plate. *Communications in Mathematics and Applications*, 14(1), 237–255. doi: 10.26713/cma. v14i1.1867

[25] Zhao, X., Mopuri, O., Raju, K. V., Farooq, S., Abdullaev, S., Alhazmi, H., Khan, S.U., & Jameel, M. (2024). Analysis of free convective flow of nanofluid due to inclined surface with thermos-diffusion effects and chemical reaction. *Tribology International*, 197, 109792. doi: 10.1016/j.triboint.2024.109792

[26] Planck, M. (1914). *The theory of heat radiation*. Blakiston.

[27] Asha, S., & Sunitha, G. (2020). Thermal radiation and Hall effects on peristaltic blood flow with double diffusion in the presence of nanoparticles. *Case Studies in Thermal Engineering*, 17, 100560. doi: 10.1016/j.csite.2019.100560

[28] Abbas, A., Ijaz, I., Ashraf, M., & Ahmad, H. (2021). Combined effects of variable density and thermal radiation on MHD Sakiadis flow. *Case Studies in Thermal Engineering*, 28, 101640. doi: 10.1016/j.csite.2021.101640

[29] Saravana, R., Reddy, R.H., Murthy, K.V.N., & Makinde, O.D. (2022). Thermal radiation and diffusion effects in MHD Williamson and Casson fluid flows past a slendering stretching surface. *Heat Transfer*, 51(4), 3187–3200. doi: 10.1002/htj.22443

[30] Gambo, J.J., & Gambo, D. (2020). On the effect of heat generation/absorption on magnetohydrodynamic free convective flow in a vertical annulus: An Adomian decomposition method. *Heat Transfer*, 50(3), 2288–2302. doi: 10.1002/htj.21978

[31] Rao, S.R., Vidyasagar, G., & Deekshitulu, G. (2021). Unsteady MHD free convection Casson fluid flow past an exponentially accelerated infinite vertical porous plate through porous medium in the presence of radiation absorption with heat generation/absorption. *Materials Today: Proceedings*, 42(3), 1608–1616. doi: 10.1016/j.matpr.2020.07.554

[32] Manjunatha, S., Puneeth, V., Gireesha, B., & Chamkha, A.J. (2022). theoretical study of convective heat transfer in ternary nanofluid flowing past a stretching sheet. *Journal of Applied and Computational Mechanics*, 8(4), 1279–1286. doi: 10.22055/ jacm.2021.37698.3067

[33] Amar, N., Kishan, N., & Goud, B.S. (2023). Viscous dissipation and radiation effects on MHD heat transfer flow of Casson fluid through a moving wedge with convective boundary condition in the existence of internal heat generation/absorption. *Journal of Nanofluids*, 12(3), 643–651. doi: 10.1166/jon.2023. 1948

[34] Ou, J.W., & Cheng, K.C. (1973). Viscous dissipation effects on thermal entrance region heat transfer in pipes with uniform wall heat flux. *Applied Scientific Research*, 28, 289–301. doi: 10.1007/ bf00413074

[35] Brinkman, H.C. (1951). Heat effects in capillary flow I. Applied Scientific Research. 2, 120– 124. doi: 10.1007/ bf00411976

[36] Swain, B., Parida, B., Kar, S., & Senapati, N. (2020). Viscous dissipation and Joule heating effect on MHD flow and heat transfer past a stretching sheet embedded in a porous medium. Heliyon, 6(10), e05338. doi: 10.1016/j.heliyon.2020.e05338

[37] Das, U.J. (2021). MHD mixed convective slip flow of Casson fluid over a porous inclined plate with Joule heating, viscous dissipation and thermal radiation. *Journal of Mathematical and Computational Science*, 11(3), 3263–3275. doi: 10.28919/jmcs/ 5713

[38] Sadia, H., Mustafa, M., & Farooq, M. (2023). Numerical and series solutions for von-Kármán flow of viscoelastic fluid inspired by viscous dissipation and Joule heating effects. *Alexandria Engineering Journal*, 75, 181–190. doi: 10.1016/j.aej. 2023.05.075

[39] Soret, C. (1880). Influence de la température sur la distribution des sels dans leurs solutions. *Comptes rendus de l'Académie des Sciences* (Paris), 91, 289.

[40] Dufour, L. (1872). The diffusion thermoeffect. *Archives des Sciences Physiques et Naturelles*, 45, 9–12.

[41] Krenn, P., Zimmermann, P., Fischlschweiger, M., & Zeiner, T. (2021). Influence of thermal diffusion on the solvent absorption kinetics of highly cross-linked epoxy resins. *Journal of Molecular Liquids*, 339, 116809. doi: 10.1016/j.molliq.2021.116809

[42] Revathi, G., Avadapu, S., Raju, C., Babu, M.J., Zidan, A., Alaoui, M.K., Shah, N.A., & Chung, J.D. (2023). Dynamics of Lorentz force and cross-diffusion effects on ethylene glycol-based hybrid nanofluid flow amidst two parallel plates with variable electrical conductivity: A multiple linear regression analysis. *Case Studies in Thermal Engineering*, 41, 102603. doi: 10.1016/j.csite.2022. 102603

[43] Ullah, S., Ullah, I., Ali, A., Shah, K., & Abdeljawad, T. (2024). Investigation of cross-diffusion effect on radiative Jeffery-Hamel flow in convergent/divergent stretchable channel with Lorentz force and Joule heating. *Alexandria Engineering Journal*, 86, 289–297. doi: 10.1016/j.aej.2023.11.054

[44] Alam, M.S., Ferdows, M., Ota, M., & Maleque, M.A. (2006). Dufour and Soret effects on steady free convection and mass transfer flow past a semi-infinite vertical porous plate in a porous medium. *International Journal of Applied Mechanics and Engineering*, 11(3), 535–545.

[45] Aruna, S., & Lakshmi, K.J. (2017). Combined effects of thermal diffusion and diffusion thermo on an unsteady MHD Casson fluid flow past a semi-infinite vertically inclined permeable moving plate. *Journal of Nanofluids*, 6(6), 1149–1159. doi: 10.1166/jon.2017.1403

[46] Ram, M.S., Ashok, N., & Shamshuddin, M.D. (2023). Numerical solution of radiative and dissipative flow on non-Newtonian Casson fluid model via infinite vertical plate with thermo-diffusion and diffusion-thermo effects. *Journal of Nanofluids*, 12(3), 777–785. doi: 10.1166/jon.2023.1976

[47] Krishna, M. V., Swarnalathamma, B., & Chamkha, A.J. (2019). Investigations of Soret, Joule and Hall effects on MHD rotating mixed convective flow past an infinite vertical porous plate. *Journal of Ocean Engineering and Science*, 4(3), 263–275. doi: 10.1016/j.joes.2019.05.002

[48] Kumar, B., Seth, G.S., Nandkeolyar, R., & Chamkha, A.J. (2019). Outlining the impact of induced magnetic field and thermal radiation on magneto-convection flow of dissipative fluid. *International Journal of Thermal Sciences*, 146, 106101. doi: 10.1016/j.ijthermalsci.2019.106101

[49] Brewster, M. Q. (1992). *Thermal radiative transfer and properties*. John Wiley & Sons.

Co-published by
Institute of Fluid-Flow Machinery
Polish Academy of Sciences
Committee on Thermodynamics and Combustion
Polish Academy of Sciences

http://www.imp.gda.pl/archives-of-thermodynamics/

Thermal instability of three-dimensional boundary layer stagnation point flow towards a rotating disc

Samir Mamache, Fatsah Mendil*, Faiçal Nait Bouda

Université de Bejaia, Faculté de Technologie, Laboratoire de Mécanique, Matériaux et Energétique (L2ME), 06000 Bejaia, Algeria.
*Corresponding author email: fatsah.mendil@univ-bejaia.dz

Received: 16.01.2024; revised: 19.06.2024; accepted: 19.07.2024

Abstract

In this paper, the thermal instability of a three-dimensional boundary layer axisymmetric stagnation point flow towards a heated horizontal rotating disk is considered. A large number of works have been done on stability analysis. However, they did not check the thermal stability of the non-parallel-flow in the face of small disturbances that occur in the vicinity of the heated rotating disk. The governing equations of the basic flow are reduced to three coupled nonlinear partial differential equations, and solved numerically with the fourth-order Runge-Kutta method. Thermal stability is examined by making use of linear stability theory based on the decomposition of the normal mode of Görtler-Hammerlin. The resulting eigenvalue problem is solved numerically using a pseudo-spectral method based on the expansion of Laguerre's polynomials. The obtained results are discussed in detail through multiple configurations. As the main result, for large Prandtl numbers (Pr), the rotation disk parameter (Ω) has a destabilizing effect while for small Pr (around the unity) it tends to stabilize the basic flow. It was found that as the disk radius $r \to 0$, the flow is linearly stable, and the disturbances grow rapidly away from the stagnation point. For low values of Pr, the flow becomes more stable, and strong thermal gradients are necessary to destabilize it. However, an increase in Pr leads to a significant expansion of the instability region.

Keywords: Thermal instability; Stagnation point; Boundary layer; Rotating disk; Spectral method

Vol. 45(2024), No. 4, 61–72; doi: 10.24425/ather.2024.151997

Cite this manuscript as: Mamache, S., Mendil, F., & Bouda, F.N. (2024). Thermal instability of three-dimensional boundary layer stagnation point flow towards a rotating disc. *Archives of Thermodynamics*, 45(4), 61–72.

1. Introduction

Different phenomena are responsible and act on the transport of matter. The latter can be transported by convection and diffusion as it is encountered in the mixed convection rotating-disk systems. In these processes, all fluids are subjected to a gravitational field in the presence of a thermal gradient that leads spontaneously to variation in the density of the fluid, which gives rise to complex convective movements within the fluid medium [1]. This dynamic behavior can be summarized as being the passage towards a secondary flow leading to the appearance of disturbances that develop within the fluid when viscous and thermal dissipation are overcome by Archimedean thrust. These instabilities, developing in the phenomena of which many applications abound, have benefited from great attention from researchers, scientists, and industrialists in various fields since the Rayleigh-Bernard era, such as gas turbines, rotating-disk air cleaners, medical equipment, etc. This frequently encountered phenomenon is the unique solid film generation process [2] with high performance and great purity. This process depends mainly

Nomenclature

a – positive constant, 1/s
f, h – similarity functions
g – gravitational acceleration, m/s^2
Gr – Grashof number
k – dimensionless wavenumber
L_N – n-th order Laguerre's polynomial
p – dimensionless pressure
P* – pressure, kPa
Pr – Prandtl number
r, z – dimensionless radial and axial coordinates
r*, z* – radial and axial coordinates, m
t – time, s
T – temperature, K
u, v, w – dimensionless velocity components
$\boldsymbol{V}$* – velocity field, m/s
Z_i – location of the collocation node

Greek symbols

α – thermal diffusivity, m^2/s
β – thermal expansion coefficient, 1/K
θ – dimensionless azimuthal coordinate
Θ – dimensionless temperature
υ – kinematic viscosity, m^2/s
ρ – density, kg/m^3
ω – dimensionless temporal growth rate
Ω – dimensionless rotation parameter
Ω* – angular velocity, s^{-1}

Subscripts and Superscripts

c – critical values
N – expansion coefficients vectors in Laguerre's polynomials
w – wall condition
' – differentiation concerning z
* – dimensional quantities
~ – perturbation quantities
^ – complex amplitude functions of perturbations quantities
∞ – free stream condition

Abbreviations and Acronyms

CVD – chemical vapor deposition

on the convection motions linked to interdependent chemical reactions (homogeneous and heterogeneous) in a fluid medium at the heated substrate [3]. Hussain et al. [4] examined the convective traveling modes instability within the boundary layer over a rotating disk in an enforced axial flow under the chemical vapour deposition (CVD) process. In-depth studies of hydrodynamics flow have been motivated by the need to avoid or delay the transition to turbulence in boundary layers. In the case of rotating disk flows, the current field of numerical mechanics requires more advanced techniques for a more precise analysis of these various physical phenomena. In this regard, the first similarity transformations designed to convert the governing partial differential equations into ordinary differential equations were introduced by von Karman [5], who studied with excellence the fluid flow due to the disk rotation. Griffiths [6] introduced von Karman similarity transformations in a generalized Newtonian fluid boundary layer flow due to a rotating disk, after using a high Reynolds number boundary-layer approximation. The corresponding results provided a more accurate description of the flow. Khan et al. [7] analyzed the thermophysical characteristics of liquids and gases near a heated rotating disk. Usman et al. [8] investigated the heat transfer characteristics of a non-isothermal wavy disk rotating in a forced flow. They presented a suitable mechanism for the rapid removal of thermal energy from the surface of the rotating disk. The combination of axisymmetric stagnation flow on a rotating disc was studied by Hannah [9]. Sarkar et al. [10] studied the problem of an axisymmetric oblique stagnation point flow over the rotating disk. Their investigation highlighted that the streamlines shift the location of the stagnation point toward the incoming flow. Forced orthogonal flow with off-center axisymmetric stagnation point flow over a rotating disk was discussed by Wang [11] and Heydari et al. [12].

The instability designates the unstable motion, which refers to small interruptions in laminar flow. These instabilities accumulate and amplify with the presence of thermal and viscous diffusion that occurs within the fluid. When these disturbances develop significantly, the flow is profoundly modified, leading to unstable behaviours under the competition between these effects. An impressive study of this instability phenomenon was presented by Amaouche et al. [13], where they were able to compare the stability characteristics of thermal convection over a non-orthogonal stagnation point flow with those occurring in Hiemenz flow over a heated horizontal plate. Moreover, they examined the presence of a constant magnetic field on the thermal instability of a two-dimensional stagnation point flow, indicating that magnetic fields act to improve its stability [14]. Nait Bouda et al. [15] investigated the effects of mass transfer on the thermal instability of a boundary layer stagnation point flow. Well afterwards, Mendil et al. [16] examined the effect of temperature-dependent viscosity on the thermal instability of two-dimensional stagnation point flow. They found that the intensification of the viscosity of the fluid due to the increase in temperature acts significantly to increase the stability of the flow.

The stability of flows impinging on curved cylindrical surfaces is the subject of several investigations in the literature due to their wide application. This type of convective motion develops a more complex behaviour than flat surfaces. Mittal [17] realized the stabilizing effect as a function of the flow regime on the stability of a flow past a cylinder. The stability of an axisymmetric stagnation flow obliquely striking a circular cylinder in uniform rotation under the effect of the Lorentz force associated with a radial magnetic field has been analyzed by Amaouche et al. [18]. Among the studies on the onset of instabilities of mixed convection over circular cylinders, a two-dimensional boundary layer problem induced by an upward flow on a heated circular horizontal cylinder was investigated by Mouloud et al. [19]. They found that growing instability accumulates in free convection flow and stable sections correspond to forced and mixed convection flow.

Mechanisms having significant effects on flows in most current research are increasingly focused on the complex chal-

lenges encountered in a wide range of current applications. Rotating surfaces with high heat transfer has been the subject of many recent works where investigations are mainly motivated by the possibility of solving the boundary layer equations. At this level, the stability theory aims precisely to prevent the development of disturbances and to determine the critical conditions for the appearance of the instabilities. In this regard, the theoretical and experimental study of linear stability in a spiral vortex in the boundary-layer transition regime on a rotating disk under the effects of streamline curvature and Coriolis force was carried out by Kobayashi et al. [20]. Malik et al. [21] examined the Coriolis effect and the streamline curvature on the stability of three-dimensional rotating disk flow. Lingwood [22] explored the characteristics of boundary layer flow over a rotating disk in an otherwise still fluid by analyzing the inviscid stability of the flow and the stability with viscous curvature, Coriolis and streamlining effects. The instability of trailing-edge flows and wakes is a considerable topic in aerodynamics. Practical interest in this area has driven research to examine the stability of these flows by theoretical and experimental means to improve the understanding of the transition to turbulent flow. In this aspect, an analytic approach for calculating absolutely unstable inviscid modes of the boundary layer on a rotating disk is examined by Türkyılmazoglu and Gajjar [23]. A recent review of the topic relating to the phenomenon of instability of fluid flows can be found in [24,25]. Miller et al. [26] investigated the stability of a heated rotating-disk boundary layer in a temperature-dependent viscosity fluid. Sharma et al. [27] performed a numerical analysis of the nonlinear characteristics of the transition to the chaos caused by thermal instability in a bottom-heated slotted channel undergoing natural convection. Roşca et al. [28] analyzed linear temporal stability of an axisymmetric rotational stagnation flow over a rotating disk under a radially stretching sheet and also presented the radial and azimuthal shear stresses in an axisymmetric rotational stagnation flow. Healey [29] examined the relation between viscous and inviscid absolute instabilities in a boundary layer flow induced by a rotating disk. In some cases, with temperature changes, the viscosity may also undergo a significant change in flow behaviour. Jasmine and Gajjar [30] investigated the absolute and convective instabilities in the incompressible boundary layer on a rotating von Karman disk flow with temperature-dependent viscosity. Wiesche and Helcig [31] investigated experimentally the effect of heating on the stability of the laminar three-dimensional boundary layer flow over a rotating disk. The stability of the three-dimensional boundary layer flow introduced into a rotating disk has been studied numerically using linear stability theory and experimentally by Lee et al. [32]. An overview of developments in the theory of hydrodynamic stability related to the concepts of absolute/convective and local/global instability was performed by Huerre and Monkewitz [33], where they demonstrated how these notions can be used effectively to obtain a description of the spatio-temporal dynamics of open shear flows. Based on the linearized incompressible Navier-Stokes equations, numerical simulations of the flow developing on the surface of a rotating disk were examined with excellence in [34]. Mechanisms having significant effects on flows in most current research are increasingly focused on the complex challenges encountered in a wide range of current applications. Rotating surfaces with high heat transfer has been the subject of many recent works where investigations are mainly motivated by the possibility of solving the boundary layer equations.

In light of these previous findings, even though the above-mentioned studies on instabilities are inherent to many applications, the novelty of this original contribution is focused on the appearance of thermal instability of three-dimensional boundary layer stagnation point flow over a heated rotating disk. For this reason, the thermal instability analysis implemented in [13–16] for two-dimensional flat plate boundary layer flow has been extended and applied to the three-dimensional boundary-layer flow rotating disk. By taking into account the Boussinesq approximation, the resulting dynamic and temperature field are coupled to each other leading to an eigenvalue problem constituted by making use of the linear stability theory. The latter is then solved numerically using the pseudo-spectral collocation method based on Laguerre's polynomials expansion. The rotating disk parameter (Ω) is also one of the novelties or key objectives of this given analysis. Indeed, great attention is given to the competition between rotation parameter and thermal buoyancy forces on the linear stability of the basic flow. Therefore, we seek to examine the evolution of the instability threshold and the effects of pertinent parameters such as the disk radius, the rotating disk parameter, the Prandtl and Grashof numbers (r, Ω, Pr, Gr) linked to the different stages of the transition to turbulence.

2. Model description

2.1. Disk geometry

We consider a heated horizontal disk with a large radius rotating about its axis (z^*) with an angular velocity Ω^* subject to an external axisymmetric orthogonal flow $\boldsymbol{V}_\infty^*(ar^*, 0, -2az^*)$, where a is a positive constant, as shown in Fig. 1. The temperature at the disk (T_w) is assumed to be constant and greater than the external temperature (T_∞). Here, the coordinate frame is not related to the disk rotation.

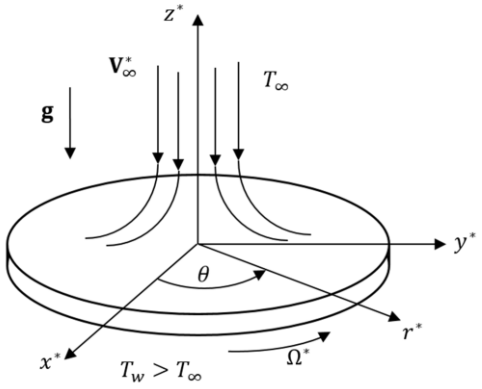

Fig. 1. Physical model and coordinate system for the stagnation point flow considered.

For the steady state, all the physical quantities are assumed to be independent of θ since the flow is axisymmetric about the z^*-axis that is measured from the stagnation point ($r^* = 0$). The physical properties of the fluid are assumed to be constant, except for the density belonging to the buoyancy term given by Boussinesq approximation. We note that in cylindrical coordinates (r^*, θ, z^*), the flow moves within the velocity field u^*, v^* and w^* in the radial, azimuthal and axial directions, respectively. The governing equations of the problem under the assumptions and approximations of the boundary layer are given by [13–16]:

$$\nabla \boldsymbol{V}^* = 0, \tag{1}$$

$$\frac{\partial \boldsymbol{V}^*}{\partial t^*} + (\boldsymbol{V}^* \cdot \nabla)\boldsymbol{V}^* = -\frac{1}{\rho}\nabla P^* + \upsilon \nabla^2 \boldsymbol{V}^* - \boldsymbol{g}\beta(T - T_\infty), \tag{2}$$

$$\frac{\partial T}{\partial t^*} + (\boldsymbol{V}^* \cdot \nabla)T = \alpha \nabla^2 T. \tag{3}$$

The appropriate boundary conditions are applied, such that the radial and azimuthal velocities on the disk are subject to no-slip conditions, while the axial one verifies the non-permeability. Far from the disk, the flow tends to the external stream. Concerning the thermal conditions, the temperature at the disk is maintained at (T_w) whereas, at infinity, the temperature is equal to that of the external flow (T_∞) such as:

$$u^* = 0,\ v^* = r^*\Omega^*,\ w^* = 0,\ T = T_w \ \text{ at } \ z^* = 0, \tag{4}$$

$$u^* = a\, r^*,\ v^* = 0,\ w^* = -2a\, z^*,\ T = T_\infty \ \text{ as } \ z^* \to \infty, \tag{5}$$

where υ designates the kinematic viscosity, ρ is the density of the fluid, $\boldsymbol{g}$ is the gravitational acceleration, β is the thermal expansion coefficient, α is the thermal diffusivity of the fluid and T is the temperature. The dimensionless form of the Eqs. (1)–(3) is obtained by injecting these scaling variables below.

$$t^* = at,\ \ r^* = \sqrt{\upsilon a^{-1}}r,\ \ \ z^* = \sqrt{\upsilon a^{-1}}z,$$

$$(u^*, v^*, w^*) = \left(\sqrt{\upsilon a}u, \sqrt{\upsilon a}v, \sqrt{\upsilon a}w\right),$$

$$(p^*, T) = (\rho(\upsilon a)p,\ \ \Theta(T_W - T_\infty) + T_\infty).$$

2.2. Solution of the basic flow

In this area, the steady state of the three-dimensional boundary layer flow (Eqs. (1)–(3)) is associated with the cylindrical coordinates r, θ, and z. The buoyancy effect has an important position in the governing differential equations through this mixed convection problem. Taking into account the axial symmetry of the steady state, the equation system is then reduced after neglecting some terms. By subtracting the equation projected along the axial direction from that projected along the radial direction, after deriving them to ($\partial/\partial r$, $\partial/\partial z$) respectively, this leads to eliminating the pressure term in the momentum equation as follows:

$$\frac{\partial}{\partial z}\left(u\frac{\partial u}{\partial r} - \frac{v^2}{r} + w\frac{\partial u}{\partial z}\right) - \frac{\partial}{\partial r}\left(u\frac{\partial w}{\partial r} + w\frac{\partial w}{\partial z}\right) - \mathrm{Gr}\frac{\partial \Theta}{\partial r} = \\ = \frac{\partial}{\partial z}\left(\frac{\partial^2 u}{\partial r^2} + \frac{1}{r}\frac{\partial u}{\partial r} - \frac{u}{r^2} + \frac{\partial^2 u}{\partial z^2}\right) - \frac{\partial}{\partial r}\left(\frac{\partial^2 w}{\partial r^2} + \frac{1}{r}\frac{\partial w}{\partial r} + \frac{\partial^2 w}{\partial z^2}\right), \tag{6}$$

$$u\frac{\partial v}{\partial r} + \frac{uv}{r} + w\frac{\partial v}{\partial z} = \left(\frac{\partial^2 v}{\partial r^2} + \frac{1}{r}\frac{\partial v}{\partial r} - \frac{v}{r^2} + \frac{\partial^2 v}{\partial z^2}\right), \tag{7}$$

$$u\frac{\partial \Theta}{\partial r} + w\frac{\partial \Theta}{\partial z} = \frac{1}{\mathrm{Pr}}\left(\frac{\partial^2 \Theta}{\partial r^2} + \frac{1}{r}\frac{\partial \Theta}{\partial r} + \frac{\partial^2 \Theta}{\partial z^2}\right). \tag{8}$$

The heat transfer is transferred by forced convection, which involves the only normal component of the flow field. Therefore, the temperature field is fully slaved to the normal component of the flow, making the basic flow independent of the Grashof number. Taking into account the following similarity variables [35]:

$$\begin{matrix} u(r,z) = r\, f'(z),\ v(r,z) = r\,\Omega\, h(z), \\ w(r,z) = -2f(z),\ \Theta(r,z) = \Theta(z) \end{matrix}. \tag{9}$$

By subsuming the above similarity transformation (9) in the previous system (Eqs. (6)-(8)), and after some development, the equations are reduced in terms of f, h, Θ, leading to the following ordinary and nonlinear coupled differential equations system:

$$f''' - 2f'^2 + 2ff'' + \Omega^2 h^2 + 1 = 0, \tag{10}$$

$$h'' - 2f'\,h + 2f\,h' = 0, \tag{11}$$

$$\Theta'' + 2\mathrm{Pr} f\Theta' = 0, \tag{12}$$

where the prime (′) denotes differentiation with respect to z, and the transformed boundary conditions are given by:

$$f(0) = f'(0) = 0,\ \ h(0) = 1,\ \ \Theta(0) = 1 \ \ \text{at} \ \ z = 0, \tag{13}$$

$$f'(z) = 1,\ \ h(z) = 0,\ \ \Theta(z) = 0 \ \ \text{as} \ \ z \to \infty. \tag{14}$$

The above equations are, for convenience, formulated in terms of dimensionless variables. The distance along the disk and time are scaled using the factors $\ell = (\upsilon/a)^{1/2}$ and a^{-1}, respectively. Prandtl and Grashof numbers are given, respectively, by $\mathrm{Pr} = \upsilon/\alpha$, $\mathrm{Gr} = g\beta\,(T_w - T_\infty)\,\ell^3\,/\,\upsilon^2$, and $\Omega = \Omega^*/a$ is the dimensionless rotation parameter. It is preliminary to analyze the basic flow before examining the critical conditions related to the transition to turbulence because the solution of this one appears as variable coefficients in the stability problem. The nonlinear differential Eqs. (10)–(12) with the associated boundary conditions (13) and (14) are solved numerically using the fourth-order Rung-Kutta method with the so-called shooting technique. By keeping an accuracy of 10^{-6}, the process is repeated until the correct results are obtained.

3. Linear stability analysis

The linear stability analysis consists in determining the complex wave numbers and frequencies of the waves that the system supports. In most stability studies, either a purely temporal or spatial instability approach is taken. The limitations of adopting a purely spatial or temporal instability analysis were made clear with the introduction of the concepts of absolute and convective instability. It seems from [22,23,30] that the choice of a temporal or spatial analysis can only be fixed after the behaviour of both the wave number and frequency have been studied in the complex plane and the convective or absolute character of the insta-

bility has been determined. In the problem at hand it is customary to focus attention on temporal instability, i.e. disturbances grow in time at every fixed point in space [19]. In this part, the work is oriented toward the three-dimensional stability analysis in order to examine the temporal growth and spatial amplification of disturbances. Investigations in this section are based on the instability of the flow that occurs after the loss of stability in order to understand the destabilizing mechanisms linked to the different stages of the transition to turbulence. We consider small disturbances propagating along the boundary layer so that the instantaneous quantities can be expressed as the sum of the quantities of the base state and that of the disturbances state as follows:

$$(\bar{u},\bar{v},\bar{w},\bar{p},\bar{\Theta})(r,\theta,z,t) = (u,v,w,p,\Theta)(r,z) + (\tilde{u},\tilde{v},\tilde{w},\tilde{p},\tilde{\Theta})(r,\theta,z,t). \tag{15}$$

By substituting the above decomposition (Eq. (15)) into the Navier-Stokes and energy equations, after subtracting the base state and eliminating the nonlinear terms, we obtain a set of equations governing the evolution of the three-dimensional perturbations in time and space as follows:

$$\left(\frac{\partial}{\partial r}+\frac{1}{r}\right)\tilde{u}+\frac{1}{r}\frac{\partial\tilde{v}}{\partial\theta}+\frac{\partial\tilde{w}}{\partial z}=0, \tag{16}$$

$$\left(\frac{\partial}{\partial t}-\nabla^2+u\frac{\partial}{\partial r}+\frac{v}{r}\frac{\partial}{\partial\theta}+w\frac{\partial}{\partial z}+\frac{\partial u}{\partial r}\right)\tilde{u}-2\frac{v}{r}\tilde{v}+\frac{\partial\tilde{p}}{\partial r}=0, \tag{17}$$

$$\left(\frac{v}{r}+\frac{\partial v}{\partial r}\right)\tilde{u}+\left(\frac{\partial}{\partial t}-\nabla^2+u\frac{\partial}{\partial r}+\frac{v}{r}\frac{\partial}{\partial\theta}+w\frac{\partial}{\partial z}+\frac{u}{r}\right)\tilde{v}+\frac{\partial v}{\partial z}\tilde{w}+\frac{1}{r}\frac{\partial\tilde{p}}{\partial\theta}=0, \tag{18}$$

$$\left(\frac{\partial}{\partial t}-\nabla^2+\frac{v}{r}\frac{\partial}{\partial\theta}+w\frac{\partial}{\partial z}+\frac{\partial w}{\partial z}\right)\tilde{w}+\frac{\partial\tilde{p}}{\partial r}-\mathrm{Gr}\,\tilde{\Theta}=0, \tag{19}$$

$$\left(\frac{\partial}{\partial t}-\frac{1}{\mathrm{Pr}}\nabla^2+\frac{v}{r}\frac{\partial}{\partial\theta}+w\frac{\partial}{\partial z}\right)\tilde{\Theta}+\frac{\partial\Theta}{\partial z}\tilde{w}=0, \tag{20}$$

where ∇^2 refers to the three-dimensional Laplace operator. It should be noted that the quantities (u, v, w, Θ) as previously indicated, represent variable coefficients corresponding to the solution of the basic flow. These coefficients show significant variations in the normal direction (z) and change linearly in the chordwise direction (r), but not in the spanwise direction (θ). The strong dependence of the basic state on radial distance in the problem at hand does not permits the introduction of eigenmodes in the chordwise direction (r), in general. However, the introduction of the eigenmodes in the spanwise (θ) direction to model the problem permits considering the solution separable in the variables θ and t, as discussed previously by Amaouche et al. [14]. Retaining self-similarity for the perturbation amplitude. The disturbance quantities of a general traveling mode can be expressed in the form of the normal mode of Görtler-Hammerlin [36,37], as follows:

$$(\tilde{u},\tilde{v},\tilde{w},\tilde{p},\tilde{\Theta})(r,\theta,z,t) = (r\hat{u},r\hat{v},\hat{w},\hat{p},\hat{\Theta})(z)\exp(ik\theta+\omega t). \tag{21}$$

In the current study, our attention is focused on temporal instability, where the wave number k is real and the temporal growth rate ω is allowed to be complex. Here, $(r\hat{u},r\hat{v},\hat{w},\hat{p},\hat{\Theta})$ are complex amplitude functions of three-dimensional small disturbances. This so-called Görtler-Hammerlin model has been the subject of many works reported before. It was also extended for three-dimensional stability analysis as in [14]. In the present study, we are interested in the region located near the stagnation point, therefore, the non-parallel flow effects of order (r^2) in the terms [$1/r^2$ ($\partial^2V^*/\partial\theta^2$)] are included, and the thermal stability analysis are examined in the concept of non-parallel flow. Introducing the decomposition given by Eq. (21), Eqs. (16)–(20) take the following algebraic system form:

$$2\,\hat{u}+ik\,\hat{v}+D\,\hat{w}=0, \tag{22}$$

$$\left(D^2+2fD-2f'-ik\Omega h-\frac{k^2}{r^2}\right)\hat{u}+2\left(\Omega h-\frac{ik}{r^2}\right)\hat{v}-f''\hat{w}=\omega\,\hat{u}, \tag{23}$$

$$-2\left(\Omega h-\frac{ik}{r^2}\right)\hat{u}+\left(D^2+2fD-2f'-ik\Omega h-\frac{k^2}{r^2}\right)\hat{v}-\Omega h'\hat{w}-\frac{ik}{r^2}\hat{p}=\omega\,\hat{v}, \tag{24}$$

$$\left(D^2+2fD-2f'-ik\,\Omega h-\frac{k^2}{r^2}\right)\hat{w}-D\hat{p}+\mathrm{Gr}\hat{\Theta}=\omega\,\hat{w}, \tag{25}$$

$$\left(D^2+2\mathrm{Pr}fD-ik\Omega\mathrm{Pr}h-\frac{k^2}{r^2}\right)\hat{\Theta}-\mathrm{Pr}\,\Theta'\hat{w}=\mathrm{Pr}\omega\,\hat{\Theta}. \tag{26}$$

The disturbances cancel each other out at the wall as well as outside the boundary layer, as indicated by these boundary conditions:

$$\hat{u} = \hat{v} = D\,\hat{w} = \hat{p} = \hat{\Theta} = 0 \quad \text{at} \quad z = 0, \tag{27}$$

$$\hat{u} = \hat{v} = \hat{p} = \hat{\Theta} = 0 \quad \text{as} \quad z \to \infty. \tag{28}$$

The pressure and azimuthal component of the velocity can be deduced from Eqs. (22) and (24) in the form:

$$\hat{v} = -\frac{1}{ik}(\lambda_1 + 2f') - i\,k\,\Omega\,h''(2\hat{u} + D\hat{w}), \tag{29}$$

$$\hat{p} = \frac{r^2}{k^2}(\lambda_1 + 2f') - ik\Omega h''[2(D^2 + 2fD - 2f' - \omega)\hat{u} + (\lambda_1 - 2f' - \omega)D\hat{w} + ik\Omega h'\hat{w}]. \tag{30}$$

The combined Eqs. (22) and (24) lead us to reduce the number of unknowns within the system itself. This simplification is achieved by extracting the term $\hat{v}$ from Eq. (22) and introducing it into Eqs. (23) and (24). Additionally, the pressure $\hat{p}$ is extracted from Eq. (24) and introduced into Eq. (25). Thereafter, we can replace the pressure term as well as the azimuthal velocity component to obtain a reduced system of an eigenvalue problem in the following form:

$$\begin{pmatrix} \lambda_1 - 2f' + 2\xi & \xi D - f'' & 0 \\ \lambda_3 & \lambda_4 & -\frac{k^2}{r^2}\mathrm{Gr} \\ 0 & -\mathrm{Pr}\Theta' & \lambda_5 \end{pmatrix} \begin{pmatrix} \hat{u} \\ \hat{w} \\ \hat{\theta} \end{pmatrix} = \omega \begin{pmatrix} 1 & 0 & 0 \\ 2D & \lambda_2 & 0 \\ 0 & 0 & \mathrm{Pr} \end{pmatrix} \begin{pmatrix} \hat{u} \\ \hat{w} \\ \hat{\theta} \end{pmatrix}, \tag{31}$$

such as

$$D = \frac{\partial}{\partial z}, \quad \lambda_1 = (\lambda_2 + 2fD - i\,k\,\Omega\,h), \quad \lambda_2 = D^2 - \frac{k^2}{r^2}, \quad \xi = \frac{2}{k^2}\left(i\,k\,\Omega\,h + \frac{k^2}{r^2}\right),$$

$$\lambda_3 = 2(D^2 + 2f\,D)D - 4f'', \quad \lambda_4 = \lambda_1 D^2 - 2f''\,D - \left[\frac{k^2}{r^2}(\lambda_1 + 2f') - ik\Omega h''\right],$$

$$\lambda_5 = \lambda_2 + 2\mathrm{Pr}fD - i\,k\,\mathrm{Pr}\,\Omega\,h.$$

This combination will not only facilitate the numerical solution of the system but also minimize the computation time.

4. Computational method

The basic flow is solved simultaneously with the stability problem, which appears in the form of variable coefficients. To approximate the solution of the problem, the flow stability characteristics are calculated by solving the generalized algebraic eigenvalue problem (31) through a pseudo-spectral method based on the expansion of Laguerre's polynomials. The most important feature of this method is exponential convergence, which allows high precision with a modest number of collocation points. However, the use of Laguerre polynomials is motivated by the distribution of their zeros, i.e. the first zeros are close to each other and this distribution is perfectly suited to describe regions of strong gradients in the boundary layers. According to mathematical models, an approach of the three-dimensional complex amplitude functions is given as an approximation in the form $\hat{\phi}_N(\hat{u}_N, \hat{w}_N, \hat{\Theta}_N)$ [13–16], defined as:

$$\hat{\phi}_N(z) = \exp(-z)\sum_{i=1}^{N} \frac{zL_N(z)}{z_i(z-z_i)\frac{dL_N(z_i)}{dz}}\phi_N(z_i). \tag{32}$$

The simplification related to this approximation gives rise to an algebraic eigenvalue system in terms of discretized square matrices ($3\times N$, $3\times N$) such as:

$$\begin{pmatrix} \boldsymbol{\lambda}_1 - 2\boldsymbol{f}' + 2\boldsymbol{\xi} & \boldsymbol{\xi}(\mathbf{D} - \mathbf{I}) - \boldsymbol{f}'' & \mathbf{0} \\ \boldsymbol{\lambda}_3 & \boldsymbol{\lambda}_4 & -\frac{k^2}{r^2}\mathrm{Gr}\mathbf{I} \\ \mathbf{0} & -\mathrm{Pr}\boldsymbol{\Theta}' & \boldsymbol{\lambda}_5 \end{pmatrix} \begin{pmatrix} \hat{\boldsymbol{u}}_N \\ \hat{\boldsymbol{w}}_N \\ \hat{\boldsymbol{\theta}}_N \end{pmatrix} = \omega \begin{pmatrix} \mathbf{I} & \mathbf{0} & \mathbf{0} \\ 2(\mathbf{D} - \mathbf{I}) & \boldsymbol{\lambda}_2 & \mathbf{0} \\ \mathbf{0} & \mathbf{0} & \mathrm{Pr}\mathbf{I} \end{pmatrix} \begin{pmatrix} \hat{\boldsymbol{u}}_N \\ \hat{\boldsymbol{w}}_N \\ \hat{\boldsymbol{\theta}}_N \end{pmatrix}, \tag{33}$$

such as

$$\boldsymbol{\lambda_1} = (\boldsymbol{\lambda_2} + 2\boldsymbol{f}\mathbf{D} - 2\boldsymbol{f} - ik\Omega\boldsymbol{h}), \qquad \boldsymbol{\lambda_2} = \mathbf{D}^2 - 2\mathbf{D} + \left(1 - \frac{k^2}{r^2}\right)\boldsymbol{I}, \quad \boldsymbol{\xi} = \frac{2}{k^2}\left(ik\Omega\boldsymbol{h} + \frac{k^2}{r^2}\mathbf{I}\right),$$

$$\boldsymbol{\lambda_3} = 2(\mathbf{D}^2 + 2(\boldsymbol{f} - \mathbf{I})\mathbf{D} + \mathbf{I})(\mathbf{D} - \mathbf{I}) - 4\boldsymbol{f}'',$$

$$\boldsymbol{\lambda_4} = \boldsymbol{\lambda_1}(\mathbf{D}^2 - 2\mathbf{D} + \mathbf{I}) - 2\boldsymbol{f}''(\mathbf{D} - \mathbf{I}) - \left(\frac{k^2}{r^2}(\boldsymbol{\lambda_1} + 2\boldsymbol{f}') - ik\Omega\boldsymbol{h}''\right),$$

$$\boldsymbol{\lambda_5} = \boldsymbol{\lambda_2} + 2\mathrm{Pr}\boldsymbol{f}(\mathbf{D} - \mathbf{I}) - ik\,Pr\,\Omega\,\boldsymbol{h}.$$

The square matrices **D** and **I** are the matrices associated with the differential operator *D* and the identity matrix, respectively. Parameters $\widehat{\boldsymbol{u}}_N, \widehat{\boldsymbol{w}}_N$ and $\widehat{\boldsymbol{\theta}}_N$ denote the expansion coefficients vector. The system (33) can be expressed in terms of square matrices **A** and **B** taking the form $(\mathbf{A} - \omega\mathbf{B})\,\widehat{\boldsymbol{\phi}}_N$. For that, the matrix system does not have a unique solution; the matrix $\mathbf{A} - \omega\,\mathbf{B}$ must be regular to have non-trivial solutions. The combination of the parameters *r*, Ω, Pr, and Gr allows us to examine the critical conditions for the appearance of instability which occurs for the minimum value of Gr that cancels the det(**A**) at marginality.

5. Results and discussion

5.1. Basic flow

Within the framework of this study, the instability of the three-dimensional stagnation point flow is examined in cylindrical coordinates. The solution of the basic flow appears as variable coefficients in the generalized algebraic eigenvalue problem (33). Parameters *f*, *h*, and Θ are some of the dominating parameters controlling the stability problem, which must be examined at the beginning.

The governing basic flow (Eqs. (10)–(12)) subject to the boundary conditions (13)–(14) is reduced using the shooting technique method, which consists of converting it into a set of first-order differential equations to facilitate its resolution. With the prescribed values of Pr and Ω, the primary solution of the basic flow (1)–(3) is first obtained numerically by the iterative fourth-order Runge-Kutta method. For a step of 10^{-6}, the calculations proved sufficiently accurate. The resolution of the equations was carried out from $z = 0$ to $z \to \infty$ under Dirichlet boundary conditions imposed on the considered problem. The numerical scheme can be optimized by reducing the step size $\Delta z = 0.001$ in the considered range [0,10]. However, for such high levels of precision, the iteration process requires a significant increase in computation time. The validation is carried out by a calculation code where the results of $f''(0)$ and $h'(0)$ are reported in Tables 1 and 2. For all given values of the rotation parameter Ω, the results show considerable agreement with respect to those reported in [10–12]. Table 3 gives computa-tional results of the effects of rotation parameter and Prandtl number on the rate of heat transfer, indicating that an increase in both parameters leads to the increase in the rate of heat transfer. Numerical calculations are carried out for Ω and Pr ranging from 0 to 10 and 0.7 to 7, respectively. Using the numerical procedures described above, the radial, azimuthal velocity and temperature distributions for the flow considered from Eqs. (10)–(12) are displayed in Fig. 2.

Table 1. Initial values of f'' for various values of Ω.

	$f''(0)$			
Ω	**Present work**	**Sarkar [10]**	**Wang [11]**	**Heydari [12]**
0	1.311938	1.31194	1.31194	1.311958
1	1.573923	1.57392	1.57539	1.573930
2	2.295649	2.29564	2.2951	2.295639
5	6.259882	6.25987	6.2602	6.259869
7	9.916523	9.91652	9.9165	9.916513

Table 2. Initial values of h' for various values of Ω.

	$h'(0)$			
Ω	**Present work**	**Sarkar [10]**	**Wang [11]**	**Heydari [12]**
0	-1.074667	-1.07467	-1.07467	-1.074697
0.5	-1.083905	–	-1.0839	-1.083934
1	-1.109996	-1.11000	-1.1100	-1.110020
2	-1.196826	-1.19676	-1.1968	-1.196841
5	-1.531978	-1.53198	-1.5320	-1.531983
7	-1.745103	-1.74511	-1.7451	-1.745106

Table 3. Initial values of $-\Theta'(0)$ for various values of Ω and Pr

	$-\Theta'(0)$	
Ω	**Pr = 0.7**	**Pr = 7**
0	0.6654	1.5458
0.5	0.6696	1.5620
1	0.6817	1.6078

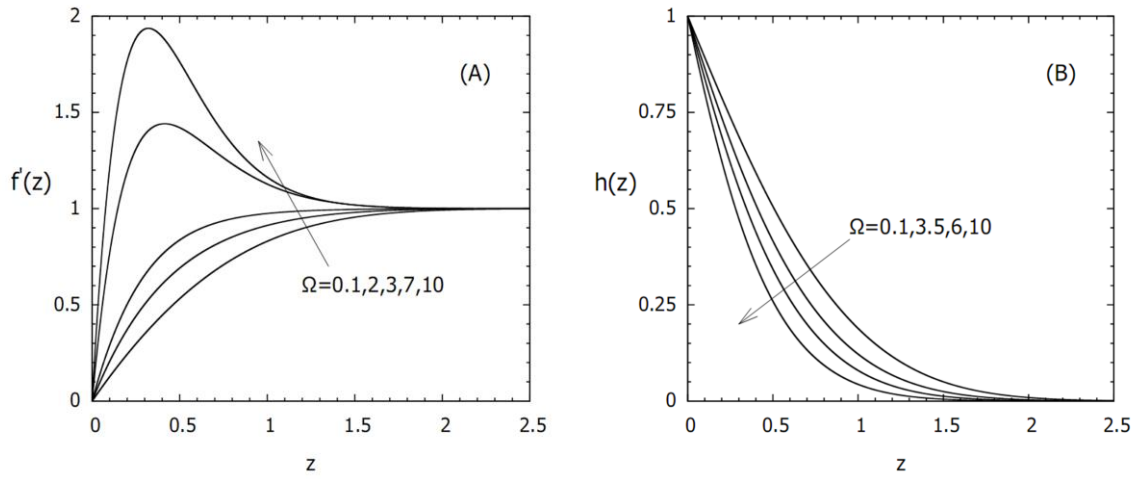

Fig. 2. Variation of $f'(z)$ and $h(z)$ for different values of Ω and Pr = 7.

Figure 2 shows the variation in velocity field $f'(z)$ and $h(z)$ functions for different values of the rotation parameter. As **Ω** is increased, the radial velocity profile increases near the stagnation point flow. When **Ω** is greater than 3.33, it is observed that with increased **Ω**, the rotation effect generates an overshoot of the radial velocity. The influence of the rotation parameter on the $h(z)$ component is presented in Fig. 2B. It can be seen that an increase in **Ω** generates a gradual decrease in the azimuthal velocity.

The results presented in Fig. 3 confirm those obtained in previous studies [14,15] indicating that the temperature of the fluid reduces for large Prandtl numbers, because with an increase in Pr the thermal diffusivity decreases. The fluid particles are able to conduct less heat and consequently temperature profiles decrease with a reduction in thermal boundary-layer thickness. In this case, temperature profiles within the fluid will be strongly influenced by the velocity profiles.

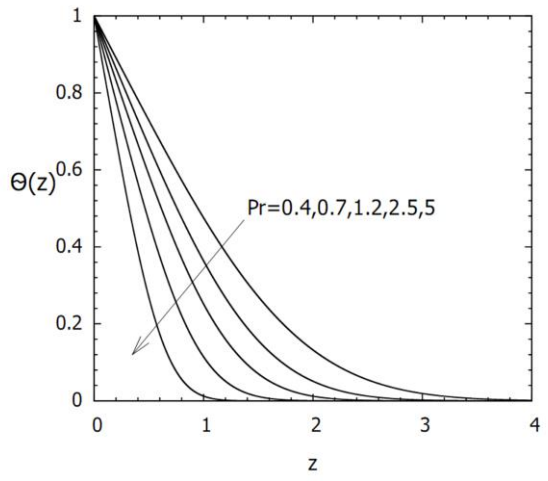

Fig. 3. Temperature profile change for a wide range of Prandtl numbers and Ω = 1.

5.2. Stability analysis

The generalized algebraic eigenvalue problem given by Eq. (33) has been solved numerically using a pseudo-spectral method based on the expansion of Laguerre's polynomials. Numerical computations are performed for several values of control parameters such as Prandtl number (Pr), disk radius (r) and rotation parameter (**Ω**). The neutral curve is generated using Newton's method where the iteration process is repeated until $|\det(\mathbf{A})|$ vanishes with the assumed tolerance $|\det(\mathbf{A})| \leq 10^{-6}$. For satisfactory convergence, the effect of the level of truncation N was taken into account on the critical conditions for the onset of instability. Convergence criteria are based on the relative difference of $|Gr_{c,i+1}-Gr_{c,i}|$. This showed that the accuracy of the numerical scheme can be improved by increasing the number of collocation nodes.

Figure 4 shows the effect of the number of collocation nodes N on the critical Grashof error. It can be clearly seen that the number of polynomials required rises by increasing the Pr number. This can be explained by the fact that an increase in Pr reduces the thermal boundary layer thickness, which requires

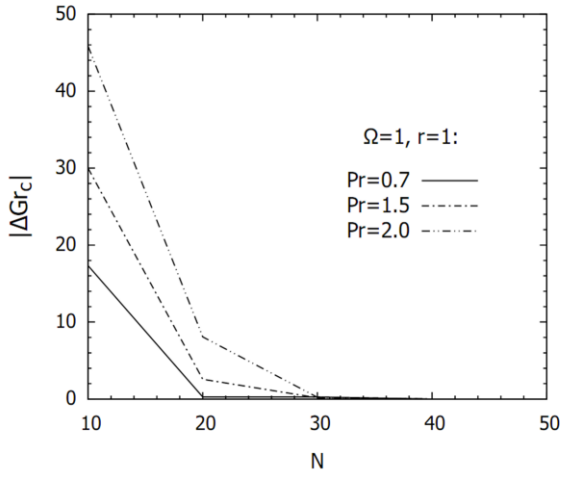

Fig. 4. Effect of the number of collocation nodes N on the critical Grashof error.

a larger number of terms in order to avoid spurious nodes and preserve the prescribed precision.

The stability analysis depicts that the critical conditions of the onset of thermal instability are significantly affected by disk rotation. Generally, one can observe that the disk radius (r), rotation parameter (Ω) and Prandtl number (Pr) act to increase or decrease the stability of the flow. An overview of the stability properties of the basic flow can be seen from the sequence of neutral stability curves displayed in Fig. 5. We recall that each curve illustrates a minimum value (critical) of the Grashof number (Gr_c) for which the boundary layer is stable or unstable. The unstable state lies above the curve, while the opposite behaviour lies below it. As it can be seen from Fig. 5A, for typical values of the rotation parameter, an increase in Ω leads to a decrease in Gr_c. Therefore, increasing Ω acts to destabilize the basic flow (i.e. Gr_c decreases and the unstable regions are expanding). This can be explained by the fact that the induced centrifugal forces by increasing Ω tend to destabilize the basic flow as previously observed in Fig. 2. In Fig. 5B, the sensitivity of the base flow to small disturbances at various locations along the disk radius (r) is examined to distinguish between the most stable and the least stable positions. For the given values of r, the corresponding neutral stability curves show that as we approach the stagnation point, the Gr_c increases and the unstable modes become imperceptible as $r \to 0$. In this region, the flow

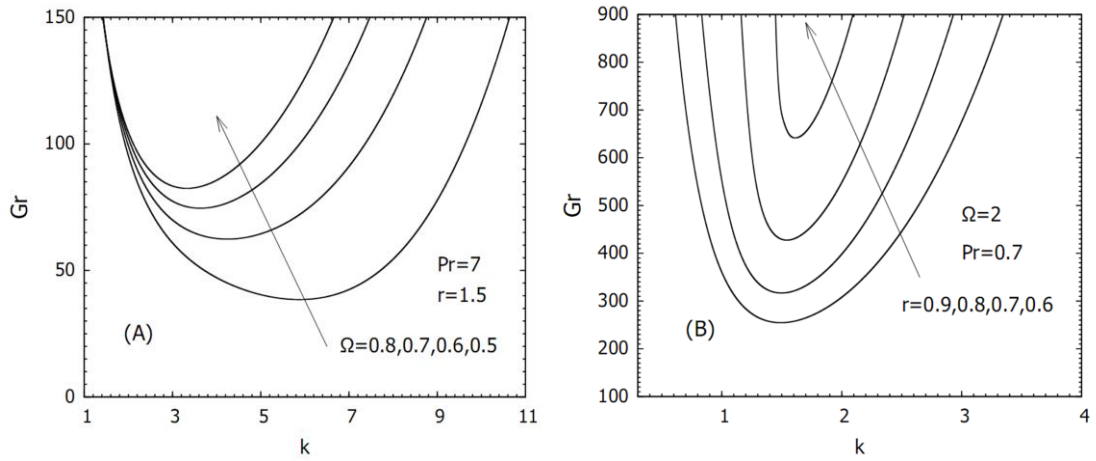

Fig. 5. Neutral stability curves for different values of: A) rotation parameter Ω, B) disk radius r.

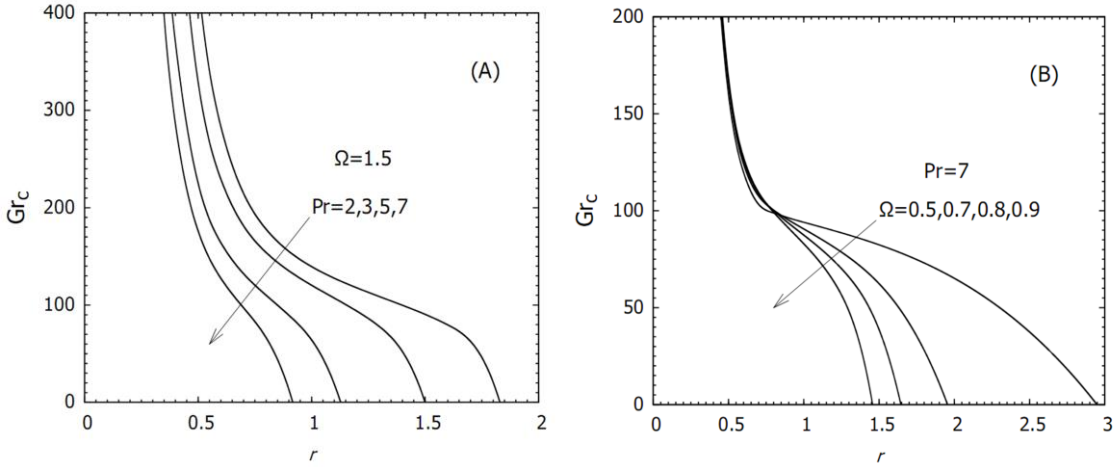

Fig. 6. Critical Grashof number as a function of the disk radius: A) for different values of Pr, B) with varying Ω.

remains more stable. In the opposite case, away from the stagnation point ($r \to \infty$), Gr_c becomes very weak and the flow becomes unstable even without heating effect.

To distinguish between stable and unstable regions along the disk radius, the results discussed in Fig. 5 can be interpreted in another aspect to check their validity. It is found that the same observation has been confirmed again. Figure 6 provides an overview of the critical Grashof number (Gr_c) as functions of the disk radius (r) for different values of Prandtl number and rotation parameter (Ω). We can see that Gr_c grows rapidly to infinity when $r \to 0$ (by approaching the stagnation point). However, the variation of Gr_c becomes significantly weaker and decreases

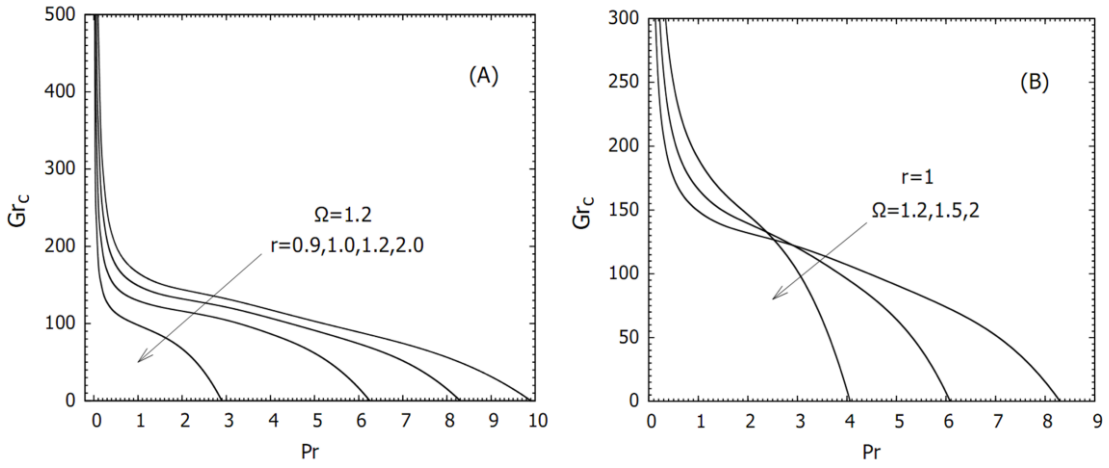

Fig. 7. Critical Grashof number (Gr_c) as a function of Pr: A) for different values of disk radius (r), B) for different values of rotation parameter (Ω).

rapidly moving away from the stagnation point. The observations show that disturbances decrease as one approaches the stagnation point (at the vicinity of the stagnation point the flow remains stable) and increase significantly as one moves away from it as shown previously in Fig. 5B. For large values of r (far away from the stagnation point), the critical Grashof number can reach zero values and the flow becomes unstable even without the thermal effects. As well, the transition to a secondary flow is linked to viscous instability.

More precisely, instability refers to the transition to a secondary flow, which occurs at a certain critical Grashof number. This transition can be explained by the influence of the buoyancy forces term in Eq. (19). The above results shown in the (k, Gr) plane indicated that the most unstable branches effectively correspond to large values of rotation parameter and disk radius. However, strong thermal gradients notably produce an opposite effect, i.e. small values of Pr are reflected with an attenuation of the instability region.

Regarding the critical conditions for the appearance of instability. Figure 7 shows an overall overview of the evolution of the critical Grashof number (Gr_c) as function of Pr. For a given values of r and Ω, both figures show that Gr_c grows very rapidly when $Pr \to 0$, i.e. a small change in the Pr affects significantly the stability threshold. However, when $Pr \to \infty$ then Gr_c becomes insensitive to Pr and decreases suddenly with a large expansion of instability region as observed previously by Amaouche et al. [13]. This can be explained by the fact that, for low values of Pr, the thermal disturbances are promoted to be dissipated rapidly, and the variation in Gr_c number corresponding to the most unstable mode remains imperceptible [15]. This means that larger thermal gradients are required to destabilize the basic flow. In contrast, for larger Prandtl numbers, thermal dissipation is slower and the thermal fields are predominated by the velocity fields, which make the equilibrium less stable. Also, the corresponding thermal boundary-layer thickness is weak, which promotes instability even close to the stagnation point. Concerning the rotation parameter, its influence on the stability of the basic flow changes for small and great Pr. For large Pr, Ω has a destabilizing effect while for small Pr (around the unity) it tends to stabilize the basic flow.

The description of the physical mechanism governing this phenomenon was also carried out by establishing a concept to justify the occurrence of these fluctuations on the least stable and the most unstable branches. Figure 8 shows the temporal

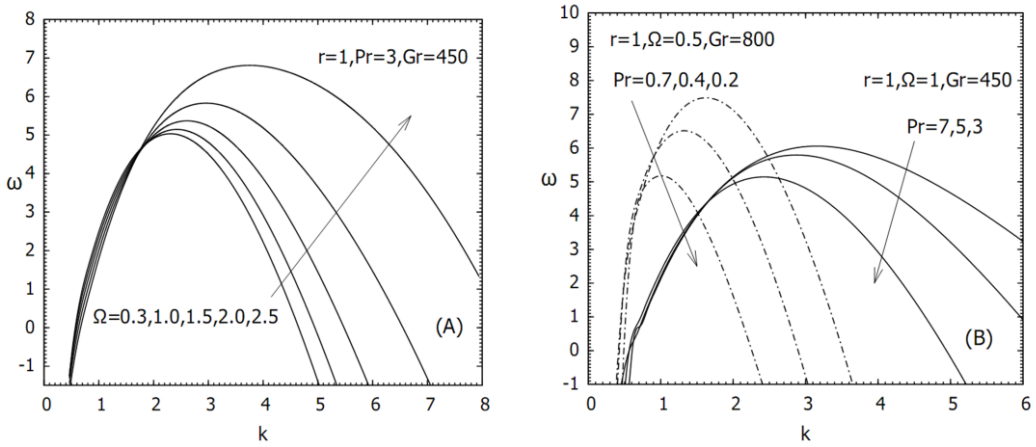

Fig. 8. Temporal growth rate as a function of wavenumber k for different values of Ω and Pr.

growth rate (ω) versus the wavenumber (k) for different values of Pr and Ω. Knowing that the stable region corresponds to negative values of temporal growth rate ($\omega < 0$), while the unstable region corresponds to positive ones ($\omega > 0$). At $r = 1$ and Gr = 450 and 800, it is seen from both figures that an increase in the Prandtl number and rotation parameter leads to a progressive expansion of the most unstable modes. However, the results indicate that the heating effect significantly increases the stability of the base flow, i.e. the most stable modes are improving as the Prandtl number decreases (Pr $\rightarrow$ 0) [19]. The graphs confirm that the effect of heating increases the stability of the flow while the effect of disk rotation decreases its stability. Within a specific range of the control parameters, the results also seem to confirm the stability analysis shown in Fig. 5.

6. Conclusions

In this paper, the thermal instability characteristics of three-dimensional stagnation point flow over a heated rotating disk is carried out under the effect of heat transfer, rotation parameter and disk radius. The eigenvalue problem governing the stability process has been constituted by applying linear stability theory, and solved numerically by making use of a pseudo-spectral method using Laguerre's polynomials. Our findings provide a significant contribution by examining the evolution of thermal instabilities in the boundary layer stagnation point flow under the appropriate control parameters, and the main results presented in this study can be summarized as follows:

i) Thermal excitation generates three-dimensional instabilities in the presence of heat transfer, which leads to a large critical Grashof number for the onset of instability.
ii) An increase in fluid temperature gives a larger critical Grashof number for the onset of thermal instability. In addition, for quite small values of the Prandtl number, the flow tends to be in a stable state.
iii) Expansion of unstable regions far from the stagnation point ($r \rightarrow \infty$), and the opposite effect turns out to be observed as we approach it ($r \rightarrow 0$). This region appears to be the most stable area with a very high critical Grashof number.
iv) The rotation parameter presents a destabilizing effect leading to the expansion of instability regions.

In perspective, the work can be improved by investigating the spatio-temporal instabilities analysis in order to identify possible convective/absolute and local/global instabilities. In addition, the asymptotic analysis of the instability can be studied and it is of capital importance to further enhance the validity of the stable and unstable regimes.

References

[1] Shevchuk, I.V. (2009). *Convective Heat and Mass Transfer in Rotating Disk Systems*. Springer, Berlin - Heidelberg. doi: 10.1007/978-3-642-00718-7

[2] Evans, G., & Greif, R. (1987). A numerical model of the flow and heat transfer in a rotating disk chemical vapor deposition reactor. *Journal of Heat Transfer*, 109(4), 928–935. doi: 10.1115/1.3248205

[3] Evans, G.H., & Greif, R. (1988). Forced flow near a heated rotating disk: A similarity solution. *Numerical Heat Transfer*, 14(3), 373–387. doi: 10.1080/10407788808913650

[4] Hussain, Z., Garrett, S.J., & Stephen, S.O. (2011). The instability of the boundary layer over a disk rotating in an enforced axial flow. *Physics of Fluids*, 23, 114108. doi: 10.1063/ 1.3662133.

[5] Kármán, Th.V. (1921). Über laminare und turbulente Reibung. ZAMM – *Journal of Applied Mathematics and Mechanics*, 1(4), 233–252 (in German). doi: 10.1002/zamm.19210010401

[6] Griffiths, P.T. (2015). Flow of a generalised Newtonian fluid due to a rotating disk. *Journal of Non-Newtonian Fluid Mechanics*, 221, 9–17. doi: 10.1016/j.jnnfm.2015.03.008

[7] Khan, M., Salahuddin, T., & Stephen, S.O. (2020). Thermo-physical characteristics of liquids and gases near a rotating disk. *Chaos Solitons & Fractals*, 141, 110304. doi: 10.1016/j.chaos.2020.110304

[8] Usman, M., Mehmood, A., & Weigand, B. (2020). Heat transfer from a non-isothermal rotating rough disk subjected to forced flow. *International Communication in Heat and Mass Transfer*, 110, 104395. doi:10.1016/j.icheatmasstransfer.2019. 104395

[9] Hannah, D.M. (1947). Forced flow against a rotating disc. *British Aeronautical Research Council Reports & Memoranda*, 2772.

[10] Sarkar, S., & Sahoo, B. (2021). Oblique stagnation flow towards a rotating disc. *European Journal of Mechanics - B/Fluids*, 85, 82–89. doi: 10.1016/j.euromechflu.2020.08.009

[11] Wang, C.Y. (2008). Off-centered stagnation flow towards a rotating disc. *International Journal of Engineering Science*, 46(4), 391–396. doi: 10.1016/j.ijengsci.2008.01.014

[12] Heydari, M., Loghmani, G.B., Rashidi, M.M., & Hosseini, S.M. (2015). A numerical study for off-centered stagnation flow towards a rotating disc. *Propulsion and Power Research*, 4(3), 169–178. doi: 10.1016/j.jppr.2015.07.004

[13] Amaouche, M., & Boukari, D. (2003). Influence of thermal convection on non-orthogonal stagnation point flow. *International Journal of Thermal Sciences*, 42(3), 303–310. doi: 10.1016/S1290-0729(02)00031-5

[14] Amaouche, M., Naït-Bouda, F., & Sadat, H. (2005). The onset of thermal instability of a two-dimensional hydromagnetic stagnation point flow. *International Journal of Heat and Mass Transfer*, 48(21-22), 4435–4445. doi:10.1016/j.ijheatmasstransfer.2005.05.003

[15] Naït Bouda, F., Mendil, F., Sadaoui, D., Mansouri, K., & Amaouche, M. (2015). Instability of opposing double diffusive convection in 2D boundary layer sta gnation point flow. *International Journal of Thermal Sciences*, 98, 192–201. doi: 10.1016/j.ijthermalsci.2015.07.014

[16] Mendil, F., Naït-Bouda, F., & Sadaoui, D. (2015). Effect of temperature dependent viscosity on the thermal instability of two-dimensional stagnation point flow. *Mechanics & Industry*, 16, 506. doi: 10.1051/meca/2015031

[17] Mittal, S. (2010). Stability of flow past a cylinder: Energy budget of eigenmodes. *International Journal for Numerical Methods in Fluids*, 63, 533–547. doi: 10.1002/fld.2084

[18] Amaouche, M., Naït-Bouda, F., & Sadat, H. (2007). Oblique axisymmetric stagnation flows in magnetohydrodynamics. *Physics of Fluids*, 19, 114106. doi: 10.1063/1.2804957

[19] Mouloud, S., Nait-Bouda, F., Sadaoui, D., & Mendil F. (2019). The onset of instabilities in mixed convection boundary layer flow over a heated horizontal circular cylinder. *Journal of Thermal Science and Engineering Applications*, 11(5), 51002. doi: 10.1115/1.4042586

[20] Kobayashi, R., Kohama, Y., & Takamadate, Ch. (1980). Spiral vortices in boundary layer transition regime on a rotating disk. *Acta Mechanica*, 35, 71–82. doi: 10.1007/BF01190058

[21] Malik, M.R., Wilkinson, S.P., & Orszag, S.A. (1981). Instability and transition in rotating disk flow. *American Institute of Aeronautics and Astronautics*, 19(9), 1131–1138. doi: 10.2514/3.7849

[22] Lingwood, R.J. (1995). Absolute instability of the boundary layer on a rotating disk. *Journal of Fluid Mechanics*, 299, 17–33. doi: 10.1017/S0022112095003405

[23] Turkyilmazoglu, M., & Gajjar, S.J.B. (2001). An analytic approach for calculating absolutely unstable inviscid modes of the boundary layer on a rotating disk. *Studies in Applied Mathematics*, 106(4), 419–435. doi.org/10.1111/1467-9590. 001733

[24] Turkyilmazoglu, M. (2019). Direct contact melting due to a permeable rotating disk. *Physics of Fluids*, 31, 023603. doi: 10.1063/1.5086724

[25] Turkyilmazoglu, M. (2010). Heat and mass transfer on the MHD fluid flow due to a porous rotating disk with hall current and variable properties. *Journal of Heat and Mass Transfer*, 133(2), 021701. doi: 10.1115/1.4002634

[26] Miller, R., Griffiths, P., Hussain, Z., & Garrett, S.J. (2020). On the stability of a heated rotating-disk boundary layer in a temperature-dependent viscosity fluid. *Physics of Fluids*, 32, 024105. doi: 10.1063/1.5129220

[27] Sharma, A., Mahapatra, P.S., Manna, N.K., Ghosh, K., Wahi, P., & Mukhopadhyay, A. (2016). Thermal instability-driven multiple solutions in a grooved channel. *Numerical Heat Transfer, Part A: Applications*, 70(7), 776–790. doi: 10.1080/ 10407782. 2016.1192936

[28] Roşca, N.C., & Pop, I. (2017). Axisymmetric rotational stagnation point flow impinging radially a permeable stretching/shrinking surface in a nanofluid using Tiwari and Das model. *Scientific Reports*, 7, 40299. doi: 10.1038/srep40299

[29] Healey, J.J. (2004). On the relation between the viscous and inviscid absolute instabilities of the rotating-disk boundary layer. *Journal of Fluid Mechanics*, 511, 179–199. doi: 10.1017/ S0022112004009565

[30] Jasmine, H.A., & Gajjar, J.S.B. (2005). Absolute and convective instabilities in the incompressible boundary layer on a rotating disk with temperature-dependent viscosity. *International Journal of Heat and Mass Transfer*, 48(5), 1022–1037. doi: 10.1016/ j.ijheatmasstransfer.2004.07.036

[31] Wiesche, S., & Helcig, C. (2022). Effect of heating on the stability of the three-dimensional boundary layer flow over a rotating disk. *E3S Web of Conferences*, 345, 02007. doi: 10.1051/ e3sconf/202234502007

[32] Lee, Y.-Y., Hwang, Y.-K., & Lee, K.-W. (2003). The flow instability over the infinite rotating disk. *KSME International Journal*, 17(9), 1388–1395. doi: 10.1007/BF02982480

[33] Huerre, P., & Monkewitz, P.A. (1990). Local and global instabilities in spatially developing flows. *Annual Review of Fluid Mechanics*, 22, 473–537. doi: 10.1146/annurev.fl.22.010190. 002353

[34] Appelquist, E., Schlatter, P., Alfredsson, P.H., & Lingwood, R.J. (2015). Global linear instability of the rotating-disk flow investigated through simulations. *Journal of Fluid Mechanics, 765*, 612–631. doi: 10.1017/jfm.2015.2

[35] Mustafa, M. (2017). MHD nanofluid flow over a rotating disk with prtial slip effects: Buongiorno-model. *International Journal of Heat and Mass Transfer*, 108(B), 1910–1916. doi: 10.1016/ j.ijheatmasstransfer.2017.01.064

[36] Görtler, H. (1955). Dreidimensionale Instabilität der ebenen Staupunktströmung gegenüber wirbelartigen Störungen. In *50 Jahre Grenzschichtforschung*, H. Görtler, W. Tollmein (Eds.), (pp. 304–314), Vieweg und Teubner Verlag, Wiesbaden (in German). doi: 10.1007/978-3-663-20219-6_30

[37] Hämmerlin, G. (1955). Zur Instabilitätstheorie der ebenen Staupunktströmung. In *50 Jahre Grenzschichtforschung*, H. Görtler, W. Tollmein (Eds.), (pp. 315–327), Vieweg und Teubner Verlag, Wiesbaden (in German). doi: 10.1007/978-3-663-20219-6_31.

Co-published by
Institute of Fluid-Flow Machinery
Polish Academy of Sciences
Committee on Thermodynamics and Combustion
Polish Academy of Sciences

http://www.imp.gda.pl/archives-of-thermodynamics/

Numerical investigation of thermal-flow processes in the ejector-condenser for selected geometrical parameters

Tomasz Kuś*, Paweł Madejski

AGH University of Krakow, Faculty of Mechanical Engineering and Robotics, Department of Power Systems and Environmental Protection Facilities, al. Mickiewicza 30, 30-059 Kraków, Poland
*Corresponding author email: kus@agh.edu.pl

Received: 31.01.2024; revised: 19.07.2024; accepted: 09.09.2024

Abstract

The paper presents the results of analysis of thermal-flow processes in the ejector-condenser for selected geometrical parameters using CFD (Computational Fluid Dynamics) methods. The ejector-condenser is the water-driven, two-phase ejector responsible for creating a sub-pressure allowing exhaust gases (steam and CO_2 mixture) to be entrained, condensing steam, and then increasing the pressure above the atmospheric conditions. The axisymmetric numerical model was developed to take into account multiphase, turbulent flow with steam condensation in the presence of inert gas. The influence of the selected geometrical parameters, such as the motive nozzle's and mixing chamber's diameters on the ejector performance was investigated. CFD analysis results are presented in the form of developed scalar distributions as well as pressure, temperature and steam mass flow changes along the flow path. Performances for different geometry modes were calculated and compared using parameters such as compression ratio, expansion ratio, mass entertainment ratio and condensation efficiency. The maximum achieved compression ratio for the analyzed geometrical variants is 1.113 for the assumed mass entertainment ratio of 0.0295. The condensation efficiency varies in a range of 49.6%–91.4% depending on motive fluid inlet conditions and geometry mode.

Keywords: Ejector; Two-phase flow, Steam condensation, Computational fluid dynamics

Vol. 45(2024), No. 4, 73–83; doi: 10.24425/ather.2024.151998

Cite this manuscript as: Kuś, T., & Madejski, P. (2024). Numerical investigation of thermal-flow processes in the ejector-condenser for selected geometrical parameters. *Archives of Thermodynamics* 45(4), 73–83.

1. Introduction

Ejectors are highly reliable, almost free-maintenance and have no moving parts. They can be used for transporting and compressing fluids and carrying out heat and mass transfer processes. For an efficient operation, the proper design is needed to minimize flow losses. Numerical modelling gives a possibility to investigate and understand more deeply the influence of various design and operating parameters on the ejector performance.

Because of complex phenomena, which take place especially in the ejectors, researchers more and more often are using CFD (Computational Fluid Dynamics) modelling to take into account turbulent flow with heat and mass transfer processes, when the ejector is working in two-phase mode.

Modelling of the flow in one-phase ejectors is connected with the appropriate reflection of the turbulent flow and thermophysical properties of fluids, which is especially important when dealing with gas ejectors working in subsonic and supersonic modes [1]. In one-phase ejectors, the momentum exchange occurs as a result of turbulence, shock train formation and boundary layer interactions [2].

A 3D CFD model of the one-phase water ejector to compute friction losses was developed by Marum et al. [3]. Three different turbulence models were used to calculate incompressible flow in the ejector and the k–ω SST model turned out to be the most suitable. Various turbulent approaches (standard k–ε,

Nomenclature

a – interfacial area per unit volume / interaction area density, 1/m
$\boldsymbol{a}$ – surface area vector, m^2
A – surface area, m^2
C – coefficient,
f – dumping functions
$\boldsymbol{f}_b$ – body force vector, N/m^3
$\dot{g}$ – mass flow rate boiling/condensation per unit volume, $kg/(m^3s)$
h – heat transfer coefficient, $W/(m^2K)$
H – total enthalpy, m^2/s^2
$\mathbf{I}$ – unit tensor
k – turbulent kinetic energy, J/kg
l – interaction length scale, m
L – phase change heat, J/kg
$\dot{m}$ – mass flow rate of steam, kg/s
N – pressure ratio
Nu – Nusselt number
p – pressure, Pa
P – production term, W/m^3
Pr – Prandtl number
r – radius, m
Re – Reynolds number
$\dot{\boldsymbol{q}}$ – heat flux vector, W/m^2
Q – heat transfer per unit volume, W/m^3
S – source term, W/m^3 or 1/s
Sc – Schmidt number
t – time scale, s
T – temperature, K
$\mathbf{T}$ – viscous stress tensor, Pa
$\boldsymbol{v}$ – velocity, m/s
V – volume, m^3

Greek symbols

α – volume fraction
γ – temperature ratio
ε – turbulent dissipation rate, J/(kg s)
η – condensation efficiency, %
θ – expansion ratio
λ – heat conductivity, W/(m K)
μ – dynamic viscosity, Pa·s
ξ – compression ratio
ρ – density, kg/m^3
σ – coefficient
τ – stresses, Pa

Subscripts

0 – specific/ambient value
1,2 – ordering numbers
c – continuous phase
CO_2 – carbon dioxide
d – at driving fluid inlet
e – energy/large eddy
g – at gas inlet
i – phase *i*
j – phase *j*
k – turbulent kinetic energy
m – mixture
o – at diffuser outlet
s – steam
t – turbulent
u – phase
w – water
ε – turbulent dissipation rate
Θ – angular direction
μ – viscosity

Abbreviations and Acronyms

CFD – computational fluid dynamics
FVM – finite volume method
XNP – nozzle exit position

RNG k–ε, realizable k–ε and k–ω SST) using CFD techniques for modelling of the supersonic steam ejector were tested by Xiao et al.[4]. The level of agreement with experimental data of each model depends on various factors: the solver type (pressure vs. density based, mesh density, discretization scheme. The k–ω SST and realizable k–ε models with the two wall treatments are recommended.

Two-phase ejector modelling is much more challenging due to complicated gas-liquid interfacial interactions and the possibility of mass transfer between the phases. Therefore, knowledge of thermodynamic and mechanical non-equilibrium effects is crucial to develop reliable numerical models [5].

Koirala et al. [6] numerically investigated two-phase flow with condensation in a water-driven steam ejector using the Eulerian method with a thermal phase-change model. Results show that the numerical model is an effective tool for solving complex flow with a phase change. A two-phase ejector operating with LNG (liquefied natural gas) as motive fluid and BOG (boiling off gas) as entrained fluid with the condensation process was computed using the CFD technique by Zheng et al. [7]. A mixture model with the standard k–ε model was applied. Assari et al. [8] conducted numerical research where the water-air ejector was modelled using two different approaches: Eulerian-Eulerian and mixture. The mixture model seems to be more efficient considering computational time, convergence and consistency with experimental data.

Computational research leading to a better understanding of the jet behaviour and gas induction in a liquid-gas ejector was conducted by Sharma et al. [9]. The axisymmetric model with the Euler-Euler framework combined with the standard k–ε model was developed. It was concluded that adding the turbulent dispersion model causes the phase profile more dispersed. The mixing process of liquid and gas in the ejector was investigated by Wang et. al. [10] using the numerical model based on the steady-state two-fluid mixture model and realizable k–ε model. The turbulent mixing process was indicated as the most efficient mechanism. The influence of applying various turbulence models on the two-phase CO_2 ejector operation was investigated by Majchrzyk et al. [11]. Multiphase flow was calculated using a homogeneous equilibrium model (HEM) taking into account real properties. The Reynolds Stress Model with linear pressure-strain approach gives the best prediction.

Operating conditions, working medium and design factors influence the ejector performance. In this study, attention will be focused on those listed last. The performance is investigated mainly using dimensionless quantity like compression ratio, pressure ratio or entrainment ratio (volumetric or mass flow), Madejski et al. [12]. In the paper [12], the authors confirmed by simulation results with adopted characteristic curves of ejector operation that the mass flow rate of water strongly depends on the ejector design and entrainment ratio.

CFD investigation of the nozzle diameter, nozzle exit position (NXP), mixing length, diffuser curve and diameter in water-water ejector was investigated by Reis et al. [13]. The following performance indicators were obtained: pressure ratio: 0.2–0.8; efficiency: 0–35%; entrainment ratio (volumetric): 0–7. In the optimized geometry, flow profiles are more homogeneous which is more profitable – less dissipative. The influence of the diffuser angle, mixing chamber length and nozzle position on the water-water ejector performance was investigated using CFD by Sheha et al. [14]. The obtained pressure ratio was in the range of 0.37–0.8 and the entertainment mass ratio up to 2. The maximum obtained efficiency was 37.8% for the optimal design. The entertainment ratio in the range of 0.5–2.6 for different chamber heights, mixing and diffuser diameters for the assumed compression ratios 1 and 1.17 was computed for an air-air ejector by Zhang et al. [15] using numerical simulation. Too small geometrical parameters lead to an increase in total pressure losses influenced by the shock wave intensity. The influence of NXP on the operation of an air-air (air+water) ejector was investigated numerically and experimentally by Chen et al. [16]. The obtained pressure ratio: 0.04–0.29 and entrainment ratio: 0.05–0.45. The optimum NXP depends on the water mass flow rate and operation mode (one-phase, two-phase, critical, subcritical). The liquid content in the gas phase for different mixing chamber lengths was investigated by Yan et al. [17] using CFD.

The achieved entertainment ratio was 0.15–0.45 and the optimal length varied depending on the liquid content in gases. Mohammadi [18] investigated numerically (CFD) the influence of the nozzle diameter, mixing chamber diameter, throat diameter, nozzle exit position on the multistage steam-air ejector performance. The following nondimensional parameters were obtained: compression ratio: 2.875, 4.25, 12.219 (multi-stage), the multistage ejector gives the possibility to achieve a high compression ratio compared to the single stage ejector.

Considering steam-steam ejectors, Foroozesh et al. [19] calculated, using the CFD method, the ejector operation for various throat diameters of the primary nozzle. The achieved entertainment ratio was in the range of 0.31–0.51. As a result of optimization, the entertainment ratio was improved by about 32%. Dong et al. [20], conducted CFD analysis of the influence of the mixing chamber length on the entertainment ratio and critical back pressure in a steam ejector. The entertainment ratio was up to 0.7 and the critical back pressure: 1.3–3.7 kPa. A too long mixing chamber leads to a decrease in entrainment ratio and critical back pressure. Han et al. [21] investigated the steam ejector performance for different throat diameters and NXPs using CFD. The achieved volumetric entertainment ratio was 0.01–1.2 and pressure ratio 0.0827. An excessively small or large throat diameter and too large NXP strengthen the boundary layer separation.

In the analyzed solution of the ejector-condenser, the stream of primary fluid leaves the nozzle cross-section in a discrete form with a huge number of droplets. In the beginning, the water jet form can be noticed and the break-up of the jet depends on the physical properties of the fluids, surface tension and velocity [22]. The velocity of the outflow stream depends on the nozzle shape. A number of small-scale phenomena occur inside the nozzle [23–26], which affect the global characteristics of the device. Even when applying the most advanced 2D/3D numerical models, experimental investigation for verification of the results is required. The complex phenomenon inside two-phase ejector-condensers requires an advanced test stand to monitor thermal and flow conditions changing through the flow inside the ejector condenser. Madejski et al. [27,28] proposed assumptions and guidelines for building a prototype experimental test-rig installation for experimental research on direct contact condensers. Pressure change and temperature change along the flow of the mixture have to be monitored simultaneously because of the high instability of this phenomenon, which is also visible during CFD studies.

This paper presents results of numerical investigations of the ejector condenser, designed to entrain steam-CO_2 mixture and condense steam with the presence of inert gas. A basic geometrical model has been developed to provide the most efficient condensation process. The expected compression ratio resulting from the created sub-pressure at the gas inlet is relatively low (max. 1.25). A CFD model with the use of mixture approach and realizable two-layer k–ε turbulence model was used to develop a numerical model of the ejector condenser, allowing us to capture the phenomenon complexity. The influence of changing geometrical parameters on the ejector performance was evaluated.

2. The object of the research

The research object is the ejector condenser, which is part of the Negative CO_2 Emission Gas Power Plant [29]. The scheme of the ejector is presented in Fig. 1, and detailed dimensions for the basic model are presented in Table 1.

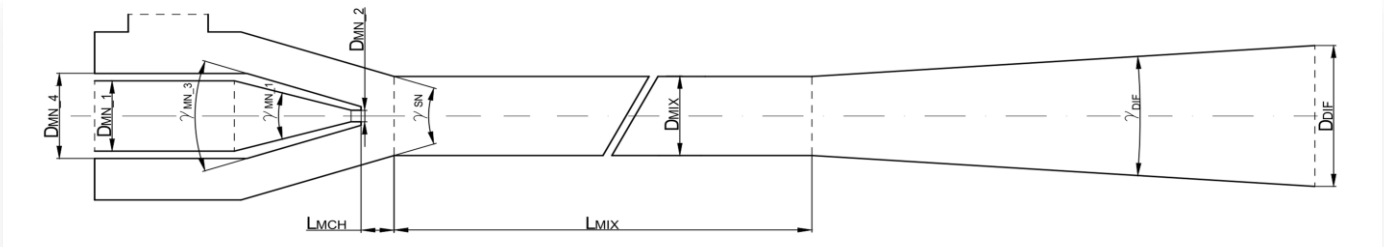

Fig. 1. Spray ejector-condenser.

Table 1. Ejector-condenser dimensions.

Parameter	Value	Parameter	Value	Parameter	Value
D_{MN_1}[mm]	25.4	D_{DIF} [mm]	100.0	γ_{MN_3} [°]	45.0
D_{MN_2}[mm]	3.0	L_{MIX} [mm]	1050.0	γ_{SN} [°]	45.0
D_{MN_4}[mm]	40.0	L_{MCH} [mm]	25.0	γ_{DIF} [°]	10.0
D_{MIX} [mm]	25.4	γ_{MN_1} [°]	30.0	-	-

3. Numerical model

3.1. Assumptions and boundary conditions

The axisymmetric numerical model was developed using a Simcenter STAR-CCM+ software based on the finite volume method (FVM). Model parameters at the boundary surfaces are presented in Fig. 2. Water properties are assumed to be constant. Steam and CO_2 properties are assumed to be temperature-dependent based on the IAPWS-IF97 [30] and NIST library [31], respectively.

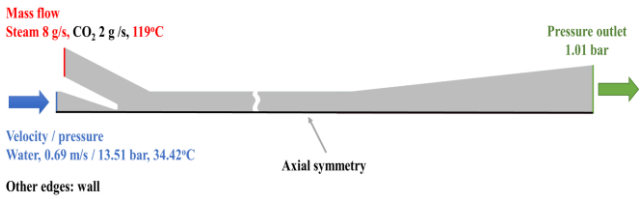

Fig. 2. Boundary conditions.

3.2. Numerical mesh

The polyhedral-elements-based mesh was developed. Mesh-sensitivity analysis was conducted based on the pressure charts along the flow path for meshes with different base sizes presented in Fig. 3. The pressure measurement points were located directly near the wall and the presented length is a distance from the motive nozzle outlet. Meshes 1–5 are characterized by the following number of elements: 60 787, 174 895, 387 221, 820 753, and 1 302 936. Taking into account the change of the solution during mesh refinement, the stability of the calculation and the available computing power, mesh 4 was selected.

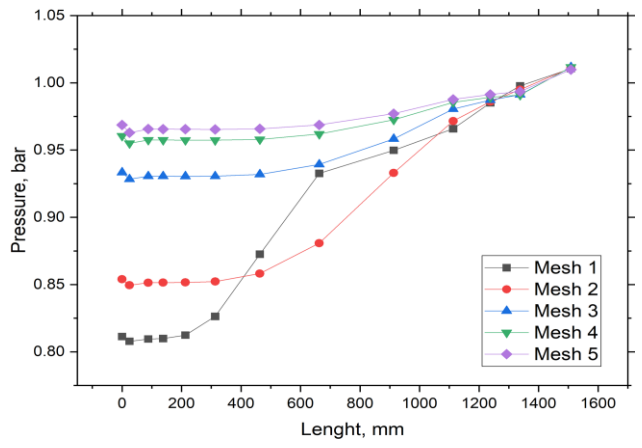

Fig. 3. Mesh independence study for ejector-condenser numerical analysis (0 mm – motive nozzle outlet).

The suction chamber and the beginning of the mixing chamber for mesh 4 is presented in Fig. 4.

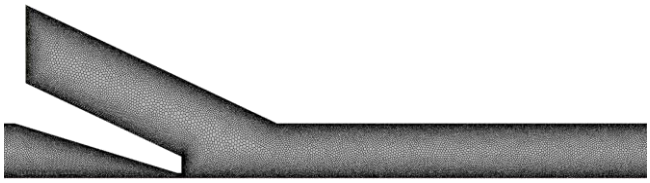

Fig. 4. Mesh at the suction chamber and at the beginning of the mixing chamber.

The base size of the chosen mesh element is 0.077 mm. It gives 820 753 elements for basic geometry and differs slightly depending on the geometry modification. The inflation layer is applied with the following properties: 3 layers, 0.03 mm total thickness and 1.6 growth ratio. The mesh was also locally refined, e.g. at the motive nozzle's trailing edge, where large pressure and velocity gradients occur.

3.3. Parameters definition

The main parameters in this paper include the compression ratio, expansion ratio, pressure ratio, mass entrainment ratio, temperature ratio and condensation efficiency.

The compression ratio ξ is the ratio between the pressures at the diffuser outlet p_o and gas inlet p_g (Eq. (1)):

$$\xi = \frac{p_o}{p_g}. \tag{1}$$

The expansion ratio θ is the ratio between the pressures at the driving fluid inlet p_d and gas inlet p_g (Eq. (2)):

$$\theta = \frac{p_d}{p_g}. \tag{2}$$

The pressure ratio N is expressed in terms of pressures at the inlets: p_g, p_d and diffuser outlet p_o (Eq. (3)):

$$N = \frac{p_o - p_g}{p_d - p_o}. \tag{3}$$

The temperature ratio k is expressed in terms of temperatures at the inlets: T_g, T_d and diffuser outlet T_o (Eq. (4)):

$$\gamma = \frac{T_o - T_g}{T_d - T_o}. \tag{4}$$

The condensation efficiency η is expressed in terms of steam mass flow rate at the gas inlet $\dot{m}_g$ and diffuser outlet $\dot{m}_o$. It describes how much steam has been condensed in the mixing chamber and diffuser (Eq. (5))

$$\eta = \left(1 - \frac{\dot{m}_o}{\dot{m}_g}\right) \cdot 100\%. \tag{5}$$

3.4. Models and governing equations

The mixture model, based on the Euler-Euler approach, is used to calculate multiphase flow. The governing equations of mass, momentum and energy are presented in Eqs. (6)–(8), and volume fractions of water, steam and CO_2 are presented in

Eqs. (9)–(11). The momentum conservation equation (Eq. (7)) uses cylindrical coordinates because the axisymmetric model is used. It is assumed that the circumferential velocity and the circumferential gradients are zero.

$$\int_A \rho_m \boldsymbol{v}_m \cdot d\boldsymbol{a} = 0, \tag{6}$$

$$\oint_{\partial A} \rho_m (\boldsymbol{v}_m \boldsymbol{v}_m) \cdot \boldsymbol{r} ds = -\oint_{\partial A} p\mathbf{I} \cdot \boldsymbol{r} ds + \oint_{\partial A} \mathbf{T}_m \cdot \boldsymbol{r} ds + \\ + \int_A \frac{1}{r} \begin{bmatrix} 0 \\ p - \tau_{\theta\theta} \\ 0 \end{bmatrix} \cdot \boldsymbol{r} dA + \int_A \boldsymbol{f}_b \, dA, \tag{7}$$

$$\int_A \rho_m H_m \boldsymbol{v}_m \cdot d\boldsymbol{a} = -\int_A \dot{\boldsymbol{q}} \cdot d\boldsymbol{a} + \\ + \int_A (\mathbf{T}_m \cdot \boldsymbol{v}_m) \cdot d\boldsymbol{a} + \int_V (\boldsymbol{f}_b \cdot \boldsymbol{v}_m + S_e) \cdot dV, \tag{8}$$

$$\int_A \alpha_w \boldsymbol{v}_m \cdot d\boldsymbol{a} = \int_V S_w \, dV + \int_A \frac{\mu_t}{\mathrm{Sc}_t \rho_m} \nabla \alpha_w \cdot d\boldsymbol{a}, \tag{9}$$

$$\int_A \alpha_s \boldsymbol{v}_m \cdot d\boldsymbol{a} = \int_V S_s \, dV + \int_A \frac{\mu_t}{\mathrm{Sc}_t \rho_m} \nabla \alpha_s \cdot d\boldsymbol{a}, \tag{10}$$

$$\int_A \alpha_{CO2} \boldsymbol{v}_m \cdot d\boldsymbol{a} = \int_A \frac{\mu_t}{\mathrm{Sc}_t \rho_m} \nabla \alpha_{CO2} \cdot d\boldsymbol{a}. \tag{11}$$

In Eq. (7), $\boldsymbol{v_m} = (v_z v_r v_\theta)^T$ and the third right hand side term contains a tensor $\begin{bmatrix} 0 \\ p - \tau_{\theta\theta} \\ 0 \end{bmatrix}$.

The realizable two-layer k–ε model was used to calculate turbulence. The turbulent dynamic viscosity μ_t is calculated according to Eq. (12). Two transport equations for turbulent kinetic energy are solved: for turbulent kinetic energy k (Eq. (13)) and turbulent dissipation rate ε (Eq. (14)).

$$\mu_t = \rho C_\mu f_\mu k T, \tag{12}$$

$$\nabla \cdot (\rho k \overline{\boldsymbol{v}}) = \nabla \cdot \left[\left(\mu + \frac{\mu_t}{\sigma_k} \right) \nabla k \right] + P_k - \rho(\varepsilon - \varepsilon_o) + S_k, \tag{13}$$

$$\nabla \cdot (\rho \varepsilon \overline{\boldsymbol{v}}) = \nabla \cdot \left[\left(\mu + \frac{\mu_t}{\sigma_\varepsilon} \right) \nabla \varepsilon \right] + \frac{1}{t_e} C_{\varepsilon 1} P_\varepsilon + \\ - \rho C_{\varepsilon 2} f_2 \left(\frac{\varepsilon}{t_e} - \frac{\varepsilon_o}{t_0} \right) + S_\varepsilon. \tag{14}$$

The condensation is calculated using a thermally driven model where the rate of boiling/condensation depends on heat transfer between saturated interphase boundary surfaces and phases. The interphase mass flow rate $\dot{g}$ per unit volume between steam s and water w can expressed as in Eq. (15)

$$\dot{g}^{(s\,w)} = \frac{Q_s^{(s\,w)} + Q_w^{(s\,w)}}{L_{s\,w}}. \tag{15}$$

One of the parameters that determine the heat transfer rate Q is the heat transfer coefficient h (Eq. (16)). It depends on the continuous phase (steam) heat conductivity λ_c, Nusselt Number Nu and interaction length scale l (droplet diameter)

$$h^{(s\,w)} = \frac{\lambda_c Nu}{l}. \tag{16}$$

The Nusselt number was calculated using the Ranz-Marshal approach supplemented with the Armenante-Kirwan correlation [32] for condensation on water droplets (Eq. (17))

$$\mathrm{Nu} = 2 + 0.6 \mathrm{Re}_t^{0.5} \mathrm{Pr}_c^{0.33}. \tag{17}$$

The Nusselt Number, thereby the heat transfer coefficient has been corrected by the correlation from Borishanskiy et al. [33], (Eq. (18)), where $\bar{h}_{co_2}$ denotes the heat transfer coefficient with inert gas and $\bar{h}$ – in the absence of inert gas

$$\frac{\bar{h}_{co_2}}{\bar{h}} = 1 - 0.25 \cdot (\alpha_{CO_2})^{0.7}. \tag{18}$$

Validation has been developed based on the results from the spray ejector condenser experimental rig located at AGH for the same boundary conditions. A detailed description of the design of the experimental rig and measurement devices is presented by Madejski et al. [34]. Pressure sensors were located near the wall at gas and water inlets, and temperature sensors were at the ejector outlet. A good agreement is obtained for the gas inlet pressure and outlet temperature, and moderate agreement for the water inlet pressure (see Table 2).

Table 2. Validation of the CFD results.

	Gas inlet pressure, bar	Water inlet pressure, bar	Outlet temperature, K
CFD	0.97	13.5	327.33
Experiment	0.95	15.6	321.60
Error, %	2.3	13.5	1.8

4. Results

4.1. Motive nozzle diameter

The following nozzle diameters are considered: 2.6 mm, 2.8 mm, 3.0 mm (basic mode), 3.2 mm, and 3.6 mm for various types of boundary conditions at the water inlet: velocity and pressure. Figure 5 shows the pressure contours located in the suction chamber for various motive nozzle diameters for a constant velocity boundary condition at the water inlet. The pressure difference is high: from 7 bar for the largest nozzle diameter (3.6 mm) to 23 bar for the smallest one (2.6 mm).

Cross-sectional average pressure and steam mass flow charts along the flow path for velocity and pressure boundary condi-

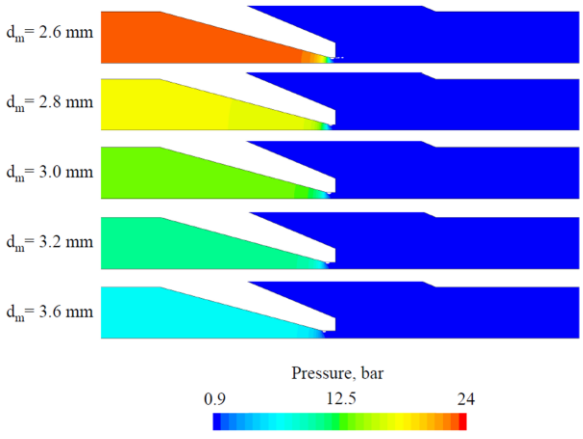

Fig. 5. Pressure contours in the suction chamber for various motive nozzle diameter for constant velocity boundary conditions.

tions (b.c.) at the water inlet are presented in Figs. 6, 7 and Figs. 8, 9, respectively. Considering the constant velocity (mass flow rate) at the water inlet: smaller nozzle diameters create a greater sub-pressure at the gas inlet (up to 0.91 bar) and intensify the condensation process, which can be noticed in the more rapid decrease in steam mass flow. A reverse trend can be noticed for pressure boundary conditions at the water inlet: better performance (condensation insensitivity, lower gas inlet pressure) is achieved for nozzles with higher diameters.

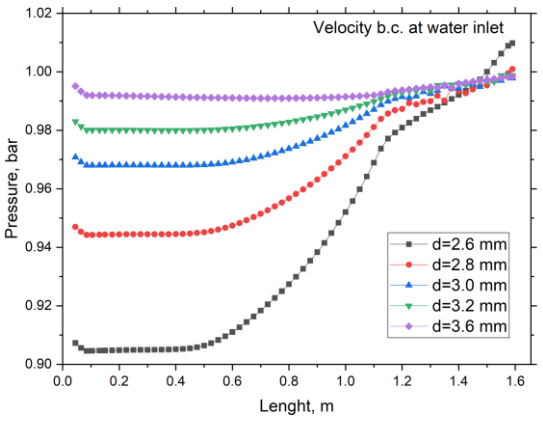

Fig. 6. Average pressure change along the flow path for velocity b.c. at water inlet (0 mm – motive nozzle outlet).

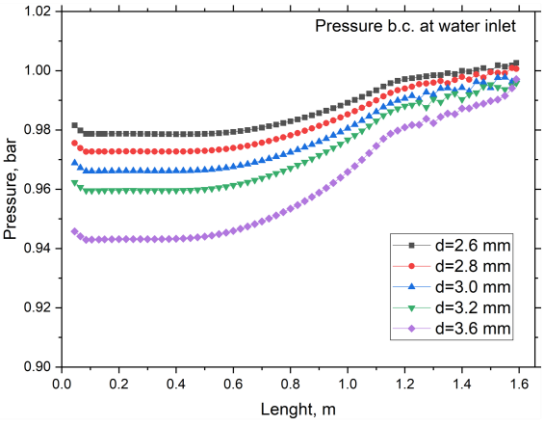

Fig. 7. Average pressure change along the flow path for pressure b.c. at water inlet (0 mm – motive nozzle outlet).

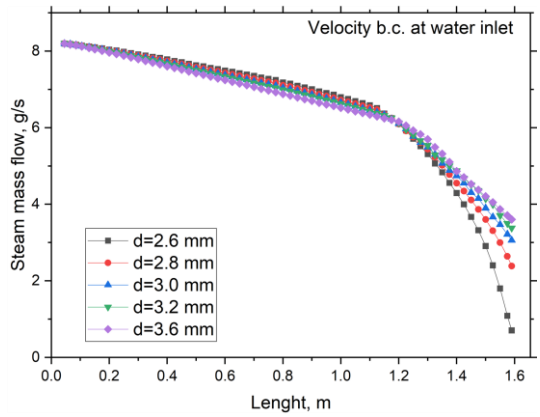

Fig. 8. Average steam mass flow change along the flow path for velocity b.c. at water inlet (0 mm – motive nozzle outlet).

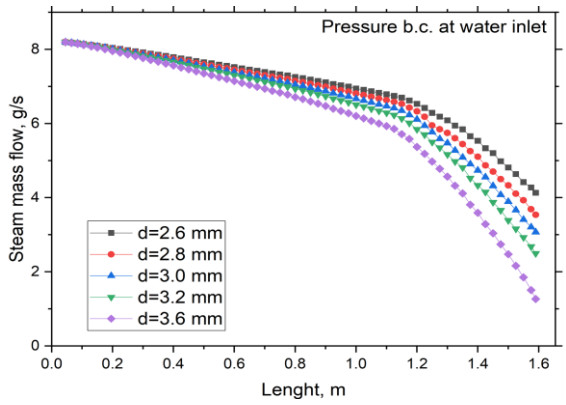

Fig. 9. Average steam mass flow change along the flow path for pressure b.c. at water inlet (0 mm – motive nozzle outlet).

Velocity contours for various nozzle diameters are presented in Fig. 10 and Fig. 11 for velocity and pressure b.c. at the water inlet, respectively. The highest velocity occurs in the region of the water jet, especially at the beginning of the mixing chamber. Considering constant velocity b.c. at the water inlet (constant mass flow rate), the smaller the nozzle diameter, the higher the velocity of the mixture.

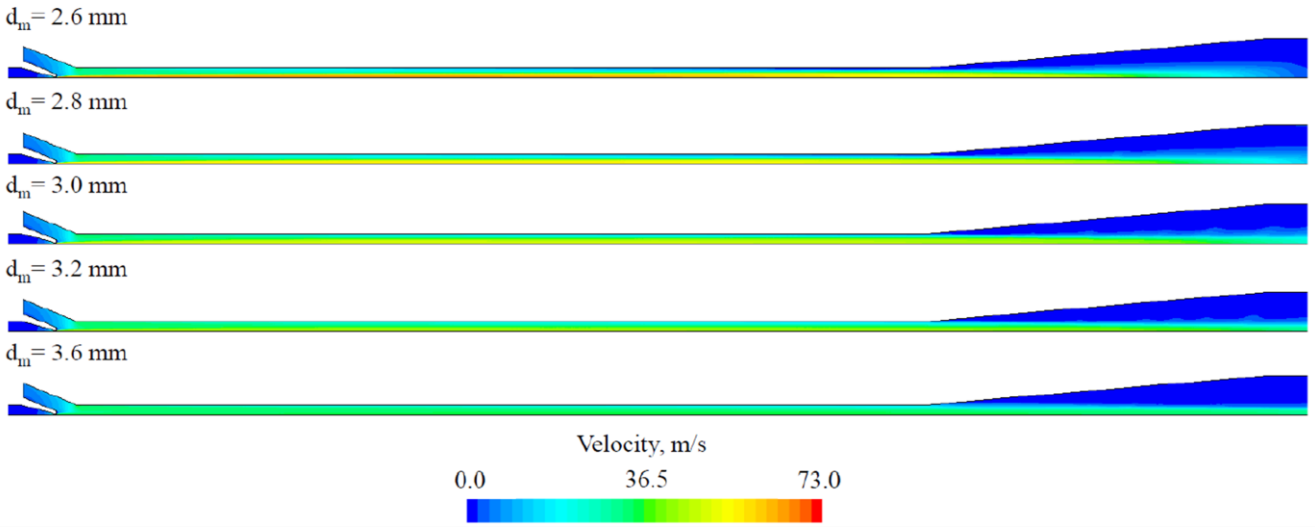

Fig. 10. Velocity contours for various nozzle diameters for constant velocity b.c.

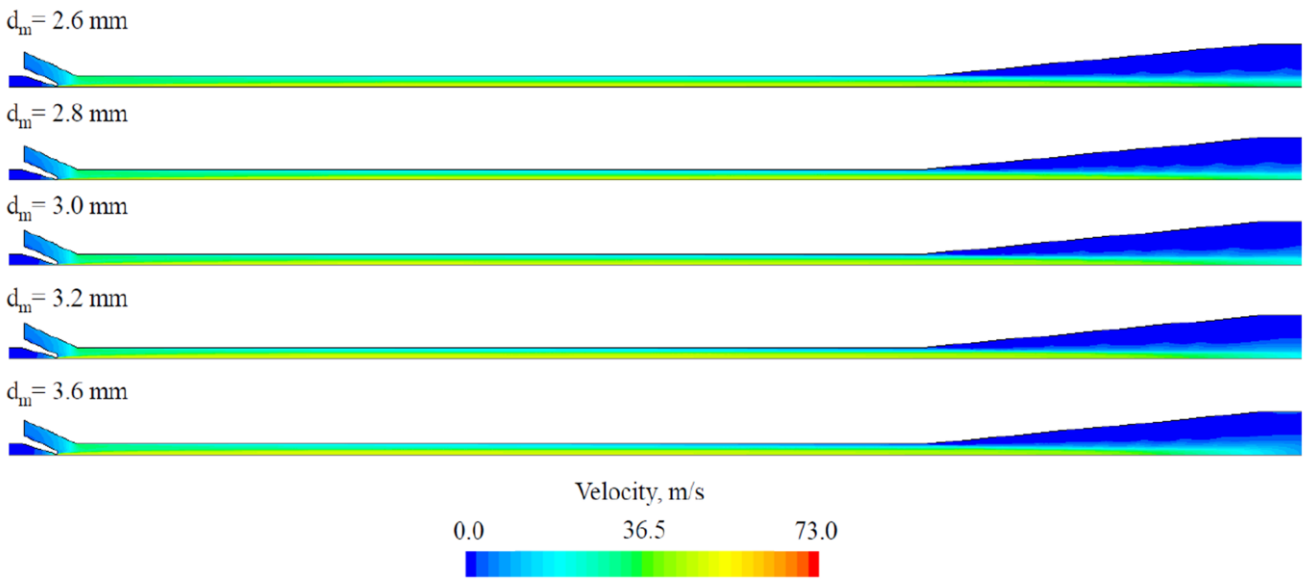

Fig. 11. Velocity contours for various nozzle diameters for constant pressure b.c.

The maximum velocity of about 70 m/s is achieved for the nozzle diameter 2.6 mm, and it occurs near the ejector axis. For the 3.6 mm diameter, the mixture velocity in the mixing chamber is uniform and about 30 m/s. Regarding velocity contours for pressure b.c. differences are not clearly visible between different nozzles diameters. The mixture velocity does not exceed 50 m/s.

Steam volume fraction contours for various nozzle diameters for velocity b.c. are presented in Fig 12. Lower values of steam volume fraction occur in the water jet region. Some part of the steam still exists near the outlet in all cases.

The performance analysis based on non-dimensional ejector indicators for different motive nozzle diameters considering two types of b.c. (velocity and pressure) is presented in Table 3. The compression ratio ranges between 1.003–1.113 and the pressure ratio 0.0017–0.0046. The maximum value is obtained for the motive nozzle diameter 2.6 mm for velocity b.c. Considering pressure b.c., the greatest compression ratio is obtained for the motive nozzle diameter 3.6 mm (1.054 and 4.844, respectively) but it is connected with quite a low mass entrainment ratio (0.0205). Considering the condensation efficiency, it varies significantly depending on the b.c. type at the water inlet and motive nozzle diameter. The highest 91.4% is obtained for the motive nozzle diameter 2.6 mm and velocity b.c. at the water inlet. The lowest 49.6% is achieved for the same motive nozzle diameter but for pressure b.c. at the water inlet.

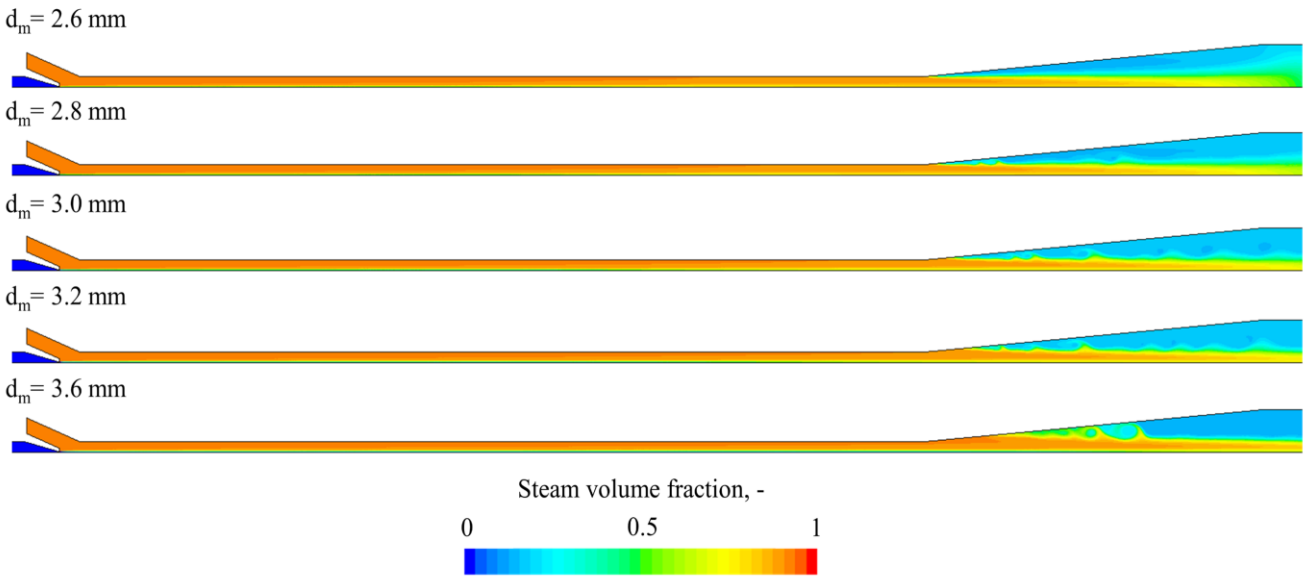

Fig. 12. Steam volume fraction contours for various nozzle diameters for constant pressure b.c.

Table 3. Performance analysis for various motive nozzle diameters using different b.c. at the water inlet.

B.c. at the water inlet	Motive nozzle diameter, mm	Compression ratio ξ,	Expansion ratio Θ,	Pressure ratio *N*,	Mass entertainment ratio ω_M,	Temperature ratio γ,	Condensation efficiency η, %
Velocity	2.6	1.113	25.506	0.0046	0.0295	2.972	91.4
	2.8	1.056	18.479	0.0032	0.0295	3.192	70.9
	3.0	1.044	13.912	0.0035	0.0295	3.283	62.7
	3.2	1.016	10.875	0.0016	0.0295	3.356	58.8
	3.6	1.003	7.131	0.0005	0.0295	4.526	56.0
Pressure	2.6	1.021	13.759	0.0017	0.0394	2.319	49.6
	2.8	1.025	13.843	0.0020	0.0339	2.769	56.8
	3.0	1.047	13.937	0.0036	0.0295	3.243	62.5
	3.2	1.034	14.031	0.0026	0.0259	3.691	69.5
	3.6	1.054	14.275	0.0041	0.0205	4.844	84.5

4.2. Mixing chamber diameter

Three mixing chamber diameters are taken into account: 20 mm, 25 mm (basic mode), and 30 mm. The mixing chamber diameter can be manipulated in two ways: shortening the size of the exhaust gas inlet line or slightly reducing the length of the mixing chamber (marked as *). The cross-sectional average pressure and temperature charts for the various mixer diameters are presented respectively in Fig. 13 and Fig. 14. Increasing the diameter of the mixing chamber causes the outlet temperature to be higher. It indicates that the condensation process is more intensive. Reducing the diameter leads to a decrease in the performance of the ejector: pressure losses can be observed in the mixing chamber, and outlet temperature is reduced.

Figure 15 shows the velocity contours for different mixing chamber diameters. A significantly higher mixture velocity (45−55 m/s) for a 20 mm mixing chamber diameter is observed. It can be the reason for the high-pressure losses. Moreover, the highest value of velocity occurs in the water jet region for 25 mm and 30 mm mixing chamber diameters. For the 20 mm diameter, the velocity value is high in the gas region near the mixing chamber wall.

Temperature contours for various mixing chamber diameters are presented in Fig 16. The differences in the radial direction are visible. With a 20 mm mixing chamber diameter, the temperature becomes uniform much more quickly. Fluctuation of the temperature in the diffuser can be observed due to the mixing and condensation processes.

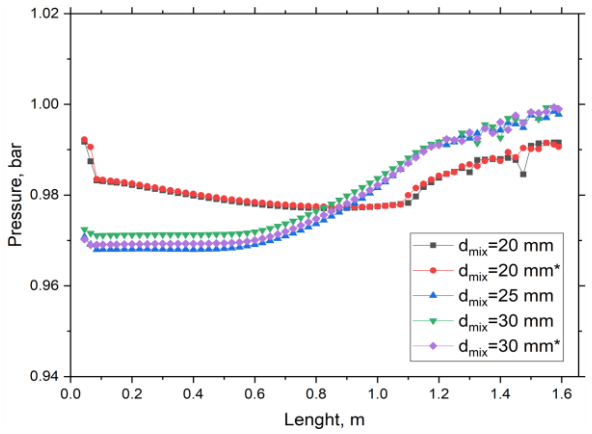

Fig. 13. Average pressure change along the flow path for various mixing chamber diameters (0 mm – motive nozzle outlet).

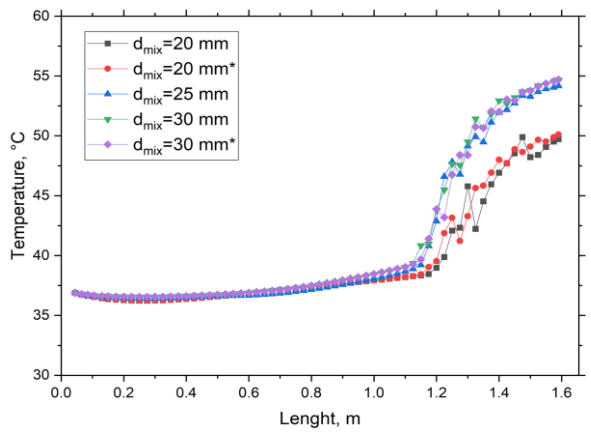

Fig. 14. Average pressure change along the flow path for various mixing chamber diameters (0 mm – motive nozzle outlet).

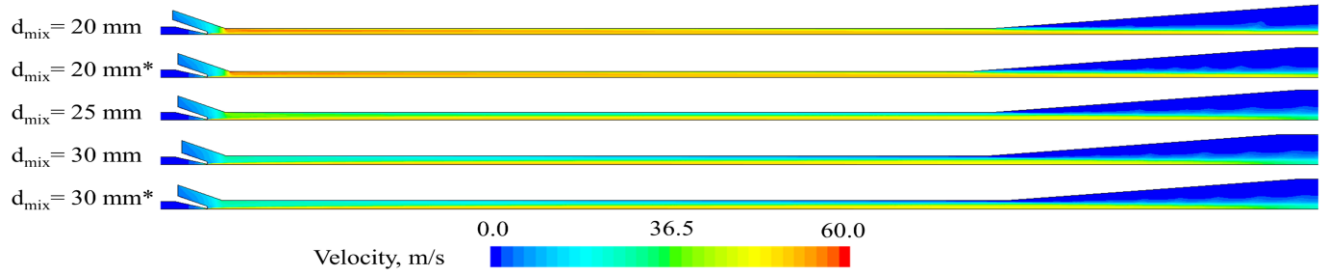

Fig. 15. Velocity contours for various mixing chamber diameters.

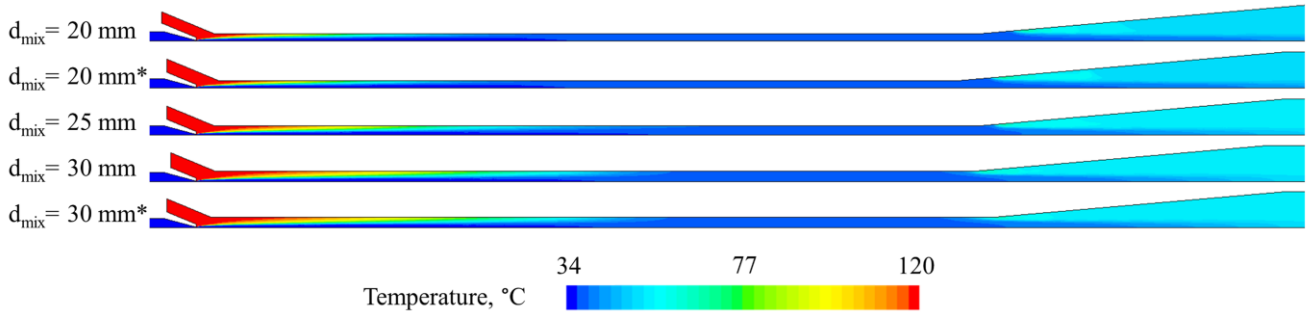

Fig. 16. Temperature contours for various mixing chamber diameter.

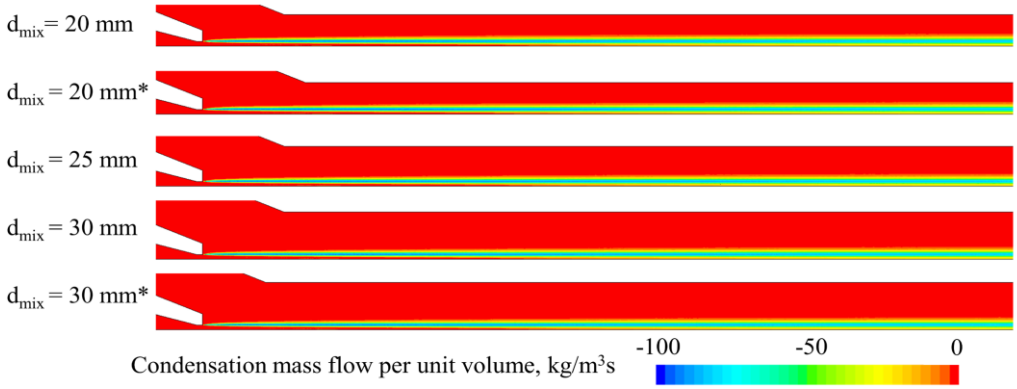

Fig. 17. Condensation mass flow contours for various mixing chamber diameter.

Table 4. Performance analysis for various mixing chamber diameter.

Mixing chamber diameter, mm	Compression ratio ξ,	Expansion ratio Θ,	Pressure ratio N,	Mass entertainment ratio ω_M,	Temperature ratio k,	Condensation efficiency η, %
20	0.999	13.646	-0.0001	0.0295	4.534	57.9
20*	0.998	13.651	-0.0002	0.0295	4.393	59.8
25	1.044	13.912	0.0035	0.0295	3.283	62.7
30	1.027	13.894	0.0021	0.0295	3.178	68.1
30*	1.029	13.928	0.0023	0.0295	3.171	66.8

Condensation mass flow contours for various mixing chamber diameters are presented in Fig. 17. The condensation occurs mainly in the water jet region. The maximum value of condensation mass flow per unit volume is about 100 kg/m^{3}s. There are no clear differences between the contours for different mixing chamber diameters.

Performance analysis using performance ejector indicators for various mixing chamber diameters is presented in Table 4. The highest compression ratio is achieved for the 25 mm mixing chamber diameter (basic mode). Considering the 20 mm mixing chamber diameter, no pressure lift is observed because the compression ratio is around 1. An increase in the mixing chamber diameter causes the compression ratio and temperature ratio to be lower. The mass entrainment ratio is the same for all considering cases because of constant mass flow rate/velocity b.c. at the water and gas inlet. The condensation efficiency is higher for the increased mixing chamber diameter.

5. Conclusions

An axisymmetric CFD model of the ejector condenser was developed to investigate the ejector performance and condensation intensity for various design modes. The presence of three phases – water, steam and CO_2 was considered using the mixture model. A thermally-driven model with the applied Nusselt correlation for direct contact condensation was used to calculate the condensation. A mesh independence test and the comparison with the experimental results were performed. The analysis considered two geometrical parameters: motive nozzle diameter (for two types of b.c. at the water inlet) and mixing chamber diameter.

Changing the diameter of the motive nozzle significantly affects the generated pressures and the efficiency of vapour condensation. For the assumed constant flow rate of the motive wa-

ter, decreasing the diameter from 3.0 mm to 2.6 mm is more profitable: lower pressure at the gas inlet and less steam at the outlet (better condensation intensity). For the assumed constant pressure at the motive water inlet, increasing the diameter from 3.0 mm to 3.6 mm improves the compression effect and condensation performance.

Reducing the mixing chamber diameter from 25 mm to 20 mm diameter causes a significant growth in the velocity of the mixture and leads to pressure losses and a decrease in the condensation efficiency. Increasing the diameter to 30 mm decreases the compression ratio by about 1.5%, and the condensation efficiency by about 6.5%–8.6%.

Results show that the developed CFD model which reflects multiphase turbulent flow with phase change in the spray ejector can be helpful for investigating thermal-flow phenomena and assessing the influence of the chosen geometric parameters on the ejector performance. Results also indicate the direction of further design improvements. Future work should investigate other geometrical parameters that can significantly affect the performance.

Acknowledgements

The research leading to these results has received funding from the Norway Grants 2014–2021 via the National Centre for Research and Development. Work has been prepared within the frame of the project: ”Negative CO_2 emission gas power plant”–NOR/POLNORCCS/NEGATIVE-CO_2-PP/0009/2019-00 co-financed by the programme ”Applied research” under the Norwegian Financial Mechanisms 2014–2021 POLNOR CCS 2019 – “Development of CO_2 capture solutions integrated in power and industry processes”.

References

[1] Croquer, S., Poncet, S., & Aidoun, Z. (2016). Turbulence modeling of a single-phase R134a supersonic ejector. Part 1: Numerical benchmark. *International Journal of Refrigeration*, 61, 140-152. doi: 10.1016/j.ijrefrig.2015.07.030

[2] Aidoun, Z., Ameur, K., Falsafioon, M., & Badache, M. (2019). Current Advances in Ejector Modeling, Experimentation and Applications for Refrigeration and Heat Pumps. Part 1: Single-phase ejector. *Inventions*, 4(1). doi: 10.3390/inventions4010015

[3] de Oliveira Marum, V.J., Reis, L.B., Maffei, F.S., Ranjbarzadeh, S., Korkischko, I., dos Santos Gioria, R., & Meneghini, J.R. (2021). Performance analysis of a water ejector using Computational Fluid Dynamics (CFD) simulations and mathematical modeling. *Energy*, 220. doi: 10.1016/j.energy.2021.119779

[4] Xiao, J., Wu, Q., Chen, L., Ke, W., Wu, C., Yang, X., Yu, L., & Jiang, H. (2022). Assessment of Different CFD Modeling and Solving Approaches for a Supersonic Steam Ejector Simulation. *Atmosphere*, 13(1), 144. doi: 0.3390/atmos13010144

[5] Ringstad, K.E., Allouche, Y., Gullo, P., Ervik, A., & Banasiak, K. (2022). A detailed review on CO2 two-phase ejector flow modeling. *Thermal Science and Engineering Progress*, 20. doi: 10.1016/j.tsep.2020.100647

[6] Koirala, R., Inthavong, K., & Date, A. (2022). Numerical study of flow and direct contact condensation of entrained vapor in water jet eductor. *Experimental and Computational Multiphase Flow*, 4, 291–303. doi: 10.1007/s42757-021-0118-2

[7] Zheng, P., Li, B., & Qin, Jingxuan. (2018). CFD simulation of two-phase ejector performance influenced by different operation conditions. *Energy*, 155, 1129–1145. doi 10.1016/j.energy.2018.04.066

[8] Assari, M.R., Tabrizi, H.B., Beik, A.J.G., & Shamesri, K. (2022). Numerical Study of Water-air Ejector using Mixture and Two-phase Models. *International Journal of Engineering*, 35(2), 307−318. doi: 10.5829/IJE.2022.35.02B.06

[9] Sharma, D., Patwardhan, A., & Ranadek, V. (2018). Effect of turbulent dispersion on hydrodynamic characteristics in a liquid jet ejector. *Energy*, 164, 10–20. doi: 10.1016/j.energy.2018.08.171

[10] Wang, X., Li, H., Dong, J., Wu, J. & Tu, J. (2020). Numerical study on mixing flow behavior in gas-liquid ejector. *Experimental and Computational Multiphase Flow*, 3, 108–112. doi: 10.1007/s42757-020-0069-z

[11] Majchrzyk, M., Dziurowicz, D., Hajda, M., Palacz, M., Bodys, J., Fingas, R., Smolka, J., & Nowak, A.J. (2020). Detailed numerical investigation of the CO two-phase ejector 3-D CFD model based on the flow visualisation experiments. *Chemical Engineering and Processing - Process Intensification*, 182. doi: 10.1016/j.cep.2022.109195

[12] Madejski, P., Banasiak, K., Ziółkowski, P., Mikielewicz, D., Mikielewicz, J., Kuś, T., Karch, M., Michalak, P., Amiri, M., Dąbrowski, P., Stasiak, K., Subramanian, N., & Ochrymiuk, T. (2023). Development of a spray-ejector condenser for the use in a negative CO_2 emission gas power plant, *Energy*, 283. doi: 10.1016/j.energy.2023.129163

[13] Reis, L.B., & dos Santos Gioria, R. (2021). Optimization of liquid jet ejector geometry and its impact on flow fields. *Applied Thermal Engineering*, 194. doi: 10.1016/j.applthermaleng.2021.117132

[14] Sheha, A.A.A., Nasr, M., Hosien, M.A., & Wahba, E.M. (2018). Computational and Experimental Study on the Water-Jet Pump Performance. *Journal of Applied Fluid Mechanics*, 11(4), 1013–1020. doi: 10.29252/jafm.11.04.28407

[15] Zhang, J., Geng, J., Yang, S., Cheng, C. Zhu, G., Wang, C., Yang, Z., & Lye, Y. (2023). Influence of geometric parameters on the performance of ejector used in aeroengine air system. *Thermal Science and Engineering Progress*, 37(1). doi: 10.1016/j.tsep.2022.101571

[16] Chen, W., Huang, C., Bai, Y., Chong, D., Yan, J., & Liu, J. (2020). Experimental and numerical investigation of two phase ejector performance with the water injected into the induced flow. *International Journal of Advanced Nuclear Reactor Design and Technology*, 2, 15–24. doi: 10.1016/j.jandt.2020.01.001

[17] Yan, J., Shu, Y., Jiang, J., & Wen, H. (2023). Optimization of Two-Phase Ejector Mixing Chamber Length under Varied Liquid Volume Fraction. *Entropy*, 2023, 25(1). doi: 10.3390/e25010007

[18] Mohammadi, A. (2019). An investigation of geometrical factors of multi-stage steam ejectors for air suction. *Energy*, 186. doi: 10.1016/j.energy.2019.07.138

[19] Foroozesh, F., Khoshnevis, A.B., & Lakzian, E. (2020). Investigation on the effects of water steam ejector geometry in the refrigeration systems using entropy generation assessment. *Journal of Thermal Analysis and Calorimetry*, 141, 1399–1411. doi: 10.1007/s10973-019-09128-1

[20] Dong, J., Hu, Q., Yu, M., Han, Z., Cui, W., Liang, D., Ma, H., & Pan, X. (2020). Numerical investigation on the influence of mixing chamber length on steam ejector performance. *Applied Thermal Engineering*, 174. doi: 10.1016/j.applthermaleng.2020.115204

[21] Han, Y., Wang, X., Sun, H., Zhang, G., Guo, L., & Tu, J. (2019). CFD simulation on the boundary layer separation in the steam

ejector and its influence on the pumping performance. *Energy*, 167. doi: 10.1016/j.energy.2018.10.195

[22] Weber, C. (1931). On the disintegration of a liquid jet. *Zeitschrift für Angewandte Mathematik und Mechanik*, 11(2), 136–154. doi: 10.1002/zamm.19310110207

[23] Mikielewicz, D., Amiri, M., & Mikielewicz, J. (2022). Direct-contact condensation from vapour-gas mixture in a spray ejector condenser for negative CO_2 power plant. *2nd International Conference on Negative CO_2 Emissions*, June 14–17, Gothenburg, Sweden.

[24] He, S., Li, Y., & Wang, R.Z. (2009). Progress of mathematical modelling on ejectors. *Renewable and Sustainable Energy Reviews*, 18(3), 1760–1780. doi: 10.1016/j.rser.2008.09.032

[25] Colarossi, M., Trask, N., Schmidt. D.P., & Bergander, M.J. (2012). Multidimensional modeling of condensing two-phase ejector flow. *International Journal of Refrigeration*, 35(2), 290–299. doi: 10.1016/j.ijrefrig.2011.08.013

[26] Ameur, K., Aidoun, Z., & Ouzzane, M. (2016). Modeling and numerical approach for the design and operation of two-phase ejectors. *Applied Thermal Engineering*, 109, 809–818. doi: 10.1016/j.applthermaleng.2014.11.022

[27] Madejski, P., Michalak, P., Karch, M., Kuś, T., & Banasiak, K. (2022). Monitoring of Thermal and Flow Processes in the Two-Phase Spray-Ejector Condenser for Thermal Power Plant Applications. *Energies*, 15(19). doi: 10.3390/en15197151

[28] Madejski, P., Karch, M., Michala, P., & Banasiak, K. (2024). Conceptual Design of Experimental Test Rig for Research on Thermo-Flow Processes During Direct Contact Condensation in the Two-Phase Spray-Ejector Condenser. *Journal of Energy Resources Technology*, 146(3). doi: 10.1115/1.4064194

[29] Ziółkowski, P., Madejski, P., Amiri, M., Kuś, T., Stasiak, K., Subramanian, N., Pawlak-Kruczek, H., Badur, J., Niedźwiedzki, Ł., & Mikielewicz, D. (2021). Thermodynamic Analysis of Negative CO2 Emission Power Plant Using Aspen Plus, Aspen Hysys, and Ebsilon Software. *Energies*, 14(19), 6304. doi: 10.3390/en14196304

[30] Wagner, W., & Kretzschmar, H.-J. (2008). *International Steam Tables—Properties of Water and Steam Based on the Industrial Formulation IAPWS-IF97. Tables, Algorithms, Diagrams, and CD-ROM Electronic Steam Tables – All of the Equations of IAPWS-IF97 Including a Complete Set of Supplementary Backward Equations for Fast Calculations of Heat Cycles, Boilers, and Steam Turbines*, 2nd Ed. Springer, New York.

[31] Linstrom, P.J., & Mallard, W.G. (2001). The NIST Chemistry WebBook: A Chemical Data Resource on the. *Journal of Chemical and Engineering Data*, 46(5), 1059–1063. doi: 10.1021/je000236i

[32] Armenante, P.M., & Kirwan, D.J. (1989). Mass Transfer to microparticles in agitated Systems. *Chemical Engineering Science*, 44(12), 2781–2796. doi: 10.1016/0009-2509(89)85088-2

[33] Borishanskiy, V.M. (1977). Effect of Uncondensable Gas Content on Heat Transfer in Steam Condensation in a Vertical Tube. *Heat Transfer - Soviet Research*, 9, 35–42.

[34] Madejski, P., Karch, M., Michalak, P., & Banasiak, K. (2024). Conceptual Design of Experimental Test Rig for Research on Thermo-Flow Processes During Direct Contact Condensation in the Two-Phase Spray-Ejector Condenser. *Journal of Energy Resources Technology*, 146(3), 1–39. doi: 10.1115/1.4064194

Co-published by
Institute of Fluid-Flow Machinery
Polish Academy of Sciences
Committee on Thermodynamics and Combustion
Polish Academy of Sciences

http://www.imp.gda.pl/archives-of-thermodynamics/

Carbon dioxide capture in large-scale CCGT power plant from flue gases obtained from various fuel mixtures

Navaneethan Subramanian*, Paweł Madejski

AGH University of Science and Technology, Faculty of Mechanical Engineering and Robotics, al. Mickiewicza 30, 30-059 Kraków, Poland
*Corresponding author email: subraman@agh.edu.pl

Received: 31.01.2024; revised: 22.07.2024; accepted: 08.10.2024

Abstract

In this study, the thermodynamic analysis of a combined cycle gas turbine integrated with post-combustion carbon capture and storage using the solvent method is performed. The syngas obtained from the gasification of sewage sludge is mixed with methane and nitrogen-rich natural gas fuels at different proportions, used in the gas turbine, and the properties of fuel and flue gases are analyzed. The flue gas obtained from the fuel mixture is passed through the post-combustion carbon capture and storage at various load conditions to assess the heat and electricity required for the carbon capture process. The solvent used for the carbon capture from flue gases enables CO_2 capture with the high efficiency of 90%. With the calculated results, the load conditions of flue gas using fuel mixtures are identified, which reduces the heat and power demand of post-combustion carbon capture and storage and provides the possibility to achieve neutral emission. The impact of selected operating conditions of post-combustion carbon capture and storage on the CO_2 emission reduction process and on the power plant performances is investigated. Considering the factors of electricity generation, energy efficiency, heat supply to the consumers, operating load of post-combustion carbon capture and storage and CO_2 emission, the 50% mixture of syngas with both fuels performs better. Also, the use of a mixture of 2-amino-2methyl-1-propanol and piperazine with reboiler duty 3.7 MJ/kgCO_2 in post-combustion carbon capture and storage slightly enhanced the performance of the power plant compared to the use of monoethanolamine with reboiler duty 3.8 MJ/kgCO_2.

Keywords: Thermodynamic modelling; Combined Cycle Gas Turbine; Post-combustion carbon capture and storage; CO_2 capture; Negative emission

Vol. 45(2024), No. 4, 85–93; doi: 10.24425/ather.2024.151999

Cite this manuscript as: Subramanian, N., & Madejski, P. (2024), Carbon dioxide capture in large-scale CCGT power plant from flue gases obtained from various fuel mixtures. *Archives of Thermodynamics*, 45(4), 85–93.

1. Introduction

A recent report by the International Energy Agency (IEA) in 2023 states that global energy-related emissions have reached 36.8 billion tons in the year 2022, which made the limiting global average temperature to 1.5°C by 2100 impossible. The expeditious actions by the conference of the parties (COP) will make it possible to limit the temperature to 1.7°C. Among the pathways suggested for limiting the increasing temperature in the energy sector, the carbon capture and storage (CCS), carbon capture utilization and carbon dioxide removal are among the many methods [1]. According to the Intergovernmental Panel on Climate Change (IPCC), as an effort to limit the global average temperature to below 2°C and to achieve net zero emission or 'negative emissions', the Bioenergy with Carbon Capture and Storage (BECCS) appears to be a feasible option [2], which can reach a potential of capturing 50 Mt CO_2/year by 2030 [3]. BECCS results in utilization of byproducts obtained from the

Nomenclature

Abbreviations and Acronyms

AEEA – aminoethyl ethanolamine
AMP – 2-amino-2methyl-1-propanol
BAE – 2-(butylamino)ethanol
BECCS – bioenergy with carbon capture and storage
CCGT – combined cycle gas turbine
CCS – carbon capture and storage
COP – conference of parties
DEA – diethanolamine
DETA – diethylenetriamine
DHN – district heating network
EAE – 2-(ethylamino)ethanol
EGBE – 2-butoxyethanol
HP – high pressure
HRSG – heat recovery steam generator
IEA – International Energy Agency
IPCC - intergovernmental panel on climate change
LP – low pressure
MAE – 2-(methylamino)ethanol
MDEA – methyl diethanolamine
MEA – monoethanolamine
PCCS – post-combustion carbon capture and storage
PZ – piperazine

thermochemical conversion process and integration with carbon capture technology, which helps not only to fight the climate change crisis but also to satisfy the energy demand [4].

The use of natural gas in combined cycle gas turbines (CCGT) integrated with post-combustion carbon capture (PCCS) provides low carbon emission and the possibility of achieving higher efficiency of CO_2 capture at a lower operational cost. During the steady state operation, CCGT with PCCS can provide a gross efficiency of 58% [5]. The cost saving of CCGT integrated with PCCS depends upon the effective operation of the power plant. When the electricity price is higher, the CCGT operation focuses on power generation and reduces the CO_2 capture process, thus producing more power output by reducing the energy penalty of CCS. When the carbon price is higher, the focus will be changed to the carbon capture process [6].

Post-combustion carbon capture works on low CO_2 concentrations and has minimised pressure loss when operated using solvents. Monoethanolamine (MEA), diethanolamine (DEA), methyl diethanolamine (MDEA), aminoethyl ethanolamine (AEEA), diethylenetriamine (DETA) are the most commonly used solvents in PCCS [7]. The PCCS process using chemical absorption solvents has a high carbon capture efficiency of 90% – 99% [8]. Despite amine loss and corrosion of utensils during the CO_2 capture process, MEA is the most widely used solvent due to its operation under partial pressure, capture rate and chemical kinetics [9]. The steam from the steam cycle of the power plant is used for the regeneration of the CO_2 capture process when operating PCCS is integrated with a power plant. Up to 10% of efficiency is reduced during the extraction of steam in the power plant due to the energy penalty, which can be minimized by introducing supplementary equipment such as a supplementary steam turbine [10]. Wu et al. [11] state that the introduction of solar energy for the PCCS regeneration process has improved the power generation in the steam cycle, which reduced the energy penalty to 6.93%.

The use of a single amine in PCCS has the drawback of consuming higher energy for regeneration and a lower absorption rate. Nowadays the use of blended solvents is gaining more attention because of the higher CO_2 capture rate and lower energy required for regeneration [12]. A simulation comparison by Ding et al. [13] shows that the blending of piperazine (PZ) with MEA and MDEA shows better performance by reducing regeneration energy and making the process more cost-effective compared to MEA and blended MEA-MDEA amines. Ping et al. [14] experimental study of nonaqueous secondary alkanolamines 2-(methylamino) ethanol (MAE), 2-(butylamino) ethanol (BAE) and 2-(ethylamino) ethanol (EAE) with 2-butoxyethanol (EGBE) used for the CO_2 capture process shows the blend of EGBE with BAE has a lower regeneration energy of 1.73 MJ/$kgCO_2$ compared to MEA which is 3.8 MJ/$kgCO_2$. The experimental study of blend solvents 2-amino-2methyl-1-propanol (AMP)-PZ-MEA with MEA shows that the blend of 6M–7M AMP-PZ-MEA solvents has 1.5–2.5 times higher mass transfer coefficient and better CO_2 capture rate than 5M MEA [15].

Due to the volatility of amine, the emission of amine with ammonia and other compounds occurs during oxidative degradation. This depends upon various factors such as operating conditions and the composition of flue gases, which can be reduced by cooling the treated flue gas at the outlet of the absorber, which is done by adding a water wash column [16].

Mathematical modelling of complex energy systems is a helpful tool in the analysis of conventional systems [17,18], those based on renewable energy sources [19], or hybrid energy systems [20]. Tools for the simulation of thermodynamics processes developed in recent years are increasingly popular, e.g. Aspen Plus, Aspen Hysys, GateCycle, IpsePRO or Ebslion Professional are used in the presented case [21,22].

The novelty of the study is that it identifies the CO_2-neutral fuel mixture and shows simulation results of the performance of CCGT when integrated with PCCS. CCGT is operated using the fuels methane and nitrogen-rich natural gas mixed with syngas obtained from gasification of sewage sludge at different proportions of 25%, 50% and 75%. The flue gas produced from CCGT is passed at different load conditions from 50% to 100% for CO_2 removal to PCCS using the solvent method. Two different aqueous solvents 30wt% MEA and a blend of 16wt% AMP – 14wt% PZ are used in PCCS. The extraction of steam from CCGT for amine regeneration has an impact on the power plant performance. Based on the power generation, DHN heat supply, emission parameters and the regeneration energy of solvents in PCCS, the CO_2-neutral fuels are identified.

2. Model and simulation description

The thermodynamic model of Ebsilon [23] for flows of pure water/steam and data of IPAWS-IF97 [24] were used. The Red-

lich–Kwong–Soave real gas formulation [25] and NIST [26] data for calculating MEA mixture properties were adopted. The equations of state, mass and energy balances were resolved iteratively, with a convergence criterion set to 10−9. This referred to the relative deviation between the second-last and the last iteration step for mass flow, pressure and enthalpy.

A model of CCGT operated with two Siemens SGT-800 gas turbines with a maximum power of 50.5 MW per turbine and a steam turbine with a maximum power of 65 MW is developed. The outlet gas from the gas turbine at 553°C is passed through the heat recovery steam generators (HRSGs) with high pressure (HP) and low pressure (LP) steam levels to produce steam for the steam turbine. An economizer is included at the last stage of HRSG for a district heating network (DHN) along with a heat exchanger, in which steam from the steam turbine is used as a hot stream to supply heat to the water. When using different fuels in the developed model of CCGT, the gas turbines increase the fuel mass flow to operate at full efficiency of 38.1%, which also depends upon the calorific value of the fuel. Gas fuels such as methane and N_2-rich natural gas are used in gas turbines. To measure the possibility of achieving a 'negative CO_2 emission', syngas is mixed with the fuel at different proportions as 25%, 50% and 75%. When operating CCGT with PCCS, CGGT is always kept in full load condition and the flue gas to PCCS is directed with various load conditions between 50% and 100%. When supplying steam to the DHN heat exchanger and PCCS for amine regeneration, the power generation in the steam cycle varies with changing the behaviour of CCGT.

PCCS uses an aqueous solution of 30wt% MEA and 16wt%+14wt% of AMP-PZ solvents and has a CO_2 capture efficiency of 90% and rich CO_2 loading of 0.5, 0.62 and 0.86 mol-CO_2/mol-amine, respectively. The absorber operates at 40°C, 1 bar and the stripper operates at 120°C, 2 bar, respectively. The model incorporates mass and energy balance equations to ensure accurate simulation of the entire process. These balances account for the flow rates, temperatures and pressures of all streams entering and exiting each component. The reaction mechanism between the amines (MEA, AMP-PZ) and CO_2 in flue gas is manually described within the absorber component, as CO_2 is selectively separated from the flue gas stream based on the capture efficiency. CO_2 is then mixed with the amine solution, resulting in the formation of rich amine flow at the bottom outlet of the absorber. A water wash system is added to the top of the absorber to minimize solvent emission by cooling the low CO_2 flue gas stream exiting the absorber, thereby condensing and capturing any solvent vapours before they are released into the atmosphere. The rich amine from the absorber is preheated before it enters the stripper. The rich amine solution is further heated in a reboiler using steam from CCGT. This heating process facilitates the separation of CO_2 from amine. When the amine flows back inside the stripper, CO_2 gets separated exiting the top of the stripper. The reaction mechanism in the stripper is described similarly to the absorber component, where CO_2 is separated using the separator component of the model according to the lean amine loading from the amine stream from the reboiler to the stripper after heating. The separated CO_2 is cooled and compressed up to 110 bar at the CO_2 compression system.

Based on the Gorzów CCGT power plant in Poland [27] and the theoretical analysis of PCCS using the solvent method for different flue gases, a model of CCGT integrated with PCCS as in Fig. 1 is developed.

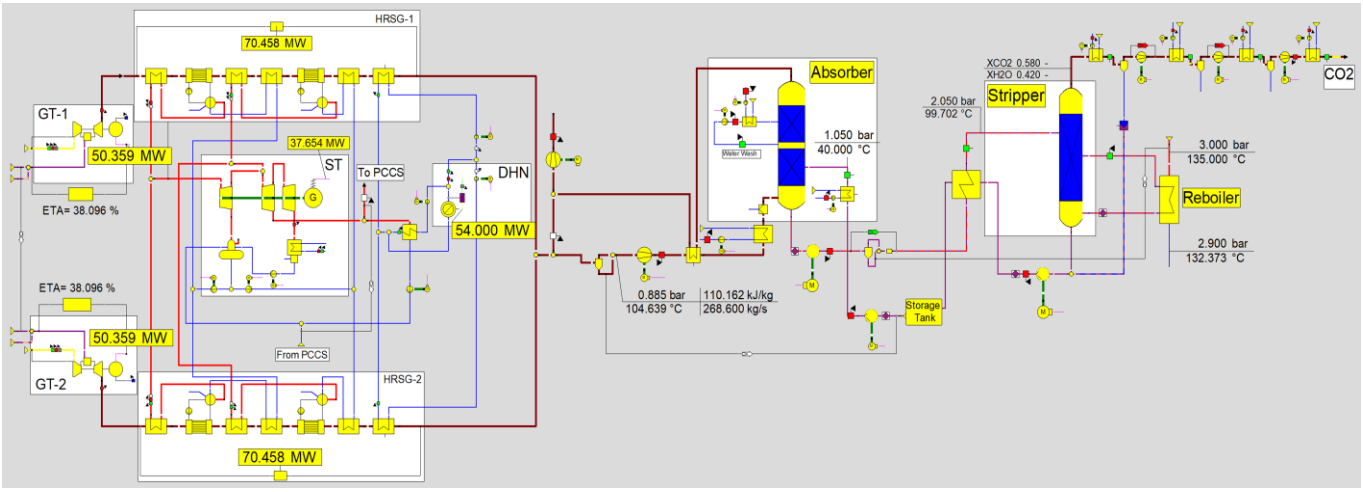

Fig. 1. Model of CCGT integrated with PCCS developed using Ebsilon® Professional 16.

Based on the rich CO_2 loading calculation and depending upon the CO_2 at the PCCS inlet, the required amount of lean solvent is given as input to the absorber model [28]. The model increases or decreases the flow of amine required for the capture to the absorber, considering the flow of CO_2 in the flue gas. Due to the absence of gas-to-liquid phase mass transfer and chemical reaction in the simulation, the internal reactions are manually described in the model using the study.

3. Results and discussion

3.1. Fuel composition and emission

The composition of the fuels and mixture of fuels used in the gas turbine for combustion such as methane with syngas and N_2-rich natural gas with syngas at different proportions changes with an increase in the proportion of syngas along with a change in the lower heating value (LHV) of the fuels. LHV of methane,

N_2-rich fuel and syngas are 50.5 MJ/kg, 18.63 MJ/kg and 17.08 MJ/kg, respectively. The presence of CO_2 content in syngas increases the CO_2 content in the other fuels when mixed. When mixing syngas with the other fuels, the lower heating value changes due to the increasing syngas content in the fuel, and the CO_2 content increases. The fuels and the mixture of fuels are given as an input to the gas turbine at 30 bar and 25°C. The fuels and mixture of fuels are used in the gas turbines of CCGT and CO_2 emissions are analyzed as in Fig. 2. Due to the CO_2 content in fuel, the combustion of the fuels results in an increase in CO_2 emission in flue gas with an increased syngas proportion. After various stages of HRSG, the flue gas at 0.885 bar and 104.6 °C is passed to PCCS for CO_2 removal process.

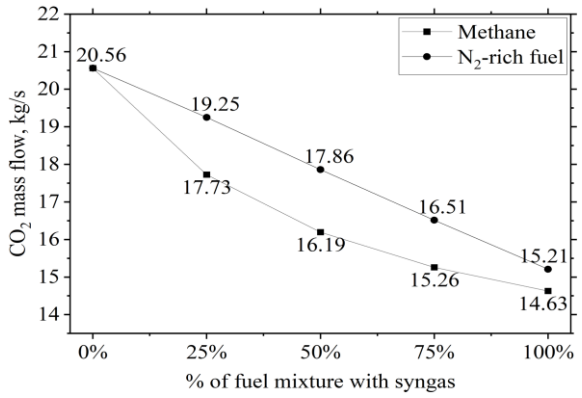

Fig. 2. CO_2 emission from fuels mixed with syngas at different proportions.

When the flue gas passes through PCCS at different load conditions, the flue gas diverted from PCCS is passed directly into the atmosphere. When passing flue gases to PCCS at different proportions from 50% to 100%, the CO_2 content at the inlet of PCCS gets reduced as in Fig. 3.

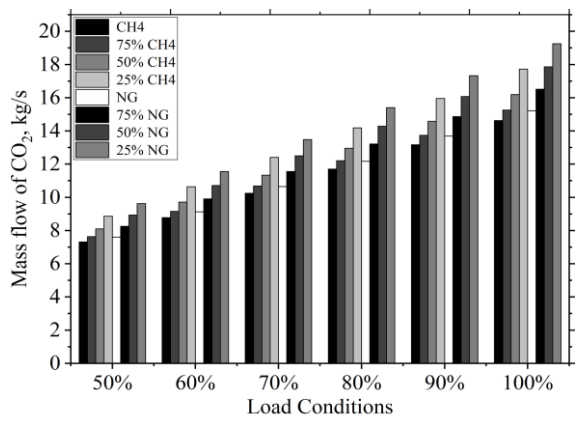

Fig. 3. CO_2 emission from different fuels at the inlet of PCCS increasing with the increase in flue gas load condition.

3.2. Performance of CCGT without PCCS

The change in content of the fuel when mixed with syngas does not have any adverse effects on the performance of CCGT without PCCS. This is because the gas turbine adjusts the mass flow rate of the fuel according to its LHV, ensuring consistent performance. With the maximum load of DHN heat supply of 54 MW, gas cycle power generation is 100.72 MW, and steam cycle power generation 37.65 MW. The performance metrics of CCGT without PCCS as detailed in Table 1 remain unchanged for using fuels and a mixture of fuels in the CCGT gas turbine.

Table 1. Performance of CCGT without PCCS operation.

Parameters	Unit	Value
Gross energy (power + heat)	MW	192.37
Net energy (power + heat)	MW	138.37
Net power	MW	128.43
Plant power consumption	MW	9.94
Gross energy efficiency	%	72.84
Net energy efficiency	%	52.4
Net power efficiency	%	48.63

Even after accounting for the power consumption of 9.94 MW by CCGT, the net power produced 128.43 MW is delivered to the grid. This demonstrates that the mixture of syngas does not impair the overall efficiency and effectiveness of the CCGT in generating electricity and supplying heat to DHN. The adaptability of the gas turbine to different fuel compositions ensures steady performance and reliable power output to the grid.

3.3. Performance of CCGT with PCCS

When operating CCGT integrated with PCCS using MEA, the Gross power production of the CCGT is maintained between 129 MW to 131 MW by adjusting the DHN heat supply. For the comparison purpose, during the PCCS operation with AMP-PZ amine, the same DHN heat supply given for PCCS using MEA is used to measure the Gross power production as shown in Fig. 4 and Fig. 5 for MEA and AMP-PZ solvents, respectively. Initially for flue gas to PCCS at full load condition, the heat supplied to DHN (Fig. 6) according to the availability of steam in the steam cycle. The reduced flue gas load conditions to PCCS reduce the steam requirement for amine regeneration, making more steam available for steam cycle power generation and increasing the DHN heat supply without much possible change in gross power. Considering the nominal load of DHN heat supply as 54 MW and depending upon the load condition and fuel used in CCGT, Fig. 7 shows the % of nominal power at different flue gas load conditions of PCCS depending on fuel mixture as net energy is maintained between 129 MW to 132 MW. Followed by the various operating procedures of CCGT integrated with PCCS operations, the change in gross energy efficiency of the power plant is noticed in Fig. 8. Since the net energy production is maintained between 130 MW to 132 MW by adjusting heat to DHN, the net energy efficiency in all the PCCS load conditions has very slight differences. Figure 9 shows the total power consumed by the equipment in CCGT and PCCS including the pumps, blowers, and CO_2 compression system.

Since the carbon capture efficiency of the solvents used in the PCCS is the same, PCCS captures 90% of CO_2 from flue gases. Considering the highest CO_2 capture from syngas of 18.62 kg/s, the nominal capture rate in percentage is given in Fig. 10. Due

to the change in the amine stream and gas stream with respect to the CO_2 content in the flue gas, the power consumption by PCCS varies. With the varying load conditions, the PCCS consumes 5.5% to 11.4% of the power from CCGT for its use. The lower the flue gas load operated, the lower the power consumed by PCCS.

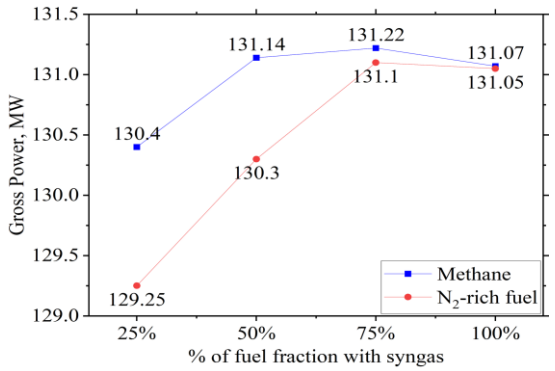

Fig. 4. Gross power generation of CCGT using fuel and fuel mixture with syngas and treating flue gas in PCCS at full load conditions using MEA.

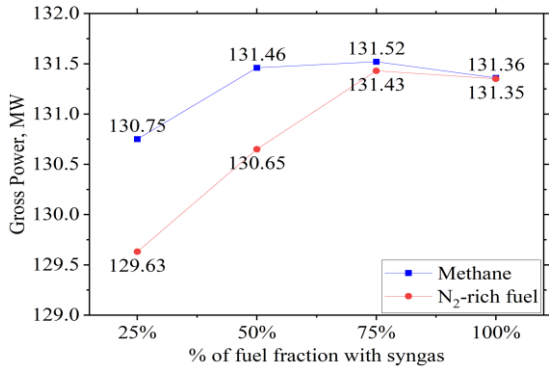

Fig. 5. Gross power generation of CCGT using fuel and fuel mixture with syngas and treating flue gas in PCCS at full load conditions using AMP-PZ.

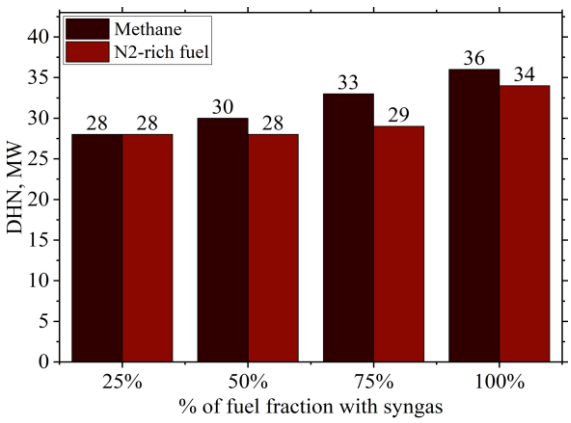

Fig. 6. Heat supplied to district heat network at full load condition of PCCS depending on fuel mixture as the net energy is maintained between 129 MW to 132 MW.

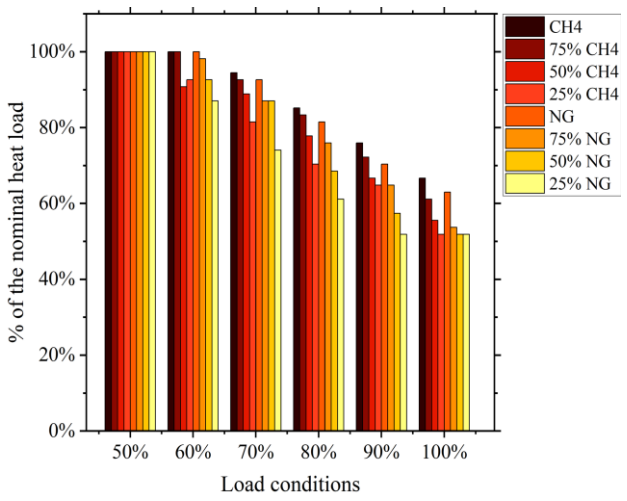

Fig. 7. Percentage of nominal heat load variation in heat supplied to district heat network at different flue gas load conditions of PCCS.

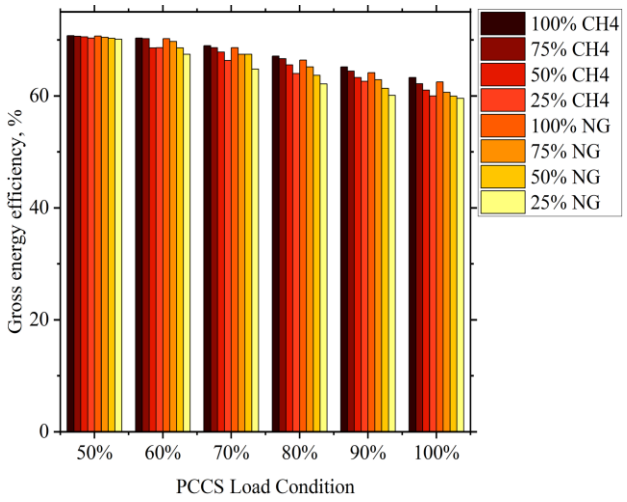

Fig. 8. Gross energy efficiency of CCGT using fuel mixture with syngas and treating flue gas in PCCS at variable load conditions.

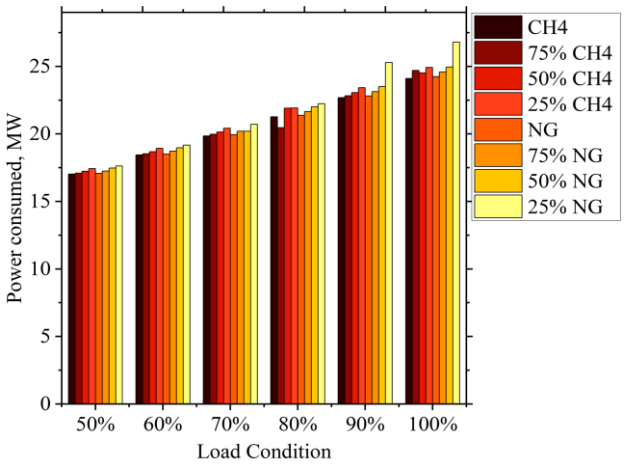

Fig. 9. Total power consumption of CCGT using different fuels and mixture of fuels with PCCS operated under different load conditions.

After the CO_2 capture process, only 10% of CO_2 is emitted into the atmosphere from PCCS operated at full load condition. When PCCS is operated at different load conditions, CO_2 in flue gas diverted from PCCS is directly passed into the atmosphere. Hence, reducing load conditions in PCCS increases the CO_2 emission into the atmosphere. The CO_2 emission is estimated by the procedure that when biogas produced from biomass is used as fuel and CCS is performed, the emission is considered as 'zero-emission'.

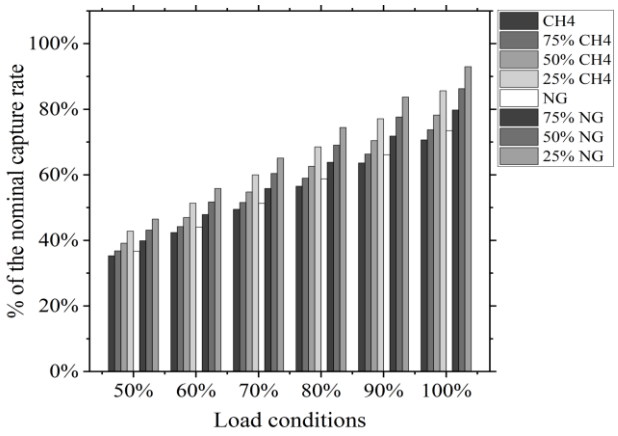

Fig. 10. Percentage of nominal CO_2 capture rate in PCCS at different load conditions from flue gases produced by different fuels.

When a syngas mixture with other fuels is used for combustion, the CO_2 emitted is estimated by the captured CO_2 from the share of syngas and the CO_2 emitted into the atmosphere according to the load changes in PCCS. When the flue gas load to PCCS is reduced, more amount of flue gas diverted from PCCS passes to the atmosphere and less amount of CO_2 from the share of syngas enters PCCS, making it less possible to achieve negative emission as in Fig. 11. The range of CO_2 emission after PCCS varies from 8.36 kg/s to –4.28 kg/s depending upon the fuel mixture and PCCS flue gas load conditions.

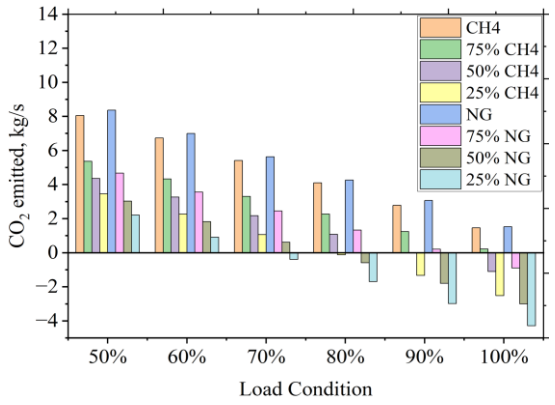

Fig. 11. CO_2 emitted into the atmosphere after flue gas from different fuel mixtures treated in PCCS at different load condition.

3.4. Analysis of PCCS using different solvents

The model regulates the flow of amines based on the proportion of CO_2 entering the PCCS at different load conditions and from flue gases produced by various fuels or mixtures of fuels, as illustrated in Fig. 12 and Fig. 13 for PCCS using MEA and a blend of AMP-PZ, respectively. The requirement of MEA and AMP-PZ changes according to the CO2 concentration in the flue gas and the rich loading of the amine used. Initially, the mass flow rate of lean amine necessary for capturing 14.63 kg/s of CO_2 produced by burning methane in a combined cycle gas turbine (CCGT) is calculated to be 136.68 kg/s for MEA and 136.73 kg/s for AMP-PZ.

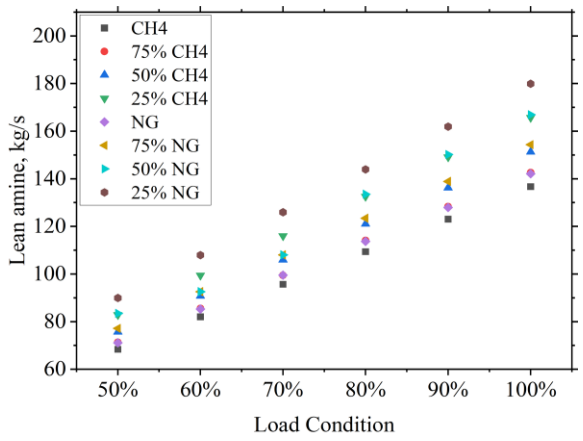

Fig. 12. Mass flow of lean MEA supplied to the absorber with PCCS operated under different load conditions to treat flue gases from different fuels and fuel mixtures.

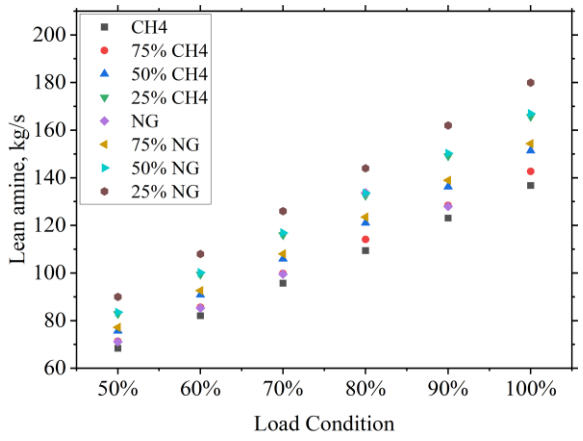

Fig. 13. Mass flow of lean AMP-PZ supplied to the absorber when PCCS operated under different load conditions to treat flue gases from different fuels and fuel mixtures.

The steam needed for the reboiler in PCCS is extracted from the LP turbine of CCGT at a temperature of 135°C and a pressure of 3 bar. Considering the reboiler duty of MEA and AMP-PZ, which is 3.8 MJ/kg-CO_2 and 3.7 MJ/kg-CO_2, respectively, the mass flow rate of steam required for processing 13.26 kg/s of captured CO_2 in rich amines is calculated to be 23.19 kg/s for MEA and 22.58 kg/s for AMP-PZ. The model adjusts these initial calculated values based on the CO_2 content in the rich amine. As the CO_2 content varies, the mass flow rate of steam extracted from CCGT for the reboiler is adjusted, as shown in Fig. 14 and Fig. 15 for PCCS utilizing MEA and AMP-PZ solvents.

The steam consumption by the reboiler for treating flue gases from a 25% N_2-rich natural gas and 75% syngas fuel mixture is higher compared to that of other fuels. The steam consumption varies from 31.38 kg/s to 15.69 kg/s for using MEA and 30.56 kg/s to 15.28 kg/s for AMP-PZ in operating PCCS at different load conditions. The minimum steam consumption for the reboiler among the fuels used is for methane, and varies from 23.85 kg/s to 11.92 kg/s for MEA and 23.22 kg/s to 11.61 kg/s for AMP-PZ depending upon the load conditions.

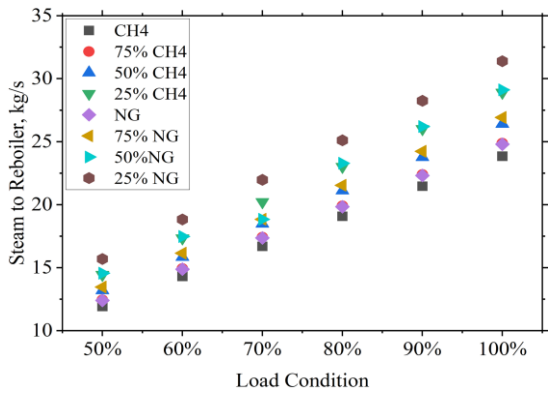

Fig. 14. Steam consumption by the reboiler of PCCS using MEA solvent for flue gases from different fuels and mixture of fuels.

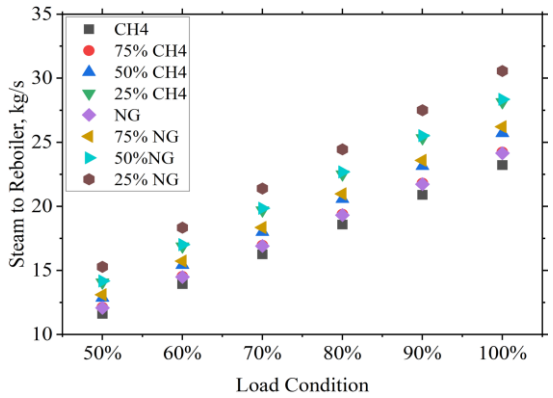

Fig. 15. Steam consumption by the reboiler of PCCS using AMP-PZ solvent for flue gases from different fuels and mixture of fuels.

3.5. Indicators of CO_2 emission level assessment

With the data obtained from CCGT and PCCS using different fuels, mixtures of fuels and different solvents, the CO_2 emission level assessment indicators are calculated using formulas given in [29]. Despite achieving a solvent CO_2 capture efficiency of 90%, due to the operational condition of PCCS, the CO_2 capture ratio fluctuates with the operational conditions of PCCS. Specifically, this ratio varies between 0.45 to 0.9, corresponding to 50% and 100% of PCCS load, respectively. Depending upon the load conditions, the capture ratio varies as the CO_2 capture is different from the CO_2 generated when changing the load conditions. The use of MEA and AMP-PZ in PCCS showed only minor differences in their impact on CCGT. Consequently, these differences did not significantly affect the specific emission and relative emissivity of CO_2.

Figures 16 and 17 illustrate the specific emission of CO_2 measured in g CO_2/kWh, for a methane mixture with syngas and N_2-rich fuel mixture with syngas, respectively. The relative emissivity of CO_2 in g/kWh is measured with the heat input from the fuel to CCGT of 264 088.22 kW as in Figs. 18 and 19. The heat input by the fuel is the same for all the fuels and fuel mixtures used in CCGT.

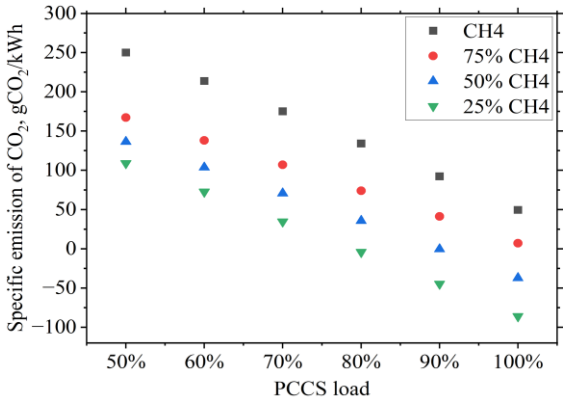

Fig. 16. Specific emission of CO_2 in g CO_2/kWh measured varying with PCCS load condition for the use of methane and its mixture with syngas in CCGT.

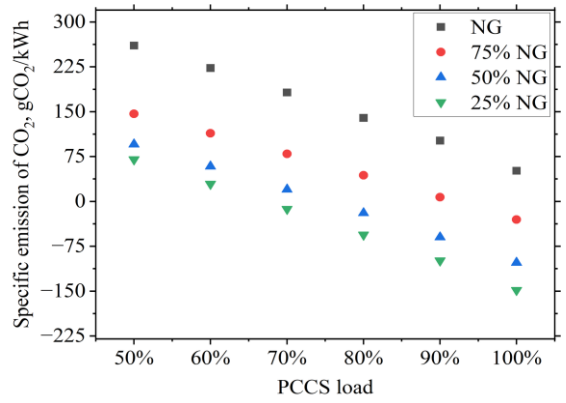

Fig. 17. Specific emission of CO_2 in g CO_2/kWh measured varying with PCCS load condition for the use of N_2-rich fuel and its mixture with syngas in CCGT.

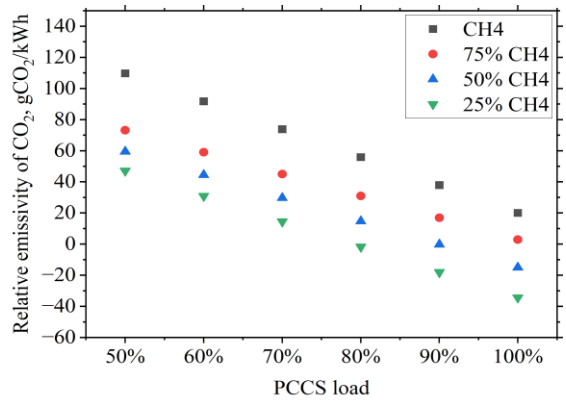

Fig. 18. Relative emissivity of CO_2 in g CO_2/kWh measured varying with PCCS load condition for the use of methane and its mixture with syngas in CCGT.

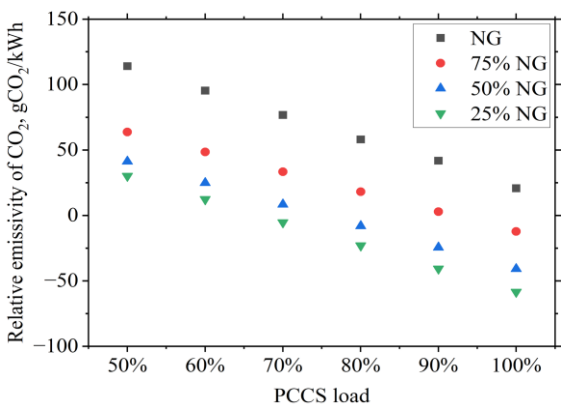

Fig. 19. Relative emissivity of CO_2 in g CO_2/kWh measured varying with PCCS load condition for the use of N_2-rich fuel and its mixture with syngas in CCGT.

When the PCCS process is not integrated into CCGT, the specific emission and relative emissivity measured from the power generation and CO_2 emission for various fuels are observed to be higher than the emission caused by CCGT as in Figs. 20 and 21 for the methane and N_2-rich fuel mixture with syngas, respectively.

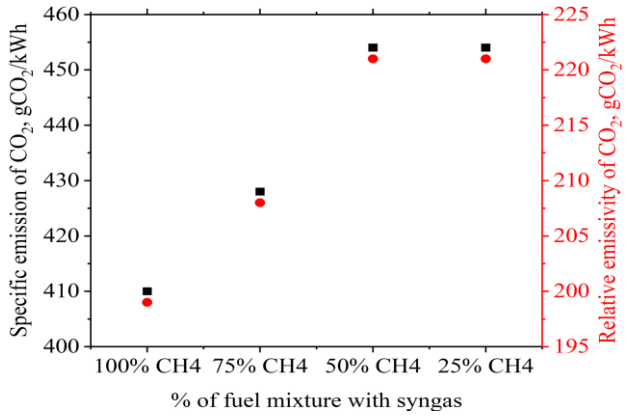

Fig. 20. Specific emission and relative emissivity of CO_2 in g CO_2/kWh measured for the use of methane and its mixture with syngas in CCGT without PCCS.

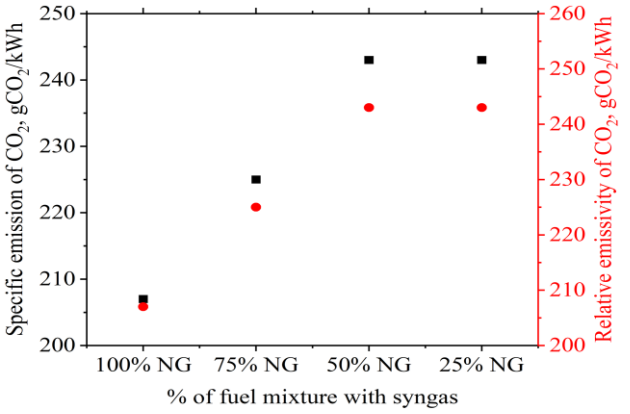

Fig. 21. Specific emission and relative emissivity of CO_2 in g CO_2/kWh measured for the use of N_2-ich fuel and its mixture with syngas in CCGT without PCCS.

4. Conclusions

The behaviour of CCGT integrated with PCCS hugely depends upon the type of fuel used in the gas turbine and the solvent used in PCCS. Since the steam required for the solvent regeneration is taken from the steam cycle of the power plant, it affects the overall efficiency and power generation. The modelling and simulation results obtained help to understand various thermodynamic properties of CCGT as well as PCCS. From the data, it is observed that when integrating CCGT with PCCS, the PCCS consumes 5.5% to 10.5% of power from the power plant for its use depending upon the load conditions and steam used for solvent regeneration. Considering the heat and power generation, and thermal efficiency of the power plant, the syngas mixture with both fuels at 50% helps achieve the possibility of zero or negative CO_2 emission without much disturbance in the heat and power generation process. Also, the load conditions of flue gas from a 50% syngas mixture with both fuels can be adjusted from 80% to 100% to PCCS to maintain a close-to-zero emission.

The increase of syngas in the mixture with methane and N_2-rich fuel increases the possibility of achieving 'negative emission' but on the other hand, the heat and power generation are reduced in the power plant, also it requires a huge resource of sewage sludge for the gasification process.

The use of AMP-PZ has very slight differences when compared to MEA in power consumption by PCCS, requirement of lean amine and heat supply to the reboiler. As referred to in [13], increasing the proportion of PZ in the solvent mixture can lower the regeneration rate, which will have a huge impact on the heat and power generation process of the power plant.

Acknowledgements

The research leading to these results has received funding from the Norway Grants 2014-2021 via the National Centre for Research and Development. Work has been prepared within the frame of the project: "Negative CO_2 emission gas power plant" – NOR/POLNORCCS/NEGATIVE-CO2-PP/0009/2019-00 co-financed by the programme "Applied research" under the Norwegian Financial Mechanisms 2014-2021 POLNOR CCS 2019 – "Development of CO_2 capture solutions integrated in power and industry processes".

References

[1] IEA (2023), Credible pathways to 1.5°C, *IEA, Paris*, License: CC BY 4.0. https://www.iea.org/reports/credible-pathways-to-150c. [accessed 17 Jan. 2024].

[2] de Coninck, H., Revi, A., Babiker, M., Bertoldi, P., Buckeridge, M., Cartwright, A., Dong, W., Ford, J., Fuss, S., Hourcade, J.C., Ley, D., Mechler, R., Newman, P., Revokatova, A., Schultz, S., Steg, L., & Sugiyam, T. (2018). Strengthening and Implementing the Global Response. In *Global Warming of 1.5ºC.* (pp. 313–444). Cambridge University Press. Cambridge USA doi: 10.1017/9781009157940.006

[3] IEA (2022), Bioenergy with Carbon Capture and Storage, *IEA, Paris*. https://www.iea.org/reports/bio-energy-with-carbon-capture-and-storage [accessed 17 Jan. 2024].

[4] Shahbaz, M., AlNouss, A., Ghiat, I., Mckay, G., Mackey, H., Elkhalifa, S., & Al-Ansari, T. (2021). A comprehensive review

of biomass based thermochemical conversion technologies integrated with CO_2 capture and utilisation within BECCS networks. *Resources, Conservation and Recycling*, 173. doi: 10.1016/j.resconrec.2021.105734

[5] Bui, M., Sunny, N., & Mac Dowell, N. (2023). The prospects of flexible natural gas-fired CCGT within a green taxonomy. *iScience*, 26. doi: 10.1016/j.isci.2023.107382

[6] Chyong, C.K., Reiner, D., M., Ly, R., & Fajardy, M. (2023). Economic modelling of flexible carbon capture and storage in a decarbonised electricity system. *Renewable and Sustainable Energy Reviews*, 188. doi: 10.1016/j.rser.2023.113864

[7] Kim, S., Ko, Y., Lee, G.J., Lee, J.W., Xu, R., Ahn, H., & Kang, Y.T. (2022). Sustainable energy harvesting from post-combustion CO_2 capture using amine-functionalized solvents. *Energy*, 267. doi:10.1016/j.energy.2022.126532

[8] Liu, F., Qi, Z., Fang, M., & Ding, H. (2023). Pilot test of water-lean solvent of 2-(ethylamino) ethanol, 1-methyl-2-pyrrolidinone, and water for post-combustion CO_2 capture. *Chemical Engineering Journal*, 459. doi: 10.1016/j.cej.2023. 141634

[9] Kindra, V.O., Milukov, I.A., Shevchenko, I.V., Shabalova, S.I., & Kovalev, D.S. (2023). Thermodynamic analysis of cycle arrangements of the coal-fired thermal power plants with carbon capture. *Archives of Thermodynamics*, 42(4), 103–121. doi: 10.24425/ather.2021. 139653

[10] Xu, C., Li, X., Liu, X., & Li., J. (2020). An integrated de-carbonization supercritical coal-fired power plant incorporating a supplementary steam turbine, process heat recovery and a modified boiler structure. *Applied Thermal Engineering*, 178. doi: 10.1016/j.applthermaleng.2020.115532

[11] Wu, Y., Dai, Y., Xie, W., Chen, H., & Zhu, Y. (2022). Performance analysis for post-combustion CO_2 capture in coal-fired power plants by integration with solar energy. *Energy*, 261. doi: 10.1016/j.energy.2022.125239

[12] Xiang, J., Wei, D., Mao, W., Liu, T., Luo, Q., Huang, Y., Liang Z., & Luo, X. (2024). Comprehensive kinetic study of carbon dioxide absorption in blended tertiary/secondary amine solutions: Experiments and simulations. *Separation and Purification Technology*, 330(part B). doi: 10.1016/j.seppur.2023.125310

[13] Ding, X., Chen, H., Li, J., & Zhou, T. (2023). Comparative techno-economic analysis of CO_2 capture processes using blended amines. *Carbon Capture Science and Technology*, 9. doi: 10.1016/j.ccst.2023.100136

[14] Ping, T., Dong, Y., & Shen., S. (2020). Energy-Efficient CO_2 Capture Using Nonaqueous Absorbents of Secondary Alkanolamines with a 2-Butoxyethanol Cosolvent. *ACS Sustainable Chemistry and Engineering*, 8(49), 18071–18082. doi:10.1021/acssuschemeng.0c06345

[15] Nakrak, S., Chalermsinsuwan, B., Tontiwachwuthikul, P., Gao, H., Liangz, Z., & Sema, T. (2023). Comparative mass transfer performance of CO_2 absorption using highly-concentrated AMP-PZ-MEA ternary amines solvent. *Energy Reports*, 9, 1–7. doi: 10.1016/j.egyr.2023.05.219

[16] Spietz, T., Dobras, S., Chwoła, T., Wilk, A., Krótki, A., & Więcław-Solny, L. (2020). Experimental results of amine emission from the CO_2 capture process using 2-amino-2-methyl-1-propanol (AMP) with piperazine (PZ). *International Journal of Greenhouse Gas Control*, 102. doi: 10.1016/j.ijggc.2020.103155

[17] Tramošljika, B., Blecich, P., Bonefačić, I., & Glažar, V. (2021). Advanced Ultra-Supercritical Coal-Fired Power Plant with Post-Combustion Carbon Capture: Analysis of Electricity Penalty and CO_2 Emission Reduction. *Sustainability*, 13. doi: 10.3390/ su13020801

[18] Madejski, P., & Żymełka, P. (2020). Calculation methods of steam boiler operation factors under varying operating conditions with the use of computational thermodynamic modeling. *Energy*, 197. doi: 10.1016/j.energy.2020.117221

[19] Başaran, T., Çetin, B., & Özdemir, M.R. (2022). Thermodynamic and mathematical analysis of geothermal power plants operating in different climatic conditions. *Case Studies in Thermal Engineering*, 30. doi: 10.1016/j.csite.2021.101727

[20] Thabit, Q., Nassour, A., & Nelles, M. (2022). Innovative hybrid waste to energy–parabolic trough plant for power generation and water desalination in the Middle East North Africa region: Jordan as a case study. *Energy Reports*, 8, 13150–13169. doi: 10.1016/j.egyr.2022.09.144

[21] Ziółkowski, P., Madejski, P., Amiri, M., Kuś, T., Stasiak, K., Subramanian, N., Pawlak-Kruczek, H., Badur, J., Niedźwiecki, Ł., & Mikielewicz, D. (2021). Thermodynamic Analysis of Negative CO_2 Emission Power Plant Using Aspen Plus, Aspen Hysys, and Ebsilon Software. *Energies (Basel)*, 14(19). doi: 10.3390/en14196304

[22] Madejski, P., & Żymełka, P. (2020). Introduction to computer simulation and calculations of energy systems using STEAG Ebsilon®Professional software. Kraków: AGH (in Polish).

[23] Steag Energy Services, *Ebsilon®Professional 15.00*. https://www.ebsilon.com/ [accessed 17 Jan. 2024].

[24] International association for the properties of water and steam, *IAPWS R7-97* (2012). www.iapws.org/relguide/IF97-Rev.html [accessed: 17 Jan. 2024].

[25] Soave, G. (1971). Equilibrium constants from a modified Redlich-Kwong equation of state. *Chemical Engineering Science.* 27(6), 1197–1203. doi: 10.1016/0009-2509(72)80096-4

[26] Linstrom, P.J., & Mallard, W.G. (2001). The NIST Chemistry WebBook: A Chemical Data Resource on the Internet. *Journal of Chemical and Engineering Data*, 46(5), 1059–1063, doi: 10.1021/je000236i

[27] Lisiecka, K. (2017). Gorzów CHP plant is full of good energy. PGE GiEK S.A. Gorzów CHP unit (in Polish)

[28] Subramanian, N., & Madejski, P. (2023). Analysis of CO_2 capture process from flue-gases in combined cycle gas turbine power plant using post-combustion capture technology. *Energy*, 282. doi: 10.1016/j.energy.2023.128311

[29] Madejski, P., Chmiel, K., Subramanian, N., Kuś, T. (2022). Methods and Techniques for CO_2 Capture: Review of Potential Solutions and Applications in Modern Energy Technologies. *Energies (Basel)*, 15, 887. doi: 10.3390/en15030887

Co-published by
Institute of Fluid-Flow Machinery
Polish Academy of Sciences
Committee on Thermodynamics and Combustion
Polish Academy of Sciences

http://www.imp.gda.pl/archives-of-thermodynamics/

Analysis of the accuracy of the inverse marching method used to determine thermal stresses in cylindrical pressure components

Magdalena Jaremkiewicz*

Cracow University of Technology, Faculty of Environmental and Energy Engineering, ul. Warszawska 24, Cracow 31-155, Poland
*Corresponding author email: magdalena.jaremkiewicz@pk.edu.pl

Received: 30.07.2024; accepted: 08.10.2024

Abstract

This paper analyses the inverse marching method used to determine the thermal stresses on the inner surface of a thick-walled cylindrical element not weakened by holes in the transient state. The heat conduction problem was considered one-dimensional, i.e. it was assumed that heat is transferred only in the radial direction. The method is based on measuring the temperature inside the pipeline wall at a single point and assuming that the pipeline is thermally insulated. The paper undertook an evaluation of the influence of the measuring point's distance from the inner surface, the number of control volumes into which the inverted area was divided and the length of the time step on the accuracy of the calculated temperature, heat transfer coefficient and thermal stresses on the inner surface of the pressure element. Verification was performed by comparing the calculation results obtained from the direct analytical method perturbed by random errors with those obtained from the numerical inverse step method.

Keywords: Thermal stresses; Inverse heat conduction problem; Finite volume method

Vol. 45(2024), No. 4, 95–105; doi: 10.24425/ather.2024.152000

Cite this manuscript as: Jaremkiewicz, M. (2024). Analysis of the accuracy of the inverse marching method used to determine thermal stresses in cylindrical pressure components. *Archives of Thermodynamics*, 45(4), 95–105.

1. Introduction

The problem of identifying thermal stresses is essential in many different industries, such as conventional, nuclear, and renewable power generation, the metallurgical industry, the semiconductor industry, the automotive and aerospace industries, and even medicine.

One of the most popular methods for determining thermal stresses, as described in publications in recent years, is the finite element method (FEM). For example, for a case from the metallurgical industry considered in [1], the authors of the paper used FEM in the Ansys software to analyse the thermal stresses of a ladle refractory layer on molten steel. This analysis allowed the authors to evaluate the effect of dilatations of different sizes on the reduction of thermal stresses. Also, it allowed the creation of temperature and stress characteristics under different operating conditions.

In the context of conventional power generation, the unpredictability of renewable energy production results in the requirement for frequent start-up and shut-down and load shifting of power units. This results in a reduced equipment lifetime due to thermo-mechanical fatigue and creep. Monitoring power plant operating conditions and residual life assessments to ensure safe operation also requires power plants that have exceeded their design life. For the reasons mentioned above, correctly identifying the thermal stresses of critical pressure components of power

Nomenclature

a, b, c – coefficients of a polynomial function
c – specific heat capacity, J/(kg K)
E – Young's modulus, MPa
Fo – Fourier number
h – heat transfer coefficient, W/(m^{2}K)
k – thermal conductivity coefficient, W/(m K)
$\mathbf{K}$ – thermal conductivity tensor
n_c – number of control volumes
N – temperature measuring point
p_n – overpressure of the fluid inside the cylindrical element, MPa
$\dot{q}_i$ – heat flux at the *i*-th node, W/m^2
$\dot{q}_v$ – energy generation rate per unit volume, W/m^3
$\dot{Q}_{i,j}$ – heat flow rate between the nodes *i* and *j*, W
r – radius, m
s – thickness, m
$s_{N,stresses}$ – mean squared error of thermal stresses, MPa
$s_{N,temp}$ – mean squared error of temperature, ºC or K
t – time, s
T – temperature, ºC or K
T_i – temperature at the *i*-th node, ºC or K
$\bar{T}$ – average temperature over wall thickness, ºC or K
v_T – rate of temperature change, K/s

Greek symbols

α – stress concentration factor
β – linear thermal expansion coefficient, 1/K
δ – distance from the internal surface to the measuring point, m
Δr – spatial step, m
Δt – time step, s
ΔV_i – volume of the *i*-th control cell, m^3
ε – tolerance, K
κ – thermal diffusivity coefficient, m^2/s
ν – Poisson's ratio
ϱ – density, kg/m^3
σ – circumferential stresses, MPa
ϕ – shape factor

Subscripts and Superscripts

al – allowable
f – fluid
in – inner
m – mean
out – outer
p – caused by pressure
P – on the edge of the hole at point P
T – thermal

Abbreviations and Acronyms

FEM – finite element method
FVM – finite volume method
DCS – distributed control systems

boilers is crucial. Knowledge of the thermal stresses is also necessary for determining the optimum temperature histories of the fluid during heating [2] and cooling [3] of pressure components when the rate of temperature change is determined from the condition of not exceeding the allowable stresses.

Recently, many articles have been devoted to determining thermal stresses in nuclear power plants, where the issue of safe operation of pressure equipment is critical. An example is the paper [4], which presents a simplified method for determining thermal stresses at the corners of pressure vessel nozzles of nuclear reactors. In order to eliminate the disadvantage of the popular FEM method, i.e. the high computational cost for three-dimensional elements, the thermal stresses are estimated based on temperature gradients. Temperature gradients are predicted in the cross-section at the corners of the nozzles based on the known geometry of the element and the way the temperature is distributed in the cylindrical element and semi-infinite plate (determined analytically). The authors of the paper [5] also addressed the study of thermal stresses at the corners of reactor nozzles. They presented simple equations for the prediction of the stress intensity factor, which was obtained from thermal loading analysis under cooling and heating conditions using the FEM. The FEM analyses were used in both cases only to validate the proposed approach.

Residual stresses arising in pressure components due to thermal shock are also investigated. An example of research on this topic is the paper [6], where the authors characterised the residual stresses in a steel pressure vessel of a nuclear reactor whose surface is plated with a nickel-based alloy. The study's authors also investigated the interaction between residual and thermal stresses during thermal shock.

A common area for conventional and nuclear power plants with a high need for thermal stress analysis are steam turbines. In [7], an algorithm for monitoring thermal stresses in rotors and bodies of shut-off and control valves of steam turbines is presented. The developed software allows the determination of stresses in critical turbine components based on measured data, and it will also enable the optimisation of the device start-up process. In [8], thermal stresses were analysed for the case of high-temperature steam inlet to steam turbines with a combined HP-IP cylinder and high- and medium-pressure rotors located in separate casings, operating with a double or single thermal bypass. On the other hand, in [9], acceptable parameter deviations were analysed to assess the quality of the start-up operation in terms of the thermal stress values of the critical elements of the power plant thermal scheme, i.e. the high-pressure turbine rotor and the high-pressure outlet header of the recovery boiler superheater. Calculations were performed using the Ansys software.

Determining thermal stresses in a thick-walled element without holes, in both quasi-stationary and transient states, requires knowledge only of the temperature distribution in the wall of the element. However, thick-walled elements often have holes, and a quasi-stationary state is difficult to achieve in practice. Given this, the thermal stresses can only be correctly calculated by knowing the stress concentration factor at the edge of the hole and, in turn, this without knowing the exact temperature of the fluid flowing through the element and the heat transfer coefficient at its internal surface.

In order to determine the heat transfer coefficient, exact transient temperature measurements are required due to the slight difference between the fluid temperature at high pressure and the internal surface temperature of the component. The heat

transfer coefficient has an essential influence on the optimum rate of change of the fluid temperature, which is determined by the condition of not exceeding the allowable thermal stresses on the inner surface of the pressure element [10]. Strain and stress analyses demonstrate that the influence of the time- and location-varying heat transfer coefficient compared to the fixed coefficient recommended by standards is a crucial factor in fatigue calculations. The importance of determining the actual heat transfer coefficient on the internal surface of pressure components based on numerical studies of steam boiler start-up and analysing deformations and stresses in the component is demonstrated in [11].

The highest thermal stresses occur on the inner surface of the pressure element, which is in direct contact with the high-pressure, high-temperature fluid. In order to determine the stresses on this surface, a temperature measurement is usually taken in practice at half the wall thickness s and a distance δ from the inner surface of the element of 6 to 10 mm [12]. This method in transient states is characterised by low accuracy. The stresses on the inner surface of the element determined in this way may differ by up to several tens per cent from the actual stresses, significantly when the steam temperature changes rapidly.

An attempt to develop a mathematical model using the finite difference method to determine the transient thermal stresses in a thick-walled pressure component was made in the article [13], among others. The developed model has been verified experimentally and compared to a model based on FEM. The model uses known temperatures of the surroundings, external surface and fluid inside the cylindrical element. The method considered is based on solving a direct problem.

Another approach to determining transient thermal stresses based on the temperature distribution inside the wall of a pressure element is to use methods based on solving the inverse heat conduction problem [14]. In the inverse heat conduction problem, the temperature at the edge of the element is determined based on temperature changes at selected points inside the analysed body. The determination of thermal stresses based on the measurement of the wall temperature of a thick-walled element with simple shapes near the inner surface is presented in the article [12]. The temperature measurement location divides the wall in the cross-section into direct and inverse areas, with the finite volume method (FVM) being used in the inverse area to determine the temperature distribution and heat flux. Knowing the heat flux and temperature at the internal surface and the temperature of the fluid washing over this surface allows the heat transfer coefficient to be determined. The technique of measuring the fluid temperature with new solid-sheathed thermometers using the inverse solution of the heat conduction problem is described in detail in [15]. In turn, papers [16,17] present a method for determining the three-dimensional temperature field in thick-walled elements based on temperature measurements at a series of points on the thermally insulated external surface. In [16], a flat element was analysed and in [17], a cylindrical one. In addition, a method for determining the heat transfer coefficient has been developed for the case of an element with complex shapes. This method is made possible by a 'measuring probe', by which the temperature is measured at 6 points near the inner surface of the component [18].

Inverse problems are characterised by a high sensitivity of the solution to input disturbances. To reduce their influence on the solution of the inverse problem, one of the regularisation methods, such as the Tikhonov method, discrete Fourier transform, energy regularisation method and others, can be used. Examples of research on Tikhonov regularisation and its modifications are presented in papers [19,20]. The paper [19] investigated the solution of an inverse problem illustrating the wall of a heating device, in which the regularisation parameter was chosen based on Morozov's principle. The paper [20], on the other hand, analysed the effect of the regularisation of the inverse problem on the stability of the calculated boundary conditions during the cooling of a sample in a thermo-chemical treatment furnace. A slightly different approach is proposed in [21], for the analysis of a ceramic-coated metal element (e.g. a turbine blade), where the temperature of the metal is controlled by solving the Cauchy problem for the heat conduction equation for a two-layer element. A regularisation method based on the energy balance formulation for the ceramic layer was used here, and the spectral radius of the equation matrix was used to analyse the stability of this computational model.

Another effective and simple solution that eliminates the influence of random errors on computational results in solving inverse problems and that can be applied in real time is smoothing measurement data by approximating the measured values with digital filters [22]. The smoothing of N-measured data in the form $f_s = f(s)$ is implemented by the least squares method using orthogonal Gram polynomials. An example of the use of digital filters for smoothing measured data is presented in the paper [15], which demonstrates the application of a new measurement technique to determine the transient temperature of superheated steam flowing out of the second superheater stage in a power boiler, based on the solution of an inverse problem.

This paper undertakes the determination of thermal stresses in thick-walled pressure elements using an inverse method based on FVM. The case of a transient and a cylindrical element not weakened by holes is considered. While the method is well-known and, for a cylindrical element, has been described in works [12,14], this article focuses on determining the best conditions for its application. The analysis of the accuracy of the inverse method consisted of selecting the most favourable division into control volumes depending on the distance of the temperature measuring point from the inner surface and the length of the time step. This was possible based on the computational tests performed, which made it possible to compare the determined temperature distribution and thermal stresses on the inner surface determined by the analytical method and the direct solution of the heat conduction problem with the results obtained from the inverse solution. The choice of the inverse method to determine the temperature distribution for thermal stresses using the control volume method to carry out accuracy analyses and conditions of applicability was due to a number of its advantages. Its use is simple in practice and does not require temperature measurements to be taken on the internal surface of pressure parts, especially as this would be very difficult in the

case of pressurised components. Furthermore, the method can be used for online stress monitoring. As described in this chapter, FEM for determining stresses is very popular. However, it requires the solution of a direct problem and, in the case of components with complex shapes, consumes a large amount of computational cost.

2. Determination of thermal stresses on the inner surface of pressure elements

Thick-walled components are used in power plant units due to the high pressure of the working fluid. The highest thermal stresses in thick-walled pressure components usually occur when there is a change in temperature during operation with a simultaneous uneven temperature distribution at the cross-section of the component walls, i.e. during start-up and shut-down. As a result of the standardisation of calculation procedures for boilers, the German regulation TRD 301 [23] and the European standard EN 12952-3 [24] were developed. These are the essential documents describing procedures for determining thermal stresses in pressure components. However, they are limited only to determining thermal stresses under the assumption of a quasi-stationary temperature field in the element wall, which is difficult to achieve in practice. Also, the assumption of a parabolic temperature distribution in the wall does not give satisfactory results for rapid and sudden temperature changes over time.

Simplified methods for determining transient thermal stresses on the surfaces of pressure parts washed with a working fluid based on the provisions mentioned above are described below. The main advantage of the methods discussed in this section is the simple formulae for determining the stresses on the inner surface of the element. Despite their approximate nature, they are used by boiler manufacturers. However, due to the development of DCS (distributed control systems) in power plants, there is now the possibility of using more complex formulas to calculate stresses online.

2.1. Thermal stresses in the plate assuming a quasi-stationary temperature field

Cylindrical pressure elements with a large diameter can be treated as flat elements. It is then assumed that the element can expand freely but not bend. An example of a cylindrical element that can be treated as a flat wall is the wall of a steam drum.

The basis for determining allowable heating and cooling rates of thick-walled cylindrical pressure elements is the condition of not exceeding the circumferential allowable stresses on the inner surface of the pressure element at the hole's edge at point P. The circumferential stresses at point P are the sum of the stresses due to pressure and thermal stresses:

$$\sigma_{\mathrm{P}} = \alpha_p \sigma_p + \alpha_T \sigma_T, \tag{1}$$

where α_p is the pressure stress concentration factor at point P lying on the edge of the hole (Fig. 1), and α_T is the thermal stress concentration factor at point P.

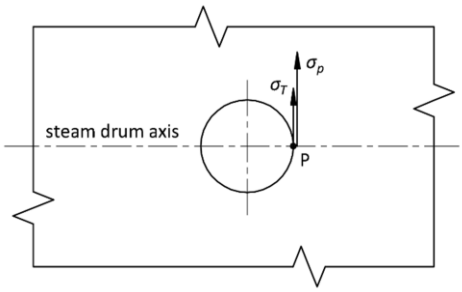

Fig. 1. Section of the wall of a steam drum with a hole.

The symbol σ_p denotes the circumferential stresses from the pressure in a cylindrical element not reinforced by holes, which are expressed by the relation:

$$\sigma_p = \frac{p_n r_m}{s}, \tag{2}$$

where p_n is the overpressure of the medium inside the element, s is the thickness of the element, and $r_m = (r_{in} + r_{out})/2$ is the mean radius of the cylindrical pressure element determined as the arithmetic mean of the inner radius r_{in} and the outer radius r_{out}.

The highest thermal stress in a cylindrical element occurs at the surface in contact with the fluid and is determined by the formula:

$$\sigma_T = \frac{E\beta}{1-\nu}\left(\bar{T} - T|_{r=r_{in}}\right), \tag{3}$$

where E is Young's modulus, β is the linear thermal expansion coefficient, ν is Poisson's ratio, T is the temperature, and $\bar{T}$ denotes the average temperature over wall thickness.

After determining the average wall temperature of the component $\bar{T}$ from the solution of the heat conduction equation, a general relationship is obtained:

$$\sigma_T = \phi \frac{E\beta}{1-\nu}\frac{v_T s^2}{\kappa}, \tag{4}$$

where the symbol ϕ is usually referred to as the shape factor, κ is the thermal diffusivity coefficient, and v_T is the rate of temperature change.

For the inner surface of a cylinder, the ends of which are free to extend, the shape factor for a cylindrical element [24,25] is expressed by the formula:

$$\phi = \frac{1}{8}\frac{(k^2-1)(3k^2-1)-4k^4 \ln k}{(k^2-1)(k-1)^2}, \tag{5}$$

where $k = r_{out}/r_{in}$.

Stress concentration factors can be determined based on EN 12952-3 [24] or can be determined by FEM in the case of vessel-to-spigot connections with more complex geometries. The allowable heating or cooling rates of a pressure element are determined by the condition:

$$\sigma_{\mathrm{P}} \leq \sigma_{al}, \tag{6}$$

where σ_{al} is the allowable stress determined from the Wöhler fatigue diagram in the standard [24].

Equation (6) gives satisfactory results when determining the permissible heating rates from the cold state when the pressure element is heated at a constant rate over a long time. With a time-varying rate of change in the fluid temperature, Eq. (1) is not very accurate, particularly with rapid temperature changes. Sudden changes in the fluid temperature occur, for example, when the evaporator is flooded with hot water at the beginning of a start-up, when cooling water is injected in superheated steam temperature controllers or when the boiler pressure is suddenly reduced due to damage to the steam evaporator tubes or superheaters.

It should be added that Eq. (1) remains valid at the pressure elements for time-varying heating or cooling rates.

This paper focuses only on the determination of thermal stresses.

2.2. Transient thermal stresses in a cylindrical element

A more general method for determining the thermal stresses in cylindrical elements without holes is the one using Eq. (3), where the average temperature $\bar{T}$ over the wall thickness is determined from the formula:

$$\bar{T} = \frac{2}{r_{out}^2 - r_{in}^2} \int_{r_{in}}^{r_{out}} rT(r,t)dr, \tag{7}$$

where r denotes the radius.

The spatiotemporal distribution of the temperature in a cylindrical wall can be obtained from the analytical solution of the heat conduction equation or by using numerical methods, for example FEM or FVM. When numerical methods are used, the wall temperature is determined only at discrete points, while the average temperature is determined using the chosen approximation method [26,27]. By calculating the integral in Eq. (7) using, for example, the trapezoidal rule for discrete points, the following expression is obtained:

$$\bar{T} = \frac{1}{r_{out}^2 - r_{in}^2} \sum_{i=2}^{N} (r_{i-1}T_{i-1} + r_i T_i)\Delta r, \tag{8}$$

where r_i is the radius at which the *i*-th node is located, Δr is the spatial step, and T_i is the temperature at the *i*-th node.

In some cases, the number of points at which the wall temperature is determined may be too small, and the accuracy of the average temperature determined from Eq. (8) may be insufficient. Another method of determining the average wall temperature can then be used, in which temperatures determined, for example, from the inverse solution of the heat conduction equation are interpolated by a second-degree polynomial [26,27]:

$$T(r,t) = a(t) + b(t)r + c(t)r^2, \tag{9}$$

where $a(t)$, $b(t)$ and $c(t)$ denote time-dependent coefficients.

For example, if the temperature is measured at two points in the wall, i.e. T_1 at the inner radius r_{in} and T_2 at half the wall thickness at radius r_m, and the pipeline is insulated at the outer surface, after determining the coefficients $a(t)$, $b(t)$ and $c(t)$ for such boundary conditions and substituting the resulting temperature distribution $T(r,t)$ expressed by Eq. (9) into Eq. (7), the following relation is obtained:

$$\bar{T} = T_1 + \frac{2}{9}\left(4 + \frac{\Delta r}{r_{in}+\Delta r}\right)(T_2 - T_1). \tag{10}$$

Both Eqs. (8) and (10) make it possible to calculate the approximate value of the average temperature over the thickness of the cylindrical wall.

3. Determination of the one-dimensional temperature distribution in a cylindrical element using the inverse marching method

Suppose the temperature measurement in the thick-walled component can only be realised at the external surface and/or inside the pipe wall. In that case, the transient temperature field in the inverse region can be determined from the solution of the inverse heat conduction problem.

The general form of the heat conduction equation for stationary solids that can be treated as incompressible is presented as follows [28]:

$$c(T)\rho(T)\frac{\partial T}{\partial t} = \nabla(\mathbf{K}\nabla T) + \dot{q}_v, \tag{11}$$

where c is the specific heat capacity, ρ is the density, **K** is the thermal conductivity tensor, and $\dot{q}_v$ is the energy generation rate per unit volume.

In [28], FVM was used to solve the inverse problem: the heat conduction equation and known boundary conditions. FVM, also known as the control volume method, is versatile and efficient for solving heat conduction problems. Assuming that the temperature field is two-dimensional and the physical properties: specific heat capacity *c*, density *ρ*, thermal conductivity coefficient *k* and energy generation rate per unit volume $\dot{q}_v$ are temperature dependent, the heat conduction equation can be transformed to the form:

$$\Delta V_i c(T_i)\rho(T_i)\frac{\partial T_i}{\partial t} = \sum_{j=1}^{n_c} \dot{Q}_{i,j} + \Delta V_i \dot{q}_v(T_i), \tag{12}$$

where $\dot{Q}_{i,j}$ is the heat flux rate transferred from node *j* inside the neighbouring cell to node i, and ΔV_i is the volume of the i-th control cell. Node i is located inside the analysed area and heat transfer occurs in n_c control volumes adjacent to the analysed control area.

In this paper, the inverse heat conduction problem will be solved for the case of a cylindrical wall when heat is transferred only in the radial direction.

The proposed inverse method is stable and has high accuracy if the condition is met [29]:

$$\Delta \mathrm{Fo} \geq 0.05. \tag{13}$$

Furthermore, due to the method's sensitivity to random errors in the temperature measurement $T(t)$, to at least partially eliminate their influence on the calculation results, the temperature waveform is proposed to be smoothed using a 9-point digi-

tal filter [22]. Filtering also makes it possible to accurately determine the values of the derivatives of the temperature function $T(t)$ from measured data perturbed by random errors.

3.1. One-dimensional transient temperature field in elements with simple shapes

In the measurement method, the temperature, heat transfer coefficient and thermal stresses on the inner surface of a thick-walled cylindrical element are determined by measuring the temperature inside the wall at a single point. For this purpose, the temperature distribution in the area $r_{in} \le r \le r_{out}$ and the heat flux density on the pipe's inner surface are investigated. The temperature measurement is taken at node *N* inside the pipe wall, which has been thermally insulated (Fig. 2). The pipeline cross-section is divided into a direct and an inverse region, where the boundary between the two is at radius r_N.

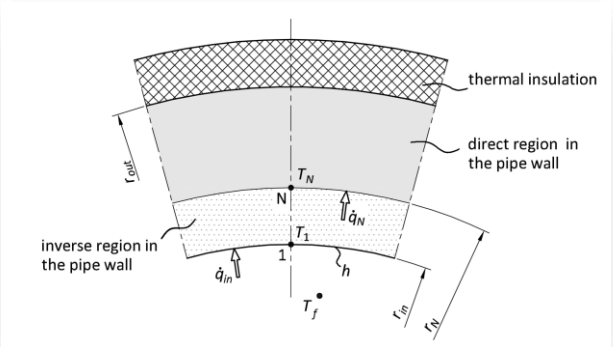

Fig. 2. Pipe wall cross-section with control volumes.

Heat transfer through the cylindrical wall is assumed to take place only in the radial direction r. In this case, the heat conduction equation in the cylindrical coordinate system takes the form [29,30]:

$$c(T)\rho(T)\frac{\partial T}{\partial t} = \frac{1}{r}\frac{\partial}{\partial r}\left[k(T)r\frac{\partial T}{\partial r}\right]. \tag{14}$$

The heat conduction equation is solved first for the direct area for the boundary conditions:

$$T|_{r=r_N} = T_N, \tag{15}$$

$$k(T)\frac{\partial T}{\partial r}\Big|_{r=r_{out}} = 0, \tag{16}$$

where T_N is the temperature measured at node *N* located inside the pipeline wall (Fig. 2). In this way, the temperature distribution in the area $r_N \le r \le r_{out}$ and the heat flux $\dot{q}_N$ at node *N* are determined. The solution assumes that the values of the physical properties of the pipe material: c, ρ, k are variable and temperature dependent.

Equation (14) is then solved for the inverse region $r_{in} \le r \le r_N$ using the boundary conditions:

$$T|_{r=r_N} = T_N, \tag{17}$$

$$k(T)\frac{\partial T}{\partial r}\Big|_{r=r_N} = \dot{q}_N. \tag{18}$$

The inverse problem described by Eqs. (14) and (16)–(18) was solved using FVM (Eq. (12)) and approximating the derivatives of the temperature function by differential quotients:

$$\frac{\partial T}{\partial r}\Big|_{r_{i+1}} = \frac{T_{i+1}-T_i}{\Delta r}, \quad \frac{\partial T}{\partial r}\Big|_{r_i} = \frac{T_i-T_{i-1}}{\Delta r}. \tag{19}$$

An illustration of the division of the inverse area into control volumes is shown in Fig. 3. As for the direct area, this solution assumes that the values of the physical properties of the pipe material c, ρ, k are temperature-dependent. FVM allows the temperature distribution in the area $r_{in} \le r \le r_N$ to be determined. Some examples of the division of the inverse area into different numbers of control volumes are shown in Fig. 3.

The energy balance equation for the control volume with node *N* has the form:

$$\pi\left[{r_N}^2 - \left(r_N - \frac{\Delta r}{2}\right)^2\right]c(T_N)\rho(T_N)\frac{dT_N}{dt} =$$
$$= 2\pi\left(r_N - \frac{\Delta r}{2}\right)\frac{k(T_{N-1})+k(T_N)}{2}\frac{T_{N-1}-T_N}{\Delta r} + 2\pi r_N\dot{q}_N, \tag{20}$$

from which the temperature T_{N-1} can be determined:

$$T_{N-1} = \frac{(\Delta r)^2\left(r_N-\frac{\Delta r}{4}\right)}{r_N-\frac{\Delta r}{2}}\frac{c(T_N)\rho(T_N)}{k(T_{N-1})+k(T_N)}\frac{dT_N}{dt} +$$
$$-\frac{2r_N\Delta r}{r_N-\frac{\Delta r}{2}}\frac{\dot{q}_N}{k(T_{N-1})+k(T_N)} + T_N. \tag{21}$$

The energy balance equation for a full-dimensional control volume (with thickness Δr) for nodes 2 to $(N-1)$ is shown in the following equation:

$$\pi\left[\left(r_{in}+(2i-1)\frac{\Delta r}{2}\right)^2 - \left(r_{in}+(2i-3)\frac{\Delta r}{2}\right)^2\right]\times$$
$$c(T_i)\rho(T_i)\frac{dT_i}{dt} = 2\pi\left(r_{in}+(2i-3)\frac{\Delta r}{2}\right)\frac{k(T_{i-1})+k(T_i)}{2}\frac{T_{i-1}-T_i}{\Delta r} +$$
$$+2\pi\left(r_{in}+(2i-1)\frac{\Delta r}{2}\right)\frac{k(T_i)+k(T_{i+1})}{2}\frac{T_{i+1}-T_i}{\Delta r},$$
$$i = 2,\dots,N-1, \tag{22}$$

from which the temperature T_{i-1} can be determined:

$$T_{i-1} = 2(\Delta r)^2\frac{2r_{in}+(2i-2)\Delta r}{2r_{in}+(2i-3)\Delta r}\frac{c(T_i)\rho(T_i)}{k(T_{i-1})+k(T_i)}\frac{dT_i}{dt} +$$
$$-\frac{2r_{in}+(2i-1)\Delta r}{2r_{in}+(2i-3)\Delta r}\frac{k(T_i)+k(T_{i+1})}{k(T_i)+k(T_{i-1})}(T_{i+1}-T_i) + T_i. \tag{23}$$

Since for individual temperatures T_{i-1} (for $i = 2,\dots,N$) the values of $k(T_{i-1})$ are not known (the equation is non-linear), the sought temperature T_{i-1} is obtained after *n* iterations. In the first iteration $(n=0)$ for individual nodes, it is assumed that $k\left(T_{i-1}^{(0)}\right) = k(T_i)$.

The iteration process continues until a condition is met [29]:

$$\left|T_{i-1}^{(n+1)} - T_{i-1}^{(n)}\right| \le \varepsilon, \tag{24}$$

where the tolerance $\varepsilon \approx 0.000\,01$ K. If the values of the physical properties are constant, iterations are not required.

FVM also allows the heat flux $\dot{q}_{in}$ at the inner surface of the pipeline to be determined from the energy balance for node 1:

$$\pi\left[\left(r_{in}+\frac{\Delta r}{2}\right)^2-r_{in}^2\right]c(T_1)\rho(T_1)\frac{dT_1}{dt}=$$
$$=2\pi r_{in}\dot{q}_{in}+2\pi\left(r_{in}+\frac{\Delta r}{2}\right)\frac{k(T_2)+k(T_1)}{2}\frac{T_2-T_1}{\Delta r}, \quad (25)$$

from which it can be determined:

$$\dot{q}_{in}=\frac{\left(r_{in}+\frac{\Delta r}{2}\right)^2-r_{in}^2}{2r_{in}}c(T_1)\rho(T_1)\frac{dT_1}{dt}+$$
$$-\frac{k(T_2)+k(T_1)}{2}\frac{r_{in}+\frac{\Delta r}{2}}{r_{in}\Delta r}(T_2-T_1). \quad (26)$$

The application of the described method in the inverse region consists in determining the temperatures at successive nodes ($(N-1)$, $(N-2)$,..., 2 and 1) marching towards the inner surface of the pipeline. Based on the measured temperature $T_N(t)$ inside the pipeline wall at node N, the temperature of node $(N-1)$ is determined from Eq. (21). If the solution of the direct problem allows this and the temperature at node $(N+1)$ is calculated, the temperature at node $(N-1)$ can be determined from Eq. (23). By substituting the calculated temperature $T_{N-1}(t)$ into Eq. (23), the temperature $T_{N-2}(t)$ at node $(N-2)$ is determined. The procedure is repeated using Eq. (23) until the temperature $T_1(t)$ at node 1 is determined. Knowing the temperatures $T_1(t)$ and $T_2(t)$ from Eq. (26) the heat flux $\dot{q}_{in}(t)$ on the inner surface of the pipe can be determined.

In order to determine the heat transfer coefficient at the internal surface of the pipe h, it is necessary to know the temperature of the fluid T_f flowing through the pipe. The boundary condition should then be used:

$$\dot{q}|_{r=r_{in}}=h\left(T_f-T|_{r=r_{in}}\right), \quad (27)$$

where

$$T|_{r=r_{in}}=T_1,\ \dot{q}|_{r=r_{in}}=\dot{q}_{in}. \quad (28)$$

A transformation of Eq. (27) gives:

$$h=\frac{\dot{q}_{in}}{T_f-T_1}. \quad (29)$$

After determining the temperature distribution at the cross-section of the cylindrical element at time t, the temperature distribution at time $t+\Delta t$ is calculated.

4. Computational validation of the inverse method

The calculations were carried out for a header with an external diameter of 355 mm and a wall thickness of 50 mm. The pipe material is P91 steel. The temperature-dependent physical properties of the steel were assumed for the calculations:

$$k(T)=-0.003\times10^{-10}T^5+4.741\times10^{-10}T^4+$$
$$-2.874\times10^{-7}T^3+6.438\times10^{-5}T^2+$$
$$-4.177\times10^{-4}T+28.676, \quad (30)$$

$$c(T)=1.41\times10^{-6}T^3-6.43\times10^{-4}T^2+$$
$$+4.88\times10^{-1}T+439.80. \quad (31)$$

The approximation of the physical properties was made using data from [28], the coefficient of determination of the two functions obtained being $r^2\cong1$. The value of the density of P91 steel was assumed to be constant, equal to $\varrho=7750$ kg/m^3, as it changes very little in the temperature range for which the calculations were carried out.

Firstly, the temperature distribution in the pipeline wall was determined using a direct, analytical method, with the assumption that the temperature of the fluid increases stepwise from 20°C to 100°C with a heat transfer coefficient at the inner surface of the pipeline of $h=1\,000$ W/(m^{2}K). The transient temperature waveforms were determined at 51 evenly spaced nodes over the wall thickness, where the first node is on the internal surface, and the last node is on the external surface, assuming ideal heat insulation on the external surface of the pipeline ($\dot{q}=0$). In addition, the heat flux and thermal stresses on the inner surface of the pipeline without holes were determined. The temperature waveforms from the selected nodes were then perturbed with random errors and were used as 'measured data' for the calculations performed using the inverse marching method.

Then, the temperature, heat flux and thermal stress on the inner surface were reconstructed using an inverse marching method based on a temperature measurement inside the pipeline wall disturbed by random errors.

In the proposed inverse marching method to monitor thermal stresses in simple shaped elements based on the measurement of the wall temperature at a single point, the sequence of operations is as follows. For a given time, the temperature distribution in the direct area is determined from the temperature measurement at node N and for the insulated outer surface, including the temperature at node $(N+1)$ located at a distance Δr from N. Then, based on the temperature waveforms at nodes N and $(N+1)$, the temperatures in the inverse region at nodes $(N-1)$, $(N-2)$,..., 1 are determined with a spatial step Δr, as well as the thermal stress and heat flux at node 1 (on the internal surface).

In the research presented in this paper, the main objective is to evaluate the influence of the number of nodes in the inverse region, the distance of node N from the inner surface and the size of the time step on the accuracy of the performed calculations using the proposed inverse method. Therefore, in the calculations made with the inverse method, the above-described sequence of operations was shortened and the 'measured data' generated by the analytical direct method at nodes N and $(N+1)$ were used immediately.

Cases where the node is located at distances δ of 6, 12 and 18 mm were analysed. In addition, the inverse area was divided into 2, 3 and 4 control volumes in each case. Calculations were performed for time steps Δt with values of 1, 2, 3, 4, 5 and 6 s.

The division of the inverse region in the cross-section of the cylindrical element into finite volumes is shown in Fig 3.

For each case, the mean squared errors of the calculated values of temperature and thermal stresses were determined relative to those determined from the solution of the direct problem. The results of the calculations are shown in Table 1. For each time step, the smallest mean squared error values for a given distance δ from the internal surface are highlighted in green in Table 1.

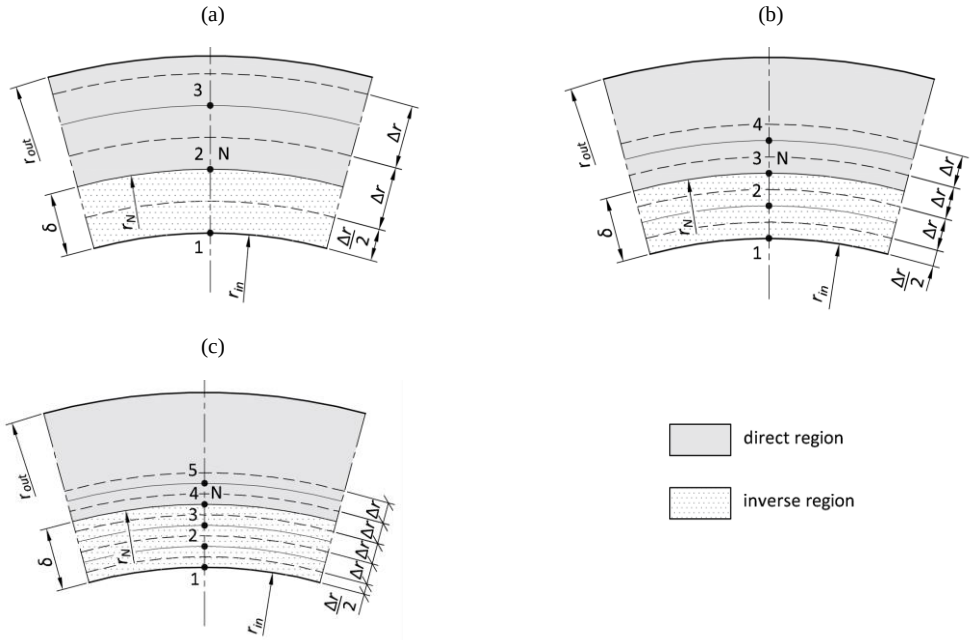

Fig. 3. Division of the inverse area in the cross-section of a cylindrical element into: (a) two control volumes, (c) three control volumes, (c) four control volumes; *N* - position of the wall temperature measurement point.

Table 1. Summary of mean square error values for the determined temperature and thermal stress depending on the value of the time step Δt, the number of control volumes and the distance from the inner surface δ.

Number of control volumes	Time step Δt, s	Distances of the measuring point from the inner surface δ					
		6 mm		12 mm		18 mm	
		$s_{N,temp}$, K	$s_{N,stresses}$, MPa	$s_{N,temp}$, K	$s_{N,stresses}$, MPa	$s_{N,temp}$, K	$s_{N,stresses}$, MPa
2	1	**0.289**	**0.871**	0.804	2.327	1.777	4.895
3		0.344	1.040	0.761	2.271	2.632	7.744
4		0.456	1.376	0.743	2.212	2.309	6.937
2	2	0.310	0.938	0.427	1.240	0.965	2.702
3		0.373	1.131	0.469	1.373	0.887	2.567
4		0.459	1.390	0.541	1.577	0.834	2.424
2	3	0.378	1.144	**0.411**	**1.197**	0.740	2.116
3		0.417	1.268	0.502	1.472	0.660	1.898
4		0.509	1.542	0.585	1.705	0.708	2.025
2	4	0.435	1.318	0.508	1.473	0.628	1.824
3		0.477	1.448	0.594	1.743	0.670	1.922
4		0.567	1.720	0.664	1.939	0.735	2.090
2	5	0.483	1.463	0.615	1.783	**0.597**	**1.760**
3		0.522	1.584	0.671	1.972	0.719	2.064
4		0.597	1.809	0.716	2.097	0.777	2.216
2	6	0.519	1.571	0.715	2.071	0.623	1.825
3		0.543	1.651	0.731	2.154	0.776	2.236
4		0.613	1.860	0.756	2.227	0.823	2.362

The best results were obtained for the position of the temperature measuring point at a distance of 6 mm from the inner surface, for which the smallest errors correspond to a time step Δt of 1 s and a division into 2 control volumes. For this case, the mean-square error of the temperature $s_{N,temp}$ determined by the inverse marching method is only 0.289 K and the error in determining the thermal stress $s_{N,stresses}$ is 0.871 MPa. For a measuring point distance δ of 12 mm from the inner surface, the smallest errors are obtained for a time step Δt of 2 s and division into 2 control volumes, and for a distance δ of 18 mm – for a time step Δt of 5 s and division also into 2 control volumes. It is not a rule that, for a given time step, a division into two control volumes is the most favourable, especially for smaller time step values, but in fact, the most favourable choice of time step length corresponds to a division into the minimum number of control volumes.

It should also be noted that very large mean squared errors were obtained for δ = 18 mm and a time step Δt of 1 s. These results should not be taken into account because, according to the condition described in Eq. (13), the minimum time step for this distance is 2 s.

The temperature and thermal stress curves calculated by the direct and inverse method on the surface of the analysed thick-walled cylindrical element for several selected cases summari-

sed in Table 1 are shown in Figs. 4 – 9. In the figures, two cases each for distance δ with, respectively, the smallest and largest mean square error of the determined temperature and thermal stresses using the inverse method are selected.

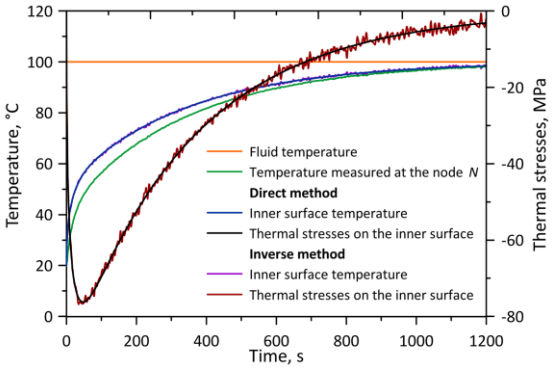

Fig. 4. Results of calculations of temperature and thermal stresses on the internal surface of a cylindrical element for measuring point N at a distance of $\delta = 6$ mm using the direct and inverse method for $\Delta t = 1$ s and division of the inverse area into 2 control volumes.

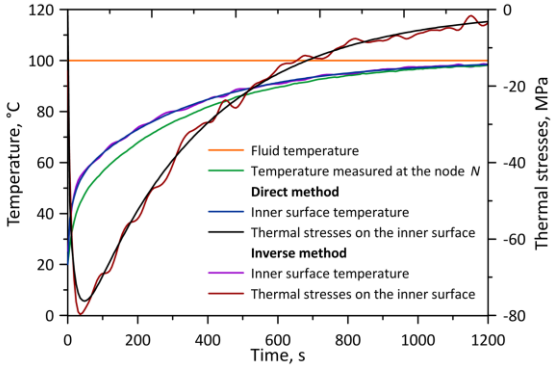

Fig. 5. Results of calculations of temperature and thermal stresses on the internal surface of a cylindrical element for measuring point N at a distance of $\delta = 6$ mm using the direct and inverse method for $\Delta t = 6$ s and division of the inverse area into 4 control volumes.

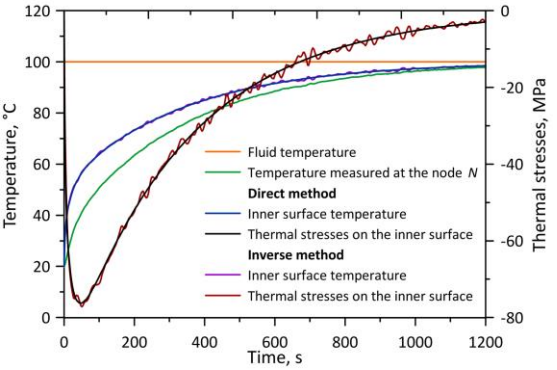

Fig. 6. Results of calculations of temperature and thermal stresses on the internal surface of a cylindrical element for measuring point N at a distance of $\delta = 12$ mm using the direct and inverse method for $\Delta t = 3$ s and division of the inverse area into 2 control volumes.

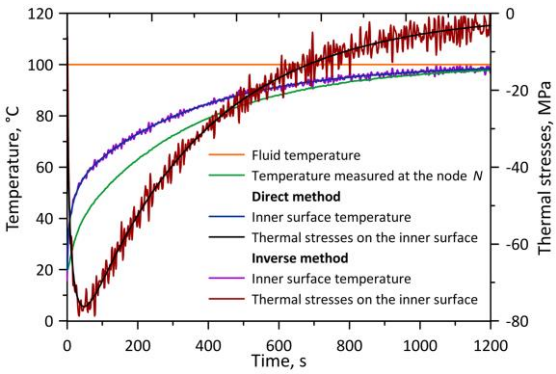

Fig. 7. Results of calculations of temperature and thermal stresses on the internal surface of a cylindrical element for measuring point N at a distance of $\delta = 12$ mm using the direct and inverse method for $\Delta t = 1$ s and division of the inverse area into 2 control volumes.

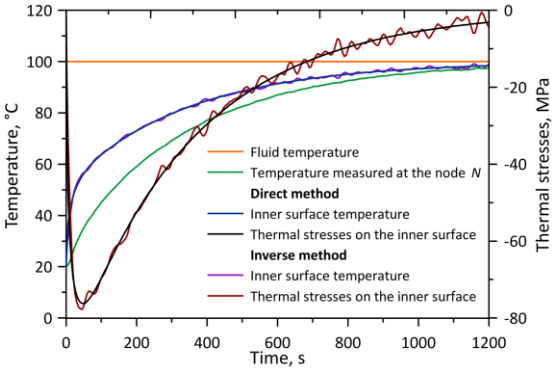

Fig. 8. Results of calculations of temperature and thermal stresses on the internal surface of a cylindrical element for measuring point N at a distance of $\delta = 18$ mm using the direct and inverse method for $\Delta t = 5$ s and division of the inverse area into 2 control volumes.

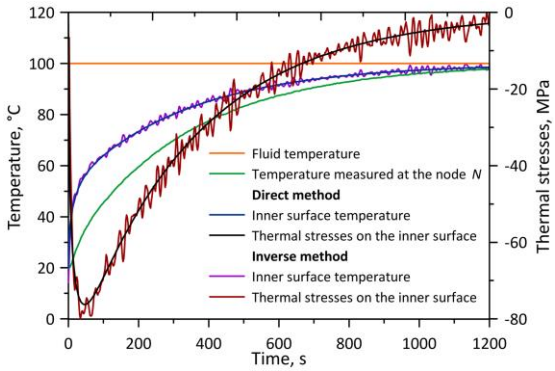

Fig. 9. Results of calculations of temperature and thermal stresses on the internal surface of a cylindrical element for measuring point N at a distance of $\delta = 18$ mm using the direct and inverse method for $\Delta t = 2$ s and division of the inverse area into 2 control volumes.

6. Conclusions

Based on analyses of the accuracy of the inverse marching method used to determine thermal stresses in cylindrical pres-

sure elements without holes, the following conclusions can be drawn:

- the best choice of time step length and number of control volumes/nodes depends on the location of the measurement point. It is advisable to select the location of the measuring point by making test calculations and checking which time step and number of nodes will give the results with the lowest errors. The results of the test calculations confirm what could be expected, i.e. the closer the measuring point is to the inner surface, the more accurate the results. If the position of the measuring point is imposed in advance, it is worth carrying out test calculations to determine the optimum number of nodes in the inverted area and the length of the time step;
- the mean squared errors for temperature measurements are less than 1 K (for those selected as most favourable for a given distance from the inner surface δ);
- the mean squared errors of the thermal stresses for the most favourable configurations of the number of control volumes and time step length for a given distance δ range from 0.871 MPa to 2.424 MPa, corresponding to temperature determination errors of 0.289 K to 0.834 K. The maximum thermal stress during pipeline heating is approximately 76 MPa. This shows how important it is to determine the exact temperature distribution in the pipeline wall and to choose the best possible conditions (time step, distance δ and number of nodes) for making the calculations using the presented inverse method;
- in addition to the calculations described, the heat transfer coefficient h on the internal surface of the pipeline was determined. However, the mean square errors of the heat transfer coefficient determination are substantial. The slightest error was obtained for the case when the time step is $\Delta t = 3$ s, the inverse area is divided into 4 control volumes, and the measuring point is located at a distance δ of 6 mm and is 215.6 W/(m^{2}K) with a reference value h of 1 000 W/(m^{2}K). This leads to the conclusion that the heat transfer coefficient should be determined either from a correlation for the Nusselt number or by another method, such as that described in [30].

Acknowledgements

This work was partially funded by the National Science Centre in Poland within the framework of research project no. 2021/43/B/ST8/01170.

References

[1] Fang, L., Su, F., Kang Z., & Zhu, H. (2024). Finite element (FE) analysis of thermal stress in production process of multi-layer lining ladle. *Case Studies in Thermal Engineering*, 57, 104307. doi: 10.1016/j.csite.2024.104307

[2] Taler, D., Dzierwa, P., Kaczmarski, K., & Taler, J. (2022). Increase the flexibility of steam boilers by optimisation of critical pressure component heating. *Energy*, 250, 1–18. doi: 10.1016/j.energy.2022.123855

[3] Taler, D., Kaczmarski, K., Dzierwa, P., Taler, J., & Trojan, M. (2024). Optimisation of the cooling of pressurised thick-walled components operating with fluid at saturation temperature. *Energy*, 290, 1–15. https://doi.org/10.1016/j.energy.2023.129975

[4] Oh, Ch., Lee,S., Jhung, M. J., & Huh N.-S. (2022). Analytical approach to estimate the thermal stress distribution of reactor pressure vessel nozzle corners with a constant cooldown rate. *International Journal of Pressure Vessels and Piping*, 197, 104608. doi: 10.1016/j.ijpvp.2022.104608

[5] Jeong, S.-H., Chung, K.-S., Ma, W.J., Yang, J.S., Choi, J.B., & Kim, M. K. (2022). Thermal stress intensity factor solutions for reactor pressure vessel nozzles. *Nuclear Engineering and Technology*, 54, 2188–2197. doi: 10.1016/j.net.2022.01.006

[6] Olivera, S. J., Mostafavia, M., Hosseinzadehb, F., & Paviera, M. J. (2019). Redistribution of residual stress by thermal shock in reactor pressure vessel steel clad with nickel alloy. *International Journal of Pressure Vessels and Piping*, 169, 37–47. doi: 10.1016/j.ijpvp.2018.11.007

[7] Radin, Y.A., Kontorovich, T.S., & Golov, P.V. (2020). Monitoring The Thermal Stress State In Steam Turbines. *Power Technology and Engineering*, 53(6), 719–723. doi: 10.1007/s10749-020-01146-6

[8] Radin, Y.A., & Kontorovich, T.S. (2021). Influence Of The Arrangement Of The Highand Intermediate-Pressure Cylinders Of Steam Turbines With Different Bypass Circuits On Their Thermal Stress State During Start-Ups And Shutdowns. *Power Technology and Engineering*, 54(5), 720–725. doi: 10.1007/ s10749-020-01276-x

[9] Radin, Y.A., & Kontorovich, T.S. (2024). Influence Of Parameter Deviations Vis-À-Vis Assignment Schedule On Thermally Stressed State Of Main Thermal Power Plant Equipment. *Power Technology and Engineering*, 57(6), 918–921. doi: 10.1007/s10749-024-01758-2

[10] Taler, J., Taler, D., Kaczmarski, K., Dzierwa, P., Trojan, M., & Jaremkiewicz, M. (2018). Allowable Rates of Fluid Temperature Variations and Thermal Stress Monitoring in Pressure Elements of Supercritical Boilers. *Heat Transfer Engineering*, 40(17–18), 1430–1441. doi: 10.1080/01457632.2018.1474584

[11] Wacławiak, K., & Okrajni, J. (2019). Transient heat transfer as a leading factor in fatigue of thick-walled elements at power plants. *Archives of Thermodynamics*, 40(3), 43–55. doi: 10.24425/ather.2019.129549

[12] Taler, J., Dzierwa, P., Jaremkiewicz, M., Taler, D., Kaczmarski, K., & Trojan, M. (2018). Thermal stress monitoring in thick-walled pressure components based on the solutions of the inverse heat conduction problems. *Journal of Thermal Stresses*, 41(10−12), 1501–1524. doi: 10.1080/01495739.2018.1520621

[13] Teixeira Júnior, M., Zilio, G., Mortean, M.V.V., de Paiva, K.V., & Oliveira, J.L.G. (2023). Experimental and numerical analysis of transient thermal stresses on thick-walled cylinder. *International Journal of Pressure Vessels and Piping*, 202, 104884. doi: 10.1016/j.ijpvp.2023.104884

[14] Taler, J., & Duda, P. (2000). Experimental verification of space marching methods for solving inverse heat conduction problems. *Heat and Mass Transfer*, 36, 325–331. doi: 10.1007/s002310000082

[15] Jaremkiewicz, M., Dzierwa, P., Taler, D., & Taler, J. (2019). Monitoring of transient thermal stresses in pressure components of steam boilers using an innovative technique for measuring the fluid temperature. *Energy*, 175, 139–150. doi: 10.1016/j.energy.2019.03.049

[16] Jaremkiewicz, M., Taler, D., Dzierwa, P., & Taler, J. (2019). Determination of transient fluid temperature and thermal stresses in pressure thick-walled elements using a new design thermometer. *Energies*, 12, 1–21. doi: 10.3390/en12020222

[17] Taler, J., Dzierwa, P., Jaremkiewicz, M., Taler, D., Kaczmarski, K., Trojan, M., Węglowski, B., & Sobota, T. (2019). Monitoring of transient 3D temperature distribution and thermal stress in pressure elements based on the wall temperature measurement. *Journal of Thermal Stresses*, 42, 698–724. doi: 10.1080/01495739.2019.1587328

[18] Taler, J., Dzierwa, P., Jaremkiewicz, M., Taler, D., Kaczmarski, K., Trojan, M., & Sobota, T. (2019). Thermal stress monitoring in thick walled pressure components of steam boilers. *Energy*, 175, 645–666. doi: 10.1016/j.energy.2019.03.087

[19] Joachimiak, M., Joachimiak, D., & Ciałkowski, M. (2022). Investigation on Thermal Loads in Steady-State Conditions with the Use of the Solution to the Inverse Problem. *Heat Transfer Engineering*, 44(11–12), 963–969. doi: 10.1080/01457632.2022.2113451

[20] Joachimiak, M., & Joachimiak, D. (2024). Stabilization of boundary conditions obtained from the solution of the inverse problem during the cooling process in a furnace for thermochemical treatment. *International Journal of Heat and Mass Transfer*, 224, 125274. doi: 10.1016/j.ijheatmasstransfer.2024.125274

[21] Ciałkowski, M., Joachimiak, M., Mierzwiczak, M., Frąckowiak, A., Olejnik, A., & Kozakiewicz, A. (2023). The analysis of the stability of the Cauchy problem in the cylindrical double-layer area. *Archives of Thermodynamics*, 44(4), 563–579. doi: 10.24425/ather.2023.149735

[22] Taler, J. (1995). *Theory and practice of identifying heat transfer processes*, Zakład Narodowy im. Ossolińskich (in Polish).

[23] TRD 301 (2001). *Zylinderschalen unter innerem Überdruck. Technische Regeln für Dampfkessel (TRD)*, Heymanns Beuth Köln-Berlin.

[24] European Standard EN 12952-3 (2001). *Water-tube boilers and auxiliary installations. Part 3: design and calculation for pressure parts*. European Committee for Standardization.

[25] Taler, J., Dzierwa, P., & Taler, D. (2011). Optimisation of heating and cooling of thick-walled boiler components. In *Thermal and flow processes in large power boilers, Modelling and monitoring* (pp. 584–625). Wydawnictwo Naukowe PWN (in Polish).

[26] Taler, J., & Zima, W. (1999). Solution of inverse heat conduction problems using control volume approach. *International Journal of Heat and Mass Transfer*, 42, 1123–1140. doi: 10.1016/S0017-9310(98)00280-4

[27] Taler, J., Zima, W., & Jaremkiewicz, M. (2016). Simple method for monitoring transient thermal stresses in pipelines. *Journal of Thermal Stresses*, 39, 386–397. doi: 10.1080/01495739.2016.1152109

[28] Taler, J., & Duda, P. (2006). *Solving Direct and Inverse Heat Conduction Problems*, Springer.

[29] Taler, J.(1999). A new space marching method for solving inverse heat conduction problems. *Forschung im Ingenieurwesen*, 64, 296–306. doi: 10.1007/PL00010844

[30] Jaremkiewicz, M., & Taler, J. (2018). Measurement of Transient Fluid Temperature in a Pipeline. *Heat Transfer Engineering*, 39(13–14), 1227–1234. doi: 10.1080/01457632.2017.1363631

Co-published by
Institute of Fluid-Flow Machinery
Polish Academy of Sciences
Committee on Thermodynamics and Combustion
Polish Academy of Sciences

http://www.imp.gda.pl/archives-of-thermodynamics/

ARCHIVES OF THERMODYNAMICS

Sizing large-scale industrial heat pump for heat recovery from treated municipal sewage in coal-fired district heating system

Jacek Kalina*

Silesian University of Technology, Konarskiego 22, Gliwice 44-100, Poland
*Corresponding author email: jacek.kalina@polsl.pl

Received: 21.02.2024; revised: 11.07.2024; accepted: 09.09.2024

Abstract

Electrification of district heating and deep integration of sectors of national economies are fundamental elements of the future smart energy systems. This paper discusses the problem of optimal sizing of large-scale high-temperature heat pumps using treated sewage water as a heat source in a coal-fired district heating system. The study presents an approach to modelling of heat pump system that enables techno-economic analysis for investment decision making. Such analysis is enabled by a black-box-type identification model of the selected industrial heat pump. The model was developed based on the data generated by physical modelling of the heat pump using Ebsilon Professional software. In addition, it is proposed that the heat pump system is integrated with a dedicated photovoltaic power plant. The case study takes into consideration site-specific technical, economic, ecological, and legal constraints, weather conditions, hydraulic performance of the heating network, and variability of loads within the sewage and the district heating systems. The results revealed that the proposed modelling approach is effective regarding multiple simulations and system optimisation. In addition, it was found that large-scale heat pump projects can be technically feasible and profitable if the heat pump is appropriately sized and operated. In the given case, the optimum size of the heat pump for a city of around 180 000 inhabitants is around 12 MW under maximum winter load.

Keywords: District heating; Heat pumps; Sewage treatment plants; Sector integration; Renewable energy

Vol. 45(2024), No. 4, 107–124; doi: 10.24425/ather.2024.152001

Cite this manuscript as: Kalina, J. (2024). Sizing large-scale industrial heat pump for heat recovery from treated municipal sewage in coal-fired district heating system. *Archives of Thermodynamics*, 45(4), 107–124.

1. Introduction

The accelerating global climate change and the growing problem of the availability of primary energy resources have resulted in an unprecedented change in approach to energy supply planning and energy system development. According to major organisations [1–3], the ongoing energy transition is nowadays driven by digitalisation, decarbonisation, decentralisation, and disruption-as-usual. Renewable energy, energy efficiency, integration of sectors, and circular economy, as well as electrification of transport and district heating and cooling are key pillars of the future energy systems. According to IRENA's report [3], to limit the rise in global temperature to well below 2°C above pre-industrial levels, the annual energy-related CO_2 emissions should decline by 2050 by 70% below today's level. To achieve this, electricity should progressively become the central energy carrier. Its share in global final consumption should gradually increase to almost 50% by 2050, and 86% of electricity

Nomenclature

c – specific heat capacity, kJ/(kg K)
C – cost, EUR
CAPEX– capital expenditures, EUR
COP – coefficient of performance
DPB – discounted payback period, year
G – sewage load, m^3/day
h – specific enthalpy, kJ/kg
IRR – internal rate of return
L – residual value, EUR
$\dot{m}$ – mass flow rate, kg/s
N – economic lifetime, year
NPV – net present value, EUR
NPVR– net present value ratio
OC – sum of operational costs, EUR
p – pressure, kPa
P – electric power, kW
$\dot{Q}$ – heat flux, W
r – discounted cash flow rate
s – specific entropy, kJ/(kg K)
sc – specific energy cost, EUR/GJ
SPB – simple payback period, year
T – temperature, K
Tx – income tax, EUR
t – time, year

Greek symbols

Δ – difference
ε – pressure ratio
η – efficiency

Subscripts and Superscripts

aux – auxiliary equipment
av – average
B – boiler
CP – central heating plant
CHP – combined heat and power (cogeneration) unit
CSTP– central sewage treatment plant
d – daily
des – at design conditions
dhw – district heating network water
el – electricity, electrical
env – environmental
f – fuel
grid – power grid
HP – heat pump
i – isentropic
in – inlet conditions
lift – heat pump temperature lift
m – mechanical, materials
max – maximum
out – outlet conditions
sw – treated wastewater
s – after isentropic process
wf – working fluid
ref – reference value
t – time step

Abbreviations and Acronyms

CSTP– central sewage treatment plant
ETS – emissions trading system
HP – heat pump
M – electric motor
PV – photovoltaic

generation should be renewable, and 60% should come from solar and wind. The report also shows that by 2050 around 334 million heat pumps should be installed globally.

Regarding the energy supply and use patterns, energy harvesting, use of distributed resources, and distributed generation are envisioned as future backbones of the European energy system. Key topics of discussions that nowadays take place globally are related to the so-called smart energy systems [4], which among other components are considerably based on 4th generation district heating, electrification, electrofuels, and energy efficiency.

In the district heating sector, a faster rollout of energy transition must take place to meet energy and climate policy. Although the European Union (EU) strategy for making heating and cooling more efficient and sustainable was announced in 2016 [5], in some European regions little has been done in this area. On average, in the EU only about 25% of district heat is currently produced from renewable sources [6]. In countries like Poland, still, around 85% of primary energy input to district heating systems comes from fossil fuels, mainly coal, and diversification of primary energy sources used for heat production is progressing very slowly [7]. In addition to this, in cities, high-temperature district heating grids prevail. Overall, according to International Energy Agency (IEA) [6], decarbonisation potential of district heating is largely untapped, and decarbonisation efforts were not enough to curb associated emissions.

According to the *Project of strategy for district heating till 2030 with a perspective till 2040* [8], there is a political commitment to reorganisation, reconfiguration, and decarbonisation of the entire district heating sector in Poland. According to the policy targets, the share of renewable energy sources should increase from the current level of 9.5% to 28.4% in 2030, and 85% of district heating systems meet the Energy Efficiency Directive (EED) (EU/2023/1791) definition of an effective system. Regarding specific technologies, the strategy, among other ventures, recommends solar systems, geothermal plants, cogeneration plants fired with biogas and hydrogen, heat pumps driven by electricity from renewable sources, as well as lowering district heating network temperatures. The decomposition of district heating systems and the introduction of new tools to integrate distributed sources are also indicated in the document.

In the market, considerable activities focused on energy transition have been recently triggered by many district heating companies across the country. In many cases, investors take into consideration that future district heating infrastructures should be designed for the future system, and as recommended by Lund et al. [9,10] should enable the integration of district heating with

the electricity sector. In this context, in the wide range of different projects in Poland, large-scale industrial heat pumps recovering heat from municipal sewages are frequently taken into consideration. The first project of this kind was carried out in 2020 by Veolia in Szlachęcin near Poznań [11]. In that project, the lower heat source for the heat pumps is treated wastewater being disposed to the Warta River. The minimum temperature of the sewage water in winter is 8°C and the flow is within the range of 50 m^3/h to 350 m^3/h. The water is directed to a 300 m^3 concrete tank and then pumped to the cascaded heat pump system of 1641 kW heating capacity, which delivers district heating water at 65°C.

Another example is the 12.5 MW heat pump ongoing project triggered by Fortum in Wrocław [12,13]. In this case, untreated sewage will be used as the heat source. The total cost of the project is estimated at PLN 82 million (around EUR 17.5 million). Large-scale heat pump projects were also triggered in 2022 by PGE Energia Ciepła in Cracow, by PGNiG Termika S.A. in Warsaw, and by PEC Gliwice Sp. z o.o. in Gliwice (*Przedsiębiorstwo Energetyki Cieplnej* – Heating Energy Company), and are considered by many other companies. In each case, projects are tailored taking into consideration local conditions for integration of sewage water treatment plant with district heating system. As in 2022, due to disruptions caused by the situation in Ukraine, which caused issues of limited coal availability, many projects of this type are focussed on the security of heat supply and resilience of the systems to market turmoil.

The use of large-scale industrial heat pumps, including high-temperature ones, for the decarbonisation of the district heating sector has gained the significant interest of many stakeholders, including industry, policymakers, and researchers globally. For example, Volkova et al. [14] claim that large-scale heat pumps are key future district heating technologies, which in the baseline scenario proposed will generate more than half of the heat for the Baltic states: Estonia, Latvia, and Lithuania in 2050. In Denmark, the total heat pump capacity in the district heating systems has increased in recent years, and experts expect this trend to continue as natural gas networks and coal are phased out [15]. Barco-Burgos et al. [16] have recently presented an extensive review paper focused on the integration of high-temperature heat pumps in district heating and cooling networks. According to their study, small district heating and cooling systems present the largest potential for heat pump use and significant reduction of consumption of fossil fuels, while, in medium and large systems this potential is lower.

David et al. [17] presented the results of the survey on the technical characteristics of 149 large-scale heat pumps in district heating systems with a total thermal heating output of 1.58 GW. The study revealed that with 54 examples in Norway, Sweden, Finland, and Switzerland and a total installed capacity of 891 MW, sewage water is the most common type of heat source. The average of the installed capacity was 17 MW per heat pump unit. Another interesting insight is that some of the heat pumps installed in the newest age group (2011–2016) were sized for the primary load and are operated continuously for 7000–8000 h/year, mainly to achieve a faster return rate of the investment. The annual operating hours of other heat pumps, especially the older ones, are in the range of 4000–7000 h.

Arpagaus et al. [18] presented an extensive review of the state-of-the-art and current research activities in the field of high-temperature heat pumps with heat sink temperatures in the range of 90°C to 160°C. They identified 13 manufacturers that can deliver heat at a sink temperature of at least 90°C, and the heating capacities range from about 20 kW to 20 MW. According to the study, most of the heat pumps examined use a single-stage thermodynamic cycle. They differ mainly in the type of refrigerant and compressor, and the coefficient of performance (COP) ranges from 2.4 to 5.8 at a temperature lift from 95°C to 40°C.

Bach et al. [19] analysed the technical and economic aspects of integrating large-capacity heat pumps in the Greater Copenhagen district heating system, which is, according to the authors, a state-of-the-art system with multiple heat sources. The results revealed that heat pumps connected to the distribution district heating networks can be operated for around 3500 full load hours and for approximately 4000 full load hours in a zero carbon-dioxide emission scenario expected in the year 2025. In the case heat pump is connected to the transmission network of an elevated temperature, the annual running time decreases to around 1000 full load hours. The main heat sources considered were drinking water, sewage water, and sea water, which resulted in average value of the COP at 3.1, 3.2, and 2.9, respectively, in the case heat pump is connected to the distribution network, and at 2.6, 2.6, and 2.5 in the case heat is delivered to the transmission network. The total heating capacity of heat pumps recovering heat from sewage water was estimated at 87 MW.

Popovski et al. [20] presented the results of a techno-economic analysis of different decarbonisation scenarios for an existing district heating network supplied by coal-fired combined heat and power plants in Germany. The main focus of the study was on large-scale heat pumps. Key conclusions of the study were that under the current regulatory and economic framework, large-scale heat pumps are not cost-competitive with the existing coal-fired cogeneration plants, and the European Union Emissions Trading System (EU ETS) CO_2 price will most likely not be a sufficient incentive in the short and medium term. To be cost-competitive, heat pumps should be operated for a significant number of hours per year, and the district heating supply temperature should be lowered.

Trabert et al. [21] theoretically examined the economic performance of electricity price-driven heat production by a river water two-stage ammonia heat pump in district heating systems using the EnergyPRO software. The heat pump was integrated with an existing cogeneration plant and a heat storage tank. The electricity for the heat pump was assumed to be supplied by the cogeneration plant, and the electricity costs resulted only from the lost revenue from a potential sale of electricity at the spot market. Four values of heating capacity were tested in the heat pump sizing exercise, i.e. 4.70, 5.17, 5.64, and 6.11 MW, respectively. The annual average COP of the heat pump was in the range from 3.4 to 3.7 depending on the heat pump size, and the annual running hours were from 6354 h/a for the smallest heat pump to 4794 h/a for the largest one. The results revealed that

the lowest levelized cost of heat (LCOH) was obtained for the heat pump of 4.70 MW heating capacity and the electricity-price driven operation was especially relevant for lower heating loads out of the heating season.

Fambri et al. [22] investigated the operation of large-scale heat pumps in district heating systems considering that the power-to-heat energy conversion process may provide flexibility for the electricity sector. They performed a case study for the city of Turin and created a potential scenario for heat pump operation based on the integration of the electric distribution system and the district heating distribution system. Results revealed that the installation of a 2.5 MW heat pump using groundwater of 15°C as a heat source and 250 m^3 heat storage tank may be profitable. The achieved simple payback period (SPB) of the project was in the range of 10.2 years with a potential reduction by 18% depending on flexibility provision incentives.

This work focuses on the heat recovery from municipal sewage water treatment plants. According to Volkova et al. [14], sewage water treatment plants are sources of heat with a high utilisation potential and are available all year round, ensuring relatively high values of COP. On the other hand, Ziemele and Dace [23] claim that usually located at a certain distance from the city, away from most heat consumers, and the full exploitation of their potential can be problematic. In their study for Riga, they sized heat pump for the heat demand of the adjacent heating area, which resulted in a much lower capacity (8 MW) than the total heat potential of the treated wastewater. This resulted in the waste water heat recovery share in annual heat production at the level of 2%.

In this paper, the techno-economic study of the integration of municipal sewage treatment system and district heating system through the installation of large-scale heat pump is performed under Polish 2022 market conditions. One of the challenges in such projects is to determine the optimal size of the equipment, which depends on several factors, such as the flow and temperature of treated wastewater, the desired district heating network water temperature, and the economic and environmental constraints of the project. In this paper, a general methodological framework for sizing industrial heat pumps for waste heat recovery from sewage treatment plants is presented. According to [16], only a few published works discuss the optimal and basic integration of heat pumps in district heating and cooling systems, while the optimal size of heat pumps for a given system widely depends on local conditions, and macroeconomic factors, such as electricity and fuel prices. The proposed methodology is analogous to the one used for sizing organic Rankine cycle (ORC) cogeneration systems in retrofitting projects of coal-fired district heating plants [24,25].

The case study was carried out for the city of Gliwice, where the share of coal in the energy mix for district heating is currently 100%. In addition, heat is produced in heat-only boilers. The main objectives of the work are:

i) to assess energy, environmental, and financial performance indicators of the heat pump implementation project,
ii) to optimally size the heat pump for the given system,
iii) to determine whether the integration of sectors through the heat pump is competitive in the district heating system,
iv) to identify key factors influencing the profitability.

Optimal selection of heat pump size, working fluids, parameters, and its integration with the existing district heating system are critical issues of the project. Considerable differences in energy, ecological, and economic results are observed for different heat pump cycle configurations and working fluids [18,26]. An important aspect of system design is also the hydraulic performance of a district heating network [27]. Regarding practical solutions, Barco-Burgos et al. [16] identified twelve generic configurations of heat pumps and how they can be integrated into district heating and cooling systems. The design task should also take into consideration an operational strategy and control of the heat pump unit under variable load and price conditions. An important problem of the optimisation task is also a selection of proper objective functions and constraints. The task must be properly formulated under the site-specific heating load profile, economic (including financial support mechanism) and legal conditions, including different strategies to supply electric energy to the heat pump plant. On the other hand, in practice, the final solution adopted for implementation is heavily dependent on the offers of heat pump manufacturers and engineering companies, as well as on the maturity of the market.

In Poland, according to the report [28], the district heating sector covers around 24% of the total demand for heat in the country, and the share of coal in heat production in the sector was 72.5% in 2018. District heating systems are responsible for more than 35 million tons of CO_2 emissions annually. In cities with a population in the range of 20–99 thousand people, the share of heat delivered from ineffective heating systems is 72.5% and in smaller cities, it is 86.2%. The heat pump market is emerging and nowadays there is only one reference system with a cascade of Mitsubishi heat pumps [11]. The heat pump was traditionally regarded as a non-competitive solution in Polish district heating systems. The reason for this was the relatively low price of coal. Moreover, according to the position of power transmission system operator (TSO) – PSE S.A., there will not be a sufficient amount of electricity available to electrify district heating in Poland in 20–30 years. The situation has dramatically changed in the year 2022 as coal prices increased several times. In addition, there has been a considerable increase in the number of European Union emission allowances (EUAs) processed under EU ETS. This together resulted in a significant increase of heat production costs. Additionally, emission limits resulting from the EU directives [29,30] force district heating companies to make strategic investment decisions.

The work presented concerns pre-feasibility study and predesign process of the heat pump plant for heat recovery from the central municipal sewage water treatment plant in the city of Gliwice. The scope of work covers the preparation and analysis of input data, heat pump modelling, system design and simulations, and financial analysis. The aim is to perform a quantitative assessment of the technical feasibility and cost-effectiveness of the project and to provide the information necessary to make an investment decision, proceed to further stages of design, and take steps to raise investment funds.

A single heat pump technology is considered for size optimisation. The main reason for this is the actual availability of

appropriate heat pumps in the Polish market. Although the number of identified companies was considerable, only a few of them responded to inquiries on potential deliveries and their willingness to cooperate within the project. The technology preliminary evaluated for this study is the SHP-C600 heat pump system proposed by Siemens Energy [31,32].

2. Decarbonisation of Gliwice district heating system

The city of Gliwice is located in the southern part of the country, in the Silesia region, where also significant coal resources and active coal mines exist. The population of the city is around 180 thousand inhabitants. The city is located in the area of an accumulation plain cut by the Kłodnica River valley, which has a symmetrically developed network of side valleys in this area. Morphologically, the Gliwice region is poorly diversified. The average annual temperature varies between 7–8°C. The average monthly temperature in January is between –3°C and –2°C, while the average monthly temperature in July varies between 14°C and 16°C. Important factors influencing the climate of the city of Gliwice are high economic activity and the concentration of residential buildings. The significant degree of urbanisation results in the emissions of gaseous and particulate pollutants much higher than in other parts of the country.

The largest heat supplier and district heating network operator in the city is the municipal district heating company PEC Gliwice Sp. z o.o. (PEC), which operates in the field of heat generation, transmission, and distribution in accordance with the concessions granted by the President of the Energy Regulatory Authority of Poland. The main source of heat for the district heating network is the central heating plant equipped with 7 coal-fired boilers of total heating capacity of 360.5 MW, which is located in the western part of the city. The technological system of the heating plant includes a boiler house consisting of three WP-70 pulverised coal-fired water-tube boilers of 81.4 MW nominal heating capacity each and a boiler house in which four WR-25 coal-fired water-tube grate boilers of 29.2 MW nominal heating capacity are installed. The minimum allowable heating output of the WP-70 boiler is around 35 MW and that of the WR-25 boiler around 10–12 MW. The indicative thermal efficiency of boilers (ratio of thermal output to fuel LHV (lower calorific value) chemical energy input) in the 2021/22 heating season was η_B = 0.84 for WP-70 boilers and η_B = 0.87 for WR-25 boilers. Total annual coal consumption in the 2021/2022 heating season was 114 207.93 tonnes, and the average LHV (lower heating value) of coal was 21.4 MJ/kg. Apart from coal, the plant also uses significant amounts of quick lime, urea, and water in exhaust gas treatment systems to keep emissions below the current limits.

The total length of the district heating network is around 235 km. The network is the 2G (second generation) high-temperature water network with a maximum winter forward water temperature of 120°C. The network arrangement is of mixed radial and ring type, with several loops in the central region. The heat carrier is led out of the heating plant via 4 transmission pipelines: North-Western (2×DN600), New Western (2×DN700), Southern (2×DN500), and Northern (2×DN350). The total number of heating substations in the network is 1682 located in 6 heating zones. Figure 1 depicts the central heating plant output, while the temperature characteristics of the district heating network is depicted in Fig. 2.

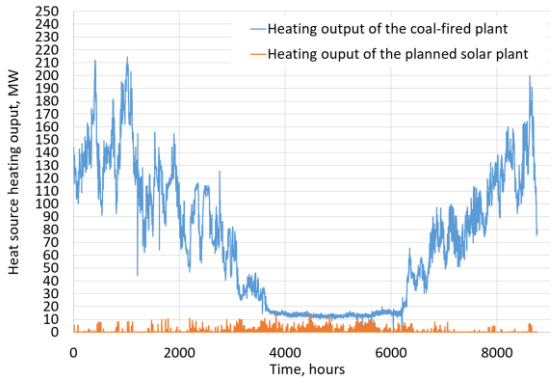

Fig. 1. Annual profile of heating plant thermal output (2022 data).

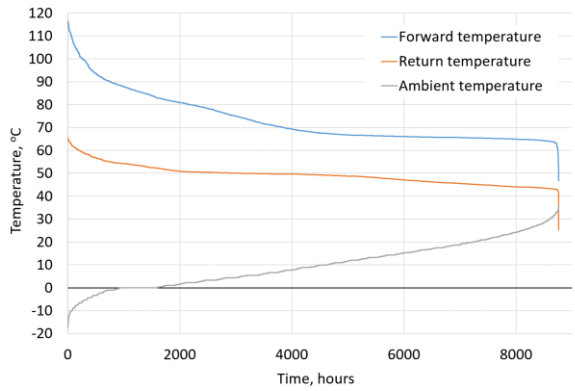

Fig. 2. Annual characteristic temperatures of the system.

As a result of the ongoing local programme of emission reduction from distributed domestic boilers and intensive development of new residential, retail, and office areas in Gliwice, the number of connected consumers and the ordered heating power are constantly increasing. For example, the heating power of facilities connected to the district heating network in the 2018/2019 season amounted to 15.65 MW, of which 5.47 MW were newly built buildings.

Recently, several new investment projects have been triggered aiming at obtaining the status of an efficient district heating system as defined by the revised EED [33]. Those include the implementation of a cogeneration plant fired with biomass and waste-derived fuels, a solar heating plant with a peak capacity of 13.3 MWp and heat storage. The investment project was publicly announced at [34]. The simulated heat output of the solar plant is already depicted in Fig. 1. In addition to this, several projects have been triggered in the field of waste heat recovery from distributed sources, including the Gliwice Central Sewage Treatment Plant. The key existing infrastructure for the project includes equipment and installations located at the heat pump and sewage treatment plant, and the district heating network.

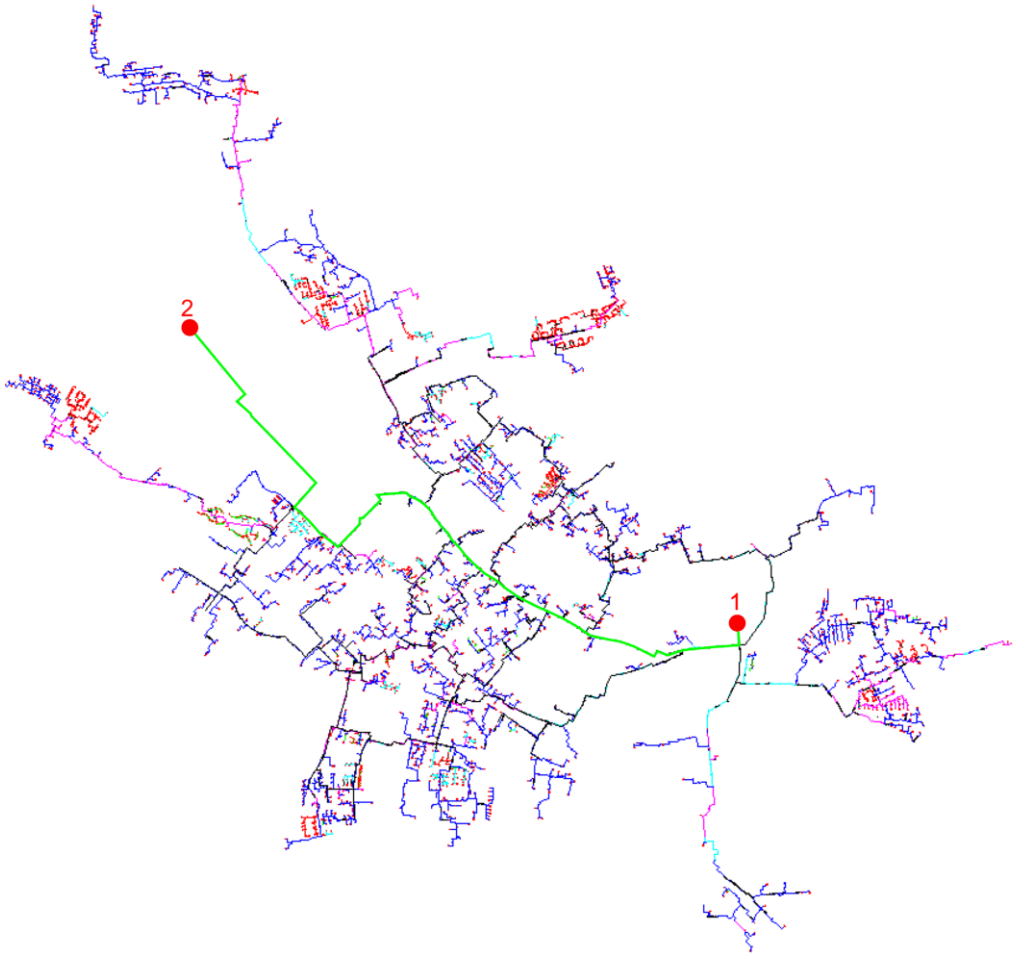

Fig. 3. Locations of the heating plant (1) and the sewage treatment plant (2) in the Gliwice district heating network.

Fig. 4. Central Sewage Treatment Plant of Gliwice (source: Google Earth).

Locations of the heating plant and the sewage treatment plant in the heating network are depicted in Fig. 3.

3. Heating potential of treated sewage water

The sewage treatment plant in Gliwice is presented in Fig. 4. It treats the city's sewage before discharging it into the Kłodnica River. The plant was designed for the maximum sewage treatment capacity of $G_{d,max}$ = 84 000 m^3/day, and daily average flow of $G_{d,av}$ = 40 000 m^3/day. Sewage treatment technology is based on mechanical and biological processes, with the possibility of chemical support. Before discharge into the river, the treated wastewater flows through a measuring station, where the flow and temperature are determined.

At the first stage of project development, the potential of treated sewage water for heat recovery was assessed. This was done by adopting flow rate and temperature measurements available from the plant's SCADA (supervisory control and data acquisition) system, and using the following formula:

$$\dot{Q}_{HP,in} = \dot{m}_{sw} c_{sw} \Delta T_{sw}. \quad (1)$$

Based on available measurement data, the annual flow and temperature models were developed with hourly resolution. Figure 5 depicts the flow of wastewater. Characteristic morning and evening peaks can be observed, as well as the night valleys, which typically occur between 2:00 and 7:00 am. Temperature of the wastewater is depicted in Fig. 6. The highest value measured is 22.9°C and the lowest one is 10.7°C. According to the acquired measurement data, the maximum thermal power that can be recovered from the treated wastewater at the temperature drop of ΔT = 5 K is 31.5 MW and the minimum is 2.7 MW. The annual average value is 8.1 MW. It was found that the peak flows occur on summer days in the time of heavy rains. The lowest heat recovery potential is in winter. The highest heat recovery potential is in July while the lowest one is in March. Figure 7 depicts the duration curve of the heat recovery potential. It can be concluded that very high recovery potential lasts for a relatively short time, and throughout most of the annual time the potential is close to average.

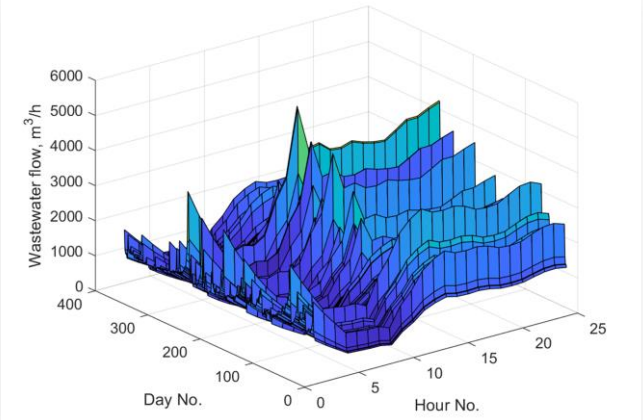

Fig. 5. Annual wastewater flow profile.

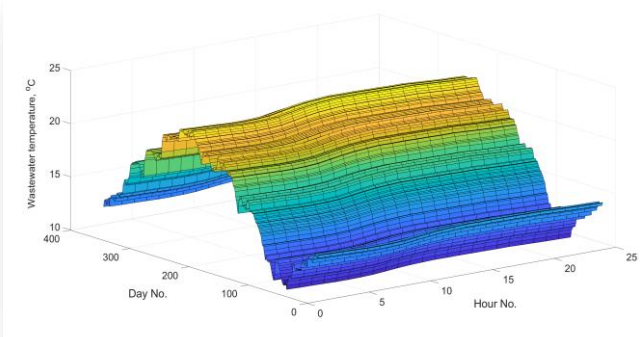

Fig. 6. Annual wastewater temperature profile.

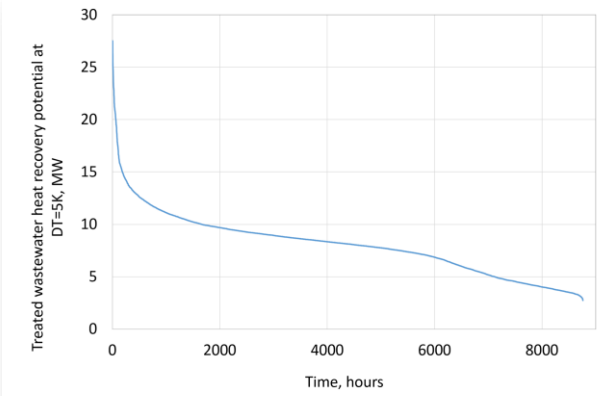

Fig. 7. Annual wastewater heat recovery potential duration curve.

There are two important features of the sewage treatment plant in Gliwice. The first one is that there are running two biogas-fired cogeneration modules of 365 kW and 210 kW installed electric power, respectively. The second favourable feature of the location is that there is available more than 20 000 m^2 of land for a photovoltaic (PV) power plant. Therefore it was decided that the PV system would be collocated with the heat pump. The realistic peak power output of the plant was assessed at around 1200 kW. The PV generation model is based on the measurements from a nearby PV plant located at the Gliwice campus of the Silesian University of Technology. The annual PV generation profile in kW is depicted in Fig. 8.

4. Materials and methods

Heat pumps are a major technology for integrating low-temperature heat sources with high-temperature district heating systems. The proposed methodology for optimal sizing of the heat pump and its integration with both the technological system of the sewage treatment plant and the district heating network is based on the following key steps:

a) acquisition of input data;
b) equipment availability assessment and selection of heat pump technology;
c) identification of key performance parameters of the heat pump system through physical modelling;
d) development of the heat pump identification model based on black-box type correlation;

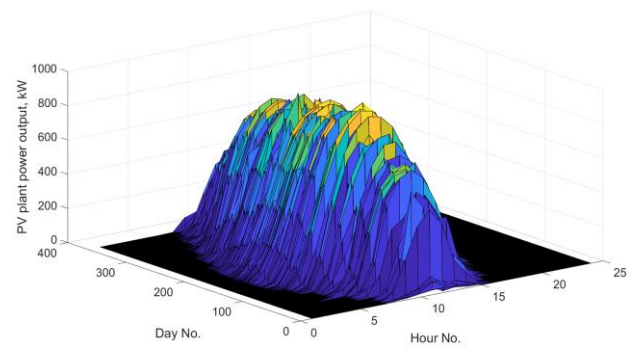

Fig. 8. Modelled annual power output of the PV plant.

e) hydraulic interconnection design for the integration of heat pump with the district heating system;
f) construction of a simulation model enabling multiple calculations and system optimisation;
g) annual system simulations with different values of decision variables, and determination of key items of the annual substance and energy balance;
h) estimation of investment expenditures for different heat pump heating capacities;
i) determination of the level of profitability of the project in the individual variants,
j) sensitivity analysis.

In the first step, relevant valid measurement data on the operation of both the district heating system and the sewage treatment plant system were acquired and analysed. Based on this, daily variation profiles of the individual parameters were determined and an annual data set was compiled for the simulation calculations of the heat pump system.

The heat pump selection for the project should take into consideration criteria such as the design temperature lift, coefficient of performance (COP), capital and operating costs, reliability, maintenance, and environmental impact. In this study, the equipment market was screened for the availability of heat pumps, as well as the available reference projects were examined. Overall, two types of approaches were identified in the field of waste heat recovery from sewage treatment plants. The first is based on cascaded systems and a larger number of heat pumps like in the case of Szlachęcin project [11]. In the second approach, large-scale industrial heat pumps are used. As there is no need to reserve heating capacity due to the possibility of supplying from the existing heating plant, the second approach was selected. It was preliminary considered to adopt for further studies the SHP-C600 industrial heat pump produced by Siemens Energy [31,32,35,36]. According to Siemens Energy publicly available data, the solution has been proven, implemented, and improved since 1981, and there are currently more than 50 units of this type in operation with a single pump heating capacity ranging between 5 MW and 30 MW. So far, the technology has proven high availability and flexibility of operation. According to the obtained information, the heat pump can potentially run for 8700 hours per year and the minimum allowable heating load of the heat pump is 30% of maximum power. This enables flexible cooperation with the heating plant, as well as with the future sources of heat in the district heating system. The single heat pump unit arrangement of the wastewater heat recovery system is also focused on minimisation of the service costs.

The heat pump can be built in a heating capacity variant from 5 MW to 70 MW. The auxiliary equipment will be supplied with 0.4 kV. Although, according to Siemens, heat sink temperature up to 150°C is possible [36], it is planned to build a typical unit, reaching a hot water temperature of up to 99ºC at the outlet to the grid. The time of occurrence of the network supply water temperatures higher than 99ºC was approximately 314 hours in the 2021/2022 season. After taking into consideration the point of heat pump interconnection, network water flows, and heated areas of the system, it was concluded that the temperatures higher than 99ºC will be required throughout around 283 hours per year.

The heat pump consists of an evaporator, a condenser with a subcooler, expansion valves, a flash tank, and a two-stage radial turbo compressor with inlet guide vanes at both compressor stages. The compressor will be driven by an electric motor (alternating current (AC) machine) with a supply voltage of 10.5 kV. A schematic diagram of the heat pump is depicted in Fig. 9. An advantageous feature of the proposed system is the direct heat exchange between heat pump working fluid and the treated wastewater, which will eliminate the demand for an intermediate heat exchanger, which would cause unfavourable temperature differences and exergy losses.

4.1. Heat pump physical model

The physical model of the heat pump is built using equations that describe the thermodynamic processes that make up the heat pump cycle. The working fluid is trans-1,3,3,3-tetrafluoropropene, which is also named refrigerant R-1234ze(E). It is used by several high-temperature heat pump manufacturers, including Siemens. The critical pressure of this fluid is 3634.90 kPa and critical temperature is 382.51 K.

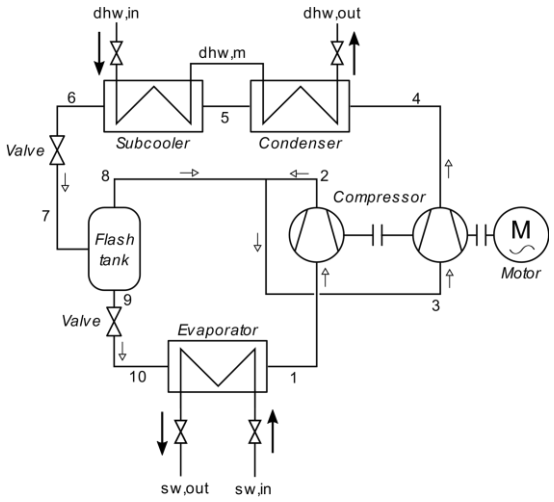

Fig. 9. Schematic diagram of the industrial heat pump.

The key performance parameters of heat pumps are heating capacity $\dot{Q}_{out}$, cooling capacity (or heat absorbed from the sink) $\dot{Q}_{in}$, temperature lift ΔT_{lift}, and coefficient of performance COP.

The heating output of the heat pump is the sum of heat extracted from the working fluid in the condenser and subcooler. Taking into account the specific points of the thermodynamic cycle defined in Fig. 9, the heat output can be presented as

$$\dot{Q}_{HP,out} = \dot{m}_{wf,4}\left(h_{wf,4} - h_{wf,6}\right). \quad (2)$$

Heat losses from the heat exchangers were neglected due to the relatively low process temperature. The values of specific enthalpy of the working fluid in points 4, 5 and 6 result from the saturation conditions at the given pressure. The pressure setpoint results from the district heating network water temperatures at

the heat pump outlet $T_{dhw,out}$. The temperature after the subcooler, and thus the enthalpy $h_{wf,6}$ result from the network water temperature at the heat pump inlet $T_{dhw,in}$.

After the subcooler, the working fluid pressure is throttled to the intermediate pressure, which results from the outlet pressure of the first compressor stage:

$$p_7 = p_2. \tag{3}$$

The throttling process occurs at constant enthalpy. Thus, equations for the two respective throttle valves are:

$$h_{wf,6} = h_{wf,7}, \tag{4}$$

$$h_{wf,9} = h_{wf,10}. \tag{5}$$

The mass and energy balances of the phase separator (flash tank) take the form

$$\dot{m}_{wf,7} = \dot{m}_{wf,8} + \dot{m}_{wf,9}, \tag{6}$$

$$\dot{m}_{wf,7} h_{wf,7} = \dot{m}_{wf,8} h_{wf,8} + \dot{m}_{wf,9} h_{wf,8}, \tag{7}$$

where specific enthalpies $h_{wf,8}$ and $h_{wf,9}$ are saturation enthalpies for liquid and vapour phase, respectively.

Heat delivered to the working fluid in the evaporator is

$$\dot{Q}_{HP,in} = \dot{m}_{wf,10}\left(h_{wf,1} - h_{wf,10}\right). \tag{8}$$

Again, the specific enthalpies of $h_{wf,1}$ and $h_{wf,10}$ results from the pressure setpoint, which depends on the treated wastewater temperature at the heat pump outlet ($T_{sw,out}$).

The most important component of the heat pump system is the compressor. In the SHP-C600, a two stage compressor is used. The respective pressure ratios of the particular stages are:

$$\varepsilon_1 = \frac{p_2}{p_1}, \tag{9}$$

$$\varepsilon_2 = \frac{p_4}{p_2}. \tag{10}$$

The entropy of the working fluid after the isentropic compression process is

$$s_2|_{p_2} = s_1|_{p_1}. \tag{11}$$

From the value of entropy s_2, the value of enthalpy $h_{2,s}$ after the isentropic compression is determined. Then the isentropic efficiency is used to calculate the enthalpy after the actual compression process:

$$h_{wf,2} = \eta_i\left(h_{wf,2,s} - h_{wf,1}\right) + h_{wf,1}. \tag{12}$$

Electrical power delivered to the electric motor driving the compressor first stage is

$$P_{el,in,1} = \frac{\dot{m}_{wf,1}\left(h_{wf,2} - h_{wf,1}\right)}{\eta_m \eta_{el}}. \tag{13}$$

The power deliver to the second stage is

$$P_{el,in,2} = \frac{\dot{m}_{wf,3}\left(h_{wf,4} - h_{wf,3}\right)}{\eta_m \eta_{el}}. \tag{14}$$

Finally, the coefficient of performance is

$$\mathrm{COP} = \frac{\dot{Q}_{HP,out}}{P_{el,in,1} + P_{el,in,2}}. \tag{15}$$

The temperature lift is defined as

$$\Delta T_{lift} = T_{dhw,out} - T_{sw,in}. \tag{16}$$

In actual operating conditions, the heat pump runs at variable parameters. The key independent parameters selected for the heat pump model are: treated sewage water temperature at the evaporator inlet ($T_{sw,in}$); water temperature at the inlet and outlet of the condenser ($T_{dhw,in}$, $T_{dhw,out}$); and heating capacity ($\dot{Q}_{HP,out}$), which can be lower than the maximum achievable at given temperatures (part load conditions). To appropriately assess annual energy balance of the system, time series simulation is required with hourly resolution. District heating network and treated sewage water parameters are known from measurements. Parameters of the heat pump must be determined from the model for each time step (t).

The heat pump cycle is depicted in the temperature – entropy (T-s) diagram in Fig. 10. Because the measurements of relevant heat pump performance parameters were not available, the relevant model was built using Ebsilon Professional simulation software [37], and calibrated with publicly available data given in [31,32,35]. The model is shown in Fig. 11. The most important issue of the modelling is the unknown pressure-flow characteristics of the compressor. In the study the Ebsilon built-in characteristics was used. Table 1 presents a comparison of results obtained by the model with parameters initially presented by Siemens Energy in [35]. The heat pump was simulated in design and off-design modes respectively, and a number of data points were generated. Those data were then used to develop regression models of key performance parameters, which were later used

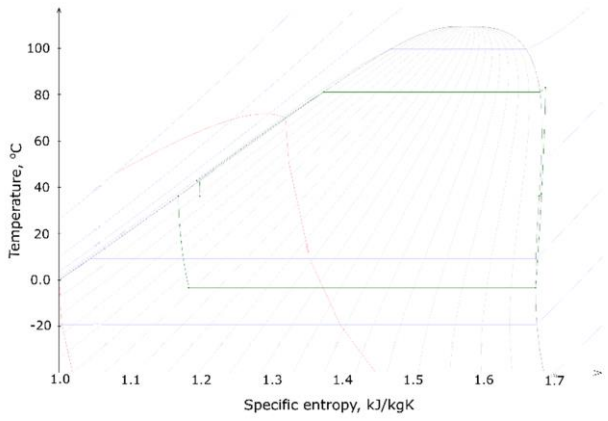

Fig. 10. Simulated heat pump cycle in T-s diagram.

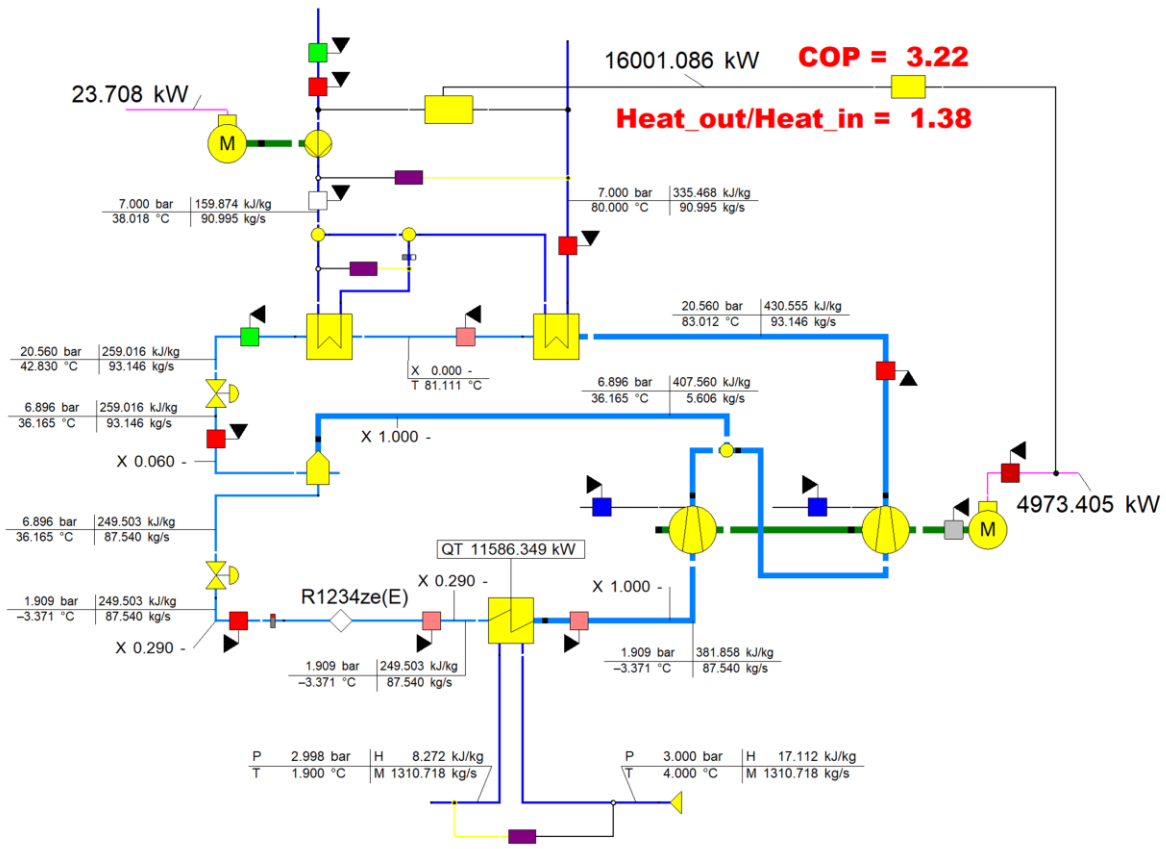

Fig. 11. Ebsilon Professional physical model of the Siemens SHP-C600 heat pump; M – electric motor, M – mass flow, H – enthalpy, P – pressure; T – temperature; QT – heat transferred, X – vapour quality.

for an annual simulation of the system's operation. Such an approach was previously demonstrated in [24,25,38].

The highest capacity and COP values are achievable in the summer when the wastewater temperature is high and the network water temperature is low. In winter, both heating output and COP decrease. Hence, the average annual efficiency of the system is influenced by the utilisation strategy of the unit and the duration of operation under winter and summer conditions respectively.

4.2. Heat pump black-box identification model

Although physical equation based modelling of heat pump performance gives relatively good predictions of the key performance parameters, it is not effective regarding multiple time series simulations required for system optimisation. The problem is long calculation times and convergence problems at some set points. For this reason, a black-box parametric model was developed that enabled multiple trouble-free simulations.

The highest assumed heating capacity of the heat pump model under winter conditions was 18 970 kW at a wastewater temperature of 14°C and a district heating network water temperature of 99°C. This value has been set as the reference one $\dot{Q}^{ref}_{HP,out,des}$. The heating capacity $\dot{Q}_{HP,out,des}$ was then used as the scaling and sizing design parameter. The Matlab software was used to fit appropriate correlations which enabled multiple annual simulations of the heat pump operation with hourly resolution. The relative achievable full load heating output under given thermal conditions, which was obtained from Ebsilon simulations, is

Table 1. Comparison of modelling results with data declared by the HP manufacturer.

Parameter	Unit	Declared data [35]	Modelling result	Relative difference
Heat source water mass flow	kg/s	1333.0	1310.72	-1.67%
Heat sink water mass flow	kg/s	94.0	90.99	-3.20%
Working fluid mass flow through the evaporator	kg/s	87.5	87.54	0.05%
Working fluid mass flow through the condenser	kg/s	93.0	93.15	0.16%
Heating capacity	kW	16510.0	16001.09	-3.08%
Cooling capacity (heat input)	kW	11563.0	11586.35	0.20%
Electric power input	kW	5124.0	4973.41	-2.94%

$$\frac{\dot{Q}_{HP,out,max}}{\dot{Q}_{HP,out,des}} = \left[-a + bT_{sw,in} + c\Delta T_{lift} - dT_{sw,in}\Delta T_{lift} - e\left(\Delta T_{lift}\right)^2\right], \quad (17)$$

where the values of coefficients are: a = 5.9340, b = 0.2129, c = 0.1386, d = 0.0021, e = 0.0007. The coefficient of determination for this correlation is R^2 = 0.9999. The results of curve fitting are depicted in Fig. 12.

The maximum value of COP achievable under given temperature conditions is

$$\mathrm{COP}_{max} = \left[a + bT_{HP,out} - cT_{sw,in} - d\left(T_{HP,out}\right)^2 + eT_{HP,out}T_{sw,in} + f\left(T_{sw,in}\right)^2\right], \quad (18)$$

where the values of coefficients are: a = 2.8150, b = 0.0368, c = 0.0597, d = 0.0004, e = 0.0003, f = 0.0014. The coefficient of determination for this correlation is R^2 = 0.9966.

Under real operating conditions, the heating capacity of the heat pump is frequently limited by the heat balance of the district heating network. Therefore, the actual COP at given time step is calculated using the following formula:

$$\mathrm{COP} = \left[-a + b\frac{\dot{Q}_{HP,out}}{\dot{Q}_{HP,out,max}} + cT_{sw,in} - d\left(\frac{\dot{Q}_{HP,out}}{\dot{Q}_{HP,out,max}}\right)^2 - e\frac{\dot{Q}_{HP,out}}{\dot{Q}_{HP,out,max}}T_{sw,in}\right], \quad (19)$$

where the values of coefficients are: a = 0.126, b = 2.047, c = 0.03105, d = 0.9205, e = 0.03109. The coefficient of determination for this correlation is R^2 = 0.999.

In the next step, hydraulic and thermal simulations of the district heating network were performed to determine the interconnecting pipe diameter and the effects of the network operation

4.3. Hydraulic integration

It was proposed to directly integrate the heat pump with the treated wastewater duct and the district heating grid. The approach is based on the construction of a concrete overflow buffer tank for the treated wastewater pumping station and a concrete heating chamber equipped with appropriate shut-off fittings, which will provide two modes of operation for the heat pump system:

- mode 1 – in parallel with the central heating plant –plugging into the supply and return pipelines;
- mode 2 – in series with the central heating plant – connection to the return pipeline only for preheating of return water.

The second mode will be applied at the lowest ambient temperatures when the heat pump will contribute only to around 5% of the total heat demand of the district heating system. A schematic diagram of the heat pump hydraulic integration is presented in Fig. 13.

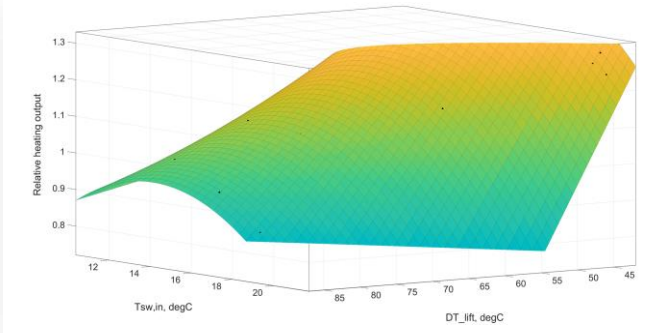

Fig. 12. Curve fitting to Ebsilon Professional simulation results.

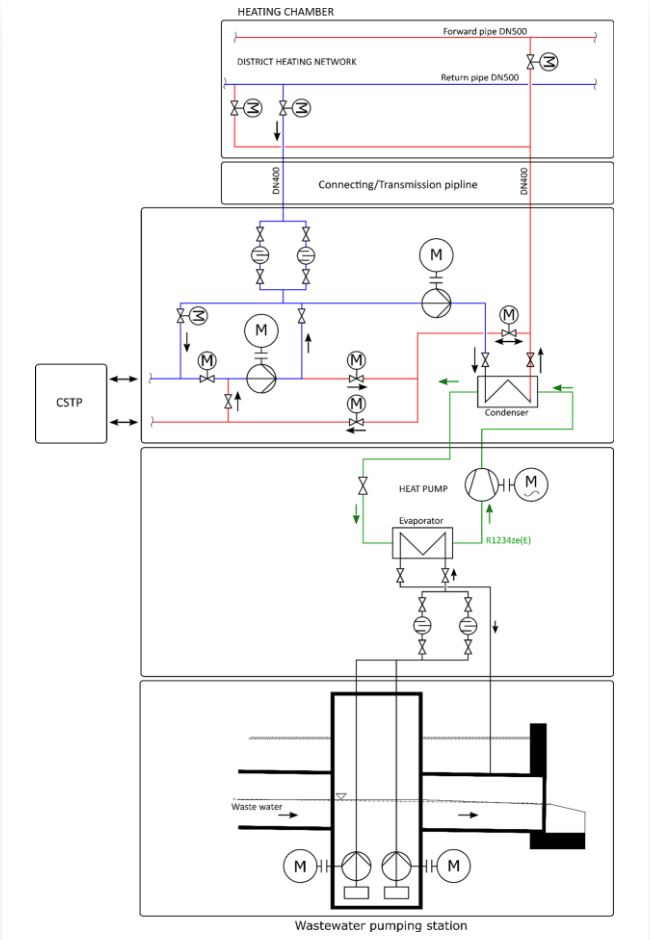

Fig. 13. Schematic diagram of the heat pump hydraulic integration.

with multiple heat sources. As it is presented in Fig. 3, the central heating plant and heat pump are located in different parts of the city and the distance between them is around 7 228 m. The district heating network model was built using the NetSim software [39] and detailed network data available in the Municipal Spatial Information System – Systemic Heat Portal (https://msip.gliwice.eu/geoportale). In particular, the routes and diameters of the pipelines were taken from the portal. The model was calibrated with measurement data for selected states of the district heating network provided by the district heating company. In the study, three pipe diameters were taken into consideration: DN200, DN400, and DN500 respectively. Sample results are depicted in Figs. 14 and 15.

It was found that the DN200 diameter of the interconnecting pipe results in high values of differential pressure at the heat pump system, thus the cost of water pumping increases. A change in pipeline diameter from DN200 to DN400 leads to a significant reduction in the required differential pressure and thus in the electrical drive power requirement of the network water pumps. The pipeline diameter is further increased to DN500, and the reduction in the required differential pressure is relatively small. Eventually, the DN400 pre-insulated pipeline was selected.

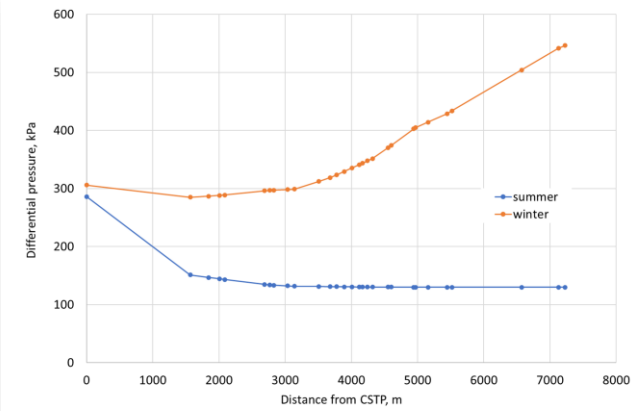

Fig. 14. Estimated distribution of differential pressure in the section connecting the heating and sewage treatment plants for a heat pump with a heating capacity of 13 MW and a transmission pipeline diameter of DN400.

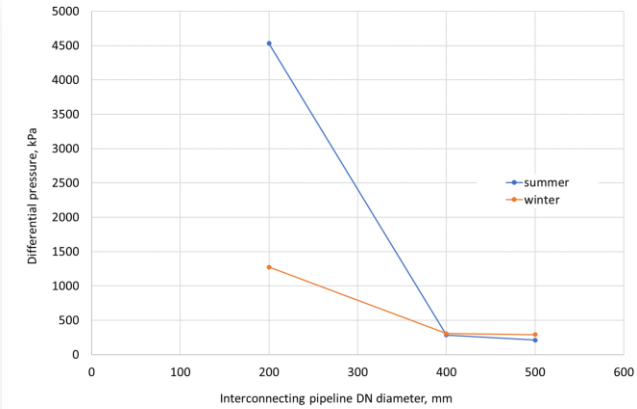

Fig. 15. Required differential pressure at the point of incorporation of a heat pump with a heating capacity of 13 MW, depending on the diameter of the transmission pipeline.

The obtained results confirmed the possibility of cooperation between the existing central heating plant and the heat pump located on the premises of the sewage treatment plant. The respective heat sources will run in parallel and supply heat to different areas of the district heating system. It was also confirmed that, under summer load conditions, it is possible to switch off the central heating plant and deliver heat to consumers from the heat pump only.

4.4. Economic model

The final step was to evaluate the feasibility and profitability of installing an industrial heat pump for waste heat recovery from sewage treatment plants. This was done by comparing the financial benefits and costs of the project over the assumed lifetime of 15 years. According to market producers estimations, the specific capital investment costs for the installed system without integration are 250 to 800 EUR/kWth, and depend mainly on heating capacity, temperature lift and scope of supply [36]. The investment costs are studied in depth in [40–42]. According to different data sources, the expected value for 10 MWth heat pump is between 350 and 500 EUR/kWth. After consulting different engineering offices and potential vendors, investment cost data were acquired. Available data from other projects were also taken into consideration. As the total capital investment costs (total CAPEX) are always site-specific and significantly influenced by system integration costs, this study uses engineering evaluation methods based on the scope of the project, which includes:

- heat pump;
- container transformer station with 20 kV input voltage with 10.5 kV outputs (heat pump) and 0.4 kV (internal installations and drives);
- connection to the external electricity grid and power supply to the transformer station (cable line of estimated length of 1500 m);
- construction of a concrete overflow buffer tank for the wastewater pumping station with an estimated volume of 125 m^3;
- installation of a system of submersible pumps for the treated wastewater to the heat pump, together with an intake filter to prevent the coarse fraction (plants, dead birds) from entering the pumps;
- variable-speed drives for treated wastewater pumps;
- machinery house building of 12 m× 35 m and height of 9 m on a floodplain, soundproofed, equipped with overhead crane and social space, including fabrication;
- machinery house building electrical, HVAC (heating, ventilation, air conditioning), and sanitary installations;
- photovoltaic plant with a peak capacity of 1.17 MWp;
- electrical installation integrating sewage treatment plant, PV, and heat pump systems;
- pre-insulated pipe DN400 district heating network transmission section, 1700 m long (complete supply, works and acceptance in the thermal-technological sector);
- concrete heating chamber at the point of connection of the system to the district heating network;
- hydraulic system and fittings of a district heating chamber ensuring change of supply modes of a district heating network;

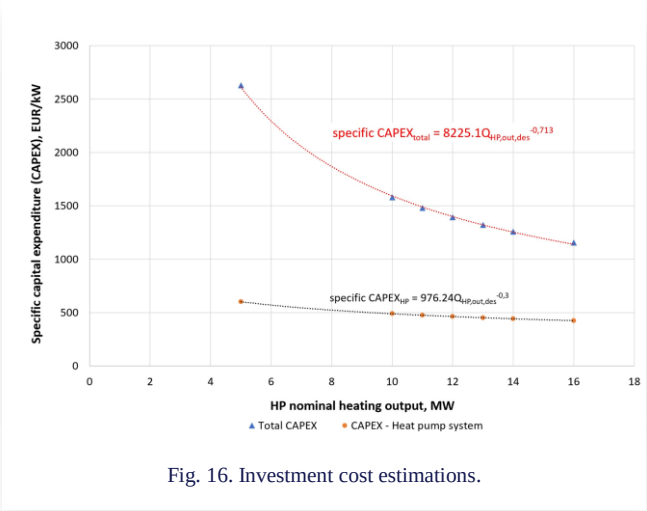

Fig. 16. Investment cost estimations.

- electrical installation of the heating chamber and power supply;
- district heating network water pumping station;
- hydraulic system to integrate the sewage treatment plant with the heat pump system and the district heating network (auxiliary equipment, fittings, pipework – complete supply, works and commissioning of the heat-technology branch);
- control system, field measurements, and telemetry for PEC (complete supply, works, and commissioning in the field of instrumentation and control engineering).

The costing curves elaborated for CAPEX estimations are depicted in Fig. 16. The investment costs for the interconnecting pipeline strongly depends on the pipe diameter, which is shown in Fig. 17. The obtained values of the estimated capital expenditures are overall in line with the literature data taking into account recent increases in costs in the construction sector. It can be also concluded that the specific scope of the project and site-specific requirements, such as hydraulic and electric interconnections, and the collocated PV plant, significantly influence the total CAPEX. Therefore, the specific total CAPEX gets very high values for the smallest heat pump option. The higher is the design heating capacity $\dot{Q}_{HP,out,des}$ the lower is the total specific CAPEX.

The optimisation problem is to select the size of the heat pump to achieve the best value of a selected quality indicator (objective function) under given constraints. The task is solved from the local financial perspective. Therefore, the net present value (NPV) calculated for the economic lifetime of the project was selected as the main objective function:

$$\max \mathrm{NPV}, \tag{20}$$

where

$$\mathrm{NPV} = \sum_{t=1}^{N} \frac{\Delta \mathrm{CF}_t}{(1+r)^t} - \mathrm{CAPEX}. \tag{21}$$

Other financial indicators such as net present value ratio (NPVR), internal rate of return (IRR), simple payback period (SPB), discounted payback period (DPB) were also calculated where it was possible.

The key component of the objective function is the differential cash flow $\Delta \mathrm{CF}_t$ resulting from cash flows after and before the project. Assuming that the project does not generate new incomes as the market for heat remains the same after the project, the differential cash flow results mainly from the changes in costs:

$$\Delta \mathrm{CF}_t = \mathrm{CF}'_t - \mathrm{CF}_t = -\Delta \mathrm{OC}_t - \Delta \mathrm{Tx}_t + \Delta L_t, \tag{22}$$

where the residual value L is calculated only for $t = 15$. The differential operational costs take into account mainly changes in costs of electricity, fuel costs, and maintenance and environmental costs related to heat sources:

$$\Delta \mathrm{OC}_t = C_{HP,t} + \Delta C_{CP,t} = \left(C_{el,HP} + C_{m,HP} + \Delta C_{f,CP} + \Delta C_{el,CP} + \Delta C_{m,CP} + \Delta C_{env,CP}\right)_t. \tag{23}$$

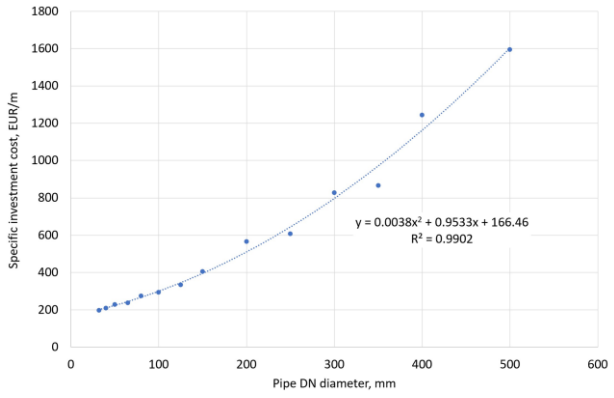

Fig. 17. Specific investment costs for the interconnecting pipeline as a function of diameter (Poland, 2022 prices, pre-insulated pipes in reinforced trench).

For tax calculations also the changes in depreciation and financial costs are taken into consideration. It must be emphasised that the cost of heat recovered from the treated wastewater was set to 0.

The key assumptions for financial calculations are as follows:

- The project is a standalone unit of analysis.
- The project's economic lifetime is 15 years.
- Construction time is 2 years.
- Discounted cash flow rate is $r = 0.03$.
- Two funding options were considered: with no subsidy (only equity and loan) and with a subsidy of 30% of the total investment cost. In the first option, the share of equity is 25%.
- Prices are valid for the year 2022.
- Coal price: 195 EUR/tonne (at LHV = 21.40 MJ/kg).
- Utility grid electricity price: 195 EUR/MWh (constant price based on current contract).
- Price of CO_2 emission allowance in EU ETS: 84 EUR/tonne.

- Heat pump service and maintenance cost (including reserves for overhauls): 2.5% of the direct investment expenditures (i.e. related to the productive assets).

The objective function is subject to both equality and inequality constraints, which result from heat load profile, heat recovery potential from the treated wastewater, parameters of district heating water, energy and substance balances, heat pump and coal-fired heat only boilers characteristics including COP and efficiency variations, range of allowable loads, etc. The basis for the sizing of the heat pump and the analyses of the quantitative effects of the project is the reference hourly distribution model of key parameters in terms of substance and energy balances. Calculations were carried out using an hour-by-hour simulation method. In the heating season, the heat pump system is covering the base heating load of the district heating system. During the off-season operation, heat for the district heating network is generated exclusively by heat pump systems and a solar thermal plant. Coal-fired boiler plants are not in operation. The heat pump works under part load conditions to enable full consumption of the solar heat.

The municipal district heating network balance takes into consideration heat supplies from different heat sources. Assuming that at each hour the heat generation by solar plant, as well as heat consumption and losses from the grid remain unchanged after the project, the differential heating power balance results in reduced heating output of coal-fired boilers:

$$-\Delta\dot{Q}_B = \dot{Q}_{HP,out} + \dot{Q}_{CHP} - \dot{Q}_{CSTP}. \quad (24)$$

Electric power balance of the heat pump system takes into account electricity from the grid and generated on-site:

$$\frac{\dot{Q}_{HP,out}}{\mathrm{COP}} + P_{aux} = P_{grid} + P_{PV} + P_{CHP} + \\ -P_{PV,CSTP} + \Delta P_{CP}. \quad (25)$$

In the base case scenario, a year-round operation of the heat pump unit was assumed (8000 hours), with two shutdowns at the beginning and end of the heating season. The assumed shutdowns aim to ensure a technical minimum for the coal-fired boilers being dispatched. An alternative operating strategy can be oriented towards minimising the cost of heat generation and dependent on the instantaneous price of electricity. Typically, this approach to pump control is used for energy purchases on the Commodity Exchange. In this study, however, constant electricity price was assumed as the electricity for PEC is procured through a tendering procedure. Therefore, the alternative strategy taken into consideration assumes shutdowns of the heat pump whenever performance parameters do not justify the momentary costs of heat production.

5. Results and discussion

Detailed annual simulations were carried out for 6 variants of the heat pump size expressed by the maximum heating power in winter conditions. In each variant, this power is: variant HP_16 – 16 MW, variant HP_14 – 14 MW, variant HP_13 – 13 MW, variant HP_12 – 12 MW, variant HP_11 – 11 MW, variant HP_10 – 10 MW, and variant HP_5 – 5 MW.

It was found that variability of treated wastewater flow and temperature, district heating network heat demand, and temperatures result in high variability of the heat pump performance parameters, such as the achievable heating capacity and COP. Depending on the heat pump design heating capacity (size), the fraction of annual time where the heat pump works under part load conditions is different. The simulated annual variations of heat pump relative heating capacity and COP in the base case operation scenario for the heat pump_12 variant are depicted in Figs. 18 and 19, respectively. It can be concluded that the highest values of COP occur in summer. However, in summer the heating output is significantly reduced due to both low heating demand and parallel operation with the solar plant. On the other

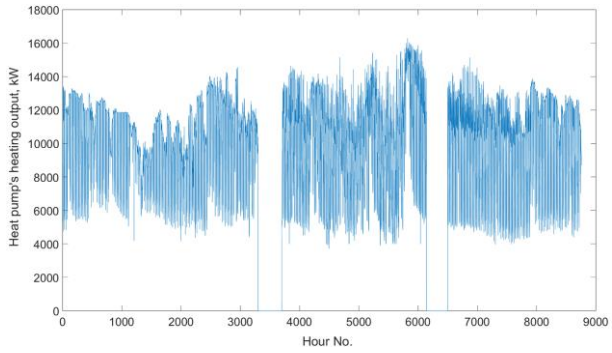

Fig. 18. Simulated annual variations of a 12 MW heat pump's heating output.

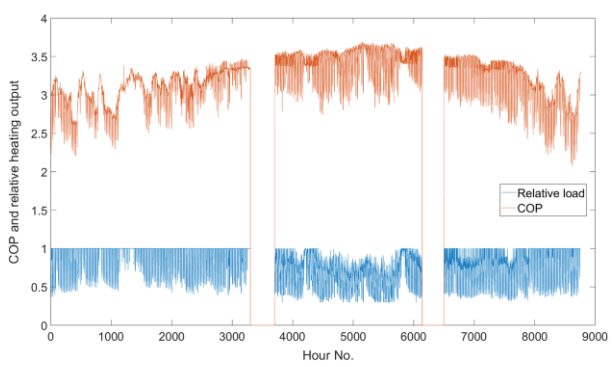

Fig. 19. Simulated annual variations of relative heating output and COP of a 12 MW heat pump.

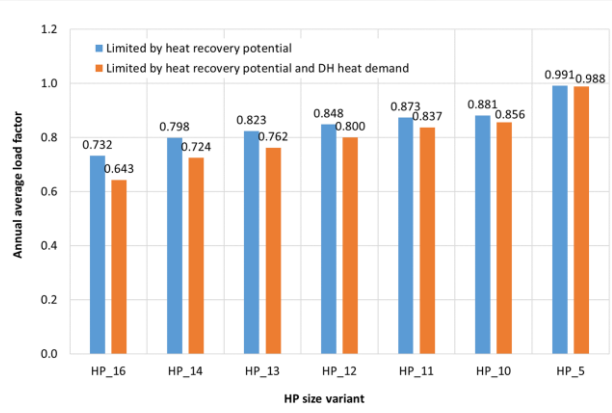

Fig. 20. Annual average load factor.

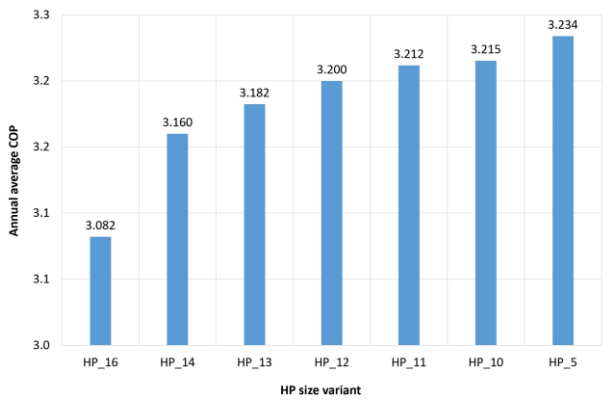

Fig. 21. Annual average COP.

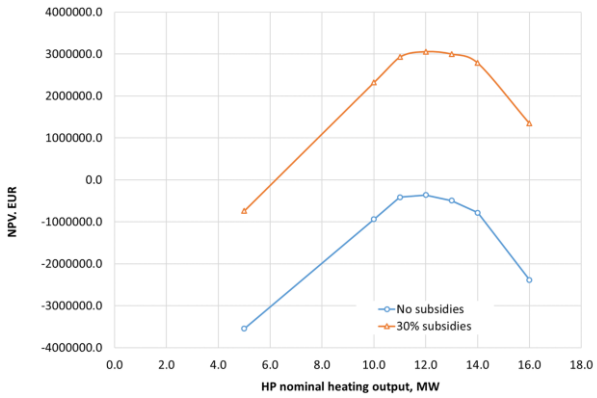

Fig. 23. NPV for different heat pump size variants.

hand, in the winter the heat pump runs closer to full load conditions, however, the achievable heating output and COP vary due to the availability of heat recovery potential.

Figures 20 to 24 summarise the key simulation results for the individual heat pump capacity variants. Figure 20 depicts the annual average load factor (defined as the ratio of the actual heating capacity to the achievable capacity under given thermal conditions) for different heat pump size options. As the installed capacity of the heat pump increases, the value of the annual average load factor decreases. It can be concluded that only the smallest heat pump can operate close to full load conditions. The larger the heat pump the actual load is limited by both the availability of the heat recovery potential and the heat demand in the district heating network. The influence of those limitations on COP is shown in Fig. 21.

Figure 22 depicts potential direct reductions in coal consumption at heating plant and related CO_2 emissions. The presented values are valid only if the electricity to drive the heat pump is supplied from renewable energy sources. In the case electricity is from coal-fired power plants, the systemic effects will be lower as the heat pump operation will result in additional fuel consumption at utility power plant.

Figures 23 and 25 present values of the objective function (NPV) for different heat pump size variants. It was found that the best option under the given assumptions is the HP_12 variant. However, the NPV curve is quite flat in the area of optimal solutions. Therefore, the potential range of heat pump design heating capacities that should be considered for the project is 11–14 MW. This gives the manufacturer a flexibility margin. Another important finding is that under given prices and operational strategy the project is not profitable without subsidies. The final value of NPV index is slightly negative for all the variants within the range of optimal solutions. The value of discounted payback period (DPB) is higher than 15 years and the value of SPB is in the range of 12 years, as depicted in Fig. 24.

As a result of the analyses carried out, the most favourable technical solution was found to be a heat pump variant with a design heating capacity of 12 MW under maximum winter load conditions. The baseline operational strategy assumed heat pump operation within 8000 hours per year. It results in an average annual heat pump load factor of 0.80 and an average annual COP of 3.20. Its implementation leads to a reduction in coal consumption at the central heating plant of approximately 15987 tonnes/year and a reduction in CO_2 emissions of approximately 34694 tonnes/year. The estimated total investment outlay (CAPEX) is at the level of EUR 14 759 183, which results in a specific investment cost of 1230 EUR/kW. The profitability indices without subsidies are slightly negative: NPV = –360070.4 EUR, NPVR = –0.025, IRR = 0.027,

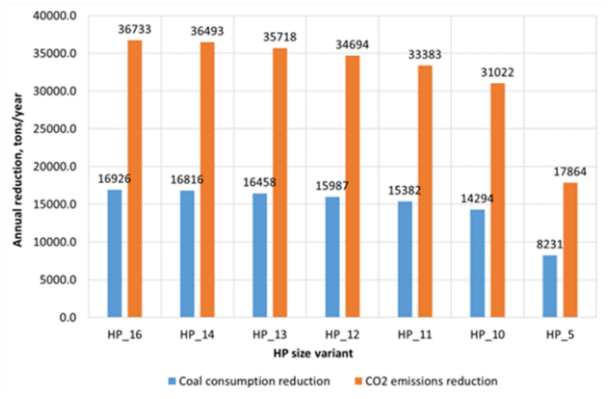

Fig. 22. Annual reduction of coal consumption and related CO_2 emissions from coal-fired boilers.

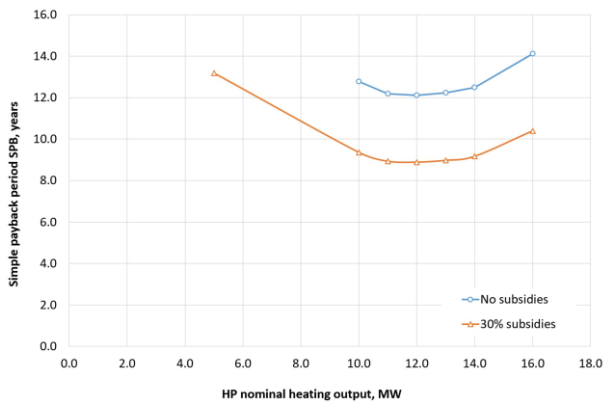

Fig. 24. SPB for different heat pump size variants.

SPB = 12.12 years, and DPB >15 years. The change in the project's value over the years is depicted in Fig. 25. Figure 26 depicts the project's sensitivity to critical financial parameters.

If the project is subsidised at 30% of CAPEX, the profitability indicators take on the values: NPV = 3,056,658.3 EUR, NPVR = 0.21, IRR = 0.068, SPB = 8.88 years, DPB = 10.73 years. Those are values typically accepted in the district heating sector.

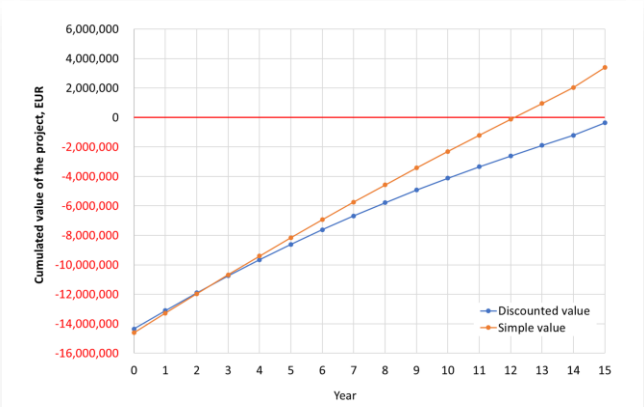

Fig. 25. Simple and discounted value of the project for HP_12 size variant.

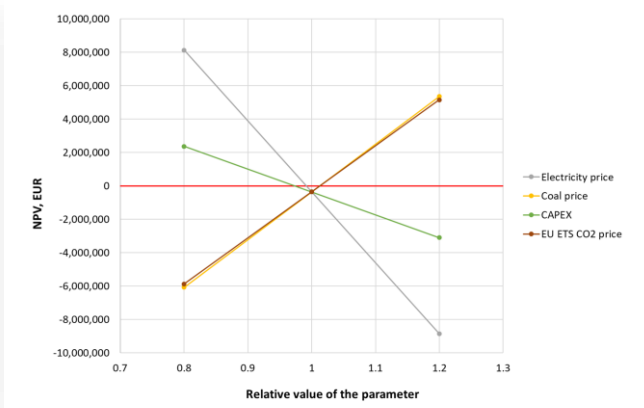

Fig. 26. Sensitivity analysis for HP_12 size variant.

The profitability of the project is highly sensitive to the variability of the critical project parameters, which include the electricity purchase price, the coal purchase price, the CO_2 emission allowance (EUA) price, and the total capital expenditure (CAPEX). The project shows the greatest sensitivity in relation to the electricity purchase price, and then to coal and EUA prices. The project is much less sensitive to CAPEX, which means operational effects are of critical importance for profitability.

After considering the specific contribution of each project effect to the final financial value, it was found that, relative to the results presented, there is a potential for improvement in energy and financial performance. This, however, requires the development of a suitable strategy for operating the heat pump.

Given that the cost-effectiveness of heat pump operation in the district heating system with coal-fired boilers is determined by the ratio of the cost of driving energy, which is the ratio of electricity cost to the sum of the costs of coal and CO_2 emissions, a potential for improving the financial effects exists in reducing the annual operating time of the heat pump to the period during which the following precondition is met:

$$\frac{sc_{el}}{\mathrm{COP}} < \frac{sc_f}{\eta_B}. \tag{26}$$

Given that the average efficiency of a coal-fired boiler at heating plant is around 0.85 and the COP is 3.2 for average annual conditions and 2.6 for winter conditions, the ratio of electricity cost to fuel cost should be below 3.76 for average annual conditions and 3.06 in the winter. The assumed prices result in a ratio of 3.11, which means that winter operation of the heat pump with low COP generates financial losses. Taking the heat pump periodically out of operation at the lowest achievable COP values will lead to reduced losses and therefore an improved annual result. Therefore, in additional simulation, it was assumed that the heat pump is taken out of service when the COP falls below 3.0. The values of the profitability indices obtained for the financing variant without financing improved (see Fig. 27), resulted in NPV = 728 508 EUR, NPVR = 0.05, IRR = 0.037, SPB = 11.15 years, and DPB = 14.19 years. The annual operating time of the heat pump in this control scenario was 6986 hours per year. The simulations also revealed that setting the COP criterion too high leads to a further reduction in operating time, which leads to a reduction in cost-effectiveness. It is therefore recommended that an algorithm be developed to control the use of the heat pump depending on the achievable COP and the actual energy cost ratio.

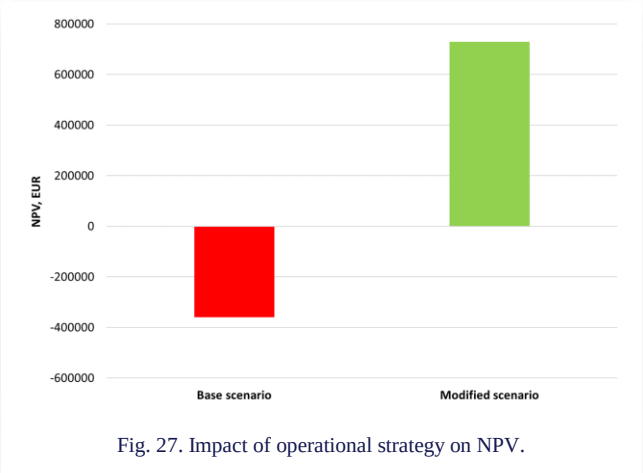

Fig. 27. Impact of operational strategy on NPV.

6. Conclusions

Using physical modelling to develop a black-box-type identification model of the industrial heat pump system appeared to be effective modelling approach that enabled multiple system simulations and techno-economic optimisation. Models of such type can deliver useful information regarding investment decision making and production planning. Heat pumps are thermodynamic systems that can be modelled relatively fast using available software tools. However, such model require calibration using measurement data form existing plants. Better accuracy of

the models can be achieved if larger collections of measurement data is available.

An important conclusion from the study is that the projects of implementation of large industrial heat pumps in Polish district heating systems may be nowadays profitable. Although the expected payback periods are quite long, the profitability indices are overall positive if the heat pump is appropriately sized and runs under given price conditions. The profitability is highly influenced by the energy performance of the system, which mainly results from the sizing of the heat pump, load conditions, and achievable COP. In the presented case study, the project of integration of sewage treatment plant and heating plant with the heat pump system is on the verge of profitability, and therefore even small changes in technical performance may significantly influence the objective function.

It was also concluded that the profitability of the project is strongly dependent on the size of the heat pump and the optimal solution exists. For the given potential for heat recovery from the treated wastewater, which is between the summer maximum of 31.5 MW and the winter minimum of 2.7 MW, the optimal size of the heat pump (regarded as maximum heating capacity under winter conditions) is 12 MWth. Such a heat pump unit ensures an annual average heat recovery rate of around 7 MW, which is slightly below the annual average heat recovery potential (7.9 MW). Smaller heat pumps are less cost-effective as a significant increase in the total CAPEX occurs once the heat pump size is reduced. The profitability of larger heat pumps is significantly influenced by part load conditions, which result in COP reductions.

As the project's profitability is very sensitive to the technical performance of the system, and considering that due to the heat pump integration with high-temperature heating grid the resulting COP is relatively low, the recommended strategy for heat pump operation is to control the momentary cost of heat generation resulting from thermal conditions, COP, electricity and fuel prices and environmental costs. Relevant algorithms and software should be implemented to assist system operators in making well-informed operational decisions.

The market trends in Poland have recently revealed a considerable decrease in electricity prices while coal and CO_2 prices remained close to the values assumed for the study. This is the result of a significant increase in power generation by PV and wind plants recently commissioned in Poland. In addition, major energy companies in Poland have recently announced strategies indicating the withdrawal of coal assets and significant investments in renewable energy sources. In June 2023, for the first time in history, negative prices of electricity occurred in the national commodity energy exchange. In the light of the obtained results of this study, it can be concluded that the profitability of projects assuming the implementation of large-scale heat pumps in the district heating sector in Poland will improve shortly and a considerable number of new projects should be expected to be triggered.

Acknowledgements

The work is co-funded by the European Union within the framework of the Programme for the Environment and Climate Action, LIFE Clean Energy Transition sub-programme. Project: Supporting Energy Transition and Decarbonisation in District Heating Sector, acronym LIFE22-CET-SET_HEAT, project number 101119793. Project website: https://setheat.polsl.pl

References

[1] International Energy Agency (2021). *Net Zero by 2050. A Roadmap for the Global Energy Sector*. IEA Special Report. IEA Publications. https://www.iea.org/reports/net-zero-by-2050 [accessed 16 Feb. 2024].

[2] World Economic Forum Global Future Council on Energy 2016-18 (2018). *Transformation of the Global Energy System*. World Economic Forum. http://www3.weforum.org/docs/White_Paper_Transformation_Global_Energy_System_report_2018.pdf [accessed 16 Feb. 2024].

[3] IREA (2019). *Global Energy Transformation. A Roadmap To 2050 (2019 edition)*. International Renewable Energy Agency, Abu Dhabi. https://www.irena.org/-/media/Files/ IRENA/Agency/Publication/2019/Apr/IRENA_Global_Energy_Transformation_2019.pdf [accessed 16 Feb. 2024].

[4] Lund, H., Østergaard, P.A., Connolly, D., & Mathiesen, B.V. (2017). Smart energy and smart energy systems. *Energy*, 137, 556−565. doi:10.1016/j.energy.2017.05.123

[5] Communication from the Commission to the European Parliament, the Council, the European Economic and Social Committee and the Committee of the Regions (2016) *An EU Strategy on Heating and Cooling*. Publications Office of the EU, Brussels, 16.2.2016. https://eur-lex.europa.eu/legal-content/en/TXT/ ?uri= CELEX:52016DC0051 [accessed 16 Feb. 2024].

[6] Delmastro, Ch., Briens, F., Husek, M., & Martinez-Gordon, R. (2022). District Heating. International Energy Agency Tracking report. IEA. https://www.iea.org/energy-system/buildings/district-heating [accessed 16 Feb. 2024].

[7] Polish Energy Regulatory Office (2022). *District Heating in Numbers*. URE (in Polish). https://www.ure.gov.pl/pl/cieplo/energetyka-cieplna-w-l/11407,2022 [accessed 16 Feb. 2024].

[8] Polish Ministry of Climate and Environment (2022). *Project of the strategy for district heating till 2030 with a perspective till 2040*. BIP (in Polish). https://bip.mos.gov.pl/strategie-plany-programy/strategia-dla-cieplownictwa-do-2030-r-z-perspektywa-do-2040-r/ [accessed 16 Feb. 2024].

[9] Lund, H., Werner, S., Wiltshire, R., Svendsen S., Thorsen J.E., Hvelplund F., Mathiesen, B.V. (2014). 4th Generation District Heating (4GDH): Integrating smart thermal grids into future sustainable energy systems. *Energy*, 68, 1−11. doi: 10.1016/j.energy.2014.02.089

[10] Lund, H. (2018). Renewable heating strategies and their consequences for storage and grid infrastructures comparing a smart grid to a smart energy systems approach. *Energy*, 151, 94−102. doi: 10.1016/j.energy.2018.03.010

[11] The project ''Construction of a Cogeneration System in Szlachęcin'' as a Step Towards District Heating Transformation. (in Polish). *Nowoczesne Ciepłownictwo*, Sept. 2022. https://nowoczesne-cieplownictwo.pl/projekt-budowa-systemu-kogeneracji-w-szlachecinie-jako-krok-w-kierunku-transformacji-cieplownictwa/ [accessed 16 Feb. 2024].

[12] Fortum (2022). Heat from wastewater will be fed into Fortum's district heating network in Wrocław (in Polish). https://www.fortum.pl/media/2022/11/cieplo-ze-sciekow-trafi-do-sieci-cieplowniczej-fortum-we-wroclawiu. [accessed 16 Feb. 2024].

[13] Wysocki, T. (2022). The largest heat pump is being built in Wrocław. Wastewater will be used to heat 5,000 flats. *wroclaw.pl* (in Polish). https://www.wroclaw.pl/dla-mieszkanca/powstaje-

wrompa-pompa-ciepla-miejska-siec-cieplownicza-fortum-mpwik [accessed 16 Feb. 2024].

[14] Volkova, A., Koduvere, H., & Pieper, H. (2022). Large-scale heat pumps for district heating systems in the Baltics: Potential and impact. *Renewable and Sustainable Energy Reviews*, 167, 112749. doi: 10.1016/j.rser.2022.112749

[15] Johansen, K., & Werner, S. (2022). Something is sustainable in the state of Denmark: A review of the Danish district heating sector. *Renewable and Sustainable Energy Reviews* 158, 112117. doi: 10.1016/j.rser.2022.112117

[16] Barco-Burgos, J., Bruno, J.C., Eicker, U., Saldaña-Robles, A.L., & Alcántar-Camarena, V. (2022). Review on the integration of high-temperature heat pumps in district heating and cooling networks. *Energy* 239(E), 122378. doi: 10.1016/j.energy.2021.122378

[17] David, A., Vad Mathiesen, B., Averfalk, H., Werner, S., & Lund, H. (2017). Heat roadmap Europe: Large-scale electric heat pumps in district heating systems. *Energies*, 10(4), 578. doi: 10.3390/en10040578

[18] Arpagaus, C., Bless, F., Uhlmann, M., Schiffmann, J., & Bertsch, S.S. (2018). High temperature heat pumps: Market overview, state of the art, research status, refrigerants, and application potentials. *Energy*, 152, 985−1010. doi: 10.1016/j.energy.2018.03.166

[19] Bach, B., Werling, J., Ommen, T., Münster, M., Morales, J.M., & Elmegaard, B. (2016). Integration of large-scale heat pumps in the district heating systems of Greater Copenhagen. *Energy*, 107, 321−334. doi: 10.1016/j.energy.2016.04.029

[20] Popovski, E., Aydemir, A., Fleiter, T., Bellstädt, D., Büchele, R., & Steinbach, J. (2019). The role and costs of large-scale heat pumps in decarbonising existing district heating networks − A case study for the city of Herten in Germany. *Energy*, 180, 918−933. doi: 10.1016/j.energy.2019.05.122

[21] Trabert, U., Jesper, M., Bergstraesser, W., Best, I., Kusyy, O., Orozaliev, J., & Vajen, K. (2021). Techno-economic evaluation of electricity price-driven heat production of a river water heat pump in a German district heating system. *International Journal of Sustainable Energy Planning and Management*, 31, 121–142. doi: 10.5278/ijsepm.6291

[22] Fambri, G., Mazza, A., Guelpa, E., Verda, V., & Badami, M. (2023). Power-to-heat plants in district heating and electricity distribution systems: A techno-economic analysis. *Energy Conversion and Management* 276, 116543. doi: 10.1016/j.enconman.2022.116543

[23] Ziemele, J., & Dace, E. (2022). An analytical framework for assessing the integration of the waste heat into a district heating system: Case of the city of Riga. *Energy*, 254(B), 124285. doi: 10.1016/j.energy.2022.124285

[24] Świerzewski, M., Kalina, J. (2020): Optimisation of biomass-fired cogeneration plants using ORC technology. *Renewable Energy*, 159, 195–214. doi: 10.1016/j.renene.2020.05.155

[25] Świerzewski, M., Kalina, J., & Musiał, A. (2021). Techno-economic optimization of ORC system structure, size and working fluid within biomass-fired municipal cogeneration plant retrofitting project. *Renewable Energy*, 180, 281–296. doi: 10.1016/j.renene.2021.08.068

[26] Mateu-Royo, C., Navarro-Esbrí J., Mota-Babiloni, A., Amat-Albuixech, M., & Molés F. (2018). Theoretical evaluation of different high-temperature heat pump configurations for low-grade waste heat recovery. *International Journal of Refrigeration*, 90, 229–237. doi: 10.1016/j.ijrefrig.2018.04.017

[27] Wang, H., Wang, H., Zhou, H., & Zhu T. (2018). Modeling and optimization for hydraulic performance design in multi-source district heating with fluctuating renewables. *Energy Conversion and Management*, 156, 113–129. doi: 10.1016/j.enconman.2017.10.078

[28] Macuk, R. (2019). *Heating in Poland. Edition 2019. Report*. Forum Energii. https://www.forum-energii.eu/en/download/ download/heating-in-poland-2019-edition [accessed 20 Feb. 2020].

[29] Directive 2010/75/EU of the European Parliament and of the Council of 24 November 2010 on Industrial Emissions (Integrated Pollution Prevention and Control). *Official Journal of the European Union*, L 334/17.

[30] Directive 2015/2193 of the European Parliament and of the Council of 25 November 2015 on the Limitation of Emissions of Certain Pollutants into the Air from Medium Combustion Plants. *Official Journal of The European Union*, L 313/1.

[31] Siemens Energy (2023). Large-scale industrial heat pumps. Siemens Energy Global. https://www.siemens-energy.com/global/en/home/products-services/product-offerings/heat-pumps.html [accessed 16 Feb. 2024].

[32] Modelon (2024). Modelon Case Study: Adapting to The Future of Energy Technology with System Simulation. Modelon Impact. https://modelon.com/support/heat-pump-technology-adapting-to-the-future-with-system-simulation/ [accessed 16 Feb. 2024].

[33] *Proposal for a Directive of the European Parliament and of the Council amending Directive (EU) 2018/2001 on the promotion of the use of energy from renewable sources*, Directive 2010/31/EU on the energy performance of buildings and Directive 2012/27/EU on energy efficiency. COM/2022/222 final. https://eur-lex.europa.eu/legal-content/EN/TXT/?uri=COM:2022:222:FIN [accessed 16 Feb. 2024].

[34] *Project ''The Green Energy Park''*. PEC Gliwice (in Polish). https://parkzielonejenergii.pl/ [accessed 16 Feb. 2024].

[35] Drzozga, A., & Obarski, D. (2022). *Industrial Heat Pumps Technology*. Siemens Energy. Business presentation. Warsaw, February 2022. (Unpublished).

[36] *Industrial Heat Pump. IEA Technology Collaboration Programme on Heat Pumping Technologies (HPT TCP). Annex 58*. Siemens Energy. https://heatpumpingtechnologies.org/annex58/wp-content/uploads/sites/70/2022/07/siemens-energy-hthp-technology.pdf [accessed 16 Feb. 2024].

[37] *Ebsilon Professional.* STEAG energy services GmbH. https://www.ebsilon.com/en/2019. [accessed 16 Feb. 2024].

[38] Kalina, J., Świerzewski, M., & Szega, M. (2017). Simulation based performance evaluation of biomass fired cogeneration plant with ORC. *Energy Procedia*, 129, 660–667. doi: 10.1016/j.egypro. 2017.09.137

[39] Vitec Energy (2023): *NetSim − Grid Simulation System.* https://www.vitec-energy.com/netsim-grid-simulation/ [accessed 16 Feb. 2024].

[40] Pieper, H., Ommen, T., Buhler, F., Paaske, B.L., Elmegaard, B., & Markussen, W.B. (2018). Allocation of investment costs for large-scale heat pumps supplying district heating. *Energy Procedia*, 147, 358–367. doi: 10.1016/j.egypro.2018.07.104.

[41] Danish Energy Agency (2023). *Technology Data for Generation of Electricity and District Heating.* https://ens.dk/en/our-services/projections-and-models/technology-data/technology-data-generation-electricity-and [accessed 16 Feb. 2024].

[42] Grosse, R., Christopher, B., Stefan, W., Geyer, R., & Robbi, S. (2017). Long term (2050) projections of techno-economic performance of large-scale heating and cooling in the EU, *Publications Office of the European Union*, EUR28859. doi: 10.2760/24422

Co-published by
Institute of Fluid-Flow Machinery
Polish Academy of Sciences
Committee on Thermodynamics and Combustion
Polish Academy of Sciences

http://www.imp.gda.pl/archives-of-thermodynamics/

Experimental research of a pumping engine in a micro-ORC system with a low-boiling medium

Tomasz Z. Kaczmarczyk[a*]

[a]Institute of Fluid-Flow Machinery, Polish Academy of Sciences, ul. Fiszera 14, Gdańsk 80-231, Poland
*Author email: tkaczmarczyk@imp.gda.pl

Received: 14.05.2024; revised: 11.10.2024; accepted: 29.10.2024

Abstract

The paper presents the results of experimental research on a pumping engine with the low-boiling medium HFE-7100. The research was conducted in a micro-ORC system with an output of about 2.5 kW_e. Among other factors, the impact of working medium temperature and pump rotational speed on the operating parameters of the gear pump and pumping engine is analyzed. The research shows that increasing the rotational speed and HFE-7100 temperature resulted in an increase in the power consumed by the pump drive and an increase in the effective power of the pump. The increase in the effective power of the pump was greater than the electrical power consumption of the pump drive, resulting in an increase in the volumetric efficiency of the pump. It has been established that, at a constant pump rotational speed of 2000 rpm, increasing the average temperature of HFE-7100 by 27 K from approximately 304 K resulted in a 4% increase in the pump's volumetric efficiency to 80%. It has been established that, for any value of pump rotational speed and working fluid temperature, there exists an optimal effective power value for the pump at which the pumping engine achieves the maximum efficiency.

Keywords: Gear pump; Pumping engine; HFE-7100; Micro-cogeneration; ORC system

Vol. 45(2024), No. 1, 125–140; doi: 10.24425/ather.2024.152002

Cite this manuscript as: Kaczmarczyk, T.Z. (2024). Experimental research of a pumping engine in a micro-ORC system with a low-boiling medium. *Archives of Thermodynamics*, 45(4), 125–140.

1. Introduction

Today, the world is seeing a continuous increase in the demand for electricity [1]. This has contributed to increased exploration and use of energy resources [2], rising energy prices [3], and the energy crisis [4]. This has caused an increase in the emission of pollutants into the natural environment [5]. As a result, many countries have tightened standards, restrictions and rigour related to the emission of pollutants into the environment [6]. Such actions have forced the search for new energy-saving technologies [7] and rational energy management [8], among other things. This involves, among other things, recovering waste energy [9,10], using renewable energy sources (RES) [11], or searching for new high-efficiency systems [12] and energy machines [13]. One possibility that meets the above requirements is the use of combined heat and power (CHP) systems [14], including organic Rankine cycle (ORC) technology [15].

It should be mentioned that ORC systems can be powered by heat sources with a wide temperature range [16]. These systems can use, among other things, waste heat [17] or RES [18], i.e. biomass [19], geothermy [20] or solar energy [21]. It should be noted that in ORC systems, in addition to expansion units (EUs),

Nomenclature

d – diameter, m
Eu – Euler number, $Eu=\Delta p/\rho v^2$
f – frequency, 1/s
g – gravitational acceleration, m/s^2
H – head, m
L – characteristic dimension, m
m – mass flow rate, kg/s
n – rotational speed, rpm
N – power, W
p – pressure, kPa
P – net pump power, W
q – volumetric flow rate, m^3/s
R – range
Re – Reynolds number, $Re=\rho vL/\mu$
t – temperature, °C
v – velocity, m/s
V – elementary capacity, m^3/rev
w – velocity, m/s
x – quality

Greek symbols

Δ – difference
η – efficiency, %
μ – dynamic viscosity, Pa s
ρ – density, kg/m^3
ω – angular velocity, rad/s
Ω – specific speed

Subscripts and Superscripts

1,2 – ordinal numbers
av – average
e – electrical
i – inner
nom– nominal
min– minimal
PE – pumping engine
r – real (measured)
t – thermal
th – theoretical
vol – volumetric
u – effective

Abbreviations and Acronyms

BWR– back work ratio
CHP – combined heat and power
EES – Engineering Equation Solver
EV – expansion valve
EU – expansion unit
GWP – global warming potential
MTG – micro turbogenerator
MR – measurement range
MV – measurement value
ORC – organic Rankine cycle
PE – pumping engine
RES – renewable energy sources
R1 – first temperature range
R2 – second temperature range
VSD – variable speed drive

flow units [22,23] and volumetric units [24], pumping engines (PEs) are essential components [25]. PEs not only determine the proper operation of the entire cogeneration system [26] but also the profitability and investment payback period [27].

One indicator determining the operating efficiency of cogeneration systems is the back work ratio (BWR), which is the ratio of the electrical power consumed by PE to the power produced by EU [28]. BWR is an important indicator considered in sensitivity analysis [29] and the optimisation process [30] of ORC systems with gas turbines [31]. Studies [32] show that BWR is directly correlated with the evaporation temperature of the working medium (R123) and has extremes at which the BWR value is minimum. The value of the BWR indicator depends on the type of working medium. For the same evaporation temperature value, the BWR value of the organic mediums used in ORC systems is higher than that obtained for water. As the critical temperature of the working medium increases, the BWR value decreases [33]. That is why in organic Rankine cycles, unlike in classical steam cycles, the BWR indicator can have a high value. That is why it can significantly affect the efficiency of the ORC system and even cause it to be negative [34]. Then the electric power consumed by PE is greater than the total electric power produced by the expansion unit(s) operating in the micro-ORC system [7].

Therefore, the efficiency of these power machines, and thus their energy intensity, should be as low as possible [35]. That is why new organic media are continually being tested in ORC systems to achieve the lowest possible BWR values [36]. However, it should be emphasised that pumps are mostly designed to operate with water as the working fluid [37]. Meanwhile, the physico-chemical properties of organic working media differ significantly from those of water [38]. Many a time such liquids have much higher density and lower viscosity in relation to water [39]. As a consequence, they can cause higher losses due to internal leaks in pump components and reduce their efficiency and effective delivery head [40]. Additionally, the working fluids used in ORC systems can have adverse effects on pump [41] and microturbine components [42,43], and they can also cause cavitation [44,45]. These phenomena can contribute to machinery malfunctions, which can eventually lead to their damage or breakdown. Therefore, to prevent and eliminate these adverse effects, analyses [46] and numerical simulations [47] are conducted, as well as experimental research [48] when these machines operate in conjunction with each other in ORC systems [49].

For example, Yang et al. [50] conducted a study on a multistage centrifugal pump, hydraulic diaphragm metering pump and roto-jet pump in an ORC system with R245fa refrigerant. The study was conducted with a working fluid temperature at

the pump supply of approximately 30°C and a pressure range of 4 to 11 bar. They determined that the maximum efficiencies of these pumps were 58.76%, 55.26% and 30.51%, respectively. On the other hand, the maximum mechanical efficiency of the multistage centrifugal pump operating in an ORC system with R245fa fluid was approximately 62% [51]. Zeleny et al. [52] conducted a study on a PE with a gear pump operating in an ORC system with a nominal electrical power of approximately 5 kW_e. The pump was supplied with the working fluid, hexamethyldisiloxane. The study shows that, at the operating point of the ORC unit, the maximum isentropic and volumetric efficiencies were approximately 70% and 81%, respectively, and the PE efficiency was approximately 45%. D'Amico et al. [53] conducted a study on a multi-diaphragm pump in a 5 kW_e ORC system. They used R134a as the working fluid. For the nominal operating parameters of the ORC system, the working fluid temperature at the pump supply was approximately 30°C. The study showed that with a differential pressure of approximately 15 bar in the pump, the maximum PE efficiency was approximately 32%, and the maximum volumetric efficiency of the pump was around 94%.

Carraro et al. [54] studied a PE with a multi-diaphragm pump in a 4 kW_e ORC system with R134a as the working fluid. The pump, operating at a supply frequency of 50 Hz, had a rotational speed of 960 rpm and could generate a maximum pressure of approximately 25 bar. The study shows that an important parameter affecting the efficiency of PE is the pump rotational speed. They determined that as the rotational speed of the pump increases, the efficiency of PE increases. At 53% of the rated frequency of the pump drive supply and within a working fluid pressure differential range of 7 bar to 15.5 bar, the efficiency of PE was in the range of 15–24%. When the drive supply frequency was increased to 80% of the rated value, and the rotational speed of the pump was thus increased to 782 rpm, a pressure differential of 15 bar and a maximum PE efficiency of approximately 48% were achieved. On the other hand, further increases in the rotational speed of the drive resulted in a decrease in PE efficiency. Numerical analysis by Zardin et al. [55] shows that at low rotational speeds and high forcing pressures, so-called critical operating conditions arise, resulting in an approximate 15% decrease in the mechanical efficiency of the gear pump.

A study by Misiewicz [56] shows that as the load rate and rotational speed decrease, the efficiency of an electric motor operating in conjunction with a frequency converter decreases. The researchers found that an electric drive operating below 70% of the rated load could result in a reduction in the efficiency of the pump unit by approximately 57%. Similar conclusions were obtained by Yang et al. [57], who studied a piston pump in an ORC system with R123 fluid. The study shows that at low rotational speeds (approximately 8 Hz), the maximum efficiency of PE was around 30%, with the pump's maximum isentropic efficiency of approximately 73%.

However, the total efficiency of PEs used in micro-ORC systems depends not only on the pump efficiency but also on the efficiency of the pump drive and additional equipment, e.g. inverter, etc. For example, a study conducted by Landelle et al. [58] on a PE unit with a reciprocating pump in an ORC system with R134a fluid shows that, regardless of the pump's rotational speed and discharge pressure, the power consumption of the variable speed drive (VSD) is constant. The power balance presented for the PE unit shows that at a maximum pressure of 35 bar and about 33% of the rated rotational speed of the pump, the power lost by VSD was about 44%, and the effective power of the pump was about 40% of the total power of the PE unit. On the other hand, pump and motor losses were 13% and 3%, respectively. Under the rated operating conditions of the pump, the effective power of the pump accounted for approximately 52% of the total power of the PE unit, and the losses in VSD, motor and pump were 19%, 12% and 17%, respectively. The researchers found that at the rated rotational speed of the pump, as the forcing pressure decreases, the effective power of the pump decreases, and the losses in VSD, motor and pump increase.

Feng et al. [59] conducted a study on a plunger pump operating in an ORC system with a capacity of approximately 2 kW_e. The cogeneration system used an expansion unit with a scroll expander, which was powered by the R123 fluid. The study found that the isentropic efficiency of the scroll expander was in the range of 69% to 85%. The researchers determined that the efficiency of the electric generator was in the range of 60% to 73%. On the other hand, the isentropic efficiency of the plunger pump was in the range of 27% to 54%. For these operating conditions of the cogeneration system, the BWR value was in the range of 14% to 32%. The work highlights that the maximum theoretical thermal efficiency of this cycle was approximately 11%, and the maximum thermal efficiency confirmed by the study was about 5%. On the other hand, a study [60] conducted on a diaphragm metering pump in an ORC system with R123 fluid demonstrates that as the BWR indicator increases, the thermal efficiency of the cycle decreases. On the other hand, the ORC system's thermal efficiency was 0.13% and was similar to the results obtained by Gao et al. [61].

On the other hand, Komaki et al. [62] found that an alternative to commercial solutions could be a rotary jet pump (known as a Pitot pump), which could ensure not only a higher delivery head but also a higher flow at a higher efficiency. Literature data [63] show that the delivery head of a Pitot tube pump can be approximately 1.6 times higher than that of a conventional centrifugal pump operating at the same speed. Because in this design (Pitot pump), high rotational speeds of the pump are not necessary to generate high forcing pressure. In addition, the Pitot pump can also produce high pressure of the liquid at a low flow rate of the working fluid.

As part of the literature review, it is worth mentioning that research is also being conducted on so-called pumpless ORC

systems. A study by Jiang et al. [64] demonstrated that the maximum electrical efficiency of a pumpless ORC system with a 1 kW_e scroll expander powered with R245fa was 2.4%. Theoretical calculations by Gkimisis et al. [65] demonstrate that pumpless micro-ORC systems can achieve a maximum thermal efficiency of approximately 5%. On the other hand, according to Richardson [66], in the case of two-stage systems with thermofluidic pumps, the theoretical efficiency of these ORC systems can be approximately 7.5%. However, it should be emphasised that these systems require advanced control and regulation systems and have a more complex structure compared to systems with PEs.

The conducted review of the thematic literature shows that, despite high pump efficiencies [67], the efficiency of the remaining components of the unit also has a fundamental impact on the total efficiency of the PE. As a result, the maximum efficiencies of PEs operating in micro-ORC systems did not exceed 48%. Moreover, the application of a different operating medium to the same type of pump gives different results obtained during experimental tests. As the review shows, the results obtained by experimental testing differed significantly from those obtained during theoretical calculations. For example, the theoretical efficiencies of the pumps and PEs were more than twice as high as the efficiencies noted during the experimental research. Hence, one can see the existing necessity to conduct experimental research on PEs operating in micro-ORC systems.

The paper presents a study conducted on a PE with a gear pump and the low-boiling fluid HFE-7100. Currently, there is a lack of experimental study on PE with such a medium in the thematic literature. It should be emphasised that HFE-7100 is environmentally friendly and possesses good thermodynamic properties as a potential working fluid for ORC systems. The HFE-7100 medium has a GWP value of 320, which is significant in terms of environmental assessment [69]. However, this medium is categorised as a solvent, which, consequently, can have an adverse effect on some construction materials of the pumps, as demonstrated in this work. That is why the experimental research results presented can also have a practical application in addition to the scientific aspects. Moreover, the research presents the effect of changing the temperature of the working fluid on the operating parameters and performance of the pump and PE, which will certainly contribute to filling the existing literature gap in this subject area. The work presents the performance characteristics of the PE and the pump based on dimensionless numbers, which will facilitate other researchers in comparing their research results and analyses. The PE characteristics presented as a function of dimensionless numbers enable researchers to compare their research results for different types of pumps effectively, spanning a wide power range. Moreover, it will be possible to compare PE research for the various working mediums used in ORC systems. The author's motivation and rationale for conducting experimental research, based on the author's experience, are presented in Section 2.

2. Motivation and rationale for conducting the experimental research

Most pumps available on the commercial market mainly have operating characteristics specified for water as the working medium. Manufacturers do not always provide the operating characteristics of pumping engines specified for the new working mediums used in ORC systems. It should be noted that there is also limited information on the durability and compatibility of pump construction elements for these new operating mediums. That is why, in the commercial market, the selection of pumping engines with the required operating parameters for the ORC system with the HFE-7100 medium was largely limited. It should be emphasised that the cost of purchasing a commercial PE is several times less than the price to be paid for individually designing and building a prototype pumping engine [49]. This means that using a commercial PE in an ORC system can be justified economically, as it can significantly reduce the total cost of the microsystem.

In ORC micro-CHP systems, pumping engines are characterised by specific operating conditions due to the required high pressure and low flow rate of the working medium in the cycle [68]. For example, for an ORC system with a 2.5 kW_e microturbine, a nominal supply pressure of approximately 1100 kPa is required at an HFE-7100 medium flow rate of approximately 0.17 kg/s [70].

The study [38] conducted on a commercial PE with a PK70-type rotodynamic pump showed that the pump's discharge pressure rise was too low in relation to the HFE-7100 medium flow rate ($\Delta p/m$). As a result, at the required nominal vapour pressure at the inlet of the expansion valve, the value of the working medium flow rate was several times higher than the nominal value. This resulted in the micro-ORC system with a 25 kW_t biomass boiler not being able to generate vapour at the required parameters, thus failing to ensure the appropriate superheating degree of HFE-7100 directed to the expansion unit. Supplying a flow expansion unit with wet vapour or liquid working medium can cause it to malfunction, reduce efficiency, and even fail. On the other hand, the study showed that the maximum efficiency of the PK70-type rotodynamic pump operating in the micro-ORC system with and without regeneration was 11.7% and 14.7%, respectively. This was due, among other factors, to internal losses in the pump, which increased the energy consumption of the pump. The HFE-7100 medium has approximately 1.5 times the density of water, and kinematic viscosity is more than twice as low.

A study conducted by Mathias et al. [71] on an ORC system with R123 medium showed that the gear pump was very energy-consuming, consuming about 2.2 kW. The researchers found that the duplex (positive-displacement) piston pump was less energy-consuming, with a power consumption of about 390 W and an isentropic efficiency of about 69% (including the motor).

On the other hand, the study [72] found that the HFE-7100 medium had virtually no lubricating properties and the use of

rolling bearings caused the grease to be washed out, increasing the vibration level and ultimately damaging the expansion unit. HFE-7100 is a solvent primarily used in industry as a cleaning and washing agent. Therefore, using a piston pump and direct contact with the HFE-7100 medium would result in its damage. That is why, based on the above experience and literature data, an intermediate option was decided upon, namely the use of a diaphragm pump (type D/G-03, produced by HYDRA-CELLTM PUMP) in the ORC system and PE tests [25]. From the experimental tests carried out, it became apparent that after approximately 5 hours of PE operation with the HFE-7100 medium, the pump diaphragms were damaged (Fig. 1), and the lubricating oil from the diaphragm pump penetrated into the working medium cycle. It should be mentioned that at the time of selection and purchase, both the sellers of the working medium and the pumping engine declared the compatibility of the construction materials used for PE with the HFE-7100 medium. Moreover, the static chemical resistance to the HFE-7100 medium (the immersion test lasted 30 days) of the material samples (EPDM, Viton, Teflon), from which the pump diaphragms were made, was also confirmed by experimental tests conducted at the Institute of Fluid-Flow Machinery of the Polish Academy of Sciences (IFFM PAS) in Gdańsk.

Thus, during these tests, it was demonstrated that the material used from the pump diaphragms lacks resistance to the HFE-7100 liquid under varying dynamic loads, rendering PE unsuitable for use in the ORC system together with the diaphragm pump. It should be emphasised that there is currently a shortage of such studies and data in both the thematic literature and pump manufacturers' databases. That is why it is worth bearing in mind that the use of new working mediums that have not been fully tested brings many uncertainties to both the design and experimental testing of the components (i.e. PE) of an ORC system. It must then be assumed that the new working medium can be one of the causes of damage to the seals of the machines and their components and cause an increase in internal leakage in these devices [49,38], which, consequently, can lead to a reduction in their functionality and efficiency.

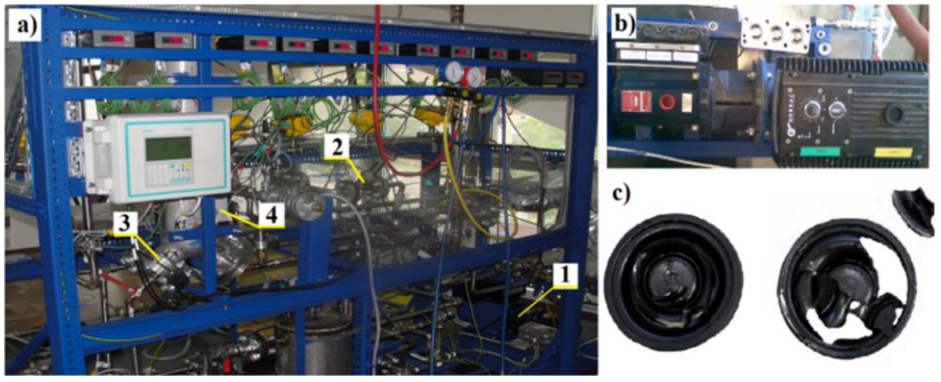

Fig. 1. a) ORC test rig, b) dismounted diaphragm pumping engine, c) damaged diaphragms; 1 – diaphragm pumping engine, 2 – expansion valve, 3 – regenerator, 4 – evaporator [25].

Research was also conducted with the HFE-7100 medium of a prototype Roto-Jet pump with a nominal rotational speed of 8000 rpm, a flow rate of 0.3 m^3/h and a specific speed of 2.19, which was designed and built at IFFM PAS, in Gdańsk [49]. The study showed that superheating of the working medium before entering the expansion valve was only achieved at a few points in the ORC system without regeneration, whereas in the system with regeneration, the HFE-7100 medium was in the wet vapour region. It was determined that the experimental results deviated to a significant extent (approximately 21%) from the design assumptions, analytical calculations, and 3D numerical calculations performed based on classical computational models [49]. Detailed analyses of the test results obtained showed that the working medium databases implemented in the computational models were incorrect. As it turned out, the properties of the mediums implemented in the commercial calculation programs, such as Engineering Equation Solver (EES) or Aspen Plus, commonly used in engineering calculations, differ significantly from the data obtained through experimental studies. For the HFE-7100 medium, for example, the maximum difference in kinematic viscosity (at 0°C) between the experimental data of Rausch et al. [73] and the data obtained from the EES program was approximately 32%. The same is true of the working medium database, e.g. REFPROP 9.1, which does not contain complete data on the thermophysical and physicochemical properties of the working medium HFE-7100. On the other hand, manufacturers of working mediums typically provide physicochemical data in their catalogues for only a single point, for normal or standard conditions (at 25°C and 1013.25 hPa). That is why ongoing efforts are being made to create reliable databases for new working mediums [74]. It should be borne in mind that the working mediums adopted for ORC systems repeatedly have a completely different application predicted by the manufacturer, as mentioned above.

To recapitulate, it can be stated that the rationale for conducting PE tests with a gear pump was driven, among other factors, by the uncertainty and lack of complete knowledge of the HFE-7100 medium used in the ORC system. Based on previous experience with this medium, it was necessary to investigate the PE under real operating conditions in a microsystem. This was due, among other factors, to the necessity of establishing the chemical interaction of this medium with the pump's structural components, determining the performance characteristics of the pump operating in the micro-ORC system, and filling the literature gap in this area. That is why this question is of interest both in terms of content and research. On the other hand, one

of the objectives of this study was to determine whether and to what extent the pumping engine can operate with the low-boiling liquid HFE-7100 in the micro-ORC system, and if so, what the actual operating characteristics of PE are.

3. Test bench

A study on a PE with a gear pump was conducted in a micro-CHP ORC system, a diagram and photograph of which are shown in Figs. 2 and 3, respectively. The micro-ORC system ultimately operates in conjunction with a 2.5 kW_e micro turbo-generator (MTG) [75] powered by the vapour of the HFE-7100 working fluid [21]. The basic physicochemical parameters of the low-boiling fluid HFE-7100 are listed in Table 1. It should be noted that HFE-7100 is a dry working medium, as shown in the T-s diagram (Fig. 4). In view of the above, the PE should ensure nominal operating parameters for MTG, among others:

- mass flow rate (m_{nom}) – 0.17 kg/s,
- nominal vapour differential pressure in the microturbine (Δp_{nom}) – 1000 kPa,
- minimal vapour differential pressure in the microturbine (Δp_{min}) – 450 kPa.

The test rig used for the research on the PE consisted of three cycles: the heating cycle, the HFE-7100 working fluid cycle and the cooling cycle. A prototype two-module induction heater with a nominal power of 2 × 24 kW_e was used to heat the thermal oil. The vapour of the working fluid from the expansion valve (EV) was directed successively to the condenser and then to the tank from which the PE was fed. The thermal oil was directed to the evaporator after being heated to a set temperature. A plate heat exchanger with a heat exchange surface area of 4.1 m^2 was used as an evaporator. The HFE-7100 working fluid, pumped by the PE, vaporised while flowing through the evaporator. It was then directed to the EV, which simulated MTG operation. The EV was used to throttle the flow of the working fluid and thus constituted the load for the tested PE. A plate heat exchanger with a heat exchange surface area of 3.2 m^2 was used as the condenser.

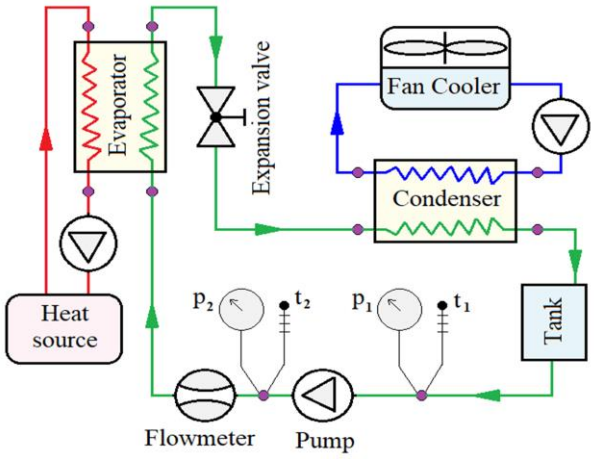

Fig. 2. Simplified diagram of a micro-ORC system: t_1 and t_2 – temperature measurement points at the pump inlet and outlet, p_1 and p_2 – pressure measurement points at the pump inlet and outlet.

Table 1. Selected physicochemical properties of the HFE-7100 working fluid at a temperature of 25°C and atmospheric pressure [21].

Properties	Values	Units
Boiling Point	61	°C
Liquid Density	1510	kg/m³
Dynamic Viscosity	0.61	mPa s
Specific Heat	1183	J/kg K
Surface Tension	0.0136	N/m

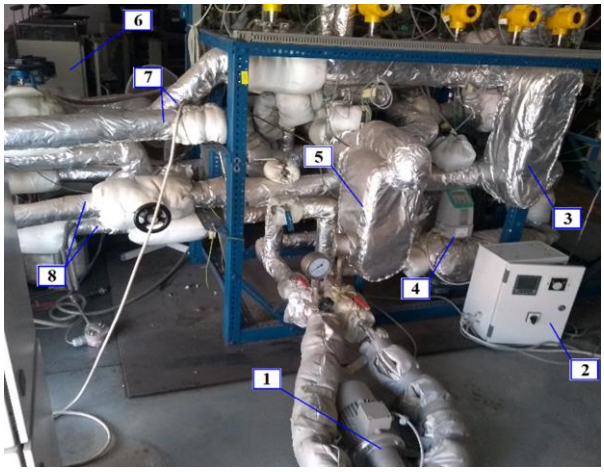

Fig. 3. Micro-ORC power plant test rig: 1 – pumping engine, 2 – frequency converter connected to the PE drive, 3 – evaporator, 4 – Coriolis mass flowmeter, 5 – condenser, 6 – control and regulation module for the induction heater, 7 – heating cycle piping, 8 – cooling cycle piping.

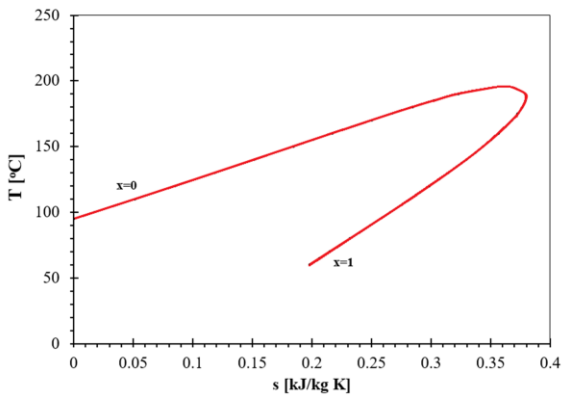

Fig. 4. T-s diagram of the HFE-7100 working medium.

The heat from the condenser on the working fluid side was dissipated using a 50 kW_t fan cooler. In the fan cooler, a 40% solution of propylene glycol in distilled water was used as the working fluid.

3.1. Pumping engine

The tested PE was a commercial design that consisted of a gear pump (1.1), which was connected to an electric drive (1.3) via a magnetic coupling (1.2), as shown in Fig. 5. The technical data and operating parameters of the gear pump and electric drive are provided in Table 2.

Table 2. Selected technical data of PE (according to manufacturer's data).

Gear pump		Electric drive	
Manufacturer	Scherzinger	Manufacturer	Küenle
Type	gear	Type	synchronous
Model	4030-450-DM 075	Model	KTENW 80 K2 KT
Displacement	4.5 cm³/rev	Class of construction	IE2
Maximum differential pressure	14 bar	Efficiency	77.4%
Maximum flow rate	15.75 l/min	Power rating	750 W
Maximum rotational speed	3,500 rpm	Rotational speed	3,000 rpm
Outer diameter of the gear wheel	25 mm	Rated voltage	230/400 V
Pitch diameter of the gear wheel	20 mm	Rated current	3.0/1.7 A
Inner diameter of the suction port	14.5 mm	Frequency	50 Hz
Inner diameter of the discharge port	14.5 mm	cos φ	0.80
Temperature range	from -20°C to +130°C	Insulation class	F
Maximum inlet pressure	100 bar	Ingress Protection code	IP55

The PE was connected to the micro-ORC system with the help of corrugated pipes (9,10) made of stainless steel. Manovacuometers (11,12) and shut-off valves (13,14) were fitted to the suction and discharge piping. The rotational speed of the gear pump was controlled by varying the frequency of the motor power supply using an inverter of the type SV015iG5A-4, manufactured by LS Electronics.

3.2. Test apparatus and measurement errors

K-type thermocouples with a diameter of 0.5 mm were used to measure the temperature of the working fluid before and after the pumping engine. On the other hand, pressure transducers and manovacuometers were used to measure pressures. The flow rate of the working fluid was measured using a Coriolis flowmeter (Fig. 2). The schedule and specifications of the measuring apparatus used for the PE tests are included in Table 3.

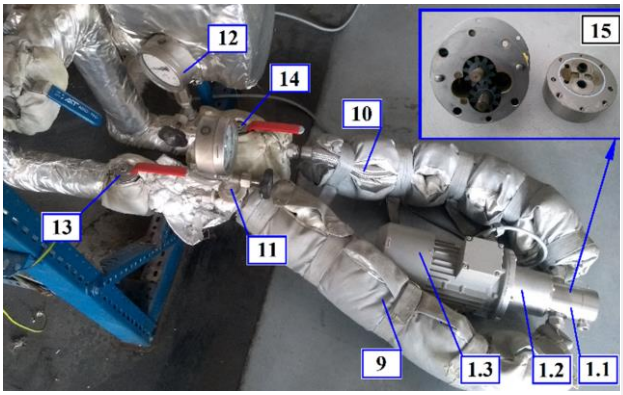

Fig. 5. Photograph of the PE on the test rig: 1.1 – gear pump, 1.2 – magnetic coupling, 1.3 – electric drive, 9 – pump supply pipe, 10 – pipe at the outlet of the gear pump, 11 and 12 – analogue manovacuometers fitted to the suction and discharge piping, respectively, 13 and 14 – shut-off valves fitted to the suction and discharge piping, respectively, 15 – the inside of the gear pump housing.

The standard uncertainties of the dimensionless numbers Re and Eu were 0.8% and 0.5%, respectively, as calculated from the relation (1):

$$u(k) = \left(\Delta k/\sqrt{3}\right) \cdot 100\%. \quad (1)$$

where: Δk – maximum uncertainty.

Table 3. Test apparatus and measurement sensors.

Instrument: type/model	Manufacturer	Range	Accuracy
Thermocouple: K-type, Class 1	Czaki Thermo-Product	-40°C – 600°C	± 0.0040·|t| [°C]
Pressure transducer: type NPXA, Class 0.1	Peltron	0 – 16 bar	± 0.1% MR
Analogue manovacuometer: Class 1.0	Wika	0 – 16 bar	± 0.16 bar MV
Coriolis mass flowmeter: model Sitrans FC, type Mass 2100	Siemens	0 – 5,600 kg/h	± 0.1% MV
Meter of network parameters, type ND20	Lumel	0.002 – 1.200 A 0.010 – 6.000 A	± 0.2% MR
		5 – 480 V	± 0.5% MR
		-1.65 – 1.65 kW	± 0.5% MR
		-1.65 – 1.65 kVar	± 0.5% MR
		1.4 – 1.65 kVA	± 0.5% MR

MR – measurement range, MV – measurement value

Manovacuometers were used as additional measuring instruments to monitor pressure during the start-up of the ORC system. A meter of network parameters, of the type ND20, was used to measure the electric power consumed by the pumping engine drive. All measured quantities were recorded and archived by

a measurement system from National Instruments (NI). A program specifically written in the LabView environment was utilised to record, archive, and visualize the measurement data. All measured quantities were recorded every 1 second on an NI measurement computer.

4. Methodology and research procedure

The research methodology of the PE is shown in Figure 6. The PE was tested at three preset rotational speeds: n_1 = 1000 rpm, n_2 = 1500 rpm, and n_3 = 2000 rpm. At each preset rotational speed, the PE was tested in two temperature ranges (R1 and R2) of the HFE-7100 working fluid, which were measured at the pump supply. The temperature waveforms of the HFE-7100 working fluid measured at the pump supply depending on the pump's differential pressure for the preset rotational speeds of the pump are shown in Fig. 7.

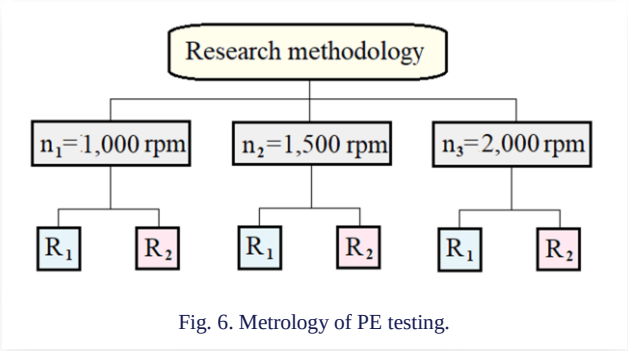

Fig. 6. Metrology of PE testing.

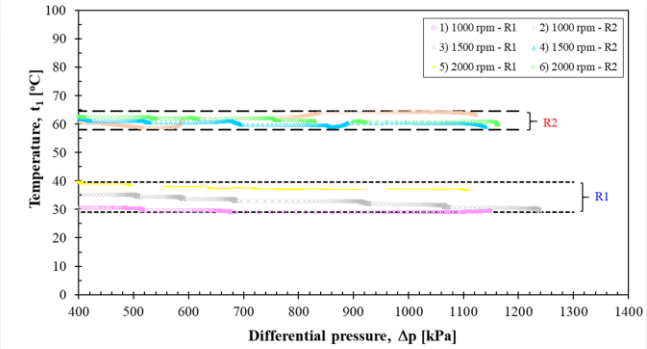

Fig. 7. Temperature ranges of HFE-7100 versus differential pressure of the pump unit.

The first temperature range (R1) of the HFE-7100 working fluid (t_1 – Fig. 7) covered the range from 29°C to 39°C, and the second (R2) from 58°C to 64°C. In R1, the average temperature value of HFE-7100 was t_{av1}=34 ±5 °C, and in R2, it was t_{av2}=61 ± 3 °C. It should be emphasised that the boiling point of HFE-7100 at atmospheric pressure is 61 °C. That is why the working fluid with a temperature of 61 °C directed from the tank to the pump's suction channel should have a pressure higher than atmospheric to avoid cavitation. The pressure of the working fluid behind EV was regulated by a condenser heat removal system (Fig. 2).

The temperature ranges R1 and R2 were determined based on the technical capabilities of the heat removal system for the heat exchangers (evaporator and condenser). The tolerances in the average temperature values of HFE-7100, and thus the ranges R1 and R2, were, among other things, due to the limited possibilities of regulating the operating parameters of the cycles as a result of the high thermal inertia of the ORC system. Therefore, maintaining small temperature tolerances with the required minimum differential pressure (450 kPa) of the working fluid for the preset rotational speeds of the pump was rendered difficult, particularly in the R2 range.

That is why the proposed research methodology had two principal objectives. Firstly, to verify: At what operating parameters will PE ensure nominal operating conditions for MTG? Secondly, at what rotational speed levels (n_1, n_2, n_3) and preset temperature levels (R1, R2) of the low-boiling fluid HFE-7100 will the efficiency of PE be the highest?

4.1. Research procedure

The research procedure involved setting the power and oil temperature on the control panel of the electric induction heater, which were 30 kW_t and 200°C, respectively, under the nominal operating conditions of MTG. Then, the oil pump was started, and a verification of the correct operation of the measuring apparatus and indications of measuring instruments was performed. After positive tests, the electric induction heater was put into operation. The rotational speed of the oil pump, and thus the value of the oil flow rate in the heating cycle, was regulated using an inverter.

The system's heating process was carried out until the thermal oil temperature reached approximately 100°C. At that time, the fan cooler and glycol pump were started, and the proper operation of the measurement system in this cycle was checked. Then, the process of starting the working fluid cycle, in which the tested PE was mounted, was initiated. Using an inverter, the present rotational speed (i.e., n_1, n_2 or n_3) of the PE, and thus the flow rate value of the HFE-7100 working fluid, was set. At this stage of the research, the expansion valve was fully open. At that time, the forcing pressure value of the working fluid was approximately 120 kPa.

For this value of working fluid pressure and a thermal oil temperature of about 100°C, the process of complete evaporation of HFE-7100 in the evaporator occurred. By varying the flow rate of the glycol solution, the average temperature of the working fluid, t_{av1} or t_{av2}, was regulated to fall within the present range of R1 or R2. Control of the flow rate of the glycol solution in the cooling cycle was realised by changing the rotational speed of the glycol pump using an inverter. Once the microsystem was warmed up and the set temperature (t_{av1} or t_{av2}) was within the tolerance limit (R1 or R2), the process of loading PE commenced. PE was loaded by means of changing the degree of opening of the expansion valve, which made it possible to determine the so-called choking characteristics. The same procedure was used for each preset rotational speed of PE.

5. Calculation methods

The effective (useful) delivery head of the pump H_u was calculated from Eq. (2):

$$H_u = \Delta p/g\rho. \quad (2)$$

The volumetric efficiency of the pump was calculated from Eq. (3):

$$\eta_{vol} = (m_r/m_{th})\ 100\%. \quad (3)$$

The value of the theoretical flow rate of the pump was calculated from Eq. (4):

$$m_{th} = \rho V f. \quad (4)$$

The specific speed of the pump was calculated from Eq. (5):

$$\Omega_s = \omega q^{1/2}/(gH)^{3/4}. \quad (5)$$

The delivery head of the pump was calculated from Eq. (6):

$$H = p_2/g\rho. \quad (6)$$

The net (effective) power of the pump, P_u, was calculated from Eq. (7):

$$P_u = q\Delta p. \quad (7)$$

The efficiency of the pumping engine, η_{PE}, was calculated from Eq. (8), which has the form:

$$\eta_{PE} = (P_u/N_e)\ 100\%. \quad (8)$$

As mentioned earlier, one of the essential parameters required from PE is an adequate differential pressure (Δp) of the working fluid. That is why the dimensionless parameter Euler number (Eu) was introduced into the analysis, which was calculated from Eq. (9):

$$Eu = \Delta p/\rho w^2. \quad (9)$$

The flow velocity was calculated from Eq. (10):

$$w = q/(\pi d_i^2/4). \quad (10)$$

The nature of flow of the working fluid through the pump was determined based on the Reynolds number (Re), which was calculated from Eq. (11):

$$Re = w\rho d_i/\mu. \quad (11)$$

6. Results and discussions

As mentioned earlier, the differential pressure in the pump (Δp) is one of the essential parameters required for the correct operation of expansion microunits. That is why the elaborated experimental performance characteristics of PE are presented as a function of differential pressure, among others, as detailed in Section 6.1. The efficiency characteristics of the pump and PE are discussed in Section 6.2. On the other hand, an analysis of PE operation in the ORC system based on dimensionless numbers is provided in Section 6.3.

6.1. Analysis of the effect of differential pump pressure

Figure 8 shows that with an increase in the differential pressure value (Δp), the useful delivery head of the pump (H_u) increased. It was observed that the pump rotational speed did not have a fundamental impact on the value of the useful delivery head of the pump.

This manifested itself in the fact that the measurement data labelled 1, 3 and 5 (see Fig. 8), being in the R1 temperature range, could be approximated by a single line. Similarly, in the R2 temperature range, the measurement data (labelled 2, 4 and 6 in Fig. 8) aligned along a single approximation line (broken line). Furthermore, it was found that irrespective of the temperature of the working fluid, the useful delivery head of the pump increased with the rise in the differential pressure generated by the pump. On the other hand, an increase in the temperature of the working fluid at the same differential pressure resulted in a further increase in the value of the useful delivery head (ΔH_U) of the pump. This was manifested by the increase in the slope value of the approximating straight lines.

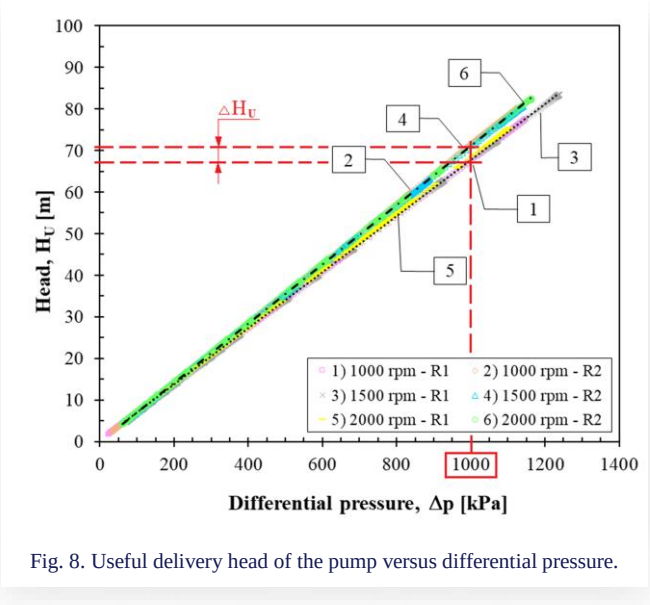

Fig. 8. Useful delivery head of the pump versus differential pressure.

Figure 9 shows the electric power (N_e) consumed by the PE drive versus differential pressure. The study reveals that, regardless of the temperature of the working fluid, the electric power consumed by the PE drive is directly proportional to the differential pressure of the pump.

It was determined that as the rotational speed and the temperature of the working fluid increase, the power consumed by the pump increases. In the analysed case, for this same value of differential pressure and at a pump rotational speed of 1000 rpm, the temperature increase from R1 to R2 resulted in an increase in the electric power ($\Delta N_{e\text{-}n1}$) consumed by the pump drive by 26 W_e. On the other hand, at a rotational speed of

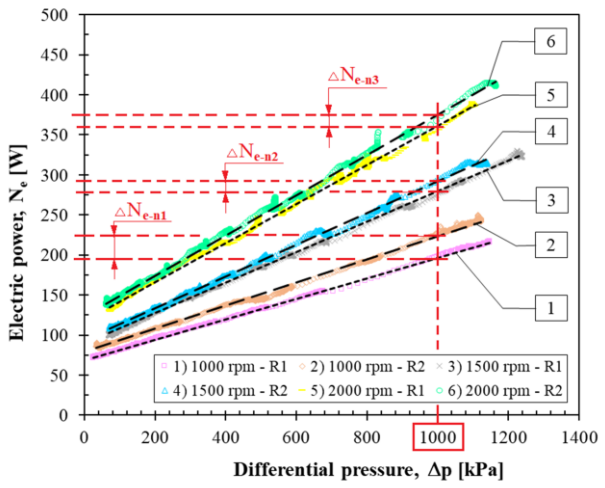

Fig. 9. Electric power consumed by the PE drive versus differential pressure.

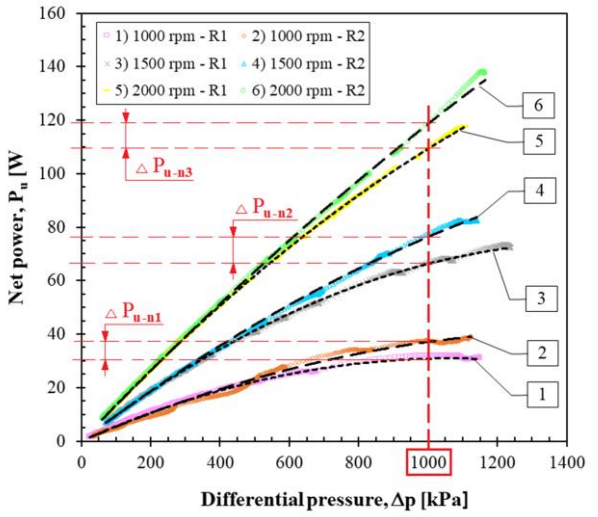

Fig. 10. Dependence of the net pump power on the differential pressure.

1500 rpm, an increase in the consumed electric power ($\Delta N_{e\text{-}n2}$) of approximately 18 W_e was recorded. In the case when the pump rotational speed was 2000 rpm, the increase in electric power consumption ($\Delta N_{e\text{-}n3}$) by the pump drive was approximately 16 W_e. This means that as the rotational speed increases, the electric power consumption by the PE drive decreases (Fig. 9). Table 4 includes the values of power consumed by the PE drive for preset pump rotational speeds and a differential pressure of 1000 kPa.

Table 4. Operating parameters of PE for a differential pressure of 1000 kPa and preset pump rotational speeds.

Characteristics	Parameters	Pump rotational speed			Units
		1000	1500	2000	rpm
$H_u(\Delta p)$	R1	67	67	67	m
	R2	71	71	71	m
	ΔH_u	*6*	*6*	*6*	%
$N_e(\Delta p)$	R1	199	278	359	W
	R2	225	295	375	W
	ΔN_e	*13.1*	*6.1*	*4.4*	%
$P_u(\Delta p)$	R1	31	66	110	W
	R2	37	77	120	W
	ΔP_u	*19.3*	*16.7*	*9.1*	%

Figure 10 shows that the effective power of the pump increases with increasing differential pressure and rotational speed of the pump. It was observed that above a differential pressure of about 450 kPa, the temperature of the working fluid has a fundamental impact on the effective power of the pump. It also results from this that at the first ($\Delta P_{u\text{-}n1}$), second ($\Delta P_{u\text{-}n2}$) and third ($\Delta P_{u\text{-}n3}$) rotational speeds, the increases in the effective power of the pump were 6 W, 9 W, and 10 W, respectively. This means that at a constant differential pressure, there was an increase in the average effective power of the pump as the temperature of the working fluid increased. As mentioned earlier, the second necessary condition for the use of PE in the micro-ORC system and the correct operation of MTG is to ensure an adequate flow rate of the working fluid.

6.2. Analysis of the effect of ORC system operating parameters on PE efficiency

As mentioned earlier (Section 3), the value of the nominal flow rate of HFE-7100 in the 2.5 kW_e MTG is approximately 0.17 kg/s. Moreover, the pump is required to have the highest possible efficiency. That is why Fig. 11 shows the dependence of the volumetric efficiency of the pump on the flow rate of the working fluid. The study (Fig. 11) reveals that as the pump rotational speed increases, the slopes (α) of the straight lines approximating the pump efficiency versus the working fluid flow rate decrease. That is why, as the pump rotational speed increases, the characteristics are steeper. For example, for a rota-

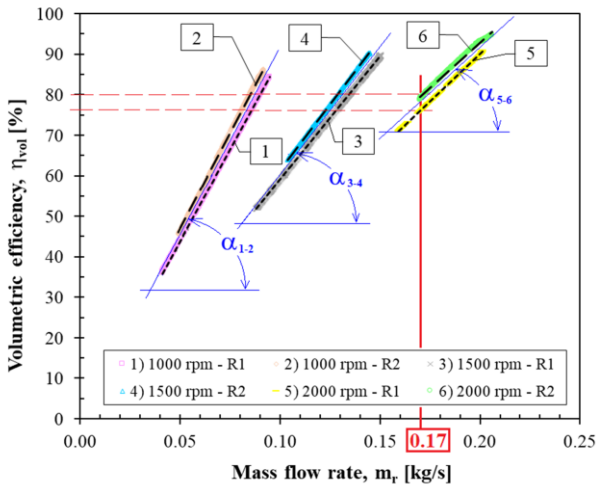

Fig. 11. Dependence of pump volumetric efficiency on the HFE-7100 flow rate.

tional speed of 1000 rpm, the average value of the angle ($\alpha_{1\text{-}2}$) within the temperature range R1 and R2 was approximately 62° (Fig. 11). For a rotational speed of 1500 rpm, the average value of the $\alpha_{3\text{-}4}$ angle was approximately 52°. On the other hand, for a pump rotational speed of 2000 rpm, the value of the $\alpha_{5\text{-}6}$ angle was approximately 42°.

It has been established that a 500 rpm change in the rotational speed of the pump results in a change of the inclination angle of the straight line approximating the volumetric efficiency of the pump by 10°. That is why, at low rotational speeds (lines 1 and 2), a small change in the flow rate of the working fluid results in a large change in the volumetric efficiency of the pump.

The study reveals that an increase in the temperature of the working fluid results in an increase in the volumetric efficiency of the pump. For example, for a flow rate of 0.17 kg/s (Fig. 11) in the R1 temperature range, the average value of the pump volumetric efficiency was approximately 76%, and in the R2 range, it was approximately 80%. Furthermore, it can be seen from Fig. 11 that achieving an HFE-7100 flow rate equal to 0.17 kg/s is only possible with a pump rotational speed of at least 2000 rpm (lines 5 and 6).

Figure 12 shows that an increase in the rotational speed of the pump resulted in an increase in the efficiency of the PE. It has been established that for each value of speed and working fluid temperature, there exists an optimum effective power value for the pump at which the efficiency of PE is maximum. For a pump rotational speed of 1000 rpm, in the R1 temperature range, the maximum PE efficiency of approximately 17.0% was achieved with an effective power of 25 W. On the other hand, an increase in the HFE-7100 temperature from R1 to R2 resulted in an increase in PE efficiency to 17.2%, which was obtained with an effective power of 30 W.

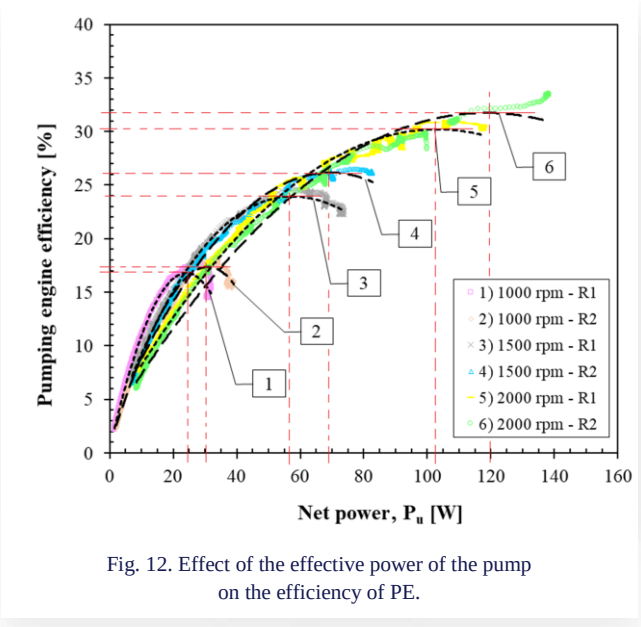

Fig. 12. Effect of the effective power of the pump on the efficiency of PE.

Similarly, at pump rotational speeds of 1500 rpm and 2000 rpm, the increase in temperature resulted in an increase in the efficiency of PE. The maximum efficiencies of PE at a rotational speed of 1500 rpm for the temperature ranges R1 and R2 were 19.0% and 26.0%, respectively. On the other hand, at a rotational speed of 2000 rpm, the efficiency maxima for the R1 and R2 ranges were 30.2% and 31.8%, respectively.

These efficiency values were obtained at the effective powers of the pump, which were 103 W and 120 W, respectively. It is worth noting that for a pump rotational speed of 2000 rpm (at the MTG's nominal operating point), regardless of the HFE-7100 temperature, the volumetric efficiencies of the pump were approximately 60% higher (Fig. 12) than the PE efficiencies obtained. This means that not only the pump but also the efficiencies of the drive and magnetic coupling have a very significant impact on the efficiency of PE. At a nominal rotational speed of 3000 rpm, the efficiency of the electric drive is approximately 77%. That is why PE operation below the rated rotational speed of the electric drive resulted in significant losses.

6.3. Analysis of PE operation in terms of dimensionless numbers

Figure 13 shows that the temperature of the working fluid has a fundamental impact on the value of the Reynolds number (Re). It was determined that at the nominal flow rate of the MTG (i.e., 0.17 kg/s), in the HFE-7100 temperature range R1, Re was approximately 30 000. On the other hand, in the R2 range of working fluid temperatures, the Re number was approximately 40 800. As can be seen in Fig. 13, the value of the Re number over the entire investigated range of temperatures (R1 and R2) and pump rotational speeds (n_1 to n_3) was above 3000. This means that the flow of the working fluid was turbulent.

Furthermore, the study reveals that the measurement data obtained in the R1 temperature range over the entire range of rotational speeds could be approximated by a single line. On the

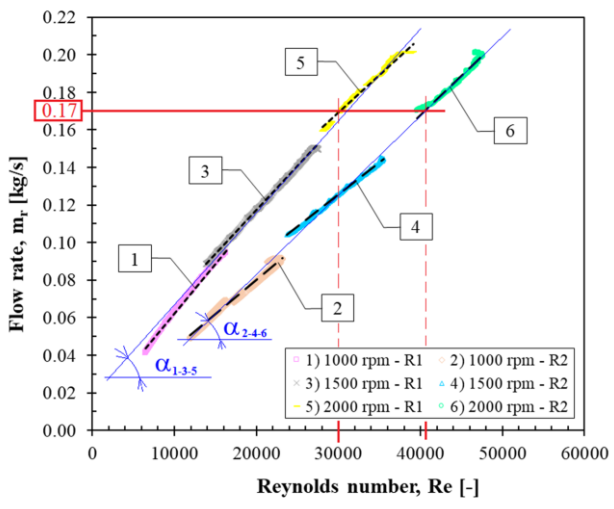

Fig. 13. HFE-7100 flow rate versus Re number.

other hand, the angle value of the slope ($\alpha_{1\text{-}3\text{-}5}$) of this straight line was approximately 48°. In the case when the working fluid temperatures were in the R2 range, the angle value ($\alpha_{2\text{-}4\text{-}6}$) was approximately 44°. That is why it can be deduced that as the temperature of the working fluid increased, the value of the Reynolds number increased.

Figure 14 shows that the value of the working fluid temperature and Re have a fundamental impact on the volumetric efficiency of the pump. It was observed that as the working fluid temperature and pump rotational speed increase, the characteristics of the pump efficiency shift to the right towards larger values of the Re number.

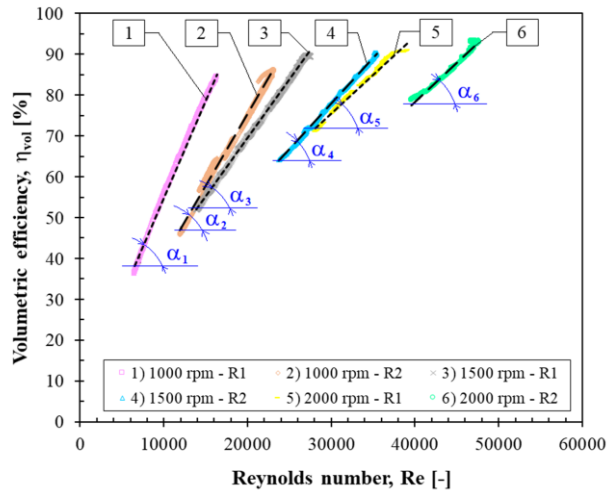

Fig. 14. Dependence of pump volumetric efficiency on Re number.

Furthermore, as the temperature increased, the characteristics were flatter, which manifested itself as a reduction in the value of the slope of the approximating straight lines. For a pump rotational speed of 1000 rpm, the inclination angle of the function (α_1) in the R1 temperature range was approximately 67°. In the same temperature range and at a rotational speed of 1500 rpm, the α_3 inclination angle was approximately 53°, and at a rotational speed of 2000 rpm, the value of the α_5 angle was approximately 44°. On the other hand, in the R2 temperature range, the values of angles α_2, α_4 and α_5 (see Fig. 14) corresponding to the pump rotational speeds of 1000 rpm, 1500 rpm and 2000 rpm were 60°, 47° and 42°, respectively.

That is why it can be deduced that at low pump rotational speeds and low working fluid temperatures, small changes in the Reynolds number result in significant changes in the volumetric efficiency of the pump.

Figure 15 shows the dependence of the electric power consumed by the PE drive on the specific speed. In addition, the study reveals that irrespective of the pump rotational speed, a change in working fluid temperature from R1 to R2 caused the pump power curves to intersect at the so-called 'characteristic points' (Fig. 15). At a pump rotational speed of 1000 rpm, the characteristics intersected at point A, where the specific speed

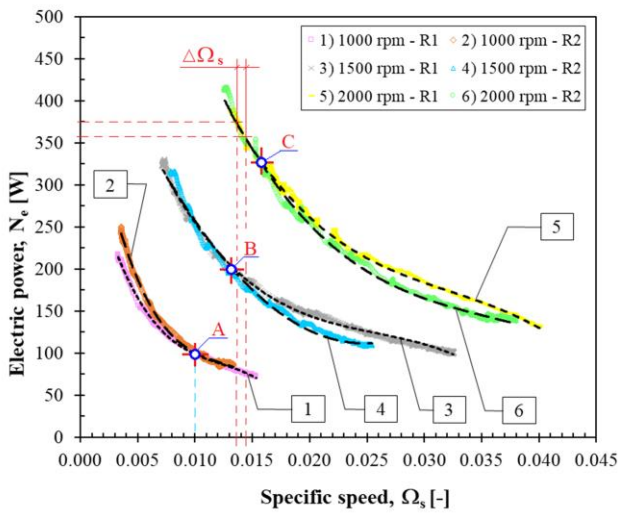

Fig. 15. Dependence of the electric power consumed by the PE drive on specific speed.

was approximately 0.010. It was observed that to the right of point A, power curves 1 and 2 coincided.

That is why the temperature of the medium had no effect on the course of the power curves. On the other hand, to the left of point A, an increase in the temperature of the working fluid resulted in an increase in the power consumed by the pump drive. The maximum increase in power consumed at a rotational speed of 1000 rpm was approximately 13.6%, and the specific speed value was approximately 0.0035. At a rotational speed of 1500 rpm, the performance curves of the pump intersected at point B.

As the pump rotational speed increased, the characteristic points shifted to the right towards higher specific speed values. It was determined that a 500 rpm increase in pump rotational speed resulted in a 0.003 increase in the value of Ω_s. It was observed that at rotational speeds of 1500 rpm and 2000 rpm to the left of characteristic points B and C, the power curves overlapped. This means that, in this area, the impact of the working fluid temperature on the course of the pump's performance curves was small. On the other hand, to the right of points B and C, an increase in the temperature of the fluid from R1 to R2 resulted in a decrease in the electric power consumption of the pump drive.

It should be noted that at MTG's nominal operating parameters (Δp=1000 kPa and m_r=0.17 kg/s), the difference in specific speed ($\Delta\Omega_s$) due to temperature changes from R1 to R2 was approximately 0.001. Therefore, at the MTG's nominal operating point, the value of Ω_s will be 0.014 ± 0.0005 regardless of the working fluid temperature.

Figure 16 shows the effect of specific speed on the effective power of the pump. It was observed that, as a result of the increase in the rotational speed, the performance curves shifted to the right towards higher specific speed values. On the other hand, irrespective of the rotational speed and working fluid tem-

perature, the effective power value of the pump decreased as the specific speed increased. It has been determined that the working fluid temperature has a fundamental impact on the value of the pump's effective power.

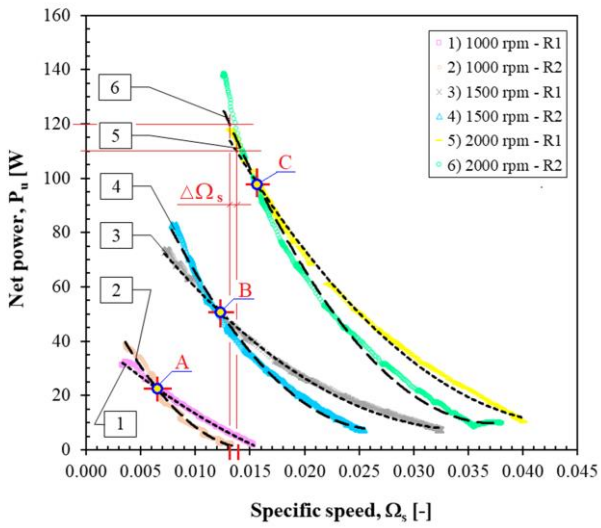

Fig. 16. Effect of specific speed on the effective power of the pump.

To the left of point A, the increase in working fluid temperature from R1 to R2 resulted in an increase in the effective power of the pump. In the R2 range, the maximum effective power value was approximately 40 W and it was approximately 23% higher than that obtained in the R1 temperature range. On the other hand, to the right of point A, an increase in temperature resulted in a decrease in the effective power value. In the R1 temperature range, with Ω_s equal to 0.014 and a rotational speed of 1000 rpm, the effective power was approximately 7.5 W, and in the R2 range, it was three times lower.

Similarly, at higher rotational speeds in the R1 temperature range and for the same Ω_s value, higher effective powers were obtained than in the R2 range. The study reveals that characteristic points B and C, determined on the effective power curves at rotational speeds of 1500 rpm and 2000 rpm respectively, were noted successively at specific speeds of approximately 0.0135 and 0.0165, respectively.

Figure 16 shows that to the left of points B and C, higher effective power values of the pump were obtained in the R2 temperature range. That is why, as the rotational speed increased, the differences in effective power decreased due to changes in the temperature of the working fluid. On the other hand, at the MTG's nominal operating point, a change in HFE-7100 temperature from R1 to R2 resulted in an increase in specific speed from approximately 0.013 to 0.014.

As mentioned earlier, an essential parameter required from PE is to ensure adequate differential pressure in the ORC system. On the other hand, in accordance with Eq. (9), differential pressure is a component of the Euler number (Eu). That is why Fig. 17 shows the characteristics of the power consumed by the pump drive versus the Eu number.

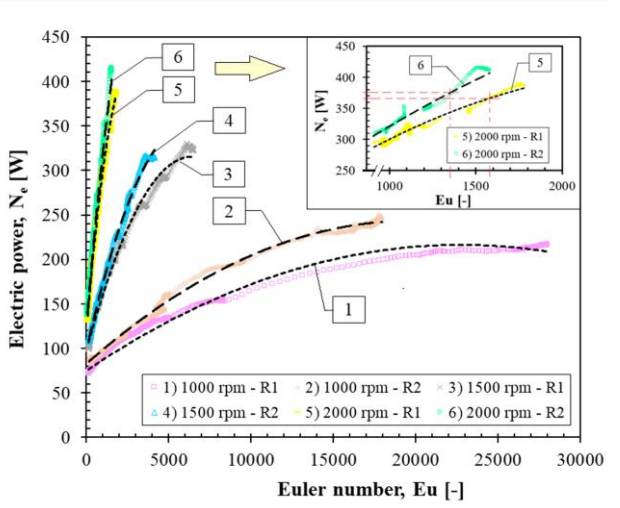

Fig. 17. Effect of the Euler number on the electric power consumed by the PE drive.

As can be deducted from Fig. 17, the value of the Eu number decreases with increasing pump rotational speed and working fluid temperature. As a result, the performance curves of PE were steeper. Therefore, a small increase in the value of the Eu number resulted in significant electric power consumption by the PE drive. On the other hand, at the MTG's nominal operating point in the temperature ranges R1 and R2, the values of the Eu numbers were 1350 and 1580, respectively. The study reveals that, at low rotational speeds, the electric power consumption by the pump drive in the R2 temperature range is greater than when operating in the R1 range. To recapitulate, it can be stated that irrespective of the pump rotational speed, an increase in the temperature of the working fluid results in a higher electric power consumption by the pump drive.

6. Conclusions

The study reveals that an increase in working fluid temperature, differential pressure in the pump and rotational speed results, firstly, in an increase in effective power. Secondly, it causes an increase in the delivery head of the pump. Thirdly, it results in an increase in the electric power consumed by the pumping engine drive. The study reveals that an increase in the temperature of the HFE-7100 working fluid results in an increase in the volumetric efficiency of the pump. For example, at a rotational speed of 2000 rpm, an increase in the average temperature of the working fluid from 34°C to 61°C resulted in an increase in the volumetric efficiency of the pump from 76% to approximately 80%. Moreover, it was stated that for each value of pump rotational speed and working fluid temperature, there exists an optimum value of the effective power of the pump at which the efficiency of the pumping engine reaches the maximum value.

Based on the study, it was established that the maximum efficiency of the pumping engine, approximately 32%, was achieved at a rotational speed of 2000 rpm. At the same time, it was observed that, regardless of the change in the temperature of the working fluid, the efficiency of the pumping engine was, on average, about 60% smaller than the volumetric efficiency of the pump.

Acknowledgements

This study was conducted as part of the statutory works of the Institute of Fluid-Flow Machinery of the Polish Academy of Sciences (IFFM PAS) in Gdańsk and part of the TechRol project financed by the National Centre for Research and Development (NCBR) (grant agreement No. BIOSTRATEG3/344128/12/NCBR/2017).

References

[1] Hasan, A., Mugdadi, B., Al-Nimr, M.A., & Tashtoush, B. (2022). Direct and indirect utilization of thermal energy for cooling generation: A comparative analysis. *Energy*, 238 (Part C), 122046. doi: 10.1016/j.energy.2021.122046

[2] Kruk-Gotzman, S., Ziółkowski, P., Iliev, I., Negreanu, G-P., & Badur, J. (2023). Techno-economic evaluation of combined cycle gas turbine and adiabatic compressed air energy storage integration concept. *Energy*, 266, 126345. doi: 10.1016/j.energy.2022.126345

[3] Montazerinejad, H., & Eicker, U. (2022). Recent development of heat and power generation using renewable fuels: A comprehensive review. *Renewable and Sustainable Energy Reviews*, 165, 112578. doi: 10.1016/j.rser.2022.112578

[4] Wei, J., Hua, Q., Yuan, L., Li, G., Wang, J., & Wang, J. (2023). A review of the research status of scroll expander. *Proceedings of the Institution of Mechanical Engineers, Part A: Journal of Power and Energy*, 237(1), 176–197. doi: 10.1177/09576509221109245

[5] Minea, V. (2014). Power generation with ORC machines using low-grade waste heat or renewable energy. *Applied Thermal Engineering*, 69(1–2), 143-154. doi: 10.1016/j.applthermaleng.2014.04.054

[6] Di Battista, D., & Cipollone, R. (2023). Waste Energy Recovery and Valorization in Internal Combustion Engines for Transportation. *Energies*, 16, 3503. doi: 10.3390/en16083503

[7] Kaczmarczyk, T.Z. (2021). Experimental research of a small biomass organic Rankine cycle plant with multiple scroll expanders intended for domestic use. *Energy Conversion and Management*, 244, 114437. doi: 10.1016/j.enconman.2021.114437

[8] Jain, S.V., Patel, R.N. (2014). Investigations on pump running in turbine mode: A review of the state-of-the-art. *Renewable and Sustainable Energy Reviews*, 30, 841–868. doi: 10.1016/j.rser.2013.11.030

[9] Kottapallia, A. & Konijeti, R. (2022). Numerical and experimental investigation of nonlubricated air scroll expander derived from a refrigerant scroll compressor. *Frontiers in Heat and Mass Transfer*, 19(1), 1–11. doi: 10.5098/hmt.19.11

[10] Zhang, X., Wang, X., Cai, J., Wang, R., Bian, X., He Z., Tian, H., & Shu, G. (2023). Operation strategy of a multi-mode Organic Rankine cycle system for waste heat recovery from engine cooling water. *Energy*, 263 (Part E), 125934. doi: 10.1016/j.energy.2022.125934

[11] Gunawan, G., Permana, D.I., & Soetikno, P. (2023). Design and numerical simulation of radial inflow turbine of the regenerative Brayton cycle using supercritical carbon dioxide. *Results in Engineering*, 17, 100931. doi: 10.1016/j.rineng.2023.100931

[12] Li, X., Lv, C., Yang, S., Li J., Deng, B., & Qing, Li Q. (2019). Preliminary design and performance analysis of a radial inflow turbine for a large-scale helium cryogenic system. *Energy*, 167, 106–116. doi: 10.1016/j.energy.2018.10.179

[13] Liaw, K.L., Kurnia, J.C., Lai, W.K., Ong, K.Ch., Zar, M.A.B.M.A, Muhammad, M.F.B., & Firmansyah. (2023). Optimization of a novel impulse gas turbine nozzle and blades design utilizing Taguchi method for micro-scale power generation. *Energy*, 282, 129018. doi: 10.1016/j.energy.2023.129018

[14] Zhar, R., Allouhi, A., Ghodbane, M., Jamil, A., & Khadija, L.K. (2021). Parametric analysis and multi-objective optimization of a combined Organic Rankine Cycle and Vapor Compression Cycle. *Sustainable Energy Technologies and Assessments*, 47, 101401. doi: 10.1016/j.seta.2021.101401

[15] Kolasiński, & P., Daniarta, S. (2021). Sizing the thermal energy storage (TES) device for organic Rankine cycle (ORC) power systems. *MATEC Web of Conferences*, 345, 00018. doi: 10.1051/matecconf/202134500018

[16] Zhang, H-H., Zhang, Y-F., Feng, Y-Q., Chang, J-Ch., Chang, Ch-W., Xi, H., Gong, L., Hung, T-Ch., & Li, M-J. (2023). The parametric analysis on the system behaviors with scroll expanders employed in the ORC system: An experimental comparison. *Energy*, 268, 126713. doi: 10.1016/j.energy.2023.126713

[17] Milewski, J., & Krasucki, J. (2018). Comparison of ORC and Kalina cycles for waste heat recovery in the steel industry. *Journal of Power Technologies*, 97(4), 302–307.

[18] Alperen B., C., & Oğuz A. (2024). Numerical analysis-based performance assessment of the small-scale organic Rankine cycle turbine design for residential applications. *Thermal Science and Engineering Progress*, 51, 102626. doi: 10.1016/j.tsep.2024.102626

[19] Ziółkowski, P., Hyrzyński, R., Lemański, M., Kraszewski, B., Bykuć, S., Głuch, S., Sowiżdżał, A., Pająk, L., Wachowicz-Pyzik, A., & Badur, J. (2021). Different design aspects of an Organic Rankine Cycle turbine for electricity production using a geothermal binary power plant. *Energy Conversion and Management*, 246, 114672. doi: 10.1016/j.enconman.2021.114672

[20] Wang, R., Jiang, L., Ma, Z., Gonzalez-Diaz, A., Wang, Y., & Roskilly, A.P. (2019). Comparative Analysis of Small-Scale Organic Rankine Cycle Systems for Solar Energy Utilisation. *Energies*, 12(5), 829. doi: 10.3390/en12050829

[21] Kaczmarczyk, T.Z., & Żywica, G. (2022) Experimental study of a 1 kW high-speed ORC microturbogenerator under partial load. *Energy Conversion and Management*, 272, 116381. doi: 10.1016/j.enconman.2022.116381

[22] Peng, N., Wang, E., & Wang, W. (2023). Design and analysis of a 1.5 kW single-stage partial-admission impulse turbine for low-grade energy utilization. *Energy*, 268, 126631. doi: 10.1016/j.energy.2023.126631

[23] Witanowski, Ł., Klonowicz, P., Lampart, P., Klimaszewski, P., Suchocki, T., Jędrzejewski, Ł., Zaniewski, & D., Ziółkowski, P. (2023). Impact of rotor geometry optimization on the off-design ORC turbine performance. *Energy*, 265, 126312. doi: 10.1016/j.energy.2022.126312

[24] Ekwonu, M.C., Kim, M., Chen, B., Nasir, M.T., & Kim, K.C. (2023). Dynamic Simulation of Partial Load Operation of an Organic Rankine Cycle with Two Parallel Expanders. *Energies*, 16(1), 519. doi: 10.3390/en16010519

[25] Kaczmarczyk, T.Z. (2022). Thermal flow and electrical power research of ORC micro-cogeneration systems and their components. *Summary of Professional Accomplishments – Appendix No. 3 to the habilitation proceedings*. Gdańsk, Poland. https://www.imp.gda.pl/en/bip/postepowania-habilitacyjne/ [accessed: 3 Oct. 2023].

[26] Casari, N., Fadiga, E., Pinelli, M., Randi, S., & Suman, A. (2019). Pressure Pulsation and Cavitation Phenomena in a Micro-ORC System. *Energies*, 12(11), 2186. doi: 10.3390/en12112186

[27] Witanowski, Ł., Ziółkowski, P., Klonowicz, P., & Lampart, P. (2023). A hybrid approach to optimization of radial inflow turbine with principal component analysis. *Energy*, 272, 127064. doi: 10.1016/j.energy.2023.127064

[28] Fakeye, A.B., & Oyedepo, S.O. (2019). Designing Optimized Organic Rankine Cycles Systems for Waste Heat-to-Power Conversion of Gas Turbine Flue Gases. *International Conference on Engineering for Sustainable World. Journal of Physics: Conference Series*, 1378, 032097. IOP Publishing. doi: 10.1088/1742-6596/1378/3/032097

[29] Xi, H., Zhang, H., He, Y-L., & Huang, Z. (2019). Sensitivity analysis of operation parameters on the system performance of organic Rankine cycle system using orthogonal experiment. *Energy*, 172, 435–442. doi: 10.1016/j.energy.2019.01.072

[30] Fatigati, F., Vittorini, D., Wang, Y., Song, J., Markides ,C.N., & Cipollone, R. (2020). Design and Operational Control Strategy for Optimum Off-Design Performance of an ORC Plant for Low-Grade Waste Heat Recovery. *Energies*, 13(21), 5846. doi: 10.3390/en13215846

[31] Ziviani, D., Gusev, S., Lecompte, S., Groll, E.A., Braun, J.E., Horton, W.T., Broek, M., & De Paepe, M. (2017). Optimizing the performance of small-scale organic Rankine cycle that utilizes a single-screw expander. *Applied Energy*, 189, 416–432. doi: 10.1016/j.apenergy.2016.12.070

[32] Meng, F., Zhang, H., Yang, F., Hou, X., Lei, B., Zhang, L., Wu, Y., Wang, J., & Shi, Z. (2017). Study of efficiency of a multistage centrifugal pump used in engine waste heat recovery application. *Applied Thermal Engineering*, 110, 779–786. doi: 10.1016/ j.applthermaleng.2016.08.226

[33] Quoilin, S., Broek M., Declaye, S., Dewallef, P., & Lemort, V. (2013). Techno-economic survey of Organic Rankine Cycle (ORC) systems. *Renewable and Sustainable Energy Reviews*, 22, 168–186. doi: 10.1016/j.rser.2013.01.028

[34] Moradi, R., Habib, E., Bocci, E., & Cioccolanti, L. (2021). Component-Oriented Modeling of a Micro-Scale Organic Rankine Cycle System for Waste Heat Recovery Applications. *Applied Sciences.* 11(5), 1984. doi: 10.3390/app11051984

[35] Kaczmarczyk, T.Z., & Żywica, G. (2022). Experimental research of a micropower volumetric expander for domestic applications at constant electrical load. *Sustainable Energy Technologies and Assessments*, 49, 101755. doi: 10.1016/j.seta.2021.101755

[36] Huo, E., Xin, L., & Wang, S. (2022). Thermal stability and pyrolysis mechanism of working fluids for organic Rankine cycle: A review. *International Journal of Energy Research*, 46(14), 19341–19356. doi: 10.1002/er.8518

[37] Hao, X., Zhou, X., Liu, X., & Sang, X. (2016). Flow characteristics of external gear pumps considering trapped volume. *Advances in Mechanical Engineering*, 8(10). doi: 10.1177/1687814016674100

[38] Kaczmarczyk, T.Z., Żywica, G., & Ihnatowicz, E. (2016). Experimental investigation on a rotodynamic pump operating in the cogeneration system with a low-boiling working medium. *Transactions of the Institute of Fluid-Flow Machinery*, 134, 63–87.

[39] Njock, J.P., Ngangué, M.N., Sosso, O.T., & Nzengwa, R. (2023). Highlighting the effect of the lower operating limit of the condenser on ORC working fluids selection. *Results in Engineering*, 19, 101369. doi: 10.1016/j.rineng.2023.101369

[40] Ping, X., Yang, F., Zhang, H., Zhang, J., Xing, Ch., Yan, Y., Yang, A., & Wang, Y. (2023). Information theory-based dynamic feature capture and global multi-objective optimization approach for organic Rankine cycle (ORC) considering road environment. *Applied Energy*, 348, 121569. doi: 10.1016/j.apenergy.2023.121569

[41] Dhote, N., Khond, M., & Sankpal, R. (2023). Wear material determination and parameters optimization of an external gear pump by Taguchi technique. *Materials Today: Proceedings*, 72 (Part 3), 679–686. doi: 10.1016/j.matpr.2022.08.374

[42] Hernandez-Carrillo, I., Wood, Ch.J., & Liu, H. (2017). Advanced materials for the impeller in an ORC radial microturbine. *Energy Procedia*, 129, 1047–1054. doi: 10.1016/j.egypro.2017.09.241

[43] Li, W., & Yu, Z. (2021). Cavitating flows of organic fluid with thermodynamic effect in a diaphragm pump for organic Rankine cycle systems. *Energy*, 237, 121495. doi: 10.1016/j.energy.2021.121495

[44] Li, W., & Yu, Z. (2021). Cavitation models with thermodynamic effect for organic fluid cavitating flows in organic Rankine cycle systems. *Thermal Science and Engineering Progress*, 26, 101079. doi: 10.1016/j.tsep.2021.101079

[45] Li, W., Mckeown A., & Yu, Z. (2020). Correction of cavitation with thermodynamic effect for a diaphragm pump in organic Rankine cycle systems. *Energy Reports*, 6, 2956–2972. doi: 10.1016/j.egyr.2020.10.013

[46] Borsukiewicz-Gozdur A. (2013). Pumping work in the organic Rankine cycle. *Applied Thermal Engineering*, 51 (1–2), 781–786. doi: 10.1016/j.applthermaleng.2012.10.033

[47] Lu, Y., Guo, Z., Zheng, Z., Wang, W., Wang, H., Zhou, F., & Wang, X. (2023). Underwater propeller turbine blade redesign based on developed inverse design method for energy performance improvement and cavitation suppression. *Ocean Engineering*, 277, 114315. doi: 10.1016/j.oceaneng.2023.114315

[48] Bianchi, G., Fatigati, F., Murgia, S., & Cipollone, R. (2017). Design and analysis of a sliding vane pump for waste heat to power conversion systems using organic fluids. *Applied Thermal Engineering*, 124, 1038–1048. doi: 10.1016/j.applthermaleng.2017.06.083

[49] Kaczmarczyk, T.Z., Ihnatowicz, E., Żywica, G., & Kaniecki, M. (2019). Experimental study of the prototype of a Roto-Jet pump for the domestic ORC power plant. *Archives of Thermodynamics*, 40(3), 83–108. doi: 10.24425/ather.2019.129995

[50] Yang, Y., Zhang, H., Xu, Y., Yang, F., Wu, Y., & Lei, B. (2018). Matching and operating characteristics of working fluid pumps with organic Rankine cycle system. *Applied Thermal Engineering*, 142, 622–631. doi: 10.1016/j.applthermaleng.2018.07.039

[51] Yang, Y., Zhang, H., Tian, G., Yonghong, X., Chongyao, W., & Jianbing, G. (2019). Performance Analysis of a Multistage Centrifugal Pump Used in an Organic Rankine Cycle (ORC) System under Various Condensation Conditions. *Journal of Thermal Science*, 28, 621–634. doi: 10.1007/s11630-019-1069-9

[52] Zeleny, Z., Vodicka, V., Novotny, V., & Mascuch, J. (2017). Gear pump for low power output ORC – an efficiency analysis. *Energy Procedia*, 129, 1002–1009. doi: 10.1016/j.egypro.2017.09.227

[53] D'Amico, F., Pallis, P., Leontaritis, A.D, Karellas, S., Kakalis, N.M., Rech, S., & Lazzaretto, A. (2018). Semi-empirical model of a multi-diaphragm pump in an Organic Rankine Cycle (ORC) experimental unit. *Energy*, 143, 1056–1071. doi: 10.1016/j.energy.2017.10.127

[54] Carraro, G., Pallis, P., Leontaritis, A.D., Karellas, S., Vourliotis, P., Rech, S., & Lazzaretto, A. (2017). Experimental performance evaluation of a multi-diaphragm pump of a micro-ORC system. *Energy Procedia*, 129:1018-1025. doi: 10.1016/j.egypro.2017.09.232.

[55] Zardin, B., Natali, E., & Borghi, M. (2019). Evaluation of the Hydro-Mechanical Efficiency of External Gear Pumps. *Energies*, 12(13), 2468. doi: 10.3390/en12132468

[56] Misiewicz W. (2007). The optimization of the pump sets with the variable-speed drives. Maszyny Elektryczne – Zeszyty Problemowe, 78, 43–52.

[57] Yang, X., Xu, J., Miao, Z., Zou, J., & Yu, Ch. (2015). Operation of an organic Rankine cycle dependent on pumping flow rates and expander torques. *Energy*, 90(1), 864–878. doi: 10.1016/j.energy.2015.07.121

[58] Landelle, A., Tauveron, N., Revellin, R., Haberschill, P., Colasson, S., & Roussel, V. (2017). Performance investigation of reciprocating pump running with organic fluid for organic Rankine cycle. *Applied Thermal Engineering*, 113, 962–969. doi: 10.1016/j.applthermaleng.2016.11.096

[59] Feng, Y-Q., Hung, T-Ch., Wu, S-L., Lin, Ch-H., Li, B-X., Huang, K-Ch., & Qin, J. (2017). Operation characteristic of a R123-based organic Rankine cycle depending on working fluid mass flow rates and heat source temperatures. *Energy Conversion and Management*, 131, 55–68. doi: 10.1016/j.enconman.2016.11.004

[60] Yang, Y., Zhang, H., Xu, Y., Zhao, R., Hou, X., & Liu, Y. (2018). Experimental study and performance analysis of a hydraulic diaphragm metering pump used in organic Rankine cycle system. *Applied Thermal Engineering*, 132, 605–612. doi: 10.1016/j.applthermaleng.2018.01.001

[61] Gao, P., Wang, Z.X., Wang, L.W., & Lu, H.T. (2018). Technical feasibility of a gravity-type pumpless ORC system with one evaporator and two condensers. *Applied Thermal Engineering*, 145, 569–575. doi: 10.1016/j.applthermaleng.2018.09.049

[62] Komaki, K., Kanemoto, T., & Sagara, K. (2012). Performances and Rotating Flows of Rotary Jet Pump. *Open Journal of Fluid Dynamics*, 2(4A), 375–379. doi: 10.4236/ojfd.2012.24A048

[63] Osborn, S. (1996). The Roto-Jet pump: 25 years new. *World Pumps*, 363, 32–36. doi: 10.1016/S0262-1762(99)81000-1

[64] Jiang, L., Lu, H.T., Wang, L.W., Gao, P., Zhu, F.Q., Wang, R.Z., & Roskilly, A.P. (2017). Investigation on a small-scale pumpless Organic Rankine Cycle (ORC) system driven by the low temperature heat source. *Applied Energy*, 195, 478–486. doi: 10.1016/j.apenergy.2017.03.082

[65] Gkimisis, L., Arapkoules, N., Vasileiou, G., Soldatos, A., & Spitas, V. (2020). Modelling and numerical simulation of a novel Pumpless Rankine Cycle (PRC). *Applied Thermal Engineering*, 178, 115523. doi: 10.1016/j.applthermaleng.2020.115523

[66] Richardson, E.S. (2016). Thermodynamic performance of new thermofluidic feed pumps for Organic Rankine Cycle applications. *Applied Energy*, 161, 75–84. doi: 10.1016/j.apenergy.2015.10.004

[67] Semkło, Ł., & Gierz, Ł. (2022). Numerical and experimental analysis of a centrifugal pump with different rotor geometries. *Applied Computer Science*, 18(4), 82–95. doi: 10.35784/acs-2022-30

[68] Datla, B.V., & Brasz J.J. (2012). Organic Rankine Cycle System Analysis for Low GWP Working Fluids. *International Refrigeration and Air Conditioning Conference at Purdue*, 16–19 July, 2012

[69] Kaczmarczyk, T.Z., & Ihnatowicz, E. (2016). The experimental investigation of scroll expanders operating in the ORC system with HFE7100 as a working medium. *Applied Mechanics and Materials*, 831, 245–255

[70] Kaczmarczyk, T.Z., Żywica, G., & Ihnatowicz, E. (2017). The impact of changes in the geometry of a radial microturbine stage on the efficiency of the micro CHP plant based on ORC. *Energy*, 137, 530–543. doi: 10.1016/j.energy.2017.05.166

[71] Mathias, J.J., Johnston, J.J., Cao, J.J., Priedeman, D.D., & Christensen, R.N. (2009). Experimental testing of gerotor and scroll expanders used in, and energetic and exergetic modeling of an organic Rankine cycle. *Journal of Energy Resources Technology. Trans. ASME*, 131, 21–24. doi: 10.1115/1.3066345

[72] Kaczmarczyk, T.Z., Żywica, G., & Ihnatowicz, E. (2017). Measurements and vibration analysis of a five-stage axial-flow microturbine operating in an ORC cycle. *Diagnostyka*, 18(2), 51–58.

[73] Rausch, M.H., Kretschmer, L., Will, S., Leipertz, A., & Fröba, A.P. (2015). Density, Surface Tension, and Kinematic Viscosity of Hydrofluoroethers HFE-7000, HFE-7100, HFE-7200, HFE-7300, and HFE-7500. *Journal of Chemical Engineering*, 60, 3759–3765. doi: 10.1021/acs.jced.5b00691

[74] Bell, I.H., Wronski, J., Quoilin, S., & Lemort, V. (2014). Pure and Pseudo-pure Fluid Thermophysical Property Evaluation and the Open-Source Thermophysical Property Library CoolProp. *Industrial & Engineering Chemistry Research*, *53*(6), 2498–2508. doi: 10.1021/ie4033999

[75] Rządkowski, R., Żywica, G., Kaczmarczyk, T.Z., Koprowski, A., Dominiczak, K., Szczepanik, R., & Kowalski, M. (2020). Design and investigation of a partial admission radial 2.5-kW organic Rankine cycle micro-turbine. *International Journal of Energy Research*, 44(14), 11029–11043. doi: 10.1002/er.5670

Co-published by
Institute of Fluid-Flow Machinery
Polish Academy of Sciences
Committee on Thermodynamics and Combustion
Polish Academy of Sciences

http://www.imp.gda.pl/archives-of-thermodynamics/

Application of innovative solutions to improve the efficiency of the low-pressure cylinder flow part of a 1000 MW steam turbine for nuclear power plant

Roman Rusanov*, Viktor Subotin, Andrii Rusanov, Viktor Shvetsov, Serhii Palkov, Ihor Palkov, Marina Chugay

Pidhornyi Institute of Power Machines and Systems of the National Academy of Sciences of Ukraine, Pozharskogo str. 2/10, Kharkiv, 61046, Ukraine
*Corresponding author email: roman_rusanov@ipmach.kharkov.ua

Received: 05.02.2024; revised: 02.07.2024; accepted: 10.10.2024

Abstract

The outcomes of gas-dynamic computations for the low-pressure cylinder component of the K-1000-60/1500-2M type low-speed steam turbine intended for use in nuclear power plants are presented in the paper. Various strategies for enhancing the low-pressure cylinder, incorporating a novel approach, which was not previously employed in low-speed high-power steam turbines, have been identified. The flow part redesign has been carried out through the comprehensive methodology and software implemented in the IPMFlow package. This methodology encompasses gas-dynamic computations of varying complexities and analytical profiling methods for spatial blade row shapes based on a limited set of parameterized values. Real thermodynamic properties of water and steam were considered in 3D turbulent flow calculations. The final stage involved end-to-end 3D computations of the 7-stage low-pressure cylinder, employing parallel computing technology. The results indicate that the innovative solutions incorporated in the developed low-pressure cylinder led to a substantial increase in both efficiency and power.

Keywords: Flow part; Low-pressure cylinder; Meridional contours; Low-speed steam turbine; Spatial flow

Vol. 45(2024), No. 4, 141–152; doi: 10.24425/ather.2024.152003

Cite this manuscript as: Rusanov, R., Subotin, V. Rusanov, A., Shvetsov, V., Palkov, S., Palkov, I., & Chugay, M. (2024). Application of innovative solutions to improve the efficiency of the low-pressure cylinder flow part of a 1000 MW steam turbine for nuclear power plant. *Archives of Thermodynamics*, 45(4), 141–152.

1. Introduction

Nowadays, the world pays a lot of attention to low-carbon [1] forms of energy sources, such as organic Rankine cycle (ORC) [2–4], but all of them are low-power ones [5–7]. Despite the existing risks, nuclear energy, just like a low-carbon one [8], is a promising source to achieve the climate policy goals stipulated by the Paris Climate Agreement [9].

In the European Union (EU), the Green Deal [10] presented in December 2019 allows nuclear energy usage by EU members as part of their national energy balance. Many developing countries have considered the construction of nuclear power plants that can provide relatively cheap electricity, which is an important factor for economies with growing energy consumption [11]. In addition, on February 2, 2022, the European Commission at the summit in Brussels proposed to classify both gas and nuclear power plants as „green energy sources" [12].

According to data from the World Nuclear Association, as of September, 2020 [13], the number of nuclear power plants operating worldwide was 439, with a total capacity equal to 391.7 GW. Currently, 52 reactors are under construction [14], and 12 of those reactors are located in China, 6 in India and 4 in South Korea. In Ukraine, it was planned to put 5 or more nuclear power plants into operation within the next 5–10 years [15], and by 2040, it is planned to have 14 nuclear power units in launch.

Nomenclature

C_3 – absolute speed, m/s
D_{av} – average diameter, m
D/L – blade fanning (ratio of the mid-diameter to the blade height)
L – blade height, m
Pk – pressure in the condenser, Pa
u/C_0 – velocity ratio (loading of stage)
y^+ – dimensionless distance from the wall

Greek symbols

η – efficiency, %
ξ_{ov} – losses with the outlet velocity, %
ρ – degree of reactivity

Abbreviations and Acronyms

HIPC – high-intermediate-pressure cylinder
HPC – high-pressure cylinder
IPC – intermediate-pressure cylinder
LPC – low-pressure cylinder
NPP – nuclear power plant
RB – rotor blade
SB – stator blade

In total, 106 more nuclear reactors are planned to be launched (with a total capacity of 113.8 GW), including in countries where there were no NPPs before, such as Turkey [16] and Uzbekistan [17]. The possibility of building nuclear power plants is also being considered in other countries [18], including Kazakhstan, Poland and Saudi Arabia.

The International Energy Association predicts a 75% increase in electricity generation at NPPs by 2050 [19].

One of the largest worldwide turbine manufacturers of nuclear power plants is JSC "Ukrainian Energy Machines" (former JSC "Turboatom"). The turbines made by JSC "Ukrainian Energy Machines" are operated at NPPs in Finland, Ukraine, Bulgaria, Hungary and other countries [20]. The modernization and reconstruction techniques have been developed in [21–23] for many produced turbines.

In this paper, options for a new LPC of a low-speed turbine (1500 rpm) of the K-1000 series are presented. The new flow part is designed to ensure the possibility of its placement within the existing turbine framework. During the development of the new flow part, the innovative solutions, implemented for the first time in the K-220-44-3 series steam turbine [24], namely, meridional contours of the special form, are involved. The advanced methodology implemented in the IPMFlow software has been used during the design stage. This methodology includes gas-dynamic evaluations with various complexity levels, as well as methods for the spatial blade rows shape construction based on a limited number of parameters. The newly developed LPC, due to the usage of blades with modern smooth profiles and the special form of meridional contours has demonstrated a significant increase in efficiency and power.

2. Computational methods and axial flow parts analytical profiling

The three-dimensional steam flow calculation as well as the steam turbine flow part design have been provided using the IPMFlow software [25]. The unsteady Reynolds-averaged Navier-Stokes equations are the basis of the software package mathematical model. The numerical integration is accomplished using the implicit quasi-monotonic ENO-scheme of high accuracy. The Menter two-equations k–ω SST turbulence model [26] is involved in calculations. The steam thermodynamic properties are incorporated by applying the interpolation-analytical approximation method to the IAPWS-95 equations [27]. The results obtained by the IPMFlow software package have the necessary trustworthiness for the qualitative flow structure analysis as well as for the quantitative estimations of isolated turbine stages [28,29] and entire flow paths of turbomachines [30–32].

The original parallel computing technology is implemented to speed up the calculation time of the IPMFlow software [33].

The effective analytical profiling method for the blade row of the axial flow turbine geometry [34] is used.

3. Research object

Steam turbines of the K-1000-60/1500 series are low-speed condensing-type steam turbines developed by JSC „Ukrainian Energy Machines”.

These mentioned turbines have the following modifications:

- K-1000-60/1500-1. A 57.4 m long turbine unit (without a generator its length is 50.7 m) with HPC, IPC and three LPCs, with a single-pass condenser is considered. The rated and maximum power is 1030 MW [35];
- K-1000-60/1500-2. The length is reduced to 52.2 m due to the combination of HPC and IPC into one double-flow HIPC [36]; the weight with a condenser is lower by 350 tons. It is capable of generating the power up to 1100 MW;
- K-1000-60/1500-2m. Slightly different from the previous one.

In total, 17 turbines of such type were installed in the 1980–1990s, 8 of them were installed in Ukraine and 2 in Bulgaria (Kozloduy NPP) [37].

The K-1000-60/1500-1 modification, according to the studies at the South Ukraine NPP, showed the best economic results [38]. Despite this, due to the large size and cost, it was abandoned.

As an object of research, an LPC flow of the latest K-1000 series turbine with 7 stages (Fig. 1) is considered in the paper. This flow part has four regenerative steam extractions (behind 1st, 2nd, 4th and 6th stages).

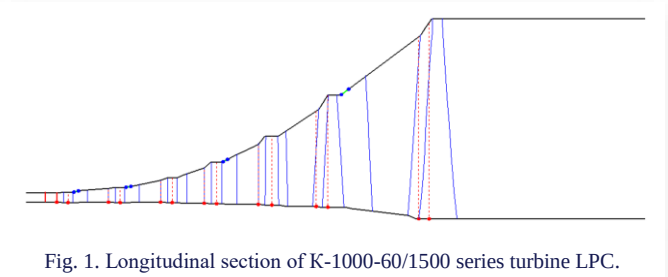

Fig. 1. Longitudinal section of K-1000-60/1500 series turbine LPC.

The following parameters are used as initial data for the flow part calculations: the inlet total pressure is 1.069 MPa, the inlet total temperature is 249.5°C, the outlet static pressure is 3.825 kPa; steam extractions: behind the first stage the value is 8.595 kg/s, behind the second stage the value is 12.588 kg/s, behind the fourth stage the value is 9.723 kg/s, behind the sixth stage the value is 7.824 kg/s.

The first five stages SBs and the first three stages RBs are of constant cross-sections, and the rest have variable cross-sections as shown in Fig. 2.

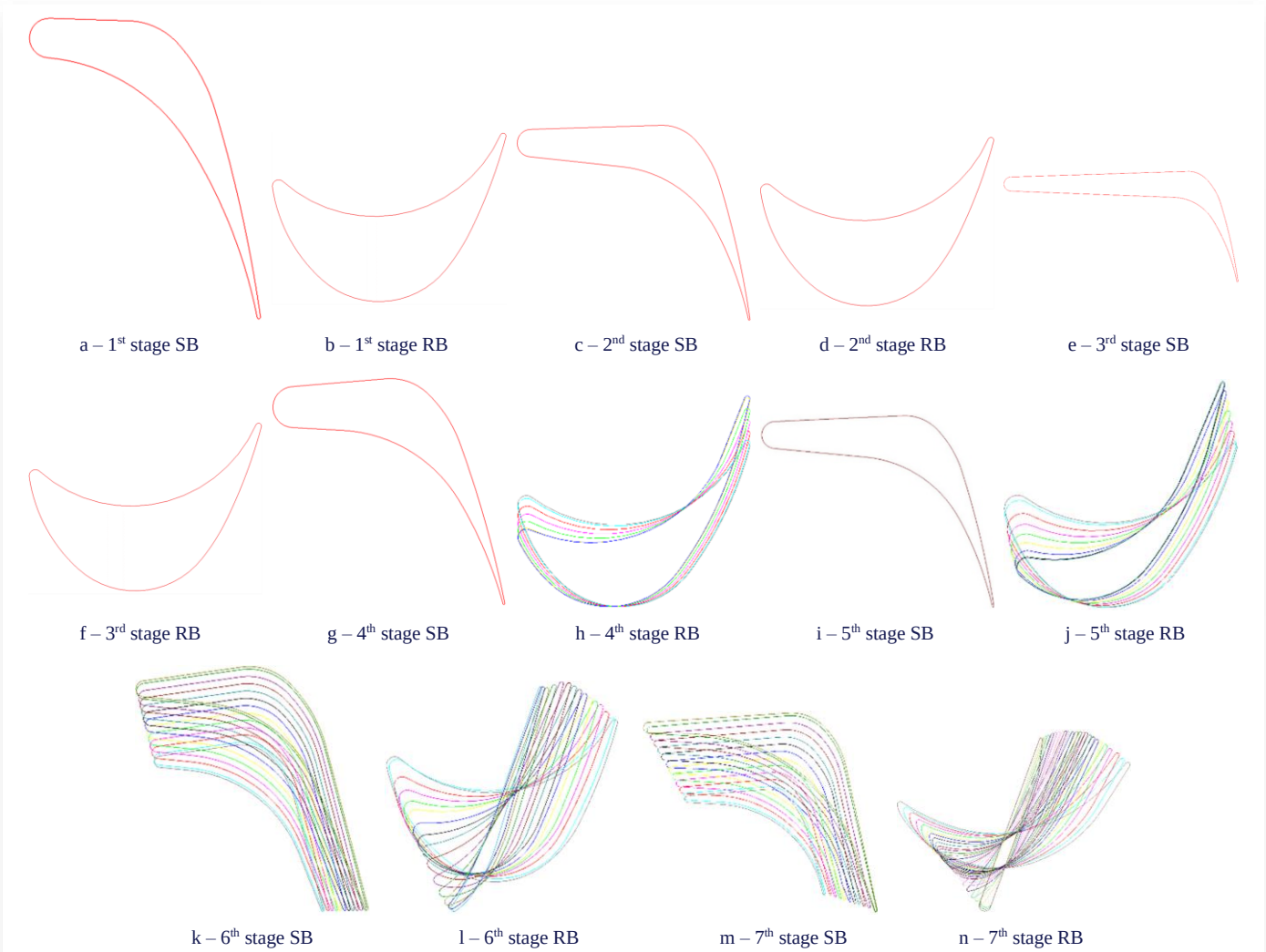

Fig. 2. View of the blades cross-sections.

4. The initial flow part analysis and choosing the directions of modernization

Numerical simulations of the three-dimensional steam flow through the original turbine flow part are provided to determine the modernization areas. End-to-end LPC computations of 7 stages are accomplished on h-type difference grids with a total number of cells of about 7 million. The computational grid refinement near rigid surfaces corresponds to $y^+ < 5$. Figure 3 visualizes the flow in the flow part, whereas Fig. 4 demonstrates the pressure distribution across the blade surfaces. The basic integral characteristics of the flow part under consideration are shown in Table 1.

The flow visualization results (Fig. 3), demonstrate the favourable flow picture. It should be noted that any flow separations or vortex flows are not observed here. However, the pressure on the blade surfaces is non-monotonic (Fig. 4). It usually leads to an increase in the kinetic energy losses. In the first six stages, a relatively low reactivity degree is observed (compared with the desired value of 0.5). The increased load (small value of u/C_0) is recognized in the first five stages (Table 1). The loading in the seventh stage is high (small value of $u/C_0 = 0.48$), with a high value of reactivity. Such a ratio of loading and reactivity is uncharacteristic and can be explained by the high supersonic flow velocity in the interblade channel (Fig. 3: m, n).

Relatively long cylindrical blades with a constant profile (small D/L) are used for the first stage blades, which leads to deterioration in the picture of flow along the blade height. Also, as it can be concluded from the graphs (Fig. 4), the pressure distributions on the blade surfaces are not monotonous. In all stages, the significant underload of the inlet stator blade is observed from the pressure distribution graphs (Fig. 4: a, c, e, g, i, k, m). It is caused by the blade extension there (Fig. 2i). Such a profile has been created using the strength conditions, but it is not optimal from the gas dynamics point of view.

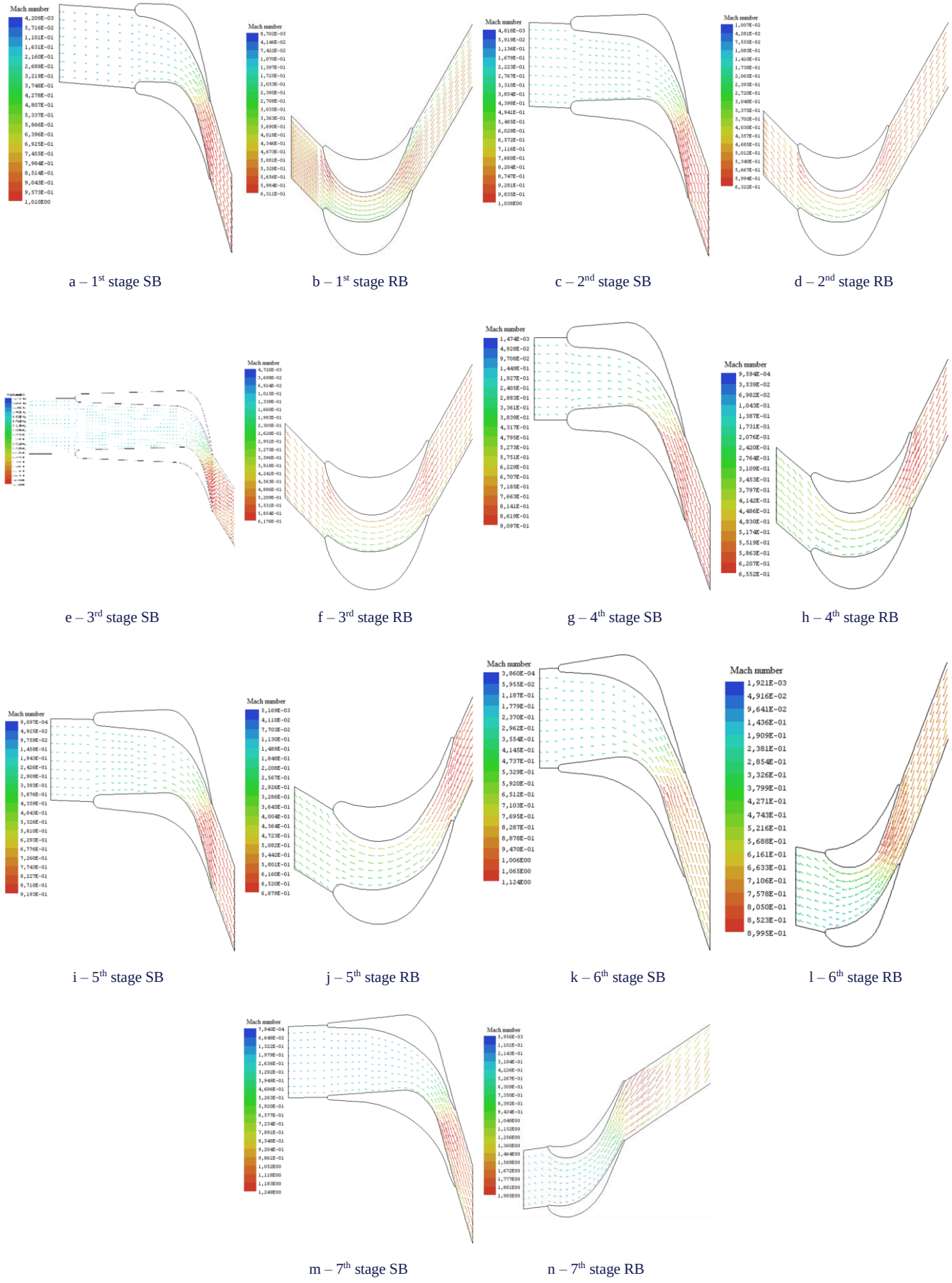

a – 1st stage SB b – 1st stage RB c – 2nd stage SB d – 2nd stage RB

e – 3rd stage SB f – 3rd stage RB g – 4th stage SB h – 4th stage RB

i – 5th stage SB j – 5th stage RB k – 6th stage SB l – 6th stage RB

m – 7th stage SB n – 7th stage RB

Fig. 3. Vectors of velocity in the mid-span blade-to-blade section.

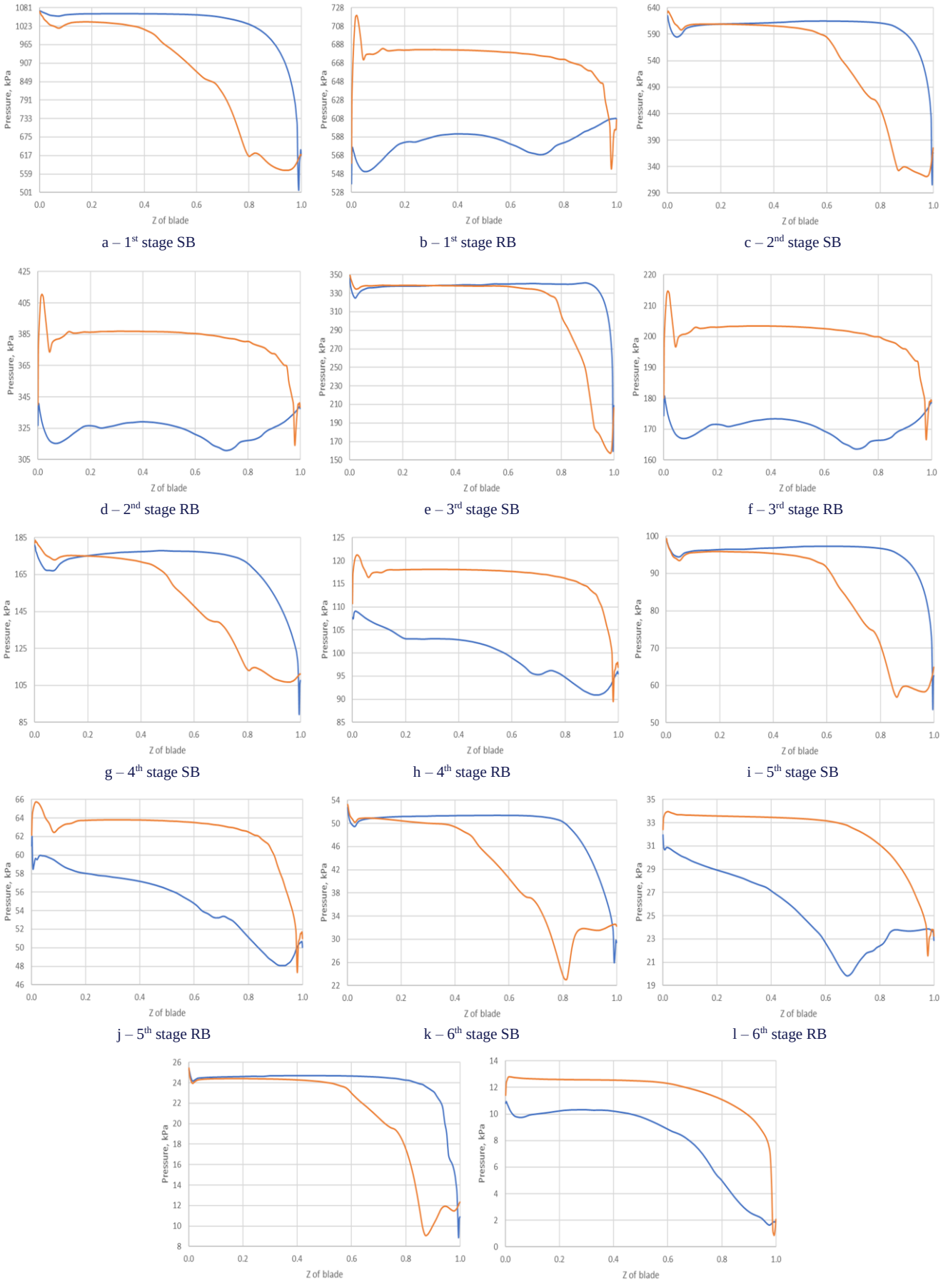

a – 1st stage SB

b – 1st stage RB

c – 2nd stage SB

d – 2nd stage RB

e – 3rd stage SB

f – 3rd stage RB

g – 4th stage SB

h – 4th stage RB

i – 5th stage SB

j – 5th stage RB

k – 6th stage SB

l – 6th stage RB

m – 7th stage SB

n – 7th stage RB

Fig. 4. Pressure distribution over the blade surfaces in the mid-span section.

Table 1. Main geometrical and integral gas-dynamical characteristics of the flow part.

Stage No.	D/L	u/C_0	ρ	η, %
1	40.68	0.48	0.0059	92.85
2	27.69	0.49	0.0584	97.56
3	17.40	0.51	0.0675	90.49
4	10.73	0.56	0.2399	94.03
5	6.80	0.59	0.3018	93.37
6	4.54	0.62	0.3614	92.92
7	2.86	0.48	0.5742	89.63

Figures 5 and 6 demonstrate some results concerning the last stage in the nominal mode. From the graph in Fig. 5, one can see that the value of reactivity degree at the hub is low.

From Fig. 6, it can be seen that there is an uneven distribution of parameters along the height. A supersonic flow is observed at the outlet of the blade row. It leads to a high value of losses with the outlet velocity (Table 2).

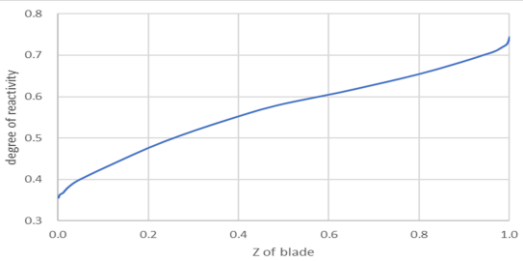

Fig. 5. Reactivity degree distribution along the rotor blade height in 7th stage.

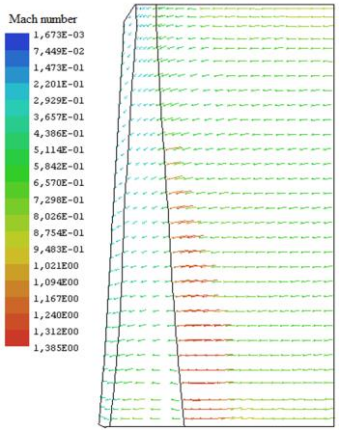

Fig. 6. Velocity vectors in 7th stage rotor at mid-meridional section.

All over the flow part, some flow separations have been observed near significant breaks in the peripheral contours, the so-called overlaps. Fig. 7 demonstrates an example of a similar separation, which occurred between the rotor and stator in the 5th stage.

Table 2 displays integral features of the entire flow part, encompassing average outlet velocity values. One can conclude

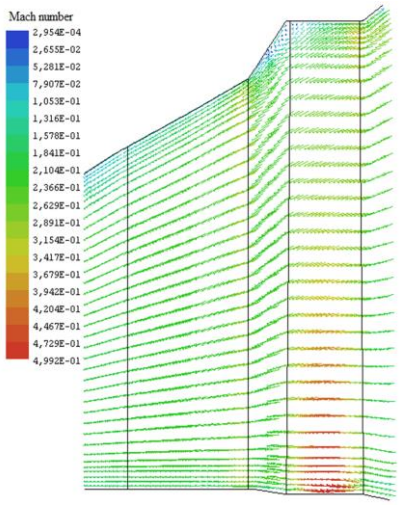

Fig. 7. Velocity vectors in 5th stage at mid-meridional section.

Table 2. The flow part main integral characteristics.

C_3, m/s	ξ_{ov}, %	η, %	Power (one flow), MW
285.7	4.74	88.60	134.095

that the flow part efficiency is relatively high, but the outlet velocity values, and so the corresponding losses, are quite large.

Based on the above shown results and their analysis, the following measures to improve the flow part are planned:

- The use of smooth meridional contours, which will ensure the absence of flow separations in the stator-rotor interspace overlap of meridional contours;
- Developing the blades with smooth (monotonic) surfaces, which will ensure the absence of non-monotonicity in the pressure diagrams on the blade surfaces;
- Developing the blades, adjusted along the flow, with variable cross-sections along the height, which will ensure the flow improvement around the blades;
- Redesigning the meridional contours (used for the low-speed steam turbine structure for the first time in the world practice), which will ensure an increase in D_{av} of the first stage, reducing the load of the stage (increase in u/C_0), increasing the reactivity degree, and more optimal distribution of thermal drops;
- Increasing the height of the last stage rotor blade, which will ensure the reduction of the outlet velocity losses;
- Developing the saber-shaped last stage stator blade, which will ensure more uniform distribution of parameters along the height and an increase in reactivity degree at the hub.

5. Modernized flow part and discussion

According to the measures described above, the new LPC flow part of the K-1000 nuclear turbine series was designed, whereas its fitting within the original framework has been reassured. The modernized flow part is shown in Figs. 8 and 9. Blades in the 3rd to 7th stages incorporate variable height profiles.

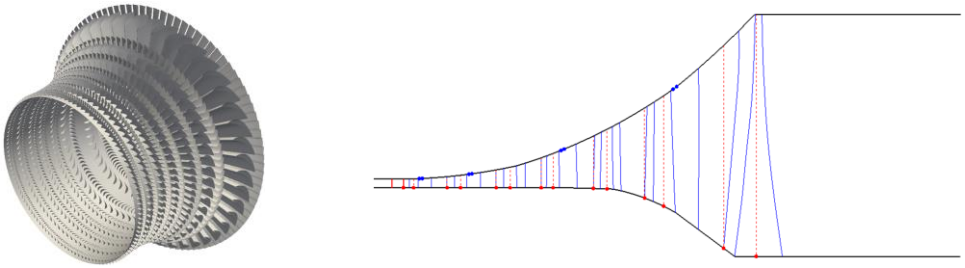

Fig. 8. Visualization of the redesigned flow part in the new LPC of K-1000-60/1500 turbine series.

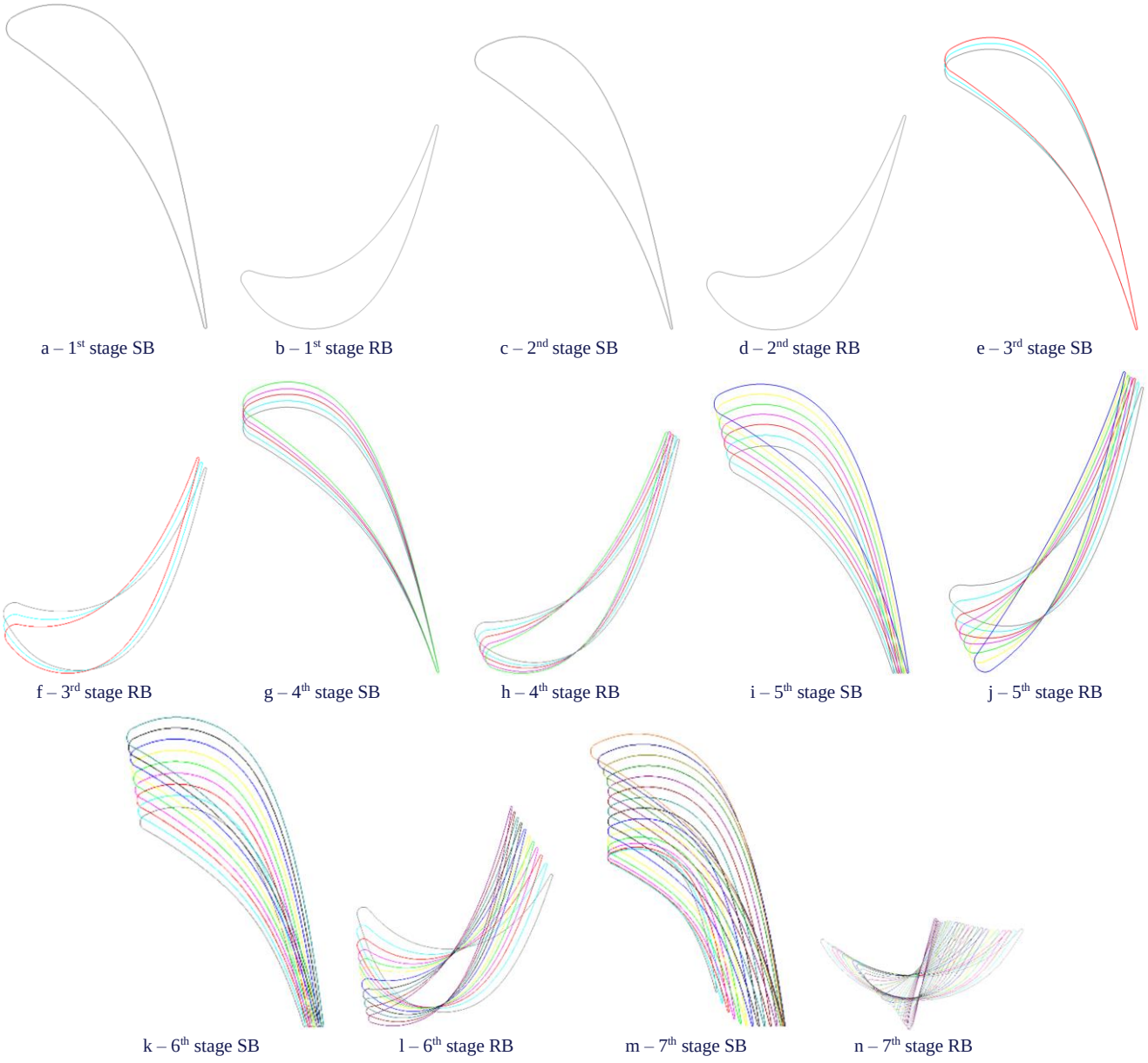

Fig. 9. New blades overview.

End-to-end calculations for the new LPC with 7 stages have been completed using h-type difference grids, akin to those utilized in the original LPC, with the total cells number about 7 million. The computational grid refinements near rigid surfaces correspond to $y^+ < 5$.

Figure 10 visualizes the flow in the designed flow part, and Fig. 11 demonstrates pressure distributions over the blade surfaces. The flow visualization results (Fig. 10) demonstrate the favourable flow picture. It should be noted that any flow separations or vortex flows are not observed here. The flow velocity in the interblade channel of the 7th stage is closer to subsonic (Fig. 10 m, n) compared to the original stage (Fig. 3 m, n). This approach leads to a lower value of kinetic energy losses.

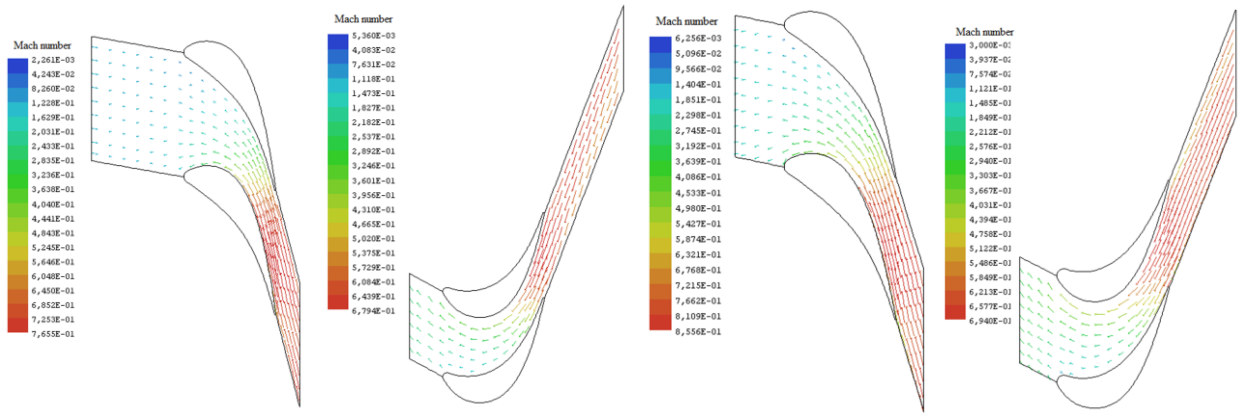

a – 1st stage SB b – 1st stage RB c – 2nd stage SB d – 2nd stage RB

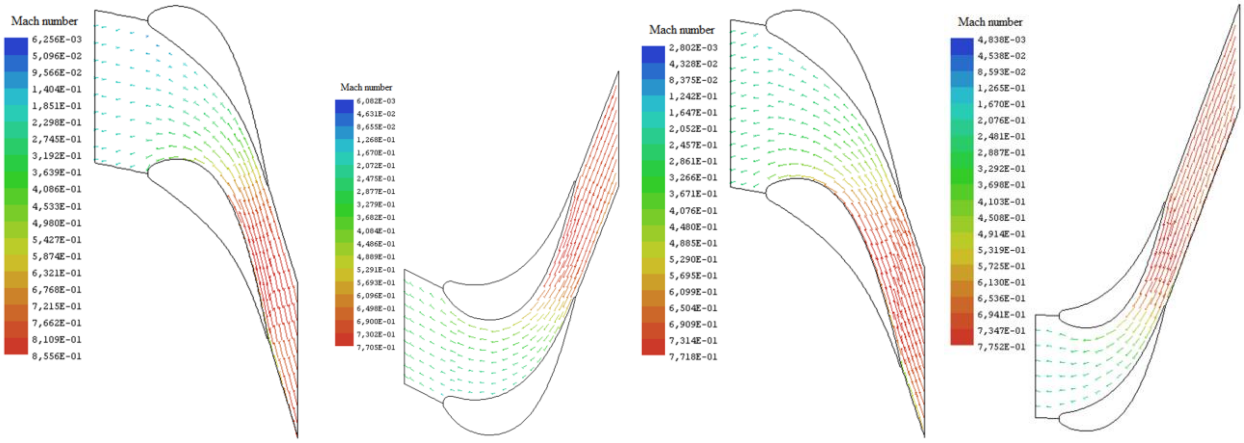

e – 3rd stage SB f – 3rd stage RB g – 4th stage SB h – 4th stage RB

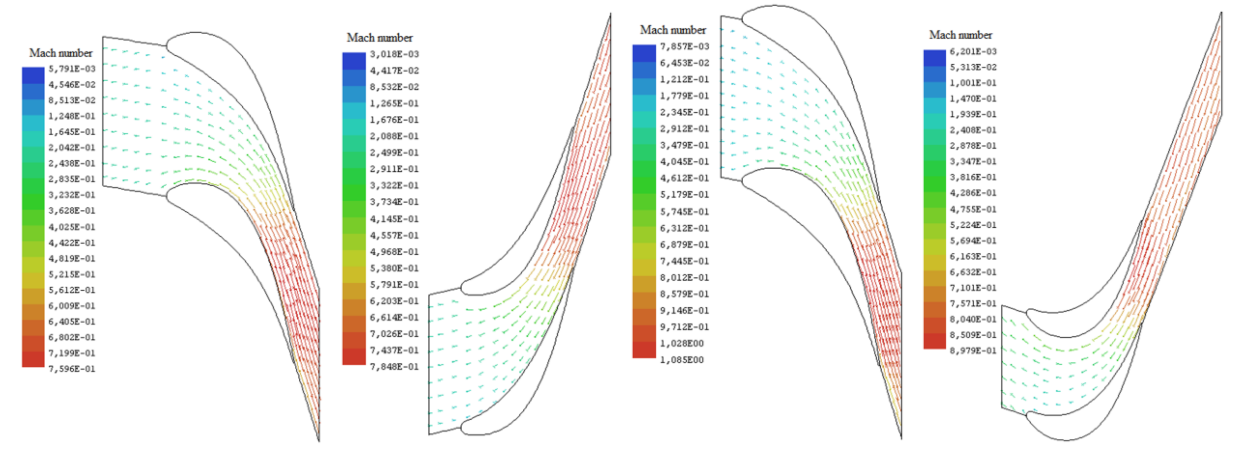

i – 5th stage SB j – 5th stage RB k – 6th stage SB l – 6th stage RB

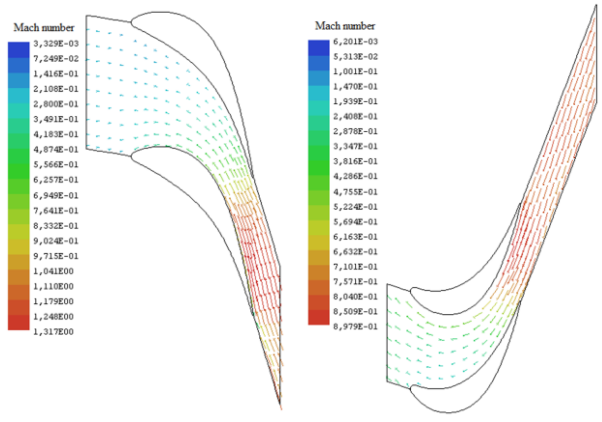

m – 7th stage SB n – 7th stage RB

Fig. 10. Velocity vectors in the mid-span blade-to-blade section.

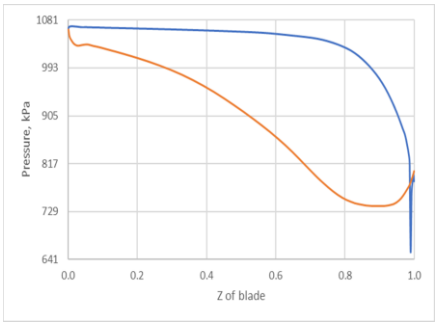

a – 1st stage SB

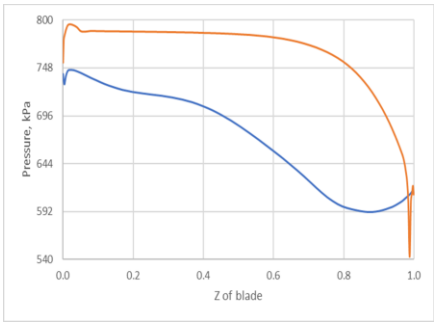

b – 1st stage RB

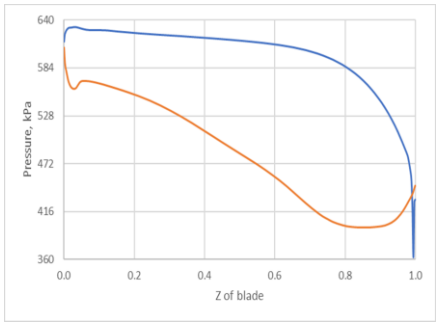

c – 2nd stage SB

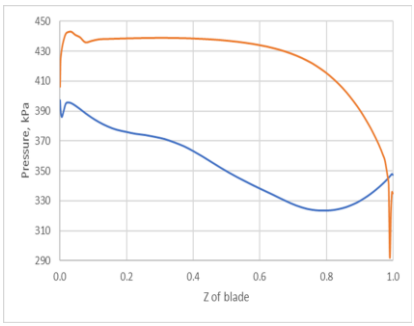

d – 2nd stage RB

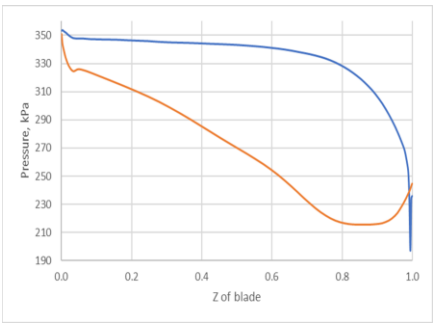

e – 3rd stage SB

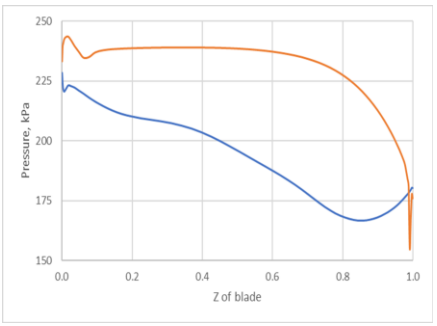

f – 3rd stage RB

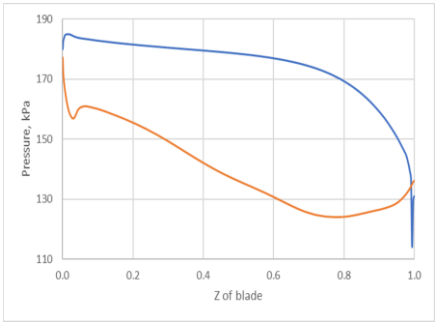

g – 4th stage SB

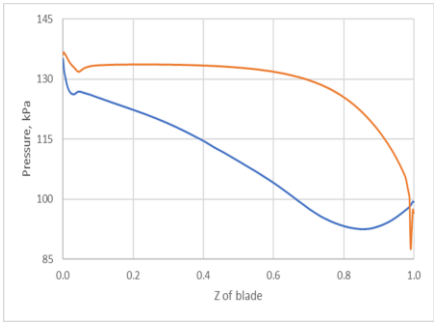

h – 4th stage RB

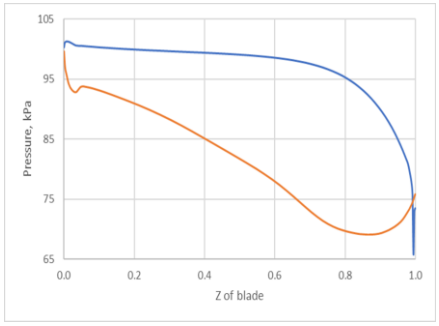

i – 5th stage SB

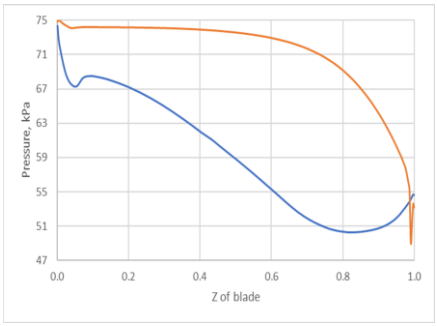

j – 5th stage RB

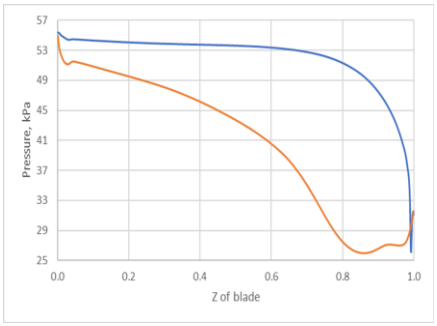

k – 6th stage SB

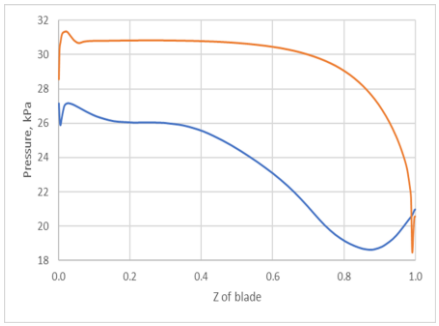

l – 6th stage RB

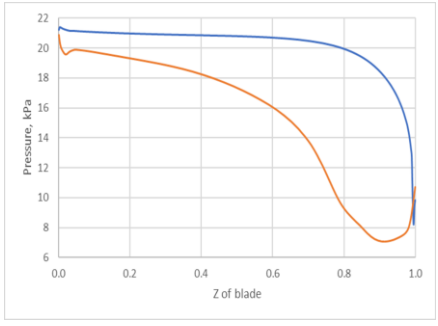

m – 7th stage SB

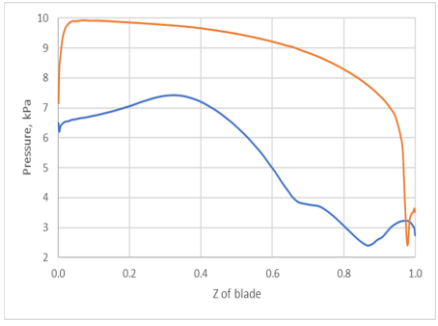

n – 7th stage RB

Fig. 11. Pressure distributions over the blade surfaces in the mid-span section.

Table 3. The primary integral and geometrical characteristics of the flow part.

Stage number	D/L	u/C_0	ρ	η, %
1	58.03	0.57	0.3979	94.77
2	27.69	0.60	0.3436	95.91
3	17.40	0.61	0.3910	93.71
4	10.73	0.66	0.4672	95.49
5	6.80	0.69	0.4861	95.78
6	4.54	0.69	0.3439	95.04
7	2.58	0.49	0.5042	90.13

From the results shown in Fig. 10, it can be concluded that a favourable flow pattern is obtained. The pressure distributions on the blade surfaces (Fig. 11) became essentially more monotonic compared to the original LPC (Fig. 4). These outcomes are obtained through the use of blades with smooth surfaces. The basic integral characteristics of the newly designed flow part are presented in Table 3.

By reprofiling the meridional contours, the increase in the average diameters for the first three stages has been successfully accomplished. It led to a number of advantages (see Table 3): decreased the relative blade height (increased value of D/L), the loading of stages became more optimal, the value of u/C_0 became closer to 0.7 [37], and the degree of reactivity increased. It is necessary to add more about this solution's innovativeness. In the steam turbine world practice, the average diameter in LPCs usually increases essentially from the first stages to the last ones, but the hub diameter remains practically the same or slightly decreases. In the proposed flow part option, the difference in average diameters between the stages has decreased, and the hub diameter in the first stages has increased substantially compared both to the last ones and the original option. So, this made it possible to achieve the above mentioned advantages. The proposed approach has been used for the first time for the low-speed turbine. It is offered for implementation by JSC «Ukrainian Energy Machines». In global practice, during the steam turbine construction, a similar approach was first proposed by the authors for a high-speed turbine of the K-220-44 series [20]. Previously, the implementation of such structures was not carried out especially due to technological problems, since in this case, the rotor becomes significantly heavier. The JSC «Ukrainian Energy Machines» has solved this problem by using the technology of welded rotors manufacturing [39] which has ensured their reasonable characteristics both in terms of mass and strength.

To reduce the outlet velocity losses, the new rotor blade of the last stage has been used with a height of 1650 mm instead of 1450 mm in the original structure. However, increasing the blade length results in an even greater decrease in fanning value (decrease of D/L) that also leads to an additional reactivity degree decrease at the hub surface of the stages. To eliminate this negative effect, the saber-shaped last stage stator blade has been developed, Fig. 12.

Figures 13 and 14 illustrate the reactivity degree variation along the blade height and the velocity vectors in the 7th stage rotor at the mid-meridional section. From the obtained results, one can see that due to using the saber-shaped blade, the unevenness in the distribution of the parameters along the height in the 5th stage has significantly decreased compared to the original design (Fig. 7). Moreover, despite the extensive fanning, there has been an increase in the reactivity degree at the hub surface (Fig. 13).

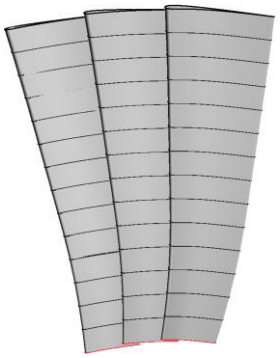

Fig. 12. 3D visual representation of the stator blades in the new design last stage.

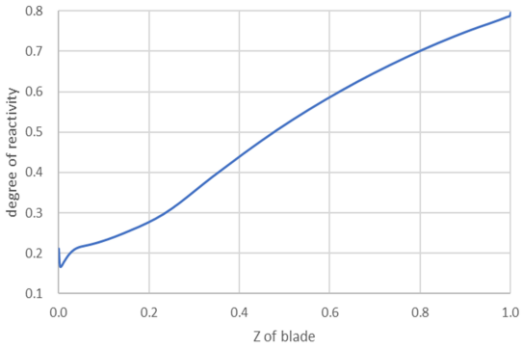

Fig. 13. Reactivity degree vs. the height of the rotor blade in 7th stage.

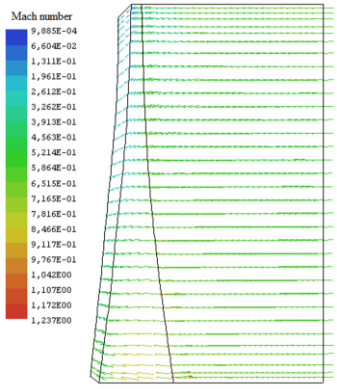

Fig. 14. Velocity vectors in 7th rotor stage at the mid-meridional section.

The redesigned flow part features smooth meridional contours without overlaps in the new configuration. This design guarantees the prevention of flow separation in these specific areas [40]. Indeed, for example, Fig. 15 visualizes the flow in the 5th stage. Compared to the original design shown in Fig. 7, the flow here is continuous.

Table 4 shows the basic flow part integral characteristics of the whole modernized turbine. One can see the significantly decreasing outlet velocity and, accordingly, the decreasing losses with outlet velocity. Due to the complex measures implemented to modernize the flow part, the efficiency increase was shown both in each individual stage (refer to Tables 1 and 3) and in the overall flow domain (refer to Tables 2 and 4).

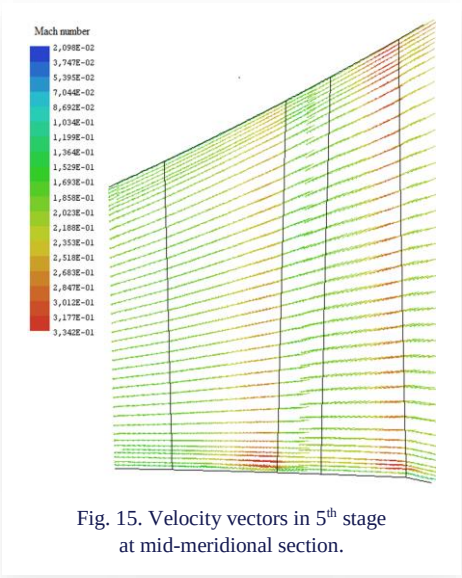

Fig. 15. Velocity vectors in 5th stage at mid-meridional section.

Table 4. The flow part main integral characteristics.

C_3, m/s	ξ_{ov}, %	η, %	Power (one flow), MW
230.8	3.1	91.42	139.387

6. Conclusions

- Analysis of 3D turbulent steam calculations in the initial design of the low-pressure cylinder flow part for the K-1000-60/1500 turbine has identified areas for improvement.
- The research has been carried using the techniques and software package for gas-dynamic calculations and the design of flow parts created at the IPMach NAS of Ukraine.
- A significant increase in the efficiency of LPC of the K-1000-60/1500 series steam turbine has been achieved.
- The total efficiency and power of the developed LPC flow part (single flow) are 91.42% and 139.387 MW, which is by 2.82% and 5.292 MW higher compared to the original one.
- LPC of this turbine consists of 6 flows, so the total increase in power is 31.752 MW.
- JSC "Ukrainian Energy Machines" (formerly PJSC "Turboatom") has approved the findings of the presented research.
- The methodology put forth, coupled with the acquired expertise, holds potential for utilization in the development and enhancement of LPC flow parts for other robust steam turbines at NPPs and TPPs within Ukraine and beyond.

Acknowledgements

The work was carried out within the framework of the scientific topic „Improvement and development of the main turbine equipment of NPP power units, including the use of technologies of small modular reactors and energy storage, in order to ensure energy security and sustainable development of the economy of Ukraine in the war and post-war periods" of the budget program „Scientific and technical (experimental) works under the priority direction – Technologies of thermal, electric and atomic energy to ensure the energy security of Ukraine" for 2023-2024", code of the program classification of expenditures 6541230 (applied research).

References

[1] Geletukha, G. (2020). Engagement of biomass CHP for power grid balancing in Ukraine. *Thermophysics and Thermal Power Engineering*, 42(3), 47−55. doi: 10.31472/ttpe.3.2020.5

[2] Engineer, Y., Rezk, A., & Hossain, A.K. (2021). Energy analysis and optimization of a small-scale axial flow turbine for organic Rankine cycle application. *International Journal of Thermofluids*, 12, 100119. doi: 10.1016/j.ijft.2021.100119

[3] Jankowski, M., Klonowicz, P., & Borsukiewicz, A. (2021). Multi-objective optimization of an ORC power plant using one-dimensional design of a radial-inflow turbine with backswept rotor blades, *Energy*, 237, 121506. doi: 10.1016/j.energy.2021.121506

[4] Musiał, A.M., Antczak, Ł., Jędrzejewski, Ł., & Klonowicz, P. (2021). Analysis of the use of waste heat from a glass melting furnace for electricity production in the organic Rankine cycle system. *Archives of Thermodynamics*, 42(1), 15–33. doi: 10.24425/ather.2021.136945

[5] Witanowski, Ł., Klonowicz, P., Lampart, P., Klimaszewski, P., Suchocki, T., Jędrzejewski, Ł., Zaniewski, D., & Ziółkowski, P. (2023). Impact of rotor geometry optimization on the off-design ORC turbine performance. *Energy*, 265, 126312, doi: 10.1016/j.energy.2022.126312

[6] Witanowski, Ł., Klonowicz, P., Lampart, P., Suchocki, T., Jędrzejewski, Ł., Zaniewski, D., & Klimaszewski, P. (2020). Optimization of an Axial Turbine for a Small Scale ORC Waste Heat Recovery System. *Energy*, 205, 118059. doi: 10.1016/j.energy.2020.118059

[7] Chantasiriwan, S. (2021). Comparative thermo-economic analysis of regenerative Rankine cycles with two feed water heaters. *Case Studies in Thermal Engineering*, 28, 101476, doi: 10.3390/en17122816

[8] Wojciechowski, W., Streimikiene, D., Wojciechowski, A., & Bilan, Y. (2023). The role of nuclear energy in low carbon energy transition: evidence from panel data approach in EU. *Environmental Science and Pollution Research International*, 30, 124353–124373. doi: 10.1007/s11356-023-30827-8

[9] Leiter, T. (2022). Too Little, Too Slow? Climate Adaptation at the United Nations Climate Change Negotiations Since the Adoption of the Paris Agreement. *Carbon & Climate Law Review*, 16(4), 243–258. doi: 10.21552/cclr/2022/4/5

[10] European Commission. (2023). *The European Green Deal*. (2019). https://ec.europa.eu/commission/presscorner/detail/en/ip_19_6691 [accessed 22 July 2024].

[11] Magazzino, C., Mele, M., Schneider, N., & Vallet, G. (2020). The relationship between nuclear energy consumption and economic growth: Evidence from Switzerland. *Environmental Research Letters*, 15, 0940. doi: 10.1088/1748-9326/abadcd

[12] European Commission. (2022) *EU Taxonomy: Commission presents Complementary Climate Delegated Act to accelerate decarbonization*. https://ec. europa.eu/commission/presscorner/detail/ en/ip_22_711 [accessed 22 July 2024].

[13] World Nuclear Association. (2023). *World Nuclear Performance Report*. COP26 Edition. https://www.world-nuclear.org/our-association/publications/ global-trends-reports/world-nuclear-performance-report.aspx [accessed 22 July 2024].

[14] Statista. (2024). *Number of under construction nuclear reactors worldwide*. https://www.statista.com/statistics/513671/number-of-under-construction-nuclear-reactors-worldwide/ [accessed 22 July 2024].

[15] Westinghouse Electric Company. (2022). *Energoatom and Westinghouse Begin AP1000® Plant License Process in Ukraine*. https://info.westinghousenuclear.com/news/energoatom-and-westinghouse-begin-plant-license-process [accessed 22 July 2024].

[16] Saylan, E., & Aygün, C. (2024). Thermoeconomic analysis and environmental impact assessment of the Akkuyu nuclear power plant. *Journal of Thermal Analysis and Calorimetry*, 149(12), 6531–6550. doi: 10.1007/s10973-024-13237-x

[17] Samatova, S.Y., Khidirovm M.M., Khamitjonov, O.B., & Mirzayarov A.U. (2021). NPP Construction Economic Benefits For Uzbekistan. *International Journal of Engineering and Information Systems*, 5(1), 162–165.

[18] Emerging Nuclear Energy Countries. (2024). *World-Nuclear report*. https://world-nuclear.org/information-library/current-and-future-generation/the-nuclear-debate [accessed 22 July 2024].

[19] World-Nuclear Association. (2024). *Nuclear Power in the World Today*. https://world-nuclear.org/information-library/current-and-future-generation/nuclear-power-in-the-world-today [accessed 22 July 2024].

[20] World-Nuclear Association. (2024). *Nuclear Power in Ukraine*. https://world-nuclear.org/information-library/country-profiles/countries-t-z/ukraine.aspx [accessed 22 July 2024].

[21] Becker, O., Decker., K., & Mraz, G. (2021). *NPP Zaporizhzhya lifetime-extension environmental impact assessment*. Umweltbundesamt GmbH Online Library: https://www.umweltbundesamt.at/fileadmin/site/publikationen/rep0775.pdf [accessed 22 July 2024].

[22] JSC "Ukrainian Energy Machines". (2023). *Geography of supplies 2023*. https://ukrenergymachines.com/en/map [accessed 22 July 2024].

[23] Oyedepo, S.O., Fakeye, B.A., Mabinuori, B., Babalola, P.O., Leramo, R.O., Kilanko, O., Dirisu, J.O., Udo, M., Efemwenkiekie, U.K., & Oyebanji, J.A. (2020). Thermodynamics analysis and performance optimization of a reheat-regenerative steam turbine power plant with feed water heaters. *Fuel*, 280, 118577. doi: 10.1016/j.fuel.2020.118577

[24] Rusanov, A., Subotin, V., Shvetsov, V., Rusanov, R., Palkov, S., Palkov, I., & Chugay, M. (2022). Application of innovative solutions to improve the efficiency of the LPC flow part of the 220 MW NPP steam turbine. *Archives of Thermodynamics*, 43(1), 63−87. doi: 10.24425/ather.2022.140925

[25] Yershov, S., Rusanov, A., Gardzilewicz, A., & Lampart, P. (1999). Calculations of 3D viscous compressible turbomachinery flows. *Proc. 2nd Symp. on Comp. Technologies for Fluid, Thermal/Chemical Systems with Industrial Applications, ASME PVP Division Conf.*, PVP, 397.2, 143−154. 1−5 August, Boston, USA.

[26] Menter, F.R. (1994). Two-equation eddy viscosity turbulence models for engineering applications. *AIAA Journal*, 32(8), 1598–1605. doi:10.2514/3.12149

[27] Rusanov, A.V., Lampart, P., Pashchenko, N.V., & Rusanov, R.A. (2016). Modelling 3D steam turbine flow using thermodynamic properties of steam IAPWS-95. *Polish Maritime Research*, 23(1), 61–67. doi: 10.1515/pomr-2016-0009

[28] Lampart, P., Gardzilewicz, A., Rusanov, A., & Yershov, S. (1999). The effect of stator blade compound lean and twist on flow characteristics of a turbine stage - numerical study based on 3D RANS simulations. *Proc. 2nd Symp. on Comp. Technologies for Fluid/Thermal/ Chemical Systems with Industrial Applications, ASME PVP Division Conf.*, PVP, 397.2, 195–204. 1-5 August, Boston, USA.

[29] Rusanov, A., Rusanov, R., Klonowicz, P., Lampart, P., Żywica, G., & Borsukiewicz, A. (2021). Development and Experimental Validation of Real Fluid Models for CFD Calculation of ORC and Steam Turbine Flows. *Materials*, 14(22), 6879. doi: 10.3390/ma14226879

[30] Lampart, P., Rusanov, A., Yershov, S., Marcinkowski, S., & Gardzilewicz, A. (2005). Validation of a 3D BANS solver with a state equation of thermally perfect and calorically imperfect gas on a multi-stage low-pressure steam turbine flow. *Transactions of the ASME, Journal of Fluids Engineering*, 127(1), 83−93.

[31] Lampart, P., Yershov, S., & Rusanov, A. (2005). Increasing flow efficiency of high-pressure and low-pressure stream turbine stages from numerical optimization of 3D blading. *Engineering Optimization*, 37, 145–166.

[32] Rusanov, A.V., Kostikov, A.O., Shubenko, O.L., Kharlampidi, D.K., Tarasova, V.O., & Senetskyi, O.V. (2019). Highly Efficient Cogeneration Power Plant with Deep Regeneration Based on Air Brayton Cycle. *Journal of Mechanical Engineering*, 22(4), 12−23. doi: 10.15407/pmach2019.04.012

[33] Fischer, P.F., & Venugopal, M. (1995). A commercial CFD application on a shared memory multiprocessor using MPI. *Parallel Computational Fluid Dynamics*, 231−238. doi: 10.1016/B978-044482322-9/50083-9

[34] Lampart, P., Gardzilewicz, A., Rusanov, A., & Yershov, S. (2001). Investigations of interaction of the main flow with root and tip leakage flows in an axial turbine stage by means of a source/sink approach for a 3D Navier-Stokes solver. *Journal of Thermal Science*, 10(3), 198–204. doi: 10.1007/s11630-001-0019-4

[35] Grigorieva, V.A., & Zorina, V.M. (1989). *Thermal and Nuclear Power Plants: A Handbook* (2nd edition., revised). Energoatomizdat.

[36] Brodov, Yu.M., & Saveliev, R.Z. (1994). *Condensing units of steam turbines: Textbook for universities*. Energoatomizdat.

[37] Levchenko, E.V., Shvetsov, V.L., Kozheshkurt, I.I., & Lobko, A.N. (2010). Experience of PJSC «Turboatom» in the development and modernization of turbines for nuclear power plants. *Bulletin of the National Technical University "Kharkiv Polytechnic Institute*", 3: *Energy and heat engineering processes and installation*, 8 p.

[38] Nguyen, K., & Laskin, A. (2015). Influence of u/c_0 ratio on Unsteady Loads and Efficiency Level of Axial Turbine Stage. *Science and Education of the Bauman*, 6, 56−66. doi: 10.7463/0615.0786614

[39] Hryshyn, M., Zaytsev, B., Palkov, I., Kantor, O., & Pashchenko, Yu. (2019). Welded combined rotor for the steam turbine K-325-23.5. *Bulletin of the National Technical University "Kharkiv Polytechnic Institute". Series: Power and Heat Engineering Processes and Equipment*, 3(1328), 66−75. doi: 10.20998/2078-774X.2019.03.10

[40] Rusanov, A., & Rusanov, R. (2021). The influence of stator-rotor interspace overlap of meridional contours on the efficiency of high-pressure steam turbine stages. *Archives of Thermodynamics*, 42(1), 97–114. doi: 10.24425/ather.2021.136

Co-published by
Institute of Fluid-Flow Machinery
Polish Academy of Sciences
Committee on Thermodynamics and Combustion
Polish Academy of Sciences

http://www.imp.gda.pl/archives-of-thermodynamics/

ARCHIVES OF THERMODYNAMICS

Operation of a hybrid heating system based on heat pumps using a photovoltaic installation

Marcin Kazimierz Turoń

Cracow University of Technology, ul. Warszawska 24, Cracow 31-155, Poland
Corresponding author email: marcin.turon@doktorant.pk.edu.pl

Received: 20.03.2024; revised: 22.08.2024; accepted: 20.10.2024

Abstract

In Poland, heating systems using renewable energy sources have gained importance in construction projects, especially in newly designed buildings. This is mainly due to the Regulation of the Minister of Infrastructure, which sets technical conditions for buildings. As of December 31, 2020, the primary energy index for newly designed single-family buildings should not exceed 70 kWh/(m^2·year). This requires efficient energy sources in building design. Renewable energy installations have significantly lower primary energy utilization rates than fossil fuel systems, making them the preferred choice. In a facility in Batowice near Krakow, a hybrid energy system with ground-source and air-source heat pumps has been installed. These pumps are powered by electricity from a photovoltaic installation connected to the grid. The study aims to determine the optimal heat pump choice based on the facility's conditions and optimize electricity consumption from the photovoltaic installation. Both heat pumps showed similar efficiencies during the heating season from December 2022 to March 2023: the ground-source heat pump achieved an annual coefficient of performance of 2.69, and the air-source heat pump achieved a seasonal coefficient of performance of 2.63. Given the high non-renewable primary energy factor for grid electricity, the feasibility of replacing gas boilers with heat pumps requires careful evaluation. The results indicate that integrating a heat pump with a photovoltaic installation substantially reduces the primary energy utilization index, supporting climate protection and the advancement of renewable energy sources. However, heat pumps alone may not be sufficiently efficient without the support of a PV installation.

Keywords: Renewable energy sources; Heat pumps; Hybrid installations; Energy efficiency; Photovoltaic installations

Vol. 45(2024), No. 4, 153–162; doi: 10.24425/ather.2024.152004

Cite this manuscript as: Turoń, M.K. (2024). Operation of a hybrid heating system based on heat pumps using a photovoltaic installation. *Archives of Thermodynamics*, 45(4), 153−162.

1. Introduction

Poland and other European Union (EU) countries have committed to preparing an energy scenario by 2050 that allows for sustainable and carbon-free energy production. Therefore, one of the critical objectives of EU energy policy is to improve the energy performance of the building stock. In achieving these objectives, heat pumps (HPs) can play an essential role in electrifying sources of heat generation and domestic hot water preparation. HPs are expected to bring the most significant environ-

Nomenclature

Abbreviations and Acronyms

AHP – air-source heat pump
COP – coefficient of performance
EP – primary energy
EU – European Union
GHP – ground-source heat pump
HP – heat pump
PEF – primary energy factor
PV – photovoltaic
RES – renewable energy sources
sCOP– seasonal (annual) coefficient of performance

mental benefits in energy markets where renewable energy, such as wind, has a considerable share. A noteworthy challenge associated with the electrification of heat is the transition of residential space heating from conventional fossil fuel-based technologies to electricity.

The primary challenge in utilizing heat pumps is the resultant primary energy utilization index. To ensure the ecological viability of replacing a fossil fuel-based heat source, it must be replaced with a device with a lower primary energy input. Given the high primary energy factor associated with grid electricity (Table 1), replacing a gas boiler with a heat pump powered by the electrical grid becomes environmentally beneficial only if the heat pump's average annual coefficient of performance (sCOP) exceeds 2.3. Otherwise, the carbon dioxide emissions from using a heat pump will surpass those from heating the building with natural gas.

Comprehensive field studies covering multiple heating seasons are required to determine the feasibility of implementing heat pumps in heating systems. It is also essential to ascertain whether the type of heat pump significantly impacts the expected outcomes. The unique characteristics of the studied facility allow for the empirical comparison of air-source and ground-source heat pumps operating under identical conditions within a single hybrid system. This study is particularly valuable because, in a standard facility, two different types of heat pumps are typically not installed within the same heating system. Furthermore, the photovoltaic (PV) installation in the building facilitates the evaluation of the potential for using solar energy to power heat pumps, substantially contributing to the reduction of the primary energy utilization index. In addition to comparing the performance of different heat pumps, this study aims to maximize the utilization of energy generated by the PV installation during its production phase.

Kim et al. [1] suggested a hybrid solar-geothermal carbon dioxide heat pump system for residential applications. By using a heat pump with CO_2 as the working medium, the temperature of the heating medium produced was significantly increased. Sridhar et al. [2] have developed a numerical algorithm that, based on intelligent measurement data, allows the selection of a hybrid heating system for a set of buildings, increased electrification of the heat sources, and improved flexibility. Yao et al. [3] analysed a residential heating system based on a heat pump with a borehole heat exchanger powered by electricity from PV-T panels. They demonstrated that the heat pump in the developed hybrid system can achieve a COP significantly above 7. Kazem et al. [4] showed that the combined use of PV-T installations to power heat pumps can reduce grid electricity consumption significantly. In addition, the waste heat from the PV-T systems enhances the heat pumps' efficiency. Long et al. [5] have proposed a combined system for heating the house and sup-plying domestic hot water. An air-source heat pump and a solar thermal collector were used to heat the residence and provide hot water. This solution enables significant energy savings [5]. Bezrodny et al. [6] proposed the use of heat pumps in air-conditioning systems. The authors showed that recirculating the exhaust air through the heat pump evaporator allows the preset room conditions to be maintained over a wider range of variations in ambient air parameters. In addition, lower specific energy consumption of the heat pump is achieved, improving its efficiency. Hanuszkiewicz-Drapała and Bury [7] conducted a thermodynamic analysis of a heat pump with a horizontal ground heat exchanger used to heat and cool a residential building. They investigated the impact of the heat supplied to the ground during the summer on the operation of the heating system and electricity consumption during the following heating season.

Heat pumps for residential heating powered by electricity from renewable sources reduce greenhouse gas emissions and dependence on imported fossil fuels [8]. Heat pumps combined with heat storage are well suited to providing short-term flexibility, shifting loads to periods of low prices and high renewable electricity supply. Harnessing the flexibility of heat pumps, a more balanced local energy system can be created [9,10]. Hybrid installations using renewable energy sources are an increasingly common solution. In his article on hybrid installations, Pater argues that it is possible to easily significantly increase the share of renewable energy sources in the production of energy for heating purposes [11], and in the next study, he analyses a hybrid based on a heat pump combined with a photovoltaic installation to supply the building with hot water [12].

The performance of photovoltaic panels is strongly dependent on external conditions such as sunshine, temperature, air pollution, cloud cover or precipitation. Although photovoltaic panels operate most efficiently in full sunlight, different atmospheric conditions still allow their use over a wide geographical and climatic range. Katoch et al. in [13] analysed the influence of the dust gathering on the photovoltaic panel on its performance and average output power and short circuit current. Kuczyński and Borowska [14] investigated the exergy efficiency of photovoltaic installations as a critical parameter to determine the maximum amount of electricity that could be produced under certain conditions. Kadhim and Al-Ghezi [15] made a comprehensive review of cooling systems that allow for increased efficiency, energy production and service life of photovoltaic modules.

The intermittent electricity production in photovoltaic panels requires such installations to be equipped with energy storage systems. Deka and Szlęk [16] investigated the different methods of storage of excess energy from renewable sources as one of the ways to reduce reliance on fossil fuels for residential heat-

ing and cooling. Excess energy can be stored in systems using phase change materials (PCM) and later used to produce cold in adsorption chillers or to support refrigerant preparation in heating systems. Karwacki et al. [17] conducted a study to identify the best phase-change material for thermal energy storage in domestic installations. Cieśliński et al. [18] carried out experimental viscosity determinations of phase-change materials, which were used to develop accurate correlation formulas for determining the viscosity of PCMs.

The conducted research aims to evaluate the feasibility of implementing hybrid systems based on renewable energy sources for powering buildings under Polish conditions. The primary objective of the study was to compare the performance of ground-source and air-source heat pumps and to investigate the potential for optimizing their integration with photovoltaic installations.

2. Legal requirements for buildings

In the context of the regulations in force in Poland, one of the most essential indicators, important for investors and building designers, is the facility's unit demand for non-renewable primary energy. The latest amendment has maintained the limitation introduced since December 31, 2020, on the primary energy (EP) index for heating, ventilation and domestic hot water preparation at 70 kWh/(m²·year) for single-family houses and 75 kWh/(m²·year) for collective residential buildings.

Public buildings, excluding healthcare facilities, have a demand limit of 45 kWh/(m²·year) [19]. These restrictions compel investors and designers to seek energy-efficient construction solutions and utilize energy sources with low primary energy utilization rates. Table 1, included in the Regulation of the Minister of Development and Technology [20], presents the values of primary energy utilization rates for various energy sources.

3. Hybrid installation

A hybrid power supply system based on multiple energy sources has been implemented in the building being considered, located in Batowice near Krakow in Poland. The primary heat sources for the heating system are two heat pumps (Table 2):

- a ground-source heat pump (GHP) with a capacity of 10.9 kW (B0/W35),
- an air-source heat pump (AHP) with a capacity of 12 kW (A7/W35).

A fireplace with a water jacket also serves as an auxiliary heat source, and a gas-condensing boiler is installed as a peak heat source.

The heating system incorporates a central heating buffer tank with a capacity of 1500 litres. Furthermore, the hot water provision includes a separate domestic hot water tank with a capacity of 800 litres. During the summer months, a solar collector installation is utilized to prepare domestic hot water. Moreover, besides being connected to the power grid, electricity generated by a 9.6 kW PV installation is also utilized. The installation layout is presented in Fig. 1. In order to conduct a comparative analysis of two different types of heat pumps, a ground and air heat pump was installed in one building, as part of one heating system. Table 2 contains a comparative summary of the most important parameters of both devices. Please remember that both heat pumps differ in their specific operation depending on the prevailing external conditions. The outside air temperature is of little importance for a ground heat pump. The air heat pump is very sensitive to weather conditions because it uses outside air as the lower heat source. From the user's point of view, it is very important to determine which source will be a more justified choice, both in terms of energy and finances. Comparing the behaviour of both devices under identical operating conditions is the best way to determine when and which device will work better.

Table 1. The effort of non-renewable primary energy factors (PEF) for the production and delivery of the energy carrier for technical systems [20].

No.	Method of Energy Supply	Type of Energy Carrier	PEF
1	Local energy production in the building	Heating oil	1.10
2		Natural gas	
3		Liquid gas	
4		Coal	
5		Lignite	
6		Solar energy	0.00
7		Wind energy	
8		Geothermal energy	
9		Biomass	0.20
10		Biogas	0.50
11	Network heating from co-generation	Coal or gas	0.80
12		Biomass, biogas	0.15
13	Network heating from a heating plant	Coal	1.30
14		Gas or heating oil	1.20
15	System power grid	Electricity	2.50

4. Research problem analysis and interpretation of measurement results

According to Table 1, in the case of an energy production system in a building, the amount of final energy for heating should be multiplied for non-renewable sources by the indicator PEF = 1.1. In practice, to meet the requirements of the regulation, we must reduce the use of usable energy in the facility to the level appropriate for low-energy buildings. The use of grid electricity carries an even greater burden on the environment, as illustrated by the PEF index value 2.5 (until April 28, 2023, this index was 3.0). Replacing heat sources using non-renewable energy (natural gas, coal, etc.) with heat pumps will be justified only if the total (weighted) coefficient PEF resulting from using renewable energy and electricity supplying the heat pump compressor is lower than 1.1. As we can see, this will be closely related to the achievable seasonal efficiency of the device used. Therefore, to obtain satisfactory results, a seasonal efficiency ra-

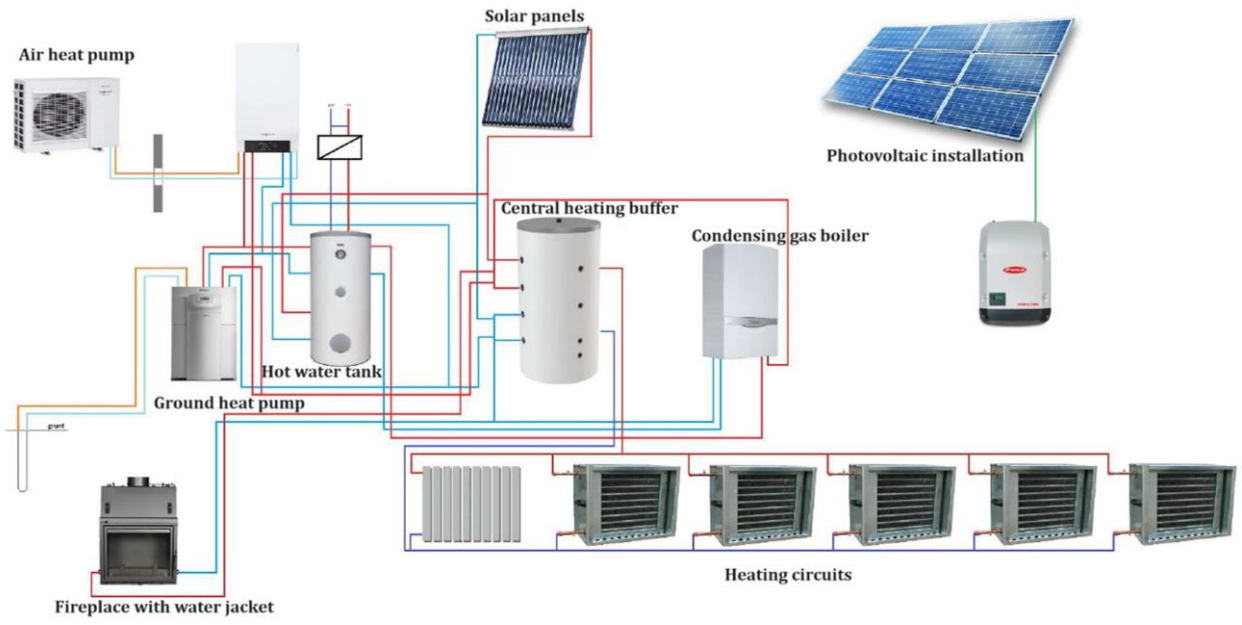

Fig. 1. Diagram of a hybrid installation powering the building in Batowice.

Table 2. Technical data of heat pumps.

Parameter	Air heat pump	Ground heat pump
HP type	Vitocal 151.A10	VWS 104/3
Refrigerant type	R290	R407C
Heating power	12 kW (A7/W35) 9.7 kW (A-7/W35) 9.37 kW (A7/W55)	10.9 kW (B0/W35) 9.7 kW (B0/W55)
Electrical power consumption	2.46 kW (A7/W35) 3.23 kW (A-7/W35) 2.6 kW (A7/W55)	2.2 kW (B0/W35) 3.2 kW (B0/W55)
COP	5.0 (A7/W35) 3.0 (A-7/W35) 3.7 (A7/W55)	4.9 (B0/W35) 3.0 (B0/W55)

tio of the heat pump should be obtained at a level higher than 2.3 (before changing the index, it was necessary to get a seasonal efficiency sCOP above 2.73). Otherwise, using a heat pump powered by network electricity will generate higher primary energy consumption than an installation with a gas or coal boiler. Figure 2 shows the average monthly COP values for the tested heat pumps from November 2022 to the end of 2023. The efficiency factor of both devices is so high that from an ecological point of view, with PEF = 2.5 for electricity from the grid, their use is profitable. This is a fundamental issue, especially when air heat pump, because the device is characterized by high vari-

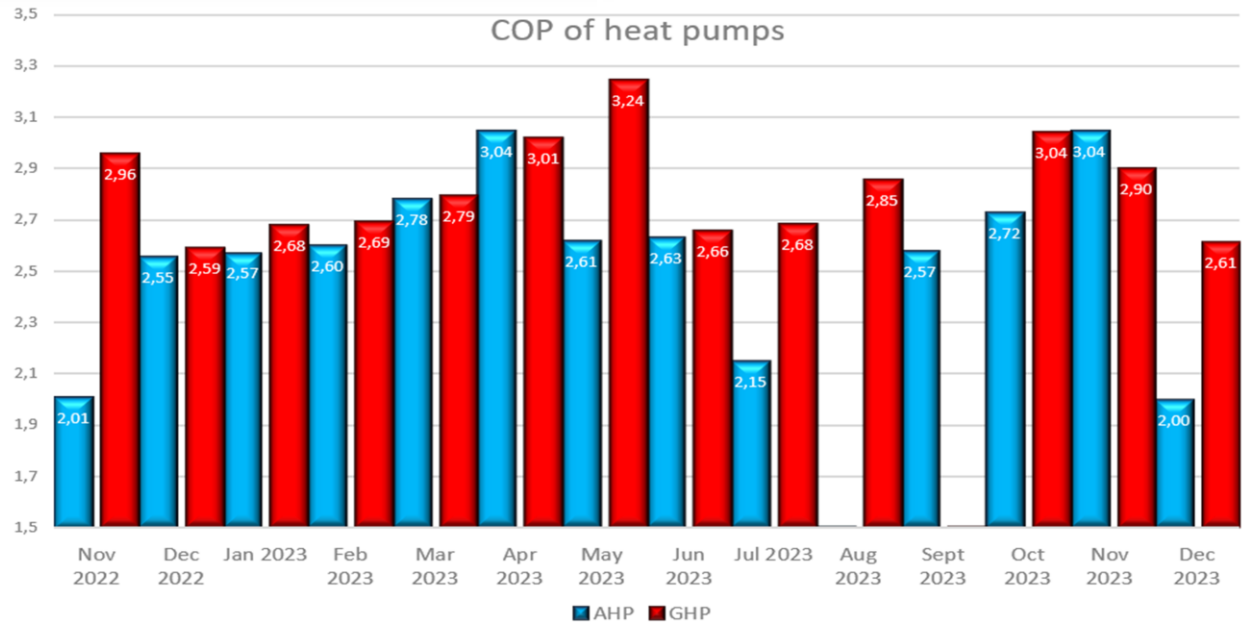

Fig. 2. Average monthly COP values of ground-source and air-source heat pumps installed in the analysed facility.
AHP – air-source heat pump, GHP – ground-source heat pump.

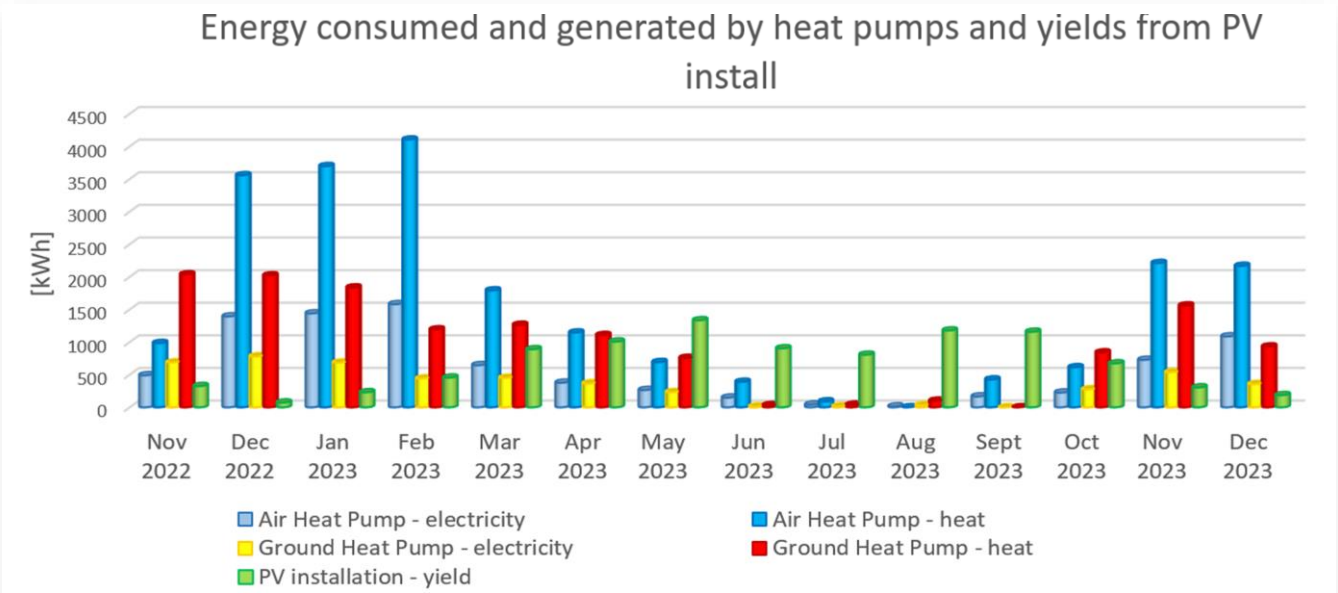

Fig. 3. Balance of energy consumed and produced by heat pumps and electricity production by the photovoltaic installation.

ability of operating efficiency with changes in outdoor air parameters. Installing a photovoltaic installation to power a heat pump comes in handy here. The PEF coefficient for solar installations is 0.0 [20], meaning that energy from a PV installation does not result in primary energy use. Another question when planning to install a photovoltaic system concerns the level of electricity used to power the heat pump compressor. We cannot ensure 100% use of energy from PV installations, and we will take part of the electricity for our pump from the network, so we will not eliminate the share of primary energy in the overall energy balance of the building. In the future, this may be possible when satisfactory efficiency of storing electricity is achieved. Still, with current technological limitations, we must assume that part of the electricity for our heat pump will come from non-renewable sources.

Two heat pumps were installed in the tested facility: a 10.9 kW ground source heat pump operating with R407C refrigerant and a 12 kW air source heat pump using R290 refrigerant. Additionally, a 9.6 kW photovoltaic installation was installed to meet the building's electricity demand partially. The photovoltaic system is connected to the power grid and operates under a prosumer net-metering system. Under this system, any surplus electricity generated by the photovoltaic installation not consumed by the building is transmitted into the grid. The prosumer will receive 80% compensation for the supplied energy for the following year. Since April 2022, a new billing system called net billing has been implemented, involving financial settlement for surplus energy. The prosumer sells surplus energy to the grid and receives a monetary credit, allowing them to purchase grid energy at a specified rate. Additionally, the prosumer is responsible for transmission fees for delivered and consumed energy.

To estimate the amount of primary energy used to operate the heat pump in the configuration with a photovoltaic installation, it is necessary to consider the methodology for calculating the share of renewable energy in the electricity used. First, we must determine how to divide energy use between the building's heat pump and other electrical devices. We have two options here: qualifying all renewable energy as consumed for the operation of the heat pump, especially in residential buildings, where the energy for lighting the building is not included in the balance of primary energy use in the building or dividing the consumption as a percentage between all electricity receivers in the considered object. The most rational and fair solution is measuring devices so that it is possible to indicate directly which source powered the heat pump in real-time during its operation. However, the solution is expensive and impractical from the point of view of an ordinary user, for whom the distribution of energy produced is irrelevant because it does not affect the economic aspect of using energy from a PV installation. A comparison of electricity consumption and production of heating energy by an air and ground heat pump and energy production by a photovoltaic installation in individual months is shown in Fig. 3.

It should be noted that the greatest energy demand for heat pump operation occurs in periods when production from PV installations is the lowest. Prosumer settlement of micro-installations enables annual balancing of energy delivered and consumed, which is a beneficial solution for the user. In turn, the use of the generated electricity for one’s own needs and the amounts of electricity fed into the network and consumed are shown in Fig. 4.

It can be said that using heat pumps enables an increase in the consumption of energy generated by the PV installation for internal needs. During months when heat pumps are used for heating, the self-consumption of electricity from the PV system significantly exceeds the amount of energy exported to the grid. The subsequent step involves determining the methodology for categorizing the electricity fed into the grid and the energy consumed in a 1:0.8 balance when employing net metering settlement [21]. In such scenarios, the grid is considered a storage facility for the generated energy, with an assumed annual efficiency of 80%. It can be presumed that the PEF index for the

energy received from the grid in the balance is also 0.0, indicating renewable energy inclusion in the primary energy balance of the grid's current. Hence, adopting a PEF value of 0.0 solely for the energy sourced from the PV installation and used for internal needs at the production point appears reasonable. However, for the remaining electricity derived from the grid, whether within or outside the balance, a PEF coefficient of 2.5 should be employed following the reduction from 3.0.

Another problem we face here is using electricity from PV installations for our needs. Depending on the daily electricity use profile, an average household can use approximately 20–30% [22] of the energy produced for its own needs. The remaining part of the production from the photovoltaic installation is fed into the power grid. Therefore, the next challenge is to develop methods for maximising electricity consumption from the photovoltaic installation at the generation site, necessarily without increasing the energy needs of the building. The data analysis covered the period from November 2022 to the end of 2023 and allowed for a preliminary assessment of the cooperation of the photovoltaic installation with the building. Figures 4, 5 and 6 present the results of the research.

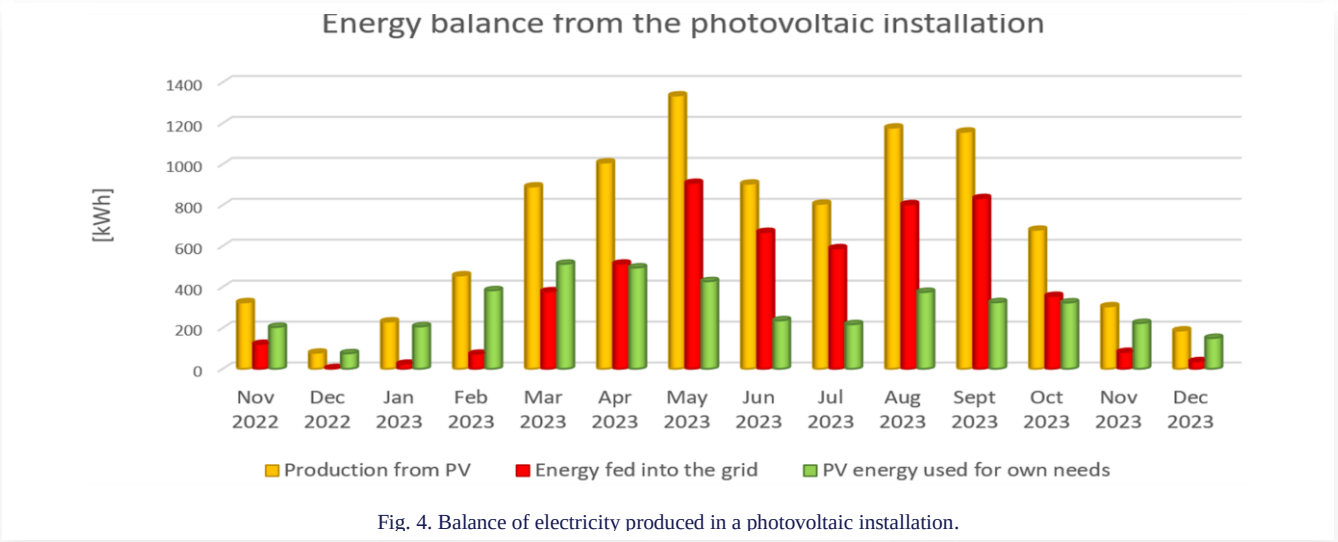

Fig. 4. Balance of electricity produced in a photovoltaic installation.

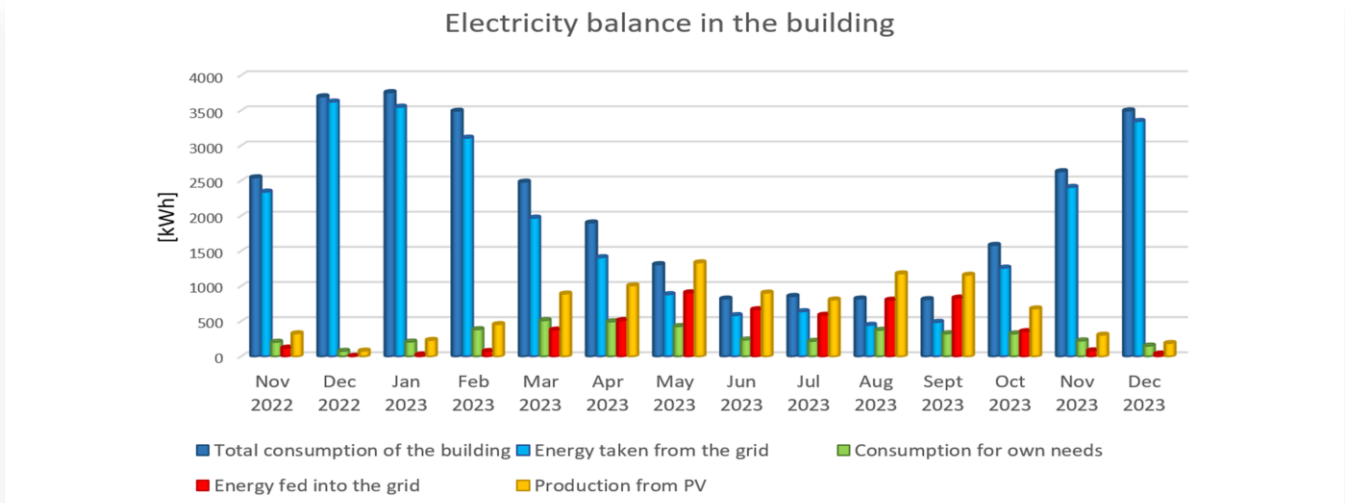

Fig. 5. Energy balance in the facility. Distribution of electricity consumed by the building and produced by the photovoltaic installation.

The analyses were conducted in the context of electricity consumption by the tested facility, energy production in the photovoltaic installation, the possibility of covering the building's demand with the energy produced by the PV installation and the use of energy from photovoltaics for own needs at the time of its production. The analysis used data from the measurement system installed in the facility and on the platform provided by the power company (Figs. 7 and 8).

During the summer months, when PV installation production is at its peak, approximately 30% [22] of the energy generated is consumed for internal needs. This aligns with the typical annual energy consumption profiles of households. Additionally, as illustrated in Fig. 5, it can be observed that only during the peak production period does the PV installation generate more energy than what is required by the building.

Conversely, the utilization of energy produced directly at the generation site to meet the facility's internal needs averages approximately 20% (refer to Fig. 6).

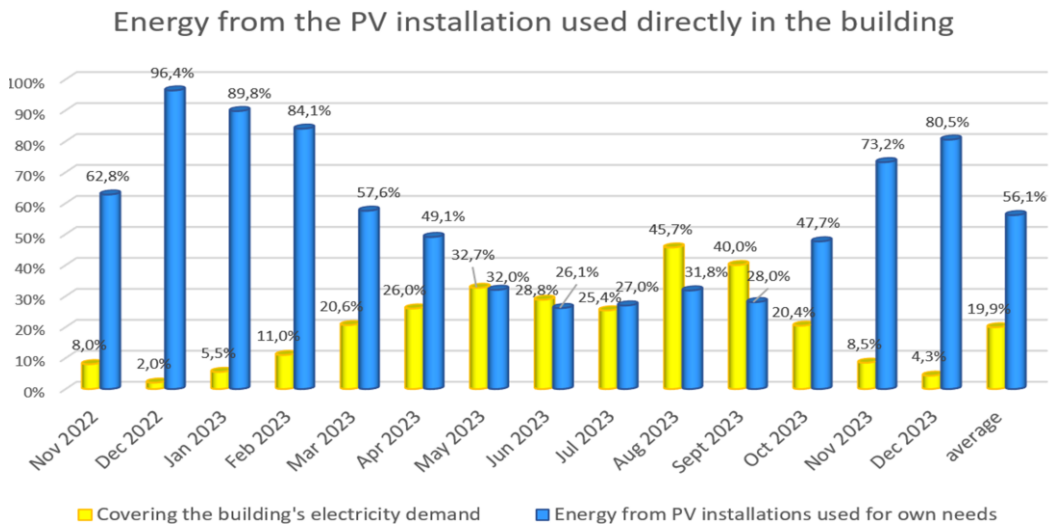

Fig. 6. Percentage of energy from the PV installation used for own needs in meeting the energy needs of the building and in the production of energy from photovoltaics.

The amount of energy generated by the photovoltaic installation is measured within the building, and information regarding the energy fed into the grid and the energy drawn from the power grid can be accessed by the customer through the platform provided by the power company (Fig. 7). Using the obtained data, it is possible to calculate the energy consumed by the prosumer for their own needs and the total energy used by the building.

Moreover, the platform provides information regarding virtual energy storage. The system converts the energy fed into the grid into equivalent units that can be credited to the prosumer's account. This enables the user to access information on the energy they can receive at no cost from the grid in the upcoming billing period (Fig. 8).

The conducted research aims to assess the more appropriate choice between a ground heat pump and an air heat pump, particularly in Polish climatic conditions. Additionally, the research endeavours to identify strategies to optimize the efficient utilization of electricity generated by photovoltaic systems to meet the energy demands of the building.

A preliminary analysis of measurement data showed that the operating parameters of both heat pumps are comparable during the heating season when the building consumes the most energy. A heat pump with a ground collector, due to the greater stability of the lower source, will have a slightly higher COP (Fig. 2 – red bars on the chart). Still, the cost of its installation will be much higher, which makes the economic viability of this project questionable. In turn, despite the expectation that in the summer, an air heat pump operating on a higher heat source parameter would have a higher COP, it turned out that this assumption was wrong. The ground heat pump, despite the lower temperature of the ground source, achieved higher operating efficiency than the air pump in the summer months. An additional experiment was conducted in August and September to investigate this dependency. Throughout August 2023, the heating of domestic hot water was supported only by a ground heat pump, while in September, an air unit was used for this purpose. The results confirmed previous observations. Despite the atmospheric air temperature being higher than the temperature of the brine feeding the ground heat pump, the efficiency of the air HP was lower than that of the ground one. The first thing that comes to mind is that an air heat pump, despite better operating parameters related to higher external air temperature, consumes more electricity due to constant readiness for operation. Heating the compressor crankcase, which is performed by an air heat pump, is not necessary in the case of a ground heat pump, which is especially noticeable during periods when heat pumps only work to heat domestic hot water, which is why they are turned on sporadically. When the compressor works more often during the heating season, this problem does not occur because there are only a few downtime periods for heating devices.

In subsequent heating periods, modifications to the system are planned, consisting of adapting the hybrid operation to the building's changing energy demand. The analysis of the collected measurement data is intended to help develop solutions that will help designers efficiently select power supply installations for a building with a specific energy class. It should significantly improve cooperation between the architectural industry and designers of sanitary installations supplying buildings with low energy demand.

The heating system in the tested facility is equipped with a central heating buffer with a capacity of 1500 l and a domestic hot water tank with a capacity of 800 l. Both tanks are located in the heated space of the building. Owing to these installation elements, energy can be accumulated, and its use can be postponed in time. Therefore, the first idea that comes to mind is the production of heat during the day, when the air temperature is higher, which is of great importance for increasing the efficiency of the air heat pump. During the day, we also obtain energy from the photovoltaic installation to use the electricity produced directly to power the heat pump. The energy collected in this way, which was generated in the most favourable conditions during the day, can later be used when our needs related to space heating and domestic hot water are the highest. However, this will

involve additional costs associated with raising the temperature in the buffer tank. This will help increase the heat capacity of the system but will force the heat pumps to work with less optimal parameters of the upper source. Analyzing measurement data collected last year and in subsequent heating seasons will allow for estimating actual savings related to these measures re-

Fig. 7. Visualization from the TAURON e-counter platform. Balance of electricity consumed and energy from the PV installation fed into the power grid [23].

Fig. 8. Visualization from the TAURON e-counter platform. Balance of electricity consumed and energy from the PV installation fed into the power grid - considering the settlement balance [23].

garding energy and economy. The calculations will require considering two variants of settlement of the photovoltaic installation with the power company. They may be considered for a maximum period of 15 years because the prosumer settlement ceases to be valid later. After the period for which the prosumer contract has been concluded, it becomes even more important to use as much energy from photovoltaics as possible for your own needs, so optimizing the operation of the building's power supply system is one of the key elements of the user's savings planning.

This research can contribute to optimising energy utilization in buildings, thereby enhancing energy efficiency in the construction sector. Moreover, by improving the correlation between the operation of heat pumps and the usage of energy generated in photovoltaic installations, the research aims to enhance the stability of the collaboration between photovoltaic systems and the power grid. This research holds significant importance, not only for economic purposes but also for climate protection, particularly in terms of enhancing the efficiency of harnessing renewable energy to mitigate the greenhouse effect.

5. Conclusions

The conducted research aims to determine the actual operating parameters of two types of heat pumps installed under identical conditions, which constitutes a unique approach to the subject. The hybrid system installed in the analyzed building allows for very flexible changes in the operating parameters of both devices. Additionally, the building's power supply system enables the study of the cooperation between the heat pumps and the photovoltaic installation. Research conducted over two heating seasons allowed for drawing conclusions that may significantly influence the approach of investors, designers and installers towards the use of RES in construction.

Summarizing the initial research, it should be noted that in the current climatic conditions in Poland, the operation of an air-source heat pump does not significantly differ from the performance of a ground-source heat pump. The efficiency indicators of both devices during the heating season differ slightly and are respectively: for the GHP 2.69; for the AHP 2.63. Considering the investment costs AHP are currently becoming a real alternative to the much more expensive GHP.

It was also noted that the cooperation of an AHP with solar collectors, in the summer, does not have a positive effect on the efficiency of the heat pump. Despite the higher temperatures of the lower source than in the heating season, the efficiency of the device decreases instead of increasing. In July, when the AHP was operating only for the domestic hot water buffer, its sCOP was only 2.16, which was the lowest value recorded during the unit's operation. The main reason for this situation is the long downtime of the heat pump in readiness for operation, which causes the consumption of electricity, despite the lack of need for the device to operate.

In turn, the cooperation of the heat pump with the photovoltaic installation can contribute to increasing the ecological efficiency of the use of the building's power supply system. In the period December 2022 – February 2023, the use of energy from PV for own needs exceeded 80%, and over the entire year amounted to 55.7%, significantly exceeding the assumed self-consumption, which in an average household is about 30%. Maximizing the use of energy generated by the PV installation for one's own needs will also contribute to increasing the economic efficiency of the project. The lack of prosumer settlement will reduce energy losses in the case of net-metering and eliminate additional energy purchase costs in the case of net-billing.

The research planned for the upcoming years aims to address these questions and alleviate any uncertainties regarding the viability of utilizing renewable energy in construction. This research is anticipated to provide valuable insights and clarification in this regard.

Acknowledgements

The Ministry of Science and Higher Education of the Republic of Poland supported the research. This project received funding from the programme: Implementation Doctorate No. DWD/5/0032/2021.

References

[1] Kim, W., Choi, J., & Cho, H. (2013). Performance analysis of hybrid solar-geothermal CO_2 heat pump system for residential heating. *Renewable Energy*, 50, 596–604, doi: 10.1016/j.renene.2012.07.020

[2] Sridhar, A., Belonogova, N., Honkapuro, S., Huuki, H., Kopsakangas-Savolainen, M., & Ruokamo, E. (2023). Identifying hybrid heating systems in the residential sector from smart meter data. *Journal of Building Engineering*, 74, 106867. doi: 10.1016/j.jobe.2023.106867

[3] Yao, J., Liu, W., Zhang, L., Tian, B., Dai, Y., & Huang, M. (2020). Performance analysis of a residential heating system using borehole heat exchanger coupled with solar assisted PV/T heat pump. *Renewable Energy*, 160, 160−175. doi: 10.1016/j.renene.2020.06.101

[4] Kazem, H.A., Chaichan, M.T., Al-Waeli A.H.A., & Sopian K. (2022). A systematic review of photovoltaic/thermal applications in heat pumps systems. *Solar Energy*, 269, 112299. doi: 10.1016/j.solener.2023.112299

[5] Long, J., Xia, K., Zhong, H., Lu, H., & Yongga A. (2021). Study on energy-saving operation of a combined heating system of solar hot water and air source heat pump. *Energy Conversion and Management*. 229, 113624. doi: 10.1016/j.enconman.2020.113624

[6] Bezrodny, M,. Prytula, N., & Tsvietkova M. (2019). Efficiency of heat pump systems of air conditioning for removing excessive moisture. *Archives of Thermodynamics*, 40(2), 151−165. doi: 10.24425/ather.2019.129546

[7] Hanuszkiewicz-Drapała, M., & Bury T. (2016). Utilization of the horizontal ground heat exchanger in the heating and cooling system of a residential building. *Archives of Thermodynamics*, 37(1), 42−72. doi: 10.1515/aoter-2016-0004

[8] Meles, T.H., & Ryan, L. (2022) Adoption of renewable home heating systems: An agent-based model of heat pumps in Ireland. *Renewable and Sustainable Energy Reviews*, 169, 112853. doi: 10.1016/j.rser.2022.112853

[9] Marijanovic, Z., Theile, P., & Czock, B.H. (2022). Value of short-term heating system flexibility – A case study for residential heat pumps on the German intraday market. *Energy*, 249, 123664. doi: 10.1016/j.energy.2022.123664

[10] You, Z., Lumpp, S.D., Doepfert, M., Tzscheutschler, P., & Goebel, C. (2024). Leveraging flexibility of residential heat pumps

through local energy markets. *Applied Energy*, 355, 122269. doi: 10.1016/j.apenergy.2023.122269

[11] Pater, S. (2019). Field measurements and energy performance analysis of renewable energy source devices in a heating and cooling system in a residential building in southern Poland. *Energy and Buildings*, 199, 115−125. doi: 10.1016/j.enbuild.2019.06.057

[12] Pater, S. (2023). Increasing Energy Self-Consumption in Residential Photovoltaic Systems with Heat Pumps in Poland. *Energies*, 16, 4003. doi: 10.3390/en16104003

[13] Katoch, M., Dahiya, V., & Yadav, S.K.: (2023). The performance analysis of dusty photovoltaic panel. *Archives of Thermodynamics*, 44(2), 49–68. doi: 10.24425/ather.2023.146558

[14] Kuczyński, W., & Borowska, A. (2023). The effect of photovoltaic system operating parameters on exergy efficiency. *Archives of Thermodynamics*, 44(4), 619–633. doi: 10.24425/ather.2023.149736

[15] Khadim, O.I.S.A., & Al-Ghezi, A.K.A. (2023). Photovoltaic panels cooling technologies: Comprehensive review. *Archives of Thermodynamics*, 44(4), 581−617. doi: 10.24425/ather.2023.149720

[16] Deka, P., & Szlęk, A. (2022). Thermal energy storage in buildings: Opportunities and challenges. *Archives of Thermodynamics*, 43(4), 21−61. doi: 10.24425/ather.2022.144405

[17] Karwacki, J., Kwidziński, R., & Leputa, P. (2022). Performance analysis and PCM selection for adsorption chiller aided by energy storage supplied from the district heating system. *Archives of Thermodynamics*, 43(4), 135−169. doi: 10.24425/ather.2022.144409

[18] Cieśliński, J.T., Fabrykiewicz, M., Wiśniewski, T.S., Kubiś, M., Smoleń, S., Eicke, A., Dutkowski, K., & Głuszek-Czarnecka, M. (2023). New empirical correlations for the viscosity of selected organic phase change materials. *Archives of Thermodynamics*, 44(4), 123−129. doi: 10.24425/ather.2023.149732

[19] Ministry of Development and Technology. (2022). *Regulation of the Minister of Infrastructure on the technical conditions to be met by buildings and their location*. Journal of Laws 2022, item 1225. https://isap.sejm.gov.pl/isap.nsf/DocDetails.xsp?id=WDU20220001225 [accessed 07 Jan. 2024].

[20] Ministry of Development and Technology. (2023) *Regulation of the methodology for determining the energy performance of building or part of a building and energy performance certificates*. Journal of Laws, 697. https://isap.sejm.gov.pl/isap.nsf/DocDetails.xsp?id= WDU20220001225 [accessed 07 Jan. 2024].

[21] Marshal of the Sejm. (2015). *Act of February 20, 2015 on renewable energy sources*. Journal of Laws, 478. https://isap.sejm.gov.pl/isap.nsf/DocDetails.xsp?id= WDU20220001378 [accessed 07 Jan. 2024].

[22] Widén, J. (2014). Improved photovoltaic self-consumption with appliance scheduling in 200 single-family buildings. *Applied Energy*, 126, 199−212. doi: 10.1016/j.apenergy.2014.04.008

[23] TAURON Dystrybucja S.A. *e-licznik – TAURON*. https://elicznik.tauron-dystrybucja.pl/energia [accessed 07 Jan. 2024].

Co-published by
Institute of Fluid-Flow Machinery
Polish Academy of Sciences
Committee on Thermodynamics and Combustion
Polish Academy of Sciences

http://www.imp.gda.pl/archives-of-thermodynamics/

Visual and microscopic tests of composite PV module samples for the construction of roof and facade type BIPV

Piotr Sprawka[a], Patryk Chaja[b*], Paweł Wujek[a]

[a]ElectroTile Sp. z o.o., Pulawska 427, 02-801 Warszawa, Poland
[b]Institute of Fluid-Flow Machinery Polish Academy of Sciences, Fiszera 14, 80-231 Gdańsk, Poland
*Corresponding author email: patryk.chaja@imp.gda.pl

Received: 03.07.2024; revised: 30.07.2024; accepted: 09.09.2024

Abstract

The introduction of new material solutions into the BIPV (Building Integrated Photovoltaics) requires the need to check their suitability in this area. This especially applies to resistance to weather conditions and resistance to UV radiation. The authors conducted a series of tests on samples of photovoltaic modules made using a composite lamination technology based on glass fibres and hardened resins. The resistance of such a structure to atmospheric conditions and degradation by UV rays was investigated. Both of these areas have a significant impact on the efficiency of such a solution in terms of converting solar energy into electricity and the service life of the solution. It was found that delamination of the composite PV modules can be avoided in the case of some studied resins (e.g. LG 385).

Keywords: Composite; Photovoltaic; Roof; Use of lightweight structures

Vol. 45(2024), No. 4, 163–168; doi: 10.24425/ather.2024.152005

Cite this manuscript as: Sprawka, P., Chaja, P., & Wujek, P. (2024). Visual and microscopic tests of composite PV-module samples for the construction of roof and facade type BIPV. *Archives of Thermodynamics*, 45(4), 163–168.

1. Introduction

Recently, growing implementation of renewable energy sources (RES) − particularly photovoltaics, pointed to a paradigm shift in global energy systems. This transformation is largely driven by the urgent call to mitigate climate change impacts and by a rapid decline in the costs of photovoltaic technologies. Consequently, an increasing number of photovoltaic modules are being connected to power grids, a trend that is particularly noticeable in urbanized regions.

However, this exponential growth has brought to the fore a new challenge regarding the installation of a significant number of heavy photovoltaic modules on roof surfaces with specific load capacities. Notably, conventional photovoltaic installations have been found to exert substantial strain on building structures, with typical modules weighing around 12−16 kg/m² and the whole installation weighing approximately 40 kg/m² [1,2]. Such considerable weight has been identified as a limitation, especially in cases where roof structures have a lower load-bearing capacity.

To address this emerging issue, the sector has witnessed a burgeoning interest in the development of lightweight photovoltaic modules, which are commonly referred to as composite photovoltaic (CPV) modules. Such modules, presumed to weigh less than 7 kg/m² [3], present a promising avenue for expanding the integration of photovoltaic technologies, especially in urban setups with roof constraints. Besides, they eliminate the need for heavy glass and frames, components that constitute around 80% of the conventional module weight, achieving a potential weight reduction of about 2 kg/m² [4]. However, it is noteworthy that the CPV technology is distinct from building integrated photovoltaics (BIPV), which seamlessly integrates into the building's roof partitions. This distinction signifies that CPV modules offer flexibility in mounting options, allowing for the utilization of conventional mounting systems.

Nomenclature

Abbreviations and Acronyms

BIPV – building integrated photovoltaics
RES – renewable energy sources
CPV – composite photovoltaic

Despite these advancements, there remains a significant research gap in identifying optimal materials and configurations that would promote efficiency while maintaining lightweight properties. Furthermore, the sector demands meticulous scrutiny in developing coating technologies that could potentially eliminate point damages to the finished products.

This research, initiated under the auspices of the "Path for Mazovia 2019" competition, ventured into this relatively uncharted territory. Drawing upon the promising potential of composite materials, this research sought to innovate composite photovoltaic elements that not only serve as renewable energy sources elements but also function as supporting structures without the necessity of additional constructions on the roof, thereby aligning with the BIPV concept [5–7].

Much attention was paid to studies of new polymeric materials encapsulating PV (photovoltaic) elements [8]. The current state-of-the-art knowledge of different types of composites, used for the PV cell enhancement was discussed in Ref. [9], with a special focus on two-dimensional (2D) materials.

Here, the work embarked on an experimental approach wherein various resin/hardener compositions were fabricated, tested and compared including 6 types described in Refs. [10–14]. Through a series of visual and microscopic examinations, this research endeavour aims to carve out new pathways into coating technologies that satisfy manufacturer requirements while averting potential damage points in the final product.

The following characteristics of CPV samples are assessed according to the quality requirements laid down here:

- delamination surface – requirement: less than 2% of the surface, delamination in the form of stratification between the layers (compact stains) and in the form of stratification between the resin and the fabric (cross-crack mesh);
- dimension of air bubbles – requirement: less than 0.1 mm.

By weaving through these layered complexities and potential innovations, this study hopes to steer the global community a step closer to realizing a sustainable energy future with an integrated, efficient and adaptable photovoltaic solution.

2. Materials and methods

During the tests described in [10–14], 6 types of CPV samples with dimensions of 380 mm × 190 mm and of the same structure (Table 1) were produced; they differ in resins and hardeners used. Two cells measuring 156 mm × 156 mm were placed in the samples, see Fig. 1. The specification of the resins with dedicated hardeners is shown in Table 2. The samples were described by the composition of the resin/hardener as shown in Table 3. Visual and microscopic examinations were carried out on 3 samples in the initial state and 9 samples after accelerated aging in the climatic chamber.

Tests in the thermoclimatic chamber were carried out in accordance with the IEC 61215:2005 standard (Fig. 2). The purpose of this test was to determine the resistance of the photovoltaic module to the effects (material fatigue, temperature stress, etc.) of rapid temperature changes from 85°C down to –40°C. These tests stress the photovoltaic module, as a result of which, the different thermal expansion coefficients of the photovoltaic module parts reveal hidden defects such as poor soldering, cracked cells, delamination, efficiency reduction and insulation resistance, etc.).

Table 1. Structure of CPV samples for quality testing.

Layer subgroup	Layer number	Layer marking	Fibre direction	Total thickness
Top layers	7	Resin	0/90	2.1 mm
	6	GFRP TKAN. 163	–	
Cell	5	2 layers of EVA* film	–	
	4	2 layers of EVA film	–	
	3	2 layers of EVA film	–	
Bottom layers	2	Resin and black pigment	–	
	1	GFRP TKAN. 390	0/90	

*EVA – ethylene vinyl acetate.

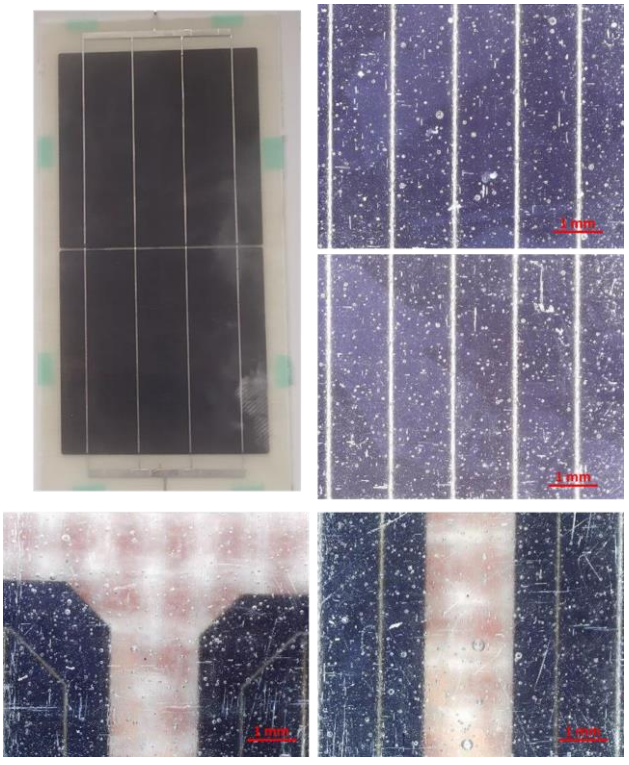

Fig. 1. Outer surface of the sample LG 385_HG 512_1.

3. Results and discussion

The results of the visual and microscopic examinations of the samples are described in Table 4 and selected examples are shown in Figs. 1 and 3. Technological and operating defects resulting from accelerated aging in the climatic chamber were observed.

Table 2. Experimental conditions.

No.	Resin	Hardener	Resin/ hardener proportion	Heating time (h)	Heating temperature (°C)
1	LG 285	H 512	100 : 40	2	120
2	LG 285	HG 287	100 : 40	2	120
3	LG 120	HG 356	100 : 35	2	120
4	LG 900UV	HG 120	100 : 25	6	115
5	LG 385	H 512	100 : 23	2	120
6	LG 385	HG 387	100 : 40	2	120

Table 3. CPV samples descriptions.

Serial no.	Sample determination CPV	Condition
1	LG 285_H 512_1	after aging
2	LG 285_HG 287_1	after aging
3	LG 120_HG 356_1	after aging
4	LG 900UV_HG 120_1	after aging
5	LG 385_H 512_1	after aging
6	LG 385_HG 387_1	initial
7	LG 285_H 512_2	after aging
8	LG 285_HG 287_2	initial
9	LG 120_HG 356_2	after aging
10	LG 900VV_HG 120_2	after aging
11	LG 385_H 512_2	after aging
12	LG 385_HG 387_2	initial

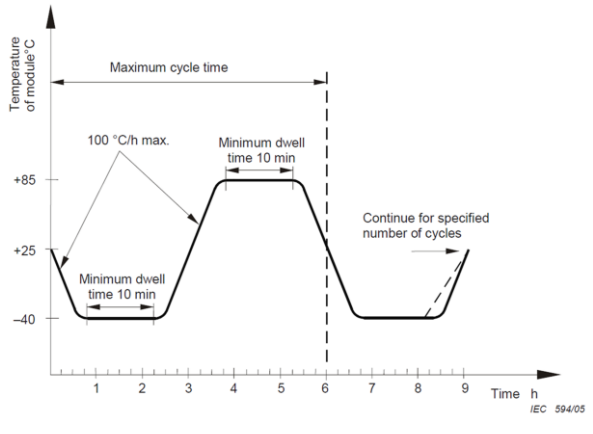

Fig. 2. Outer surface of the sample LG 385_HG 512_1.

Technical faults:

- small air bubbles of diameter less than 0.1 mm on all analysed samples (Figs. 1 and 3);
- air bubbles with dimensions from 0.2 mm to 0.5 mm on test samples: LG 285_HG 287_1, LG 120_HG 356_1, LG 900VV_HG 120_1, LG 285_HG 512_2, LG 285_HG 287_2, LG 120_HG 356_2 (Fig. 3), LG 385_HG 512_2.

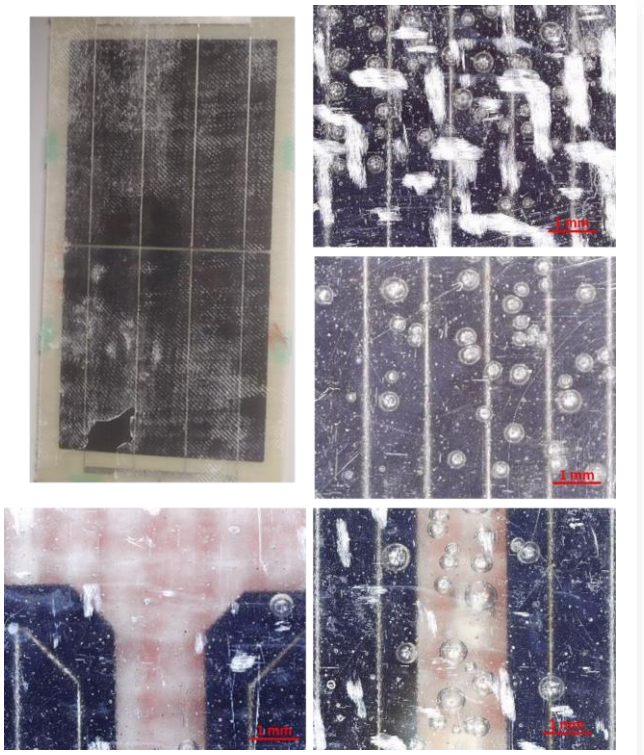

Fig. 3. Outer surface of the sample LG 120_HG 356_2 after aging.

Operating faults (after ageing):

- white structure of delamination between glass fabric and resin seen on samples: LG 285_HG 287_1, LG 120_HG 356_1, LG 285_HG 512_2, LG 900UV_HG 120_2, LG 385_HG 512_2 (see left top in Fig. 3);
- white dots on the sample LG 120_HG 356_2 (see bottom of Fig. 3);
- extensive white fields covering most of the surface of the top layer resulting from the degradation of the resin during aging (see right top in Fig. 3).

Efficiency testing of the manufactured composite modules indicates that small air inclusions with a diameter below 0.1 mm are acceptable. Larger inclusions cause delamination and ultimately degradation and rapid destruction of the module. Air inclusions have also a strong impact on the mechanical strength of the composite, causing the formation and propagation of micro-cracks. This leads to mechanical damage to the CPV module. Table 5 summarizes the characteristics examined and compares them with the required quality criteria.

Performed studies have shown that defects in the form of delamination are formed only after the aging process – see Figs. 1 and 3. No delamination was observed in the initial samples immediately after the production process. In most test samples, delamination after aging takes various forms, such as dense bleaching (delamination between layers) and gradual fad-

Table 4. The results of visual and microscopic examinations of CPV samples.

Sample	Examined feature	Description	Sample condition	Sample	Examined feature	Description	Sample condition
LG 285_H 512_1	Delamination	Extensive whiteness covering most of the outer surface of the upper layer. White cross-mesh indications of trace delamination between the fabric and the top layer resin covering most of the surface of the top layer.	After aging	LG 285_H 512_2	Delamination	Extensive whiteness covering most of the outer surface of the upper layer. White cross-mesh indications of trace delamination between the fabric and the top layer resin covering most of the surface of the top layer.	After aging
	Air bubbles	Small air bubbles of less than 0.1 mm.			Air bubbles	Small air bubbles of less than 0.1 mm in size. Air bubbles with a dimension between 0.2 and 0.5 mm in size located in.	
	Other	Colouring resin in yellow.			Other	Colouring resin in yellow.	
LG 285_HG 287_1	Delamination	White cross-mesh indications of trace delamination between the fabric and the top layer resin covering most of the surface of the top layer.	After aging	LG 285_HG 287_2	Delamination	Absence	Initial
	Air bubbles	Small air bubbles with a dimension of less than 0.1 mm. Air bubbles with a dimension between 0.2 and 0.5 mm.			Air bubbles	Small air bubbles with a dimension of less than 0.1 mm. Air bubbles with a dimension between 0.2 and 0.5 mm	
	Other	Colouring resin in yellow.			Other	Colouring resin in green.	
LG 120_HG 356_1	Delamination	White cross-mesh indications of trace delamination between the fabric and the top layer resin.	After aging	LG 120_HG 356_2 (Fig. 2)	Delamination	White indications of trace delamination at short sections of the upper edge of the glass fabric, located on a significant surface of the top layer.	After aging
	Air bubbles	Small air bubbles with a dimension of less than 0.1 mm. Air bubbles with a dimension between 0.2 and 0.5 mm, located in small areas of the top layer.			Air bubbles	Small air bubbles of less than 0.1 mm.	
	Other	Colouring resin in yellow.			Other	Colouring resin in yellow. Flaking on the outer surface.	
LG 900VV_HG 120_1	Delamination	Absence	After aging	LG 900VV_HG 120_2	Delamination	White indications of trace delamination at short sections of the upper edge of the glass fabric, located on a significant surface of the top layer.	After aging
	Air bubbles	Small air bubbles with a dimension of less than 0.1 mm. Air bubbles with a dimension between 0.2 and 0.5 mm, located in small areas of the top layer.			Air bubbles	Small air bubbles with a dimension of less than 0.1 mm. Air bubbles with a dimension between 0.2 and 0.5 mm.	
	Other	Colouring resin in yellow.			Other	Colouring resin in yellow.	
LG 385_H 512_1 (Fig. 1)	Delamination	Absence	After aging	LG 385_H 512_2	Delamination	White cross-mesh indications of trace delamination between the fabric and the top layer resin covering most of the surface of the top layer.	After aging
	Air bubbles	Small air bubbles of less than 0.1 mm.			Air bubbles	Small air bubbles with a dimension of less than 0.1 mm. Air bubbles with a dimension between 0.2 and 0.5 mm.	
	Other	Colouring resin in yellow.			Other	Colouring resin in yellow.	
LLG 385_HG 387_1	Delamination	Absence	Initial	LLG 385_HG 387_2	Delamination	Short cracks in one direction along the fibre of the glass fabric, which are a trace of delamination of the individual fibres of the outer fabric of the glass, covering most of the outer surface.	Initial
	Air bubbles	Small air bubbles of less than 0.1 mm.			Air bubbles	Small air bubbles of less than 0.1 mm.	
	Other	Colouring resin in green.			Other	Colouring resin in green.	

Table 5. Characteristics of the tested CPV samples – fulfilment of the design requirements.

Sample	Examined feature	Measured value	Limit value	Is condition met?
LG 285_H 512_1	Delamination	~ 60%	< 2% total surface	NO
	Air bubbles	up to 0.5 mm	< 0.1 mm	NO
LG 285_HG 287_1	Delamination	~ 50%	< 2% total surface	NO
	Air bubbles	up to 0.5 mm	< 0.1 mm	NO
LG 120_HG 356_1	Delamination	~ 60%	< 2% total surface	NO
	Air bubbles	up to 0.5 mm	< 0.1 mm	NO
LG 900UV_ HG 120_1	Delamination	< 2%	< 2% total surface	YES
	Air bubbles	up to 0.5 mm	< 0.1 mm	NO
LG 385_H 512_1 (Fig. 1)	Delamination	< 2%	< 2% total surface	YES
	Air bubbles	< 0.1 mm	< 0.1 mm	YES
LG 385_HG 387_1	Delamination	< 2%	< 2% total surface	YES
	Air bubbles	< 0.1 mm	< 0.1 mm	YES
LG 285_H 512_2	Delamination	~ 70%	< 2% total surface	NO
	Air bubbles	up to 0.5 mm	< 0.1 mm	NO
LG 285_HG 287_2	Delamination	< 2%	< 2% total surface	YES
	Air bubbles	up to 0.5 mm	< 0.1 mm	NO
LG 120_HG 356_2 (Fig. 2)	Delamination	~ 100%	< 2% total surface	NO
	Air bubbles	up to 0.5 mm	< 0.1 mm	NO
LG 900VV_ HG 120_2	Delamination	~60%	< 2%total surface	NO
	Air bubbles	< 0.1 mm	< 0.1 mm	YES
LG 385_H 512_2	Delamination	~ 60%	< 2%total surface	NO
	Air bubbles	< 0.1 mm	< 0.1 mm	YES
LLG 385_ HG 387_2	Delamination	~ 60%	< 2% total surface	NO
	Air bubbles	< 0.1 mm	< 0.1 mm	YES

ing. This ultimately leads to damage to the element at a level that prevents its further use.

Studies have shown that the size of the air bubbles can be divided into two ranges: 1) below 0.1 mm (evenly distributed over the surface of the sample): and 2) from 0.2 to 0.5 mm (locally distributed).

Two test samples based on LG 385 resin (LG 385_H 512_1 and LG 385_HG 387_1) met the quality requirements both in terms of the allowable delamination surface and the allowable size of air bubbles. These criteria are also met by samples based on crystalline resin, which were used in other tests as part of the first stage of the investigations.

Samples that meet the requirements have inclusions, but their number and size do not affect the efficiency and durability of the PV module.

The following conclusions can be drawn from the studies:

- Air bubbles above 0.1 mm in size can be prevented or significantly reduced when the established technological regime is kept during production.
- The selection of the appropriate resin and hardener as well as the appropriate preparation of PV panels will reduce the formation of delamination during operation.

Moving forward, the results from the current study propose a promising solution for further research. Here, we have identified that adherence to established technological regimes can effectively reduce or even eliminate the formation of air bubbles that exceed 0.1 mm. This insight necessitates a detailed exploration into optimizing the technological regimes to further enhance the efficiency and longevity of CPV modules. Moreover, a meticulous selection and preparation of resins, hardeners and PV panels could substantially mitigate the formation of delaminations during operation, indicating a vital area where future research could be channelized.

Furthermore, future research should aim at:

- developing a deeper understanding of the aging process and its influence on delamination, possibly steering towards the innovation of aging-resistant materials and technologies;
- exploring new composite materials that potentially could offer better resilience against the formation of air inclusions and delaminations;
- designing real-time monitoring systems to detect and address defects at early stages, preventing rapid degradation and promoting the longevity of the modules;
- collaborating with industry to facilitate the transition from research to real-world applications, ensuring that the advancements made in the labs can significantly impact the global movement towards sustainable energy.

The study presents a significant step towards optimizing the production and efficiency of composite photovoltaic modules. By leveraging the insights gained from this research, there exists a potential pathway to revolutionize the renewable energy sector with lightweight, efficient and durable photovoltaic solutions. As we forge ahead, continuous exploration and innovation in material science and technology regimes stand pivotal in steering the global community towards a sustainable energy future.

6. Conclusions

Qualitative research of aging of PV modules indicated that defects in the form of delamination arise only after the aging process. Delamination was not observed in the baseline samples, immediately after the manufacturing process. Delamination after aging in most test samples takes various forms such as compact bleaching (stratification between layers) and bleaching in the form.

Studies have shown that the size of air bubbles can be divided into two ranges: 1) below 0.1 mm (evenly distributed over the sample surface) and 2) from 0.2 to 05 mm (locally distributed). Air bubbles above 0.1 mm can be reduced or removed

completely as a result of strict compliance with the established technological regime.

Choosing the right resin and hardener and proper preparation of the PV panels will allow us to reduce the formation of delamination during operation. Two LG 385 resin-based test samples met the quality requirements both in terms of the permissible delamination surface and the acceptable size of air bubbles. These criteria are also met by samples based on crystalline resin which were tested in previous studies.

Further work related to BIPV is planned as part of the cooperation between ElectroTile Sp. z o.o. and IMP PAN/KEZO Research Centre. A newly conducted research project focuses on the implementation of new PV products into series production.

Acknowledgements

This work was carried out as part of the implementation of the research project entitled: "Building Sun System – photovoltaic composite roofing and facade system: BIPV II generation", MAZOWSZE/0134/19 and was also supported by the Polish Ministry of Science and Higher Education in the frame of Implementation Doctorate Programme (II edition) – Agreement No. 0063/DW/2018 from 2 August 2018.

References

[1] Ferroni, F., & Hopkirk, R.J. (2016). Energy Return on Energy Invested (ERoEI) for photovoltaic solar systems in regions of moderate insolation. *Energy Policy*, 94, 336–344. doi: 10.1016/j.enpol.2016.03.034.

[2] Mik, K., Zawadzki, P., Tarłowski, J., & Bykuć S. (2022). Assessment of prototype lightweight photovoltaic modules after over 1-year field test in Polish conditions. *Renewable Energy*, 198, 1008–1020. doi: 10.1016/j.renene.2022.08.104

[3] Martins, A.C., Chapuis, V., Virtuani, A., Perret-Aebi, L.-E., & Ballif, C. (2017). Hail resistance of composite-based glass-free lightweight modules for building integrated photovoltaics applications. *33rd European Photovoltaic Solar Energy Conference and Exhibition*, 25–29 September 2017, Amsterdam, Netherlands. doi: 10.4229/EUPVSEC20172017-6BV.3.62

[4] Oreski, G., Stein, J.S., Eder, G.C., Berger, K.A., Bruckman, L.S., Vedde, J., Weiß, K., Tanahashi, T., French, R.H., & Ranta, S. (2021). *Designing new materials for photovoltaics: Opportunities for lowering cost and increasing performance through advanced material innovations*. Report IEA-PVPS T13-13:2021. doi: 10.2172/1779380

[5] Berger, K., Cueli, A.B., Boddaert, S., Buono, M.D., Delisle, V., Fedorova, A.S., Frontini, F., Hendrick, P., Inoue, S., Ishii, H., Kapsis, C., Kim, J., Kovács, P., Chivelet, N.M., Maturi, L., Machado, M., Schneider, A., & Wilson, H.R. (2018). *International definitions of "BIPV"*. Report IEA-PVPS T15-04: 2018: doi: 10.13140/RG.2.2.15351.68007

[6] Ghosh, A (2020). Potential of building integrated and attached/applied photovoltaic (BIPV/BAPV) for adaptive less energy-hungry building's skin: A comprehensive review. *Journal of Cleaner Production*, 276, 123343. doi: 10.1016/j.jclepro.2020.123343

[7] Martins, A.C., Chapuis, V., Sculati-Meillaud, F., Virtuani, A., & Ballif, C (2018). Light and durable: Composite structures for building-integrated photovoltaic modules. *Progress in Photovoltaic Research and Applications.* 26(9), 718–729. doi: 10.1002/pip.3009

[8] Gaddam, S.K., Pothu, R., & Rajender Boddula, R. (2021). Advanced polymer encapsulates for photovoltaic devices − A review. *Journal of Materiomics*, 7, 920–928. doi: 10.1016/j.jmat.2021.04.004.

[9] Olorunfemi, T.R., Nwulu, N.I., & Ismail, S.O. (2022). Composites as candidate materials for photovoltaic cells. *Advances in Materials and Processing Technologies*, 8(4), 2378–2397. doi: 10.1080/2374068X.2022.2046328

[10] Kajisa, T., Miyauchi, H., Mizuhara, K., Hayashi, K., Tokimitsu, T., Inoue, M., Hara, K., & Masuda, A. (2014). Novel lighter weight crystalline silicon photovoltaic module using acrylic-film as a cover sheet. *Japanese Journal of Applied Physics*, 53, 092302. doi: 10.7567/JJAP.53.092302

[11] Mik, K., Bugaj, M., & Chaja, P. (2021). The evaluation of the snail track affected photovoltaic modules by different methods after 3-year operating in central Poland. *Renewable Energy*, 163, 504–516. doi: 10.1016/j.renene.2020.09.005

[12] Nussbaumer, H., Klenk, M., & Keller, N. (2016). Small unit compound modules: a new approach for light weight PV modules. 32rd European Photovoltaic Solar Energy Conference and Exhibition, 20–24 June 2016, Munich, Germany. doi: 10.4229/EUPVSEC20162016-1BO.12.5

[13] Schindler, S., Götz, D., & Dassler, D. (2019). Lightweight PV module approach − field test study and yield evaluation. *36th European Photovoltaic Solar Energy Conference and Exhibition*, 9–13 September 2019, Marseille, France. doi: 10.4229/EUPVSEC20192019-1BO.9.5.

[14] Martins, A.C., Chapuis, V., Virtuani, A., & Ballif, C. (2019). Robust glass-free lightweight photovoltaic modules with improved resistance to mechanical loads and impact. *IEEE Journal of Photovoltaics*, 9(1), 245–251. doi: 10.1109/JPHOTOV.2018.2876934

Co-published by
Institute of Fluid-Flow Machinery
Polish Academy of Sciences
Committee on Thermodynamics and Combustion
Polish Academy of Sciences

http://www.imp.gda.pl/archives-of-thermodynamics/

ARCHIVES OF THERMODYNAMICS

Investigating the effect of an inclined magnetic field on heat and mass transmission in turbulent squeeze flow of UCM fluid between parallel plates

Sreenivasa Somireddy Reddy[a], Kamatam Govardhan[b], Ganji Narender[c*], Santoshi Misra[d]

[a]Department of Humanities and Science (Mathematics), Viganana Bharathi Institute of Technology, Hyderabad-501301, Telangana, India
[b]Department of Mathematics, GITAM University, Hyderabad-502329, Telangana, India
[c]Department of Humanities and Sciences (Mathematics), CVR College of Engineering, Hyderabad-501510, Telangana, India
[d]Department of Mathematics, St. Ann's College for Women, Hyderabad, Telangana, India
*Corresponding author email: gnriimc@gmail.com

Received: 23.11.2023; revised: 21.06.2024; accepted: 10.09.2024

Abstract

This paper investigates the effects of an inclined magnetic field on heat and mass transfer in turbulent squeeze flow of a viscoelastic fluid with an upper-convected Maxwell model. Squeezing flow is an important phenomenon in various industrial and mechanical processes related to flows between parallel surfaces. Mathematical modelling for the law of conservation of mass, momentum, heat and concentration of nanoparticles is executed. The study employs a system of partial differential equations to describe the flow issue. Governing nonlinear partial equations are reduced into nonlinear ordinary differential equations. The modelled equations are then solved numerically by utilizing the efficient Adams-Moulton method of the fourth order based on the shooting technique using the Fortran programming language. Numerical results are compared with another numerical approach and an excellent agreement is observed. The effects of various factors on the non-dimensional velocity, temperature, and concentration patterns are presented using graphs, while tables are used to assess the numerical values of the skin friction, Nusselt and Sherwood numbers. It is found that the temperature profile decreases as the compression parameter increases but increases with an increase in the Eckert number. The results of this study could be useful in designing heat and mass transfer equipment for applications in viscoelastic fluid flows under an inclined magnetic field.

Keywords: Magnetic field; Upper-convected Maxwell (UCM) fluid; Chemical reaction parameter; Viscous dissipation; Squeezing parameter; Adams-Moulton method

Vol. 45(2024), No. 4, 169–178; doi: 10.24425/ather.2024.152006

Cite this manuscript as: Reddy, S.S., Govardhan, K., & Narender, G. (2024). Investigating the effect of an inclined magnetic field on heat and mass transmission in turbulent squeeze flow of UCM fluid between parallel plates. *Archives of Thermodynamics*, 45(4), 169–178.

1. Introduction

The study of mass and heat transmission with various physical factors has attracted more attention in recent years as it occurs in a wide range of industries, including food processing, lubricant systems, hydrodynamic machinery, chemical processing equipment, and polymer processing. The impact of extrusion and squeezing factors on the rate of heat conduction of the compressed viscous fluid between two parallel plates was reported by Duwairi et al. [1]. They found that increasing the squeezing parameter caused the local coefficient of friction to reduce and the rate of heat conduction to increase, whereas increasing the extrusion parameter caused the rate of heat transfer to decline and the skin friction coefficient to increase.

In the study conducted by Kai-Long Hsiao [2], the focus was on the incompressible mixed convection 2D flow of a Maxwell fluid over an extending surface. The author specifically investigated the physical properties of energy conversion, conjugate mass transfer and heat transfer, considering radiative thermal effects. Ahmadi et al. [3] studied the unsteady flow of nanofluids and the transfer of heat by a uniformly moving disc. Given that the unstable parameter is a key component of the velocity pro-

Nomenclature

B_m – magnetic flux density, A/m
C – concentration, mol/m^3
C_f – skin friction coefficient
D – diffusion coefficient, m^2/s
Ec – Eckert number
f, f' – dimensionless velocity components
k – thermal conductivity, W/(m K)
K_1 – rate of reaction, 1/s
Nu – Nusselt number
p – pressure, Pa
Pr – Prandtl number
S – squeezing number
Sc – Schmidt number
Sh – Sherwood number
T – temperature of the fluid, K
T_H – temperature of the upper wall, K
u – velocity in x direction, m/s
v – velocity in y direction, m/s
x, y – Cartesian coordinates, m

Greek symbols

α – thermal diffusivity, m^2/s
γ – chemical reaction parameter
η – dimensionless coordinate
θ – dimensionless temperature
λ_r – viscoelastic parameter
ν – kinematic viscosity, m^2/s
μ – dynamic viscosity, Pa s
ρ – fluid density, kg/m^3
σ – electrical conductivity, S/m
ϕ – dimensionless concentration
ω – inclination angle, rad

Abbreviations and Acronyms

ADM– Adomian decomposition method
BCs – boundary conditions
HAM– homotopy analysis method
IVP – initial value problem
MHD– magnetohydrodynamics
ODEs– ordinary differential equations
PDEs– partial differential equations
UCM– upper-convected Maxwell

file, it has been suggested that raising this parameter will improve the velocity profile. In addition to the magnetic effect and chemical reaction, Afify [4] addressed the mass transfer in a convective, incompressible and electrically conducting movement of viscous fluid in the direction of expanding surfaces. According to this research, as the magnetic component is increased, the friction coefficient rises while the Nusselt and Sherwood numbers fall.

A substance droplet's mobility can be explained by the squeeze-flow process. Squeezing flow has many uses in industry and sciences, including rheological testing, connecting composite materials, hot plate welding, etc. In the presence of slip impact, Bhatta et al. [5] noticed the unsteady compression of water-based nanofluid flow between two plates held parallel to one another. It was found that a rise in the Lewis number caused a fall in the proportion of nanoparticles. Adesanyao et al. [6] conducted a study on the unsteady MHD compressing Eyring-Powell fluid flow over an infinite channel. Their findings indicated that with an increase in the chemical reaction parameter, the concentration profile decreases. The researchers came to the additional conclusion that while the rate of heat transmission declines with heat absorption and compressed channel walls, it increases with the expansion of thermal radiation, channel walls, and internal heat production parameters. Farooq et al. [7] described the effect of melting heat transfer in the compressing flow of nanofluid over a Darcy porous medium. They discovered that for the prevalent thermophoresis parameter values, the temperature distribution rises.

Hayat et al. [8] conducted a study on the flow of an incompressible micropolar fluid confined between two parallel plates, considering the magnetic effect. Mahmood et al. [9], on the other hand, investigated the heat transfer and flow characteristics over a sensor surface submerged in a squeezed channel. Their findings revealed that increasing suction through the sensor surface leads to an increase in heat transfer and skin friction coefficient. Conversely, an increase in injection has the opposite effect, decreasing the skin friction and heat transfer coefficient. Mohyud-Din et al. [10] examined the MHD flow of a squeezing fluid between two plates held parallel to one another, one of which is impervious and the other porous. Ojjela et al. [11] provided an explanation of the entropy production caused by the influence of a magnetic field on an unsteady incompressible 2D squeezing flow and the mass transfer of Casson fluid between two plates kept parallel to one another. They used the Prandtl and Hartmann numbers to evaluate whether the fluid's temperature was raised, and its content was reduced.

Sheikholeslami et al. [12] utilized the Adomian decomposition technique (ADM) to determine the analytical solution for the unsteady flow of nanofluid compressed between two parallel sheets. It was determined that the Nusselt number and nanoparticle volume fraction have a straight relationship; otherwise, when the two plates travel together, they have an opposite relationship with the squeezing number. Saltwater, liquid metals, electrolytes and plasmas are a few examples of electrically conducting fluids that are studied in magnetohydrodynamics for their magnetic characteristics and activity. According to Gholinia et al. [13], who examined the effects of various physical factors on Eyring-Powell fluid, including slip flow, magnetic fields, and homogeneous and heterogeneous processes brought on by spinning discs, the temperature profile decreases as the pressure increases. A 2D second-degree fluid flow between two parallel plates that was unsteady was noticed by Hayat et al. [14] to be affected by magnetism.

Jha and Aina [15] computed an approximate solution for an incompressible, viscous, electrically conducting fluid in a vertical microporous channel created by electrically non-conducting vertical slabs held parallel to one another in the presence of induced magnetic effects. They observed that the suction or injection measure increases fluid velocity and slip velocity. Additionally, it was found that as the magnetic component and Hartmann

number rise, the volume flow rate decreases.

In addition to the magnetic effect, Khan et al. [16] looked at the heat transmission in the nanofluid flow between two plates that were kept parallel to one another. They observed that the form component has no impact on the fluid velocity. Additionally, it was found that nanoparticles with a greater shape factor would raise temperatures and slow down heat transmission. With the aid of volume portions of nanoparticles, radiation, chemical processes and viscous dispersion, Mabood et al. [17] provided the computational solution of stagnation point flow of MHD nanofluid based on water (Cu and Al_2O_3) over a porous surface. The homotopy perturbation technique was used by Siddiqui et al. [18] to calculate the solution for an unsteady 2D squeezing fluid flow of MHD between two parallel plates. They observed that for both a constant value and for various values of the magnetic parameter, the velocity curve increases monotonically.

According to slip conditions at the boundaries, Abbasi et al. [19] showed the MHD flow of UCM fluid over a porous material. They discovered a correlation between a decline in the velocity curve and a rise in the Hartmann number. A two-dimensional, incompressible, constant flow through a porous surface conduit was studied by Choi et al. [20] to determine how inertia and viscoelasticity interacted. The 2D boundary layer of UCM fluid over a porous conduit with chemical processes was studied by Hayat and Abbas [21]. They came to the conclusion that the motion behaves differently for rising Reynolds number values in viscoelastic fluid. The similarity solutions for the unstable boundary layer flow and heat transfer in a Maxwell fluid flowing over a permeable stretching sheet in the presence of a heat source or sink were examined by Mukhopadhyay and Vajravelu [22]. For the rising levels of the Maxwell fluid and magnetic field, they observed a decrease in the velocity field.

Prasad et al. [23] conducted a study on the effects of thermal conductivity, internal heat source and heat sink on the MHD flow and heat transfer in the stretching surface of UCM fluid. The findings revealed that, when temperature-dependent thermo-physical properties were considered, increasing the magnetic parameter and Maxwell parameter led to a reduction in the velocity profile within the boundary layer. Additionally, they observed that thermal conduction and the presence of a heat source/sink raised the temperature in the flow region. In another study, Sadeghy et al. [24] investigated the flow of upper convective Maxwell fluid past a rigid plate in continuous motion. Several authors [25–33] have solved many problems under generalized thermal theories. Zeeshan et al. [34], Elgazery et al. [35] and Bhatti et al. [36] have presented the solutions to some problems under various boundary conditions in porous mediums.

To the best of the Authors' knowledge, no information is available on the effects of an inclined magnetic field on heat and mass transfer in the turbulent squeeze flow of a viscoelastic fluid with an upper-convected Maxwell model. The present work aims to fill the gap in the existing literature. Therefore, in the present paper, we consider an inclined magnetic field and UCM squeezing flow of viscous fluid between parallel plates. We shall apply the shooting technique along with the Adams-Moulton method of fourth order to solve the similarity equations obtained from the governing boundary layer equations with the help of similarity transformation. The structure of the present paper is as follows. The problem is formulated in Section Two. The numerical solution for both fluid and temperature fields are presented in Section Three. Section Four contains results and discussions. The concluding remarks are eventually given in Section Five.

2. Materials and methods

An incompressible, 2-D unsteady UCM fluid flow, which is squeezed between two plates held parallel to each other (Fig. 1), along with the inclined magnetic field effect, has been considered.

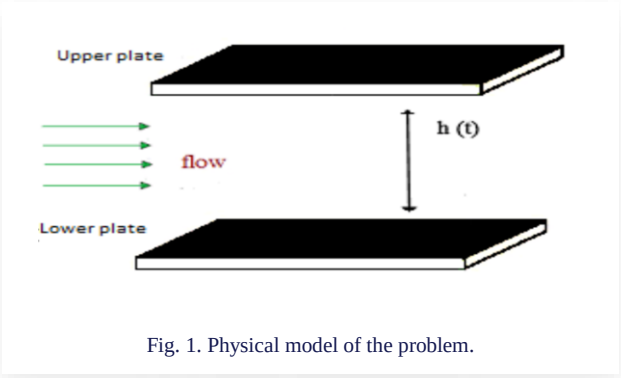

Fig. 1. Physical model of the problem.

The spacing between the plates is $y = l(1 - \alpha t)^{1/2} = h(t)$. For $\alpha > 0$, the two plates are squeezed until they touch $t = 1/\alpha$ and for $\alpha < 0$, the two plates are separated. Due to the viscous dissipation effect, the generation of heat due to friction caused by shear in the flow is retained. This effect is quite important in the case when the fluid is largely viscous or flowing at a high speed. This behaviour occurs at a high Eckert number. Mass transfer with a chemical reaction rate is accounted for. Moreover, the flow is considered symmetric. The continuity, momentum, energy and mass transfer in view of all these assumptions and approximations are given below [37]:

$$\frac{\partial u}{\partial x} + \frac{\partial v}{\partial y} = 0, \tag{1}$$

$$\left.\begin{aligned} \frac{\partial u}{\partial t} + u\frac{\partial u}{\partial x} + v\frac{\partial u}{\partial y} = -\frac{1}{\rho}\frac{\partial p}{\partial x} + \nu\left(\frac{\partial^2 u}{\partial x^2} + \frac{\partial^2 u}{\partial y^2}\right) + \\ + \frac{\sigma B_m^2}{\rho}\sin(\omega)\left(v\cos(\omega) - u\sin(\omega)\right) + \\ -\beta\left(u^2\frac{\partial^2 u}{\partial x^2} + v^2\frac{\partial^2 u}{\partial y^2} + 2uv\frac{\partial^2 u}{\partial x \partial y}\right) \end{aligned}\right\}, \tag{2}$$

$$\left.\begin{aligned} \frac{\partial v}{\partial t} + u\frac{\partial v}{\partial x} + v\frac{\partial v}{\partial y} = -\frac{1}{\rho}\frac{\partial p}{\partial y} + \nu\left(\frac{\partial^2 v}{\partial x^2} + \frac{\partial^2 v}{\partial y^2}\right) + \\ + \frac{\sigma B_m^2}{\rho}\sin(\omega)\left(v\cos(\omega) - u\sin(\omega)\right) + \\ -\beta\left(u^2\frac{\partial^2 v}{\partial x^2} + v^2\frac{\partial^2 v}{\partial y^2} + 2uv\frac{\partial^2 v}{\partial x \partial y}\right) \end{aligned}\right\}, \tag{3}$$

$$\left.\begin{aligned} \frac{\partial T}{\partial t} + u\frac{\partial T}{\partial x} + v\frac{\partial T}{\partial y} = \frac{k}{\rho C_p}\left(\frac{\partial^2 T}{\partial x^2} + \frac{\partial^2 T}{\partial y^2}\right) + \\ + \frac{\nu}{C_p}\left[4\left(\frac{\partial u}{\partial x}\right)^2 + \left(\frac{\partial u}{\partial y} + \frac{\partial v}{\partial x}\right)\right] \end{aligned}\right\}, \tag{4}$$

$$\frac{\partial C}{\partial t} + u\frac{\partial C}{\partial x} + v\frac{\partial C}{\partial y} = D\left(\frac{\partial^2 C}{\partial x^2} + \frac{\partial^2 C}{\partial y^2}\right) - K_1(t)C. \tag{5}$$

The boundary conditions for the above modelled problem are [37]:

$$\left.\begin{aligned} y=h(t):\ u=0, v=v_w=\frac{dh}{dt},\\ T=T_H,\ C=C_H,\\ y=0:\ u=\frac{\partial u}{\partial y}=\frac{\partial T}{\partial y}=\frac{\partial C}{\partial y}=0. \end{aligned}\right\} \quad (6)$$

Here, ρ is the fluid density, u and v are the velocities in the x and y directions, respectively, T denotes the temperature, C represents the concentration, p denotes the pressure, ν represents the kinematic viscosity, C_p is the specific heat, D denotes the coefficient of diffusion, and $B_m(t)=\frac{B_0}{(1-\alpha t)}, K_1(t)=\frac{k_1}{(1-\alpha t)}$ (see [25]) define the magnetic field and rate of reaction, which depend both on time.

A set of the following transformations is formed for the velocity components u and v, temperature T, concentration C and similarity variable η as [37]:

$$\left.\begin{aligned} u=\frac{\alpha x}{2(1-\alpha t)}f'(\eta), \quad v=\frac{-\alpha l}{\left[l(1-\alpha t)^{\frac{1}{2}}\right]}f(\eta),\\ \theta=\frac{T}{T_H}, \quad \phi=\frac{C}{C_H}, \quad \eta=\frac{y}{\left[l(1-\alpha t)^{\frac{1}{2}}\right]}, \end{aligned}\right\} \quad (7)$$

where the unknown function $f(\eta)$ represents the axial velocity component, $\theta(\eta)$ represents the temperature function and $\phi(\eta)$ is the concentration distribution. The new variables in Eq. (7) are submitted to the governing PDEs (1)–(5), and we get the following system of ODEs:

$$\left.\begin{aligned} f^{(iv)}(\eta)-\frac{S\left(\begin{matrix}3f^{"}(\eta)+\eta f'^{"}(\eta)+f'(\eta)f^{"}(\eta)\\ -f(\eta)f'^{"}(\eta)\end{matrix}\right)}{\left[1+S\lambda_r(f(\eta))^2\right]}+\\ -\frac{M^2\sin(\omega)\left(f^{"}(\eta)\sin(\omega)+2\delta\cos(\omega)\right)}{\left[1+S\lambda_r(f(\eta))^2\right]}+\\ -\frac{2S\lambda_r\left[f(\eta)\left(f^{"}(\eta)\right)^2+\left(f'(\eta)\right)^2f^{"}(\eta)\right]}{\left[1+S\lambda_r(f(\eta))^2\right]}=0 \end{aligned}\right\}, \quad (8)$$

$$\theta^{"}(\eta)+\mathrm{Pr}[S\left(f(\eta)\theta'(\eta)-\eta\theta'(\eta)\right)+ +\mathrm{Ec}\left(f'(\eta)\right)^2+\mathrm{Ec}(x)\left(f^{"}(\eta)\right)^2]=0, \quad (9)$$

$$\phi^{"}(\eta)+\mathrm{Sc}\left[\left(f(\eta)\phi'(\eta)-\eta\phi'(\eta)\right)-\gamma\phi(\eta)\right]=0. \quad (10)$$

The dimensionless boundary conditions are as follows:

$$\left.\begin{aligned} f(0)=0, \quad f^{"}(0)=1, \quad \theta'(0)=0, \quad \phi'(0)=0,\\ f(1)=1, \quad f'(1)=0, \quad \theta(1)=\phi(1)=1, \end{aligned}\right\} \quad (11)$$

where S is the squeeze number, Pr is the Prandtl number, Ec is the Eckert number, Sc is the Schmidt number, γ is the chemical reaction parameter, M is the magnetic parameter, λ_r is the viscoelastic parameter, Ec(x) is the local Eckert number, The various parameters utilized in the aforementioned equations can be expressed as follows:

$$\left.\begin{aligned} S=\frac{\alpha l^2}{2\nu}, \quad \mathrm{Pr}=\frac{\mu C_p}{k}, \quad \mathrm{Ec}=\frac{\alpha^2 l^2}{T_H C_p(1-\alpha t)}, \quad \mathrm{Sc}=\frac{\nu}{D},\\ \gamma=\frac{k_1 l^2}{\nu}, \quad M^2=\frac{\sigma B_0^2 l^2}{\rho\nu}, \quad \lambda_r=\frac{\alpha\beta}{2(1-\alpha t)},\\ \mathrm{Ec}(x)=\frac{\alpha^2 x^2}{4C_pT_H(1-\alpha t)^2}. \end{aligned}\right\} \quad (12)$$

It is important to note that the squeeze number S describes the movement of the plate ($S>0$ corresponds to the plates moving apart, while $S<0$ corresponds to the plates moving together) and Ec = 0 corresponds to the case when the viscous dissipation effect is absent, $\gamma>0$ represents the destructive chemical reaction and $\gamma<0$ represents the generative chemical reaction.

Expressions for the skin friction coefficient, local Nusselt number and local Sherwood number are as below [26]:

$$\left.\begin{aligned} C_f=\frac{\mu\left(\frac{\partial u}{\partial y}\right)\Big|_{y=h(t)}}{\rho v_w^2} \Rightarrow \frac{l^2}{x^2}(1-\alpha t)\mathrm{Re}_xC_f=f^{"}(1),\\ \mathrm{Nu}=\frac{-lk\left(\frac{\partial T}{\partial y}\right)\Big|_{y=h(t)}}{kT_H} \Rightarrow \sqrt{(1-\alpha t)}\mathrm{Nu}=-\theta'(1),\\ \mathrm{Sh}=\frac{-lD\left(\frac{\partial C}{\partial y}\right)\Big|_{y=h(t)}}{DC_H} \Rightarrow \sqrt{(1-\alpha t)}\mathrm{Sh}=-\phi'(1). \end{aligned}\right\} \quad (13)$$

3. Solution methodology

The system of ODEs (8)–(10) along with BCs (11) is solved numerically by utilizing the shooting technique with the Adams-Moulton method. A system of first order ODEs is required for the implementation of the shooting technique. The nonlinear differential equations are first decomposed into a system of first order differential equations. For this purpose, we introduce the new variables:

$$f=y_1, \quad f'=y_1'=y_2, \quad f^{"}=y_1^{"}=y_2'=y_3, \quad f^{"'}=y_4.$$

By using the above notations in Eq. (8), the following system of ODEs is obtained:

$$y_1'=y_2, \quad y_1(0)=0,$$

$$y_2'=y_3, \quad y_2(0)=r,$$

$$y_3'=y_4, \quad y_3(0)=0,$$

$$y_4'=\frac{\left[\begin{matrix}S(\eta y_4+3y_3+y_2y_3-y_1y_4)\\ +M^2\sin(\omega)(\sin(\omega)y_3+2\delta\cos(\omega)y_2)\\ +2S\lambda_r(y_2^2y_3+y_1y_3^2)\end{matrix}\right]}{1+S\lambda_ry_1^2}, \quad y_4(0)=s.$$

To solve the above initial value problem arising in the shooting technique, the Adams-Moulton method of the fourth order is used. Here the missing conditions r and S are to be determined so that:

$$\left.\begin{aligned} y_1(\eta_\infty,r,s)_{\eta=1}-1=0,\\ y_2(\eta_\infty,r,s)_{\eta=1}=0. \end{aligned}\right\} \quad (14)$$

To solve the above system of algebraic Eqs. (14), we use Newton's method which has the following iterative scheme:

$$\begin{pmatrix} r^{(k+1)} \\ s^{(k+1)} \end{pmatrix} = \begin{pmatrix} r^{(k)} \\ s^{(k)} \end{pmatrix} - \begin{pmatrix} \frac{\partial y_1}{\partial r} & \frac{\partial y_2}{\partial r} \\ \frac{\partial y_1}{\partial s} & \frac{\partial y_2}{\partial s} \end{pmatrix}^{-1}_{\eta=1} \begin{pmatrix} y_1(\eta, r^{(k)}, s^{(k)}) - 1 \\ y_2(\eta, r^{(k)}, s^{(k)}) \end{pmatrix}_{\eta=1}.$$

Here, k is the number of iterations (k = 0, 1, 2, 3, …). The missing initial conditions r and S are updated by using Newton's scheme. The iterative procedure is stopped when the following criterion is met:

$$\max\{|r^{(k+1)} - r^{(k)}|, |s^{(k+1)} - s^{(k)}|\} < \in, \qquad (15)$$

where ∈ denotes a small positive number.

The step size is taken as $\Delta\eta$ = 0.01. The process is repeated until we obtain the result correct up to the desired accuracy of 10^{-7}, which fulfils the convergence criterion.

Now Eq. (15) will be treated similarly by considering f as a known function. For this, let us denote θ by y_{13} and $\theta' = y'_{13}$ by y_{14}.

By using the above notations in Eq. (15), we get the system of equations:

$$y'_{13} = y_{14}, \qquad y_{13}(0) = m,$$

$$y'_{14} = \mathrm{Pr}S(\eta y_{14} - y_1 y_{14}) - \mathrm{Pr}\mathrm{E}c y_2^2 - \mathrm{Pr}\mathrm{E}c(x), \quad y(0) = 0.$$

The above initial value problem will be numerically solved by the fourth order Adams-Moulton method. In the above initial value problem, the missing condition m is to be chosen such that:

$$y_{13}(\eta, m)_{\eta=1} - 1 = 0. \qquad (16)$$

To solve the above algebraic Eq. (16), we use Newton's method which has the following iterative scheme:

$$m^{(k+1)} = m^{(k)} - \left(\frac{\partial y_{13}}{\partial m}\right)^{-1} \left(y_{13}(\eta, m^{(k)})_{\eta=1} - 1\right).$$

To incorporate Newton's method, we further use the following notations:

$$\frac{\partial y_{13}}{\partial m} = y_{15}, \qquad \frac{\partial y_{14}}{\partial m} = y_{16}.$$

As a result of these new notations, the Newton's iterative scheme gets form:

$$m^{(k+1)} = m^{(k)} - \left(y_{15}(\eta, m^{(k)})_{\eta=1}\right)^{-1} \left(y_{13}(\eta, m^{(k)})_{\eta=1} - 1\right). \qquad (17)$$

Here, k is the number of iterations (k = 0, 1, 2, 3, …). Now differentiating the above system of two first order ODEs with respect to m, we get another system of four ODEs. Writing all these four ODEs together, we have the following initial value problem (IVP):

$$y'_{13} = y_{14}, \qquad y_{13}(0) = m,$$

$$y'_{14} = \mathrm{Pr}\,S\,(\eta y_{14} - y_1 y_{14}) - \mathrm{Pr}\mathrm{E}c y_2^2 - \mathrm{Pr}\mathrm{E}c(x) y_3^2,$$

$$y_{14}(0) = 0,$$

$$y'_{15} = y_{16}, \qquad y_{15}(0) = 1,$$

$$y'_{16} = \mathrm{Pr}\,S\,(\eta y_{16} - y_1 y_{14}), \qquad y_{16}(0) = 0.$$

The Adams-Moulton method of the fourth order has been used to solve the IVP consisting of the above four ODEs for some suitable choices of m. The missing condition m is updated by using Newton's scheme (17). The iterative procedure is stopped when the following condition is met:

$$|m^{(k+1)} - m^{(k)}| < \in,$$

for an arbitrarily small positive value of ∈. Throughout this article ∈ has been taken as 10^{-8}.

In a similar manner, Eq. (10) can be treated numerically by the shooting techniques by considering f as a known function.

4. Results and discussion

This section examines how different physical factors affect the ranges of velocity, temperature, and concentration. It has been given and examined how the dimensionless mathematical model can be solved numerically. Mustafa et al. [37] used the HAM method for the numerical solution of the discussed model. In the present survey, the shooting method along with the Adams-Moulton method has been opted for reproducing the solution. The present results will be compared with those of [37] for verification of the code. The impact of different parameters, e.g. squeezing parameter S, Pr, Sc, γ and Ec is observed graphically.

Figures 2 and 3 show the impact of S on the dimensionless velocity profile. It can be noted that the fluid velocity reduces with the increasing values of the squeezing parameter.

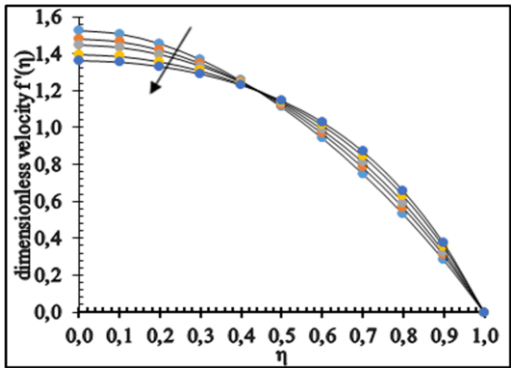

Fig. 2. Influence of S = −1.0, −0.5, 0.01, 1.0, 2.0 on $f'(\eta)$ for Pr = M = Ec = Ec(x) = Sc = γ = 1, $\delta = \lambda_r$ = 0.2, $\omega = \pi/4$.

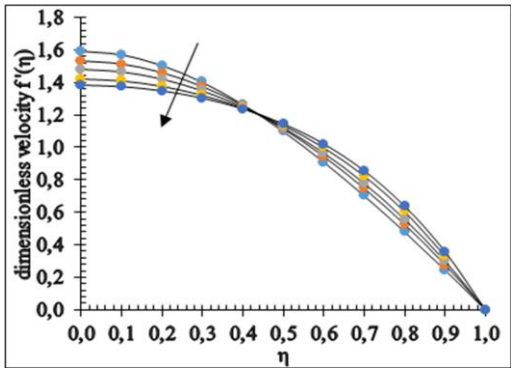

Fig. 3. Influence of S = −1.0, −0.5, 0.01, 1.0, 2.0 on $f'(\eta)$ for Pr = M = Ec = Ec(x) = Sc = γ = 1, $\delta = \lambda_r$ = 0.2, $\omega = \pi/6$.

Figures 4 and 5 present the impact of both the positive and negative squeezing parameters on the temperature distribution. Greater values of S give a noteworthy decrease in the temperature profile. Physically, an increase in S can be associated with a decrease in the kinematic viscosity, an increase in the distance between the plates and an increase in the speed at which the plate moves.

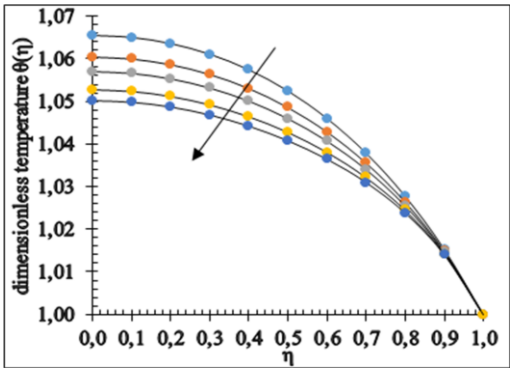

Fig. 4. Influence of $S = -1.0, -0.5, 0.01, 1.0, 2.0$ on $\theta(\eta)$ for Pr = M = Ec = Ec(x) = 0.2, Sc = γ = 1, $\delta = \lambda_r$ = 0.2, $\omega = \pi/4$.

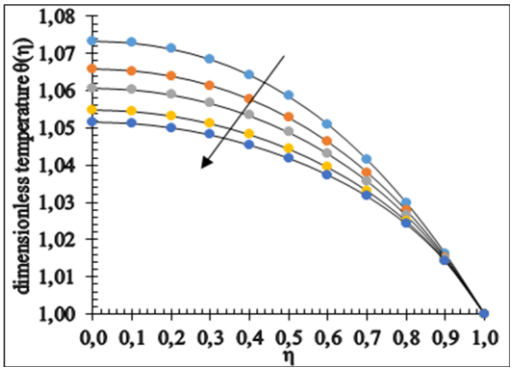

Fig. 5. Influence of $S = -1.0, -0.5, 0.01, 1.0, 2.0$ on $\theta(\eta)$ for Pr = M = Ec = Ec(x) = 0.2, Sc = γ = 1, $\delta = \lambda_r$ = 0.2, $\omega = \pi/6$.

Figures 6 and 7 show the impact of Pr on the field $\theta(\eta)$. The field $\theta(\eta)$ is rising due to the viscous dissipation effect. The Prandtl number Pr < 1 describes the liquid materials with a high thermal diffusivity but low viscosity, whereas the viscosity of liquid materials is high for the Prandtl number Pr > 1.

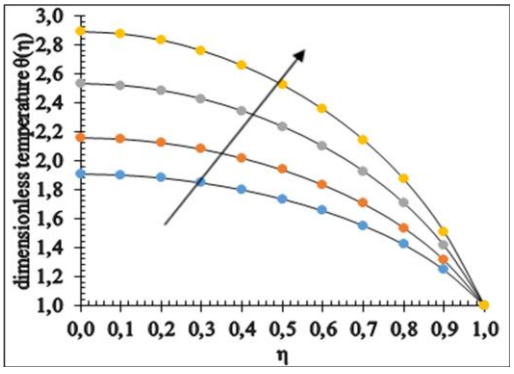

Fig. 6. Influence of Pr = 0,7, 0.9, 1.2, 1,5 on $\theta(\eta)$ for S = M = Ec = Ec(x) = Sc = γ = 1, $\delta = \lambda_r$ = 0.2, $\omega = \pi/4$.

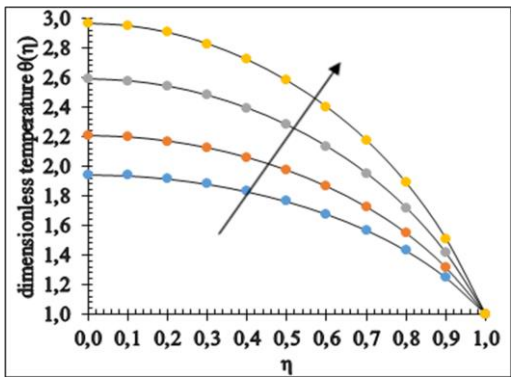

Fig. 7. Influence of Pr = 0,7, 0.9, 1.2, 1,5 on $\theta(\eta)$ for S = M = Ec = Ec(x) = Sc = γ = 1, $\delta = \lambda_r$ = 0.2, M = 3, $\omega = \pi/6$.

Figures 8 and 9 are delineated to show the impact of Ec on the temperature field $\theta(\eta)$. These figures describe that on the rising estimations of Ec, the temperature profile is also increased. Thus, the compactness of the thermal layer at the boundary is reduced by the increasing estimations of Pr and Ec.

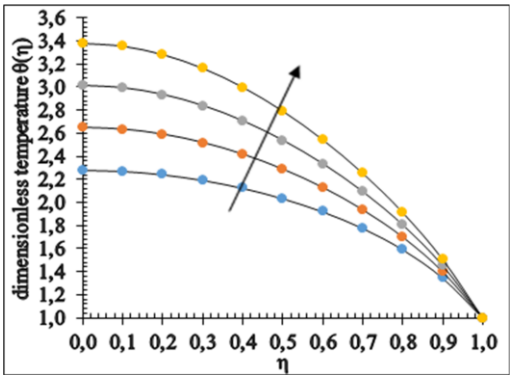

Fig. 8. Influence of Ec = 1.0, 1.5, 2.0, 2,5 on $\theta(\eta)$ for S = Pr = Ec(x) = Sc = γ = 1, $\delta = \lambda_r$ = 0.2, M = 3, $\omega = \pi/4$.

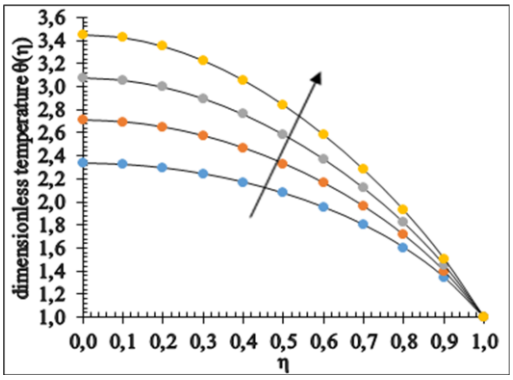

Fig. 9. Influence of Ec = 1.0, 1.5, 2.0, 2,5 on $\theta(\eta)$ for S = Pr = Ec(x) = Sc = γ = 1, $\delta = \lambda_r$ = 0.2, M = 3, $\omega = \pi/6$.

Figure 10 presents the temperature distribution for different values of the magnetic parameter M.

Figure 11 shows the behaviour of the temperature profile for the increasing values of the inclination angle ω of the applied

magnetic field. So, the influence of the magnetic inclination angle on the temperature profile of a fluid is similar to that of the magnetic parameter. Thus, in practical applications related to controlling the momentum and heat transfer of fluid in squeezing flow, the effects produced by changing the magnetic field strength can also be approximately achieved through adjusting the inclination angle of the magnetic field.

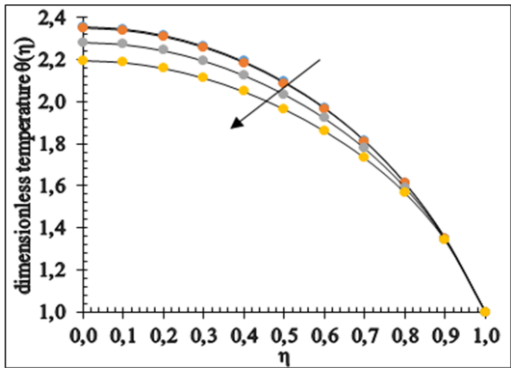

Fig. 10. Influence of M = 0, 1.0, 3.0, 5.0 on $\theta(\eta)$ for S = Pr = Ec = Ec(x) = Sc = γ = 1, $\delta = \lambda_r$ = 0.2, M = 3, $\omega = \pi/4$.

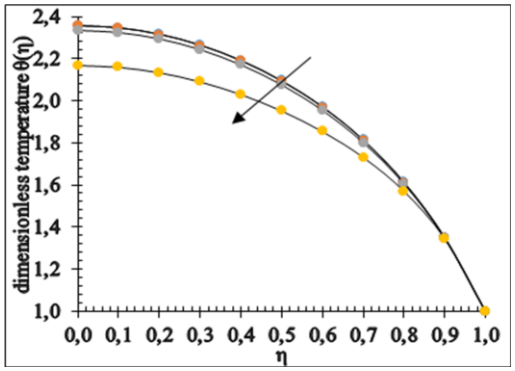

Fig. 11. Influence of ω = 0, $\pi/8$, $\pi/6$, $\pi/4$, $\pi/2$ on $\theta(\eta)$ for S = Pr = Ec = Ec(x) = Sc = γ = 1, $\delta = \lambda_r$ = 0.2, M = 3.

Figures 12 and 13 are to show the impact of S on the concentration field ϕ. A similar trend is noticed for the concentration profile as for the case of temperature field.

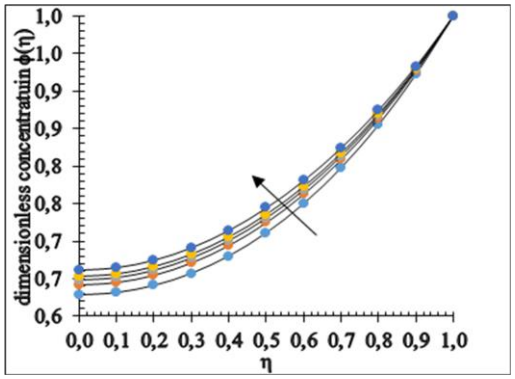

Fig. 12. Influence of S = −1.5, −0.5, 0.01, 0.5, 1.5 on $\phi(\eta)$ for Pr = M = Ec = Ec(x) = 0.2, Sc = γ = 1, $\delta = \lambda_r$ = 0.2, $\omega = \pi/4$.

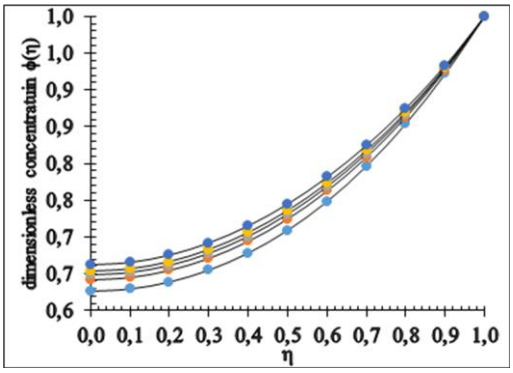

Fig. 13. Influence of S = −1.5, −0.5, 0.01, 0.5, 1.5 on $\phi(\eta)$ for Pr = M = Ec = Ec(x) = 0.2, Sc = γ = 1, $\delta = \lambda_r$ = 0.2, $\omega = \pi/6$.

The outcomes of Sc on the field ϕ are presented in Figs. 14 and 15. It can be noted that the molecular diffusivity turns more fragile, and the boundary layer thickness ends up slenderer because of the gradual increase in Sc.

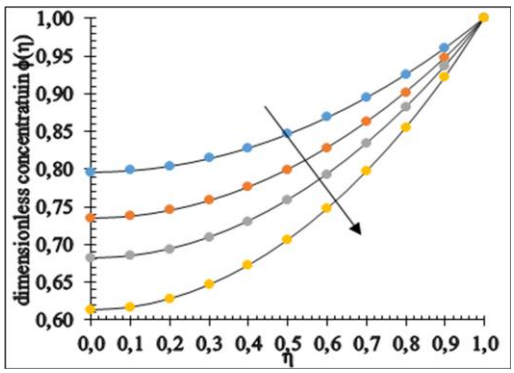

Fig. 14. Influence of Sc = 0.5, 0.7, 0.9, 1.2 on $\phi(\eta)$ for Pr = Ec = Ec(x) = γ = 1, $\delta = \lambda_r$ = 0.2, M = 3, $\omega = \pi/4$.

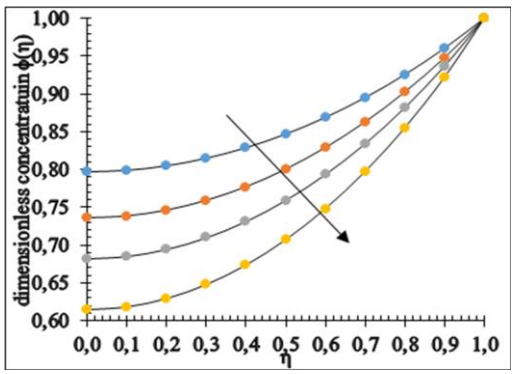

Fig. 15. Influence of Sc = 0.5, 0.7, 0.9, 1.2 on $\phi(\eta)$ for Pr = Ec = Ec(x) = γ = 1, $\delta = \lambda_r$ = 0.2, M = 3, $\omega = \pi/6$.

Figures 16 and 17 delineate the impact of concentration fields. For $\gamma > 0$, the concentration field ϕ declines significantly, whereas an increase in the concentration profile ϕ is very much visible for $\gamma < 0$. Steeper curves are observed when larger estimations of the reaction are accompanied by severe conditions, as shown in Figs. 16 and 17.

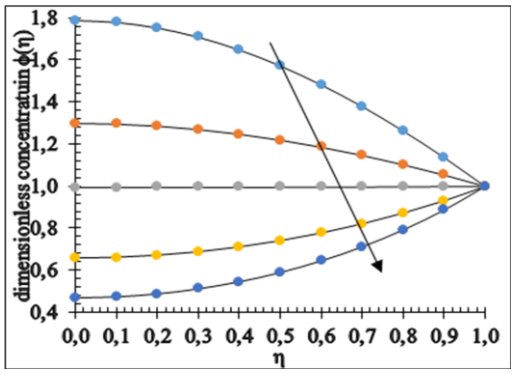

Fig. 16. Influence of $\gamma = -1.0, -0.5, 0.01, 1.0, 2.0$ on $\phi(\eta)$ for Pr = Ec = Ec(x) = S = Sc = 1, $\delta = \lambda_r = 0.2$, $M = 3$, $\omega = \pi/4$.

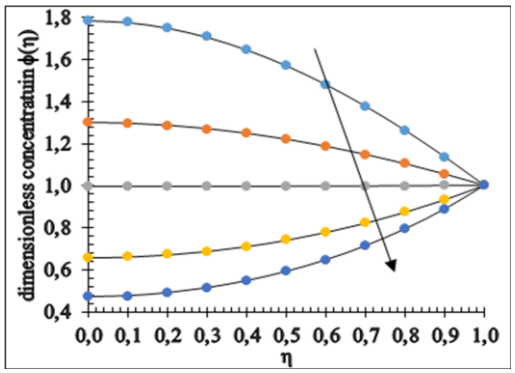

Fig. 17. Influence of $\gamma = -1.0, -0.5, 0.01, 1.0, 2.0$ on $\phi(\eta)$ for Pr = Ec = Ec(x) = S = Sc = 1, $\delta = \lambda_r = 0.2$, $M = 3$, $\omega = \pi/6$.

The numerical results of the coefficient of skin friction, the Sherwood number and Nusselt number for the distinct values of squeezing parameter S with some fixed parameters are shown in Tables 1−3.

Table 1. Skin friction coefficient for different parameters.

S	M	ω	δ	λ_r	$-f''(1)$	
					Mustafa et al. [37]	Present
-1.0	3.0	$\pi/4$	0.2	0.2	3.036639	3.037298
-0.5					3.357444	3.357991
0.01					3.612109	3.612580
0.5					3.808987	3.809395
2.0					4.232647	4.232942

Table 2. Sherwood number for $\omega = \pi/4$ rad, $M = 3.0$, $\lambda_r = \delta = 0.2$.

S	Sc	γ	$-\phi'(1)$	
			Mustafa et al. [37]	Present
-1.0	1.0	1.0	0.800351	0.8002988
-0.5			0.779759	0.7451639
0.01			0.761250	0.7612504
0.5			0.745138	0.7451639
2.0			0.702388	0.7024820

Table 3. Nusselt number for $\omega = \pi/4$ rad, $M = 3.0$, $\lambda_r = \delta = 0.2$.

S	Pr	Ec	Ec(x)	$-\theta'(1)$	
				Mustafa et al. [37]	Present
-1.0	0.2	0.2	0.2	0.170218	0.1701446
-0.5				0.168694	0.1686023
0.01				0.168541	0.1684339
0.5				0.169009	0.1688881
2.0				0.171515	0.1713616
2.0	0.4	0.2	0.2	0.339028	0.3387297
	0.6			0.502699	0.5022627
	0.8			0.662681	0.6621146
2.0	0.2	0.4	0.2	0.215831	0.2156981
		0.6		0.260147	0.2600345
		0.8		0.304463	0.3043713
0.2	0.2	0.2	0.4	0.298714	0.2983872
			0.6	0.425913	0.4254117
			0.8	0.553112	0.5524375

5. Conclusions

This article presents the simulation effects of heat and mass transfer on the UCM flow of a viscous fluid between parallel plates studied by considering the inclined magnetic field effect in the velocity equation. The set of nonlinear momentum, energy and concentration equations are transformed into the dimensionless ODEs by an appropriate transformation. Numerical solutions are obtained by using the shooting technique with the Adams-Moulton method. Our results are in excellent agreement with the existing numerical literature results. The influence of distinct physical parameters such as the Eckert number (Ec), Schmidt number (Sc), squeezing parameter (S), Prandtl number (Pr) and the chemical reaction parameter (γ) on the velocity profile, temperature field and the concentration profile are elaborated in the graphical and tabular form. The above-mentioned analysis of the UCM flow has led us to the following conclusions:

- A decrease in the temperature profile is noted with the increasing values of the squeezing parameter;
- It is observed that an increment in the temperature occurs with the increasing values of the Eckert number;
- An increment in the Schmidt number is observed to decrease the concentration profile;
- The temperature distribution decreases due to the boosting value of the magnetic parameter;
- When the values of the chemical reaction parameter are increased, the concentration profile decreases, whereas when the chemical reaction parameter is decreased, the concentration profile increases;
- The problem can be extended by a stretching surface in different types of fluids for instance a Maxwell nanofluid;
- The problem can be further extended for the cylindrical and rotating disk geometries. Some other parameters can also be included like porous media, yielding Soret and Dufour effects;

– Different numerical techniques can be utilized to solve fluid flow problems.

Acknowledgements

The authors acknowledge the constructive suggestions received from the reviewers and the editor which led to definite improvements in the paper.

References

[1] Duwairi, H., Tashtoush, B., & Damseh, R.A. (2004). On heat transfer effects of a viscous fluid squeezed and extruded between two parallel plates. *Heat and Mass Transfer*, 41(2), 112−117. doi: 10.1007/s00231-004-0525-5

[2] Hsiao, K.-L. (2017). Combined electrical MHD heat transfer thermal extrusion system using Maxwell fluid with radiative and viscous dissipation effects. *Applied Thermal Engineering*, 112, 1281−1288. doi: 10.1016/j.applthermaleng.2016.08.208

[3] Ahmadi, A.R., Zahmatkesh, A., Hatami, M., & Ganji, D.D. (2014). A comprehensive analysis of the flow and heat transfer for a nanofluid over an unsteady stretching at plate. *Powder Technology*, 258, 125−133. doi: 10.1016/j.powtec.2014.03.021

[4] Afify, A.A. (2004). MHD free convective flow and mass transfer over a stretching sheet with chemical reaction. *Heat and Mass Transfer*, 40(6−7), 495−500. doi: 10.1007/s00231-003-0486-0

[5] Bhatta, D.P., Mishra, S.R., & Dash, J.K. (2019). Unsteady squeezing flow of water-based nanofluid between two parallel disks with slip effects: Analytical approach. *Heat Transfer Asian Research*, 48(5), 1575−1594. doi: 10.1002/htj.21447

[6] Adesanya, S.O., Ogunseye, H.A., & Jangili, S. (2018). Unsteady squeezing flow of a radiative Eyring Powell fluid channel flow with chemical reactions. *International Journal of Thermal Sciences*, 125, 440−447. doi: 10.1016/j.ijthermalsci.2017.12.013

[7] Farooq, M., Ahmad, S., Javed, M., & Anjum, A. (2019). Melting heat transfer in squeezed nanofluid flow through Darcy Forchheimer medium. *Journal of Heat Transfer*, 141, 012402. doi: 10.1115/1.4041497

[8] Hayat, T., Nawaz, M., Hendi, A.A. & Asghar, S. (2011). MHD squeezing flow of a micropolar fluid between parallel disks. *Journal of Fluids Engineering*, 133(11), 111206. doi: 10.1115/1.4005197

[9] Mahmood, M., Asghar, S., & Hossain, M.A. (2007). Squeezed flow and heat transfer over a porous surface for viscous fluid. *Heat and Mass Transfer*, 44(2), 165−173. doi: 10.1007/s00231-006-0218-3

[10] Mohyud-Din, S.T., Khan, S.I., Khan, U., Ahmed, N., & Xiao-Jun, Y. (2018). Squeezing flow of MHD fluid between parallel disks. *International Journal for Computational Methods in Engineering Science and Mechanics*, 19(1), 42−47. doi: 10.1080/15502287

[11] Ojjela, O., Ramesh, K., & Das, S.K. (2018). Second law analysis of MHD squeezing flow of Casson fluid between two parallel disks. *International Journal of Chemical Reactor Engineering*, 16(6). doi: 10.1515/ijcre-2017-0163

[12] Sheikholeslami, M., Ganji, D., & Ashorynejad, H.(2013). Investigation of squeezing unsteady nanofluid flow using ADM. *Powder Technology*, 239, 259−265. doi: 10.1016/j.powtec.2013.02.006

[13] Gholinia, M., Hosseinzadeh, K., Mehrzadi, H. Ganji, D., & Ranjbar, A. (2019). Investigation of MHD Eyring Powell fluid flow over a rotating disk under effect of homogeneous-heterogeneous reactions. *Case Studies in Thermal Engineering*, 13, 100356. doi: 10.1016/j.csite.2018.11.007

[14] Hayat, T., Yousaf, A., Mustafa, M., & Obaidat, S. (2012). MHD squeezing flow of second-grade fluid between two parallel disks. *International Journal for Numerical Methods in Fluids*, 69(2), 399−410. doi: 10.1002/fld.2565

[15] Jha, B.K. & Aina, B. (2018). Magnetohydrodynamic natural convection flow in a vertical micro-porous channel in the presence of induced magnetic field. *Communications in Nonlinear Science and Numerical Simulation*, 64, 14−34. doi: 10.1016/j.cnsns.2018.04.004

[16] Khan, U., Ahmed, N., & Mohyud-Din, S.T. (2018). Analysis of magnetohydrodynamic flow and heat transfer of Cu-water nanofluid between parallel plates for different shapes of nanoparticles. *Neural Computing and Applications*, 29(1), 695−703 doi: 10.1007/s00521-016-2596-x

[17] Mabood, F., Shateyi, S., Rashidi, M., Momoniat, E., &. Freidoonimehr, N. (2016). MHD stagnation point flow heat and mass transfer of nanofluids in porous medium with radiation, viscous dissipation and chemical reaction. *Advanced Powder Technology*, 27(2), 742−749. doi: 10.1016/j.apt.2016.02.033

[18] Siddiqui, A.M., Irum, S., & Ansari, A.R. (2008). Unsteady squeezing flow of a viscous MHD fluid between parallel plates, a solution using the homotopy perturbation method. *Mathematical Modelling and Analysis*, 13(4), 565–576. doi: 10.3846/1392-6292.2008.13.565-576

[19] Abbasi, M., Khaki, M., Rahbari, A., Ganji, D., & Rahimipetroudi, I. (2016). Analysis of MHD flow characteristics of a UCM viscoelastic flow in a permeable channel under slip conditions. *Journal of the Brazilian Society of Mechanical Sciences and Engineering*, 38(3), 977−988. doi: 10.1007/s40430-015-0325-5

[20] Choi, J., Rusak, Z., & Tichy, J. (1999). Maxwell fluid suction flow in a channel. *Journal of Non-Newtonian Fluid Mechanics*, 85(2−3), 165−187. doi: 10.1016/S0377-0257(98)00197-9

[21] Hayat, T., & Abbas, A. (2008). Channel flow of a Maxwell fluid with chemical reaction. *Zeitschrift four angewandte Mathematik und Physik*, 59(1), 124−144. doi: 10.1007/s00033-007-6067-1

[22] Mukhopadhyay, S., & Vajravelu, K. (2012). Effects of transpiration and internal heat generation/absorption on the unsteady flow of a Maxwell fluid at a stretching surface. *Journal of Applied Mechanics*, 79(4), 044508. doi: 10.1115/1.4006260

[23] Prasad, A., Sujatha, A., Vajravelu, K., & Pop, I. (2012). MHD flow and heat transfer of a UCM fluid over a stretching surface with variable thermophysical properties. *Meccanica*, 47(6), 1425−1439. doi: 10.1007/s11012-011-9526-x

[24] Sadeghy, K., Najafi, A.H., & Saffaripour, M. (2005). Sakiadis flow of an upper-convected Maxwell fluid. *International Journal of Non-Linear Mechanics*, 40(9), 1220−1228. doi: 10.1016/j.ijnonlinmec.2005.05.006

[25] Hayat, T., Qasim, M., & Abbas, Z. (2010). Radiation and mass transfer effects on magnetohydrodynamic unsteady flow induced by a shrinking sheet. *Z Naturforsch*, 65(3), 231–239. doi: 10.1515/zna-2010-0312

[26] Abbas, I.A. (2007). Finite element analysis of the thermoelastic interactions in an unbounded body with a cavity. *Forschung Im Ingenieurwesen*, 71, 215–222. doi: 10.1007/s10010-007-0060-x

[27] Alzahrani, F., Hobiny, A., Abbas, I., & Marin, M. (2020). An Eigenvalues Approach for a Two-Dimensional Porous Medium Based Upon Weak, Normal and Strong Thermal Conductivities. *Symmetry*, 12(5), 848. doi: 10.3390/sym12050848

[28] Abbas I.A., & Kumar, R. (2016). 2D deformation in initially stressed thermoelastic half-space with voids. *Steel and Composite Structures*, 20(5), 1103−1117. doi: 10.12989/scs.2016.20.5.1103

[29] Zenkour, A., & Abbas, I.A. (2014). Nonlinear Transient Thermal Stress Analysis of Temperature-Dependent Hollow Cylinders

Using a Finite Element Model. *International Journal of Structural Stability and Dynamics*, 14(6), 1450025. doi: 10.1142/S0219455414500254

[30] Abbas, I., Hobiny, A., & Marin M. (2020). Photo-thermal interactions in a semi-conductor material with cylindrical cavities and variable thermal conductivity. *Journal of Taibah University for Science*, 14(1), 1369−1376. doi: 10.1080/16583655.2020.1824465

[31] Marin, M., Hobiny, A., & Abbas, I. (2021). The Effects of Fractional Time Derivatives in Por thermoelastic Materials Using Finite Element Method. *Mathematics*, 9(14), 1606. doi: 10.3390/math9141606

[32] Narender, G., Govardhan, K., & Sreedhar Sarma, G. (2020). Magnetohydrodynamic stagnation point on a Casson nanofluid flow over a radially stretching sheet. *Beilstein Journal of Nanotechnology*, 11, 1303–1315. doi: 10.3762/bjnano.11.114

[33] Narender, G., Govardhan, K., & Sreedhar Sarma, G. (2021). MHD Casson Nanofluid Past a Stretching Sheet with the Effects of Viscous Dissipation. Chemical Reaction and Heat Source/Sink. *Journal of Applied Computational Mechanics*, 7(4): 2040–2048. doi: 10.22055/JACM.2019.14804

[34] Zeeshan, A., Ahmad, M., Ellahi, R., Sait, S.M., & Shehzad, N. (2023). Hydromagnetic flow of two immiscible nanofluids under the combined effects of Ohmic and viscous dissipation between two parallel moving plates. *Journal of Magnetism and Magnetic Materials*, 575(1), 170741. doi: 10.1016/j.jmmm.2023.170741

[35] Elgazery, N.S., Elelamy, A.F., Bobescu, E., & Ellahi, R. (2021). How do artificial bacteria behave in magnetized nanofluid with variable thermal conductivity: application of tumor reduction and cancer cells destruction. *International Journal of Numerical Methods for Heat and Fluid Flow*, 32(9), 2982−3006. doi: 10.1108/HFF-11-2021-0722

[36] Bhatti, M.M., Marin, M., Ellahi, R., & Fudulu, I.M. (2023). Insight into the dynamics of EMHD hybrid nanofluid (ZnO/CuO-SA) flow through a pipe for geothermal energy applications. *Journal of Thermal Analysis and Calorimetry*, 24, 14261–14273. doi: 10.1007/s10973-023-12565-8

[37] Mustafa, M., Hayat, T., & Obaidat, S. (2012). On heat and mass transfer in the unsteady squeezing flow between parallel plates. *Meccanica*, 47(7), 1581−1589. doi: 10.1007/s11012-012-9536-3

Co-published by
Institute of Fluid-Flow Machinery
Polish Academy of Sciences
Committee on Thermodynamics and Combustion
Polish Academy of Sciences

http://www.imp.gda.pl/archives-of-thermodynamics/

Analysis of unsteady heat and mass transfer in rotating MHD convection flow over a porous vertical plate

Mohanasundaram Narmatha[a], R. Kavitha[b*],

[a]Department of Mathematics, KPR Institute of Engineering and Technology, Coimbatore, India
[b]Department of Mathematics and Statistics, Faculty of Science and Humanities, SRM Institute of Science and Technology, Chengalpattu, India
*Corresponding author email: kavibalki13@gmail.com

Received: 24.11.2023; revised: 12.07.2024; accepted: 30.09.2024

Abstract

The aim of this research paper is to investigate the rotational flow of an unsteady magnetohydrodynamic heat and mass transfer flow due to convection over a vertical porous semi-infinite plate. The plate undergoes continuous circular motion, maintaining a constant velocity. To achieve this, we worked on both numerical methods and analytical techniques, particularly utilizing perturbation methods to solve the governing partial differential equations. Consequently, we derive an expression for the Nusselt and Sherwood numbers. We delve into the analysis of the velocity profile, temperature distribution, and concentration variation, exploring their behaviour under different physical parameters, including the magnetic field parameter, Grashof number, Soret number and Schmidt number, as well as the Prandtl number. Our findings reveal that the velocity increases with rising values of Grashof, modified Grashof and Soret numbers, whereas it decreases with declining values of the magnetic field parameter, Prandtl number and Schmidt number. Additionally, as rotation gradually intensifies, the fluid velocity closely follows the boundary and becomes negligible as it moves away from it. To facilitate a comprehensive examination of the fluid flow and heat and mass transfer characteristics, we employ graphical representations. Furthermore, this paper offers an in-depth discussion of the underlying physical aspects and their implications.

Keywords: Heat transfer; Magnetohydrodynamics; Mass transfer; Rotation; Soret number; Perturbation law; Porous plate; Heat source

Vol. 45(2024), No. 4, 179–187; doi: 10.24425/ather.2024.152007

Cite this manuscript as: Narmatha, M., & Kavitha, R. (2024). Analysis of unsteady heat and mass transfer in rotating MHD convection flow over a porous vertical plate. *Archives of Thermodynamics*, 45(4), 179−187.

1. Introduction

Combined heat and mass transfer (HMT) plays a crucial role in various engineering applications. Recent research suggests that mass transfer (MT) can potentially reduce heat transfer (HT) in high-speed vehicles like aircraft and missiles, making it an attractive area of exploration. Rotating flows are fundamental to numerous scientific and engineering fields. From designing jet engines, pumps and vacuum cleaners to understanding geophysical phenomena, the analysis of rotating incompressible fluids holds significant importance. Its applications even extend to space science and engineering thermodynamics.

This research builds upon existing studies such as Chamkha et al. [1] investigations of magnetohydrodynamic (MHD) flow with hall current, and Mohyud Din et al. [2] work on nanofluids using Buongiorno's model. Both employed numerical methods for their analyses. Furthermore, Kataria and Patel's [3] research explored the influence of oscillating plates in Casson fluid flow.

Nomenclature

A –velocity ratio parameter
B_0 – magnetic induction, T
C_p – specific heat, J/(kg K)
C_w*– dimensional wall concentration, kg/m^3
C* – dimensional concentration, kg/m^3
C_∞ – ambient concentration, kg/m^3
D_M – coefficient of chemical molecular diffusivity, m^2/s
D_T – coefficient of thermal diffusivity, m^2/s
g – gravitational acceleration, m/s^2
Gm– modified Grashoff number
Gr – Grashoff number
k – thermal conductivity, W/(m K)
K – permeability, m^2
K* – mean absorption coefficient, m^{-1}
M – magnetic field parameter
n* – arbitrary constants
N – components of microrotation
Nu – Nusselt number
Pr – Prandtl number
q_r – radiative heat flux, W/m^2
q_W – the rate of heat transfer, W/m^2
Q – heat source, W/m^3
R – thermal radiation, W/m^2
Re$_x$ – local Reynold number
Sc – Schmidt number
Sh – Sherwood number
So – Soret number
t – time, s
T* – dimensional temperature, K
T_w*– dimensional wall temperature, K
T_∞ – ambient temperature, K
u, v – non-dimensional components of velocity
u^*, v^*– components of velocity, m/s
U_0, V_0– arbitrary constants, m/s
U_∞ – free stream velocity, m/s
x, y – Cartesian coordinates, m

Greek symbols

β – coefficient of thermal expansion
β^* – coefficient of concentration expansion
ε – factor of higher order
ϑ – non-dimensional temperature
μ – dynamic viscosity, Pa·s
ρ – density, kg/m^3
ρ_∞ – ambient density, kg/m^3
σ – electrical conductivity, S/m
σ* – Stefan-Boltzmann constant, W/(m^{2}K^4)
τ – shear stress, Pa
υ – kinematic viscosity, m^2/s
Ω – angular velocity, rad/s

Abbreviations and Acronyms

PDEs– partial differential equations
HMT – heat and mass transfer
HT – heat transfer
MHD– magnetohydrodynamic
MT – mass transfer

Subscripts

w – condition at the surface
∞ – condition at the free stream

The significance of MHD (magnetohydrodynamics) extends beyond theoretical aspects. Engineers utilize MHD principles in heat exchanger design, compressors and spacecraft power systems. Additionally, MHD finds application in separating molten materials and developing novel power generation methods. These diverse applications highlight the necessity of investigating problems involving MHD effects.

Existing literature highlights the importance of studying rotational and MHD effects in fluid flow. Several studies by Seth et al [4,5], Shevchuk [6], Takhar et al., [7], and Jha and Apere [8] have explored these areas in various contexts, including rotating convective flow, MHD on rotating disks and MHD flow between parallel plates. MHD effects near porous media have also been investigated by Abdel Rahman [9], while research on unsteady rotating flows was carried out by Veera Krishna et al. [10], which provides insights into drag experiences in specific geometries. Ahmmed et al. [11] examined the MHD unsteady flow with a heat source engrossed in a porous medium. Seddeek [12] investigated MHD's unsteady thermal convective flow past a semi-infinite flat plate. Furthermore, the performance of a centrifugal compressor fitted with a rotating tapered vaneless diffuser was investigated by Niveditha and Prasad [13] using the numerical ANSYS CFX software. Combined effects of rotation and other factors were studied by Narayanan et al. [14] and Rudziva et al. [15].

Motivated by the gap in Ahmmed et al.'s work [11] which lacked a combined analysis of MHD unsteady convection, HMT, and a porous medium, this study aims at: investigating MHD unsteady convective HMT flow past a vertical porous plate, employing both numerical (MATLAB) and analytical (perturbation technique) methods to solve the governing equations; obtaining expressions for the Nusselt and Sherwood numbers; analyzing the characteristics of fluid flow, HMT; and discussing the physical implications through the use of graphs.

2. Mathematical formulation

Consider the 2D unsteady MHD rotating convective HMT flow of an incompressible, viscous fluid past a vertically moving porous plate with a uniform magnetic field. We choose the x*-axis to run vertically along the plate and the y*-axis to run perpendicular to the plate which is shown in Fig. 1. It is assumed that no voltage is applied, implying that no electric field exists. The transverse magnetic field and magnetic Reynolds number are both extremely low. The induced magnetic field is insignificant.

The governing equations are as follows:

$$\frac{\partial v^*}{\partial y^*} = 0, \tag{1}$$

$$\rho\left(\frac{\partial u^*}{\partial t^*} + v^*\frac{\partial u^*}{\partial y^*}\right) = \frac{\partial p^*}{\partial x^*} + \mu\frac{\partial^2 u^*}{\partial y^*} - \rho\beta - \frac{\mu}{K^*}u^* + \\ -\sigma B_0^2 u^* + 2\Omega u^*, \tag{2}$$

$$\frac{\partial T^*}{\partial t^*} + v^* \frac{\partial T^*}{\partial y^*} = \frac{k}{\rho C_p}\frac{\partial^2 T^*}{\partial y^{*2}} - \frac{1}{\rho C_p}\left(\frac{\partial q_r^*}{\partial y^*}\right) - \frac{Q_0}{\rho C_p}(T^* - T_\infty^*), \quad (3)$$

$$\frac{\partial C^*}{\partial t^*} + v^* \frac{\partial C^*}{\partial y^*} = D_M \frac{\partial^2 C^*}{\partial y^{*2}} + D_T \frac{\partial^2 T^*}{\partial y^{*2}}. \quad (4)$$

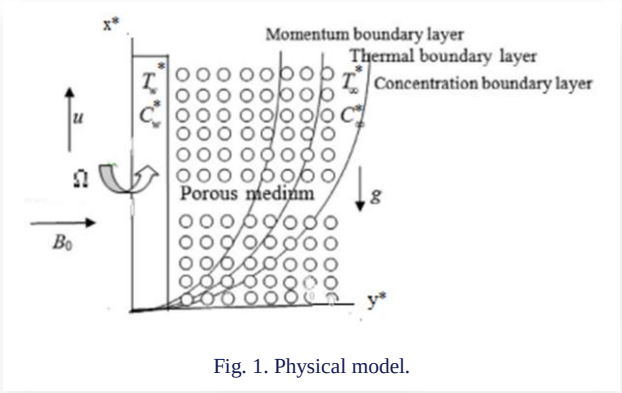

Fig. 1. Physical model.

The boundary conditions are as follows:

– at $y^* = 0$

$$u^* = u_p^*, T^* = T_w^* + \varepsilon(T_w^* - T_\infty^*)e^{n^* t^*}, \quad C^* = C_w^* + \varepsilon(C_w^* - C_\infty^*)e^{n^* t^*}, \quad (5)$$

– at $y^* \to \infty$

$$u^* \to U_\infty^* = U_0\left(1 + \varepsilon e^{n^* t^*}\right), \quad T^* \to T_\infty^*, \quad C^* \to C_\infty^*. \quad (6)$$

From Eq. (1), we deem an exponential form for the velocity:

$$v^* = -v_0(1 + \varepsilon A e^{n^* t^*}), \quad (7)$$

$$\rho\frac{dU_\infty^*}{dt^*} = \frac{\partial p^*}{\partial x^*} - \rho_\infty g - \frac{\mu}{K^*}U_\infty^* - \sigma B_0^2 U_\infty^*, \quad (8)$$

$$\rho\left(\frac{\partial u^*}{\partial t^*} + v^*\frac{\partial u^*}{\partial y^*}\right) = (\rho_\infty - \rho)g + \rho\frac{dU_\infty^*}{dt^*} + \mu\frac{\partial^2 u^*}{\partial y^{*2}} - \frac{\mu}{K^*}(U_\infty^* - u^*) - \sigma B_0^2(U_\infty^* - u^*). \quad (9)$$

Utilizing the equation of state:

$$\frac{(\rho_\infty - \rho)}{\rho_\infty} = \beta\frac{(T^* - T_\infty^*)}{T_\infty^*} + \beta^*\frac{(C^* - C_\infty^*)}{C_\infty^*}, \quad (10)$$

and plugging Eq. (10) into Eq. (9), we have:

$$\frac{\partial u^*}{\partial t^*} + v^*\frac{\partial u^*}{\partial y^*} = \frac{dU_\infty^*}{dt^*} + \mu\frac{\partial^2 u^*}{\partial y^{*2}} + g\beta\frac{(T^* - T_\infty^*)}{T_\infty^*} + g\beta^*\frac{(C^* - C_\infty^*)}{C_\infty^*} + \frac{v}{K^*}(U_\infty^* - u^*) + \frac{\sigma B_0^2}{\rho}(U_\infty^* - u^*). \quad (11)$$

The radiative heat flux term, as expressed using the Rosseland approximation, is given by:

$$q_r^* = \frac{4\sigma^*}{3k_1^*}\frac{\partial T^{*4}}{\partial y^*}. \quad (12)$$

Within the flow, the temperature difference is considered small, so that T^{*4} can be expressed as a temperature-dependent linear function. This is achieved by expanding $T_\infty{}^*$ in a Taylor series while ignoring higher-order terms, resulting in:

$$T^{*4} \cong 4T_\infty^{*3} - 3T_\infty^{*4}. \quad (13)$$

By using Eqs. (12) and (13) in Eq. (3), we get:

$$\frac{\partial T^*}{\partial t^*} + v^*\frac{\partial T^*}{\partial y^*} = \frac{k}{\rho C_p}\frac{\partial^2 T^*}{\partial y^{*2}} - \frac{16\sigma^* T_\infty^{*3}}{3\rho C_p k_1^*}\frac{\partial^2 T^*}{\partial y^{*2}} - \frac{Q_0}{\rho C_p}(T^* - T_\infty^*). \quad (14)$$

2.1. Solution of the problem

Non-dimensional quantities are introduced to find the solution of Eqs. (1) to (4) with boundary conditions (5) and (6):

$$u^* = uU_0, \quad v^* = vV_0, \quad T^* = T_\infty^* + \vartheta(T_w^* - T_\infty^*), \quad C^* = C_\infty^* + C(C_w^* - C_\infty^*), \quad U_\infty^* = U_\infty U_0,$$

$$u_p^* = U_p U_0, \quad K^* = \frac{Kv^2}{V_0^2}, \quad y^* = \frac{yv}{V_0}, \quad \mathrm{Gm} = \frac{vg\beta^*(C_w^* - C_\infty^*)}{V_0^2 U_0 C_\infty^*},$$

$$\mathrm{Gr} = \frac{vg\beta(T_w^* - T_\infty^*)}{V_0^2 U_0 T_\infty^*}, \quad \mathrm{Pr} = \frac{v\rho C_p}{k}, \quad M = \frac{\sigma B_0^2 v}{\rho V_0^2}, \quad Q = \frac{Q_0 v}{\rho V_0^2 C_p},$$

$$R = \frac{4\sigma^* T_\infty^{*3}(T_w^* - T_\infty^*)}{k_1^* k}, \quad \mathrm{Sc} = \frac{v}{D_M}, \quad t^* = \frac{tv}{V_0^2}, \quad n^* = \frac{V_0^2}{v}. \quad (15)$$

As a result, the dimensionless governing equations are expressed by Eqs. (16) to (19) with boundary conditions (20):

$$\frac{\partial v}{\partial y} = 0, \quad (16)$$

$$\frac{\partial u}{\partial t} + v\frac{\partial u}{\partial y} = \frac{dU_\infty}{dt} + \frac{\partial^2 u}{\partial y^2} + \mathrm{Gr}\vartheta + \mathrm{Gm}C + N(U_\infty - u), \quad (17)$$

$$\frac{\partial \vartheta}{\partial t} + v\frac{\partial \vartheta}{\partial y} = \frac{1}{\mathrm{Pr}}\left(1 + \frac{4R}{3}\right)\frac{\partial^2 \vartheta}{\partial y^2} - Q\vartheta, \quad (18)$$

$$\frac{\partial C}{\partial t} + v\frac{\partial C}{\partial y} = \frac{1}{\mathrm{Sc}}\frac{\partial^2 C}{\partial y^2} + \mathrm{So}\frac{\partial^2 \vartheta}{\partial y^2}. \quad (19)$$

The corresponding initial and boundary conditions are:

– at $y = 0$

$$u = U_p, \quad \vartheta = 1 + \varepsilon e^{nt}, \quad C = 1 + \varepsilon e^{nt}, \quad (20)$$

– as $y \to \infty$

$$u \to U_\infty \to 1 + \varepsilon e^{nt}, \quad \vartheta \to 0, \quad C \to 0.$$

We consider the following solutions for the perturbation technique to solve Eqs. (16) to (19):

$$u = u_0(y) + \varepsilon e^{nt}u_1(y) + o(\varepsilon^2), \quad \vartheta = \vartheta_0(y) + \varepsilon e^{nt}\vartheta_1(y) + o(\varepsilon^2), \quad C = C_0(y) + \varepsilon e^{nt}C_1(y) + o(\varepsilon^2). \quad (21)$$

By plugging Eqs. (21) into Eqs. (16)–(20), and then equating the harmonic and non-harmonic terms and ignoring higher order terms of $o(\varepsilon^2)$, we get the following pairs of equations:

$$u_0'' + u_0' + (2\Omega - N)u_0 = -N - \mathrm{Gr}\vartheta_0 - \mathrm{Gm}C_0, \quad (22)$$

$$u_1'' + u_1' - (N + n + 2\Omega)u_1 = -(N + n) - Au_0' - \mathrm{Gr}\vartheta_1 - \mathrm{Gm}C_1, \quad (23)$$

$$(3+4R)\vartheta_0^{''} + 3\mathrm{Pr}\vartheta_0' - 3Q\mathrm{Pr}\vartheta_0 = 0, \quad (24)$$

$$(3+4R)\vartheta_1^{''} + 3\mathrm{Pr}\vartheta_1' - (3n+Q)\mathrm{Pr}\vartheta_1 = -3A\mathrm{Pr}\vartheta_0', \quad (25)$$

$$C_0^{''} + \mathrm{Sc}C_0' = -\mathrm{SoSc}\vartheta_0^{''}, \quad (26)$$

$$C_1^{''} + \mathrm{Sc}C_1' - n\mathrm{Sc}C_1 = -A\mathrm{Sc}C_0' - \mathrm{SoSc}\vartheta_1^{''}. \quad (27)$$

The corresponding boundary conditions can be written as:

– at $y = 0$

$$u_0 = U_p, \quad u_1 = 0, \quad \vartheta_0 = 1, \quad \vartheta_1 = 1, \quad C_0 = 1, \quad C_1 = 1, \quad (28)$$

– as $y \to \infty$

$$u_0 \to u_1 \to 1, \quad \vartheta_0 \to 0, \quad \vartheta_1 \to 0, \quad C_0 \to 0, \quad C_1 \to 0.$$

Finally, by solving Eqs. (22) to (27), we obtain analytical solutions in the form of Eqs. (29) to (34), which satisfy the above boundary conditions (28):

$$u_0 = 1 + J_1 e^{m_2 y} + J_2 e^{m_6 y} + J_3 e^{m_2 y} + J_4 e^{m_{10} y}, \quad (29)$$

$$u_1 = 1 + J_6 e^{m_{10} y} + J_7 e^{m_2 y} + J_8 e^{m_6 y} + J_9 e^{m_2 y} + \\ + J_{10} e^{m_4 y} + J_{11} e^{m_2 y} + J_{12} e^{m_8 y} + J_{13} e^{m_6 y} + \\ + J_{14} e^{m_2 y} + J_{15} e^{m_2 y} + J_{16} e^{m_4 y} + J_{17} e^{m_{12} y}, \quad (30)$$

$$\vartheta_0 = e^{m_2 y}, \quad (31)$$

$$\vartheta_1 = D_1 e^{m_2 y} + D_2 e^{m_4 y}, \quad (32)$$

$$C_0 = B_1 e^{m_2 y} + B_2 e^{m_6 y}, \quad (33)$$

$$C_1 = B_3 e^{m_6 y} + B_4 e^{m_2 y} + B_5 e^{m_6 y} + \\ + D_3 e^{m_2 y} + D_4 e^{m_4 y}. \quad (34)$$

The shapes of functions that appear in Eqs. (29)–(34) are explained in Appendix.

Distributions of velocity, temperature and concentration along with the boundary conditions, become visible in an overview of the aforementioned solutions:

$$u(y,t) = 1 + J_1 e^{m_2 y} + J_2 e^{m_6 y} + J_3 e^{m_2 y} + J_4 e^{m_{10} y} + \\ + \varepsilon e^{nt}(1 + J_6 e^{m_{10} y} + J_7 e^{m_2 y} + J_8 e^{m_6 y} + J_9 e^{m_2 y} + \\ + J_{10} e^{m_4 y} + J_{11} e^{m_2 y} + J_{12} e^{m_8 y} + J_{13} e^{m_6 y} + J_{14} e^{m_2 y} + \\ + J_{15} e^{m_2 y} + J_{16} e^{m_4 y} + J_{17} e^{m_{12} y}),$$

$$\vartheta(y,t) = e^{m_2 y} + \varepsilon e^{nt}(D_1 e^{m_2 y} + D_2 e^{m_4 y}),$$

$$C(y,t) = B_1 e^{m_2 y} + B_2 e^{m_6 y} + \varepsilon e^{nt}(B_3 e^{m_6 y} + B_4 e^{m_2 y} + \\ + B_5 e^{m_6 y} + D_3 e^{m_2 y} + D_4 e^{m_4 y}).$$

It is critical to compute the basic physical quantities of interest, which are the local surface heat and mass flux. Using the temperature field in the boundary layer, we can calculate the local surface heat flux, represented by the Nusselt number (Nu):

$$\mathrm{Nu} = \frac{q_w^*}{k(T_w^* - T_\infty^*)} \implies \mathrm{Nu}\,\mathrm{Re}_x = \left(1 + \frac{4R}{3}\right)\left(\frac{\partial \vartheta}{\partial y}\right)_{y=0} \\ = \left(1 + \frac{4R}{3}\right)[m_2 + \varepsilon e^{nt}(m_2 D_1 + m_4 D_2)],$$

where $\mathrm{Re}_x = \frac{V_0 L}{\nu}$.

For the mass flux, we can calculate:

$$\mathrm{Sh} = \left(\frac{\partial C}{\partial y}\right)_{y=0} = m_2 B_1 + m_6 B_2 + \\ + \varepsilon e^{nt}(m_6 B_3 + m_2 B_4 + m_8 B_5).$$

3. Results and discussion

Graphs are utilized in this section to visually present numerical outcomes, aiding in the comprehension of the underlying physical phenomena. The investigation primarily focuses on analyzing velocity, temperature and concentration profiles across a spectrum of parameter values. Figures 2–19 are specifically generated for this purpose. Within these figures, Fig. 2 elucidates the impact of the Grashof number (Gr) on velocity profiles. Gr represents the approximate ratio between thermal buoyancy and viscous forces exerted on a fluid; alterations in Gr lead to changes in buoyancy while concurrently influencing viscous forces. A reduction in fluid viscosity corresponds to a decrease in internal resistance, consequently resulting in an augmentation of fluid velocity.

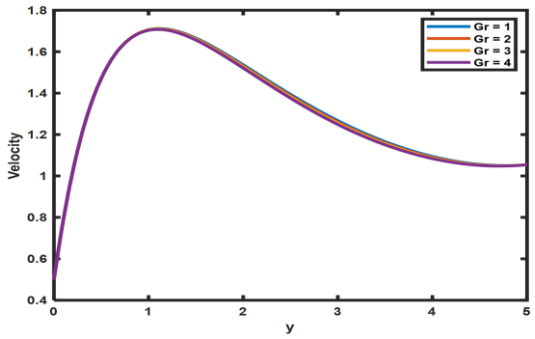

Fig. 2. Velocity profile for different values of Gr against *y*.

Figure 3 shows how the modified Grashof number (Gm) affects the velocity profiles. Gm is approximately the proportion of the buoyancy concentration to the viscous force acting on the fluid; a Gm increase leads to an enlarging buoyancy force while decreasing the viscous force. Viscosity is a type of internal resistance that occurs when a fluid is in motion. As the fluid's viscosity decreases, so does its internal resistance, increasing the velocity.

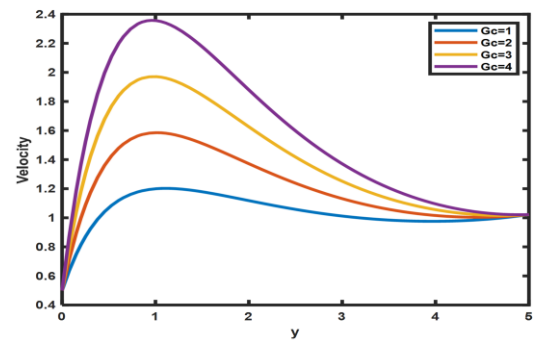

Fig. 3. Velocity profile for different values of Gm against *y*.

The velocity is depicted in Fig. 4 for various permeability values (N). It is self-evident that as permeability increases, so does the peak velocity. Due to the increase in permeability, there are more and larger pathways available for fluid flow within the porous medium, this allows for greater fluid movement and higher velocities. Higher permeability reduces the pressure drop across the porous medium for a given flow rate. With less pressure drop, there is less resistance to flow, enabling the fluid to move more freely and at high velocities.

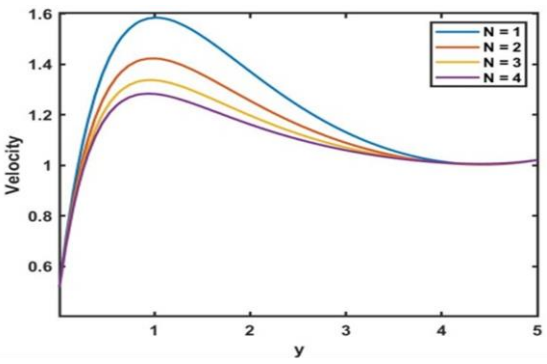

Fig. 4. Velocity profile for different values of N against y.

The modifications of velocity profiles with the Prandtl number Pr are shown in Fig. 5. This explains the motion of fluid which slows the resultant velocity because of the rise in Pr. The Prandtl number is the relationship between two diffusions, momentum and thermal, and is described as the ratio of momentum diffusion and thermal diffusion. Enhancing the Prandtl number reduces the thermal diffusion, causing the thermal boundary layer to thin. As a result, Pr increases across the fluid's occupied region, and the resultant velocity decreases. It is reasonable because the fluid has a large Prandtl number and a greater viscosity due to its thickness.

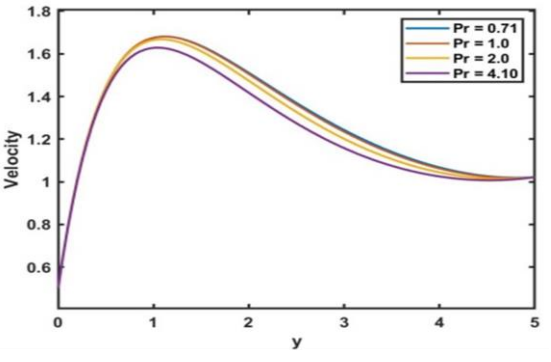

Fig. 5. Velocity profile for different values of Pr against y.

Figure 6 depicts the Soret number (So), which is observed to affect velocity profiles. This figure shows that as So increases, the velocity profiles increase, implying that the velocity of the fluid increases due to larger thermal diffusion. The effect of thermal diffusion is visible in this figure, as the fluid flow is accelerated.

The velocity profile with Schmidt number (Sc) values is depicted in Fig. 7. The velocity distribution will usually decrease as the Schmidt number increases. In terms of physics, a higher Schmidt number indicates a lower molecular diffusivity, resulting in a thinner momentum boundary layer. A decrease in velocity distribution with the increasing Sc number may be associated

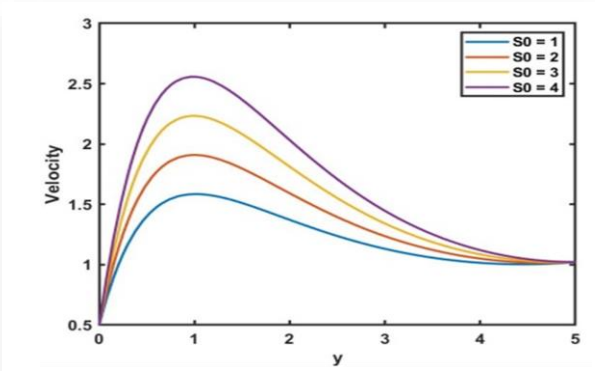

Fig. 6. Velocity profile for different values of So against y.

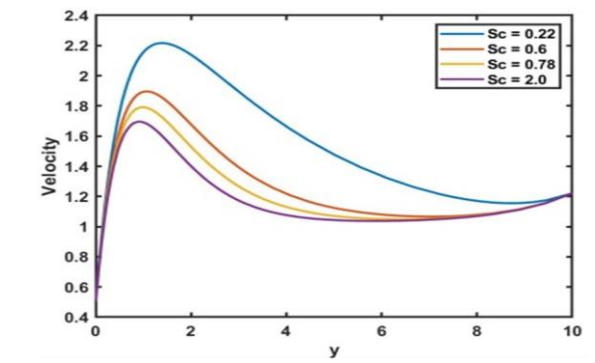

Fig. 7. Velocity profile for different values of Sc against y.

with increased flow stability. The slower diffusion of mass can lead to more stable concentration profiles, which in turn can lead to more uniform flow and reduced velocity gradients.

Figures 8 and 12 illustrate the impact of the heat source (Q) on velocity and concentration profiles. Figures 8 and 12 demonstrate that as heat is produced, the buoyancy force enhances, as a result of which the velocity curves coincide and the flow rate increases, resulting in concentration profiles. The deviation of velocity distribution concerning the thermal radiation R, is shown in Fig. 9. This shows that as thermal radiation enlarges, the velocity within the boundary layer increases. The momentum boundary layer thickness rises in proportion to the increase in thermal radiation. Temperature profiles for various heat source parameter (Q) settings are shown in Fig. 10. As shown in Fig. 10, increasing the heat source parameters reduces the temperature profiles. As the heat source parameters increase, there is more thermal energy available to dissipate throughout the system. This increased energy availability results in more efficient heat dissipation, leading to lower temperature gradients and reduced temperature profiles.

Figure 11 depicts the effect of Prandtl number (Pr) on temperature profiles. The Prandtl number is approximately the ratio of the kinematic viscosity and thermal diffusivity. Higher Prandtl values can aid in the reduction of thermal diffusiveness, which leads to a decrease in temperature profiles. It is clear from Fig. 13 that as the thermal radiation (N) is increased, the concen-

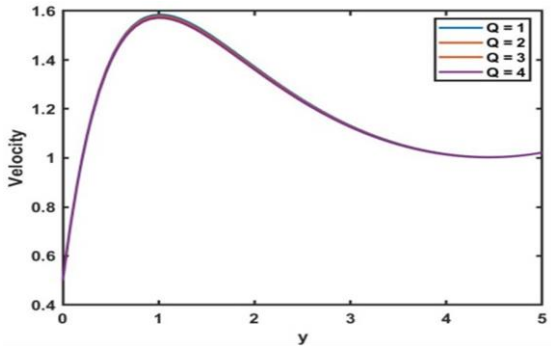

Fig. 8. Velocity profile for different values of Q against y.

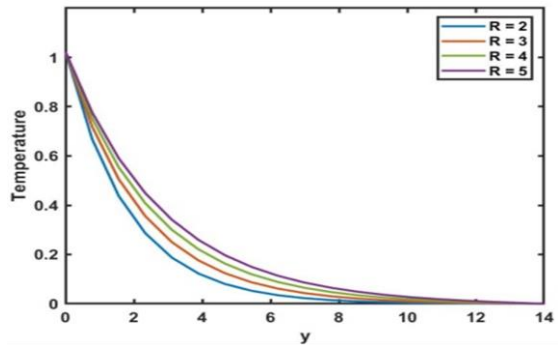

Fig. 9. Temperature profile for different values of R against y.

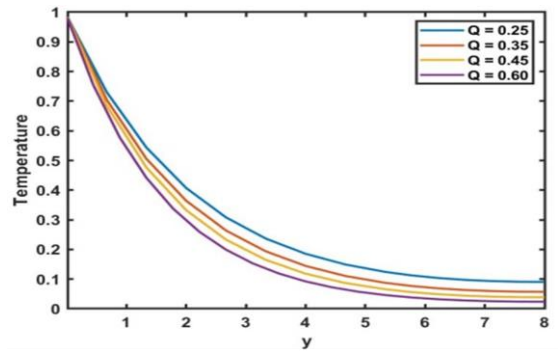

Fig. 10. Temperature profile for different values of Q against y.

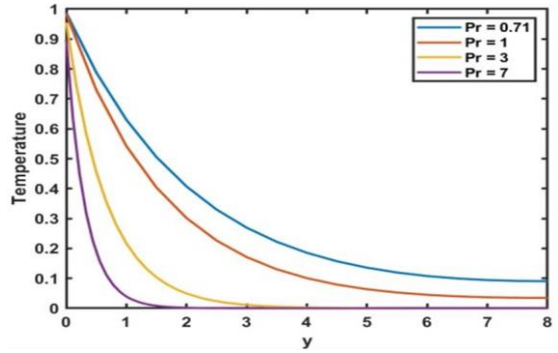

Fig. 11. Temperature profile for different values of Pr against y.

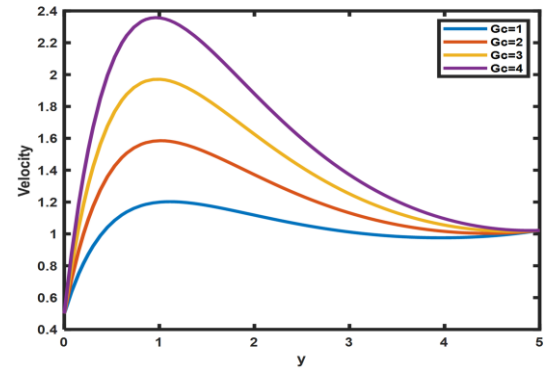

Fig. 12. Concentration profile for different values of Q against y.

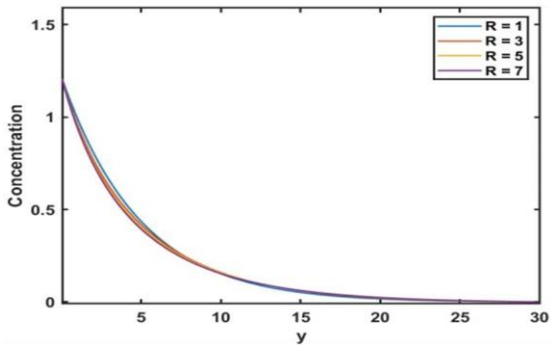

Fig. 13. Concentration profile for different values of R against y.

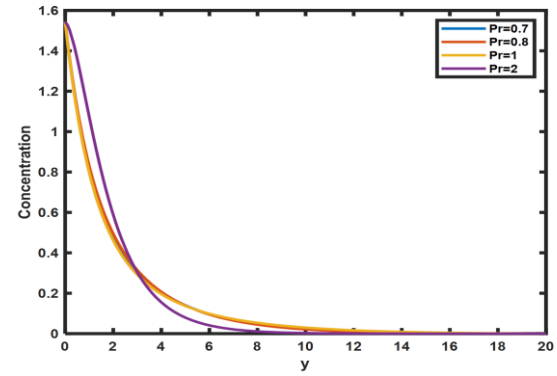

Fig. 14. Concentration profile for different values of Pr against y.

tration decreases. Higher N values cause the fluid concentration to be delayed. Similarly, for the concentration distribution: with the increasing Pr number, the boundary layer thickness shrinks, which is shown in Fig. 14.

Figure 15 illustrates the influence of the Schmidt number (Sc) on concentration profiles. It is observed that higher Sc values, representing lower diffusivity, lead to a reduction in concentration throughout the flow region. An increase in Sc correlates with reduced solute diffusivity, limiting the dispersion of solute effects. Consequently, while the concentration within the flow region increases, the boundary layer thickness decreases, resulting in an overall reduction in concentration as Sc rises. The Soret effect is a phenomenon that occurs when the concentration distribution is influenced by a temperature gradient. In physical

terms, higher Soret numbers indicate a more pronounced temperature gradient, leading to increased convective flow. Consequently, the concentration distribution expands, as illustrated in Fig. 16.

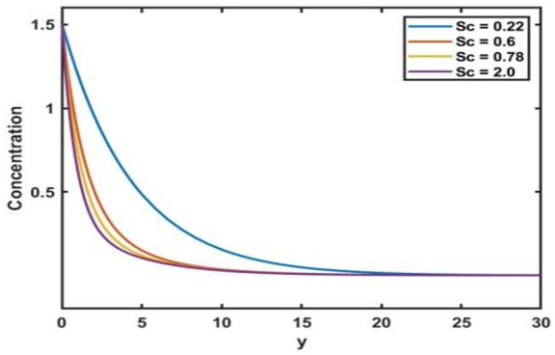

Fig. 15. Concentration profile for different values of Sc against *y*.

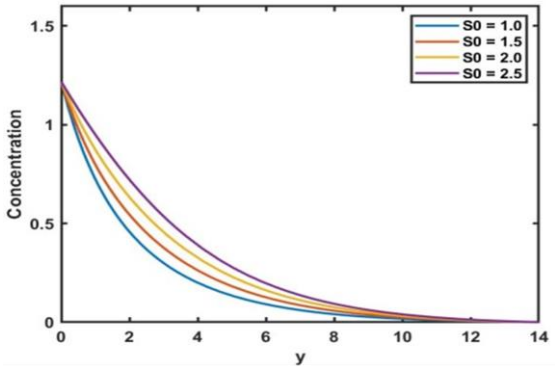

Fig. 16. Concentration profile for different values of So against *y*.

Figure 17 illustrates the influence of radiation (R) on the heat transfer rate, represented by the Nusselt number (Nu). As the radiation parameter enlarges, the rate of heat transfer (Nu) decreases. This reduction occurs because increasing the radiation parameter can diminish the effectiveness of convective heat transfer. Radiation heat transfer tends to suppress convective heat transfer, especially in regions where radiation predominates. Consequently, an increase in the radiation parameter may lead to a decrease in the convective heat transfer coefficient, resulting in lower overall heat transfer rates.

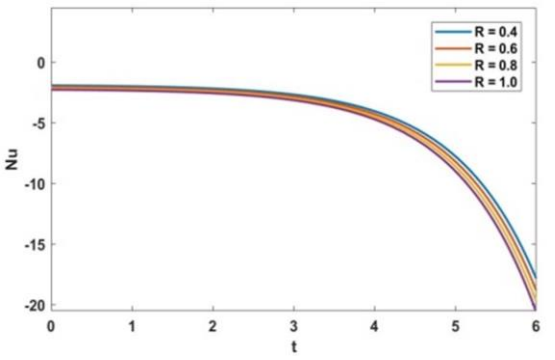

Fig. 17. Nusselt number profile for different values of *R* against *t*.

Figure 18 showcases the effect of the Soret number (So) on the Sherwood number (Sh) on the porous plate. The findings demonstrate that augmenting the value of So leads to an increase in the Sherwood number, indicating enhanced mass transfer rates.

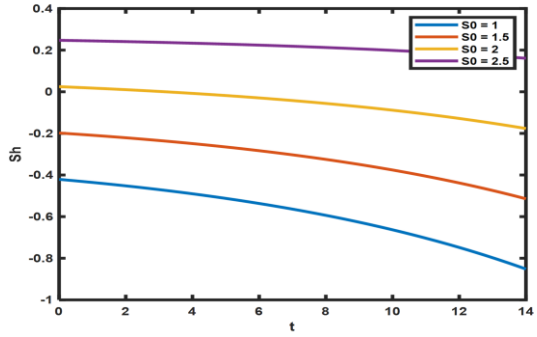

Fig. 18. Sherwood number for different values of So against *t*.

Figure 19 depicts the impact of rotation parameters on fluid velocity. Increasing the rotation parameter decreases the fluid velocity. With a gradual increase in rotation, the fluid's velocity closely adheres to the boundary and gradually diminishes as the distance from the boundary increases.

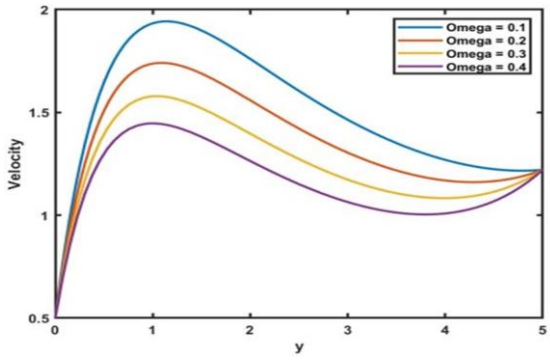

Fig. 19. Velocity profile for different values of Ω against *y*.

4. Conclusions

The main focus of this study revolves around examining the influence of rotation on the magnetohydrodynamic unsteady heat and mass transfer flow of a convective, viscous fluid through a porous medium past a vertically moving plate. The governing equations are solved using the perturbation technique. The resulting profiles, including the temperature, velocity and concentration, are graphically presented and extensively discussed for various parameter configurations. The principal discoveries of this investigation are as follows:

– The velocity increases as Gr, Gm, N, and So increase. Whereas the velocity decreases as the Pr, M, and Sc increase. The velocity profiles are unaffected by the heat source parameter (Q). The heat source parameter represents an external heat input into the system, such as thermal

radiation. This heat input affects the temperature distribution within the fluid but does not directly exert a force on the fluid particles to change their velocity. Therefore, variations in the heat source parameter do not directly alter the velocity profile;

- The temperature increases as radiation enhances, while the temperature decreases as Pr and *Q* increase;
- The rotation is increased gradually, and the fluid's velocity follows the boundary and is trivially far away from it. As the system rotates, the fluid near the boundary experiences a centrifugal force directed away from the axis of rotation. This centrifugal force causes the fluid to move tangentially along the boundary, following its curvature. The fluid velocity along the boundary tends to be higher compared to the fluid velocity in the interior of the flow domain due to the influence of the rotating motion;
- The Nu number reduces as *R* enlarges, while the Sh number enhances as the So number increases.

Appendix

In this Appendix, functions that appear in Eqs. (29)–(34) are explained below:

$$\beta_1 = \left(\frac{3+4R}{3\mathrm{Pr}}\right),$$

$$m_2 = \left(\frac{-1+\sqrt{1+4Q\beta_1}}{2\beta_1}\right),$$

$$m_4 = \left(\frac{-1+\sqrt{1+4(n+Q)\beta_1}}{2\beta_1}\right),$$

$$m_6 = -\mathrm{Sc},$$

$$m_8 = \left(\frac{-\mathrm{Sc}+\sqrt{(\mathrm{Sc})^2+4n\mathrm{Sc}}}{2}\right),$$

$$m_{10} = \left(\frac{-1+\sqrt{1-4(2\Omega-N)}}{2}\right),$$

$$m_{12} = \left(\frac{-1+\sqrt{1+4(N+n+2\Omega)}}{2}\right),$$

$$J_1 = -\left(\frac{\mathrm{Gr}}{m_2^2+m_2+(2\Omega-N)}\right),$$

$$J_2 = -\left(\frac{\mathrm{Gm}B_1}{m_6^2+m_6+(2\Omega-N)}\right),$$

$$J_3 = -\left(\frac{\mathrm{Gm}B_2}{m_{10}^2+m_{10}+(2\Omega-N)}\right),$$

$$J_4 = (U_p - 1 - J_1 - J_2 - J_3),$$

$$J_6 = -\left(\frac{AJ_4m_{10}}{m_{10}^2+m_{10}-(N+n+2\Omega)}\right),$$

$$J_7 = -\left(\frac{AJ_1m_2}{m_2^2+m_2-(N+n+2\Omega)}\right),$$

$$J_8 = -\left(\frac{AJ_3m_6}{m_6^2+m_6-(N+n+2\Omega)}\right),$$

$$J_9 = -\left(\frac{AJ_2m_2}{m_2^2+m_2-(N+n+2\Omega)}\right),$$

$$J_{10} = -\left(\frac{\mathrm{Gr}D_2}{m_4^2+m_4-(N+n+2\Omega)}\right),$$

$$J_{11} = -\left(\frac{\mathrm{Gr}D_1}{m_2^2+m_2-(N+n+2\Omega)}\right),$$

$$J_{12} = -\left(\frac{\mathrm{Gm}B_5}{m_2^2+m_2-(N+n+2\Omega)}\right),$$

$$J_{13} = -\left(\frac{\mathrm{Gm}B_2}{m_6^2+m_6-(N+n+2\Omega)}\right),$$

$$J_{14} = -\left(\frac{\mathrm{Gm}B_4}{m_2^2+m_2-(N+n+2\Omega)}\right),$$

$$J_{15} = -\left(\frac{\mathrm{Gm}D_3}{m_2^2+m_2-(N+n+2\Omega)}\right),$$

$$J_{16} = -\left(\frac{\mathrm{Gm}D_4}{m_4^2+m_4-(N+n+2\Omega)}\right),$$

$$J_{17} = -\left(\begin{matrix}1+J_7+J_8+J_9+J_6+J_{11}+J_{10}+\\+J_{13}+J_{14}+J_{12}+J_{15}+J_{16}\end{matrix}\right),$$

$$D_1 = -\left(\frac{Am_2}{\beta_1 m_2^2+m_2-(n+Q)}\right),$$

$$D_2 = (1 - D_1),$$

$$D_3 = -\left(\frac{\mathrm{ScSo}m_2^2D_1}{m_2^2+\mathrm{Sc}m_2-n\mathrm{Sc}}\right),$$

$$D_4 = -\left(\frac{\mathrm{ScSo}m_4^2D_2}{m_4^2+\mathrm{Sc}m_4-n\mathrm{Sc}}\right),$$

$$B_1 = \frac{-\mathrm{Sc}\,\mathrm{So}m_2}{m_2+\mathrm{Sc}},$$

$$B_2 = (1 - B_1),$$

$$B_3 = -\left(\frac{A\mathrm{Sc}m_6B_2}{m_6^2+\mathrm{Sc}m_6-n\mathrm{Sc}}\right),$$

$$B_4 = -\left(\frac{A\mathrm{Sc}m_2B_1}{m_2^2+\mathrm{Sc}m_2-n\mathrm{Sc}}\right),$$

$$B_5 = (1 - B_3 - B_4 - D_3 - D_4).$$

References

[1] Chamkha, A., Mansour, M.A., & Aly, A. (2011), Unsteady MHD free convective heat and mass transfer from the vertical porous plate with Hall current, thermal radiation and chemical reaction effects. *International Journal for Numerical Methods in Fluids*, 65(4), 432−447. doi: 10.1002/fld.2190

[2] Mohyud–Din, S.T., Khan, U., Ahmed, N., & Rashidi, M.M. (2018). A Study of heat and mass transfer on Magnetohydrodynamic (MHD) flow of nanoparticles. *Propulsion and Power Research*, 7(1), 72–77. doi: 10.1016/j.jppr.2018.02.001

[3] Kataria, H., & Patel, H. (2018), Heat and mass transfer in Magnetohydrodynamic (MHD) Casson fluid flow past over an oscillating vertical plate embedded in a porous medium with ramped wall temperature. *Propulsion and Power Research*, 7(3), 257−267. doi: 10.1016/j.jppr.2018.07.003

[4] Seth, G.S., Sarkar, S., & Hussain, S.M. (2014). Effects of Hall current radiation and rotation on natural convection heat and mass transfer flow past a moving vertical plate. *Ain Shams Engineering Journal*, 5(2), 489−503. doi: 10.1016/j.asej.2013.09.014

[5] Seth, G.S., Hussain, S.M., & Sarkar S. (2014). Effects of Hall current and rotation on unsteady MHD natural convection flow

with heat and mass transfer past an impulsively moving vertical plate in the presence of radiation and chemical reaction. *Bulgarian Chemical Communications,* 46(4), 704−718.

[6] Shevchuk, I.V. (2016). *Modelling of Convective Heat and Mass Transfer in Rotating Flows*. Mathematical Engineering, Springer International Publishing. doi: 10.1007/978-3-319-20961-6

[7] Takhar, H.S., Singh, A.K, & Nath. G. (2002). Unsteady MHD flow and heat transfer on a rotating disk in an ambient fluid. *International Journal of Thermal Sciences*, 41(2), 147−155. doi: 10.1016/S1290-0729(01)01292-3

[8] Jha, B.K., & Apere, C.A. (2010), Combined effect of Hall and ion-slip currents on unsteady MHD Couette flow in a rotating system. *Journal of the Society of Japan*, 79(10), 104401. doi: 10.1143/ JPSJ.79.104401

[9] Abdel Rahman, G.M. (2008), Thermal Diffusion and MHD effects on combined free forced convection and mass transfer of a viscous fluid flow through a porous medium with heat generation. *Chemical Engineering and Technology*, 31(4), 554-559. doi: 10.1002/ceat.200700487

[10] Veera Krishna, M., Ameer Ahamad, N., & Chamkha, A.J. (2020), Hall and ion slip effects on unsteady MHD free convective rotating flow through a saturated porous medium over an exponential plate. *Alexandria Engineering Journal*, 59(2), 565−577. doi: 10.1016/j.aej.2020.01.043

[11] Ahmmed, S.F., Das, M.K., & Ali, L.E. (2015). Analytical study on unsteady MHD free convection and mass transfer flow past a vertical porous plate. *American Journal of Applied Mathematics*, 3(2), 64−74. doi: 10.11648/j.ajam.20150302.16

[12] Seddeek, M.A. (2002). Effects of radiation and variable viscosity on a MHD free convection flow past a semi-infinite flat plate with an aligned magnetic field in the case of unsteady flow. *International Journal of Heat Mass Transfer*, 45(4), 931−935. doi: 10.1016/S0017-9310(01)00189-2

[13] Niveditha, P. & Prasad, B.V.S.S.S. (2021). Computational Analysis on the Performance of Centrifugal Compressor with Tapered Wall and Rotating Tapered Wall Vaneless Diffuser. *Journal of Applied Fluid Mechanics*, 14(2), 641–656. doi: 10.47176/jafm.14.02.32008

[14] Anirudh Narayanan, B., Lakshmanan, G., Mohammad, A. & Ratna Kishore V. (2021). Laminar Flow over a Square Cylinder Undergoing Combined Rotational and Transverse Oscillations. *Journal of Applied Fluid Mechanics*, 14(1), 259-273. doi: 10.47176/jafm.14.01.30706

[15] Rudziva, M., Sibanda, P., Noreldin, O.A.I., & Goqo, S.P. (2022). A Numerical study of heat and mass transfer in a Darcy porous medium saturated with a couple of stress fluid under rotational modulation. *Applied Mathematical Modelling*, 104, 455–473. doi: 10.1016/j.apm.2021.12.004

Co-published by
Institute of Fluid-Flow Machinery
Polish Academy of Sciences
Committee on Thermodynamics and Combustion
Polish Academy of Sciences

http://www.imp.gda.pl/archives-of-thermodynamics/

A comparative numerical evaluation of solar air heater performance having W-contoured, taper-contoured and reverse taper-contoured turbulators

Abhishek Ghildyal[a], Vijay Singh Bisht[a], Prabhakar Bhandari[b], Subham Thapliyal[c], Shivasheesh Kaushik[d*], Lalit Ranakoti[e], Raghubeer Singh Bangari[f], Ayushman Srivastav[g], Nikhil Kanojia[g], Ashwarya Raj Paul[h]

[a]Department of Mechanical Engineering, Veer Madho Singh Bhandari Uttarakhand Technical University, Dehradun 248007, India
[b]Department of Mechanical Engineering, School of Engineering and Technology, K.R. Mangalam University, Gurugram, Haryana 122103, India
[c]Department of Mechanical Engineering, Uttaranchal University, Dehradun, India
[d]Department of Mechanical Engineering, Shivalik College of Engineering Dehradun, India
[e]Department of Mechanical Engineering, Graphic Era Deemed to Be University, Dehradun 248002, Uttarakhand, India
[f]Department of Mechanical Engineering, Graphic Era Hill University, Dehradun 248002, Uttarakhand, India
[g]Department of Mechanical Engineering, U.P.E.S., Dehradun, India
[h]Department of Mechanical Engineering, Vellore Institute of Technology, Vellore, India
*Corresponding author email: shivasheeshkecua@gmail.com

Received: 01.02.2024; revised: 17.09.2024; accepted: 29.10.2024

Abstract

The use of different turbulators in solar air heaters can significantly impact their thermal and hydraulic performance. This study compares solar air heaters equipped with W-contoured, taper-contoured, and reverse taper-contoured turbulators. It examines heat transfer coefficients, pressure drops, velocity contours, turbulent kinetic energy contours, and thermal performance factors for these systems under varying operating conditions. The air Reynolds number ranges from 4000 to 18 000, while design parameters such as relative roughness height and relative pitch ratio remain constant for accurate comparison. The simulations were conducted with a uniform heat flux of 1200 W/m^2. The W-shaped contour roughness achieved the greatest heat transfer coefficient, surpassing both the tapered and reverse tapered configurations. In terms of friction factor, the tapered contour on the absorber plate led, followed by the reverse tapered and W-shaped contours. Overall, the W-shaped contour delivered the best performance. At lower Reynolds numbers, the reverse tapered contour outperformed the tapered contour, whereas at higher Reynolds numbers, the tapered contour showed superior performance compared to the reverse tapered contour.

Keywords: W-contoured; Taper-contoured; Reverse taper-contoured; Turbulent kinetic energy; Thermo-hydraulic performance

Vol. 45(2024), No. 4, 189–196; doi: 10.24425/ather.2024.152008

Cite this manuscript as: Ghildyal, A., Bisht, V.S., Bhandari, P., Thapliyal, S., Kaushik, S., Ranakoti, L., Bangari, R.S., Srivastav, A., Kanojia, N., & Paul, A.R. (2024). A comparative numerical evaluation of solar air heater performance having W-contoured, taper-contoured and reverse taper-contoured turbulators. *Archives of Thermodynamics*, 45(4), 189–196.

1. Introduction

Commercial energy sources have played a role in fostering economic development, but they have also had a harmful impact on the environment and society's health due to the greenhouse effect and global warming. In contrast, renewable energy sources offer a solution to meet global energy demands while safeguarding our surroundings. Additionally, sustainable energy systems,

Nomenclature

C_p – specific heat, J/(kg K)
D_h – hydraulic diameter, mm
e – roughness height, mm
f – friction factor
h – heat transfer coefficient, W/(m^2 K)
k – thermal conductivity, W/(m K)
L – length, mm
Nu – average Nusselt number
δp – pressure drop, Pa
P – roughness pitch, mm
Re – Reynolds number
T – temperature, K
u, v – velocity components, m/s
x, y – Cartesian coordinates, m

Greek symbols

α – thermal diffusivity, m^2/s
ν – kinematic viscosity, m^2/s
ρ – fluid density, kg/m^3

Subscripts and Superscripts

f – test section
r – roughened
s – smooth

Abbreviations and Acronyms

PEC – performance evaluation criterion
SAH – solar air heater

often smaller and region-specific, address concerns related to electricity distribution, environmental impact, and capital costs. Unlike centralised plants based on commercial sources, sustainable equipment like wind turbines, solar panels, and biomass can be mass-produced cost-effectively and tailored to meet the energy needs of specific locations. Among all sustainable energy sources [1], solar power has gained significant prominence due to its abundance, cost-effectiveness, cleanliness, and noiseless operation, while also being environmentally friendly.

Various methods are present for collecting solar energy, the most common of which is the flat plate solar collector, which has a basic design and requires relatively less receiving. Flat plate collectors are used less frequently. Whereas, solar water heaters and solar air heaters (SAH) require regulating for all anticipated temperature ranges [2,3]. However, one significant challenge with SAHs is their suboptimal heat/thermal efficiency due to the slow heat transfer from the absorbing plate (AP) to the air in the duct. To address this issue, artificial turbulators like baffles and ribs are employed [4,5]. These create turbulence within the air duct, enhancing the heat transfer coefficient. However, they also lead to increased friction loss, so it is essential to place turbulators solely in the laminar subzone layer.

Various methods have been proposed by researchers to increase heat transfer through SAH like nanoparticles [6,7], phase change materials [8,9], microchannels [10−12], minichannels [13,14], active techniques [15], etc. It is observed that various design modifications in SAH were taken from other thermal devices like microchannels heat sinks [16,17], heat exchangers [18−20], spiral tube exchangers [21], heat pipes with inserts and baffles [22,23], electric vehicle battery cooling [24], electrical device cooling with fins [25], car radiator [26,27], etc. Some of the recent work covered in the area of SAH has been covered herein.

Khanlari et al. [28] study aimed to enhance the utilization time of a solar air collector by integrating a PCM (phase change material) unit and adding porous fins to shorten PCM melting time. The numerical analysis showed that adding the PCM unit extended the collector's utilization time, and increasing the number of porous fins significantly improved the system's performance and energy efficiency. Abdulmejeed et al. [29] examined the performance of SAH with grooved absorber and triple-flow air channel modifications using numerical modelling and experimental evaluation. The combined SAH showed greater temperature differences than parallel-flow and triple-flow SAHs, with the parallel-flow SAH achieving thermal and exergy efficiencies of 59.51% and 29.09%, respectively, at a mass flow rate of 0.012 kg/s.

Tuncer et al. [30] study aimed to improve a solar drying system (SDS) by using a ZnO nano-enhanced absorber coating and an infrared heating system. The results showed that the combined use of these modifications significantly increased thermal and exergetic efficiencies and reduced drying time by 43.75% compared to the unmodified SDS.

Solar air heater performance can be enhanced using turbulators like Z-shaped baffles on the absorber plate as reported by Bohra et al. [31]. They found that for a blockage ratio of 0.3, with a relative pitch ratio of 1.5 and an attack angle of 45°, the maximum effective efficiency was achieved for Reynolds numbers between 5000 and 10 000. In another similar work, Semalty et al. [32] examined the effectiveness of a solar air heater with multiple ribs and an arc-shaped circular protrusion on the absorber plate, using Fluent simulations. The results indicated that the optimal thermal performance was achieved at a Reynolds number of 20 000, with specific roughness and protrusion parameters, improving thermal performance with minimal frictional pressure drop.

Singh et al. [33] performed a numerical investigation analysing the hydrothermal characteristics of SAH with S-shaped dimple roughness on the absorber plate, using Ansys Fluent for Reynolds numbers 4000 to 20 000. The study found that the optimal configuration, with a dimple diameter of 2.8 mm and relative roughness pitch of 10, yielded significantly higher Nusselt numbers and friction factors compared to smooth plates, achieving maximum thermo-hydraulic performance at a Reynolds number of 20 000. Haldia et al. [34] presented a numerical study comparing the effects of S-shaped and broken arc roughness on solar air heaters, finding that the optimal configuration for heat transfer is a gap of 0.9 mm and a pitch of 25 mm. This specific configuration significantly improves heat transfer but increases the friction factor, achieving the highest thermal performance

factor of 2.9 to 3.3, while a gap of 0.3 mm and the same pitch length shows the lowest performance.

Kumar et al. [35] explored the impact of S-shaped ribs and protrusions on the thermo-hydraulic performance of a SAH, examining various operating and design parameters. The optimal configuration, with a relative pitch roughness of 20, gap of 0.5 mm, and protrusion diameter of 0.3 mm, achieved the highest thermal performance factor of 2.5 to 3.1, while the least effective configuration had a pitch of 12 and protrusion diameter of 0.5 mm, resulting in a factor of 1.4 to 1.7. Kumar [36] experimentally analyses the heat transfer and friction factor of three-side artificially roughened solar air heaters with multiple-V and transverse wires compared to one-side roughened heaters. The three-side roughened heaters show a 24–76% increase in heat transfer rate and a 4–36% increase in friction factor, with air temperatures 34.6% higher than those in one-side roughened heaters, proving their superior performance both qualitatively and quantitatively. Ghritlahre [37] analyzes the energy and exergy performance of roughened solar air heaters with arc-shaped wire ribs using two flow arrangements: apex upstream and apex downstream. Results show that the apex upstream flow configuration achieves a maximum thermal efficiency of 73.2% and exergy efficiency of 2.64% at a mass flow rate of 0.022 kg/s, while the apex downstream flow configuration reaches a thermal efficiency of 69.4% and exergy efficiency of 1.89% under the same conditions.

Patel and Lanjewar [38] use exergy analysis to evaluate the performance of a solar air heater with a W-shaped roughened absorber surface, comparing it to a smooth plate under identical conditions. The analysis shows that the W-shaped roughened surface improves exergetic efficiency by up to 51% with a relative roughness height of 0.03375 and a rib angle of 60°, helping to optimize the design parameters for better performance. Chaudhari et al. [39] focus on optimizing the exergetic efficiency of a solar air heater with inverted L-shaped ribs by improving heat transfer rates. The analysis, conducted at a constant heat flux of 1000 W/m², determined that a relative roughness pitch of 17.86 within Reynolds numbers of 3000 to 18 000 yields optimal exergy performance, with temperature rises between 0.005 and 0.04. Ghildyal et al. [40] considered D-shaped, Reverse D-shaped and U-shaped turbulators in SAH and observed that the U-shaped turbulator achieved the best overall performance.

The present research work focuses on investigating the effects of W-contoured, taper-contoured, and reverse taper-contoured turbulators in solar air heaters, as depicted in Fig.1. The novelty of this research lies in its comparative numerical evaluation of solar air heater performance using three distinct turbulators geometries. This study is pioneering in its approach to geometric diversity, numerical simulation, comprehensive comparison and practical implications. Employing advanced numerical methods to simulate and evaluate the performance of these geometries, provides detailed insights into their thermal and hydraulic characteristics. Offering a direct comparison of the performance enhancements and efficiency gains of each turbulator type helps to identify the most effective design for solar air heaters.

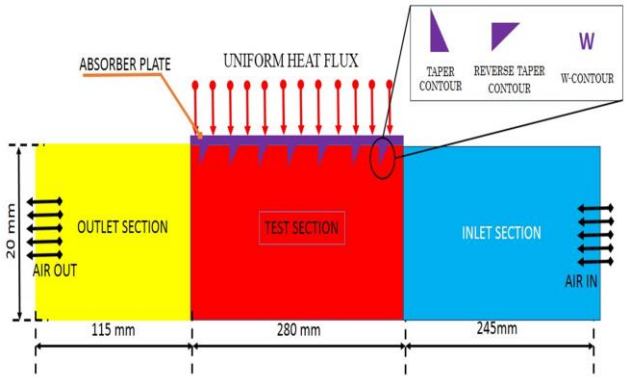

Fig. 1. Schematic diagram of solar air heaters with dimensions and different contours used for roughness.

The primary objective of this research is to enhance the performance of solar air heaters by evaluating and comparing the effectiveness of W-contoured, taper-contoured, and reverse taper-contoured turbulators. This is done by determining the impact of each turbulator design on heat transfer rates, pressure drop, and overall thermal efficiency. Further, the study also highlights potential areas for future research exploration of additional turbulator geometries or configurations.

2. Details of computational domain and grid generation

A two-dimensional computational fluid dynamics study was performed to determine how the performance of SAH changes when a roughened absorber plate is utilized. In the present research work, W-contour, taper-shaped contour, and reverse taper-contoured turbulators were used. The computational domain has 3 regions and is rectangular, measuring 20 mm in height and 640 mm in length: the entry length (L_1 = 245 mm), the test region (L_2 = 280 mm), and the exit length (L_3 = 115 mm). Under the absorber plate, turbulators are mounted. In the current study, constant relative roughness height (e/D_h = 0.021) and pitch ratio (P/e = 14.285) are used for all three turbulators. The choice of particular dimensions was based on previous literature. The air temperature at the inflow is considered to be 300 K.

Solar air heater modelling is done in Ansys Design Modular during the pre-processing phase of this investigation. The Ansys ICEM platform is used for computational domain meshing. The simulations were conducted using Ansys Fluent, a commercial software based on the finite volume method. The momentum and energy equations were discretized using a second-order upwind scheme. The pressure-velocity coupling was addressed using the SIMPLE (semi-implicit method for pressure-linked equations) algorithm. To solve the resulting system of algebraic equations, the Gauss-Seidel iterative method was employed. This numerical approach has been widely used by various researchers for similar problems [41,42].

A homogeneous structural quadrilateral mesh with y^+ = 1 (nondimensional distance from the wall) is used to build the computational domain. To accomplish uniform blending throughout the sector, featured face mesh has been adapted with a 0.2 mm body size. Figure 2 depicts the uniform structural mesh of SAH with W-contoured turbulators. To perform the grid independence test, the smooth SAH was simulated for a number of grid cells ranging from 115 200 to 480 000 for a Reynolds number of 12 000. The complete details of the test are tabulated in Table 1. It was observed that a mesh of 320 000 cells has provided optimum results in lesser computational time. So, the same grid cells were opted for all simulations.

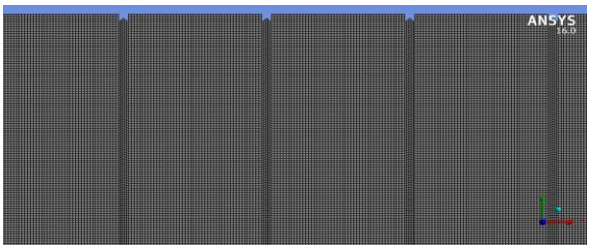

Fig. 2. Face integration of SAH with W-contoured turbulators.

Table 1. Grid independence test performed on smooth SAH.

No.	Number of grid cells	Nusselt number
1	115 200	44.00
2	192 000	39.0
3	320 000	36.44
4	480 000	36.1

2.1. Governing equations

The governing equations for the numerical model of a solar air heater are as follows:

- The continuity equation for two-dimensional steady fluid flow, which represents the conservation of mass for a fluid under motion:

$$\frac{\partial u}{\partial x}+\frac{\partial v}{\partial y}=0, \tag{1}$$

where u and v are the velocity vector components in x and y directional coordinates, respectively.

- The momentum equations for the X and Y directions are given by:
X-momentum equation:

$$u\frac{\partial u}{\partial x}+v\frac{\partial u}{\partial y}=\frac{1}{\rho}\frac{\partial p}{\partial x}+\nu\left(\frac{\partial^2 u}{\partial x^2}+\frac{\partial^2 u}{\partial y^2}\right), \tag{2}$$

Y-momentum equation:

$$u\frac{\partial v}{\partial x}+v\frac{\partial v}{\partial y}=\frac{1}{\rho}\frac{\partial p}{\partial y}+\nu\left(\frac{\partial^2 v}{\partial x^2}+\frac{\partial^2 v}{\partial y^2}\right), \tag{3}$$

where ρ is the fluid density, p is the pressure and ν is the kinematic viscosity.

- For steady and incompressible flow with constant thermal conductivity, no compression work and no heat generation, the energy equation is given by:

$$u\frac{\partial T}{\partial x}+v\frac{\partial T}{\partial y}=\alpha\left(\frac{\partial^2 T}{\partial x^2}+\frac{\partial^2 T}{\partial y^2}\right), \tag{4}$$

where T represents temperature and α is the thermal diffusivity.
The mean Nusselt number is defined as:

$$\mathrm{Nu}_r=\frac{hD_h}{k}, \tag{5}$$

where h, D_h and k stand for the coefficient of heat transfer, hydraulic diameter and thermal conductivity, respectively.
The factor of friction (f) is defined as:

$$\mathrm{f}=\frac{2(\delta p)D_h}{4\rho L_f V^2}, \tag{6}$$

where δp represents the pressure difference, L_f is the length and V is the velocity.
Performance evaluation criterion is defined as

$$\mathrm{PEC}=\frac{h_r}{h_s}\Big/\left(\frac{\delta p_r}{\delta p_s}\right)^{\frac{1}{3}}, \tag{7}$$

where h and δp stand for the heat transfer coefficient and pressure drop, respectively, and subscripts r and s refer to roughened and smooth SAHs, respectively.

2.2. Confirmation of findings

The numerical model for the smooth solar air heater was validated by comparing the average Nusselt number and the friction factor with the well-known equations, as depicted in Fig.3. The average Nusselt number from the model was compared with the Dittus-Boelter equation, and the results showed a slight variation of 2−4% between them. Additionally, the friction factor was compared with the Blasius friction equation, and the results were found to be in good agreement, validating the numerical model. The Dittus-Boelter equation and the Blasius equation for smooth solar air heater are as follows:

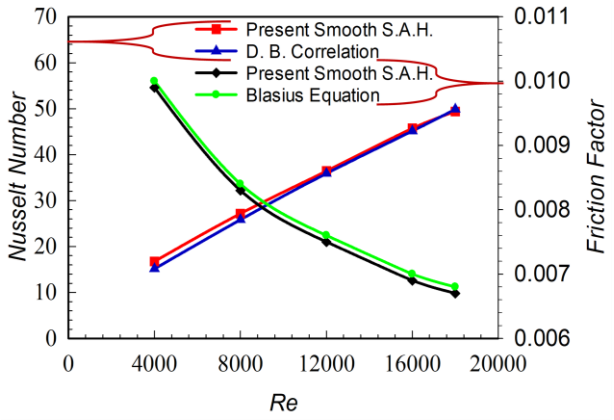

Fig. 3. Validation plot of smooth SAH with established correlation.

$$Nu_s = 0.023 Re_s^{0.8} Pr_s^{0.4}, \quad (8)$$

$$f_s = 0.0791 Re_s^{-0.25}. \quad (9)$$

3. Results and discussion

The variation of heat transfer coefficient with Reynolds number (Re) for different configuration of SAH is depicted in Fig. 4. The utilization of a textured surface on the solar air heater duct demonstrated a noteworthy improvement in the heat transfer rate compared to a smooth surface solar air heater. Nevertheless, the enhancement in heat transfer is minimal at low Reynolds numbers and escalates as the Reynolds number increases. Two main observations can be deduced from Fig. 4. Firstly, as the Reynolds number rises, there is a concurrent increase in the heat transfer coefficient for all solar air heater configurations. The rate of this increase in the heat transfer coefficient is higher for the roughened configuration compared to the smooth solar air heater case. Secondly, regardless of the variation in surface roughness, it was noted that the trend of heat transfer coefficient with Reynolds number remains consistent for all cases. Moreover, the W-shaped contour roughness exhibited the highest heat transfer coefficient value, followed by the tapered contour and reverse tapered contour configurations.

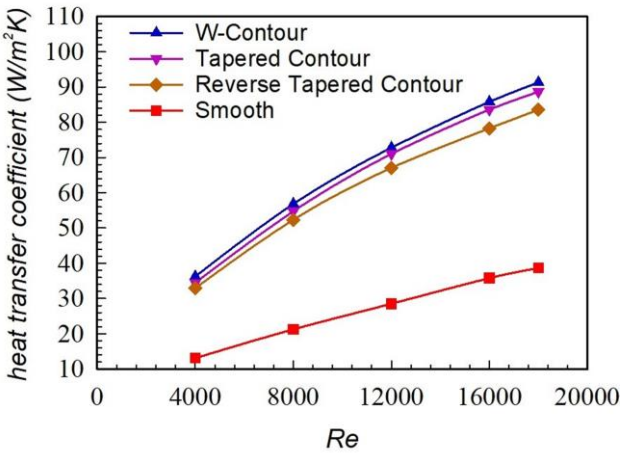

Fig. 4. Heat transfer coefficient variation with Reynolds number for different cases of SAH.

Just like the examination of heat transfer, an analysis of fluid flow was conducted by considering the pressure drop for various solar air heater configurations. It is recognized that incorporating vortex generators or turbulators on the solar air heater impacts the fluid flow parameter, specifically the pressure drop. Figure 5 demonstrates the variation of pressure drop in the SAH with Re for different configurations. It is obvious that the pressure drop in SAH with turbulators is greater than in the smooth SAH, due to obstruction in the flow field and disturbance of laminar sublayer.

Consequently, SAH with tapered contour roughness on the absorber plate yields a higher friction factor, followed by reverse tapered and W-shaped contour roughness. Both reverse tapered and W-shaped contour roughness SAHs show very marginal difference in pressure drop while tapered contour SAH demonstrates less difference at low Re value and the difference with other roughened SAH keeps on increasing with Re value.

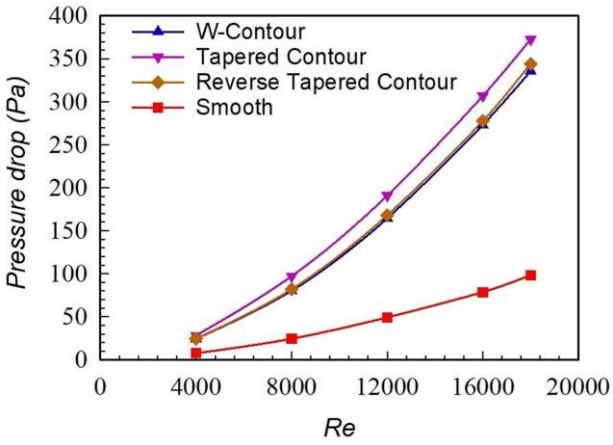

Fig. 5. Pressure drop variation with Reynold number for different cases of SAH.

Figure 6 shows the contours of velocity for each of the three coarsenesses in SAH. Once the flow is stabilized, contours of velocity reveal the creation of an eddy near the rib. A separation occurs as a result of the abrupt expansion of fluid downstream of the rib. This causes a rise in flow velocity at the upper surface of the rib, which generates turbulence. As a result, vortices form on the upper surface of the rib.

The turbulator/ribs prevent the creation of the boundary layer. As a result, the turbulent kinetic energy increases. Figure 7 displays the contours of turbulence kinetic energy for each of the three coarsenesses. The W-contour has a succession of comparable and recurring turbulence kinetic energy profiles, which simply illustrate the intensification of instability in turbulator, which increases the rate of the transfer of heat. W-contour turbulators outperform the other two types of turbulators in terms of heat transfer augmentation.

Figure 8 depicts variation of performance evaluation criterion (PEC) with Re for roughened SAH, considering smooth SAH as a reference model. As all roughened SAHs showed values above 1, this denotes that SAH with turbulators has better overall performance.

Further, it was observed that PEC keeps on decreasing with Re value for all cases. Among all the cases, W-contour has shown highest performance. While at low Re value, reverse tapered contour is better than tapered contour and at higher Re value, tapered contour is better than reverse tapered contour.

4. Conclusions

In present research work, a thorough 2D computational fluid dynamic analysis of a solar air heater with three types of turbulators are performed. The numerical analysis outcome can be summarized as follows:

- With the use of the k-ε turbulence model the verification and the computational domain are justified;

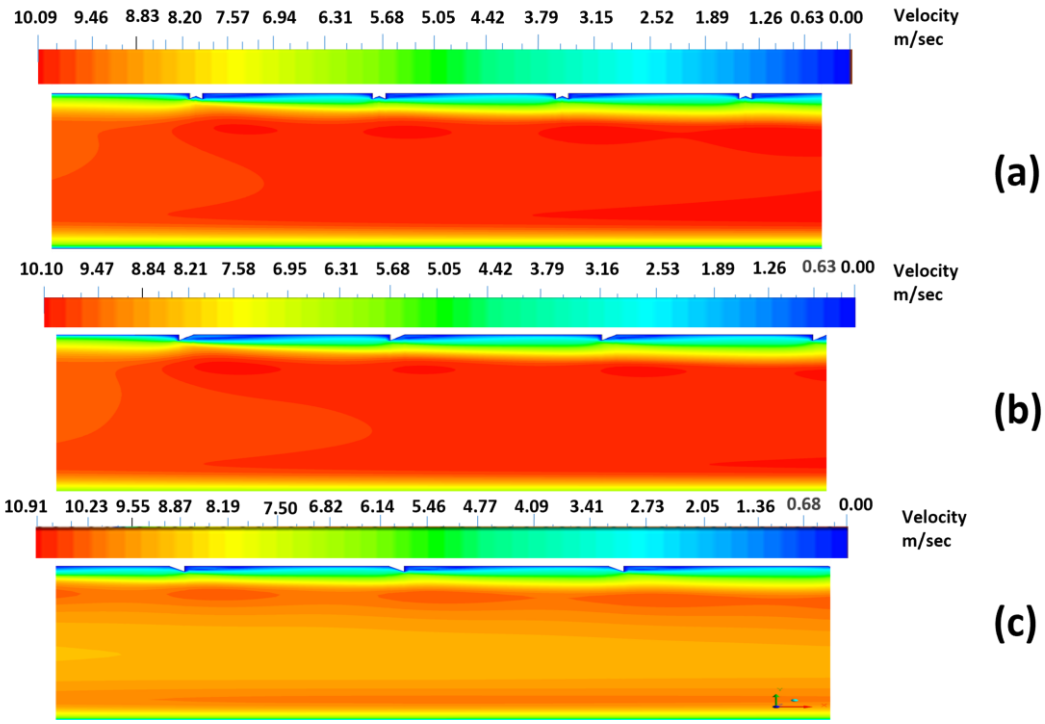

Fig. 6. Velocity contour for (a) W-contour, (b) reverse tapered contour, (c) tapered contour.

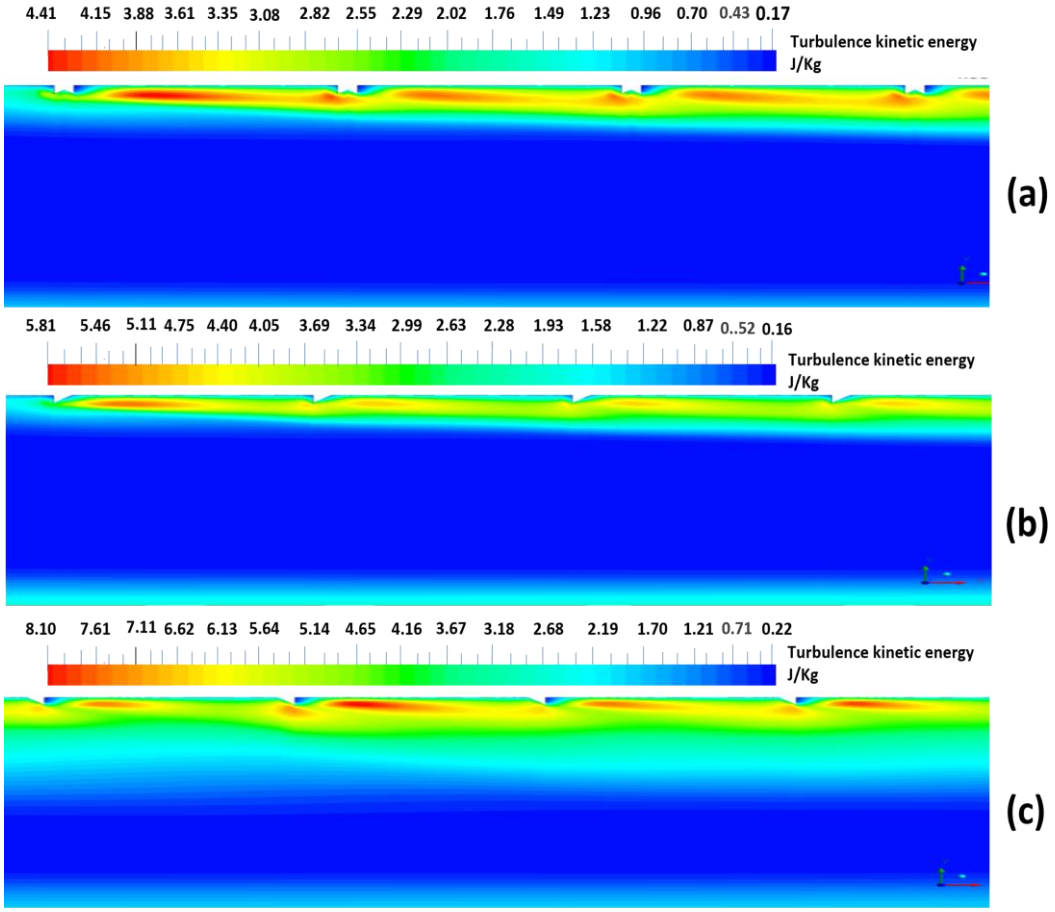

Fig. 7. Turbulence kinetic energy contour for (a) W-contour, (b) reverse tapered contour, (c) tapered contour.

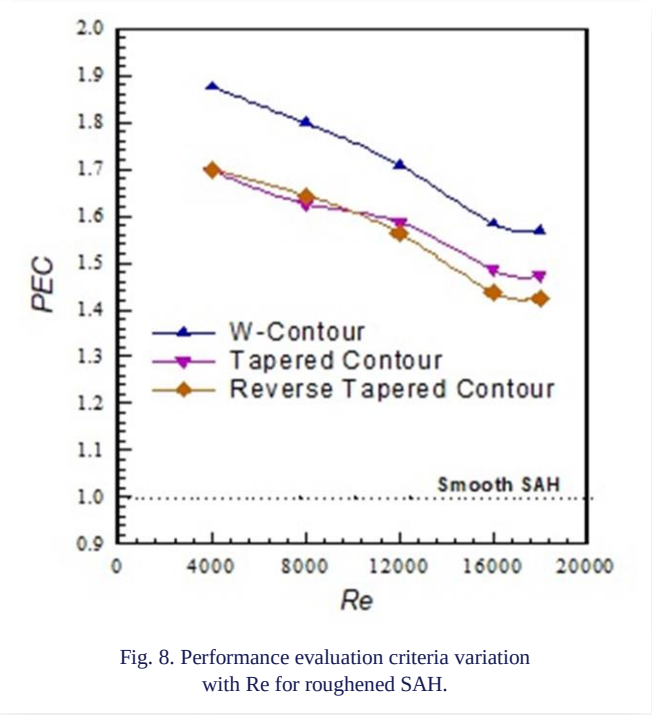

Fig. 8. Performance evaluation criteria variation with Re for roughened SAH.

- Among all configurations, SAH with W-contoured coarseness has the highest value of heat transfer coefficient, followed by taper-contoured and reverse taper-contoured configurations;
- In terms of hydraulic performance, SAH with taper-contoured roughness on the absorber plate yields a higher pressure drop, followed by reverse taper-contoured and W-shaped roughness configurations;
- Performance evaluation criterion, i.e. overall performance of the W-contour turbulator, is the highest irrespective of Reynolds number value.

As a result, a W-contoured turbulator might be explored for further experimental analysis and research on SAHs.

References

[1] Bisht, V.S., Patil, A.K., & Gupta, A. (2018). Review and performance evaluation of roughened solar air heaters. *Renewable and Sustainable Energy Reviews*, 81(1), 954−977. doi: 10.1016/j.rser.2017.08.036

[2] Bhandari, P., Varshney, L., & Bisht, V.S. (2018). Numerical analysis of hybrid solar water heating system using wire screen packed SAH. *1st International Conference on New Frontiers in Engineering, Science & Technology*, (pp. 415−142), 28-12 January, New Delhi, India.

[3] Varshney, L., Bhandari, P., & Bisht, V.S. (2014). Performance evaluation of hybrid solar water heating system using wire screen packed solar air heater. *International Journal of Engineering Research and Applications (IJERA)*, 311–316. https://www.ijera.com/special_issue/ICETMEE/ME18%20rp5%20final.pdf

[4] Kaushik, S., & Singh, S. (2019). Analysis on heat transmission and fluid flow attributes in solar air accumulator passage with diverse faux jaggedness silhouettes on absorber panel. *International Journal of Engineering and Advanced Technology*, 8(5S3), 32–41. doi: 10.35940/ ijeat.E1011.0785S319

[5] Kaushik, S., Panwar, K., & Vashisth, S. (2022). Investigating the thermionic effect of broken perforated curved ribs on solar preheater through CFD simulation. *Res Militaris* 12(5), 1508–1524.

[6] Kumar, N., Singh, P., Redhewal, A.K., & Bhandari, P. (2015). A review on nanofluids applications for heat transfer in microchannels. *Procedia Engineering*, 127, 1197–1202. doi: 10.1016/j.proeng.2015.11.461

[7] Kaushik, S., Ali, S., Kanojia, N., Uniyal, V., Verma, A.K., Panwar, S., Uniyal, S., Goswami, S., Kindo, S., Som, D., & Yadav, N.K. (2023). Experimental and CFD analysis of fluid flow in a rectangular strip-based microchannel with nanofluid. *Materials Today: Proceedings.* doi: 10.1016/j.matpr.2023.05.647

[8] Negi, A., Ranakoti, L., Bhandari, P., Khargotra, R., & Singh, T. (2024). Thermo-physical characteristics and storage material compatibility in nano-enhanced phase change materials for solar distillation applications: A critical assessment. *Solar Energy Materials and Solar Cells*, 271, 112870. doi: 10.1016/j.solmat.2024.112870

[9] Uniyal, A., Prajapati, Y.K., Ranakoti, L., Bhandari, P., Singh, T., Gangil, B., Sharma, S., Upadhyay, V.V., & Eldin, S.M. (2022). Recent advancements in evacuated tube solar water heater: A critical review integration of phase change materials and nano-fluids with ETCs. *Energies*, 15(23), 8999. doi: 10.3390/en15238999

[10] Bhandari, P., Prajapati Y.K., & Bisht, V.S. (2021). Heat transfer augmentation in micro pin fin heat sink using out of plane fluid mixing. *Proceedings of the 26th National and 4th International ISHMT-ASTFE Heat and Mass Transfer Conference*, (pp. 1595–1600), 17–20 December, Madras, India. doi: 10.1615/IHMTC-2021.2400

[11] Bhandari, P., & Prajapati Y.K. (2020). Numerical analysis of different arrangement of square pin-fin microchannel heat sink. *Advances in Mechanical Engineering. Lecture Notes in Mechanical* Engineering (pp. 879–891). *Springer*, *Singapore*. doi: 10.1007/978-981-15-0124-1_79

[12] Kaushik, S., Verma, A.K., Singh, S., Kanojia, N., Panwar, S., Uniyal, S., Goswami, S., Kindo, S., Som, D., & Yadav, N.K. (2023). Comparative analysis of fluid flow attributes in rectangular shape micro channel having external rectangular inserts with hybrid AL_2O_3+ZNO+H_2O nano fluid and (H_2O) base fluid. *Evergreen − Joint Journal of Novel Carbon Resource Sciences & Green Asia Strategy*, 10(2), 851–862. doi: 10.5109/6792839

[13] Kaushik, S., Uniyal, V., Ali, S., Kanojia, N., Verma, A.K., Joshi, S., Makhloga, M., Pargai, P.S., Sharma, S.K., Kumar, R., & Pal, S. (2023). Comparative analysis of fluid flow in mini channel with nano fluids and base fluid. *Materials Today: Proceedings.* doi: 10.1016/j.matpr.2023. 05.363

[14] Kaushik, S., Uniyal, V., Verma, A.K., Jha, A.K., Joshi, S., Makhloga, M., Pargai, P.S., Sharma, S.K., Kumar, R., & Pal, S. (2023). Comparative experimental and cfd analysis of fluid flow attributes in mini channel with hybrid CuO+ZnO+H_2O nano fluid and (H_2O) base fluid. *Evergreen − Joint Journal of Novel Carbon Resource Sciences & Green Asia Strategy*, 10(1), 182–195. doi: 10.5109/6781069

[15] Bhandari, P., Singh, J., Kumar K., & Ranakoti, L. (2022). A review on active techniques in microchannel heat sink for miniaturization problem in electronic industry: *Acta Innovations*, 45, 45−54. doi: 10.32933/ActaInnovations.45.4

[16] Bhandari, P., Rawat, K.S., Prajapati, Y.K., Padalia, D., Ranakoti, L., & Singh, T. (2023). A review on design alteration in microchannel heat sink for augmented thermohydraulic performance. *Ain Shams Engineering Journal*, 15(2), 102417. doi: 10.1016/j.asej.2023.102417

[17] Bhandari, P., Rawat, K., Prajapati, Y.K., Padalia, D., Ranakoti, L., & Singh, T. (2023). Design modifications in micro pin fin configuration of microchannel heat sink for single phase liquid flow: A review. *Journal of Energy Storage*, 66, 107548. doi: 10.1016/j.est.2023. 107548

[18] Kaushik, S., Singh, S., & Panwar, K. (2023). Experimental study of fluid flow properties in spiral tube heat exchanger with varying insert shape over spiral tube profile. *Materials Today Elsevier*, 80(1), 78–84. doi: 10.1016/j.matpr. 2022.10.117

[19] Kaushik, S., Singh, S., & Panwar, K. (2021). Comparative analysis of thermal and fluid flow behaviour of diverse nano fluid using Al_2O_3, ZnO, CuO nano materials in concentric spiral tube heat exchanger. *Materials Today: Proceedings*, 46(15), 6625–6630. doi: 10.1016/j.matpr.2021. 04.1000

[20] Singh, P., Bisht, V.S., & Bhandari, P. (2021). Numerical study of heat exchanger having protrusion and dimple roughened conical ring inserts. *Advances in Fluid and Thermal Engineering. Lecture Notes in Mechanical Engineering* (pp. 151–161). *Springer, Singapore*. doi: 10.1007/ 978-981-16-0159-0_14

[21] Kaushik, S., Singh, S., Kanojia, N., Rawat, K., & Panwar, K. (2020). Comparative study for thermal and fluid flow peculiarities in cascading spiral inner tube heat exchanger with or without diverse inserts over spiral tube. *IOP Conference Series: Materials Science and Engineering*, 802, 012009. doi: 10.1088/1757-899X/802/1/012009

[22] Kaushik, S., Mahar, V.S., Singh, S., Kshetri, R., Kumar, B., Mehta, J.S., Paul, A.R., Kumar, S., Vashisth, S., Pundir, R.S., & Kumar, A. (2024). Comparative experimental analysis of fluid flow in a concentric tube exchanger having semi hollow cylindrical macro inserts with nanofluid and base fluid. *Archives of Thermodynamics*, 45(2), 205–212. doi: 10.24425/ather. 2024.150866

[23] Uniyal, V., Joshi, S.K., Kaushik, S., & Kanojia, N. (2021). CFD investigation of transfer of the heat and turbulent flow in circular copper tube with perforated conical rings of aluminium material. *Materials Today: Proceeding*, 46(15), 6719–6725. doi: 10.1016/j.matpr.2021.04.217

[24] Bisht, A.S., Bisht, V.S., Bhandari, P., Rawat, K.S., Alam, T., & Blecich, P. (2023). The use of a vortex generator for the efficient cooling of lithium-ion batteries in hybrid electric vehicles. *Processes*, 11(2), 500. doi: 10.3390/ pr11020500

[25] Kaushik, S., Singh, S., Kanojia, N., Naudiyal, R., Kshetri, R., Paul, A.R., Kumari, R., Kumar, A., & Kumar, S. (2021). Effect of introducing varying number of fins over LED light bulb on thermal behavior. *Materials Today: Proceeding*, 46(19), 9794–9799. doi: 10.1016/j.matpr. 2020.10.876

[26] Thapa, R.K., Bisht, V.S., Bhandari, P., & Rawat, K. (2022). Numerical study of car radiator using dimple roughness and nanofluid. *Archives of Thermodynamics*, 43(3), 125–140. doi: 10.24425/ather.2022.143175

[27] Thapa, R.K., Bisht, V.S., Rawat, K., & Bhandari, P. (2023). Computational analysis of automobile radiator roughened with rib roughness. *Journal of Heat and Mass Transfer Research*, 9(2), 209–218. doi: 10.22075/jhmtr.2023.27617. 1382

[28] Khanlari, A., Aytaç, I., Tuncer, A.D., Variyenli, H.I., & Şahin, H.N. (2014). Improving the performance of a PCM integrated solar air collector by adding porous fins over the bottom side of the absorber: A transient CFD study. *Journal of Energy Storage*, 90(A), 111847. doi: 10.1016/j.est. 2024.111847

[29] Abdulmejeed, A.E.A., Tuncer, A.D., Khanlari, A., & Gungor, A. (2024). Investigation of combined parallel and triple-pass v-corrugated solar air heater: A numerical and experimental study. *Process Safety and Environmental Protection*, 185, 1385–1398, doi: 10.1016/ j.psep.2024.03. 107

[30] Tuncer, A.D., Amini, A., & Khanlari, A. (2023). Developing an infrared-assisted solar drying system using a vertical solar air heater with perforated baffles and nano-enhanced black paint. *Solar Energy*, 263, 111958, doi: 10.1016/ j.solener.2023.111958

[31] Bohra, J., Bisht, V.S., Bhandari, P., Rawat, K.S., Singh, J., Kumar, K., & Rawat, B. (2022). Effect of variable blockage height ratio on performance for solar air heater roughened with 45°-shaped baffles. *Materials Today: Proceedings*, 69(2), 153−157. doi: 10.1016/j.matpr.2022.08.279

[32] Semalty, A., Bisht, V.S., Bhandari, P., Rawat, K.S., Singh, J., Kumar, K. & Dixit, A.K. (2022). Thermodynamic investigation on solar air heater having roughness as multiple broken arc and circular protrusion. *Materials Today: Proceedings*, 69(2), 181–186. doi: 10.1016/j.matpr.2022.08. 336

[33] Singh, J., Bisht, V.S., Bhandari, P., Kumar, K., Singh, J., Alam, T., Dixit, S., Singh, S., & Khusnutdinov, R. (2024). Computational parametric investigation of solar air heater with dimple roughness in S-shaped pattern. *International Journal on Interactive Design and Manufacturing*, 18, 2969–2979. doi: 10.1007/s12008-023-01392-8

[34] Haldia, S., Bisht, V.S., Bhandari, P., Ranakoti, L., & Negi, A. (2024). Numerical assessment of solar air heater performance having broken arc and broken S-shaped ribs as roughness, *Archives of Thermodynamics*, 2024, 45(1), 23−31. doi: 10.24425/ather.2024.150435

[35] Kumar, S., Bisht, V.S., Bhandari, P., Ranakoti, L., Negi, A., Bisht, A.S., & Padalia, D. (2024). Computational analysis of modified solar air heater having combination of ribs and protrusion in S-shaped configuration. *International Journal on Interactive Design and Manufacturing*. doi: 10.1007/s12008-024-01972-2

[36] Kumar, D. (2023). Heat transfer and friction characteristics in three-side solar air heaters with the combination of multi-v and transverse wire roughness. *Archives of Thermodynamics*, 44(1), 63–87. doi: 10.24425/ ather.2023. 145877

[37] Ghritlahre, H.K. (2021). An experimental study of solar air heater using arc shaped wire rib roughness based on energy and exergy analysis. *Archives of Thermodynamics*, 42(3), 115–139. doi: 10.24425/ather.2021. 138112

[38] Patel, S. S., & Lanjewar, A. (2019). Exergy based analysis of solar air heater duct with W-shaped rib roughness on the absorber plate. *Archives of Thermodynamics*, 40(4), 21–48. doi: 10.24425/ather.2019.130006

[39] Chaudhari, M., Sharma, S.L., & Debbarma, A. (2023). Exergetic performance analysis of solar air heater with inverted L-shape ribs as roughness element. *Archives of Thermodynamics*, 44(3), 241–267. doi: 10.24425/ather. 2023.147546

[40] Ghildyal, A., Bisht, V.S., Rawat, K.S., & Bhandari, P. (2023). Effect of D-shaped, reverse D-shaped and U-shaped turbulators in solar air heater on thermo-hydraulic performance. *Archives of Thermodynamics*, 44(2), 3–20. doi: 10.24425/ather.2023.146556

[41] Bhandari, P., Vyas, B., Padalia, D., Ranakoti, L., Prajapati, Y.K., & Bangri, R.S. (2024). Comparative thermo-hydraulic analysis of periodic stepped open micro pin-fin heat sink. *Archives of Thermodynamics*, 45(3), 99–105. doi: 10.24425/ather.2024.151228

[42] Bhandari, P., & Prajapati, Y.K. (2021). Numerical study of fluid flow and heat transfer in stepped micro-pin–fin heat sink. *Fluid Mechanics and Fluid Power. Lecture Notes in Mechanical Engineering* (pp. 373–381). *Springer, Singapore*,. doi: 10.1007/978-981-16-0698-4_40

Co-published by
Institute of Fluid-Flow Machinery
Polish Academy of Sciences
Committee on Thermodynamics and Combustion
Polish Academy of Sciences

http://www.imp.gda.pl/archives-of-thermodynamics/

Influence of vortex generator dimensions on film cooling efficiency

Mohammed Larbi[a], Khadidja Boualem[b*], Siham Kerrouz[b], Fatima Benali Kouchih[a], Tayeb Yahiaoui[a], Abbes Azzi[a]

[a]University of Sciences and Technology of Oran - Mohammed Boudiaf, P.O. Box 1505, El-M'Naouer, 31000, Oran, Algeria
[b]University of Relizane, Algeria
*Corresponding author email: khadidja.boualem@univ-relizane.dz

Received: 06.01.2024; revised: 13.09.2024; accepted: 29.10.2024

Abstract

Enhancements in gas turbine blade cooling techniques, such as film cooling, have significantly advanced the aerothermal efficiency of turbines, especially in transportation sectors like aeronautics and automotive industries. This study aims to enhance turbine blade cooling by incorporating an obstruction at the jet exit. The vortex generator angle has been modified to 25°, 45°, 60°, 90° and 110°. These five designs were assessed in comparison to the conventional cylindrical hole configurations. Two injection ratios (M = 0.25, and M = 0.5) were studied within the ANSYS CFX 16 software, utilizing the finite volume method to solve the average Reynolds equations and the energy equation. The findings show qualitative alignment with experimental data for the base scenario, indicating that the vortex generator angle notably amplifies film cooling effectiveness. Typically, the vortex generator configured at 90° exhibits a stronger mixing capability compared to the other cases and cylindrical design.

Keywords: Film cooling efficiency; Vortex generator angle; Vortex structures; Area weighted film cooling

Vol. 45(2024), No. 4, 197–203; doi: 10.24425/ather.2024.152009

Cite this manuscript as: Larbi, M., Boualem, K., Kerrouz, S., Benali Kouchih, F., Yahiaoui, T., & Azzi, A. (2024). Influence of vortex generator dimensions on film cooling efficiency. *Archives of Thermodynamics*, 45(4), 197−203.

1. Introduction

Gas turbine blade cooling techniques such as film cooling have helped improve the aerothermal efficiency of turbines. Film cooling stands out as the predominant and most efficient system employed in the industry to cool gas turbine blades. Pioneering studies in film cooling, especially exploring advancements in film geometries were initiated by the work of Goldstein [1]. The film cooling efficiency and the heat transfer coefficients were experimentally established by Liess [2], accounting for the impact of blowing ratios and Mach numbers. Paradis [3] demonstrated the effects of blowing rates and temperature variations on the efficiency of film cooling. The findings reported in the work of Jabbari and Goldstein [4] demonstrate that, at unity, the blowing ratio causes the heat transfer coefficient to increase.

The most common disadvantage of film cooling system is that the flow rises from the surface in the form of two vortices. Counter-current vortices introduce hot air into the jet and destroy the protective film of cold air. Several shapes have been used to improve the cooling performance. Azzi and Jubran [5] conducted a numerical study of a configuration console for controlling the intensity of counter-rotating vortex pairs (CRVP). It was demonstrated that the two counter-rotating vortices that cause the protective coating to deteriorate are absent from the flow structure provided by the new geometry. According to Khorsi and Azzi [6], the converging slot hole (console) provides greater efficiency than the traditional cylinder hole in the same situation. According to Guangchao et al.'s research [7], raising the momentum flux ratio for the injection through fanned holes causes the heat transfer to decrease and the effectiveness of film

Nomenclature

c_p – specific heat at constant pressure, J/(kg K)
D – film-cooling hole diameter, mm
k – turbulent kinetic energy, m^2/s^2
L – spanwise dimension of the flat plate, mm
M – blowing ratio
P_k – production term, W
T – temperature, K
Tu – turbulence intensity, %
u_i – velocity components, m/s
x, y, z – Cartesian coordinates, m

Greek symbols

$\delta_{i,j}$ – unit tensor components
ε – dissipation rate of turbulent kinetic energy, m^2/s^3
η – adiabatic film cooling efficiency
λ – thermal conductivity, W/(m K)
μ – dynamic viscosity, Pa·s
μ_t – turbulent dynamic viscosity, Pa s
ρ – density, kg/m^3

Subscripts and Superscripts

c – cooling
i, j – indexes
w – wall (flat plate)
∞ – freestream condition

Abbreviations and Acronyms

CRVP – counter-rotating vortex pair
VG – vortex generator

cooling to increase dramatically. Liu et al. [8] measured the waist-shaped slot hole's film cooling performance and compared it to two different kinds of console holes. Console holes with a narrow area ratio provided the best thermal protection. Moreover, Zaman et al. [9] conducted experimental research on the flow structure of an inclined jet interacting with a vortex generator to enhance film-cooling techniques. Their work contributes significantly to advancing our understanding of film cooling mechanisms. The film cooling performance and flow characteristics of backward injection with combined holes is the focus of the investigations of Ben Ali Kouchih et al. [10].The findings suggest that backward injection achieves a uniform coverage, resulting in optimal cooling performance. Specifically, the most significant enhancement in film cooling is observed with the employment of combined holes in backward injection, especially at a blowing ratio of 1.5. The studies conducted by Boualem and Azzi [11] and Boualem and al. [12] focused on assessing the efficacy of cooling holes embedded within various trench designs. The primary finding indicates that utilizing jets installed within trenches significantly improves film cooling effectiveness, particularly at elevated blowing ratios.

Na and Shih [13] positioned a ramp preceding a coolant orifice to either eliminate or diminish the counter-rotating vortex pair (CRVP). Their findings showcase that managing the size of this counter-rotating vortex pair significantly enhances the cooling performance. Additionally, Zaman et al. [9] and Shinn et al. [14] have illustrated the film cooling distributions behind micro-ramps. These structures generate anti-vortices, effectively delaying the lifting-off of the jet. An et al. [15] carried out an experiment to investigate how the cooling performance was affected by a short crescent-shaped block positioned downstream of a cylindrical cooling hole. The results showed that this cresent-shaped block increases the lateral averaged film cooling when it is present. Meanwhile, Zhou and Hu [16,17] introduced a ramp design inspired by Barchan sand dunes. Their innovation significantly affects the Counter-Rotating Vortex Pair (CRVP), enhancing film cooling efficiency while minimizing aerodynamic losses. Grine et al. [18] combined two anti-vortex systems to enhance the film cooling efficiency. Ben Ali Kouchih et al. [19] investigated the effect of Barchan sand dunes on forward and backward injection hole. Their findings reportedly show a substantial enhancement in area-weighted film cooling.

The focus of many researchers revolves around altering the film hole shape at high ejection ratios to optimize film cooling efficiency. This paper specifically evaluates and compares the efficacy of a cylindrical hole placed within a vortex generator (VG) at low and medium blowing ratios against conventional cylindrical holes for enhancing film cooling efficiency without resorting to an increase in blowing. The assessment delves into the impact of various angle scales constituting the VG shape, including angles of 25°, 45°, 60°, 90° and 110°. These five configurations are tested across two blowing ratios 0.25 and 0.5 to comprehensively understand their performance under varying conditions.

2. Computational model and grid sensitivity study

Figure 1a presents the physical domain under consideration. The chosen base case aligns with Sinha et al.'s study [20], featuring hole dimensions of D = 1.27 cm and a length-to-diameter ratio of L/D = 1.75. The jet hole is inclined at a 35° angle to the flow direction. Within the computational space, dimensions span 20 times the diameter in height and 50 times the diameter in length.

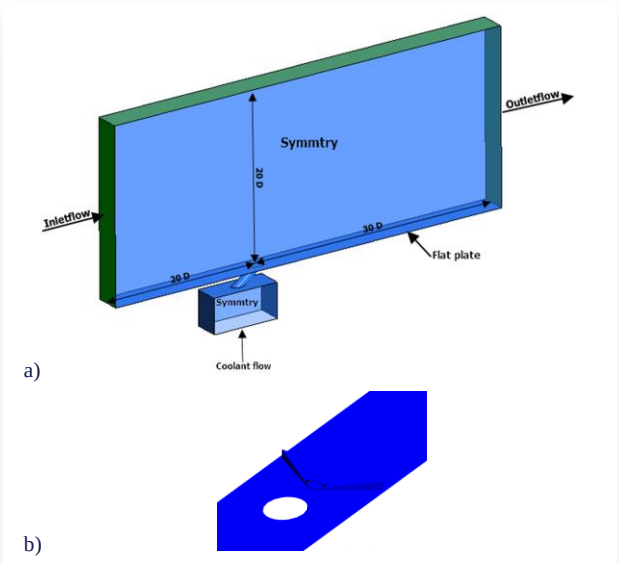

Fig. 1. a) Computational domain and boundary conditions; b) Vortex generator design.

The novel design proposed in this paper is to install a vortex generator at the outlet jet by changing the angle of the vertex of the triangle to 25°, 45°, 60°, 90° and 110° as presented in Fig. 1b. Two injection ratios $M = \rho_c U_c/(\rho_\infty U_\infty) = 0.25$ and 0.5 were investigated. The ratio ρ_c/ρ_∞ is fixed to 1.2. The methods used should be general, allowing one to solve a similar class of problems. The boundary conditions are presented in Table 1.

Table 1. Boundary conditions.

Factor	Velocity [m/s]	Temperature [K]
Hot flow inlet	20	300
Cold flow inlet	$(MU_\infty\rho_\infty)/\rho_\infty$	250

The most important parameter in this topic is the adiabatic film cooling efficiency, which is defined by the following expression:

$$\eta = \frac{T_\infty - T_w}{T_\infty - T_c}. \quad (1)$$

2.1. Turbulence modelling

To carry out this work, several simulations were conducted using ANSYS CFX 14.0 software. In the solver package, the solution of the Reynolds averaged Navier–Stokes equations (RANS) is obtained by using the finite volume method for discretization of the continuity, momentum and energy equations. The second-order upwind solution scheme is used to solve the momentum, energy and turbulence model equations. The SIMPLEC algorithm is employed to solve the pressure–velocity coupling. The governing equations that include the conservation of mass, momentum and energy can be written as follows:

$$\frac{\partial(\rho u_i)}{\partial x_i} = 0, \quad (2)$$

$$\rho\bar{u}_j\frac{\partial\bar{u}_i}{\partial x_j} = -\frac{\partial\bar{p}}{\partial x_i} + \frac{\partial}{\partial x_j}\left[\mu\left(\frac{\partial\bar{u}_i}{\partial x_j} + \frac{\partial\bar{u}_j}{\partial x_i}\right) - \overline{\rho u_i' u_j'}\right], \quad (3)$$

$$\frac{\partial}{\partial x_i}(\rho u_i T) = \frac{\partial}{\partial x_j}\left[\left(\frac{\lambda}{C_p} + \frac{\mu_t}{Pr_t}\right)\frac{\partial T}{\partial x_j}\right], \quad (4)$$

where μ_t and Pr_t are the turbulent viscosity and turbulent Prandtl number, respectively.

Modelling of the Reynolds stresses $\left(-\rho\overline{u_i'u_j'}\right)$ in Eq. (3) is done using the Boussinesq hypothesis which relates the Reynolds stresses to the mean velocity gradients via Eq. (5) below:

$$-\rho\overline{u_i'u_j'} = \mu_t\left(\frac{\partial u_i}{\partial x_j} + \frac{\partial u_j}{\partial x_i}\right) - \frac{2}{3}\left(\rho k + \mu_t\frac{\partial u_i}{\partial x_i}\right)\delta_{ij}. \quad (5)$$

Turbulent quantities in the Navier–Stokes equations are treated using the turbulent viscosity μ_t given by:

$$\mu_t = \rho C_\mu\frac{k^2}{\varepsilon}, \qquad C_\mu = 0.085.$$

According to the literature survey, the RNG k–ε model is more consistent with the experimental data for the prediction of film cooling effectiveness than other models. This model has been adopted in our work. A detailed explanation of the model formulation and test case validations can be found in specific literature, whereas only the mathematical equations of the model are presented here:

$$\frac{\partial}{\partial t}(\rho k) + \frac{\partial}{\partial x_i}(\rho k u_i) = \frac{\partial}{\partial x_j}\left[\left(\mu + \frac{\mu_t}{\sigma_k}\right)\frac{\partial k}{\partial x_j}\right] + P_k - \rho\varepsilon, \quad (6)$$

$$\frac{\partial}{\partial t}(\rho\varepsilon) + \frac{\partial}{\partial x_i}(\rho\varepsilon u_i) = \frac{\partial}{\partial x_j}\left[\left(\mu + \frac{\mu_t}{\sigma_\varepsilon}\right)\frac{\partial\varepsilon}{\partial x_j}\right] + C_{1\varepsilon}\frac{\varepsilon}{k}P_k - C_{2\varepsilon}^*\rho\frac{\varepsilon^2}{k}, \quad (7)$$

where:

$$C_{2\varepsilon}^* = C_{2\varepsilon} + \frac{C_\mu\eta^3(1-\eta/\eta_0)}{1+\beta\eta^3},$$

$$\eta = Sk/\varepsilon, \qquad S = \left(2S_{ij}S_{ij}\right)^{1/2}.$$

The constants of the RNG k–ε model are mentioned in Table 2.

Table 2. Constants of the turbulence model.

C_μ	σ_k	σ_ε	$C_{1\varepsilon}$	$C_{2\varepsilon}$	η_0	β
0.0845	0.7194	0.7149	1.42	1.68	4.38	0.012

2.2. Mesh generation

In this study, geometry generation and mesh generation were performed using ICEM. The ANSYS CFX solver was used to solve the momentum equation, energy equation, and turbulence equation. The RNG k–ε model was used in this study. The ability of this model to predict film-cooling properties has been demonstrated by [21] and [22].

In the present investigation, the lowest freestream turbulence was chosen according to the work of Mayhew, who showed that at low blowing ratio the coverage area is reduced due to increased mixing with the main flow.

Validity of the calculation is ensured by comparing the results obtained in this study with the experimental data presented by [20], taking into account the sensitivity of the mesh. Three meshes are investigated: 1000000 nodes (coarse), 1500000 nodes (fine), and 2000000 nodes (very fine). The fine mesh adjustment is near the outlet jet area. Figure 2 shows the zoom area of a multi-block hexahedral mesh.

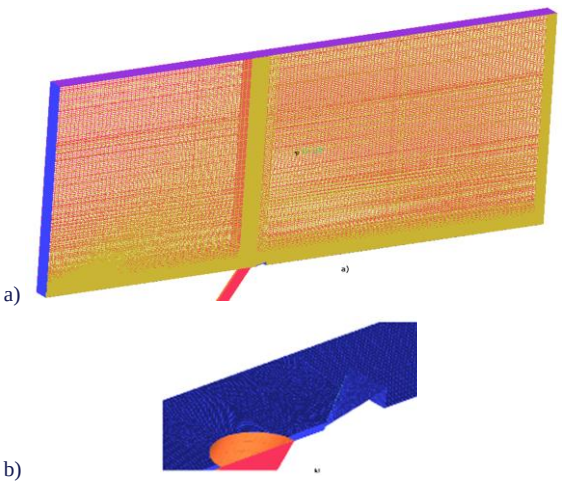

Fig. 2. a) Calculation grid, b) zoomed area of VG mesh.

Figure 3 shows the grid independence for a blowing ratio of M = 0.5. According to Fig. 4, the fine and very fine meshes give somewhat the same adiabatic film cooling in the flow direction, in contrast to the coarse mesh, which is less accurate, especially far from the jet hole. Since increasing the mesh nodes to 2 million does not make a significant difference, a fine mesh (1.5 million) was chosen and implemented in other configurations.

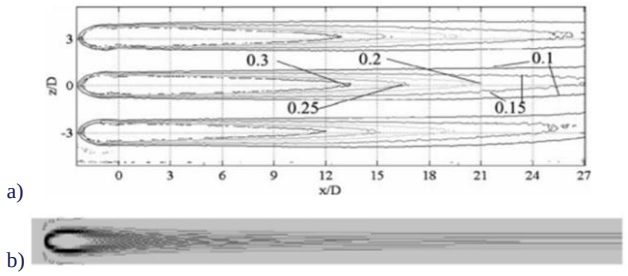

Fig. 3. Comparison of cooling efficiency contours, M = 0.5, Tu = 0.1%: a) Mayhew et al. [23], b) present investigation.

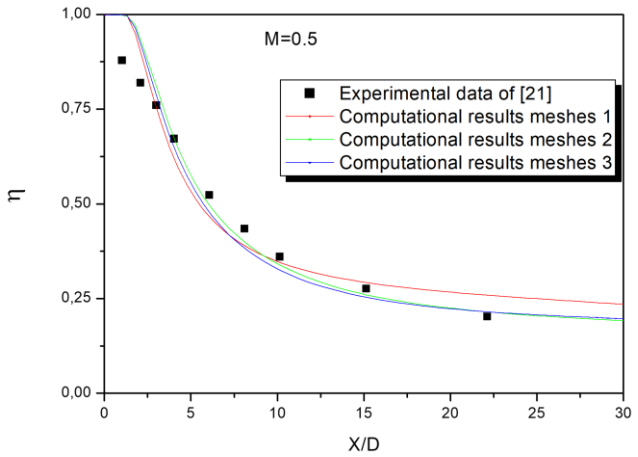

Fig. 4. Centreline adiabatic film cooling effectiveness for three different meshing.

The results indicate that the traditional film cooling design exhibits the lowest efficiency, while the new configurations demonstrate a substantially higher film cooling efficiency at both blowing ratios, 0.25 and 0.5. In some instances, the improvement rate exceeds 100%, emphasizing the significant enhancement achieved by employing these novel configurations with vortex generators in comparison to the conventional approach.

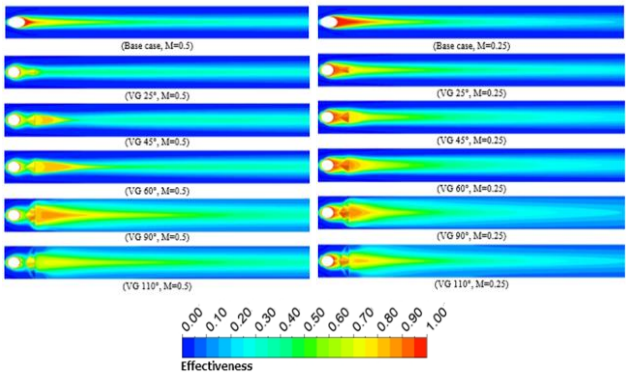

Fig. 5. Contours of adiabatic film cooling efficiency on the flat plate.

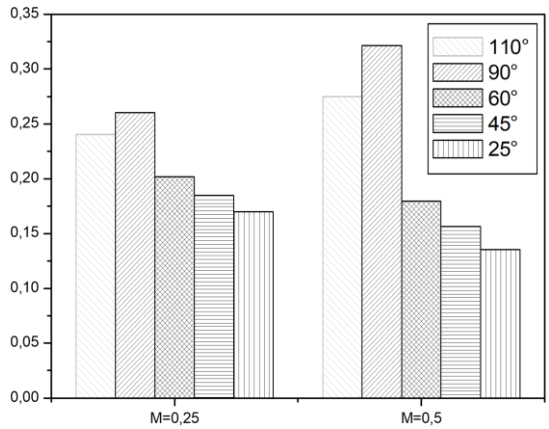

Fig. 6. Area weighted average film cooling efficiency.

3. Results and discussion

3.1. Film cooling efficiency

In Fig. 5, a comparison between the adiabatic cooling efficiency distributions on the flat plate is presented for the baseline case against the novel designs proposed in this study, particularly at low and medium blowing ratios (M = 0.25 and 0.5). The baseline case exhibits uneven coolant distribution due to jet lift-off, affecting the surface coverage. In contrast, the new designs, specifically with the degree of vortex generator configurations at 90° and 110° angles showcase notably improved film cooling efficiency distributions. This enhancement is attributed to the ability of the vortex generators to shape the coolant flow, ensuring more even distribution across the flat plate surface.

Figure 6 illustrates a quantitative assessment comparing the area-weighted average film cooling efficiency between two scenarios: the traditional case (flat plate without vortex generators) and the novel configurations (flat plate with vortex generators).

Figure 7 demonstrates the variation in film cooling efficiency for the two blowing ratios (0.25 and 0.5) across the twelve cases, including five new configurations alongside the baseline case. Notably, it is evident that the maximum efficiency occurs behind the film hole and decreases as the distance from the hole (x/D) increases across all configurations.

In the baseline cases, the cooling efficiency diminishes with increasing blowing ratios, which can be attributed to the jet take-off. However, with the incorporation of vortex generators (VGs), there is a substantial improvement in film cooling performance compared to the reference case.

Comparing the different angles of vortex generators with the traditional cylindrical hole case, it is observed that VG with a right angle generally delivers superior efficiency, except at M = 0.25, where there is a slight difference after x/D > 10, favouring the accurate trench configuration. Notably, at both blowing ratios, VG set at 90° consistently achieves the highest film cooling efficiency among the configurations tested.

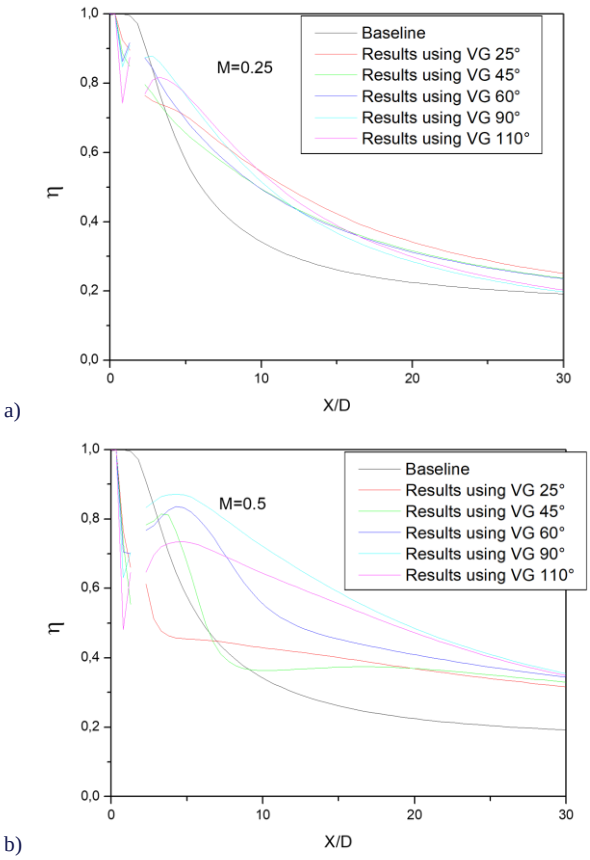

Fig. 7. Centreline adiabatic film cooling efficiency for all cases: a) M = 0.25, b) M = 0.5.

3.2. Flow structure

The formation of counter-rotating vortices (CRV), often termed kidney vortices, arises from the interaction between the mainstream and jet flows. These vortices significantly influence film-cooling performance, especially under high blowing ratios. Their passive nature involves reheating the air from the main flow, potentially compromising the protection provided to turbine blades or flat surfaces.

To gain deeper insights into the underlying physics and assess the impact of new designs on flow structures at blowing ratios of M = 0.25 and M = 0.5, Fig. 8 displays temperature contours in the y–z plane at x/D = 3, 6 and 10 for vortex generators with acute, right and obtuse angles. In the baseline case, higher injection rates lead to the jet moving away from the plate surface, enlarging the vortices. However, placing the vortex generator downstream of the jet outlet reduces the strength of the rotating vortices (CRV), encouraging the cooler flow to adhere more closely to the flat plate.

Figure 9 presents the vortex structures to better understand the flow behaviour. This figure shows that the distribution and efficiency of the cooling film are influenced by CRVP, horseshoes and shear layers. Due to the difference in momentum, the cooling jet can break away from the surface, creating a recirculation zone before reconnecting which we can observe from the baseline case. Notably, VGs with acute angles 25° exhibit lower efficiency in reducing CRVs compared to VGs with right and obtuse angles (90° and 110°), emphasizing the differential impact of VG angles on mitigating these detrimental vortices and enhancing film cooling performance.

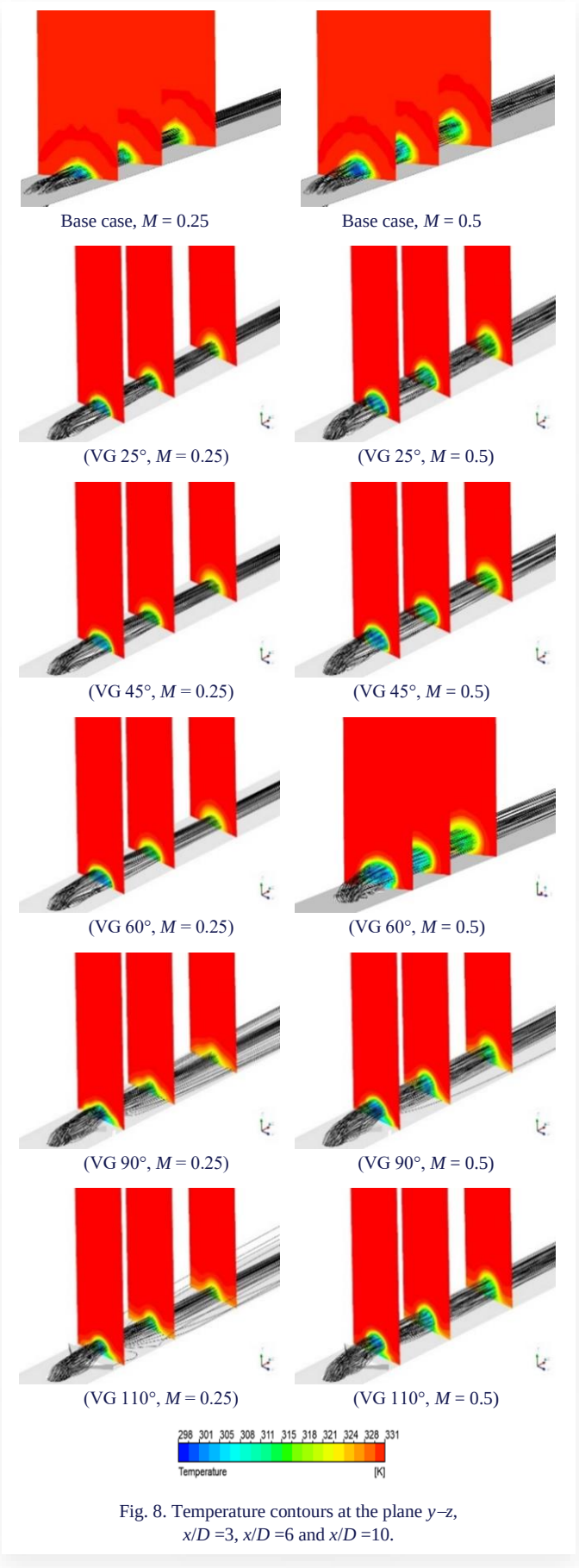

Fig. 8. Temperature contours at the plane y–z, x/D =3, x/D =6 and x/D =10.

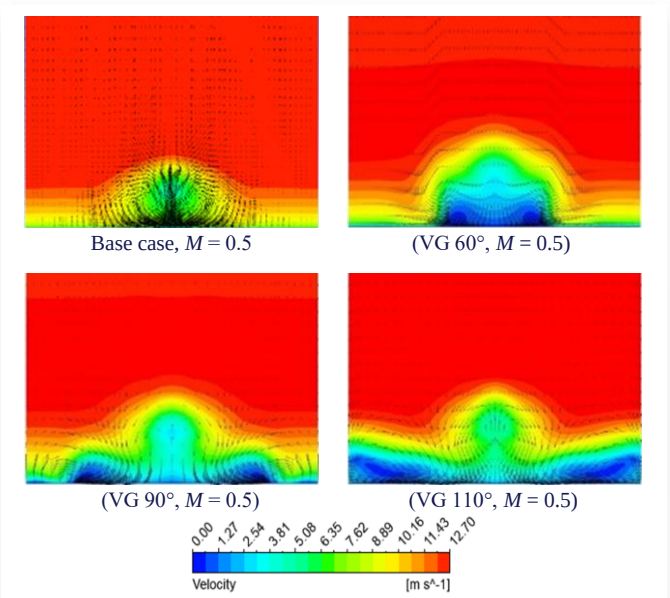

Fig. 9. Counter rotating vortex pairs at the plane y–z, x/D =3.

4. Conclusions

The numerical study focused on investigating the flow behaviour and thermal characteristics of film cooling across six different configurations. This analysis specifically considered the variation in the blowing ratio parameter, examining scenarios at M = 0.25 and M = 0.5. By exploring these different configurations and varying blowing ratios, the study aimed to understand in a comprehensive manner how changes in parameters affect flow patterns and thermal attributes, providing valuable insights into optimizing film cooling performance.

In the initial case, serving as the baseline for validation purposes, the efficiency of film cooling along the centreline was compared to the existing data. The results indicated that the computational model employed, based on the RNG k–ε model, accurately predicted the flow structure and thermal behaviour in line with the available data. Moreover, an enhancement in film cooling performance was achieved by introducing vortex generators with 90° as an improvement over the original streamwise cylindrical injection method.

The main results from this work can be summarized as follows:

- the ability of vortex generators to distribute the coolant flow over the flat plate surface,
- the new configurations demonstrate significantly higher film cooling efficiency at both blowing ratios, 0.25 and 0.5, reaching or exceeding 100% in some cases,
- right or obtuse angle vortex generators help reduce the size of counter-rotating vortices, helping to distribute cool air.

References

[1] Goldstein, R.J. (1971). Film cooling. *Advances in heat transfer*, 7, 321–379. doi: 10.1016/S0065-2717(08)70020-0

[2] Liess, C. (1975). Experimental investigation of film cooling with ejection from a row of holes for the application to gas turbine blades. *Journal of Engineering for Gas Turbines and Power*, 97(1), 21–27. doi: 10.1115/1.3445904

[3] Paradis, M.A. (1977). Film cooling of gas turbine blades: a study of the effect of large temperature differences on film cooling effectiveness. *Journal of Engineering for Gas Turbines and Power*, 99(1), 11–20. doi: 10.1115/1.3446240

[4] Jabbari, M.Y., & Goldstein, R.J. (1978). Adiabatic wall temperature and heat transfer downstream of injection through two rows of holes. *Journal of Engineering for Gas Turbines and Power*, 100(2), 303–307. doi: 10.1115/1.3446350

[5] Azzi, A. & Jubran, B.A. (2007). Numerical modelling of film cooling from converging slot-hole. *Heat and Mass Transfer (Warme und Stoffubertragung)*, 43(4), 381–388. doi: 10.1007/s00231-006-0115-9

[6] Khorsi, A., & Azzi, A. (2010). Computation film cooling from three different holes geometries. *Mechanika*, 86(6), 32–37. doi: 10.5755/j01.mech.86.6.15971

[7] Guangchao, L., Huiren, Z., & Huiming, F. (2008). Influences of hole shape on film cooling characteristics with CO2 injection. *Chinese Journal of Aeronautics*, 21(5), 393–401. doi: 10.1016/s1000-9361(08)60051-5

[8] Liu, C.L., Zhu, H.R., Bai, J.T., & Xu, D.C. (2011). Film cooling performance of converging-slot holes with different exit-entry area ratios. *Journal of Turbomachinery*, 133(1), 1–11. doi: 10.1115/1.4000543

[9] Zaman, K.B.M.Q., Rigby, D.L., & Heidmann, J.D. (2010). Experimental study of an inclined jet-in-cross-flow interacting with a vortex generator. *48th AIAA Aerospace Sciences Meeting Including the New Horizons Forum and Aerospace Exposition*, 4–7 January, Orlando, USA. doi: 10.2514/6.2010-88

[10] Ben Ali Kouchih, F., Boualem, K., & Azzi, A. (2021). Effect of backward injection with combined hole on film cooling performance. *Journal of Mechanical Engineering and Sciences*, 15(3), 8418–8427. doi: 10.15282/jmes.15.3.2021.18.0662

[11] Boualem, K., & Azzi, A. (2020). Blowing Ratio Effect on Film Cooling Performance for a Row Holes Installed in Different Trench Configurations. *Diffusion Foundations*, 28, 65−75. doi: 10.4028/www.scientific.net/DF.28.65

[12] Boualem, K., Bordjane, M., Bourdim, M., Grine, M., Ben Ali Kouchin, F., & Azzi, A. (2023). Numerical investigation of V-shaped trench on film cooling performance. *Thermophysics and Aeromechanics*, 30 (2), 305−315. doi: 10.1134/S0869864323020117

[13] Na, S. & Shih, T.I.-P. (2006). Increasing Adiabatic Film-Cooling Effectiveness by Using an Upstream Ramp. *Heat Transfer, Parts A and B*, 3, 931–938. *ASME Turbo Expo 2006: Power for Land, Sea, and Air*. 8−11 May, Barcelona, Spain. doi: 10.1115/GT2006-91163.

[14] Shinn, A.F., & Pratap Vanka, S. (2013). Large Eddy Simulations of Film-Cooling Flows With a Micro-Ramp Vortex Generator. *Journal of Turbomachinery*, 135(1). doi: 10.1115/1.4006329

[15] An, B., Liu, J., Zhang, C., & Zhou, S. (2013). Film Cooling of Cylindrical Hole With a Downstream Short Crescent-Shaped Block. *Journal of Heat Transfer*, 135(3). doi: 10.1115/1.4007879

[16] Zhou, W., & Hu, H. (2016). Improvements of film cooling effectiveness by using Barchan dune shaped ramps. *International Journal of Heat and Mass Transfer*, 103, 443–456, 2016, doi: 10.1016/j.ijheatmasstransfer.2016.07.066

[17] Zhou, W., & Hu, H. (2017). A novel sand-dune-inspired design for improved film cooling performance. *International Journal of Heat and Mass Transfer*, 110, 908–920. doi: 10.1016/j.ijheatmasstransfer.2017.03.091

[18] Grine, M., Boualem, K., Dellil, A.Z., & Azzi, A. (2020). Improving adiabatic film-cooling effectiveness spanwise and lateral directions by combining BDSR and anti-vortex designs. *Thermophysics and Aeromechanics*, 27(5), 749−758. doi: 10.1134/S0869864320050091

[19] Ben Ali Kouchih, F., Boualem, K., Grine, M., & Azzi, A. (2022). The Effect of an Upstream Ramp On Forward and Backward Injection Hole Film Cooling. *Journal of Heat Transfer*, 142(12). doi: 10.1115/1.4047643

[20] Sinha, A.K., Bogard, D.G., & Crawford, M.E. (1991). Film cooling effectiveness downstream of a single row of holes with variable density ratio. *Journal of Turbomachinery*, 113(3), 442–449. doi: 10.1115/1.2927894

[21] Silieti, M., Divo, E.B., & Kassab, A.J. (2009). The effect of conjugate heat transfer on film cooling effectiveness. *Numerical Heat Transfer, Part B: Fundamentals: An International Journal of Computation and Methodology*, 56(5), 335–350. doi: 10.1080/10407790903508046

[22] El Ayoubi, C., Ghaly, W., & Hassan, I. (2015). Aerothermal shape optimization for a double row of discrete film cooling holes on the suction surface of a turbine vane. *Engineering Optimization*, 47(10), 1384–1404. doi: 10.1080/0305215X.2014.969725

[23] Mayhew, J.E., Baughn, J.W., & Byerley, A.R. (2002). The effect of freestream turbulence on film cooling heat transfer coefficient. Paper GT2002-30173, *ASME Turbo Expo 2002: Power for Land, Sea, and Air*, 3-6 June, Amsterdam, The Netherlands. doi.org/10.1115/GT2002-30173

Co-published by
Institute of Fluid-Flow Machinery
Polish Academy of Sciences
Committee on Thermodynamics and Combustion
Polish Academy of Sciences

http://www.imp.gda.pl/archives-of-thermodynamics/

Coal-to-nuclear modernization of an existing power plant with a IV-th generation nuclear reactor

Wojciech Kosman*, Henryk Łukowicz, Łukasz Bartela,
Dorota Homa, Jakub Ochmann

Silesian Univeristy of Technology, ul. Konarskiego 18, Gliwice 44-100, Poland
*Corresponding author email: wojciech.kosman@polsl.pl

Received: 31.05.2024; revised: 23.10.2024; accepted: 15.11.2024

Abstract

The paper presents an analysis of a transition from a coal-fired power plant to a nuclear unit. The main focus is set on the extensive usage of the existing parts of the already operating system. The key problem is the correct matching of a nuclear reactor and the steam island. It is assumed here that the reactor module operates under nominal conditions and the steam turbine is adapted to fit the reactor. The paper describes the numerical model of the steam turbine cycle for the off-design simulations. The developed model allows us to determine the changes in the steam cycle in order to match the required water and steam temperature values at the inlets and the outlets of the steam generator. The paper presents the suggested modifications and the evaluation of the operation after the transition.

Keywords: Decarbonization; Nuclear reactor; Steam turbine

Vol. 45(2024), No. 4, 205–213; doi: 10.24425/ather.2024.152010

Cite this manuscript as: Kosman, W., Łukowicz, H., Bartela, Ł., Homa, D., & Ochmann, J. (2024). Coal-to-nuclear modernization of an existing power plant with a IV-th generation nuclear reactor. *Archives of Thermodynamics*, 45(4), 205–213.

1. Introduction

One of the possibilities to decarbonize the energy sector is a transformation from coal-fired power generating units to nuclear energy sources. This pathway has become more recognized in the recent years – a number of publications deal with the modern problems of nuclear power plants. In [1], the Authors presented research on the parameters of the live steam in a cycle with a steam generator and a nuclear reactor. Cogeneration systems with nuclear reactors are under investigation in [2]. Transient thermal loading problems are the subject of the study in [3].

However, the publications mentioned above deal with nuclear reactors that are capable of delivering the steam at temperatures significantly lower than in fossil-fuelled power plants – in the range of 280–320 degrees of Celsius.

Also, the steam turbine cycles presented in these publications are closely integrated with the reactor module. It means that a nuclear power plant of this type must be built from the ground as a complete cycle including the steam turbine and the reactor core [4]. This feature is a handicap when considering a smooth transition from a coal-fired energy system to the one with low emissions. When it comes to repowering the existing power plants, only some of their infrastructure may be used: the water cooling systems, the power output systems and the connections to the energy grid [5].

Much more options are available with the so-called IV-th generation reactors [6]. In this case, a reactor core and a steam

Nomenclature

c_f – constant in the pressure-flow relation, kg/s/MPa
i – enthalpy, kJ/kg
N – electric power, MW
p – pressure, MPa
Q – heat delivered to the steam/water system, MW
T – temperature, °C

Greek symbols

η – efficiency, %

Subscripts and Superscripts

cond – condensate
el – electric, refers to generator power
fw – feed water
in – inlet
live – live steam, HP turbine inlet
N – nominal
out – outlet
reheat– reheat steam, IP turbine inlet
s – isentropic
sat – saturation conditions

Abbreviations and Acronyms

COND– condenser
DAE – deaerator
FW – feed water
FWT – feed water tank
HP – high pressure, HP turbine inlet
IP – intermediate pressure, IP turbine inlet
LP – low pressure
SE – steam expander
SR – steam pressure and temperature reducing station
XC – condensate heater
XR – additional feed water heater
XSP – steam cooler

generator may be delivered as separate enclosed modules to any site and connected to a steam cycle. A strategy that is proposed for energy systems with a significant number of fossil-fuelled power generating units is based on retrofits of the existing steam cycles [7]. Coal steam boilers may be replaced with nuclear reactors and steam generators [8].

A new generation of nuclear reactors allows for generation of steam at a high temperature [9]. The IV-th generation reactors are still in development with some of them being already at the testing stage [10] and others at the concept stage [11]. Yet the transition of the steam temperature from a typical level of around 300°C to over 500°C opens new alternatives for the implementation of the reactors in the existing power generating systems [12]. Nuclear reactors may deliver the steam at a temperature level similar to fossil-fuelled boilers [13]. It means that a steam island with a power generator may remain intact. This approach may greatly improve the economic side of decarbonisation [14] and fasten the process of the transition towards low-emission power generation [15]. The economic projections are promising according to [16]. Increasing the number of nuclear power plants will also enable us to stabilize the energy grid and allow for further development of renewable energy sources, which is emphasized by a number of researchers, for example in [17] and [18]. The carbon-fuelled plants must be carefully selected for the coal-to-nuclear transition [19]. An example of the analysis to choose the optimal plant is described in [20].

The research presented in this paper aims to evaluate the possibility of matching an existing steam cycle to a high temperature reactor. The evaluation is conducted through numerical modelling and simulations of the steam cycle before and after the boiler is replaced with a nuclear reactor. An existing power plant is chosen for the evaluation with a 900 MW power generating unit. In order to properly simulate the operation of the steam turbine and the auxiliary systems, a model is built based on the available results of measurements taken during the tests of the unit.

The key problem is the matching of the steam and feed water parameters between the implemented reactor module and the existing turbine. The main assumption is that all the necessary modifications are made in the steam system, while the reactor module – including the nuclear core and the steam generator – operates at its design conditions.

The following sections describe the methodology of the research and the results of the modelling obtained for a tested reactor. This paper discusses the technical aspects only and verifies whether and how it is possible to connect a nuclear reactor to a steam island. This work is a foundation for further economic study.

2. Methodology

The following assumptions are made for the modelling and the evaluation of the cooperation between an existing steam cycle and a nuclear reactor:

- The key parameters are values of the pressure and temperature of the live steam, reheat steam and feed water;
- After the modernization and under operation at the full load, the nuclear reactor module operates in its design conditions meaning that the aforementioned values of the pressure and temperature at the inlets and outlets of the steam generator are kept equal to their design values;
- All the adjustments are made to the steam cycle, while the reactor core and steam generator operate at their design conditions. Hence, the steam cycle operates at off-design conditions even at the full load regime;
- The adjustments may include additional heat exchangers added to the cycle and rerouting of the pipelines;
- The modifications must not increase the live and reheat steam temperature above the design levels for the turbine.

The research is conducted using numerical simulations. The model of the steam cycle includes its main machines and auxiliary systems: turbines, heat recovery exchangers, pumps and a condenser. The model is built using a source code developed

in the Department of Power Engineering and Turbomachinery at the Silesian University of Technology. It was verified against measurement data obtained from the existing power plants in previous works and projects, for example [21] and [22]. The source code allows us to analyse the thermodynamic processes that occur in power generating units.

The model is adjusted to fit the measurement data from a particular power plant. The algorithm for the data processing is shown in Fig. 1. The first stage is the preparation of the input data, mostly the structure of the cycle. The model is built by adding machines and devices that constitute the steam cycle.

At this stage, measurements are also chosen for the input data. The preferred set of measurements comes from the performance tests of a cycle, which are conducted before a new power generating unit is commissioned or after every major repair. This type of measurements is performed at several levels of load with the unit not being controlled by the power demand from the grid. These measurements are preferred because they are preceded by periods of operation at a constant load, which guarantees stable conditions. In case such measurements are not available, one should use the measurements from a period of stable load during a standard operation.

Once the input data including the measurements and the cycle structure are set, the numerical model is applied to determine the values that describe the health state (the technical state) of the machines and devices in the thermodynamic cycle. The type of these values depends on the particular machine or device under the analysis. For example, a steam turbine is divided into groups of expander stages. Each group includes stages either between two consecutive steam extractions or between a turbine inlet or outlet and an extraction. Two parameters describe the health state of a group of expander stages. The first one is the isentropic efficiency of expansion defined as:

$$\eta_i = \frac{i_{in} - i_{out}}{i_{in} - i_{s,out}} \tag{1}$$

with the subscripts referring to the cross-sections of the steam path at the inlet and outlet of a group of expander stages. See also the nomenclature section of the paper.

The second parameter for the groups of turbine stages is the constant defined as:

$$c_f = \frac{m_N}{\sqrt{p_{N,in}^2 - p_{N,out}^2}} \tag{2}$$

from the pressure-mass flow relation:

$$m = c_f \sqrt{p_{in}^2 - p_{out}^2}. \tag{3}$$

The simplified Fluegel-Stodola equation is applied here. Since the flow is measured in chosen locations of a steam cycle only, a model of the whole cycle is required in order to obtain the flow through each group of the expander stages and to calculate the constants defined in Eq. (2).

The isentropic efficiency may be calculated directly for the groups of stages in the high-pressure and intermediate-pressure sections of a turbine for the pressure and temperature values measured at the inlets, outlets and at steam extractions. The calculations of the isentropic efficiency in the low-pressure sections are conducted using the following approach. One value of the efficiency is assumed for all the expansion stages, where the flowing fluid is wet steam. Then, the model of the whole steam island is applied to determine the efficiency using, among others, the measured electric power as the input data. This approach requires the equations that describe the following aspects of the operation:

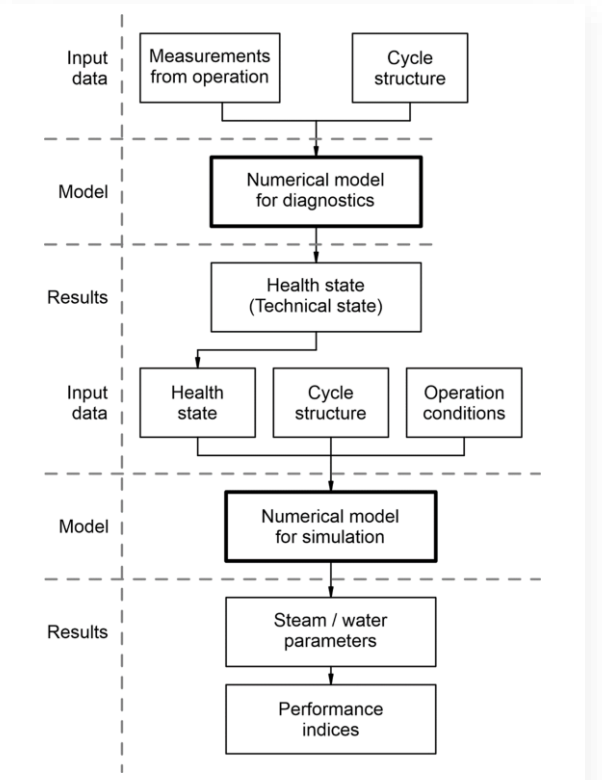

Fig. 1. Data processing to establish the numerical model of the steam cycle.

- mass and energy balances for turbine sections,
- mass and energy balances for heat recovery exchangers and deaerator,
- mass and energy balances for the condenser including the cooling water flow,
- pressure losses in pipelines,
- balance of the power output from turbine sections delivered to the power generator, including mechanical losses.

For the heat recovery exchangers, the values of the temperature differences are used as health state indicators. They are shown in Fig. 2. The differences are taken between the saturation temperature for the pressure in a heat exchanger and the outlet temperature values for cold and hot streams:

$$\Delta T_{fw} = T_{fw,out} - T_{sat}, \tag{4}$$

$$\Delta T_{cond} = T_{cond,out} - T_{sat}. \tag{5}$$

The resulting values may be positive or negative and reflect the ability of the exchanger to deliver the heat from the steam to the feed water. The health state indicators are established as functions of the load represented by the flow through the analysed machines and devices.

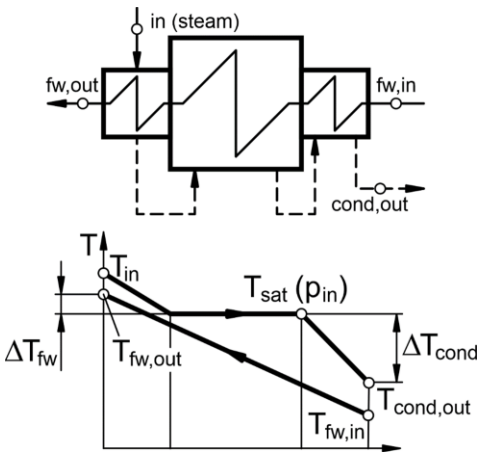

Fig. 2. Temperature differences in a heat exchanger.

Once the set of the health state indicators is obtained, the numerical model may be applied to the simulations of the off-design operation of a steam cycle. A new structure of the cycle is then established to reflect the proposed modifications required to match the reactor and the existing steam island. The operating conditions to be tested in the simulations are expressed in a set of values including:

- live steam pressure and temperature,
- reheat steam temperature
- cooling water temperature for the condenser,
- feed water temperature.

The simulation model determines the parameters of the working fluids in the main locations of the thermodynamic cycle. Then, it calculates performance indices, which include:

- power output N_{el},
- power required to drive the condensate pumps N_{cond} and the feed water pumps N_{fw},
- heat delivered to the steam/water in the steam generator Q,
- cycle efficiency η.

The cycle efficiency is used in the research presented here to compare different modernization options. It does not include the reactor efficiency since different reactor modules may be applied. This efficiency is defined as:

$$\eta = \frac{N_{el} - N_{fw} - N_{cond}}{Q}. \quad (1)$$

The proposed modifications to the steam cycle are verified against a range of values that affect the operation of the turbine and the auxiliary systems. The details of the modifications are described in the further sections of the paper.

3. Steam island

The arrangement of the steam cycle under investigation is shown in Fig. 3. It is a condensing steam turbine with high pressure, intermediate pressure and three low pressure turbine parts. Except for the high pressure turbine, all the parts are double opposed flow expanders.

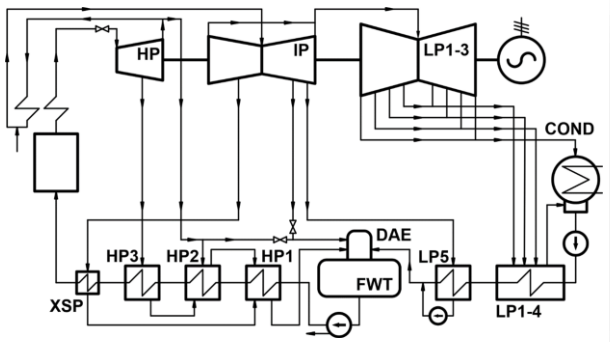

Fig. 3. Steam turbine cycle.

The heat recovery system consists of five main low pressure and three high pressure heat exchangers. There are additional exchangers located in both sections including a steam cooler / feed water heater fed from the intermediate part of the turbine. This is the last heat exchanger on the feed water path and its performance affects the final feed water temperature. The high and low pressure sections of the heat recovery system are separated by the deaerator and the feed water tank. The feed water pumping system consists of six pumps in a serial and parallel arrangement 3 by 2, but are shown for simplicity as a single pump in Fig. 3. The minimal permissible load is 40 per cent of the nominal load. Table 1 presents values of the main parameters that describe the operation of the turbine.

Table 1. Steam turbine design data.

Parameters	Symbol	Unit	Value
Electric power	N_{el}	MW	900
Live steam pressure	p_{HP}	MPa	25
Live steam temperature	T_{HP}	°C	600
Live steam flow	m_{HP}	t/h	2380
Reheat steam temperature	T_{IP}	°C	600
Steam to air heaters	-	t/h	40
Cycle efficiency	?	%	48.9

The health state analysis of the investigated steam island according to the methodology explained in Section 2 allowed us to obtain the values that may be applied in the off-design model of the turbine. The available measurement included five sets of data for five levels of the load.

The results of the simulations for the existing power plant are shown in Figs. 4–6. Figure 4 presents isentropic efficiencies for two chosen groups of turbine stages: an intermediate pressure one and a low pressure one. The efficiencies are shown as functions of the steam flow in these groups of stages and the range of curves in the horizontal direction reflects the range of flow in the turbine sections.

Figure 5 presents characteristic temperature differences for the second high pressure heat exchanger marked as HP2 in Fig. 3.

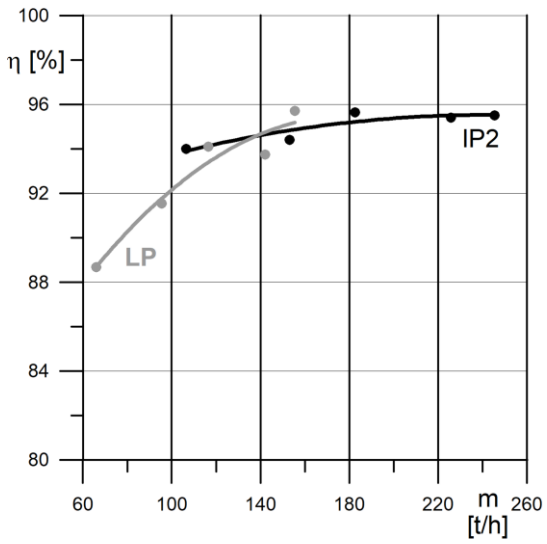

Fig. 4. Calculated isentropic efficiency of IP and LP groups of turbine stages.

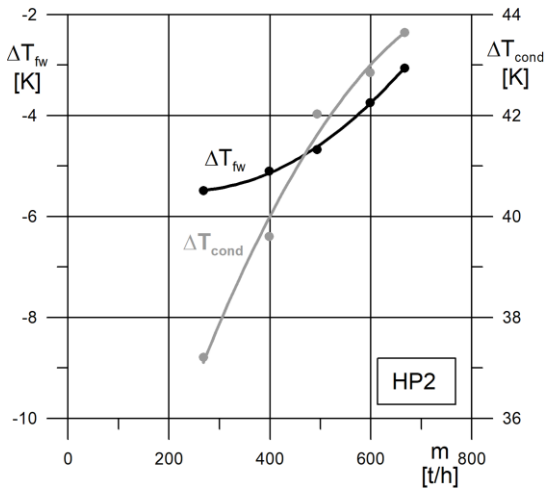

Fig. 5. Calculated temperature differences between saturation temperature in the HP2 heat exchanger and the feed water and condensate temperature.

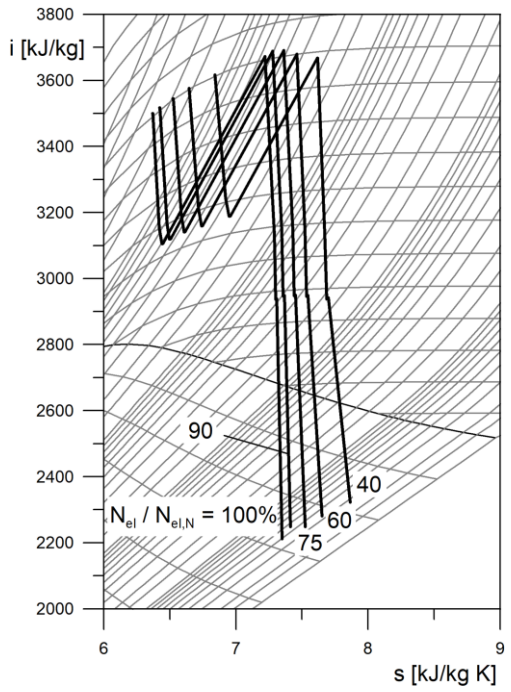

Fig. 6. Expansion lines for five different loads in the enthalpy-entropy diagram.

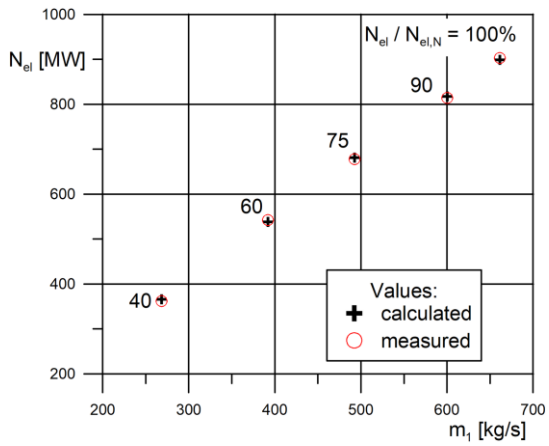

Fig. 7. Comparison between values of electric power – measured and calculated in the numerical model.

The results of the simulation are shown in Fig. 6 in the form of the expansion lines of the steam. They are drawn in the enthalpy-entropy diagram. The expansion lines show the thermodynamic processes that occur in the turbines and in the reheater. Five lines refer to the five levels of load, for which the measurements were available.

The performance of the model with the steam island health state determined according to the described methodology may be verified against the measurement of the power output. The power output is calculated in the model and it depends on the performance of all the machines and auxiliary systems implemented in the model. Thus, the difference between the calculated and the measured values of the electric power indicates the quality of the numerical model. This comparison is shown in Fig. 7.

The obtained results indicate a very good quality of the numerical module. The differences between the calculated and the measured values are less than 0.5% for loads higher than 60% of the nominal load and less than 1.1 per cent for loads less than 60% of the nominal load. This is satisfactory since the modified steam cycle with a nuclear reactor is expected to operate under regimes close to the full load.

4. Steam island modifications

There are two problems to solve when connecting a nuclear reactor with a steam generator to an existing steam cycle: matching the parameters of the live/reheat steam and matching the parameters of the feed water.

Regarding the steam parameters, the following case is under investigation in this research: the steam temperature and pressure at the outlet of the steam generator are equal to or lower than the design values for the turbine. If the steam entering the turbine has parameters lower than the design values, then the turbine operates in off-design conditions. An important issue is the temperature of the reheat steam. Values lower than the design ones result in the possibility that the expansion in the low pressure turbine ends in the area of enthalpy-entropy diagram, where steam quality is lower than in design conditions. This would cause more intensive corrosion and faster component wear in the low pressure turbine.

The simulations performed within the research presented here proved that for the turbine described in Section 3 the quality of the steam was lower by no more than 2 percentage points when compared to the conditions corresponding to the same live steam pressure (the same live steam flow) for the design conditions. In some cases, the quality was even higher. The conclusion is that for the investigated turbine the decrease of the reheat steam temperature did not result in hazardous corrosion wear.

Regarding the feed water temperature, two cases are possible: the required temperature of the water entering the steam generator may be lower or higher than the feed water temperature at the outlet of the last recovery heat exchanger in the steam cycle. A simpler case is the first one when the feed water temperature must be lowered before entering the steam generator. The water may be cooled by a flow that bypasses the high pressure regeneration system. This is shown in Fig. 8.

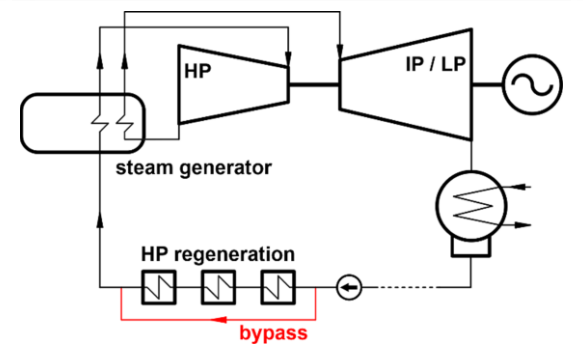

Fig. 8. Feed water cooled by a by-pass flow to match the required temperature for a steam generator.

The bypass water is extracted from the outlet of the feed water pump. The flow rate of the bypass stream must be chosen according to the temperature and the flow in the current conditions of the operation and should be added to the control system of the steam cycle. Since high pressure recovery heat exchangers typically have bypass pipes this modernization does not add to the investment costs, when implementing a nuclear reactor.

In the opposite case, when the temperature of the feed water is lower than required by a steam generator, an additional heat exchanger is necessary. Since the assumption in Section 2 is that the modifications are made on the steam cycle side, the additional exchanger must be fed with the additional steam. A suggested design is shown in Fig. 9.

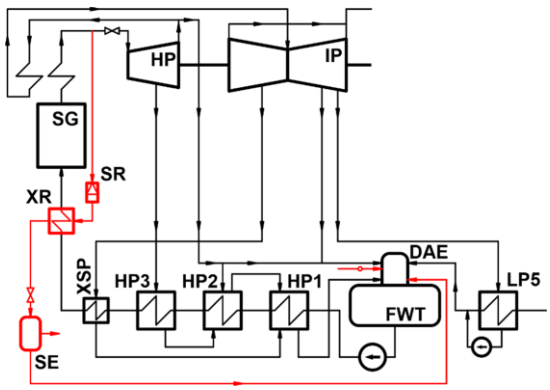

Fig. 9. Design with an additional feed water heater XR.

The additional heat exchanger XR is located upstream of the high pressure heat recovery system. The steam that feeds this exchanger is taken from the live steam pipeline. It is throttled in the station SR to the pressure value that corresponds to the saturation temperature that is higher by ΔT than the required water inlet temperature to the steam generator. The basic (reference) value of the temperature difference ΔT is 10 degrees Kelvin, although it may be optimized. For example, the steam generator inlet temperature of 300°C requires the saturation temperature in the additional heat exchanger equal to 310°C and it corresponds to the pressure of 9.867 MPa.

The steam is saturated in the expander delivering the heat to the feed water. The flow rate of the additional steam must be adjusted according to the flow of the feed water. This must be added to the control system of the power generating unit.

The condensate from the additional heat exchanger is still at a high pressure. For this reason, it flows into an expander SE. The pressure there is reduced to a level that is equal to the pressure in the deaerator. The steam and water fractions are delivered to the deaerator through separate pipelines.

It should be noted that in the presented modified arrangement of the steam cycle, the steam flow rate through the generator is higher when compared to the flow through the boiler in the original cycle for the same amount of steam entering the turbine. This is due to the additional flow of the steam that heats the feed water. This flow also goes through the high pressure heat recovery exchangers causing them to operate in off-design conditions.

5. Modified power plant

The results of the numerical simulations are presented for a fluoride salt-cooled high-temperature reactor module [23]. It is shown in Fig. 10 as already connected to a steam turbine. There is an inner loop of salt that flows through the reactor core. The heat delivered in the core is rejected in the intermediate heat exchangers and delivered to the outer loop of molten salt. The second loop feeds the steam generator.

The design data important to the research presented here are gathered in Table 2 and refer to the water/steam parameters only. Since the reactor is assumed to operate at its design conditions, the parameters in the core and the intermediate system are not

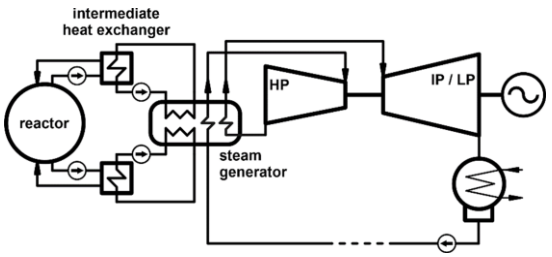

Fig. 10. Fluoride salt-cooled high-temperature reactor and steam turbine.

important to the analysis. The thermal power output of the nuclear module is much lower than the amount of heat required to generate steam for the turbine. For this reason, it is assumed that the module includes a number of reactors stacked in packages.

Table 2. Parameters of the fluoride salt-cooled high-temperature reactor.

Parameters	Symbol	Unit	Value
Live steam pressure	p_{HP}	MPa	19
Live / reheat steam temperature	T_{HP}, T_{IP}	°C	585
Feed water temperature	T_{FW}	°C	300
Power output	Q_{SG}	MW	140

The removal of the fossil-fuelled steam boiler and the addition of the nuclear reactor leads to the two main modifications listed below:

- There are no steam extractions to air heaters. In the original system, steam was taken from the extractions in the intermediate part of the turbine to heat the air flowing into the boiler. There is no need for that once the boiler is removed;
- There are no water injections to the live and reheat steam. This assumption is made to compare the operation of the cycle before and after the modifications. The water for the injections is taken from the feed water pumps outlets. It is used to maintain the temperature of the steam at desired levels. A perfect operation does not require any injections at all because the appropriate temperature levels are provided by the heat source, whether it is a fossil steam boiler or a nuclear module.

Table 3 compares the gross power output generated by the steam cycle under different conditions. The cases analyzed are as follows (with the symbols according to Table 3):

- 600/600/25 boiler – steam cycle before the modification, design steam temperature,
- 585/585/25 boiler – steam cycle before the modification, steam temperature lowered to the maximal permissible value for the steam generator,
- 585/585/19 boiler – steam cycle before the modification, steam temperature and pressure lowered to the maximal permissible values for the steam generator,
- 585/585/25 reactor – steam cycle with the reactor, steam temperature lowered to the maximal permissible value for the steam generator,
- 585/585/19 reactor – steam cycle with the reactor, steam temperature and pressure lowered to the maximal permissible values for the steam generator.

The temperature of the cooling water for the condenser is adjusted to be constant across the simulations. As mentioned above there are no water injections to the live and reheat steam. Yet the results for the steam cycle with fossil-fuelled boiler are shown with the steam extractions for the heating of the air flowing into the boiler. This is because the reference point is the original cycle with the extractions.

Table 3. Gross power output for the modified steam cycle.

p_{HP} [MPa]	T_{HP} [°C] / T_{IP} [°C] / p_{HP} [MPa] / boiler or reactor				
	600/600 25 boiler	585/585 25 boiler	585/585 19 boiler	585/585 25 reactor	585/585 19 reactor
25	900.56	880.79	-	883.23	-
19	665.61	651.65	651.65	658.92	658.92

The 19 MPa pressure level is the maximal specified for the steam generator delivered with the nuclear reactor mentioned at the beginning of this section. However, this level is too low for supercritical steam turbines, for which the live steam pressure should be above the critical value of 22 MPa for the full load operation. It is expected that the final permissible pressure for the steam generator will be higher because the steam temperature level is suitable for supercritical steam turbines. Also, a higher steam pressure requires modifications in the steam generator only and not in the nuclear reactor. For this reason, the matching between the reactor module and the steam turbine is analyzed here for the total range of pressure for the steam turbine that is up to 25 MPa.

The values of the cycle efficiency obtained from the numerical simulations are shown in Fig. 11. The presented cases are the same as in Table 3. The dashed parts of the curves for the modified turbine cycle refer to the range of pressure that may be applied to the currently available steam generator that is up to the limit of 19 MPa. The rest of the curves drawn with solid lines refer to the steam generators able to withstand higher pressure – here up to 25 MPa.

The efficiency is lower for lower steam temperatures, which results from the thermodynamic principles of power plant cycles. It is further lowered for the cycle cooperating with the nuclear reactor because an additional steam flow is used to heat the feed water and that flow also goes through the steam generator. In each point for each curve in the presented graph, the steam cycle operates in off-design conditions.

Figure 12 presents the heat transfer conditions in the additional heat exchanger XR. Firstly, the steam flow is shown that is required to increase the feed water temperature to the level appropriate for the steam generator – here it is 300°C, see Ta-

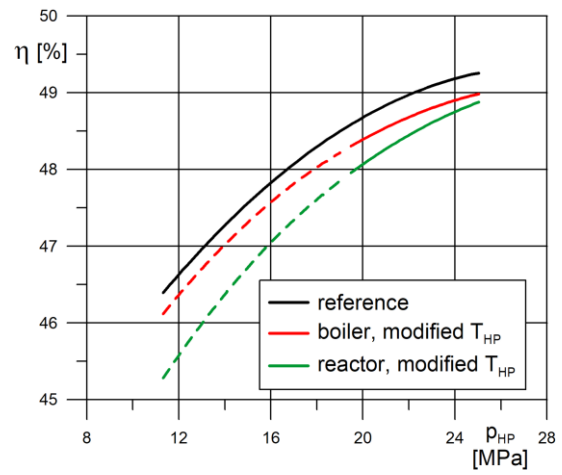

Fig. 11. Cycle efficiency for the modified steam cycle.

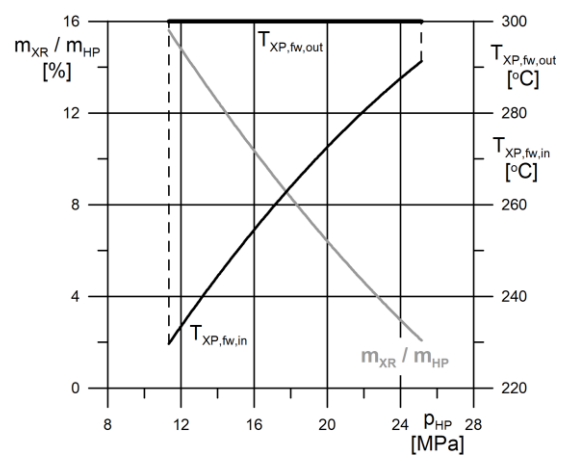

Fig. 12. Relative steam flow to the XR heat exchanger and temperature at the exchanger inlet and outlet.

ble 2. Secondly, Fig. 12 shows the temperature of the feed water at the inlet and outlet of the exchanger.

The steam flow is presented as a value relative to the live steam flow to the HP turbine section. This relative steam flow becomes higher for a lower load represented by the live steam pressure. This is because the temperature of the feed water entering the XR exchanger becomes lower for a lower load and more portions of steam are needed to increase its temperature. These heat exchange conditions are reflected in the values of the cycle efficiency in Fig. 11.

6. Conclusions

The results of numerical simulations show that the coupling of a nuclear reactor with a steam generator to an existing steam island is technically possible. The required modifications are done on the steam/water side only. The investments include new heat exchangers, steam expander, valves and piping.

The efficiency for the steam cycle analysed here is lower than for the unmodified cycle. This is because the steam generator described here required a lower steam temperature. A dedicated steam generator with a higher allowable pressure level should be designed and applied to a specific existing cycle converted from carbon to nuclear. Nevertheless, the cooperation is possible between any high pressure reactor module and an already operating steam cycle.

The pressure restriction for the steam generator described in Section 5 is expected to be neglected in the future. It is irrational to manufacture high temperature reactors with a low steam pressure because the potential of supercritical steam turbines would not be used.

Acknowledgements

This paper was created as a result of the project: “Plan of decarbonization of the domestic power industry through modernization with the use of nuclear reactors”, financed by the National Centre for Research and Development under the Programme “Social and economic development of Poland in conditions of globalizing markets” GOSPOSTRATEG (Contract No. Gospostrateg VI/0032/2021-00 dated March 15, 2022).

References

[1] Laskowski, L., Smyk, A., Jurkowski, R., Ance, J., Wołowicz, M., & Uzunow, N. (2022). Selected aspects of the choice of live steam pressure in PWR nuclear power plant. *Archives of Thermodynamics*, 43(3), 85–109. doi: 10.24425/ather.2022. 143173

[2] Jędrzejewski, J., & Hanuszkiewicz-Drapała, M. (2021). Utilization of organic Rankine cycles in a cogeneration system with a high-temperature gas-cooled nuclear reactor – thermodynamic analysis. *Archives of Thermodynamics*, 42(2), 71–87. doi: 10.24425/ather.2021.137554

[3] Banaszkiewicz, M., & Skwarło, M. (2023). Numerical investigations of transient thermal loading of steam turbines for SMR plants. *Archives of Thermodynamics*, 44(4), 197–220. doi: 10.24425/ather.2023.149715

[4] Qvist, S, Gładysz, P., Bartela, Ł., & Sowiżdżał, A. (2021). Retrofit decarbonization of coal power plants - a case study for Poland. *Energies*, 14(1), 120. doi: 10.3390/en14010120

[5] Hansen, J., Jenson, W., Wrobel, A., Stauff, N., Biegel, K., Kim, T., Belles, R., & Omitaomu, F. (2022). Investigating Benefits and Challenges of Converting Retiring Coal Plants into Nuclear Plants. Nuclear Fuel Cycle and Supply Chain. *U.S. Department of Energy Report*, 13 September, INL/RPT-22-67964.

[6] Shultis, J. K., & Faw, R. E. (2017). *Nuclear Science and Engineering. 3rd edition.* CRC Press, Taylor & Francis Group.

[7] Haneklaus, N., Qvist, S., Gładysz, P., & Bartela, Ł. (2023). Why coal-fired power plants should get nuclear-ready. *Energy*, 280, 128169. doi: 10.1016/j.energy.2023.128169

[8] Xu, S., Lu, Y.H.M., Mutailipu, M., Yan, K., Zhang, Y., & Qvist, S. (2022). Repowering Coal Power in China by Nuclear Energy – Implementation Strategy and Potential. *Energies*, 15(3), 1072. doi: 10.3390/en15031072

[9] Bartela, Ł., Gładysz, P., Ochmann, J., Qvist, S., & Sancho, L.M. (2022). Repowering a Coal Power Unit with Small Modular Reactors and Thermal Energy Storage. *Energies*, 15(16), 5830. doi: 10.3390/en15165830

[10] International Atomic Energy Agency. (2020). *Advances in Small Modular Reactor Technology Development, Supplement to: IAEA Advanced Reactors Information System (ARIS), 2020 Edi-*

tion. https://aris.iaea.org/publications/smr_book_2020.pdf [accessed 28 Nov. 2024]

[11] Dąbrowski, M.P., Boettcher, A., Brudek, W., Malesa, J., Muszyński, D., Potempski, S., Skrzypek, E., Skrzypek, M., & Sierchuła, J. (2024). Concept of the Polish high temperature gas-cooled reactor HTGR-POLA. *Nuclear Engineering and Design*, 424, 113197, doi: 10.1016/j.nucengdes.2024.113197

[12] Weng, T., Zhang, G., Wang, H., Qi, M., Qvist, S., & Zhang, Y. (2024). The impact of coal to nuclear on regional energy system. *Energy*, 302, 131765. doi: 10.1016/j.energy.2024.131765

[13] Van Hee, N., Peremans, H., & Nimmegeers, P. (2024). Economic potential and barriers of small modular reactors in Europe. *Renewable and Sustainable Energy Reviews*, 203, 114743. doi: 10.1016/j.rser.2024.114743

[14] Mignacca, B., & Locatelli, G. (2020). Economics and finance of Small Modular Reactors: A systematic review and research agenda. Renew. Sustain. *Energy*, 118, 109519. doi: 10.1016/j.rser.2019.109519

[15] Ingersoll, E., Gogan, K., Herter, J., & Foss, A. (2020). The ETI Nuclear Cost Drivers Project Full Technical Report. *Energy Systems Catapult*, Birmingham, UK, 2020.

[16] Bartela, Ł., Gładysz, P., Andreades, C., Qvist, S., & Zdeb, J. (2021). Techno-Economic Assessment of Coal-Fired Power Unit Decarbonization Retrofit with KP-FHR Small Modular Reactors. *Energies*, 14(9), 2557. doi: 10.3390/en14092557

[17] Weng, T., Zhang, G., Wang, H., Qi, M., Qvist, S., & Zhang, Y. (2024). The impact of coal to nuclear on regional energy system. *Energy*, 302, 131765. doi: 10.1016/j.energy.2024.131765

[18] Marques, A.C., & Junqueira, T.M. (2022). European energy transition: Decomposing the performance of nuclear power. *Energy*, 245, 123244. doi: 10.1016/j.energy.2022.123244

[19] Khosravi, A., Olkkonen, V., Farsaei, A., & Syri, S. (2020). Replacing hard coal with wind and nuclear power in Finland - impacts on electricity and district heating markets. *Energy*, 203, 117884. doi: 10.1016/j.energy.2020.117884

[20] Abdussami, M. R., Daley, K., Hoelzle, G., & Verma, A. (2024). Investigation of potential sites for coal-to-nuclear energy transitions in the United States. *Energy Reports*, 11, 5383–5399. doi: 10.1016/j.egyr.2024.05.020

[21] Kosman, W. (2017). The influence of the measurement inaccuracies on the assessment of the health state of gas turbines in diagnostic systems. *Journal of Power Technologies*, 97(2), 142–148.

[22] Kosman, W., Rusin, A., & Reichel, P. (2023). Application of an energy storage system with molten salt to a steam turbine cycle to decrease the minimal acceptable load. *Energy*, 266, 126480. doi: 10.1016/j.energy.2022.126480

[23] Blandford, E., Brumback, K., Fick, L., Gerardi, C., Haugh, B., Hillstrom, E., Johnson, K., Peterson, P.F., Rubio, F., Sarikurt, F.S., Sen, S., Zhao, H., & Zweibaumet, N. (2020). Kairos power thermal hydraulics research and development. *Nuclear Engineering and Design*, 364 (3), 110636. doi: 10.1016/j.nucengdes.2020.110636

Co-published by
Institute of Fluid-Flow Machinery
Polish Academy of Sciences
Committee on Thermodynamics and Combustion
Polish Academy of Sciences

http://www.imp.gda.pl/archives-of-thermodynamics/

ARCHIVES OF THERMODYNAMICS

Experimental investigation of inside zigzag pipe collector solar air heaters: energy and exergy analyses

Murat Kaya

Hitit University Mechanical Engineering, Çorum 1900, Turkey
Author email: mrtkaya@hotmail.com

Received: 06.09.2023; revised: 12.09.20243; accepted: 09.10.2024

Abstract

In this study, collectors with two different designs as solar air heaters were examined. Both collectors have equal dimensions and panels with the same features are placed inside. A zigzag strip is placed within the cavities of the collector I panel. The inside of the cavities of the collector II panel is left empty. The thermal efficiency of the panel was observed by providing air flow from the bottom of both collectors. A good design is essential for an efficient collector. As a result of the studies carried out, according to the second law of thermodynamics, the efficiency of collector I, which has a zigzag inside the panel, is between 20.2% and 38.8%, whereas the efficiency of collector II, which is hollow inside the panel, varies between 17% and 32.2%.

Keywords: Solar air heating; First law of thermodynamics; Second law of thermodynamics; Exergy; Collector efficiency

Vol. 45(2024), No. 4, 215–222; doi: 10.24425/ather.2024.152011

Cite this manuscript as: Kaya, M. (2024). Experimental investigation of inside zigzag pipe collector solar air heaters: energy and exergy analyses. *Archives of Thermodynamics*, 45(4), 215–222.

1. Introduction

Turkey obtains most of its fossil-based energy from foreign countries. A large amount of this energy is used for heating purposes in industry, workplaces and homes. Foreign dependency on energy use is quite high. However, in terms of renewable resources, it is in a position to benefit greatly from solar energy, especially in terms of its location in the world. In the drying of grain products, healthier and more efficient grain drying can be done by using solar energy instead of traditional methods. In this respect, it has a remarkable potential.

Solar energy is energy that has no fuel costs. Many studies have been carried out to benefit more from this energy. Many scientific studies have been conducted on collectors of different designs to determine the greater efficiency of such systems. In these works, the use of flat sheet panels is generally common. Different types of solar radiation air heat exchangers are produced by adding various geometrically shaped parts into these panels to increase the heat transfer rate. Solar air heated collectors have many advantages. Easy and clean energy can be obtained, there is no fuel cost, and it is easy to produce locally. Small volumes can be heated, and some leaf-type plants can be dried. For this reason, different designs have been developed recently to make collectors more efficient.

Abene et al. [1] designed two types of collectors for drying grapes. They placed various obstacle particles in rows within the collector panel and examined the increase in thermal efficiency. They compared collector WDL1 (waisted delta lengthways) and collector WO (without obstacles), which they designed. At a certain airflow rate, the thermal efficiency of the WDL1 col-

Nomenclature

A_{col} – absorber area of the collector, m^2
c_p – specific heat capacity at constant prerssure, kJ/(kg K)
$\dot{E}_x$ – dimensionless inlet exergy flow
$\dot{Q}$ – heat rate, kW
h – enthalpy, kJ/kg
I_T – solar radiation, W/m^2
$\dot{m}$ – fluid mass flow rate, kg/s
P – pressure, Pa
R – ideal gas constant, kJ/(kg K)
Re – Reynolds number
s – entropy, kJ/(kg K)
$\dot{S}$ – entropy production, kJ/(kg K s)
T – temperature, K

Greek symbols

α – absorption factor of the solar receiver
ε – specific exergy, kJ/kg
η – thermal efficiency
τ – effective transmission
ψ – exergy efficiency

Subscripts

air – air
col – collector
gen – generation
in – inlet
out – outlet
o – ambient
r – radiation

lector was 25% and 23%, respectively. In the WO heat collector, it was 29% and 24%.

Zima et al. [2] simulated the transient processes occurring in liquid flat-plate solar collector tubes using a one-dimensional mathematical model. Boundary conditions were assumed as time dependent. Differential equations were derived under boundary conditions and operating conditions, and the equations were solved using the finite difference method.

In the study of Krawczyk [3], sewage sludge from a wastewater treatment plant in Błonie near Warsaw was examined in 2012. This mud is dried with solar energy. Experimental evidence is presented in the study that there is a relationship between the cumulative drying potential of ventilation air and the condition of dried sludge. The amount of water evaporated from the dried sludge mass was determined. They determined the weight values in three groups based on the initial unitary mass. These values are between 5 and 8.3 kg/m^2 in group I, between 8.3 and 12.5 kg/m^2 in group II, and between 12.5 and 20 kg/m^2 in group III.

Khatri, R. et al. [4] in their experimental study, investigated the performance of a solar air heater with an absorber plate made of aluminium material with perforated cylindrical wing geometry. They applied the liquid at three different speeds. In measurements made on the wing-arched wavy absorber plate at a flow rate of 5 m/s, the best performance was measured in the temperature range of 55–70 °C.

Khawajah et al [5] studied 2-fin, 4-fin and 6-fin double-pass solar air heater. Instead of absorber plates, layers of wire mesh were placed between the wings. The mass flow rate was in the range of 0.0121–0.042 kg/s. The maximum efficiency was determined as 75.0%, 82.1% and 85.9%, respectively, for the 2, 4, 6 fin solar air heaters when the flow rate was 0.042 kg/s. The temperature difference ΔT was greater in the 6 fin solar air heater than in the 2 and 4 fin solar air heaters. The peak ΔT was 43.1 °C and 62.1 °C, respectively, when the mass flow rate was 0.0121 kg/s in a 6 fin solar air heater.

Sachın et al. [6] conducted solar air heater experiments on six different roughened surfaces. The air flow on rough surfaces – transverse, pit, side curved, spring, and sine wave surfaces was examined. Experiments were carried out in a wide range of Reynolds numbers (Re). They achieved the best result for a sine wave surface at Re = 15 000.

Petela [7] assumed that the energy of the atmosphere was infinite and its exergy was zero. Solar air heaters get their energy directly from the atmosphere. The exergy entering the air heaters is the exergy of E_x from solar radiation alone. Derivation procedures for three radiation categories are discussed in the study. A closed system, black flux and any arbitrary radiation flux were studied. Formulas have been created for the conversion of radiation into work or heat.

In the work of Sıvakumar et al. [8], the transformation, quality and irreversibility of the energy in the systems are determined more clearly by exergy analysis. By comparing the theoretical values of cumulative efficiency, energy efficiency and exergy efficiency, it was found that taking into account the heat capacities of the glass cover and panel gives a higher output in all thermal models.

Farahat et al. [9] determined the exergy efficiency by developing a mathematical model for linear parabolic solar collectors.

Çomakli et al. [10] conducted the experiment in February, March, April, May, June and July. They made a different plate design inside each of the four different collectors. The highest energy efficiency occurred when a distorted roughened surface was made between the absorber plate and the back plate.

Karsli [11] designed four different air-heated solar collectors. The experiments were carried out from March to July in Erzurum province in 2004. The first law efficiency varied between 26% and 80% for collector I, between 26% and 42% for collector II, between 70% and 60% for collector III, and between 26% and 64% for collector IV. The second law efficiency values varied between 0.27 and 0.64 for all collectors.

Altfeld et al. [12] studied how much the total surface area properties of the collectors affect the energy efficiency. It has been determined that the exergy efficiency is better when the collector surface is enlarged and the air flow is reduced.

Altfeld et al. [13] used different types of designed collectors in their studies. The collectors were examined for high heat and low friction losses. They determined the net input and output exergy values of solar collectors. They concluded that it is not appropriate to have a high density of rough surface fins attached to the panel surfaces inside the collector.

In their study, Gupta et al. [14] determined the exergy efficiency of solar air heater systems having various parameters such as the aspect ratio of the collector, the mass flow rate per unit area of the collector plate and the channel depth of the plate.

2. Experimental setup and measured values

In this study, two different collectors with solar air heating were designed and installed in the city of Çorum, Turkey – 39:14 North latitude; at 38:27 East longitude. The surface of the collectors is fixedly facing the sun at 12 o'clock. The collector surface was adjusted according to the azimuth angle of the sun.

The system was designed as composed of two different collectors. The collectors were manufactured from two metal sheets, on which half circle grooves were formed. Then, these metal sheets were placed upon each other in such a way that circle channels were formed. The diameter of each groove was 6 cm. In the first experiment, zigzag metal parts of 4 cm width were placed along the grooves of panel I. In this application, it was aimed to increase the contact of flowing air and the collector's inner surface in order to improve the heat transfer rate. In the second panel II, grooves were left empty for the flow experiment.

The frame of the collector from outside to outside measures 96 cm × 200 cm × 15 cm and is made of 2 cm thick wood. The glass surface area of the collector (A_{col}) is 0.92 m ×1.96 m = 1.8 m^2. The panels placed inside the collector are designed to measure 90 cm × 180 cm × 0.1 cm and be manufactured from a galvanized metal sheet. The surface area of the two panels is the same ($A_{p1} = A_{p2}$), and is equal to 0.9 m ×1.8 m = 1.62 m^2. Insulation of the panels was assured by installing 5 cm thick glass wool, which was placed between the bottom and side surfaces of the panel. The front surfaces of the panels were covered by glasses that have a thickness of 0.7 cm. As can be seen in Fig. 1, the inner and outer surfaces of the collectors were painted black. A hole of 10 cm diameter was drilled, in order to maintain inflow of the air outside. Then, in order to sustain equal distribution of air to the grooves of the panel, a part that is made of perforated sheet metal was fixed to the edges of groove entrances. The air outside was sucked into the collectors by a fan. The designed solar collector has a glass surface and a corrugated panel placed inside; the cross section profile is shown in Fig. 2. The flow rates of the air flowing through the collectors were equal. The temperature of inflowing air was that of the ambient

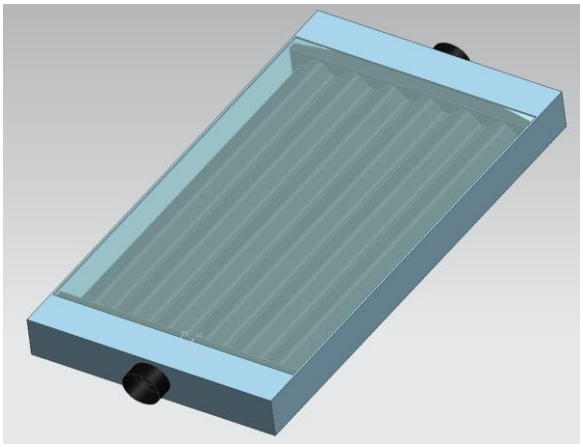

Fig. 1. The panel and collector with zigzags in the grooves.

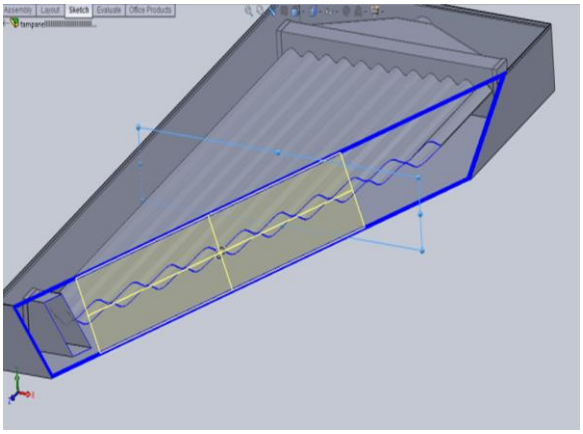

Fig. 2. Air heater heat exchanger cutaway profile.

temperature. The heating surface area (A_{col}) was 1.8 m^2. The collector was placed on a wheeled setup that was made of stainless profile steel. In addition, a special worm screw setup was placed behind the collector frame. According to the azimuth angle of the sun that changes daily and seasonally, the collectors were adjusted with the use of a worm screw for a better exposure angle and better absorption of sunlight. In the experimental study, the energy coming from the sun to the collector surface, the surface temperature, temperature and pressure values of the air entering and leaving the collector were measured.

In order to measure the required values in the experimental system, thermocouples were placed on the collector surface, at the air inlet and outlet points, and at ambient conditions. Thermocouple tips are well attached to the measuring surfaces. Experimental values were measured 30 min after the collector was exposed to the sun. Values were recorded every 30 min. The same time period of 8:30 and 17:00 daily was recorded.

The experimental setup consists of two different plates, as in Fig. 3. The inside of the first plate I is flat and the second plate II is zigzag. The designed solar collector is covered with a flat plate and glass, and the air passing through it is heated. A fan, air valve, pyrometer and multimeter were used to measure the required test results.

3. Energy and exergy analysis

Exergy analysis is a thermodynamic analysis technique based on the second law of thermodynamics. Exergy analysis helps improve and optimize designs and analyses. The authors of [15] stated it is the only analysis to compare systems with their actual values. They examined exergy on two features: (1) how close the actual performance is to the ideal one and (2) more precisely determine from energy analysis the types, causes and locations of thermodynamic losses.

Esen [16] performed the solar collector tests in two stages. In the first stage, he placed different geometrical blocks inside the collector. In the second stage, he presented an energy and exergy analysis in both cases without placing any geometrically shaped blocks. Air flow at different flow rates into the collector is made first over the panel and then under the panel. The author determined the optimum efficiency depending on the heat absorbency of the panels. Bejan [17] and Wark [18] stated that the

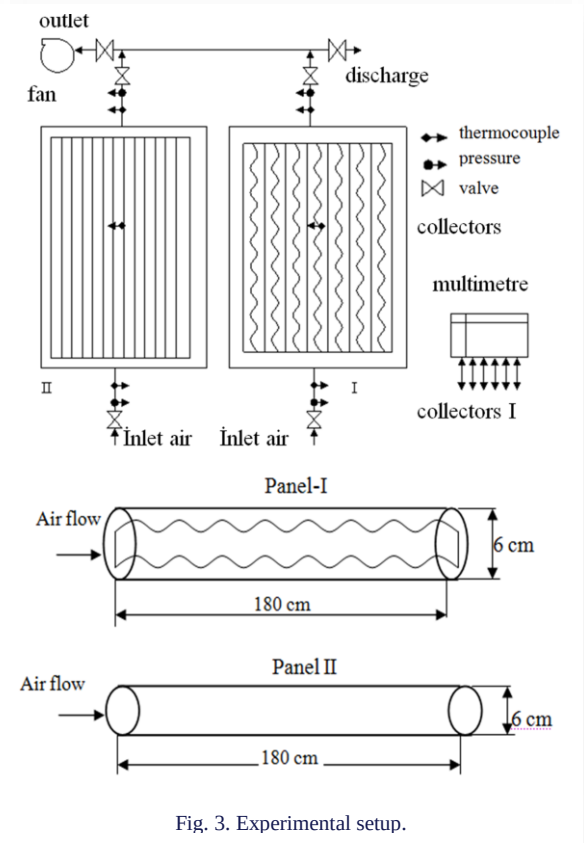

Fig. 3. Experimental setup.

efficiency of collector systems will be determined according to the second law of thermodynamics. They carried out the study firstly with an auxiliary substance method that increases fluid flow, and secondly with the heat transfer method.

In order to use the energies of the systems at the most efficient level, they must be determined clearly [19]. They argued that this could only be possible by applying exergy analysis to systems. The conversion, quality and irreversibility of energy in systems are determined more clearly by exergy analysis. They tested the performance by attaching fins to the plates to increase absorbency.

Table 1. Values adopted for the flat-plate solar collector.

Quantity	Value
Absorber material	Galvanized steel sheet
Absorber plate	0.92 m × 1.96 m
Thickness	0.001 m
Absorptance	0.9
Emittance	0.1
Absorber coating	Dull black paint
Absorptivity of the absorber	α = 0.65
Tube external diameter	0.06 m
Tube internal diameter	0.059 m
Reflectivity of the absorber	ρ = 0.16
Sealant	Silicon rubber
Back insulation	Glasswool (thickness 0.05 m)
Side insulation	Glasswool (thickness 0.025 m)
Effective product transmittance--absorptance	$\tau\alpha$ = 0.78
Panel heat transfer area	$A_{p1} = A_{p2}$ =1.62 m^2
Uncertainty in reading values of table	± 0.1%–0.2%

3.1. Energy analysis

The amount of energy coming to the collector surface due to solar radiation constitutes the thermal energy of the system. The equation that determines the solar energy coming to the solar air heater collector surface is

$$\dot{Q}_{sun} = I_T \tau\alpha A_{col}, \quad (1)$$

where A_{col} is the surface area of the collector corresponding to the sun radiation direction, $\tau\alpha$ gives the solar energy radiation value of the collector surface, A_{col} is the collector area, and $\dot{Q}_{sun}$ is the thermal energy from the sun absorbed depending on the collector surface permeability ability [11,16,20].

Exergy calculations of air entering and exiting the glass-covered solar collector at different flow rates have been made. The amount of useful energy gained by the air flow entering the collector is:

$$\dot{Q}_{air,col} = \dot{m}_{air} c_{p,air} \left(T_{air,out} - T_{air,in}\right). \quad (2)$$

The energy efficiency of the system, according to the first law of thermodynamics, is defined as the ratio of the thermal energy gained by the flow to the radiant energy coming from the sun to the collector surface:

$$\eta = \frac{\dot{m}_{air} c_{p,air} \left(T_{air,out} - T_{air,in}\right)}{I_T \tau\alpha A_{col}}. \quad (3)$$

3.2. Exergy analysis

In many energy systems, exergy analysis is applied to the systems to obtain accurate numerical values. An attempt was made to prove its usability by applying exergy analysis to the systems. It was found that high exergy losses could be reduced by designing efficient solar collectors [8,20–22].

Exergy analysis has been applied to accurately evaluate the thermal energy efficiency of different types of designed solar collector panels. It has been applied to all components of the collectors, including glass cover, sun ray angle, water flow rate and environmental conditions [23,24].

Exergy analysis more clearly determines the transformation, quality and irreversibility of the energy in the systems. However, some assumptions were made initially for solar collectors. The mass balance of solar collectors is:

$$\sum \dot{m}_{in} = \sum \dot{m}_{out}. \quad (4)$$

The exergy flow in the control region is given by Eq. (5):

$$\sum \dot{E}_{x,in} = \sum \dot{E}_{x,out}, \quad (5)$$

If there is exergy storage ($\dot{E}_{x,dest}$) in the control region, Eq. (6) is written:

$$\sum \dot{E}_{x,in} - \sum \dot{E}_{x,out} = \sum \dot{E}_{x,dest}. \quad (6)$$

There is exergy entering ($\dot{E}_{x,mass,in}$), exiting ($\dot{E}_{x,mass,out}$) the control region, as well as exergy produced ($\dot{E}_{x,heat}$), workable ($\dot{E}_{x,work}$) and stored ($\dot{E}_{x,dest}$). In this case, the exergy flow in the control region is written as Eq. (7):

$$\dot{E}_{x,heat} - \dot{E}_{x,work} + \dot{E}_{x,mass,in} - \dot{E}_{x,mass,out} = \dot{E}_{x,dest}, \quad (7)$$

where in terms of exergy

$$\varepsilon_{in} = (h_{in} - h_o) - T_o (s_{in} - s_o), \quad (8)$$

$$\varepsilon_{out} = (h_{out} - h_o) - T_o (s_{out} - s_o). \quad (9)$$

Substituting Eqs. (8) and (9) into Eq. (7) yields

$$\left(1 - \frac{T_o}{T_{sun}}\right) \dot{Q}_{sun} - \dot{m}[(h_{out} - h_{in}) - T_o(s_{out} - s_{in})] = \dot{E}_{x,dest} \quad (10)$$

The enthalpy and entropy change of the flowing air in the collector are determined by [25]:

$$\Delta h = h_{out} - h_{in} = c_{p,air}\left(T_{air,out} - T_{air,in}\right), \quad (11)$$

$$\Delta s = s_{out} - s_{in} = c_{p,air} \ln \frac{T_{air,out}}{T_{air,in}} - R \ln \frac{P_{air,out}}{P_{air,in}}. \quad (12)$$

If Eqs. (1)–(12) are substituted in Eq. (10), it becomes

$$\left(1 - \frac{T_o}{T_{sun}}\right) I_T \tau\alpha A_{col} - \dot{m} c_{p,air}\left(T_{air,out} - T_{air,in}\right) + \dot{m} c_{p,air}\, T_o \ln \frac{T_{air,out}}{T_{air,in}} - \dot{m} R T_o \ln \frac{P_{air,out}}{P_{air,in}} = \dot{E}_{x,dest}. \quad (13)$$

The exergy loss and irreversibility of the system are

$$\dot{E}_{x,dest} = T_o \dot{S}_{gen}. \quad (14)$$

After determining the exergy gain and exergy loss irreversibility of the solar collector, the second law efficiency is written as equation (15). It is defined as the ratio of the useful exergy leaving the system to the total exergy entering the system:

$$\psi = \frac{\dot{E}_{x,out}}{\dot{E}_{x,in}} = \frac{\dot{m}\,[(h_{out} - h_{in}) - T_o(s_{out} - s_{in})]}{\left(1 - \frac{T_o}{T_{sun}}\right)\dot{Q}_{sun}} = \frac{\dot{m}\, c_p\left[(T_{out} - T_{in}) - T_o \ln \frac{T_{out}}{T_{in}}\right]}{\left(1 - \frac{T_o}{T_{sun}}\right)\dot{Q}_{sun}}. \quad (15)$$

4. Results and discussion

This study was carried out in the city of Çorum in Turkey. The solar air collector with two different flow surfaces was investigated as an experimental device. The collector is isolated from the bottom and the sides against the environment. The collector receives its energy from the sun. This energy is transferred to the air flowing through the corrugated panels. The temperature change values of the collector are explained in Fig. 4. The energy transfer ability determines the efficiency of the collector and is shown in Fig. 5.

Experimental values were measured in June and July. The ambient temperature was measured between 28°C and 35°C during the daytime. The design of both solar collectors is different, but the inlet temperatures are the same for both because the inlet airflow is connected to the same manifold. The outlet temperatures from the collectors are different. During the experiment, the highest inflowing air temperature was measured at 13 o'clock (31.8°C), see Fig. 4.

The more the air flow comes in contact with the surface of the corrugated panel heated by the sun, the more the temperature

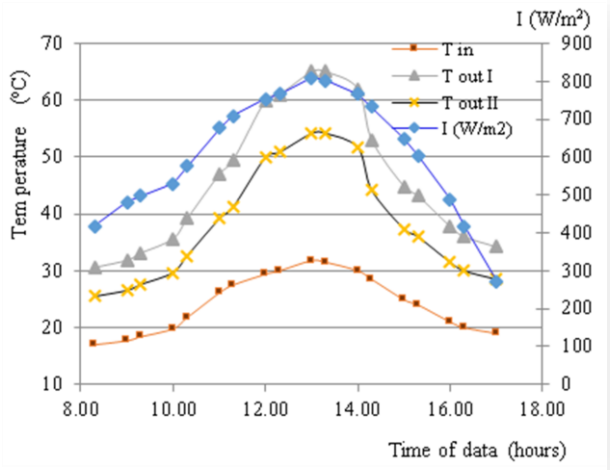

Fig. 4. The weather conditions and temperature increase across the solar air collectors on June14, 2021.

of the air increases. It may be good to keep the surface large in such collector systems, but large dimensions require larger space. Corrugated panels were created to increase the surface and reduce the length of the panel. By making zigzag rough surfaces inside the panel groove, the flow air is ensured to come into contact with the larger surface area.

The measured outflowing air temperatures in collector I and collector II are 65°C and 54.2°C, respectively. It is seen from Fig. 5 that the collector efficiency reaches its maximum values between the hours 08:30 and 17:00.

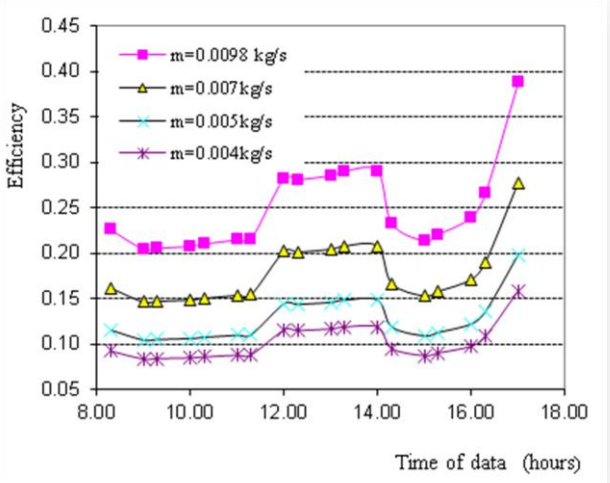

Fig. 5. Efficiency versus time of day in collector I.

The panel efficiency of the fan was observed at four different flow rates. The collector efficiency is maximum at the value of air mass flow $\dot{m}$ = 0.0098 kg/s. In the case of mass flow rate $\dot{m}$ = 0.004 kg/s, collector I's exergetic efficiency is very low. As the air flow rate decreases, the second law efficiency of the panel also decreases.

Karim and Hawlader [26] conducted an experimental study of three types of solar air collectors under Singapore climatic conditions. These collectors have flat plates, fins and V-grooves. It was found that the V-groove collector is the most efficient collector, while the flat plate collector is the least efficient collector. It was also shown that the V-slot collector has a 7−12% higher efficiency than the flat collector.

As seen from Fig. 6, when the inlet and outlet air temperature difference is compared for the same radiation values of both panels, the air temperature difference is higher in collector I.

Radiation values and temperature input-output values of both panels were compared. It is understood that at the same radiation values, the inlet-outlet temperature difference in collector I is higher. The reason for this is that there is a zigzag strip inside the panel.

In Fig. 7, changing radiation values were observed while keeping the flow rate and input temperature of air constant for both collectors. According to the second law, the exergetic efficiency of collector I, which has a zigzag inside the panel, is between 20.2% and 38.8%. It was concluded that the exergetic efficiency of collector II, which is hollow inside the panel, varies between 17% and 32.2%. In both collectors, the highest efficiency was obtained when the ambient temperature was lower.

As seen in Fig. 8, when the solar radiation reaches its maximum at 13:00, the exergetic efficiencies of both collectors reach its maximum at 29.8% for collector I and 24.8% for collector II. Although exposed to the same radiation, the exergetic efficiency of collector I is higher than that of collector II.

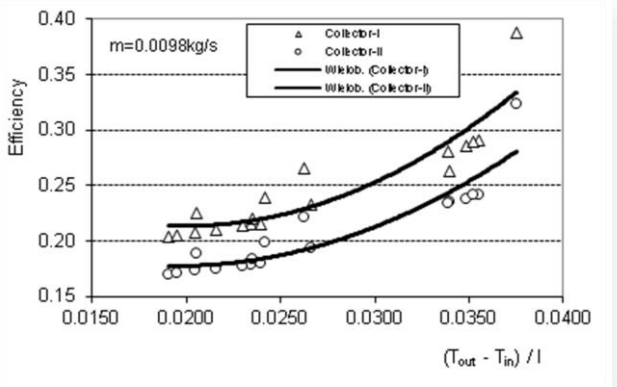

Fig. 7. Variation of collector efficiency versus parameter $(T_{out} - T_{in})/I$ at mass flow rate 0.0098 kg/s for different types of absorber plates.

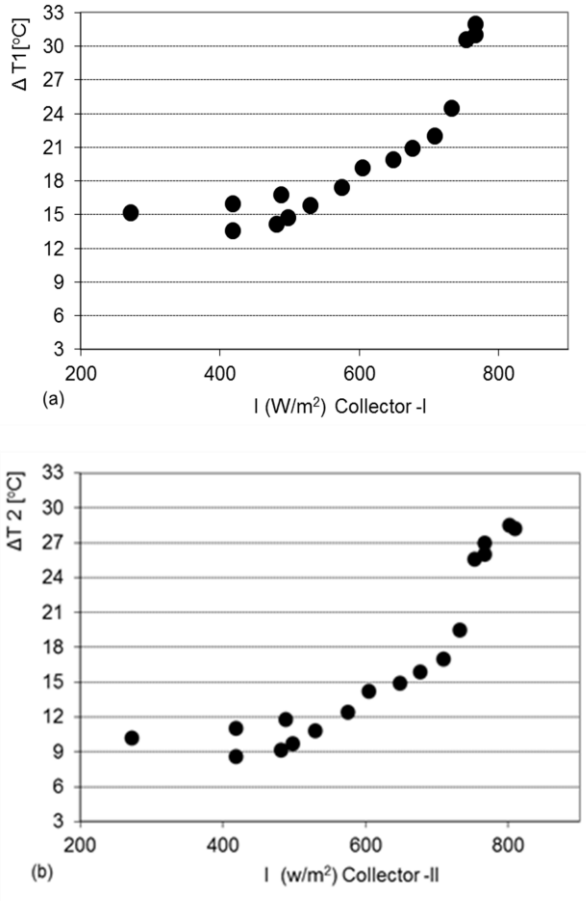

Fig. 6. Variation of temperature difference with incident radiation.

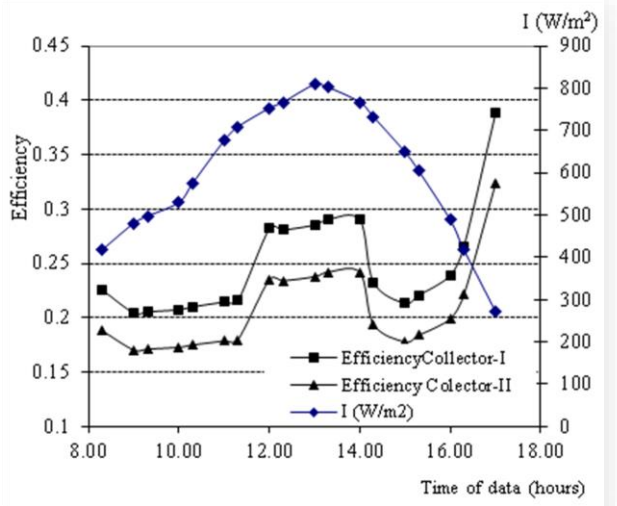

Fig. 8. The productivity changes of collector I and collector II at different radiation values.

The Ansys programme [27] was used for the display of floe parameters in the panel. The programme outputs are shown in Figs. 9−11. The air flow was observed with the highest values at the inlet and outlet of the panels (Fig. 9). It is seen in Fig. 10 that the pressure inside the panel grooves is lower than in the collector inlet–outlet. This is due to the pressure formation against the air flow inside the groove panels. Vortex changes inside panels can be seen in Fig. 11.

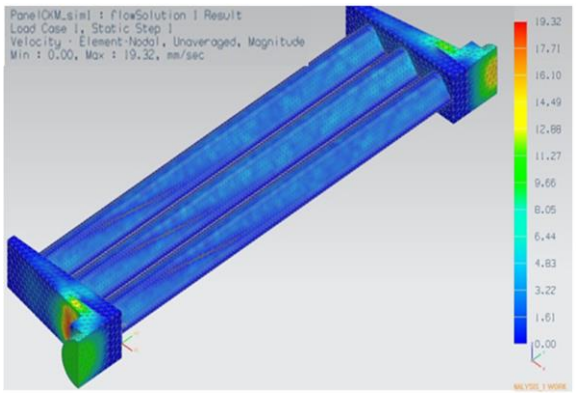

Fig. 9. Full width figure example: Panel I CKM sim l; flow Solution 1 Result; Load case 1; Static step 1; Velocity – element nodal, unaveraged, magnitude: min 0.00, max 19.32 mm/sec.

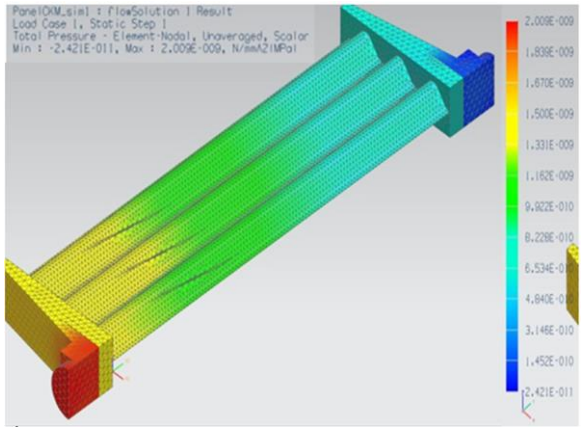

Fig. 10. Flow pressure change along the channel: Panel I CKM sim l; flow Solution 1 Result; Load case; Static step 1; Total pressure – element nodal, unaveraged, scalar: min $2.42I^{-011}$, max 2.009^{-009} N/mm^2 (MPa).

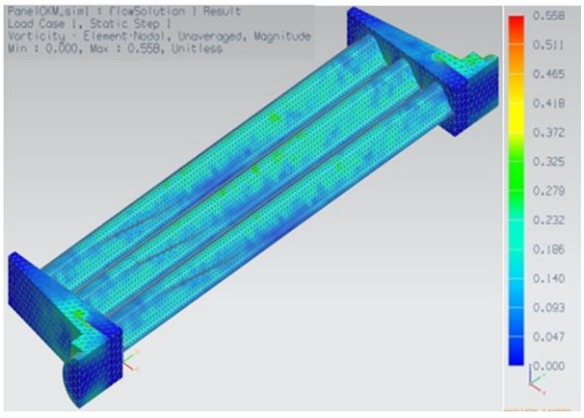

Fig. 11. Vortex along the channel change: Panel 1 CKM sim l: flow Solution 1 Result; Load Case 1; Static step 1; Vorticity – element nodal, unaveraged, magnitude: min 0.00, max 0.558 (unitless).

5. Conclusions

This study aims to investigate the effect of using various fin arrangements inside a corrugated panel with a solar thermal source. The study experiments were carried out in Corum in June–July. The experiment was carried out between 8:30 and 17:00 and the thermodynamic parameters were measured and recorded. Under the same conditions, the air temperature leaving collector I was higher than that of collector II. The highest exit temperature was reached at 13:00 in both collectors and is graphed in Fig. 4. Another important parameter for both collectors is the amount of air flow passing through the collector grooves. The collector efficiency analysis was carried out by considering the changes in these air flow amounts. The air flow was measured from Collector I between 11:00 and 15:00, at approximately 54.2ºC and 65ºC. The results presented in this study show that the efficient fin arrangement has a great effect on the heat energy transfer performance of the plate. A zig-zag fins placed inside the corrugated panel show that heat transfer is significantly improved.

References

[1] Abene, A., Dubois, V., Le Ray, M., & Ouagued, A. (2004). Study of a solar air flat plate collector use of obstacles and application for the drying of grape. *Journal of Food Engineering*, 65(1), 15– 22. doi: 10.1016/j.jfoodeng.2003.11.002

[2] Zıma, W., & Dzierwa, P. (2010). Mathematical modelling of heat transfer in liquid flat-plate solar collector tubes. *Archives of Thermodynamics*, 31(2), 45–62. doi: 10.2478/v10173-010-0008-7

[3] Krawczyk, P. (2013). Cumulative ventilation air drying potential as an indication of dry mass content in wastewater sludge in a thin-layer solar drying facility. *Archives of Thermodynamics*, 34(4), 23–34. doi: 10.2478/aoter-2013-0027

[4] Khatri, R., Goswami, S., Anas, M., Sharma, S., Agarwal, S., & Aggarwal, S. (2020). Performance evaluation of an arched plate solar air heater with porous aluminum wire mesh cylindrical fins. *Energy Reports*, 6(9), 627–633. doi: 10.1016/j.egyr.2020.11.177

[5] El-Khawajah, M.F. Aldabbagh, L.B.Y., & Egelioglu, F. (2011). The effect of using transverse fins on a double pass flow solar air heater using wire mesh as an absorber. *Solar Energy*, 85(7), 1479–1487. doi: 10.1016/j.solener.2011.04.004

[6] Sharma, S., Kumar, D.R., & Kulkarni, K. (2021). Computational and experimental assessment of solar air heater roughened with six different baffles. *Case Studies in Thermal Engineering*, 27, 101350. doi:10.1016/j.csite.2021.101350

[7] Petela, R. (2003). Exergy of undiluted thermal radiation. *Solar Energy*, 74(6), 469–488. doi: 10.1016/S0038-092X(03)00226-3

[8] Sivakumar, V., & Sundaram, G.E., (2016). MATLAB modelling and examination of the effect of heat capacity of basin and glass cover on performance of solar still by thermal models. *International Journal of Ambient Energy*, 39(1), 1–10. doi: 10.1080/01430750.2016.1222956

[9] Farahat, S., Ajam, H., & Sarhaddi, F. (2004). Method and basis of flat plate collector optimization with exergy concept. *Proceedings of First Iranian Conference on Ecoenergy*, Urmia, Iran.

[10] Çomakli, Ö., & Yüksel, F. (1994). Experimental investigation of the exergetic efficiency of air heating flat-plate solar collector with distorted plates. *Energy Conversion and Management*, 35(2), 121–126. doi: 10.1016/0196-8904(94)90072-8

[11] Karsli, S. (2007). Performance analysis of new-design solar air collectors for drying applications. *Renewable Energy*, 32(10) 1645–1660. doi: 10.1016/j.renene.2006.08.005

[12] Altfeld, K., Leiner, W., & Fiebig, M. (1988). Second law optimization of flat-plate solar air heaters Part I: The concept of net exergy flow and the modeling of solar air heaters. *Solar Energy*, 41(2), 127–32. doi: 10.1016/0038-092X(88)90128-4

[13] Altfeld, K., Leiner, W., & Fiebig, M. (1988). Second law optimization of flat-plate solar air heaters Part 2: Results of optimization and analysis of sensibility to variations of operating conditions. *Solar Energy*, 41(4), 309–317. doi: 10.1016/0038-092X(88)90026-6

[14] Gupta, M.K., & Kaushik, S.C. (2008). Exergetic performance evaluation and parametric studies of solar air heater. *Energy*, 33(11), 1691–702. doi: 10.1016/j.energy.2008.05.010

[15] Dincer, I., & Rosen, M.A. (2008). *Thermal Energy Storage: Systems and Applications*. Wiley & Sons, New York.

[16] Esen, H. (2008). Experimental energy and exergy analysis of a double-flow solar air heater having different obstacles on absorber plates. *Building and Environment*, 43(6), 1046–1054. doi: 10.1016/j.buildenv.2007.02.016

[17] Bejan, A. (1988). *Advanced Engineering Thermodynamics* (2nd ed.) (pp.133–137 & 462-465). Wiley & Sons.

[18] Wark Jr., K. (1997). *Advanced Thermodynamics for Engineers*. McGraw-Hill, New York.

[19] Ucar, A., & Inalli, M. (2006). Thermal and exergy analysis of solar air collectors with passive augmentation techniques. *International Communications in Heat and Mass Transfer*, 33(10), 1281–1290. doi: 10.1016/j.icheatmasstransfer.2006.08.006

[20] Akpinar, E.K., & Kocyigit, F. (2010). Energy and exergy analysis of a new flat-plate solar air heater having different obstacles on absorber plates. *Applied Energy*, 87(11), 3438–3450 doi: 10.1016/j.apenergy.2010.05.017

[21] Sivakumar, V., Sundaram, E.G., & Sakthivel, M. (2016). Investigation on the effects of heat capacity on the theoretical analysis of single slope passive solar still. *Desalinational and Water Treatment*, 57(20), 9190–9202. doi: 10.1080/19443994.2015.1026284

[22] Kaushik, S.C., Abhyankar, Y.P., Bose, S., & Mohan, S. (2001). Exergoeconomic evaluation of a solar thermal power plant. *International Journal of Solar Energy*, 21(4), 293–314. doi: 10.1080/01425910108914377

[23] Yousef, M., Hassan, H., Ahmed, M., & Ookawaraa, S. (2017). Energy and exergy analysis of single slope passive solar still under Egyptian climate conditions. *Energy Procedia*, 141, 18–23. doi: 10.1016/j.egypro.2017.11.005

[24] Torres-Reyes, E., Navarete-Gonzales, J.J., Zaleta-Aguilar, A., & Cervantes-De Gurtari, J.G. (2001). Exergy analysis of irreversible flat-plate solar collectors. *ECOS '01, The International Congress on Efficiency, Costs, Optimization, Simulation and environmental aspects of energy systems and processes*, July 4–6, Istanbul, Turkey.

[25] Cengel, Y.A., & Boles, M.A. (2006). *Thermodynamics: An Engineering Approach* (5th ed.). McGraw-Hill, New York.

[26] Karim, M.A., & Hawlader, M.N.A. (2004). Development of solar air collectors for drying applications. *Energy Conversion and Management*, 45(3), 329–344. doi: 10.1016/S0196-8904(03)00158-4

[27] http://www.ansys.com

Co-published by
Institute of Fluid-Flow Machinery
Polish Academy of Sciences
Committee on Thermodynamics and Combustion
Polish Academy of Sciences

http://www.imp.gda.pl/archives-of-thermodynamics/

Coupled heat, mass and momentum transfer model of a napa cabbage refrigerated storage chamber

Mirosława Kołodziejczyk[a], Kamil Śmierciew[b], Jerzy Gagan[b], Dariusz Butrymowicz[b]*, Paweł Jakończuk[b], Mateusz Pawłowski[b]

[a]PRONAR, R&D Department, Mickiewicza 101A, 17-210 Narew, Poland
[b]Department of Thermal Engineering, Bialystok University of Technology, Wiejska 45C, 15-351, Bialystok, Poland
*Corresponding author email: d.butrymowicz@pb.edu.pl

Received: 30.09.2024; revised: 14.12.2024; accepted: 16.12.2024

Abstract

Results of numerical simulation of heat, mass and momentum transfer in cold storage chambers for vegetables along with experimental validation are presented in the paper. The case of an experimental napa cabbage cold store was analysed. Coupling of processes occurring in the bulk of vegetables and in the air cooler accomplished by means of the user-defined functions in Ansys Fluent are presented. The model combines the cooling capacity with the processes occurring in the bed of cabbage, namely transpiration and respiration, and other heat gains/losses that occur in the chamber. The model of porous media was applied in terms of the bed of vegetables and air cooler. A thermal non-equilibrium model was assumed. The output of simulations were the heat and mass transfer coefficients. The numerical results were compared with the measurements. A good agreement between numerical results and experimental data in terms of temperatures in the bulk of vegetables and relative humidity was achieved. The moisture loss in stored products resulting in total loss of weight was analysed. Good agreement with experimental results and regions of the highest shrinkage of the stored vegetables were indicated.

Keywords: CFD modelling; Heat and mass transfer; Porous model; Cold storage; Napa cabbage

Vol. 45(2024), No. 4, 223–235; doi: 10.24425/ather.2024.152012

Cite this manuscript as: Kołodziejczyk, M., Śmierciew, K., Gagan, J., Butrymowicz, D., Jakończuk, P., & Pawłowski, M. (2024). Coupled heat, mass and momentum transfer model of a napa cabbage refrigerated storage chamber. *Archives of Thermodynamics*, 45(4), 223–235.

1. Introduction

It is estimated by the United Nations Department of Economic and Social Affairs that by 2050 the world's population will increase to 9.3 billion, which will require at least 70% and in some scenarios even a 100% increase in global crop production [1]. This means that the food production needs to increase by 100% and the demand for storage, and related factors—such as climate change, power consumption, hunger and land use—are expected to rise accordingly [2]. The need for refrigerated storage of fruits and vegetables causes significant energy consumption and greatly influences the cost of postharvest handling of agricultural products.

Inappropriate storage conditions in the cold storage chambers may generate drying of the product and under too low temperatures may cause the products injury that strongly deteriorates the quality of the stored products. Losses may occur mainly due to non-uniformity of the environmental conditions inside the bed of the stored products. The most important factors that protect the product against damage are air temperature, air velocity and air humidity. Important are also load arrangements and physical properties of vegetables and fruits. The macroscopic

Nomenclature

A_{fs} – heat transfer surface area, m^2
c_p – specific heat, J/kgK
C_2 – resistance coefficient
$D_{i,m}$ – mass diffusion coefficient
E – total fluid phase energy, J/kg
$\vec{g}$ – gravitational acceleration, m^2/s
h – convective mass transfer coefficient
$\vec{J}_i$ – diffusion flux vector
k – thermal conductivity, W/(m K)
L – latent heat of evaporation/condensation, J/kg
Le – Lewis number
$\dot{m}$ – transpiration rate, kg/s
Nu – Nusselt number
p – pressure, Pa
Pr – Prandtl number
R_v – water vapour gas constant, J/(kg K)
RH – relative humidity, %
$\dot{Q}$ – cooling capacity, kW
Sc – Schmidt number
$\vec{S}$ – body force term
t – time, s
t, T – temperature, K
V – volume, m^3
V – magnitude of velocity, m/s
$\vec{V}$ – velocity vector
W – heat generation, W/kg
Y_t – species mass fraction

Greek symbols

α – permeability of porous medium
β – interfacial area density, kg/m^3
δ – relative difference, %
Δl – length, m
Δp – static pressure jump across the fans, Pa
ε – porosity
η – effectiveness
μ – dynamic viscosity, Pa·s
ρ – density, kg/m^3

Subscripts and Superscripts

a – air
f – fluid
p – pressure
s – solid
t – turbulent
v – vapour
w – wall

Abbreviations and Acronyms

CAD – computer-aided designed
CFD – computational fluid dynamics
RANS – Reynolds-averaged Navier-Stokes
RNG – re-normalization group
SAS – scale adaptive simulations
SIMPLE – semi-implicit method for pressure linked equations
SST – shear stress transport
UDF – user-defined functions
VPL – vapour pressure lowering

energy balance approach cannot give the answers to the questions how these factors influence the local temperature and relative humidity inside the bulk and where in the bulk warm and cold zones are placed, causing excessive drying or chilling injuries of the vegetable tissue. In light of this fact, numerical modelling of the air conditions in the cold storage chambers seems to be the best approach in examining the reasons for unfavourable heterogeneity of thermal and flow parameters inside the bulk. Therefore, numerical modelling of the cold storage chamber may be attractive for its cost-saving potential and ability to adapt to different model parameters quicker than e.g. experimental investigations. In fact, numerical modelling using CFD (computational fluid dynamics) approach allows us to fully understand the complexity of biological systems. For this reason, the CFD approach became the basic tool that allows replicating and predicting phenomena in physics, chemistry and biology [3]. The variety of CFD applications related to heat and mass transfer in adsorption packed beds [4], cold storage rooms [5], and drying beds can be found in the literature. The papers [6–8] provided analysis of air flow and heat transfer through the package design. The aspects of energy consumption and savings are presented in papers [9,10]. The operation of the cooler is the major factor that influences the storage conditions. The forced-air cooling units for the cold storage chambers are usually mounted just under the ceiling of the chamber and they are equipped with several fans and the air cooler. The evaporator of the refrigeration system or alternatively the heat exchanger for glycol cooling installations may be applied as air coolers. Its thermal performance depends on the storage conditions and should be analysed together with the entire chamber with its load as one computational task. This may be thought as a challenge for a wide range of geometric scales of the modelled objects in the analysed cold store. The entire geometry consists of empty spaces filled with humid air only, however, there are also large areas in which a large number of small objects exist, i.e. pieces of products located inside the boxes or palloxes as well as elements of the cooling unit (fins and tubes of the air cooler). It is a challenging and time-consuming task from the pre-processing and simulation point of view to build a geometric model of the cold storage chamber which retains the exact shape of all these relatively small details. For that reason, a porous media model with large pores is widely used in modelling the bed of products and the air cooler. Using the porous model is a reasonable compromise between the computational cost and accuracy of the results [11, 12]. A space occupied by a large number of small objects is treated as a fictitious continuum of resistance to flow that is equal to the resistance of real objects. This is taken into account by means of the additional negative source term in the momentum equation. The containers of vegetables are usually modelled by a packed bed approach including both viscous and inertia resistance calculated according to the Ergun equation, which was demonstrated for the packed bed of apples [13] with the use of

the Brinkman-modified Ergun equation. In paper [14] with the use of the Ergun equation, an average accuracy of 20% on the velocity magnitudes was observed on the basis of own experimental data. The effects of blowing duct on ventilation homogeneity around stored products were analysed experimentally and numerically using the Ergun equation in [15]. However, there are also works in which the containers were treated as impenetrable solid areas with specified boundary conditions on the walls [16]. There are also works where the resistance of the bed is calculated on the basis of the experimental data for an enclosure loaded with slotted pallets [17] and inside slotted obstacles in a ventilated enclosure [18].

There are also additional problems associated with the complex geometry of the flow through the containers with stored products. The confinement effect of the porous medium, causing different flow conditions in the vicinity of the walls and inside the bed core as well as narrow gaps between the containers cause a strong increase in the number of computational cells. Both problems were studied by Moureh et al. for refrigerated trucks [19], a slot-ventilated enclosure partially loaded with vented boxes filled by spherical objects [20–22]. Near the wall, the porosity is higher which causes higher velocity gradients than inside the core of the porous medium. The common approach is based on the ratio of the hydraulic diameter to the geometric scale of the pores. Therefore, if this ratio is greater than 10, then the impact of the wall on the flow through the bed can be neglected. The interstices between the boxes in the bulk can be included by increasing the porosity, which can be considered as the additional (fictitious) aerodynamically equivalent porous medium with laminar flow that requires a much smaller number of computational cells than for real gaps [17,21]. Another problem is associated with slotted walls of boxes which are usually modelled as equivalent resistance obtained from the measurements [18,20,21]. One more approach to possible geometric simplification commonly applied is the use of symmetry of geometry [23,24]. However, such a simplification is assumed even though the real flow in such complex geometries is always non-symmetrical.

The air cooler is usually modelled by means of simplified geometry and physics. The fans that force air flow inside the chamber may be taken into account in the model by many different methods, mostly as infinitely thin plates with a given pressure jump in 3D problems [25,26], or alternatively as line segments in 2D problems [27]. In the earlier work of Hoang et al. [16], the changes in pressure in the fan and in the air cooler were modelled. The performance curve of the fan and the resistance curve of the cooler were applied in order to obtain the operation point of the fan, neglecting thus the effect of the chamber. In the paper by Nahor et al. [14], the fan and the cooler were represented by distributed body forces and resistance that was taken from the characteristics of these devices and applied to the block of air cooler dimensions. Hoang et al. [5] modelled the swirling air jets blown out by the fans by means of both nominal data and the measurements of air velocity at the fans outflows. The varying supply air temperature was modelled by the exponential function with adjustments taken from the measurements. Heat transfer in the air cooler is modelled in various ways. Hoang et al. [16] considered only the airflow in the chamber assuming temperature to be constant across the room. In the work [27], the square-shaped fins of the evaporator in 2D simulation were assumed to be at a constant temperature obtained from the measurements. Nahor et al. [14] incorporated a lumped model of heat transfer between the air cooler and the air. Delele et al. [25,26] considered the cooler as a porous medium. The model includes losses due to wall friction. Acceleration and deceleration effects as well as entrance and exit conditions were also included. Cooling capacity and condensation/evaporation effects in the air cooler were also incorporated into the model.

A thermal equilibrium is usually assumed when heat transfer in the bulk of products is modelled. Thus, the difference in temperature between the products and humid air is neglected as in papers [25−27]. Nahor [14] applied the thermal non-equilibrium approach in which the temperature difference between products and cooling air was taken into account. However, the heat transfer model used in this case neglects the thermal conductivity in the bulk. The temperature difference was also taken into account in the paper [28] in which the multi-scale model was applied including conduction inside the separate products, but heat conduction in a bed of vegetables was neglected there. Hoang et al. [5] achieved good agreement between numerical and experimental investigations. The conduction in the separate products was also included by modification of the heat transfer coefficient with the aid of additional internal resistance.

In the present study, a model is formulated for the air flow, heat, mass and momentum transfer in the storage chamber of napa cabbage. This model was verified with the use of own experimental data during long-term storage tests. Due to specific properties of napa cabbage, the coupling of heat and mass transfer as well as flow resistance processes are thought of as a novel contribution to the state of the art in modelling the refrigerated storage of foodstuff. In this approach, the cooling unit and the bulk of vegetables were considered as a whole. The aim of the calculation is the prediction of the non-uniformity of velocity, temperature and humidity distributions that consequently enables the identification of the unfavourable storage conditions, i.e. too high, too low air velocity, temperature or relative humidity. These non-uniformities were validated experimentally. In order to include the close relationship between the phenomena occurring inside the stored vegetables and in the air cooler, the user-defined functions (UDF) in Ansys Fluent were used [29].

2. Description of the model

The experimental cold store chamber of the Research Institute of Horticulture in Skierniewice, Poland, was used for the analysis with the help of a CFD model. Figure 1 shows the photo of the investigated experimental storage chamber seen from the cooler side. The CAD (computer-aided designed) model of the chamber is presented in Fig. 2, and the CAD model of the air cooler – in Fig. 3. The overall dimensions of the cold storage chamber were 2.05 m × 4.33 m × 2.93 m. The geometry of the antechamber is presented in Fig. 2. The chamber was loaded with 2940 kg of products. The napa cabbage was packed in plastic boxes placed on wooden pallets. The basic arrangement of the boxes is a block of dimensions 1.8 m × 2.8 m × 2.17 m. The

block occupies most of the chamber space. As it is seen in Fig.2, the boxes are also stored in the antechamber. The ceiling-type air cooler of a nominal thermal capacity of 1148 W and air flow rate of 1105 m^3/h was connected to the indirect cooling system operating with glycol solution. The continuous, non-stop flow

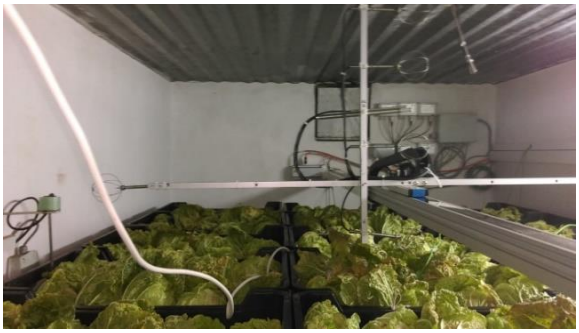

Fig. 1. Photo of the experimental cold store: view from the air cooler side. The elements of the mobile measurement system are visible.

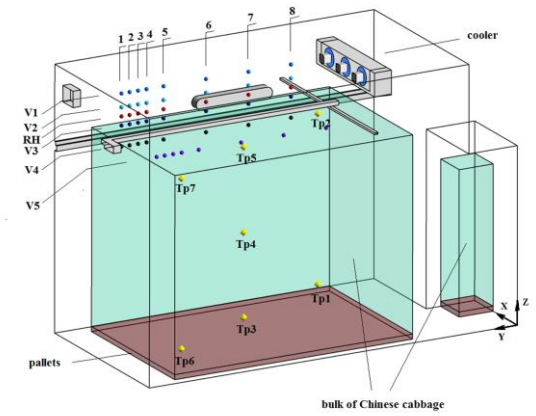

Fig. 2. Geometry of the cold storage chamber along with the antechamber. The points of the measurement system grid are shown (*V* – velocity; RH – relative humidity); *Tp* denotes temperature measurement locations in the vegetable bulk.

of air was provided by three axial fans of 0.2 m of diameter rotating at 1300 rpm, placed at the outflow of the cooler.

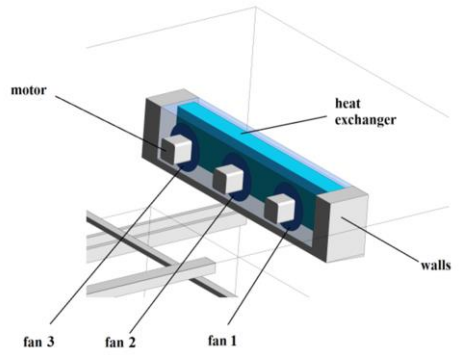

Fig. 3. Geometry of the applied air cooler.

Optimum storage conditions for napa cabbage are: temperature in the range 0°C − +3°C, however, as close as possible to 0°C without freezing is preferred, and the range of relative humidity between 95% and 98%. In order to take into account variable moisture content, the species transport method without chemical reactions was applied in modelling. Humid air was treated as a mixture of oxygen, nitrogen and water vapour. The air was considered an ideal incompressible gas. The physical properties of the air depend on temperature only with coefficients taken from the Fluent library [29].

The flow through the bulk of napa cabbage, heat exchanger in the cooling unit, and wooden pallets with supporting boxes with vegetables were modelled with the use of the porous medium model. Moist air constituted the fluid zone in all regions filled with the porous medium, but the solid zones were formed from different materials depending on the case: cabbage for the bulk of vegetables, aluminium for the air cooler, and wood for the pallets. Properties of aluminium and wood were taken from the Fluent library [18]. Thermophysical properties of napa cabbage (specific heat and thermal conductivity) were obtained through the own measurements performed for the assumed storage temperature of 1°C. The density of cabbage was determined by Bohojło-Wiśniewska [30]. Detailed numerical data are given in Table 1.

3. Mathematical model

The mathematical model of flow in a storage chamber of vegetables includes basic conservation equations with additional equations presented in the next part of this section. The model includes two energy equations for fluid and solid zones of porous media for the dual cell approach or one – for the thermal equilibrium model, and two species transport equations for oxygen and water vapour.

The continuity equation for humid air is as follows:

$$\frac{\partial(\varepsilon\rho)}{\partial t} + \nabla\cdot\left(\varepsilon\rho\vec{V}\right) = 0, \tag{1}$$

where: ε − porosity (for empty space outside the porous material $\varepsilon = 1$), ρ − density of the mixture of oxygen, nitrogen and water vapour as components of humid air, $\vec{V}$ – velocity vector.

The conservation of momentum for incompressible fluid with natural convection is as follows:

$$\frac{\partial(\varepsilon\rho\vec{V})}{\partial t} + \nabla\cdot\left(\varepsilon\rho\vec{V}\vec{V}\right) = \left(\rho - \rho_0\right)\vec{g} - \varepsilon\nabla p + \nabla\cdot\left(\varepsilon\mu\left(\nabla\vec{V} + \nabla\vec{V}^{\mathrm{T}}\right)\right) - \vec{S}, \tag{2}$$

where: p − air pressure, $\vec{g}$ − gravitational acceleration, ρ_0 − operating density, μ − viscosity of moist air including turbulent viscosity, $\vec{S}$ – body force term due to the loss of momentum in the porous medium.

Two transport equations of oxygen and water vapour are taken into account:

$$\frac{\partial}{\partial t}(\rho Y_i) + \nabla\cdot\left(\rho\vec{V}Y_i\right) = -\nabla\cdot\vec{J}_i + S_i, \tag{3}$$

Table 1. Model parameters.

Parameter	Unit	Value
Bulk of napa cabbage		
Density of a cabbage head	kg/m³	568
Specific heat	J/(kg·K)	3955
Thermal conductivity	W/(m·K)	0.4425
Number of cabbages in one box		12–13
Number of boxes in the main bulk		147
Volume of the bulk	m³	11.06
Mass of cabbage in the main bulk	kg	2940
Bulk porosity		0.532
Interfacial area density	m²/m³	7.95
Viscous resistance	1/m²	2777181
Inertial resistance	1/m	412.56
Air cooler		
Volume of heat exchange	m³	0.0189
Heat exchange surface area	m²	5.703
Surface efficiency under wet conditions		0.81
Porosity		0.60
Viscous resistance	1/m²	1.5×10^7
Inertial resistance	1/m	92.468
Interfacial area density	m²/m³	301.75
Fan power	W	3×10
Fan speed, rpm	1300	
Pallets		
Height	m	0.055
Porosity		0.99
Inertial resistance	1/m	1
Material		wood
Walls		
Overall heat transfer coefficient	W/(m²K)	0.25
Wall thickness	m	0.3
Free stream temperature	°C	12

where *i* is the indicator of the species (oxygen or water vapour), Y_i is the species mass fraction, $\vec{J}_i$ – diffusion flux; S_i − rate of species creation, taking a non-zero value only for water vapour. The nitrogen mass fraction is calculated as a supplement to unity.

In turbulent flows, the diffusion flux can be described as, Ansys Fluent [29]:

$$\vec{J}_i = -\left(\rho D_{i,m} + \frac{\mu_t}{\mathrm{Sc}_t}\right)\nabla Y_i - D_{T,i}\,\frac{\nabla T}{T}, \tag{4}$$

where: $D_{i,m}$ – mass diffusion coefficient; μ_t – turbulent viscosity; Sc_t – turbulent Schmidt number, $D_{T,i}$ – turbulent diffusivity, T – temperature.

Vegetables and fruits during postharvest storage are still living organisms, so metabolic processes occur. The most important of them that affect heat and mass balance in the cold storage chamber are the respiration and transpiration processes. In order to include the heat generation inside a porous medium, which is the bulk of vegetables, but also the heat exchanger, solid and fluid phases are not in thermal equilibrium. Furthermore, napa cabbage heads are relatively large in size and the differences in temperature between the solid and fluid phases of the porous medium making the bulk cannot be neglected. For that reason, the non-equilibrium model of heat transfer in the porous medium (a dual cell approach) was used assuming that the solid zone of the porous medium is spatially coincident with the fluid zone, and two equations of energy, for humid air (5) and for the solid material (6), are solved separately:

$$\frac{\partial(\varepsilon\rho E)}{\partial t} + \nabla\cdot\left[\vec{V}\,(\rho E + p)\right] = \nabla\cdot\left[k\,\nabla T - \sum_i h_j J_j + \left(\bar{\bar{\tau}}_{eff}\cdot\vec{V}\right)\right] + S_f^h + h_{fs}\beta_{fs}\,(T - T_s), \tag{5}$$

$$\frac{\partial\left[(1-\varepsilon)\,\rho_s E_s\right]}{\partial t} = \nabla\cdot\left[(1-\varepsilon)\,k_s\,\nabla T_s\right] + S_s^h + h_{fs}\beta_{fs}\,(T_s - T), \tag{6}$$

where $\bar{\bar{\tau}}_{eff}$ is the stress tensor. The above equations are connected by the heat transferred through the fluid/solid interface. Source terms in both equations represented by Newton's law describe this connection. This requires heat transfer coefficients h_{fs} to be determined. The symbol β_{fs} stands for the interfacial area density. The meaning of other terms in energy equations is as follows: E and E_s – total fluid and solid phase energy, ρ_s – density of the solid matrix, k and k_s – fluid and solid thermal conductivity, T and T_s – temperature of the fluid and solid phases, respectively, S_f^h and S_s^h − energy sources terms in fluid and solid zones, which will be defined in the next part of this section. This model of heat transfer in the porous medium was applied for the bulk of vegetables and for the heat exchanger. The wooden pallets which supported the boxes with vegetables, because of a very high porosity of this region, were also treated as the porous medium, but using the equilibrium single-phase porous medium model.

In modelling the flow physics, the geometry of the cooling unit was simplified to the heat exchanger considered as a box of porous medium (shown in blue in Fig. 3), and fans being infinitely thin plates with a pressure jump (shown in dark blue in Fig. 3). The pressure jump depends on the local normal velocity component according to the fan performance curve:

$$\Delta p = -0.085\,V_n^3 + 1.9046\,V_n^2 - 14.998\,V_n + 60.604, \tag{7}$$

where Δp is the static pressure jump across the fans and V_n is the local normal velocity.

The jets of air from the fans were visualised using fibre tufts. The measurement allows for modelling the performance of the fans more completely. The divergent cones of air blown out by the fans were observed. The angle of divergence was close to 90°. The inclination angle of the velocity vector was about 10°. Based on these results, the radial and tangential components of velocity were defined.

In both cases of flow through the cabbage bulk and the heat exchanger, a porous medium was considered to be an isotropic material with the loss of momentum S expressed by a pressure gradient ∇p [29]:

$$S = \nabla p = \frac{\Delta p}{\Delta l} = \frac{\mu}{\alpha}\,V + \frac{1}{2}\,C_2\,V^2. \tag{8}$$

The first term on the right-hand side of Eq. (8) is the viscous resistance; μ is the viscosity, α − permeability of the porous medium; V − magnitude of the velocity. The second term is the inertial resistance which contains the resistance coefficient C_2. These terms – the heat exchanger permeability α and inertial resistance coefficient C_2 were obtained from performance curves calculated by Śmierciew et al. [31] through numerical simulations of the flow and corresponding pressure drop in the actual cooling unit of the width of heat exchanger Δl = 0.09 m. The bed of vegetables was modelled as a porous medium. For the derivation of pressure loss coefficients due to viscosity and inertia, a series of experimental investigations were conducted in a controlled wind channel with napa cabbage [32]. The napa cabbage bulk characteristic curve was obtained based on the pressure drop measurements for several mean velocities on the length of the bed Δl = 0.6 m. The permeability α of the bed and its inertial coefficient C_2 were computed from Eq. (8). The results for the heat exchanger and cabbage bed are collected in Table 1.

Transpiration and water vapour condensation processes have an influence on the moisture content in the air in the cold storage chamber. As previously stated, the napa cabbage is stored in the range of temperatures between 0°C and 3°C under a relative humidity (RH) range of 95−98%. Therefore, there may appear some spots in the chamber where the condensation process occurs, both, in the heat exchanger and at the vegetable surface. The model of evaporation and condensation processes was incorporated into the proposed modelling approach. This model consists of the spatial distribution of volume water vapour sources or sinks in the regions modelled as porous media (cabbage bulk and heat exchanger). As a consequence, thermal effects of phenomena such as transpiration, condensation and respiration were also represented by the volumetric sources.

The model of evaporation/condensation in the bulk assumed that the process is driven by a difference between the water vapour pressure in the boundary layer at the surface of a vegetable and in the surrounding air [33]. The transpiration rate defined as a mass flow rate of moisture transpired per surface area of a vegetable can be expressed as follows:

$$\dot{m} = \ k_t(\mathrm{VPL}\, p_{sat} - p_v), \tag{9}$$

where: VPL$p_{sat} - p_v$ means the deficit in the water vapour pressure. Because of dissolved substances, the vapour pressure at the vegetable surface is lower than the saturation pressure at the vegetable surface temperature p_{sat}. The vapour pressure lowering coefficient VPL was evaluated after Becker et al. [33] at 0.99. The transpiration coefficient k_t and the convective mass transfer coefficient h_a are related by the perfect gas law:

$$k_t = \frac{1}{R_\mathrm{v}\, T}\, h_a, \tag{10}$$

where: T − local absolute temperature of the boundary layer; R_v − water vapour gas constant. The Lewis relationship can be used for the calculation of the convective mass transfer coefficient h_a, assuming that the Lewis number Le = 1,

$$h_a = \frac{h_{tc}}{\rho\, c_p \mathrm{Le}^{2/3}}, \tag{11}$$

where ρ is the humid air density, c_p is the specific heat of humid air and h_{tc} can be calculated from the correlation for low velocity force convection in a packed bed of spheres [34]. This correlation was applied also by Nguyen et al. [35] for the prediction of water loss for pears. Thus, the dimensionless relationship describing the convective heat transfer is as follows:

$$\mathrm{Nu} = 2.19\ \mathrm{Re}^{0.33}\ \mathrm{Pr}^{0.33} \tag{12}$$

with the definition of Nusselt number Nu as follows:

$$h_{tc} = \frac{\mathrm{Nu}k}{d_{pe}}, \tag{13}$$

where h_{tc} is the convective heat transfer coefficient, k denotes the thermal conductivity of moist air and d_{pe} – diameter of the sphere with a volume equal to the actual volume of a vegetable.

The process of transpiration/condensation in the bulk of vegetables was introduced into the model by transpiration rates distributed along the volume of the bed, in kg/(m^{3}s):

$$S_v = \pm \dot{m}\, \beta, \tag{14}$$

where $\dot{m}$ is calculated by Eq. (9). The positive sign is used for the transpiration process, and the negative one for the condensation process. The symbol β denotes the interfacial area density. The thermal effect of the process is also modelled as a volumetric heat source/sink by the following formula:

$$E_v = \ -S_v\, L, \tag{15}$$

where the latent heat of evaporation/condensation L is considered as a function of temperature T as follows [36]:

$$L = C_1\, T^2 + C_2\, T + C_3, \tag{16}$$

where C_1 = 0.0091×10^3, C_2 = −7.5129091×10^3, and C_3 = 3875.1×10^3. Sources due to evaporation and condensation were distributed in the fluid phase of the porous medium.

Becker and Fricke [37] related the heat generation rate due to respiration, expressed in W/kg, to the temperature from the carbon dioxide production correlation:

$$W = \frac{10.7f}{3600}\left(\frac{9}{5}t\ + 32\right)^g. \tag{17}$$

Here, t is the temperature in °C. The coefficients are: f = 6.0803×10^{-04}, g = 2.6183 [38]. Heat of respiration was distributed in the solid phase of the porous medium (cabbage) as volumetric sources and calculated in the following manner:

$$E_r = \frac{Wm}{V}, \tag{18}$$

where m denotes the mass of cabbage in the chamber and V is the volume of the bulk.

The model of heat and mass transfer in the heat exchanger was based on the cooling capacity including the sensible $\dot{Q}_s$ and latent $\dot{Q}_l$ heat transfer rates:

$$\dot{Q} = \ \eta\left(\dot{Q}_s + \ \dot{Q}_l\right) \tag{19}$$

with the overall surface efficiency η under wet conditions evaluated after Ma et al. [39] at 0.81. The air side sensible heat transfer rate was calculated from Newton's law:

$$\dot{Q}_s = h_{tx} A_{fs} (T - T_{sat}), \quad (20)$$

where: h_{tx} – air side heat transfer coefficient; A_{fs} − heat transfer surface area, T − temperature of moist air (of the porous medium modelling the heat exchanger), T_{sat} – temperature in the boundary layer at the surface of the solid phase (coils and tubes) of the heat exchanger under saturation conditions.

Condensation in the air cooler was modelled in a similar way as evaporation/condensation in the bulk of vegetables. The water vapour condensation rate was calculated using Eq. (9) with VPL = 1. Following this assumption, the latent heat transfer rate can be expressed as:

$$\dot{Q}_l = k_{tx} A_{fs} (p_v - p_{sat}) L, \quad (21)$$

where: p_v − vapour pressure of surrounding air; p_{sat} − pressure in the boundary layer at the solid surface under saturation conditions. The coefficient of condensation in the heat exchanger k_{tx} was calculated similarly as for vegetables using Eqs. (10) and (11). Volumetric water vapour sinks and corresponding condensation heat sources were modelled following Eqs. (14) and (15) and distributed in the fluid phase of the heat exchanger.

The convective heat transfer coefficient h_{tx} on the air side can be calculated from the total heat transfer rate $\dot{Q}$ according to Eqs. (19)−(21) as

$$h_{tx} = \frac{\dot{Q}}{\eta A_{fs} \left[(T_a - T_{sat}) + \frac{L}{R_v T_a \rho c_p \mathrm{Le}^{2/3}} (p_v - p_{sat}) \right]}, \quad (22)$$

provided that the total cooling capacity $\dot{Q}$ can be evaluated experimentally or provided by the manufacturer.

Local flow parameters should be the basis for determining the heat transfer coefficients in the bulk of vegetables [40]. According to this suggestion, in this paper, all quantities describing the heat transfer in the cabbage bulk, heat of respiration rate and the heat exchanger itself were distributed in space. The actual quantities of the flow are provided by the solver. Subsequently, all sources of heat and mass in the vegetable bulk and in the heat exchanger were treated as field variables. Eventually, it became possible to compute the required cooling capacity $\dot{Q}$ basing on the actual macroscopic heat balance.

The macroscopic heat balance in the cooler, adopted for this work, can be expressed by the formula

$$\dot{Q} = \dot{Q}_t + \dot{Q}_r + \dot{Q}_k + \dot{Q}_w, \quad (23)$$

where: $\dot{Q}$ – cooling capacity, $\dot{Q}_t$ – total heat flux due to transpiration/condensation in the vegetable bulk, $\dot{Q}_r$ – total heat flux due to respiration of vegetables in the bulk; $\dot{Q}_k$ – heat flux due to convection in the air cooler resulting from the temperature difference in the chamber and in the cooler, $\dot{Q}_w$ – total heat flux gain/loss through external walls.

The total heat flux due to transpiration/condensation processes $\dot{Q}_t$ in the vegetable bulk was determined by summing up the bulk heat of transpiration/condensation sources through all computational cells of the fluid phase E_v^i calculated according to Eq. (15) with the cell volumes V_i:

$$\dot{Q}_t = \sum_i E_v^i V_i. \quad (24)$$

The total heat flux due to the respiration process of vegetables was computed in a similar manner:

$$\dot{Q}_r = \sum_i E_r^i V_i, \quad (25)$$

where E_r^i is the volumetric respiratory heat source calculated from Eq. (18) at cell i; and V_i is its volume. The summing is performed through all cells of the solid zone of the cabbage bulk.

The negative source of the cooling capacity was distributed along the cells of the solid phase in the heat exchanger treated as a porous medium according to the formula

$$E_{xt} = -\frac{\dot{Q}}{V_{xt}}, \quad (26)$$

where $\dot{Q}$ is computed according to Eq. (23) and V_{xt} is the volume of the heat exchanger. The value of heat flux $\dot{Q}$ is updated at each iteration of the solution.

Condensation on the coils and fins of the heat exchanger was modelled by spatially distributed negative sources of water vapour given by

$$S_{conxt} = -\max \begin{cases} S_{conxt1} = k_{tx} (p_v - p_{sat}) \beta_{xt} \\ S_{conxt2} = \frac{1}{V_{xt}} \sum_i S_v^i V_i \end{cases}, \quad (27)$$

where $\beta_{xt} = A_{fs}/V_{xt}$ is the interfacial area density in the heat exchanger. The term S_{conxt1} denotes the volumetric condensation rate in the cooler and S_{conxt2} denotes the volumetric source of water vapour generated in the whole bulk of the heat exchanger. The summing in S_{conxt2} is performed through all V_i cells of the fluid zone of the cabbage bulk, and S_v^i is computed according to Eq. (14). This method of determination of the condensation process in the cooler prevented us from an uncontrollable growth of moisture content in the chamber above 100%, which sometimes can occur during the simulation, especially at an initial period.

The governing equations Eqs. (1)−(6) were transformed to RANS equations with the k–ω SST (shear stress transport) turbulence closing equations. The detailed turbulence model equations are given in Ansys Fluent [29], and for this reason, they are not presented in the paper.

A computational grid of 22.7 million control volumes was obtained in Ansys 16.0 using the *cut cell* method. The pressure-velocity coupling was modelled using the SIMPLE (semi-implicit method for pressure linked equations) algorithm.

4. Results and discussion

The experimental investigations were carried out during the post-harvest storage. These studies allow for obtaining data concerning distributions of important parameters required by the computational model. The database includes distributions of velocity, temperature and relative humidity of air. The measurements of air velocity and relative humidity were carried out in the mid-plane of the chamber located at X = 0.99 m above the

vegetable bulk and on one level near the wall located at X = 0.25 m using the mobile measurement system which is seen in Fig.1. As seen in Fig. 2 the velocity and humidity sensors were moved between the points of the measurement grid. The velocity magnitude was measured at elevations denoted as *V1*−*V5* and the relative humidity was measured at RH level. The data were collected at 8 verticals with a frequency of 1 Hz during 10 min of rest at each position. For the air temperature measurements inside the bulk of cabbages, 7 representative points were selected as shown in Fig. 2. The details of the grids are presented in Tables 2 and 3 with respect to the system of coordinates shown in Fig. 2.

The magnitude of the velocity vector was measured using

Table 2. Dimensions of the measurement grid of a mobile system.

Level						
	V1	*V2*	*RH*	*V3*	*V4*	*V5*
X **(m)**	1.01	1.01	1.01	1.01	1.01	0.25
Z **(m)**	2.88	2.73	2.63	2.53	2.3	2.41

Vertical							
	1	2	3	4	5	6	7
Y **(m)**	4.11	4.015	3.915	3.815	3.615	3.115	2.615

Table 3. Dimensions of the measurement grid in the bulk of vegetables.

Point							
	Tp1	*Tp2*	*Tp3*	*Tp4*	*Tp5*	*Tp6*	*Tp7*
X **(m)**	1.61	1.61	1.01	1.01	1.01	0.41	0.41
Y **(m)**	1.47	1.47	2.67	2.67	2.67	3.73	3.73
Z **(m)**	0.21	2.07	0.21	1.14	2.07	0.21	2.07

omnidirectional transducers Delta Ohm HD103t with the accuracy of ±0.04 m/s in the range of 0−0.99 m/s, and ±0.2 m/s in the range of 1−5 m/s. For relative humidity measurements, an EE Elektronik sensor of J type was used. The accuracy of this sensor is 2.7% in the range above 90% RH and 1.5% below 90% RH. The air temperature in the bulk of cabbage was measured with T-type thermocouples Czaki with a precision of ±0.2 K.

Thermal conditions in the cold storage chamber were changing constantly mainly because of the requirements to defrost the air cooler. The defrost cycle was performed two times a day and was executed by the electric heaters. The fans were stopped at this time. However, during most periods of time, the conditions in the chamber were stable. The measured velocities at levels *V1*−*V5* during 6 runs of the transducers (approx. 12 hours) are presented as a function of time in Fig. 4. Data collected at this time were selected after averaging for the purpose of the comparison with theoretical prediction obtained for the steady state conditions.

Cooling units are equipped with fans mounted either at the inlet or at the outflow from the chamber. The second location creates important problems for simulations due to difficulties in modelling the details of the jets flowing out from the fans, their

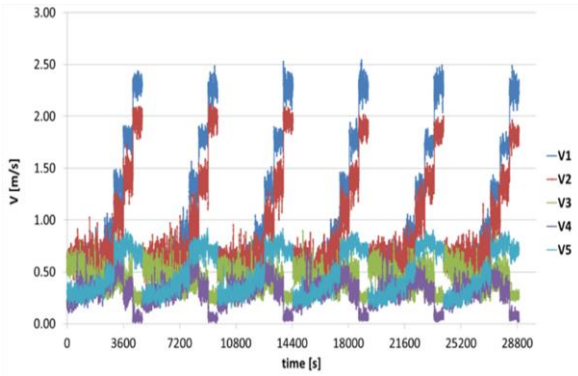

Fig. 4.Velocities measured by the mobile measurement system *vs*. time.

shapes and their swirls. They are the first important factor affecting the flow pattern above the vegetable bed. The other difficulty is the selection of the model of turbulence since this has an impact on the way the air jets flow out of the cooler and interact with each other and with the surroundings. In the present paper, the SST model of turbulence was selected because of its better ability to represent the airflow above the bed. Several models were tested, i.e. the standard model k–ε, RNG k–ε, realizable k–ε, k–ω SST, and SAS. The realizable k–ε and k–ω SST models occurred as the most promising. The realizable k–ε model was slightly better in representing the velocity distribution at the elevations *V1* and *V2* than the SST model, but it was not able to reproduce the velocity profile at *V3*, *V4* and *V5* elevations. Three interfering jets have formed one stream with a contraction near the wall opposite to the cooler, see Fig. 5b. However, the free stream above the bulk is quite wide not too far from the cooler, which may be indicated by the results of measurements collected at *V5* level, see Fig. 6e. The k–ω SST model was the only one which managed to form the air jets wide enough to get close to experimental results obtained at *V5* level, see Fig. 5a.

The experimental and calculated velocities with the use of k–ω SST model of turbulence are compared in Figs. 6−10 for various velocity measurement levels *V1* to *V5* indicated in Fig. 2. The experimental results shown in Figs. 6−10 include the lowest and the highest velocity readings at each grid point. As it can be seen, most of the numerical results lie exactly in the experimental range, however, part of them fall beyond this range, especially at *V3* level. Numerical results of the velocity distribution are shown in Fig. 11. Based on these results, the Coanda effect is seen at which the air jet is attached to and detached from the ceiling and the top of the vegetable bulk. Its shape strongly affects the results at *V1* and *V3* levels. The velocity magnitude at *V3* level depends also on the disturbances caused by the guide of the measurement system. The results obtained for *V2* and *V4* levels seem to be in better agreement with experimental data. The reason for better agreement is the fact that this was a less dynamic region. Figures 6−10 show that the range of velocity readings taken at the same position is fairly wide. That means that the air flow in the stream blown out by

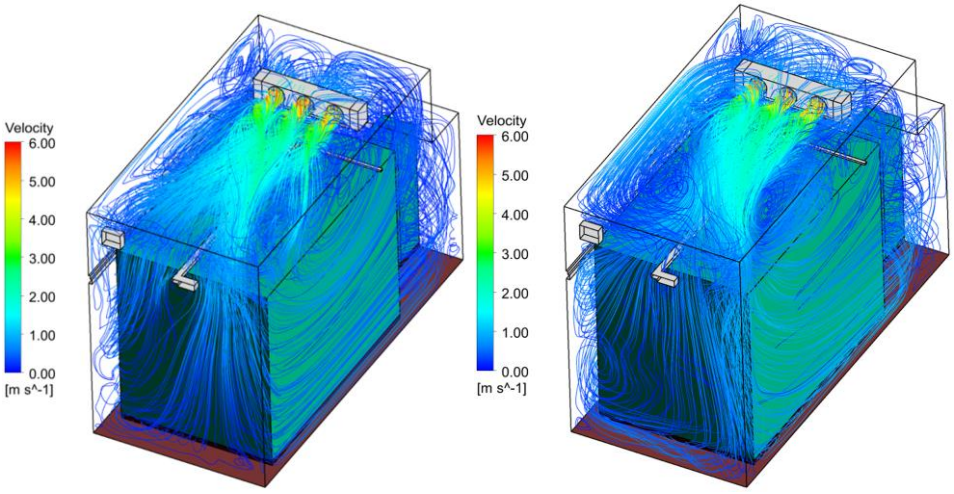

a) b)

Fig. 5. Streamlines in the chamber for two models of turbulence: a) k–ω SST, b) realizable k–ε.

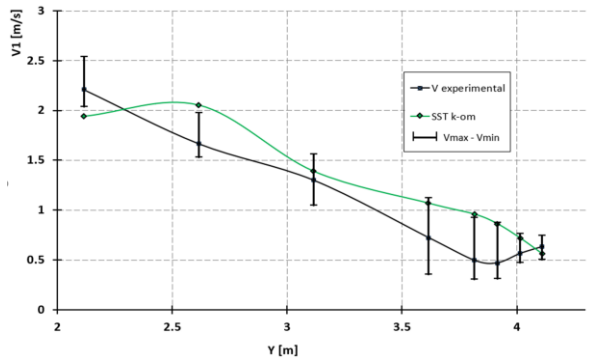

Fig. 6. Experimental and calculated velocities at *V1* level.

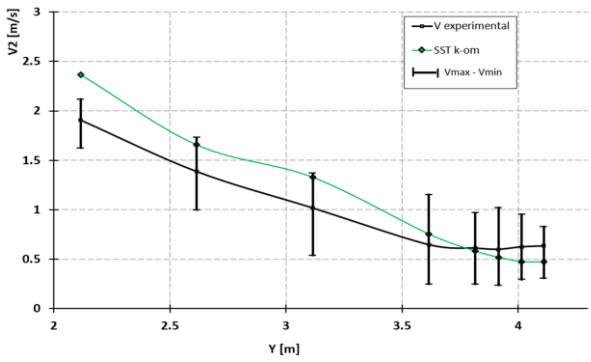

Fig. 7. Experimental and calculated velocities at *V2* level.

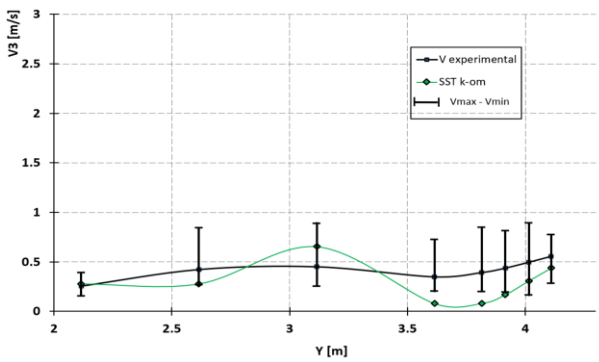

Fig. 8. Experimental and calculated velocities at *V3* level.

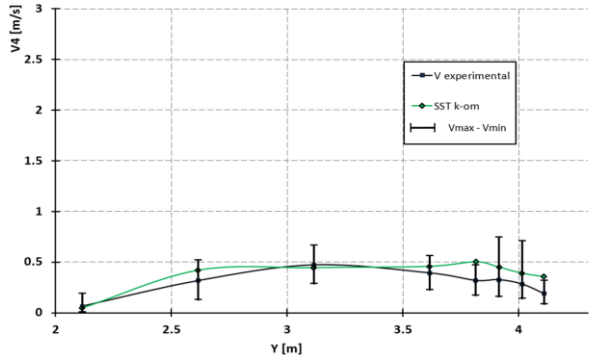

Fig. 9. Experimental and calculated velocities at *V4* level.

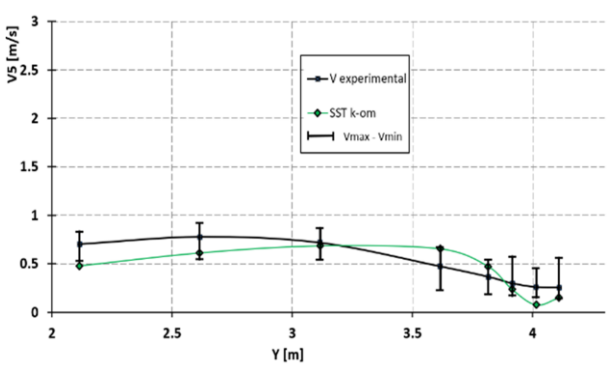

Fig. 10. Experimental and calculated velocities at *V5* level.

the fans is highly turbulent and unstable, and the instantaneous velocity fluctuates continuously around the mean value.

The interfering jets reach the vegetable bulk top surface and the supporting elements of the measurement system. Thus, the stationary process assumed here may be only a quite rough approximation of a real flow that occurs in such a complex system. The comparison shows that further research is required in modelling the air stream from the cooler. The k–ω SST turbulence model proved to be the best one from all the RANS models tested. However, the other time dependent models should be considered in future research, bearing in mind that the use of the SAS model has made no significant improvement.

From our own experience, we can conclude that modelling the physical properties of the outflow from the fans is equally important as modelling the turbulence, because of its great impact on the Coanda effect. An improper divergence angle or jet swirling may have a great impact on the air flow causing gross errors. The obtained results reveal that improvements in modelling of the outflow and turbulence require joint treatment as a single task, which is a very tedious and laborious process.

Table 4 presents the comparison of experimental results and predicted numerical results in terms of relative humidity of air and temperature in the vegetable bulk. Symbols δ_{RH} and δ_t denote mean relative differences between computed and measured values. The best agreement between calculated and experimental results of the relative humidity occurs to be at 7 and 8 verticals, i.e. at the points located below the main stream of air. Based on these results it can be stated that models of transpiration and respiration of vegetables, their coupling with processes occurring in the air cooler as well as the air flow in the vegetable bed are the most crucial issues affecting the relative humidity distribution. Other correlations than those used in this study may better predict the relative humidity distributions. Another factor that is not taken into account in the present model but potentially influencing the results is the freezing of water in the cooler. Accumulation of ice is a serious problem in the real operation of air coolers, requiring periodic defrosting which, in turn, disturbs thermal equilibrium in the chamber and produces a serious impact on the measurements executed even long after the defrost process [41]. During the measurements performed in this case, the air cooler was free of frost, as indicated by the level of velocity magnitude in Fig. 4. In the case of frost accumulation at the air cooler surface, the velocity gradually decreases in time, because of a gradually increasing drag.

Experiments show that the loss-in-weight caused by the drying process after 90-day storage depends on the location in the chamber. The greatest loss of about 11% was obtained in the external rows of the vegetable bulk (at the corner of the bulk opposite to the cooler). This loss is decreasing significantly in the direction of the cooler up to 5% in the column of boxes located at the corner under the cooler. The least shrinkage due to the drying process (about 2−3%) occurred in the column of boxes located in the middle of the bulk and in the column located just under the cooler (about 5%). The overall humidity of air in the jet blown by the fans was moderately low, about 88−89 % (see Table 4), and this was the reason for the shrinkage due to the drying process that occurred at the sides of the bulk most ventilated by the air.

In the middle of the bulk and near the cooler, the lower air flow in the bulk indicated in Fig. 7 did not disturb the humidity generated by transpiration of the cabbage, which resulted in lower shrinkage in these areas.

Based on the calculated velocity and relative humidity distributions presented in Figs. 11 and. 12, the areas in the bulk near the side opposite the cooler, its left and right sides, and the top of the bed − are the most ventilated places of the cabbage bed. Although they have a lower temperature (see Fig. 13), the relative humidity there is lower than in the middle of the bulk. This is a result of higher transpiration caused by the intensive air flow. The water vapour sources distribution S_v, which is shown in Fig. 14, illustrates the process of transpiration of the stored vegetables.

The areas of the greatest magnitude of S_v cover the areas of the least magnitudes of relative humidity and the areas of the highest velocities in the vegetable bulk. The computed water vapour generation rate in the whole bulk was equal to 0.124 kg/h, which after 90-day storage gives a mass loss of 8.8%. This result as well as the relative humidity and S_v distributions prove not only the quali-

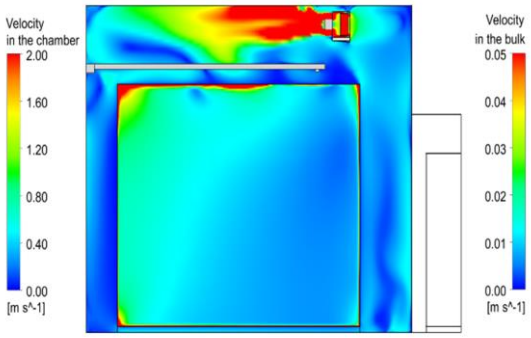

Fig. 11. Velocity distribution in the mid-plane (X = 0.99 m).

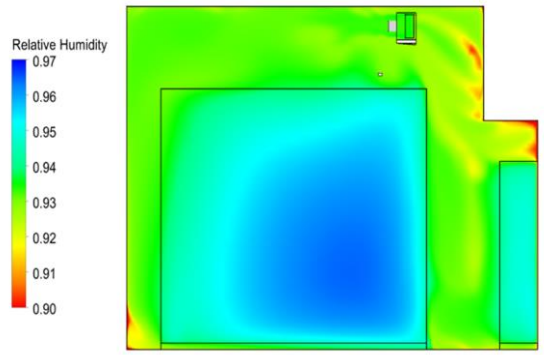

Fig. 12. Relative humidity distribution in the section of the chamber through the fan 1 (X = 0.64 m).

Table 4. Experimental results vs. calculated results.

	Relative humidity of air at RH level (%)								Air temperature in the bulk (K)						
	1	2	3	4	5	6	7	8	1	2	3	4	5	6	7
Exp. values	88.4	88.2	88.0	87.9	87.2	89.1	89.7	88.8	274.36	274.36	274.13	273.93	273.93	274.00	273.94
Calc. values	93.20	93.20	93.20	93.19	93.20	93.22	93.22	93.19	274.33	274.32	274.31	274.32	274.28	274.15	274.19
δ_{RH} (%)	5.43	5.67	5.90	6.02	6.88	4.62	3.92	4.94	–	–	–	–	–	–	–
δ_t (%)	–	–	–	–	–	–	–	–	0.01	0.02	0.07	0.14	0.13	0.06	0.09

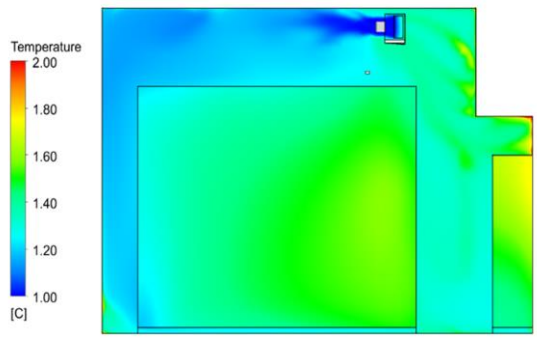

Fig. 13. Temperature distribution in the section of the chamber

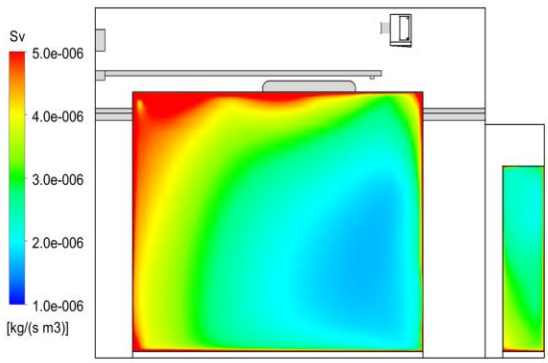

Fig. 14. The distribution of water vapour sources S_v due to transpiration of the cabbage in the section of the chamber through the fan 1 (X = 0.64 m).

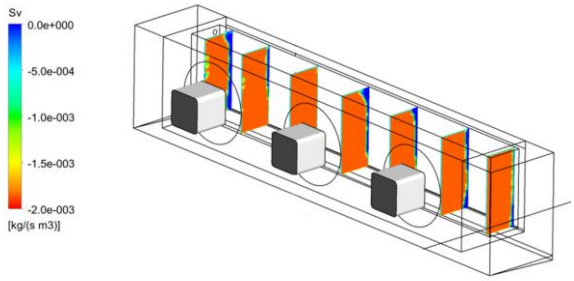

Fig. 15. Condensation rate distribution in the heat exchanger.

tative, but also quantitative reasonable agreement of experimental and computed results, and confirm the validity of the model.

Condensation occurred in the air cooler evaluated as the volumetric water vapour sinks distribution is shown in Fig. 15. The regions where condensation starts are clearly visualised by the sharp boundaries between blue and red colours. The overall condensation rate was equal to 0.116 kg/h, which gives an imbalance of 6.5% between the water vapour generation and destruction in the whole cold storage chamber.

Despite the moderate agreement between numerical and experimental results of velocity, the relative humidity and air temperatures in the vegetable bulk well correspond to each other, see Table 4. The highest temperature difference between experimental data and calculated results was found to be 0.39 K at point *Tp4* located in the middle of the bulk.

The influence of airflow outside the bulk on the conditions inside the bulk is not as large as it was expected. The temperature distribution at the plane cutting the fan 1 (X = 0.64 m) of air in a free space of the chamber and air inside the vegetable bulk is presented in Fig. 13. The greatest temperature was obtained in the boxes in the antechamber as a result of poor ventilation. The impact of heat transfer through outer walls and the highest respiration of the vegetables is presented in Fig. 16. In the main bulk the maximum vegetable temperature was inside the bulk beneath the cooler, where the air penetration was the poorest and the respiretion at its highest. The range of spatial differences of respiratory heat generation rates was very narrow due to small temperature differences in the bulk. This means that the air flow has the greatest impact on the stored vegetable temperature.

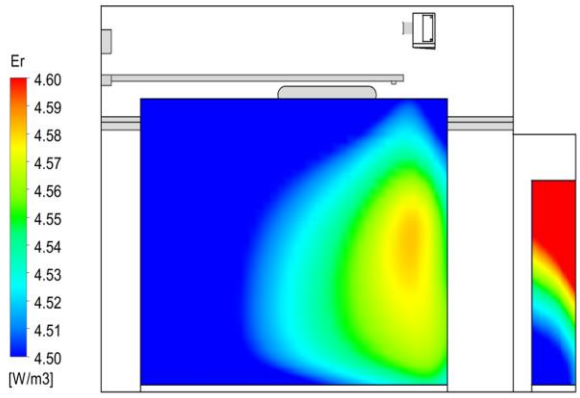

Fig. 16. Respiratory heat generation rate distribution in the section of the chamber through the fan 1 (X = 0.64m).

The heat transfer coefficient between air and cabbage was found to be in the range of 1−7 W/(m^{2}K) and reached the greatest values in the areas of the highest velocities, see Fig. 17. The heat transfer coefficient distribution in the heat exchanger was very uniform. It ranged between 32 W/(m^{2}K) and 34 W/(m^{2}K). The total cooling capacity at the steady-state operation conditions was found to be 256.3 W which is much less than the nominal capacity of the cooler 1148 W declared by the manufacturer. The flow rate of air was equal to 0.307 m^3/s (1105.3 m^3/h), i.e. exactly equal to the nominal data.

5. Conclusions

The following conclusions can be drawn based on the presented results:

- Postharvest life processes of the vegetable bed and heat transfer in the bulk should be considered together with heat and mass transfer in the cooling unit as one computational task;
- The coupling between the vapour production in the bulk and condensation in the cooler is the most distinctive featu-

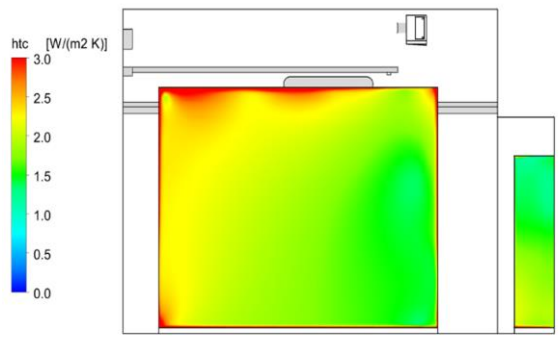

Fig. 17. Contour map of convective heat transfer coefficient between cabbage and air in the section of the chamber through the fan 1 (X = 0.64 m).

re of the model. This feature is vitally important for operation under conditions close to saturation;

- The proper modelling is a complex task that requires the thermal non-equilibrium approach, supported by UDFs. In this paper, the porous media were applied both to the bulk of vegetables and to the air cooler;
- Numerical simulations well predict the relative humidity of air and temperature. The mean relative differences between the results were in the range of 3−7% for the relative humidity and less than 0.2 % for the temperature;
- The heat transfer coefficient between the air and cabbage predicted by numerical simulations was found to be in the range of 1−7 W/(m^{2}K);
- Further works will involve an improved model of prediction of the cooling capacity, including heat transfer between the air side and the inside of the exchanger tubes, and the frosting on the tubes and fins. Further research has also to be done in order to include in the model the biological processes that occur in the vegetables that is still open issue.

Acknowledgements

The research results presented in the paper are supported by the Project No. WZ/WM-IIM/2/2023 supported by the Ministry of Science and Higher Education, Poland.

References

[1] Tian, X., Engel, B.A., Qian, H., Hua, E., Sun, S., & Wang, Y. (2021).Will reaching the maximum achievable yield potential meet future global food demand? *Journal of Cleaner Production*, 294, 126285. doi: 10.1016/j.jclepro.2021.126285

[2] Glaros, A., Marquis, S., Major, C., Quarshie, P., Ashton, L., Green, A.G., Kc, K.B., Newman, L., Newell, R., Yada, R.Y., & Fraser, E. (2022). Horizon scanning and review of the impact of five food and food production models for the global food system in 2050. *Trends in Food Science & Technology*, 119, 550–564. doi: 10.1016/j.tifs.2021.11.013

[3] Bournet, P.E, & Rojano, F. (2022). Advances of Computational Fluid Dynamics (CFD) applications in agricultural building modelling: Research, applications and challenges. *Computers and Electronics in Agriculture*, 201, 107277. doi: 10.1016/j.compag.2022.107277

[4] Janusz, S., Szudarek, M., Rudniak, L., & Borcuch M. (2023). Analysis of heat and mass transfer in an adsorption bed using CFD methods. *Archives of Thermodynamics*, 44(2), 177–194. doi: 10.24425/ather.2023.146564

[5] Hoang, H., Duret, S., Flick, D., & Laguerre, O. (2015). Preliminary study of airflow and heat transfer in a cold room filled with apple pallets: Comparison between two modelling approaches and experimental results. *Applied Thermal Engineering*, 76, 367−381. doi: 10.1016/j.applthermaleng.2014.11.012

[6] Krawczyk, K., & Badyda, K. (2011). Two-dimensional CFD modeling of the heat and mass transfer process during sewage sludge drying in a solar dryer. *Archives of Thermodynamics*, 32(4), 3–16. doi: 10.2478/v10173-011-0028-y

[7] Han, J.W., Zhao, C.J., Yang, X.T., Qian, J.P., & Fan, B.L. (2015). Computational modelling of airflow and heat transfer in a vented box during cooling: Optimal package design. *Applied Thermal Engineering*, 91, 883−893. doi: 10.1016/j.applthermaleng.2015.08.060

[8] Nalbandia, H., Seiiedlou, S., Ghasemzadeh H.R., & Rangbar, F. (2016). Innovative parallel airflow system for forced-air cooling of strawberries. *Food and Bioproducts Processing*, 100(A), 440–449. doi: 10.1016/j.fbp.2016.09.002

[9] Defraeye, T., Lambrecht, R., Delele, M.A., Tsige, A.A., Opara, U.L., Cronjé, P., Verboven, P., & Nicolai, B. (2014). Forced-convective cooling of citrus fruit: Cooling conditions and energy consumption in relation to package design. *Journal of Food Engineering*, 121, 118–127. doi: 10.1016/j.jfoodeng.2013.08.021

[10] Zhang, R., & Long, J. (2017). Study on drying uniformity of static small-sized drying box for fruits and vegetables. *Procedia Engineering*, 205, 2615–2622. doi: 10.1016/j.proeng.2017.10.201

[11] Gautam, K.R., Rong, L., Iqbal, A., & Zhang, G. (2021). Full-scale CFD simulation of commercial pig building and comparison with porous media approximation of animal occupied zone. *Computers and Electronics in Agriculture*, 186, 106206. doi: 10.1016/j.compag.2021.106206

[12] Doumbia, E.M., Janke, D., Yi, Q., Amon, T., Kriegel, M., & Hempel, S. (2021). CFD modelling of an animal occupied zone using an anisotropic porous medium model with velocity depended resistance parameters. *Computers and Electronics in Agriculture*, 181 105950. doi: 10.1016/j.compag.2020.105950

[13] Verboven, P., Hoang, M.L., Baelmans, L., & Nicolai, B.M. (2004). Airflow through beds of apples and Chicory roots. *Biosystems Engineering*, 88(1), 117−125. doi: 10.1016/j.biosystemseng. 2004.02.002

[14] Nahor, H.B., Hoang, M.L., Verboven, P., Baelmans, M., & Nicolai B.M. (2005). CFD model of the airflow, heat and mass transfer in cool stores. *International Journal of Refrigeration*, 28(3), 368−380. doi: 10.1016/j.ijrefrig.2004.08.014

[15] Mirade, P.-S., Rougier, T., Daudin, J.-D., Picque, D., & Corrieu, G. (2006). Effect of design of blowing duct on ventilation homogeneity around cheeses in a ripening chamber. *Journal of Food Engineering*, 75(1) 59−70. doi: 10.1016/j.jfoodeng.2005. 03.053

[16] Hoang, M.L., Verboven, P., De Baerdemaeker, J., & Nicolai, B.M. (2000). Analysis of the air flow in a cold store by means of computational fluid dynamics. *International Journal of Refrigeration*, 23(2), 127−140. doi: 10.1016/S0140-7007(99) 00043-2

[17] Tapsoba, M., Moureh, J., & Flick, D. (2006). Airflow patterns in an enclosure loaded with slotted pallets. *International Journal of Refrigeration*, 29(6), 899−910. doi: 10.1016/j.ijrefrig.2006.01.011

[18] Tapsoba, M., Moureh, J., & Flick, D. (2007). Airflow patterns inside slotted obstacles in a ventilated enclosure. *Computers & Fluids*, 36(5), 935−948. doi: 10.1016/j.compfluid.2006.04.002

[19] Moureh, J., Menia, N., & Flick, D. (2002). Numerical and experimental study of airflow in a typical refrigerated truck configuration loaded with pallets. *Computers and Electronics in Agriculture*, 34(1-3), 25−42. doi: 10.1016/S0168-1699(01) 00178-8

[20] Moureh, J., Tapsoba, M., & Flick, D. (2009). Airflow in a slot-ventilated enclosure partially filled with porous boxes: Part I – Measurements and simulations in the clear region. *Computers & Fluids*, 38(2), 194−205. doi: 10.1016/j.compfluid.2008.02.006

[21] Moureh, J., Tapsoba, S., & Flick, D. (2009). Airflow in a slot-ventilated enclosure partially filled with porous boxes: Part II − Measurements and simulations within porous boxes. *Computers & Fluids*, 38(2), 206−220. doi: 10.1016/j.compfluid.2008.02.007

[22] Moureh, J., & Flick, D. (2004). Airflow pattern and temperature distribution in a typical refrigerated truck configuration loaded with pallets. *International Journal of Refrigeration*, 27(5), 464−474. doi: 10.1016/j.ijrefrig.2004.03.003

[23] Ferrua, M.J., & Singh, R.P. (2009). Modeling the forced-air cooling process of fresh strawberry packages, Part I: Numerical model. *International Journal of Refrigeration*, 32(2), 335−348. doi: 10.1016/j.ijrefrig.2008.04.010

[24] Ferrua, M.J., & Singh, R.P. (2009). Modeling the forced-air cooling process of fresh strawberry packages, Part II: Experimental validation of the flow model. *International Journal of Refrigeration*, 32(2), 349−358. doi: 10.1016/j.ijrefrig.2008.04. 009

[25] Delele, M.A., Schenk, A., Tijskens, E., Ramon, H., Nicolai, B.M., & Verboven, P. (2009). Optimization of the humidification of cold stores by pressurized water atomizers based on a multi-scale CFD model. *Journal of Food Engineering*, 91(2), 228−239. doi: 10.1016/j.jfoodeng.2008.08.027

[26] Delele, M.A., Schenk, A., Ramon, H., Nicolai, B.M., & Verboven, P. (2009). Evaluation of a chicory root cold store humidification system using computational fluid dynamics. *Journal of Food Engineering*, 94(1), 110−121. doi: 10.1016/j.jfoodeng. 2009.03.004

[27] Chourasia, M.K., & Goswami, T.K. (2007). Steady state CFD modeling of airflow, heat transfer and moisture loss in a commercial potato cold store. *International Journal of Refrigeration*, 30(4), 672−689. doi: 10.1016/j.ijrefrig.2006.10. 002

[28] Xu, Y., & Burfoot, D. (1999). Simulating the bulk storage of foodstuffs. *Journal of Food Engineering*, 39(1), 23−29. doi: 10.1016/S0260-8774(98)00139-3

[29] Ansys Inc. (2015). *Ansys Fluent Theory Guide*, Release 16.0. Ansys Inc., Canonsburg.

[30] Bohojło-Wiśniewska, A. (2015). Numerical modelling of humid airflow around a porous body. *Acta Mechanica et Automatica*, 9(3), 161−166. doi: 10.1515/ama-2015-0027

[31] Śmierciew, K., Kołodziejczyk, M., Gagan J., & Butrymowicz D. (2018). Numerical modeling of fin heat exchanger in application to cold storage. *Heat Transfer Engineering*, 39(10), 874−884. doi: 10.1080/01457632.2017.1338862

[32] Butrymowicz, D., Łapiński, A., Gagan, J., & Śmierciew, K. (2016). Application of single blow technique for heat transfer measurement in packed bed of vegetables. *16th International Refrigeration and Air Conditioning Conference at Purdue*, 11–14 July, West Lafayette, USA.

[33] Becker, B.R., & Fricke, B.A. (1996). Simulation of moisture loss and heat loads in refrigerated storage of fruits and vegetables. *New Developments in Refrigeration for food Safety and Quality* (pp. 210−221), 2–4 October, Lexington, USA, International Institute of Refrigeration and American Society of Agricultural Engineers.

[34] Bird, R.B., Stewart, W.E., & Lightfoot, E.N. (2002). *Transport Phenomena*. John Wiley, New York.

[35] Nguyen, T.A., Verboven, P., Schenk, A., & Nicolai, B.M. (2007). Prediction of water loss from pears during controlled atmosphere storage a affected by relative humidity. *Journal of Food Engineering*, 83(2), 149−155. doi: 10.1016/j.jfoodeng.2007.02. 015

[36] Dehghannya, J., Ngadi, M., & Vigneault, C. (2008). Simultaneous aerodynamic and thermal analysis during cooling of stacked spheres inside ventilated packages. *Chemical Engineering Technology*, 31, (11), 1651−1659. doi: 10.1002/ceat.200800290

[37] Becker, B.R., & Fricke, B.A. (1996). Transpiration and respiration of fruits and vegetables. *New Developments in Refrigeration for Food Safety and Quality* (pp. 110−121), 2–4 October, Lexington, USA, International Institute of Refrigeration and American Society of Agricultural Engineers.

[38] ASHRAE (2006). Thermal properties of foods (Chap. 9). In *Handbook – Refrigeration*, (pp. 9.1−9.31). Inch-Pound Edition, American Society of Heating, Refrigerating and Air-Conditioning Engineers, Inc.

[39] Ma, X., Ding, G., Zhang, Y., & Wang K. (2007). Airside heat transfer and friction characteristics for enhanced fin-and-tube heat exchanger with hydrophilic coating under wet conditions. *International Journal of Refrigeration*, 30(7), 1153−1167. doi: 10.1016/j.ijrefrig.2007.03.001

[40] Kondjoyan, A. (2006). A review on surface heat and mass transfer coefficients during air chilling and storage of food products. *International Journal of Refrigeration*, 29(6), 863−875 doi: 10.1016/j.ijrefrig.2006.02.005

[41] Kołodziejczyk M., Butrymowicz D., Gagan J., & Śmierciew K. (2016). Investigations of Chinese cabbage cold storage chamber operation. *16th International Refrigeration and Air Conditioning Conference at Purdue*, 11–14 July, West Lafayette, USA

Co-published by
Institute of Fluid-Flow Machinery
Polish Academy of Sciences
Committee on Thermodynamics and Combustion
Polish Academy of Sciences

http://www.imp.gda.pl/archives-of-thermodynamics/

Mixed convection flow in a porous channel under the effects of exothermic chemical reactions and local thermal non-equilibrium

Camelia Berghian-Grosan[a], Rares Serban Pop[b], Teodor Silviu Grosan[c*]

[a]National Institute for Research and Development of Isotopic and Molecular Technologies, Donat 67-103, 400293 Cluj-Napoca, Romania
[b]University of Chester, School of Computer and Engineering Sciences, Parkgate Road, Chester, CH1 4BJ, United Kingdom
[c]Babes-Bolyai University, Department of Mathematics, M. Kogalniceanu 1, 400084 Cluj-Napoca, Romania
*Corresponding author email: teodor.grosan@ubbcluj.ro

Received: 09.04.2024; revised: 02.07.2024; accepted: 03.12.2024

Abstract

The effect of a first-order exothermic chemical reaction on the mixed flow in a vertical channel filled with a porous medium has been studied using the local thermal non-equilibrium model. A mathematical model including the exponential term for heat generation in the fluid phase and interphase heat transfer terms in both the fluid and solid phases was considered. The above dimensionless model has been solved numerically using the Matlab routine bvp4c for the energy equations together with an in-house developed code for the momentum equation. The existence of dual solutions is reported for certain values of the Frank-Kamenetskii number. The obtained profiles of temperature and velocity have been plotted. In addition, the ranges of existence of the dual solutions are reported.

Keywords: Fully developed flow; Local thermal non-equilibrium; Exothermic chemical reaction

Vol. 45(2024), No. 4, 237–242; doi: 10.24425/ather.2024.152013

Cite this manuscript as: Berghian-Grosan, C., Pop, R.S., & Grosan, T.S. (2024). Mixed convection flow in a porous channel under the effects of exothermic chemical reactions and local thermal non-equilibrium. *Archives of Thermodynamics*, 45(4), 237–242.

1. Introduction

Thermal non-equilibrium between solid and fluid phases in porous media is an important effect which is usually present when high-speed flows are involved or height porosities are present, see Vafai and Sozen [1] and Kuznetsov and Vafai [2]. Such situations are related to the study of nuclear reactor cores and in hypothetical nuclear reactor accidents, chemical reactors, etc. (see Nield and Bejan, [3]). Detailed reviews of mathematical models of heat transfer in porous media, when the thermal non-equilibrium is present, can be found in Kuznetsov [4,5]. Rees and Pop [6,7] performed a numerical and analytical study on the free convective boundary-layer flow and stagnation-point flow when the thermal non-equilibrium is taken into account. They reported that, when the solid matrix and the filling fluid are not in local thermal equilibrium, the behaviour of the flow is modified substantially. Baytas and Pop [8] studied free convection in a differentially heated square cavity using a thermal non-equilibrium model for heat transfer and the Darcy model for fluid flow. Compared to the case of thermal equilibrium, lower values of the Nusselt number were obtained in the case of thermal non-equilibrium. These values also depend on the interphase heat transfer parameters.

Self-ignition or thermal explosion can occur in heat transfer problems (e.g. in storage technology) due to chemical exothermic reactions. Such undesirable behaviour can be described using the mathematical model given by Semenov [9]. The appearance of the self-ignition/explosion is characterized by the Frank-Kamenetskii number. Critical values of this number, at which the impact occurs, are reported by Lazarovici et al. [10] for a ca-

Nomenclature

a – concentration of reactant A in Eq. (6)
c – specific heat at constant pressure, J kg^{-1}K^{-1}
Da – Darcy number
E – activation energy, J
g – gravitational acceleration, m^{2}s^{-1}
Gr – Grashof number
h – interphase heat transfer coefficient, W m^{-2}K^{-1}
H – modified inter-phase heat transfer parameter,
k – thermal conductivity, W m^{-1}K^{-1}
k_0 – pre-exponential factor
K – Frank-Kamenestkii number
K_c – critical Frank-Kamenestkii number
$\tilde{K}$ – permeability, m^2
L – characteristic length, m
N – grid dimension
p – pressure, N m^{-2}
P – dimensionless pressure
Q – exothermicity of reaction, J mol^{-1}
r_T – dimensionless value of the temperature on the boundary
R – universal gas constant, J mol^{-1}K^{-1}
Re – Reynolds number
T – temperature, K
T_0 – reference temperature, K
u, v – filtration velocity components, m s^{-1}
U – dimensionless filtration velocity
U_0 – reference velocity, m s^{-1}
x, y – Cartesian coordinates, m
X, Y – dimensionless Cartesian coordinates

Greek symbols

β – volumetric thermal expansion coefficient, K^{-1}
γ – dimensionless pressure gradient
θ – dimensionless temperature
θ' – derivative of the dimensionless temperature with respect to y
κ – thermal conductivities ratio
λ – dimensionless mixed convection parameter
μ – dynamic viscosity, kg m s^{-1}
$\tilde{\mu}$ – effective dynamic viscosity, kg m s^{-1}
μ^* – viscosities ratio
ρ – density, kg m^{-3}
ϕ – porosity

Subscripts and Superscripts

f – fluid phase
s – solid phase

vity filled with a porous medium under local thermal equilibrium conditions.

The effect of heat generated by exothermic reactions in porous media in a state of local thermal non-equilibrium has not yet been studied. Therefore, in this work, we will deal with the analysis of the effect of heat generated by an exothermic chemical reaction on the flow and heat transfer in a porous medium that is in a state of thermal non-equilibrium.

2. Mathematical model

We consider the mixed convection flow and heat transfer in the presence of exothermic chemical reactions in a vertical channel filled by a fluid porous medium (see Fig. 1). The mathematical model for convective flow in a porous medium, using the Darcy-Brinkman formulation, and considering the thermal non-equilibrium is given in [8], while details of the heat generation term due to an exothermic chemical reaction can be found in [10]. On the boundaries, the fluid and solid phases are assumed to be in local

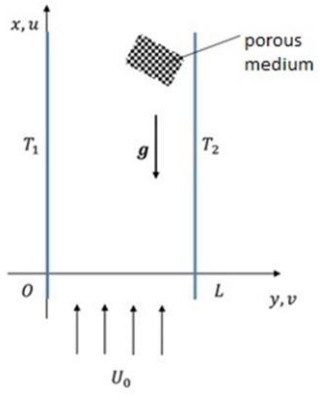

Fig. 1. Geometry of the problem.

thermal equilibrium ($T_f = T_s$). Thus, for the governing equations, a combined two temperatures model is used, considering that the heat is generated in the fluid phase. The equations of continuity, momentum and energy for fluid and solid phases are:

$$\frac{\partial u}{\partial x} + \frac{\partial v}{\partial y} = 0, \tag{1}$$

$$\frac{\partial p}{\partial x} = -\frac{\mu}{\tilde{K}} u + \tilde{\mu} \nabla^2 u + \rho g \, \beta \left(T_f - T_0\right), \tag{2}$$

$$\frac{\partial p}{\partial y} = -\frac{\mu}{\tilde{K}} v + \tilde{\mu} \, \nabla^2 v, \tag{3}$$

$$(\rho \, c)_f \left(u \frac{\partial T_f}{\partial x} + v \frac{\partial T_f}{\partial y}\right) =$$

$$= \phi k_f \left(\frac{\partial^2 T_f}{\partial x^2} + \frac{\partial^2 T_f}{\partial y^2}\right) + h\left(T_f - T_s\right) + Q k_0 a \, \mathrm{e}^{-E/RT_f}, \tag{4}$$

$$0 = (1 - \phi) k_s \left(\frac{\partial^2 T_s}{\partial x^2} + \frac{\partial^2 T_s}{\partial y^2}\right) + h\left(T_f - T_s\right). \tag{5}$$

In Eqs. (1) to (5), u and v are the components of the Darcian velocity, p is the pressure, T_f is the temperature of the fluid phase and T_s is the temperature of the solid phase. The physical properties of the fluid are given in Nomenclature.

Following the Arrhenius kinetics (see [10]) where the reactant A is transformed in the product B

$$A \rightarrow B + \text{heat}, \quad \text{rate} = k_0 a \, \mathrm{e}^{-E/RT}, \tag{6}$$

and the heat generated by a first order exothermic chemical reaction in the fluid phase is expressed by adding the term $Q k_0 a \, \mathrm{e}^{-E/RT_f}$ in Eq. (4).

Next, we assume that the process takes place far from the channel entrance and that the flow is fully developed, see Aung and Worku [11]:

$$v = 0, \quad \frac{\partial u}{\partial x} = 0, \quad \frac{\partial T}{\partial x} = 0, \quad \frac{\partial p}{\partial y} = 0, \quad \frac{\partial p}{\partial x} = \frac{dp}{dx} = \text{const.} \quad (7)$$

Thus, using assumptions (7) in Eqs. (1) to (5), the governing equations are:

$$\frac{dp}{dx} = -\frac{\mu}{\tilde{K}}u + \tilde{\mu}\,\frac{d^2u}{dy^2} + \rho g\,\beta\left(T_f - T_0\right), \quad (8)$$

$$0 = \phi k_f \frac{d^2T}{dy^2} + h\left(T_s - T_f\right) + Qk_0 a\, e^{-E/RT_f}, \quad (9)$$

$$0 = (1-\phi)k_s \frac{d^2T_s}{dy^2} + h\left(T_f - T_s\right), \quad (10)$$

along with the boundary conditions:

$$\begin{gathered} u = 0 \quad \text{at } y = 0 \quad \text{and} \quad y = L, \\ T_f = T_s = T_1 \quad \text{at } y = 0, \\ T_f = T_s = T_2 \quad \text{at } y = L, \\ T_1 > T_2. \end{gathered} \quad (11)$$

In order to solve Eqs. (8)–(11) and find the pressure gradient $\frac{dp}{dx}$, it is necessary to add a new equation related to the conservation of mass flow rate (see, Aung and Worku [11] and Cimpan [12]):

$$\int_0^L u dy = M = U_0 L. \quad (12)$$

By using the following dimensionless variables in Eqs. (8)–(12):

$$X = \frac{x}{\mathrm{Re}L}, \quad Y = \frac{y}{L}, \quad U = \frac{u}{U_0}, \quad P = \frac{p}{\rho U_0^2}, \quad \theta_f = \frac{T_f - T_0}{RT_0^2/E},$$

$$\theta_s = \frac{T_s - T_0}{RT_0^2/E}, \quad \mathrm{Re} = \frac{U_0 L}{\nu}, \quad T_0 = \frac{T_1 + T_2}{2}, \quad (13)$$

the mathematical model in the dimensionless form is obtained:

$$\gamma = -\frac{1}{\mathrm{Da}}U + \mu^* \frac{d^2U}{dY^2} + \lambda\theta_f, \quad (14)$$

$$0 = \frac{d^2\theta_f}{dY^2} + H\left(\theta_s - \theta_f\right) + \mathrm{K}\, e^{\theta_f}, \quad (15)$$

$$0 = \frac{d^2\theta_s}{dY^2} + \kappa H\left(\theta_f - \theta_s\right), \quad (16)$$

$$\begin{gathered} U = 0 \quad \text{at } Y = 0 \quad \text{and} \quad Y = 1, \\ \theta_f = \theta_s = r_T \quad \text{at } Y = 0, \\ \theta_f = \theta_s = -r_T \quad \text{at } Y = 1, \end{gathered} \quad (17)$$

$$\int_0^1 U dY = 1. \quad (18)$$

The governing parameters in Eqs. (14)–(17) are:

$\gamma = \frac{dP}{dX}$ (dimensionless pressure gradient),

$\mathrm{Da} = \frac{\tilde{K}}{L^2}$ (Darcy number),

$\mu^* = \frac{\tilde{\mu}}{\mu}$ (viscosities ratio in the Brinkman model),

$\lambda = \frac{\mathrm{Gr}}{\mathrm{Re}}$ (mixed convection parameter),

$\mathrm{Gr} = \frac{g\beta\left(\frac{RT_0^2}{E}\right)L^3}{\nu^2}$ (Grashof number),

$\mathrm{K} = \frac{Qk_0 aL^2}{\phi k_f\left(\frac{RT_0^2}{E}\right)} e^{-\frac{E}{RT_0}}$ (Frank-Kamenestkii number),

$\kappa = \frac{\phi k_f}{(1-\phi)k_s}$ (thermal conductivity ratio),

$r_T = \frac{T_1 - T_2}{2RT_0^2/E}$ (boundary condition parameter).

Assuming a large activation energy $\left(\frac{RT_0}{E} \ll 1\right)$, a Taylor expansion was used to derive the energy equation for the fluid phase, Eq. (15). Here, the Frank-Kamenestkii number K measures the heat produced by the reaction relative to its loss by Newtonian cooling and is responsible for the occurrence of the thermal explosion/ignition, see [10].

3. Numerical solution and results

We have solved the system of Eqs. (15) and (16) using the routine *bvp4c* from Matlab, using a prescribed error set to 10^{-9}. This routine uses a collocation method on a non-uniform mesh to solve boundary value problems. The method requires an initial mesh and an initial approximate solution, then during the solution process the error is estimated at each subinterval, and the mesh is adjusted to achieve the convergence. The energy equation (15) is very close to the well-known Bratu's equation [13], where $\theta(0) = \theta(1) = 0$. Similar to [13], it was found that there is a critical value of the parameter $\mathrm{K}_c(r_T, H, \kappa)$, which is the point of thermal explosion.

For $0 < \mathrm{K} < \mathrm{K}_c$, there are two solutions for the temperature θ_f, for $\mathrm{K} = \mathrm{K}_c$, we have one solution (for this value the explosion occurs), and for $\mathrm{K} > \mathrm{K}_c$, the equation has no solution. Following [13,14], we can conclude that the lower solution is the stable one. In the particular case of local thermal equilibrium, the obtained critical values K_c were compared with those obtained by Petrusel et al. [15] (for $r_T = 0$) and Pop et al. [14], see Table 1. Increasing the value of the parameter r_T leads to a reduction of the solution domain.

Next, we study the effect of local thermal nonequilibrium on the existence of the solutions of Eqs. (15) and (16). The values, for the modified interphase heat transfer parameter and the thermal conductivity ratio, were chosen on the basis of the paper by

Table 1. Values of the critical Frank-Kamenetskii number for different values of the parameter r_T.

r_T	K_c		
	Petrusel et al. [14]	Pop et al. [15]	Present
0	3.513830719	–	3.513959
0.1	–	3.51	3.510533
0.5	–	3.419	3.419371
1	–	3.155	3.155131
2	–	2.332	2.332904

Baytas and Pop [8]. The effect of varying the parameters H and κ on the range of existence of solutions is shown in Figs. 2 to 5.

The variation of the stable temperature profiles of the two phases (fluid phase and solid phase) with the boundary condition parameter r_T are given in Figs. 6 and 7. The maximum value of the temperature increases with the increase of r_T. For large values of r_T, there is an overshoot of the left boundary condition value for the θ_f profile. The same effect on the temperature profiles is observed for large values of the Frank-Kamenetskii number K, see Figs. 8 and 9.

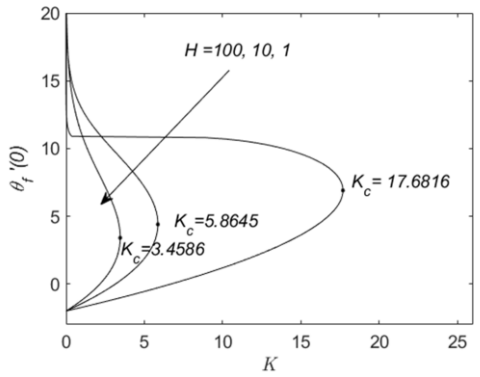

Fig. 2. Existence of dual solution and values of $\theta_f'(0)$ for different values of H when $r_T = 1$ and $\kappa = 0.1$.

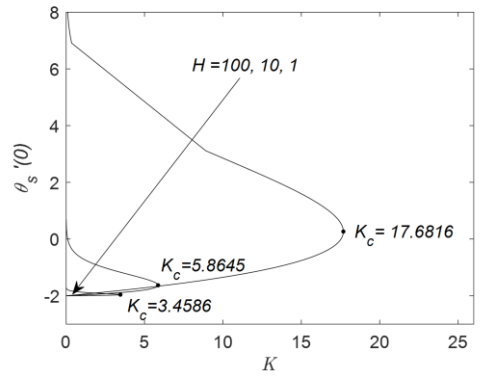

Fig. 3. Existence of dual solution and values of $\theta_s'(0)$ for different values of H when $r_T = 1$ and $\kappa = 0.1$.

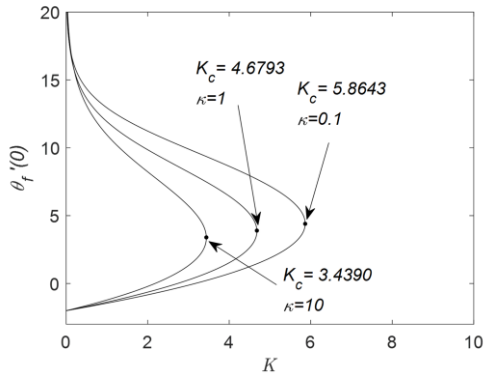

Fig. 4. Existence of dual solution and values of $\theta_f'(0)$ for different values of κ when $r_T = 1$ and $H = 10$.

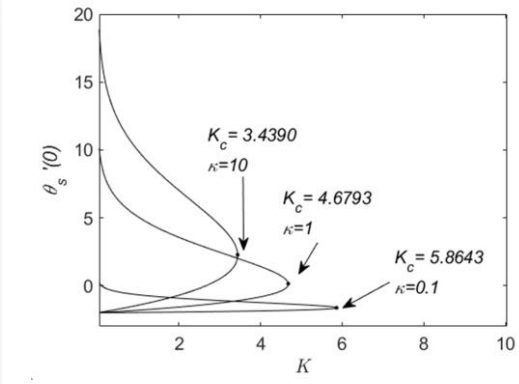

Fig. 5. Existence of dual solution and values of $\theta_s'(0)$ for different values of κ when $r_T = 1$ and $H = 10$.

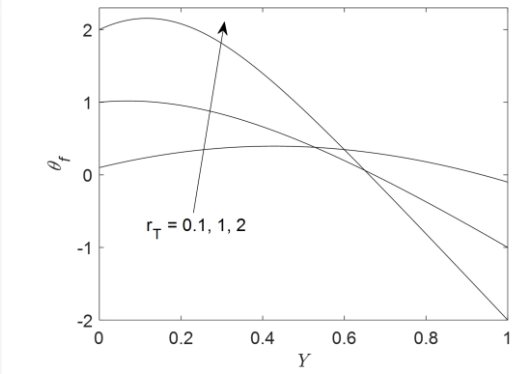

Fig. 6. Profiles of $\theta_f(Y)$ for different values of r_T when $\kappa = 2$, $H = 10$ and K = 3.

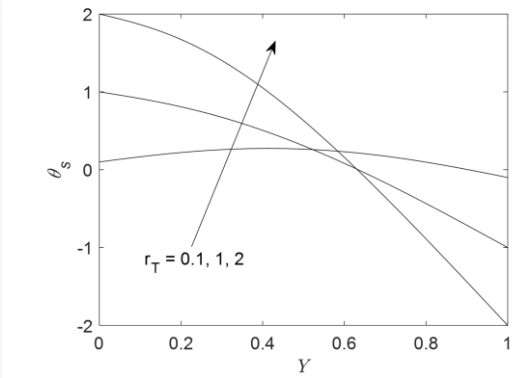

Fig. 7. Profiles of $\theta_s(Y)$ for different values of r_T when $\kappa = 2$, $H = 10$ and K = 3.

With the temperature profile obtained by solving the system of Eqs. (15) to (17), we focus on the solution of the momentum equation (14) along with the boundary conditions (17). The momentum equation was discretized using central finite differences on a uniform grid of dimension N. In addition, for the mass flux conservation equation, a midpoint quadrature formula was used. The obtained system of algebraic equations was solved using an in situ-built program using Matlab routines. In order to choose the size of the grid, a dependence simulation (see Table 2) was

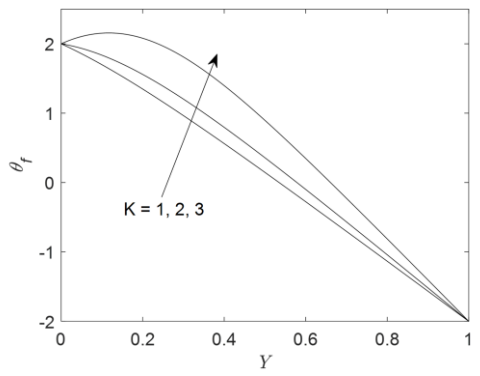

Fig. 8. Profiles of $\theta_f(Y)$ for different values of K when $\kappa = 2,\ H = 10$ and $r_T = 2$.

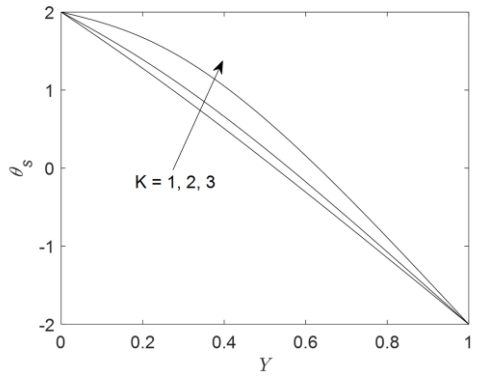

Fig. 9. Profiles of $\theta_s(Y)$ for different values of K when $\kappa = 2,\ H = 10$ and $r_T = 2$.

performed for the following values of the involved parameters: H = 10, K = 4, κ = 1, r_T = 1, λ = 1000, μ^* = 6, and Da = 10^{-2}. According to the results obtained, the numerical simulations are further carried out using a grid of dimension N = 401.

Profiles of the velocity were obtained for some typical values of the involved parameters. In this problem, the value of the viscosity ratio parameter was fixed, μ^* = 6, see Gentile and Straughan [16]. The effect of variation of parameters Da and λ on the mixed convective fully developed flow is well known. Thus, for fixed values of the flow parameters, Da = 10^{-3} and λ = 1000, we focused on the study of the effect of thermal parameters on the velocity profiles.

In Fig 10, the variation of the velocity profile with the parameter r_T is depicted. For large values of the parameter r_T, we notice the presence of the reverse flow near the cold (right) wall. Large values of r_T imply a large temperature difference between the left and right walls, and this leads to negative buoyancy forces near the cold wall, which determine the reverse flow.

Next, in order to study the effect of the interphase heat transfer parameter H on the flow, computational simulations were performed for H = 1, 10, and 100. The increase of the value of H leads to an increase of the maximum values of the velocity; the reverse flow is more visible for large values of H near the right (cold) wall, see Fig 11.

The effect of the thermal conductivities ratio κ on the velocity is shown in Fig. 12. The magnitude of U increases slowly with the increase of κ. Finally, the variation of velocity profiles with the parameter K is presented in Fig. 13. The convective flow is augmented by the increase of K due to the higher profile of temperature, see Fig. 8. The increase of the parameter also intensifies the reverse flow.

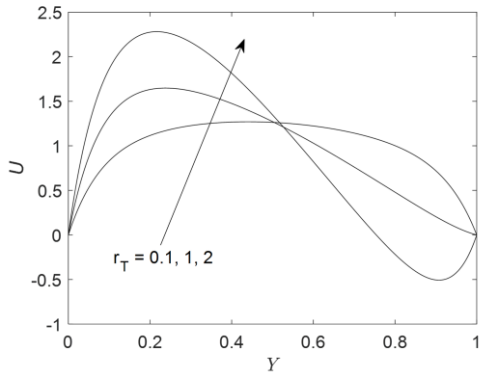

Fig. 10. Variation of velocity profiles U with r_T for K = 4, $H = 10,\ \kappa = 2$.

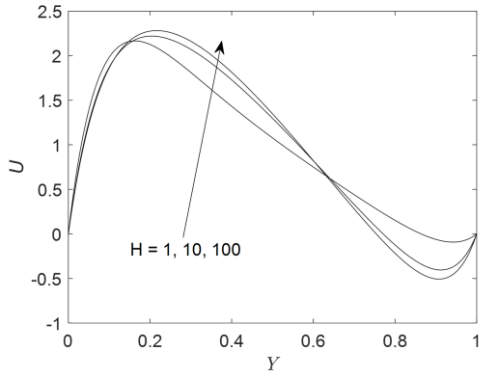

Fig. 11. Variation of velocity profiles U with H for $r_T = 2,$ K = 4, $\kappa = 2$.

Table 2. Grid dependence test.

Grid dimension, N	$\max(U)$	γ
101	3.206797	295.004812
201	3.206853	294.984245
401	3.206974	294.979059
2001	3.206979	294.977760

4. Conclusions

The effect of first order exothermic chemical reactions on the mixed convective flow in a porous medium was studied considering a thermal non-equilibrium model.

- The solution of the energy equation depends on the Frank-Kamenestkii number, K. For 0 < K < K_c (critical number), there are two solutions, for K = K_c, we have one solution and for K > K_c, the equation has no solution.

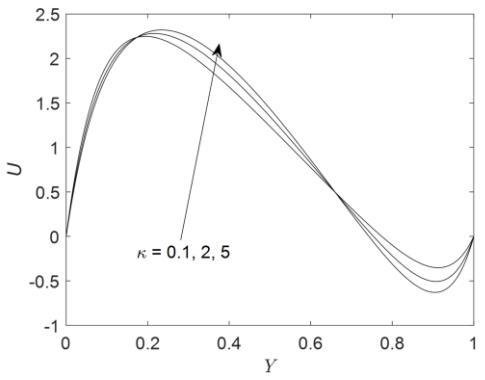

Fig. 12. Variation of velocity profiles U with κ for $r_T = 2,\ H = 10,\ K = 3$.

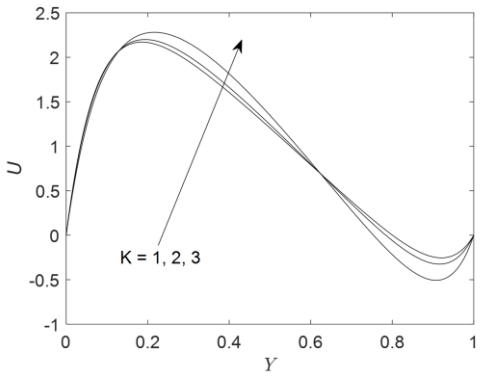

Fig. 13. Variation of velocity profiles U with K for $r_T = 2,\ H = 10,\ \kappa = 2$.

- The increase of the r_T parameter determines the apparition of the reverse flow near the cold wall.
- The magnitude of U increases with the increase of the heat transfer parameters H and κ.
- For more realistic physical modelling of the ignition/explosion occurrence, unsteady effects can be considered [17,18], while for sparse porous media Darcy-Forchheimer or Brinkman mathematical models have to be used [19].

Acknowledgements

The authors would like to acknowledge the financial support received from the grant PN-III-P4-PCE-2021-0993 (contract PCE 69/2022), UEFISCDI (Romanian Ministry of Sciences).

References

[1] Vafai, K., & Sozen, M. (1990). Analysis of energy and momentum transport for fluid flow through a porous bed. *ASME Journal of Heat Transfer*, 112(3), 690–699. doi: 10.1115/1.2910442

[2] Kuznetsov, A.V., & Vafai, K. (1995). Analytical comparison and criteria for heat and mass transfer models in metal hydride packed beds. *International Journal of Heat and Mass Transfer*, 38(15), 2873–2884. doi: 10.1016/0017-9310(94)00331-O

[3] Nield, D.A., & Bejan, A. (2017). *Convection in Porous Media.* Springer.

[4] Kuznetsov, A.V. (1996). A perturbation solution for a non thermal equilibrium fluid flow through a three dimensional sensible storage packed bed. *ASME Journal of Heat Transfer*, 118(2), 508–510. doi: 10.1115/1.2825881

[5] Kuznetsov, A.V. (1998) Thermal nonequilibrium forced convection in porous media. In *Transport Phenomena in Porous Media*, (pp. 103–129). Pergamon Oxford.

[6] Rees, D.A.S., & Pop, I. (1999). Free convective stagnation-point flow in a porous medium using a thermal nonequilibrium model. *International Communications in Heat and Mass Transfer*, 26(7), 945–954. doi: 10.1016/S0735-1933(99)00084-6

[7] Rees, D.A.S., & Pop, I. (2000). Vertical free convective boundary-layer flow in a porous medium using a thermal nonequilibrium model. *Journal on Porous Media*, 3(1), 31–44. doi: 10.1615/JPorMedia.v3.i1.30

[8] Baytas, A.C., & Pop, I. (2002). Free convection in a square porous cavity using a thermal nonequilibrium model. *International Journal of Thermal Sciences*, 41(9) 861–870. doi: 10.1016/S1290-0729(02)01379-0

[9] Semenov, N.N. (1940). Thermal theory of combustion and explosion. III Theory of normal flame propagation. *Progress of Physical Science*, 24 (4).

[10] Lazarovici, A. Volpert, V., & Merkin, J.H. (2005). Steady states, oscillations and heat explosion in a combustion problem with convection. *European Journal of Mechanics B/Fluids*, 24(2), 189–203. doi: 10.1016/j.euromechflu.2004.06.007

[11] Aung, W., & Worku, G. (1986). Developing flow and flow reversal in a vertical channel with asymmetric wall temperatures. *ASME Journal of Heat Transfer*, 108(2), 299−304. doi: 10.1115/1.3246919

[12] Cimpean, D.S. (2022). Dynamics of colloidal mixture of Cu-Al_2O_3/water in an inclined porous channel due to mixed convection: Significance of entropy generation. *Coatings*, 12(9), 1347. doi: 10.3390/coatings12091347

[13] Bratu, G. (1914). Sur les équations intégrales non linéaires. *Bulletin de la Société Mathématique de France,*, 42, 113−142. doi: 10.24033/bsmf.943

[14] Pop, I., Grosan, T., & Revnic, C. (2010). Effect of heat generated by an exothermic reaction on the fully developed mixed convection flow in a vertical channel. *Communications in Nonlinear Science and Numerical Simulation*, 15(3), 471–474. doi: 10.1016/j.cnsns.2009.04.010

[15] Petrusel, A., Rus, I.A., & Serban, M.A. (2021). Theoretical and numerical considerations on Bratu-type problems. *Studia Universitatis Babes-Bolyai Matematica*, 66(1), 29–46. doi: 10.24193/subbmath. 2021.1.03

[16] Gentile, M., & Straughan, B. (2020). Bidispersive thermal convection with relatively large macropores. *Journal of Fluid Mechanics*, 898, A14. doi: 10.1017/jfm.2020.411

[17] Anjali, D., Reddimalla, N., & Ramana Murthy, J.V. (2024). Unsteady flow of a couple stress fluid due to sudden withdrawal of pressure gradient in a parallel plate channel. *Archives of Thermodynamics*, 45(3), 179–184. doi: 10.24425/ather.2024.151220

[18] Mathews, J., & Hymavathi, T. (2024). Unsteady magnetohydrodynamic free convection and heat transfer flow of Al2O3–Cu/water nanofluid over a non-linear stretching sheet in a porous medium. *Archives of Thermodynamics*, 45(1), 165–173. doi: 10.24425/ather.2024.150449

[19] Jagadha, S., Madhusudhan Rao, B., Durgaprasad, P., Gopal, D., Prakash, P., Kishan, N., & Muthunagai, K. (2023). Darcy Forchheimer two-dimensional thin flow of Jeffrey nanofluid with heat generation/absorption and thermal radiation over a stretchable flat sheet. *Archives of Thermodynamics*, 45(2), 247-259. doi: 10.24425/ather.2024.150869

Co-published by
Institute of Fluid-Flow Machinery
Polish Academy of Sciences
Committee on Thermodynamics and Combustion
Polish Academy of Sciences

http://www.imp.gda.pl/archives-of-thermodynamics/

Non-destructive measurements of fuel cladding thickness

Zbyněk Hlávač[a*], Martin Dostal[b], Ondřej Pašta[a], René Filipi[a], Marcin Kopeć[a], Leoš Assmann[a]

[a]Research Centre Řež, Hlavni 130, 250 68 Husinec-Řež, Czechia
[b]ÚJV Řež, a. s., Hlavni 130, 250 68 Husinec-Řež, Czechia
*Corresponding author email: zbynek.hlavac@cvrez.cz

Received: 13.11.2024; revised: 14.12.2024; accepted: 16.12.2024

Abstract

The method of non-destructive measuring the thickness of small-diameter thin-walled pipes consists of using the resonant frequency of vibrations in the plane of the pipe cross-section to determine the pipe wall thickness. The relative ratio of the measured frequencies determines the thickness of the thin-walled pipe with great accuracy. For small pipe diameters, the method achieves the most accurate results. The accuracy of the measurement is directly dependent on the thickness of the pipe wall and for very thin walls the method achieves the highest accuracy. The invention relates to a method of non-destructively measuring the thickness of pipes that can only be accessed from the outside or just possibly from the inside. Particularly good results are obtained with thin-walled pipes of small diameter, such as nuclear fuel cladding or steam generator pipes. Measurement of the cladding thickness is important for downstream activities such as nuclear fuel inspections or thermomechanical calculations. The non-destructive form of measuring the thickness of thin-walled components such as fuel claddings opens the possibility of expanding activities within the inspection of energy equipment to other areas of industry, testing, or structural diagnostics.

Keywords: Wall thickness; Non-destructive testing; Impact-echo; Fuel cladding; Resonant method

Vol. 45(2024), No. 4, 243–250; doi: 10.24425/ather.2024.152014

Cite this manuscript as: Hlaváč, Z., Dostal, M., Pašta, O., Filipi, R., Kopeć, M., & Assmann, L. (2024). Non-destructive measurements of fuel cladding thickness. *Archives of Thermodynamics*, 45(4), 243–250.

1. Introduction

For decades, the non-destructive testing (NDT) techniques like x-ray radiography, eddy currents or ultrasonic testing (UT) [1,2] control processes of the fuel cladding to verify its behaviour and ensure the best quality of the fuel that directly relates to the nuclear safety and efficient operation of the power unit. The tube wall measurements with the use of NDT are one of the key aspects of the surveillance and monitoring policy during the maintenance of any technological unit based on piping with an internal medium. Among the methods used for the measurements of fuel claddings (and its coatings), the UT technology is probably in the widest use due to the long history of this technology, and not only in the nuclear industry [1,3]. To address the problems of thin-wall measurements of fuel cladding, especially in a still non-active state, the methods from other industry branches can be applied.

Current technologies developed with the high-precision principle allow for the measurements with the precision of low tens of microns [2–4]. The producers of the equipment for the coating and protective layer measurements are working to increase the precision due to the added layer nominal thicknesses being mostly below the standard resolution [5]. In the case of measuring pipes with very thin walls, such as nuclear fuel claddings, where the wall thickness is less than 600 μm, the accuracy of the UT method is in many cases insufficient.

Nomenclature

B_n – multiplier of n-mode of oscillation
d – diameter, m
E – elastic modulus, m^2/s
f – frequency, Hz
f_r – ring mode frequency, Hz
f_n – in-plane mode frequency, Hz
L – length of the tube, m
m – mass, kg
t – wall thickness, m
T – transit time, s
v – wave propagation speed, m/s
V – volume, m^3

Greek symbols
ρ – density, kg/m^3

Subscripts and Superscripts
n – number of high harmonics

Abbreviations and Acronyms
CVR – Research Centre Řež
NDT – non-destructive testing
UT – ultrasonic testing

Especially crucial components, extremely endangered to the material loss, are thin-walled parts widely used in e.g. aerospace industry, technological paths of the medium distribution [6,7] or nuclear fuel claddings [8,9]. In this way, from the gas industry and chemical processes up to the nuclear technologies, the precise measurements of the medium piping are a key factor to estimate the manufacturing quality, wear and endurance of the used tubes.

In the case of nuclear fuel claddings, the control of their wall thickness is important during the manufacturing to ensure the designed condition of the fuel, also during the performance in the power unit to investigate any potential defects.

The measurement of the wall thickness of thin-walled parts in the mechanical engineering industry is most often carried out by micrometric measurement [10]. This measurement is carried out randomly on the production lines to check the accuracy of production, taking into account the requirements of the end customer. The measurement itself is carried out using a micrometre, the accuracy of which is around 10 μm and is mainly influenced by the temperature of the instrument, the object to be measured, but also by the personnel performing the measurement, the roughness of the surface and the degree of surface contamination. This method cannot be applied on closed pipes or in inaccessible locations, for example far from the pipe edges. An example of such a situation is a fuel rod containing nuclear fuel, the opening of which would result in contamination of the immediate environment [11].

Metallographic cuttings and subsequent microscopic measurements represent a very precise destructive method [12]. The great advantage of this method is its accuracy which is in the order of several microns, Fig. 1. The disadvantage is the low flexibility in terms of determination of the thickness location, and the time and technologically consuming process of sample preparation for microscopy. In terms of industry, the use of this method is very limited and is reserved almost exclusively for laboratory environments. The technology can be performed on radioactive samples such as nuclear fuel claddings [13]. However, the transport of fuel assemblies to the hot cells usually takes place several years after the fuel has been removed from the reactor core and the method is therefore in principle unsuitable.

The shortcomings of the conventional methods are eliminated by the resonant method measuring the pipe's wall thickness. It works without the need to disassemble or damage the structure, in a relatively short time and at an arbitrarily chosen location in the pipe. It uses one or more resonant frequencies of the pipe, which are allowed to oscillate in the plane of the pipe cross-section.

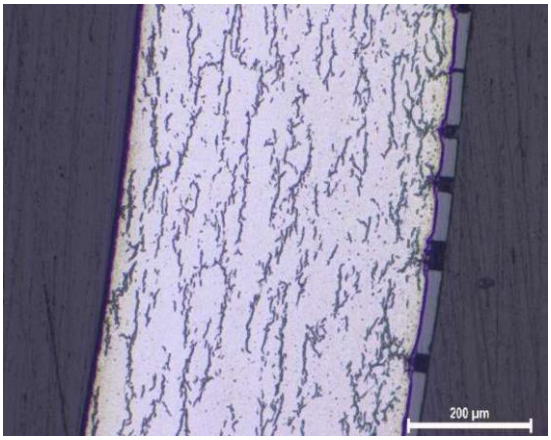

Fig. 1. The metallographic cross-section for E110 fuel cladding of 585 μm wall thickness [14].

The Research Centre Řež (Czech − *Centrum výzkumu Řež*, CVR) during the last few years has been working on the UT technology being able to measure the thin-wall tube thickness with a resolution of less than 1 μm. The main motivation for this activity was to investigate the fuel rod batches for their homogenous production (quality) and its following issues: fuel pellet gap, on-surface sedimentation, mechanical degradation of the fuel cladding and wear determination [15,16]. Currently, CVR is able to introduce a method that is capable of reaching the precision of 1 micrometre. The method was verified and validated on the fuel rod mock-ups prepared from Zr-1%Nb cladding tubes with the end caps and able to be pressurized to verify the cladding behaviour under real conditions. The conducted research and development (R&D) activities lead towards the patenting of the method with the potential use in a whole variety of industrial branches [17].

2. Resonant frequency of O-tube wall

Non-destructive method of thickness measurement of pipes works uses one or more resonant frequencies in the plane of the

pipe cross-section. It can be triggered by a short blow with a rigid object such as a hammer. This is the so-called impact-echo method.

It is also possible to excite by gradual sweeping, i.e. forced harmonic oscillation, where its wavelength gradually changes over time to cover a wider frequency spectrum, while the amplitude of the excited signal remains the same. This is a classical resonance method. Tested O-shape pipes oscillate more intensely at fundamental frequencies, with a greater amplitude. This is then scanned by an electro-acoustic probe, recorded and displayed by an oscilloscope. The oscillations with the highest amplitudes then correspond to the fundamental frequencies, i.e. the resonant frequencies of the pipe.

The pipe's excited oscillations come in a variety of different shapes, but this method only deals with some of them. For thickness measurements of small diameter thin-walled pipes, it has been proven useful to work with higher frequencies and to use the frequency of oscillation of the pipe in the plane of its cross-section. These natural fundamental frequencies can not only be measured but also predicted by calculation.

Important parameters that enter the fundamental frequency calculation are the material and geometrical properties of the pipe, and possibly also external influences that affect the pipe. The method does not consider these external influences further for the calculations. However, they cannot be neglected. It is therefore advisable to avoid such influences during the measurement. These are mainly external boundary conditions such as the way the pipe is supported or suspended, the filling or wrapping of the pipe or its pressurisation. A specific case of such external conditions are coatings or oxidation layers. The use of these circumstances will be shown in the section with examples of implementation of the invention.

Among the material properties of the pipe, the elastic modulus and the density of the pipe material are particularly important properties for predicting the fundamental frequency. Both these properties can also be expressed in terms of the propagation speed of longitudinal elastic waves.

Among the geometrical properties, the diameter of the pipe and its wall thickness are important for frequency prediction. From the following equations for predicting the selected natural frequencies, it is possible to express just the pipe wall thickness as a function of the above-mentioned variables [18–20]:

$$f_r = \frac{v}{\pi d}, \tag{1}$$

$$f_n = \frac{n(n^2-1)}{\pi d^2\sqrt{n^2+1}}\sqrt{\frac{1}{3}\frac{Et^2}{\rho}}, \quad n = 1, 2, 3. \tag{2}$$

Here f_r and f_n are the ring mode and in-plane bending mode frequencies, n is the number of high harmonics, v is the P-wave propagation speed, d is the diameter of the circular pipe, E is the elastic modulus, t is the wall thickness, and ρ the specific density of the pipe material.

Generally, the method works for all pipe sizes and shapes. However, its extraordinary accuracy is depended on the wall thickness, and also on the diameter of the pipe. For very small, thin-walled pipes, such as nuclear fuel claddings, the precision can be achieved even in the range of microns.

Probes for measuring the local thickness of the cladding can be part of the standard equipment used for fuel inspection, for example in spent fuel pools. Being watertight and having high resistance to radiation are prerequisites.

The undeniable advantage of the non-destructive thickness measurement method is that the oscillation sensor can be an ultrasonic probe that is sufficiently resistant to water and radioactive gamma radiation. It is advantageous that the evaluation equipment, which is sensitive to radioactive radiation, can be concealed at a sufficient distance from the source of ionising radiation.

The invention is further elucidated by means of the drawings, where Fig. 2 shows the oscillation shapes of a circular cross-section pipe. Figure 3 shows an example of the frequency spectrum of the measured signal including the peaks of some interesting resonant frequencies of the pipe.

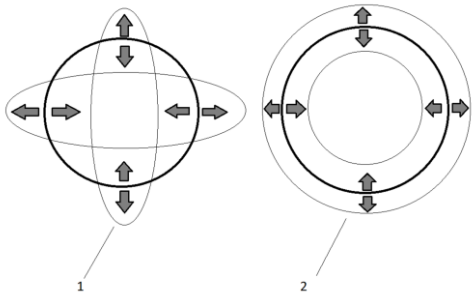

Fig. 2. The shape of the pipe oscillation in the cross-section plane via in-plane bending mode – *1*, ring mode – *2*.

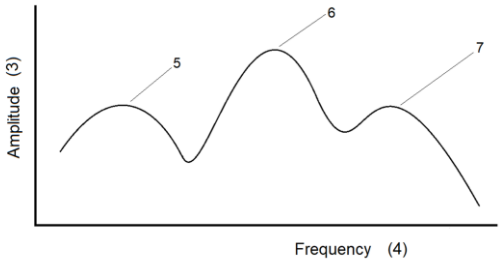

Fig. 3. Example of frequency response diagram: *3*− amplitude axis, *4* − frequency axis, *5* − resonance frequency peak of the cross-section for the in-plane bending mode and *6* − for the ring mode, *7* − for a higher harmonic.

2.1. Thin-walled tube measurement

One specific example of the use of this method is the measurement of the local thickness of nuclear fuel claddings during periodic inspections where the local geometry enters in a further calculation and/or measurement. An example is the measurement of the pressure inside a fuel rod, where the wall thickness is determined by the design of the specific fuel, but long-term measurements show standard deviations of up to 20 μm from the designed value. However, such accuracy cannot be counted on in sensitive fuel rod calculations.

Another application of the method is to verify the thickness of the oxidation layer, or the thickness of the healthy pipe material. This is particularly advantageous when oxidation occurs inside the pipe and the accuracy of conventionally used methods is not sufficient.

The method can be used even if the pipe is coated with a coating that cannot be removed for some reason. Even in this case, it is possible to determine the thickness of the pipe material accurately enough. However, slight variations due to the unknown stiffness of the coating must be taken into account.

There are many inherent oscillation shapes that could be used to predict pipe thickness. However, the best results are achieved by combining the fundamental frequency of oscillation in the plane of the pipe cross-section with in-plane bending mode and ring mode, Fig. 2. Incorporating both frequencies *5* and *6* into the appropriate relationship along with the pipe diameter will give a reasonably accurate pipe thickness result. One of the above-mentioned frequencies can then be replaced in the calculation of the pipe wall thickness by the velocity of propagation of longitudinal elastic waves, or by the square root of the ratio of the elastic modulus and density of the pipe material

$$v = \sqrt{\frac{E}{\rho}}, \tag{3}$$

where v is the propagation speed of longitudinal elastic waves, E is the elastic modulus and ρ is the specific density of the pipe's material.

The fundamental frequencies can be found in Fig. 3 where the amplitude (axis *3*) is a function of frequency (axis *4*). Fundamental frequencies appear as so-called frequency peaks (*5* to *7*). However, without the first estimation of the two peaks *5* and *6* as accurately as it could, it is impossible to find the frequency peaks in the complex frequency spectrum, Fig. 2. The spectrum contains also a number of high harmonic's peaks *7*, noise and other obscured peaks.

Nevertheless, the method, location and intensity of excitation must be adapted to the measurement of each frequency. All instruments must be set up for the particular oscillation that may be measured. It is also recommended to verify the gain of the correct values by fitting them to the pre-prepared relations, Eqs. (1) and (2). Those have been based on a good estimation of the pipe wall thickness and the longitudinal elastic-wave propagation velocity.

2.2. Fuel cladding computer model and oscillation

The Abaqus program was used for modelling the nuclear fuel cladding type Zr-1%Nb and its oscillation modes. Results fit well with the measurement, see Section 4. The best results of in-plane bending mode oscillation f_n, within n = 2 to 4, were obtained using a 23.4 mm long model (see Figs. 5 to 7). The outer diameter of Zr-1%Nb cladding is 9.1 mm. The ring mode oscillation f_r correlates more with the reality in the case of a short tube or ring of the length L = 2.34 mm, Fig. 4.

The material was modelled as elastic, using Young's modulus and Poisson's ratio of Zr-1%Nb at room temperature. Quadratic finite elements were applied in a static analysis, which was conducted just prior to the frequency analysis (using the Lanczos solver) to enable the modelling of various conditions. The examples of the oscillation shapes at frequencies f_2 (or f_2'), f_3 (or f_3') and f_4 (or f_4') are shown in Figs. 5, 6 and 7, respectively.

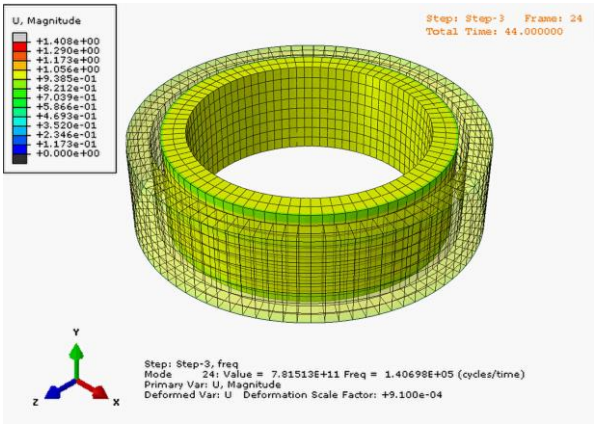

Fig. 4. Ring mode of Zr-1%Nb cladding oscillation modelled in the Abaqus program: mode 24, frequency f_r = 140 698 Hz).

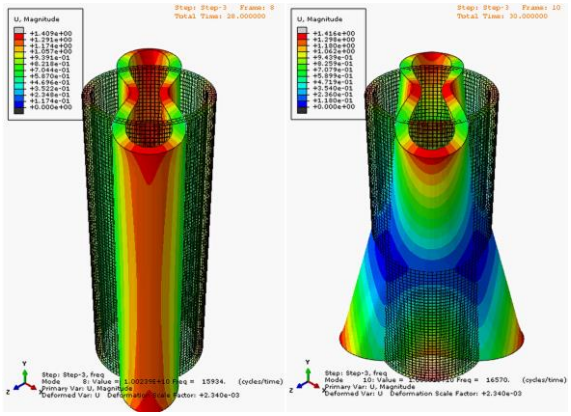

Fig. 5. In-plane bending mode of Zr-1%Nb cladding oscillation modelled in Abaqus: mode 8, frequency f_2 = 15 934 Hz (left); mode 10, frequency f_2' = 16 570 Hz (right).

3. Analog calculation of the wall thickness

The O-tube wall thickness can be measured either by commonly used destructive and non-destructive testing methods or by a newly developed resonant method.

3.1. Resonant method

One specific when it is necessary to express the wall thickness of the pipe t based on the constant speed of the ultrasonic signal propagation v, the outer diameter d_1, and the frequency of the in-plane bending mode of the cross-section f_n, for n = 1 to infinity, the following approach can be taken on the basis of Eq. (2):

$$f_n = \frac{\sqrt{B_n}}{\pi} \frac{v}{(d_1 - t)^2} t. \tag{4}$$

Thus

$$(d_1 - t)^2 = \frac{\sqrt{B_n}}{\pi} \frac{v}{f_n} t,$$

$$t^2 - 2d_1 t + d_1^2 = \frac{\sqrt{B_n}}{\pi} \frac{v}{f_n} t,$$

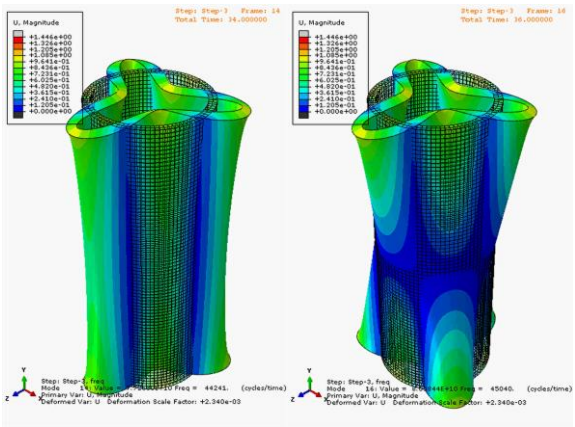

Fig. 6. In-plane bending mode of Zr-1%Nb cladding oscillation modelled in Abaqus, mode 14: frequency f_3 = 44 241 Hz (left), mode 16: frequency f_3' = 45 050 Hz (right).

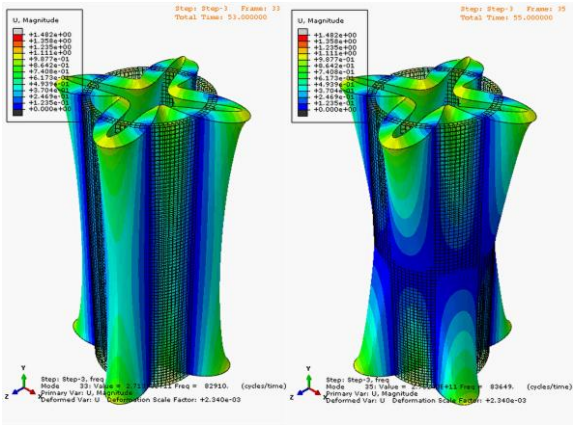

Fig. 7. In-plane bending mode of Zr-1%Nb cladding oscillation modelled in Abaqus, mode 33: frequency f_4 = 82 910 Hz (left), mode 35: frequency f_4' = 83 649 Hz (right).

$$t^2 + \left(-2d_1 - \frac{\sqrt{B_n}}{\pi}\frac{v}{f_n}\right)t + d_1^2 = 0,$$

and since

$$at^2 + bt + c = 0,$$

we get

$$a = 1, \quad b = -2d_1 - \frac{\sqrt{B_n}}{\pi}\frac{v}{f_n}, \quad c = d_1^2.$$

This results in

$$t = \frac{-b \pm \sqrt{b^2 - 4ac}}{2a} = \frac{2d_1 + \frac{\sqrt{B_n}}{\pi}\frac{v}{f_n} \pm \sqrt{\left(-2d_1 - \frac{\sqrt{B_n}}{\pi}\frac{v}{f_n}\right)^2 - 4d_1^2}}{2}. \quad (5)$$

Equation (5) can use the speed of ultrasonic signal propagation v calculated by Eq. (3), where E is the known modulus of elasticity and ρ is the known density of the material. For Eq. (4), to work well, it is necessary to determine the quantities v, E, or ρ sufficiently accurately, which can pose a minor challenge, especially when measuring only a single pipe. The coefficient B_n varies for each mode shape n from 1 to infinity. For illustration, several values will be provided in Table 1.

Table 1. Values of the coefficient B_n for individual mode shapes (number n).

Shape of oscillation n	1	2	3	4
B_n	0	2.400	19.20	70.60

A more precise but harder-to-measure method is the comparison of two resonance frequencies f_n and f_r for n = 1 to infinity. The frequency f_r is the so-called ring mode of the tube's cross-section, and Eq. (2) is expressed as

$$f_r = \frac{v}{\pi d} = \frac{v}{\pi(d_1 - t)}. \quad (6)$$

The velocity v can be expressed using Eq. (4) or (6):

$$v = f_r\pi(d_1 - t) = \frac{f_n\pi(d_1 - t)^2}{\sqrt{B_n}t},$$

$$f_r\sqrt{B_n}t = f_n(d_1 - t),$$

$$f_r\sqrt{B_n}t + f_nt = f_nd_1,$$

The wall thickness t can be derived from:

$$t = \frac{f_nd_1}{f_r\sqrt{B_n} + f_n},$$

$$t = \frac{d_1}{\frac{f_r}{f_n}\sqrt{B_n} + 1}. \quad (7)$$

Equation (7) has the undeniable advantage of being independent of the material properties and characteristics, eg. modulus E, density ρ or velocity v. However, it requires measuring two different frequencies f_r and f_n for n = 2 or higher, which may necessitate two different measurement methods, and possibly two separate devices, probes, frequency filters, etc. Ideally, if the frequencies are not too far apart, e.g. 15 kHz and 44 kHz, everything can be measured with a single apparatus.

Other methods for determining the tube wall thickness include measurements using a micrometre and bore gauge or they are based on the mass and known material density comparison.

3.2. Mass/density method

Although the density of basic materials is known, it varies across different alloys. If the alloy type is known, it is possible to calculate thickness t using Eq. (8), derived from the formula for material density, based on the known volume V and mass m:

$$\rho = \frac{m}{V} = \frac{m}{AL},$$

where

$$A = \frac{m}{\rho L} = \frac{\pi(d_1^2 - d_2^2)}{4}.$$

Here, d_1 is the outer diameter of the tube measured with a micrometre; the inner diameter of the tube d_2 can be expressed as:

$$d_2 = d_1 - 2t.$$

Out of this:

$$d_1^2 - d_2^2 = d_1^2 - (d_1 - 2t)^2 = d_1^2 - d_1^2 + 4d_1t - 4t^2$$

$$= 4d_1t - 4t^2 = \frac{4}{\pi}\frac{m}{\rho L}.$$

Hence

$$\frac{m}{\rho L \pi} = d_1t - t^2,$$

and therefore

$$t = \frac{d_1 - \sqrt{(-d_1)^2 - 4\frac{m}{\rho L \pi}}}{2}, \quad (8)$$

where L is the length of the tube.

For the reasons mentioned above, Eq. (8) is considered the most realistic.

3.3. Micrometre – bore gauge method

In the case of measuring the inner diameter d_2 with a bore gauge, the following applies:

$$t = \frac{d_1 - d_2}{2}. \quad (9)$$

Compared to Eq. (8), Eq. (9) can determine the thickness t at any end of the tube. However, it does not reach nearly the same level of accuracy as in Eq. (8).

3.4. Ultrasonic testing

The most popular method for the non-destructive determination of thickness, and not only of metal products, is the ultrasonic reflection method (ultrasonic pulse echo), based on the measurement of the transit time of flight of ultrasonic pulses [21–23]. The principle of the method is that the signal sent by the ultrasonic probe passes through the material of the body under examination, is reflected from its opposite wall and returned to the receiving probe (this might be the same ultrasonic probe as the sending one). The thickness is then determined according to the physical properties of the material under test and the measured time of flight. This method is a very frequently used non-destructive method in the engineering industry as well as in testing and diagnostics of structures, it is included in Czech and European standards, e.g. ISO 16809 [24]. The accuracy of this method depends on the sensitivity and resolution of the probes and the sensing device. For thin-walled components, measurement accuracy is in the tens of microns.

4. Nuclear fuel cladding measurement

In a specific case, the determination of wall thickness for a small-diameter zirconium tube will be compared using different approaches, based on various measured quantities. This example involves a model of a fuel rod, or in other words, nuclear fuel cladding. The measured values are shown in Table 2. An example of measured frequencies f_r is shown in Fig. 8. Table 3 presents a comparison of the results and accuracy of calculations based on the individual Eqs. (5), (7), (8) and (9).

5. Conclusions

The presented method for measuring the thickness of small-diameter thin-walled tubes using the resonant frequencies of the tube's cross-section can determine the wall thickness with an accuracy of up to 1 μm. This sets it apart from convention-al methods, such as the ultrasonic thickness gauge, which typically measures with an accuracy of ±10 μm.

The method can be applied in all areas of industry where non-destructive determination of the wall thickness of a closed pipe is required. It is particularly suitable for thin-walled closed pipes and tubes where the accuracy of standard methods is not sufficient, and the measured value can have a significant influence on further work with the measurement results.

The method can be used, for example, to check the thickness of nuclear fuel cladding, which is also essentially a closed thin-walled tube of small diameter. The method might be applicable for the qualification of nuclear fuel assemblies for a deep underground repository where a repeat verification of the fuel condition will be required. It can be used for non-destructive investigation of radioactive fuel in the hot cells using mechanical manipulators.

Outside the nuclear industry, the method can be applied to the inspection of piping in laboratory apparatuses where highly abrasive media are used, e.g. liquids or gases with solid particles or acid admixtures. In this way, it is possible to check the degree of wear of the piping without dismantling the installation and without interrupting the technological process for a significant length of time and without leaking liquids or vapours into the surroundings.

Table 2. Values of the measured quantities, including the estimated accuracy of each measurement.

Quantity	Symbol	Unit	Value measured	Measurement inaccuracy	No. of executed measurements	Measuring instrument
Specimen length	L	mm	500.0	±0.5	3	Metal gauge
Weight	m	g	50.360	±0.001	2	Digital weight
Density	ρ	kg/m³	6506	±1	>100	Nominal unit
Outer diameter	d_1	mm	9.114	±0.002	3	Micrometre
Inner diameter	d_2	mm	7.952	±0.001	3	Bore gauge
Sound velocity	v	m/s	3906	±15	>50	Oscilloscope
In-plane bending mode frequency	f_2	Hz	15 545	±175	3	
	f_3		44 060	Non-determined	1	
	f_4		84 790	±159	3	
Ring mode	f_r		147 800	±510	3	

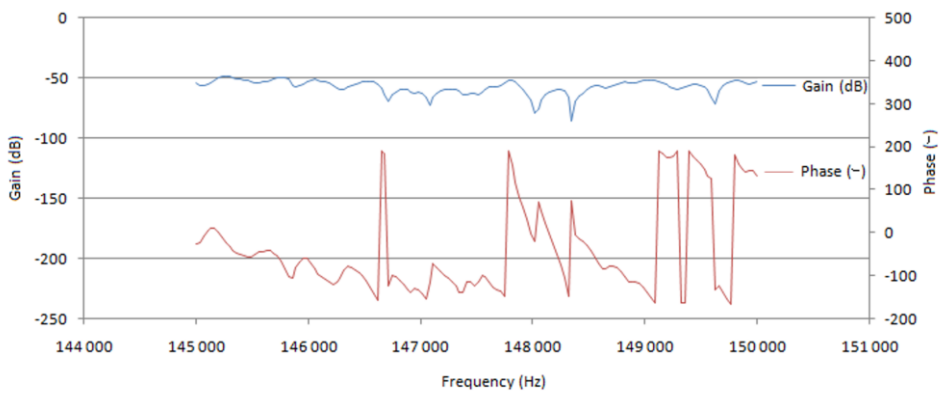

Fig. 8. Ring mode measurement in fuel rod No. 7 using classical resonance method approach, sweeping the signal (frequency f_r = 148 000 or 148 300 Hz).

Table 3. Calculated values of thickness t of the thin-walled tube made from zirconium alloy.

.Used approach	Used quantity 1	Used quantity 2	Used Eq. (#)	Calculated value [mm]	Inaccuracy determined statistically
Nominal value	t	–	–	0.585	±0.010
Micromere and bore gauge	d_2	d_1	(9)	0.581	±0.003
Weight and density	m	ρ	(8)	0.581	±0.001
Ring mode frequency	f_r	f_2	(7)	0.579	-0.002
		f_3		0.581	±0.000
		f_4		0.582	+0.001
In-plane bending mode frequency	f_2	v	(5)	0.577	-0.004
	f_3			0.578	-0.003
	f_4			0.580	-0.001
UT thickness gauge	*Transit time T*		$t = vT$	0.583	±0.010
Metallographic cross-section	t	–	–	0.581	±0.001

The above presented data come from the classical resonance approach whose accuracy reaches one or more micrometres. Future work will focus on refining measurements using the impact-echo method, combining different approaches, also on the more precise modelling of oscillation modes under various external or internal conditions. All these could decrease the measurement error by 50% or more. This would make the approach very effective and attractive for all fields of industry, not just the nuclear one.

Acknowledgements

The presented work has been realized within Institutional Support by the Ministry of Industry and Trade of the Czech Republic.

References

[1] Lee, Y.S., Park, S.J., So, W.J., & Joo, Y.S. (2016). A cladding thickness measurement of the research reactor fuel plate using nondestructive testing method. *European Research Reactor Conference, Conference Proceedings*, 13–17 March, Berlin, Germany.

[2] Park, J.W., Ko, D., Jang, H., Kim, H., Lee, J., & Choi, W. (2024). Algorithm for estimating Cr coating thickness for accident tolerant fuel cladding using a pancake ECT sensor. *Nuclear Engineering and Technology*. doi: 10.1016/j.net.2024.09.019

[3] Guo, J., Xu, Y., Pan, B., Zhang, J., Kang, R., Huang, W., & Du, D. (2021). A new method for precision measurement of wall-thickness of thin-walled spherical shell parts. *Micromachines* 12(5), 467. doi: 10.3390/mi12050467

[4] Meng, L., Liu, H., Zhang, T., Bo, Q., Li, T., & Wang, Y. (2019) Ultrasonic on-machine scanning for thickness measurement of thin-walled parts: modeling and experiments. *International Journal of Advanced Manufacturing Technology*, 104(5−8), 2061−2072. doi: 10.1007/s00170-019-04021-5

[5] Olympus. (2024). https://www.olympus-ims.com/en/72dl-plus/#!cms[focus]=cmsContent15237 [accessed 8 Nov. 2024].

[6] Majdak, M., Gradziel, S., Zima, W., Cebula, A., Rerak, M., & Kozak-Jagiela, E. (2023). Numerical and experimental analysis of thermal and flow operating conditions of waterwall tubes connected by fins. *Archives of Thermodynamics*, 44(4), 81–102. doi: 0.24425/ather.2023.149719

[7] Majkut, M., Dykas, S, & Smołka, K. (2020). Light extinction and ultrasound method in the identification of liquid mass fraction content in wet steam, *Archives of Thermodynamics*, 41(4), 63–92. doi: 10.24425/ather.2020.135854

[8] Liu, H.-B., Wang, Y.-Q., Jia, Z.-Y., & Guo, D.-M. (2015). Integration strategy of on-machine measurement (OMM) and numerical control (NC) machining for the large thin-walled parts with

surface correlative constraint. *International Journal of Advanced Manufacturing Technology*, 80, 1721–1731.

[9] Naveed, A., Muhammad, A.-N., Ateekh, U.-R., Madiha, R.; Usama, U., & Adham, E.-R. (2021). High aspect ratio thin-walled structures in D2 steel through wire electric discharge machining (EDM). *Micromachines*, 12, 1. doi: 10.3390/mi12010001

[10] Fowler, K.A., Elfbaum, G.M., Smith, K.A., & Nelligan, T.J. (1997). Theory and Application of precision ultrasonic thickness gauging. *e-Journal of Nondestructive Testing (eJNDT Articles & News)*, 2, 10.

[11] Vlassopoulos, E., Pautz, A., Papaioannou, D., Fongaro, L., Nasyrow, R., Gretter, R., Somers, J., Rondinella, V.V., Caruso, S., Raffuzzi, V., Grunberg, P., Helfenstein, J., & Schwizer, P. (2018). Mechanical integrity of spent nuclear fuel: from experimental to numerical studies. *TopFuel – Reactor Fuel Performance*, 30 September – 4 October, Prague, Czech Republic.

[12] Megzari, A., Le Clézio, E., Stepnik, B., & Despaux, G. (2022). Fuel plate cladding thickness estimation thanks to acoustic microscopy. *42nd International Meeting on Reduced Enrichment for Research and Test Reactors*, 3–5 October, Vienna, Austria.

[13] Michau, A., Maskrot, H., Gazal, Y., Maury, F., Duguet, T., Boichot, R., Pons, M., Brachet, J.-C., & Monsifront, E. (2018). Inner surface protection of nuclear fuel cladding, towards a full-length treatment by DLI-MOCVD, an optimized coating process. *TopFuel – Reactor Fuel Performance*, 30 September – 4 October, Prague, Czech Republic.

[14] Namburi, H.K., Halodova, P., Bublikova, P., Janura, R., & Krejčí, J. (2016). Microstructural evaluation of high temperature creep behavior in hydrided E110 cladding. *25th International Conference Nuclear Energy for New Europe*, 5–8 September, Portorož, Slovenia.

[15] Lee, Y.-H., & Byun T.S. (2015). A comparative study on the wear behaviors of cladding candidates for accident-tolerant fuel. *Journal of Nuclear Materials*, 465, 857−865. doi: 10.1016/j.jnucmat.2015.05.017

[16] Winter, T.C., Neu, R.W., Singh, P.M., Kolaya, L.E., & Deo, C.S. (2018), Fretting wear comparison of cladding materials for reactor fuel cladding application. *Journal of Nuclear Materials*, 508, 505−515. doi: 10.1016/j.jnucmat.2018.05.069

[17] Hlaváč, Z., Pašta, O., Assmann, L., & Kopeć, M. (2024). *A method of non-destructive measurement of thickness of light-gauge pipes with a small diameter*, Czech Patent 310172, Sep. 12.

[18] Bentley Hammer Connect Edition, *Celerity and Pipe Elasticity*, https://docs.bentley.com/LiveContent/web/Bentley%20HAMMER%20SS6-v1/en/GUID-860F7792-1873-46A7-A07D-06FB40F62D8B.html [accessed 10 Nov. 2024].

[19] Omer, I., Arsenie, D.I., & Florea, M. (2009). The influence of longitudinal elastic systems on the celerity (speed of elastic waves). *WIT Transactions on Ecology and the Environment*, 125, 393−399. doi: 10.2495/WRM090351

[20] Irvine, T. (2014). Ring vibrations modes (Revision D). *Vibrationdata*. http://www.vibrationdata.com/tutorials_alt/ringmode.pdf [accessed 10 Nov. 2024].

[21] Álvarez-Arenas, T.G., & Camacho J. (2019). Air-Coupled and Resonant Pulse-Echo Ultrasonic Technique. *Sensors (Basel)*, 19(10), 2221. doi: 10.3390/s19102221

[22] Pan, J., Chen, F., Song, Z., & Feng, Y. (2020). Ultrasonic pulse reflection method of thickness measurement system based on FPGA. *5th International Conference on Mechanical, Control and Computer Engineering (ICMCCE)*, 25−27 Dec., Harbin, China.

[23] Scholtz, L.K. (2016). *Ultrasonic Pulse-Echo Method, Bayern Collab*. https://collab.dvb.bayern/display/TUMzfp/ Ultrasonic+Pulse-Echo+Method [accessed 10 Nov. 2024].

[24] ISO 16809. (2017). *Non-destructive testing — Ultrasonic thickness measurement* (2nd ed.). https://www.iso.org/standard/72430.html [accessed 10 Nov. 2024].

Co-published by
Institute of Fluid-Flow Machinery
Polish Academy of Sciences
Committee on Thermodynamics and Combustion
Polish Academy of Sciences

http://www.imp.gda.pl/archives-of-thermodynamics/

Comment on the paper: Ochrymiuk, T., Dudda, W., & Badur, J. (2023). On a Carnot working continuum with non-equilibrium state parameters. Archives of Thermodynamics, 44(4), 285−316. doi: 10.24425/ather.2023.149714

P.D. Gujrati

University of Akron, Akron, OH 44325, USA
Author email: pdg@uakron.edu

Received: 22.06.2024; accepted: 29.10.2024

Vol. 45(2024), No. 4, 251–252; doi: 10.24425/ather.2024.152015

Cite this manuscript as: Gujrati, P.D. (2024). Comment on the paper: Ochrymiuk, T., Dudda, W., & Badur, J. (2023). On a Carnot working continuum with non-equilibrium state parameters. Archives of Thermodynamics, 44(4), 285−316. doi: 10.24425/ather.2023.149714. *Archives of Thermodynamics*, 45(4), 251–252.

In a recent paper in this journal, Ochrymiuk, Dudda and Badur [1], to be denoted collectively by ODB in short here, have compared their results with a fundamental theorem of non-equilibrium thermodynamics that I had derived in 2011 [2]. The authors claim that it "is an unacceptable paradoxical result" to justify why their results do not agree with this theorem. This is unfortunate and is caused by their partial understanding of the first law as commonly stated in textbooks, see Callen [3], in terms of exchange heat $d_{\rm e}Q$ and work $d_{\rm e}W$ in Eq. (2), and not appreciating its subtle difference with the second law that is always stated in terms of system-intrinsic (SI) heat dQ and work dW. Correcting these deficiencies will show that the theorem is unassailable.

We will use the most common notation in [2], which can be expressed in terms of the notation by ODB as follows: $d_{\rm e}$ is $d_{\rm eq}$ and $d_{\rm i}$ is $d_{\rm irr}$, here e refers to external or exchange with the outside and i refers to internal or irreversible. In contrast, d refers to SI changes so we have the operator identity $d = d_{\rm e} + d_{\rm i}$. Any irreversibility is due to processes that occur internally [4], so it is better to focus on an isolated system Σ for which $d = d_{\rm i}$ as there is no outside to it, so that $dQ = d_{\rm i}Q$ and $dW = d_{\rm i}W$; similarly $dE = d_{\rm i}E$, where $d_{\rm i}E$ is the internal change in the energy E and $dS = d_{\rm i}S$ for the entropy S.

Let E_k denote the SI energy of the kth microstate of the Hamiltonian of Σ, which occurs with probability p_k in the ensemble. Then

$$E \doteq \sum_k p_k E_k,$$

which is defined for any system, isolated or not and of any size, not necessarily macroscopic. From the definition, we obtain

$$dE \doteq \sum_k E_k dp_k + \sum_k p_k dE_k = dQ - dW, \qquad (1)$$

where the first sum is the SI heat dQ that appears in the system, and the SI work dW done by the system; the latter follows immediately from the ensemble average of the work $dW_k = -dE_k$ done by the kth microstate, which happens at the cost of reducing E_k. Thus, Eq. (1) is nothing but a statement of energy conservation and represents the first law in terms of SI quantities, including the entropy governed by the second law through dQ. This is contrasted with the conventional form

$$dE \doteq d_{\rm e}Q - d_{\rm e}W \qquad (2)$$

of the first law in terms of exchange quantities controlled by the outside and does not include the entropy as part of it. Therefore, dE here truly represents the energy change $d_{\rm e}E$ due to exchange only. This will imply that $d_{\rm i}E = 0$ due to internal processes, which is consistent with the well-known fact that internal processes cannot change the energy of any system [5]. For our isolated Σ, this means that $dE = d_{\rm i}E = 0$. Using Eq. (1), this immediately proves the theorem

$$d_{\mathrm{i}}Q \equiv d_{\mathrm{i}}W \tag{3}$$

for Σ, whose physical significance is the following: the theorem finally justifies the well-known experimental result of classical thermodynamics that *any internal work is completely dissipated in the form of internal heat* as noticed by Count Rumford (Benjamin Thomson) [6] while drilling cannons to argue that heat could not be a caloric fluid. It is truly an irreversibility principle governing irreversible processes through the first law:

$$d_{\mathrm{i}}E \doteq \sum_k E_k d_{\mathrm{i}}p_k + \sum_k p_k\, d_{\mathrm{i}}\, E_k = d_{\mathrm{i}}Q - d_{\mathrm{i}}W = 0, \tag{1}$$

for any system, not necessarily an isolated one [7]. Thus, the theorem is not "(...) an unacceptable paradoxical result", and ODB is incorrect in the assessment. The first law in Eq. (2) makes no connection with the second law, but that in Eq. (1) is equivalent to the second law as claimed in [2].

I do not make any inference of the theorem about other results ODB has obtained in [1].

References

[1] Ochrymiuk, T, Dudda, W., & Badur J. (2023). On a Carnot working continuum with non-equilibrium state parameters. *Archives of Thermodynamics*, 44(4), 285−316. doi: 10.24425/ather.2023.149714

[2] Gujrati, P.D. (2011). Generalized non-equilibrium heat and work and the fate of the Clausius inequality. *UATP/1103arXiv:1105.5549*. doi: 10.48550/arXiv.1105.5549

[3] Callen, H.B. (1985). *Thermodynamics and an Introduction to Thermostatistis* (2nd ed.). John Wiley, New York.

[4] de Groot, S.R., & Mazur, P. (1984). *Nonequilibrium Thermodynamics* (1st ed.) Dover, New York.

[5] Prigogine, I. (1971). *Thermodynamics of Irreversible Processes*. Wiley-Interscience, New York.

[6] Klassen, S., Dietrich, S., & Klassen, C.F. (2011). Biography: Sir Benjamin Thompson, Count Rumford. *Storytelling Teaching Model, http://science-story-telling.eu.* https://www.science-story-telling.eu/fileadmin/content/projekte/storytelling/biografien/biografien-eng/thompson-rumford-biografie-gb.pdf

[7] Gujrati, P.D. (2023). Foundations of nonequilibrium statistical mechanics in extended state space. *Foundations*, 3(3), 419−548. doi: 10.3390/foundations3030030

Answer of Authors of the original paper

Dear Editor-in-Chief,

In our paper *On a Carnot working continuum with non-equilibrium state parameters* published in your journal, we quoted a four-page work by Professor Gujrati under the title: *Generalized non-equilibrium heat and work and the fate of the Clausius inequality* from 2011.

The reason we quoted Gujrati's article was that we were looking for premises in the literature to justify different from the classical formulations of the first law of thermodynamics. Now, in Prof. Gujrati's article, we have found an extended form of the first law of thermodynamics, which has some analogies to our formulation of the first law of thermodynamics.

What was valuable to us was the fact that both our work and the work of Professor Gujrati are based on a new, hardly acceptable, surprising model postulate, requiring further justification, research and new premises. This new, hardly acceptable, element of the model is: our "uncompensated work transformation $\mathcal{N}_{work}$" and the "irreversible internal work d_iW", in the Gujrati's paper.

As for the unfortunate wording: "an unacceptable and paradoxical result". This was the wording originally used at the JETC 2023 conference at Salerno in relation to the concept of "uncompensated work transformation $\mathcal{N}_{work}$" that we have introduced.

We are glad that it was noted that our extended form of the first law of thermodynamics is based on this new element of $\mathcal{N}_{work}$ – which *per se* is difficult to be accepted and sounds paradoxical. Perhaps it is good that during the discussion with one of the authors, the strong words "an unacceptable and paradoxical result" were used – they are the best way to draw attention to the importance of the problem.

From the history of thermodynamics, we remember Lord Kelvin's words about the result of Davy's work as: "a lame and impotent conclusion" – it was not at all an unintentional harm to anyone. Rather, they were an indication of the place where we should focus our attention in the future.

Why did we also take the liberty of applying these words to Prof. Gujrati's result? Because we see many analogies between our extended formulation of the first law of thermodynamics and the extended formulation proposed by Prof. Gujrati.

This means that the criticisms are also similar. Therefore, we relate to Gujrati's irreversible internal work d_iW in an equivalent way as others relate to our $\mathcal{N}_{work}$. We understand well that d_iW is a novelty among thermodynamic proposals and we accept it – in our new explanatory paper, *Around the invalid formulations of the first law of thermodynamics*, we are proving that there is: a historical, logical and physical analogy of d_iW with our uncompensated transformation of the work $\mathcal{N}_{work}$.

After a series of discussions in the community, we know that both: d_iW and $\mathcal{N}_{work}$ are new, difficult to accept and paradoxically sounding proposals for thermodynamics. Therefore, we are glad that in his reply to our article, Prof. Gujrati gives one more premise for the validity of the d_iW – this time derived from statistical thermodynamics. We thank Professor Gujrati for putting the research focus at the heart of the problem, and we apologize for the linguistic misunderstanding.

Yours sincerely,
Tomasz Ochrymiuk, Waldemar Dudda and Janusz Badur